



HAL
open science

Analysis of Solar Energy Power Generation in Urban Environments

Alessia Boccalatte

► **To cite this version:**

Alessia Boccalatte. Analysis of Solar Energy Power Generation in Urban Environments. Engineering Sciences [physics]. Université Savoie Mont Blanc; Università degli studi (Gênes, Italie), 2023. English. NNT : 2023CHAMA044 . tel-04770873

HAL Id: tel-04770873

<https://theses.hal.science/tel-04770873v1>

Submitted on 7 Nov 2024

HAL is a multi-disciplinary open access archive for the deposit and dissemination of scientific research documents, whether they are published or not. The documents may come from teaching and research institutions in France or abroad, or from public or private research centers.

L'archive ouverte pluridisciplinaire **HAL**, est destinée au dépôt et à la diffusion de documents scientifiques de niveau recherche, publiés ou non, émanant des établissements d'enseignement et de recherche français ou étrangers, des laboratoires publics ou privés.

THÈSE

Pour obtenir le grade de

DOCTEUR DE L'UNIVERSITÉ SAVOIE MONT BLANC

Spécialité : **Energétique et Génie des Procédés**

Arrêté ministériel : 25 Mai 2016

Présentée par

Alessia BOCCALATTE

Thèse dirigée par **Christophe MENEZO** et **Marco FOSSA**
codirigée par **Julien RAMOUSSE**

préparée au sein du **Laboratoire LOCIE**
dans l'**École Doctorale SIE**

Analyse de la production d'énergie solaire en milieu urbain

Thèse soutenue publiquement le **14 Novembre 2023**,
devant le jury composé de :

M. Benoit BECKERS

Professeur, Université de Pau et des Pays de l'Adour, Rapporteur

M. Andreas ATHIENITIS

Professeur, Concordia University, Rapporteur

M. Valéry MASSON

Directeur de recherche, Centre National de Recherches Météorologiques,
UMR3589, Météo-France & CNRS, Président

Mme. Anne MIGAN-DUBOIS

Professeure, Université Paris Saclay-Centrale Supélec, Examinatrice

M. Mattheos SANTAMOURIS

Professeur, University of New South Wales, Invité

M. Christophe MENEZO

Professeur, Université Savoie Mont Blanc Laboratoire LOCIE, Directeur de
thèse

M. Marco FOSSA

Professeur, Università degli Studi di Genova, DIME, Directeur de thèse

M. Julien Ramousse

Professeur, Maître de conférences HDR, Université Savoie Mont-Blanc,
Co-Directeur de thèse

M. Martin THEBAULT

Chargé de recherche, CNRS Section 10, Examineur

Acknowledgements - Remerciements

At this point, the acknowledgments section is undoubtedly one of the most challenging. Unlike the various parts of a scientific article (abstract, introduction, methodology, results, and conclusions), no one teaches you how to write them, and no one will have the courage to correct them (at least I think so), so if they turn out poorly, there's no way to fix it. I'll try to do my best and write them in the most straightforward manner, avoiding getting lost in excessively detailed sentences dictated by my unbearable perfectionism (which hasn't been a great ally even in writing the following articles in this manuscript).

Let's start with my thesis advisors (my only certainty is that acknowledgments always start with the thesis advisors), Christophe and Marco. Our collaboration began back in 2018 (although theirs dates back a few years earlier in a faraway land), fortunately not because my Ph.D. lasted for six long years, but on the occasion of my master's thesis co-supervised by both of them. From that moment on, they were and have remained my thesis advisors. I thank both of them immensely for supporting and guiding me in my scientific journey with two very different approaches, and perhaps this was the true strength. Both of them have given me a lot, both scientifically and personally, and have made it possible over the years to create countless opportunities to enrich my scientific knowledge and find the path that was most consistent with my interests and inclinations.

I sincerely thank Julien, co-advisor, whom I met later during the Ph.D., and who has always supported me from a scientific standpoint, and not least, from a psychological one, teaching me that my resources are not infinite, and that at some point, it's necessary to put a brake on the aforementioned perfectionism. This lesson is worth much more than many "scientific" lessons, and I will carry it with me in the years to come.

Enfin et surtout, ultimo ma non ultimo, last but not least, of course, Martin, the co-encadrant, that I would describe as "in itinere" which in Latin means "along the way". I would define him this way for two reasons: first, because at the beginning it wasn't certain if he was part of the official thesis direction, and second, because he literally followed me through every single step of this journey, supporting and encouraging me step by step with great patience from the first day, making everything lighter with his extremely kind and sunny (to stay on theme!) personality.

On the international level, I thank all the experts from IEA Task 63, which I was a part of, who greatly enriched my scientific journey. A special thanks also goes very far away in Australia to Professors Mattheos Santamouris and Riccardo Paolini, who accompanied and guided me during my stay in Sydney, sharing their deep knowledge of urban microclimate and mitigation strategies, which I hope to further explore in my future scientific journey.

I would also like to thank all the professors and colleagues from the DIME Department at the University of Genoa, Professor Antonia Priarone, and my fellow travelers in Italy, Mattia, Samuele, and Stefano, with whom we shared many moments of both discouragement and fun,

brightened especially by Mattia's inimitable "freddure", Samuele's irony, and Stefano's sense of humor.

A huge thank you also to all the members of LOCIE in France, my "second" home, who made me feel at home in no time (despite the obvious culinary differences, including the beloved Genovese pesto, but I don't want to start the complex debate between French and Italian cuisine). I thank all the fellow Ph.D. students with whom we shared countless trips to the lake and the Savoyard mountains: Arnat, Cedric, Julie, Prince (the prince of geothermal), Romain (who is not a Ph.D. student but might as well be along with Justine), Taini, Ramez, Guillaume, Apolline, Ali, Laurence, Benjamin, Hafsa, Yago, and all the others. Among them, a special thanks goes to Alessia, the second Italian in the lab, and also the second Alessia (it was complicated in these years to figure out if they were referring to Alessia Solar or Alessia Earth), who has been much more than a colleague but a true friend, always present in times of need and, above all, always ready to accompany me on long walks in the woods.

Finally, I will personally thank my wonderful family, friends, and my beloved animals.

Abstract

Analysis of Solar Energy Power Generation in Urban Environments

In today's global energy and climate context, there's an urgent need to shift towards renewable energy sources. This need is underscored by the increasing urbanization, coupled with the heightened frequency and severity of extreme weather events due to climate change. These factors have placed high pressure on our energy infrastructure, environment, economy, and society. Addressing this pressure requires a decisive shift from fossil fuel-based to renewable energy resources.

Central to this transition are urban systems. High population density and increasing energy demand in cities position them at the center of the energy issue. Recent concepts such as Nearly Zero Energy Buildings (nZEB) and Districts (nZED) have brought forth discussions on energy efficiency, introducing the idea of on-site or nearby renewable energy production.

In this context, solar energy is one of the most direct means of integration. Yet, a comprehensive understanding of the urban solar potential demands careful planning, design, and optimization for effective integration. This entails a comprehensive, interdisciplinary scientific approach that accounts for the complex interplay of geometric, physical, morphological, and climatic attributes within the urban environment. Challenges such as shading, inter-reflections, and microclimatic effects like the Urban Heat Island (UHI) reduce the effectiveness of solar systems and increase building energy needs.

This thesis investigates this intricate subject, spanning solar engineering, building design, urban planning and climate studies. It presents a series of scientific publications, each addressing a distinct yet interconnected aspect. Initially, it focuses on the physical characterization of urban systems, with specific attention to the Urban Heat Island, emphasizing its pivotal role in urban planning and its impact on building energy simulation and performance. The research then shifts to studying solar radiation distribution in relation to urban morphological attributes. Following this, the performance of photovoltaic installations in urban settings is analysed, with a particular focus on local climatic conditions and mounting configurations. Finally, it addresses the application of concentrated solar systems, specifically Linear Fresnel Collectors (LFCs), offering a promising alternative for solar integration for industrial applications in peripheral urban areas.

The key goal is to assess the challenges in implementing city-wide solar energy integration. This is mainly achieved through real-world case studies, proposing integrated workflows with diverse and coupled simulation tools. One of the key issues is to minimize the computational resources required for such large-scale analyses. Notably, these investigations encompass not only the city-scale but also extend to district-level and individual production system scales.

Methodologically, a wide range of tools is employed, including analytical models and numerical simulations, tailored to each study's specific scope and scale. These encompass simulations of urban microclimate, building energy performance, photovoltaic energy production, and ray-tracing techniques. Statistical methods also play a key role, particularly in Geographic Information System (GIS) data analyses. Data-driven techniques aid in aggregating and analyzing spatial data, enhancing understanding of urban morphologies and solar radiation distribution. Unsupervised machine learning techniques, like clustering, are deployed to unveil patterns within extensive datasets.

The results of this thesis aim to prioritize the integration of solar systems in urban environments, highlighting the significance of climate mitigation strategies. Moreover, the research endeavors to provide practical urban planning guidelines for effectively addressing the requirements of energy-efficient urban development.

Résumé

Analyse de la Génération d'Énergie Solaire en Milieu Urbain

Dans le contexte actuel, la nécessité de se tourner vers les énergies renouvelables est urgente, compte tenu de l'urbanisation croissante et de l'aggravation des phénomènes météorologiques extrêmes liés au changement climatique. Cela met une pression considérable sur les infrastructures énergétiques, l'environnement, l'économie et la société, exigeant une transition rapide des combustibles fossiles vers les énergies renouvelables.

Au cœur de cette transition se trouvent les systèmes urbains. La densité de population élevée et la demande croissante d'énergie dans les villes les placent au centre de la problématique énergétique. Des concepts récents tels que Nearly Zero Energy Buildings (nZEB) and Districts (nZED) ont suscité des discussions sur l'efficacité énergétique, introduisant l'idée de production d'énergie renouvelable intégré.

L'énergie solaire se distingue comme la ressource la plus disponible à l'échelle urbaine. Cependant, une compréhension complète du potentiel solaire urbain nécessite une planification, une conception et une optimisation minutieuses pour être efficace. Cela exige une approche scientifique globale et interdisciplinaire, tenant compte des attributs géométriques, physiques, morphologiques et climatiques dans un environnement urbain complexe. Des défis tels que l'ombrage, les réflexions entre bâtiments et les effets microclimatiques comme l'îlot de chaleur urbain (UHI) limitent l'efficacité des systèmes solaires intégrés et augmentent les besoins énergétiques des bâtiments.

Cette thèse aborde l'ingénierie solaire, la conception des bâtiments, l'urbanisme et la climatologie. Elle présente une série de publications interconnectées abordant des aspects distincts mais liés. Elle débute par la caractérisation physique des systèmes urbains, mettant l'accent sur l'îlot de chaleur urbain et son influence sur la performance énergétique des bâtiments. Ensuite, la distribution du rayonnement solaire en relation avec la morphologie urbaine est étudiée. La performance des installations photovoltaïques, en mettant l'accent sur les conditions climatiques et les configurations de montage est ensuite analysée. Enfin, l'application de systèmes solaires concentrés, notamment les Collecteurs Linéaires Fresnel (LFC), est explorée comme alternative prometteuse pour l'intégration solaire dans les applications industrielles en périphérie urbaine.

L'objectif principal est d'évaluer les défis de l'intégration de l'énergie solaire à l'échelle urbaine. Cela se fait à travers des études de cas réels, mettant en oeuvre des stratégies intégrées avec divers outils de simulation couplés. Minimiser les ressources numériques mobilisées pour les analyses à grande échelle est un enjeu clé. Les investigations couvrent non seulement l'échelle de la ville, mais s'étendent également aux échelles du quartier et des systèmes de production individuels.

Sur le plan méthodologique, divers outils sont utilisés, dont des modèles analytiques et des simulations numériques, adaptés à l'objectif et à l'échelle de chaque étude. Cela inclut des simulations du microclimat urbain, les performances énergétiques des bâtiments, la production d'énergie photovoltaïque et les techniques de lancer de rayons. Les méthodes statistiques, en particulier dans l'analyse des données du Système d'Information Géographique (SIG), ainsi que l'apprentissage automatique non supervisé, comme le clustering, sont déployées pour extraire des motifs des ensembles de données étendus.

Les résultats de cette thèse visent à donner la priorité à l'intégration des systèmes solaires dans les environnements urbains soulignant ainsi l'importance des stratégies d'atténuation du climat. De plus, la recherche vise à fournir des directives pratiques pour la planification urbaine afin de répondre efficacement aux exigences du développement durable.

Impact Statement

As briefly outlined in the Abstract, this research aims to explore innovative approaches to assess the integration and performance of solar systems within urban environments. The primary objective is to develop data-driven methodologies that incorporate local climate data to analyze large scale urban datasets encompassing the whole city.

The Ph.D. project is a collaboration between Université Savoie Mont Blanc (USMB) in Chambéry, France, and Università degli Studi di Genova (UNIGE) in Genoa, Italy, with an additional five-months visiting period at the University of New South Wales (UNSW) in Sydney, Australia.

The research and its findings have been disseminated through various academic and institutional platforms. The author has led the publication of 11 peer-reviewed journal articles, with one currently undergoing revision. Within this manuscript, seven of these publications will be presented in detail. Two conference papers have been accepted to the 6th International Conference on Countermeasures to Urban Heat Islands, scheduled to be held in Melbourne, Australia, from December 4th to 7th, 2023. The author has also contributed to the preparation of the final report for the IEA Task 63 "Solar Neighbourhood Planning"¹ (Subtask C: Solar Planning Tools) and provided preliminary estimations of urban PV solar potential, as well as contributed to the drafting of the relevant section in the Regional Energy Environmental Plan of the Liguria Region (Piano Energetico Ambientale Regionale-PEAR 2030), currently under review by the regional authorities. Additionally, the findings have been presented at national conferences (Journées Nationales de l'énergie Solaire-JNES, Journées Nationales du PhotoVoltaire-JNPV) and national scientific outreach events (Biomim'expo, Journée Scientifique Pôle PEM).

¹<https://task63.iea-shc.org/news>

Aim of the thesis

The primary objective of this thesis is to advance the understanding and application of solar energy systems within urban environments. To achieve this objective, the following specific goals have been formulated:

- Develop data-driven methodologies with limited computational resources aimed at better characterizing the urban system from a physical perspective, with particular attention to the urban heat island phenomenon and its impact on building energy consumption and integrated photovoltaic (PV) production.
- Investigate the relationship between urban morphology, urban microclimate, and the distribution of solar radiation on urban surfaces, with the aim of optimizing the utilization of solar energy within urban areas and generating preliminary estimates of solar potential at the city-scale.
- Evaluate the impact of local climate conditions and PV mounting configuration on the performance of photovoltaic systems.
- Explore alternative solutions based on specific concentration solar technologies for peripheral areas and industrial applications.

Structure of the manuscript and appended publications

This manuscript investigates the relationships among diverse research domains, critically evaluating them to highlight the complexity of the examined issues. By integrating knowledge from solar and energy engineering, urban planning and climate, and geospatial data management, this dissertation is characterized by a cross-disciplinary approach.

The manuscript is structured as a series of scientific publications that I have realized during my researches. The first and last chapters serve as Introduction and Conclusions, respectively, while the central chapters contain one or more publications related to a specific topic.

The detailed structure of the manuscript as well as a short description of the appended publications is schematically presented below:

Chapter 1

The Introduction contextualizes the research domains explored in this dissertation, offering an overview of the scientific issues addressed. It emphasizes the significance of the conducted research and establishes the link among the various investigations. As previously noted, the topics addressed in each publication exhibit a considerable degree of diversity. Consequently, the state of the art, literature review, and methodologies pertinent to each theme are extensively discussed within each publication. This approach acknowledges the challenge of constructing a cohesive discourse that encompasses all the addressed topics.

Chapter 2

This chapter aims to define the major scientific issues related to the integration of solar energy within the urban environment. It is based on the following publication:

- **Paper 1.** Manni, M., Formolli, M., **Boccalatte, A.**, Croce, S., Desthieux, G., Hachem Vermette, C., Kanters, J., Ménézo, C., Snow, M., Thebault, M., Wall, M., Lobaccaro, G. (2023). Ten questions concerning planning strategies and design principles for solar neighborhoods. *Building and Environment* (under revision)

Paper 1: This article presents the collaborative efforts of experts in the solar energy field as part of the IEA Task 63 "Solar Neighbourhood Planning". It introduces key principles for planning solar systems in urban environments through a concise 10-question paper, focusing on strategies and design principles for solar neighborhood planning.

Chapter 3

After delineating the key issues related to solar energy integration within the built environment, this chapter is dedicated to the physical characterization of the urban system and local climate, which is crucial as it constitutes the boundary conditions for the conducted analyses. It is based on two publications:

- **Paper 2. Boccalatte, A.**, Fossa, M., Thebault, M., Ramousse, J., Ménézo, C. (2023). Mapping the urban heat island at the territory scale: An unsupervised learning approach for urban planning applied to the Canton of Geneva. *Sustainable Cities and Society*, 96(February), 104677. <https://doi.org/10.1016/j.scs.2023.104677>
- **Paper 3. Boccalatte, A.**, Fossa, M., Ménézo, C. (2020). Best arrangement of BIPV surfaces for future NZEB districts while considering urban heat island effects and the reduction of reflected radiation from solar façades. *Renewable Energy*, 160, 686–697. <https://doi.org/10.1016/j.renene.2020.07.057>

Paper 2: The research proposes a new data-driven methodology to characterize the urban heat island (UHI) phenomenon at a large scale using limited computational resources. The approach combines unsupervised machine learning techniques (Gaussian Mixture Model clustering) with parametric microclimate simulations (Urban Weather Generator tool). The study is applied to the entire Canton of Geneva (Switzerland), covering an area of approximately 300 km², and enables the creation of a preliminary microclimate map for urban planning applications. The methodology can be generalized to any urban area, provided that the necessary data is available.

Paper 3: This study shifts the focus from the urban scale to the district scale. It presents a comprehensive analysis of energy demand and supply modeling for an energy-efficient urban district with solar building envelopes. The research incorporates building energy simulations using EnergyPlus, models for power generation from Building Integrated Photovoltaics (BIPV) employing the Sandia PV Array Performance model, and simulations of the Urban Heat Island effect using the Urban Weather Generator tool. By zooming in on the district level, the study investigates the impact of the urban microclimate on building energy demand and explores the potential "darkening" effects resulting from the extensive integration of PV systems on building facades.

Chapter 4

After characterizing the microclimatic complexity of the urban system, this chapter examines the influence of morphological complexity on the distribution of solar resources on urban surfaces. The analysis in this chapter builds upon the findings presented in the following article:

- **Paper 4. Boccalatte, A.,** Thebault, M., Ménézo, C., Ramousse, J., Fossa, M. (2022). Evaluating the impact of urban morphology on rooftop solar radiation: A new city-scale approach based on Geneva GIS data. *Energy and Buildings*, 260, 111919. <https://doi.org/10.1016/j.enbuild.2022.111919>

Paper 4: The article proposes a general methodology based on the processing and analysis of a large-scale GIS dataset. Utilizing building footprints and height data, a dataset of 40 morphological features is calculated for 60,000 buildings in the Canton of Geneva (Switzerland). The relationship between the morphological features and the shading rate of urban surfaces is then investigated. The findings provide insights into the distribution of solar irradiation within the city and its dependence on urban morphology.

To complement this chapter, a technical report is included, which presents the **Preliminary Estimation of the Solar Potential in the Liguria Region (Italy)**. This estimation was conducted as part of the Regional Energy Environmental Plan of the Liguria Region (PEAR 2030).

Chapter 5

In this chapter, the performance of various types of photovoltaic systems in urban environments is investigated, with particular attention to the impact of local climate conditions and extreme heat events. It is based on the following publication:

- **Paper 5. Boccalatte, A.,** Thebault, M., Paolini, R., Fossa, M., Ramousse, J., Ménézo, C., Santamouris M. (2023). Assessing the Combined Effects of Local Climate and Mounting Configuration on the Electrical and Thermal Performance of Photovoltaic Systems. Application to the Greater Sydney Area. *Renewable Energy* (revised version submitted)

Paper 5: This research, conducted during the visiting period at the University of New South Wales, investigates the electrical and thermal performance of PV systems in Greater Sydney (NSW, Australia). The study focuses on the influence of mounting configuration and local climate, with particular attention to the negative impact of extremely hot conditions on PV operation. Experimental data from ten weather stations across Greater Sydney are utilized as input for the Sandia PV Array Performance model to predict cell temperatures and power production. Additionally, a PV thermal model is implemented to analyze daytime convection and radiation heat fluxes from PV surfaces.

Chapter 6

This concluding chapter integrates the discussion on solar energy integration in urban areas by investigating alternative solutions for industrial applications and peripheral areas. Specifically, an insight into the modeling and geometric optimization of linear Fresnel solar concentration systems is presented, including two articles on the topic:

- **Paper 6.** Fossa, M., **Boccalatte, A.,** Memme, S. (2021). Solar Fresnel modeling, geometry enhancement, and 3D ray-tracing analysis devoted to different energy efficiency definitions and applied to a real facility. *Solar Energy*, 216, 75–89. <https://doi.org/10.1016>
- **Paper 7. Boccalatte, A.,** Fossa, M., Ménézo, C. (2021). Calculation of the incidence angle modifier of a Linear Fresnel Collector: The proposed declination and zenith angle

model compared to the biaxial factored approach. *Renewable Energy*. <https://doi.org/10.1016/j.renene.2021.12.017>

Paper 6: This research focuses on evaluating the performance of Linear Fresnel Reflectors (LFR). The study employs 3D ray-tracing simulations and parametric optimization using an in-house developed code at the University of Genoa. The investigation addresses shading, blocking, and end effect issues while considering different optical and energy efficiency definitions. A parametric analysis explores the impact of mirror distance and receiver height for the geometrical optimization of the reference plant.

Paper 7: Building upon Paper 6, this study presents a novel approach to reduce the size of ray tracing datasets and generate compact analytical equations for efficient hourly performance simulations. The model integrates newly developed Incidence Angle Modifier (IAM) correlations based on declination and zenith angles, resulting in improved accuracy and computational efficiency compared to existing methodologies.

Chapter 7

This final chapter presents the main conclusions and future perspectives that can be drawn from this work.

Other publications by the Author not included in the thesis manuscript

Peer-reviewed journal articles

- **Boccalatte, A.**, Fossa, M., Gaillard, L., Menezo, C. (2020). Microclimate and urban morphology effects on building energy demand in different European cities. *Energy and Buildings*, 224, 110129. <https://doi.org/10.1016/j.enbuild.2020.110129>
- **Boccalatte, A.**, Fossa, M., Sacile, R. (2021). Modeling, Design and Construction of a Zero-Energy PV Greenhouse for Applications in Mediterranean Climates. *Thermal Science and Engineering Progress*, 25(August), 101046. <https://doi.org/10.1016/j.tsep.2021.101046>
- Memme, S., **Boccalatte, A.**, Brignone, M., Delfino, F., Fossa, M. (2022). Simulation and design of a large thermal storage system: Real data analysis of a smart polygeneration micro grid system. *Applied Thermal Engineering*, 201, 117789. <https://doi.org/https://doi.org/10.1016/j.applthermaleng.2021.117789>
- Morchio, S., Fossa, M., Priarone, A., **Boccalatte, A.** (2021). Reduced Scale Experimental Modelling of Distributed Thermal Response Tests for the Estimation of the Ground Thermal Conductivity. *Energies*, 14(21). <https://doi.org/10.3390/en14216955>

Conference articles

- Boccalatte, A., Ménézo, C., Thebault, M., Ramousse, J., Fossa, M. (2023). Urban Climate and Radiation Conditions for BIPV and Nearly Zero Energy District Design. Accepted

for the 6th *International Conference on Countermeasures to Urban Heat Islands*, RMIT University Melbourne (Australia), 4-7 December 2023. <https://www.ic2uhi2023.com/>

- Boccalatte, A., Ménézo, C., Thebault, M., Ramousse, J., Fossa, M. (2023). Temperature Derating and Photovoltaic Efficiency in Urban Climates: A Case Study of Sydney Metropolitan Region. Accepted for the 6th *International Conference on Countermeasures to Urban Heat Islands*, RMIT University Melbourne (Australia), 4-7 December 2023. <https://www.ic2uhi2023.com/>

Notes on my contribution in the appended publications

In Paper 1 I wrote mainly the parts related to urban microclimate and to the digitalization of the built environment. Regarding the other papers, I did all the tasks, from conceptualization to final publication, under the guidance of my supervisors.

Table of contents

List of figures	19
List of tables	25
Nomenclature	27
1 Introduction	35
1.1 Background and Motivation	36
1.2 Cities and City-Scale	38
1.3 Integrating Solar Energy into the Urban Environment	39
1.4 Digitalization of the Urban Environment	40
1.5 Urban Morphology	45
1.5.1 Urban Microclimate	46
1.5.2 Implications of Urban Morphology and Microclimate on Integrated Solar Systems	49
1.6 Alternative Solutions Based on Solar Concentration for Urban Industrial Appli- cations	50
1.6.1 Linear Fresnel Collectors (LFCs)	51
1.6.2 Rooftop-Integrated LFCs Applications	52
1.6.3 LFCs Modelling and Geometrical Optimization	54
2 Key Principles of Solar Energy Integration in the Urban Environment	57
2.1 Ten Questions Concerning Planning and Design Strategies for Solar Neighbor- hoods	60
2.1.1 Introduction	60
2.1.2 Ten questions (and answers) concerning solar neighborhoods	64
2.1.3 Conclusions and further developments	100
3 Characterizing the Urban Environment for Solar Energy Integration	103

3.1	Mapping the Urban Heat Island at the Territory Scale: an Unsupervised Learning Approach for Urban Planning Applied to the Canton of Geneva	105
3.1.1	Introduction	105
3.1.2	Data Sources, Models and Methods	109
3.1.3	Results	120
3.1.4	Discussion	130
3.1.5	Limitations and Future Perspectives	131
3.2	Best Arrangement of BIPV Surfaces for Future NZEB Districts while considering Urban Heat Island Effects and the Reduction of Reflected Radiation from Solar Façades	132
3.2.1	Introduction	132
3.2.2	Modelling a Solar Urban District	135
3.2.3	The Reference BIPV District Test Case	143
3.2.4	Towards the Nearly Zero Energy District: Results and Discussion . . .	145
3.2.5	Conclusions	153
4	Influence of Urban Morphology on City-Scale Solar Resource Distribution	155
4.1	Evaluating the Impact of Urban Morphology on Rooftop Solar Radiation: a New City-Scale Approach based on Geneva GIS Data	157
4.1.1	Introduction	157
4.1.2	Data and Methods	159
4.1.3	Definition of I^* , the Scaled Solar Insolation	161
4.1.4	Morphological Tessellation and Calculation of Urban Form Features . .	164
4.1.5	Data Pre-processing	167
4.1.6	Results and Discussion	167
4.1.7	Conclusions and Perspectives	176
4.2	Preliminary Estimation of the Solar Potential in the Liguria Region (Italy) . . .	178
4.2.1	Executive Summary	178
5	Performance of Photovoltaic Systems in Urban Environments	187
5.1	Assessing the Combined Effects of Local Climate and Mounting Configuration on the Electrical and Thermal Performance of PV Systems. Application to Greater Sydney	189
5.1.1	Introduction	189
5.1.2	Materials and Methods	194
5.1.3	Results and Discussion	204
5.1.4	Conclusions and Future Perspectives	221

6	Modeling and Optimization of Linear Fresnel Solar Concentration Systems	223
6.1	Solar Fresnel Modelling, Geometry Enhancement and 3D Ray Tracing Analysis devoted to Different Energy Efficiency Definitions and applied to a Real Facility	225
6.1.1	Introduction	225
6.1.2	Modelling a Linear Fresnel Concentrator based on a Ray-tracing Technique	229
6.1.3	Optical Optimization Methodology	241
6.1.4	Results and Discussion	247
6.1.5	Conclusions	253
6.2	Calculation of the Incidence Angle Modifier of a Linear Fresnel Collector: the Proposed Declination and Zenith Angle Model compared to the biaxial factored approach	255
6.2.1	Introduction	255
6.2.2	Modelling the Linear Fresnel System and Define its Figures of Merit	257
6.2.3	The 3D Optical Model of a Linear Fresnel Concentrator and Efficiency Definitions	258
6.2.4	The Case Study and the Geometry Optimization	259
6.2.5	The Incidence Angle Modifier in LFC and the Biaxial Factored Approach	260
6.2.6	The Present Model for Sun Angle-Based Incidence Angle Modifier	263
6.2.7	Results	270
6.2.8	Conclusions	278
7	Conclusions and Future Perspectives	281
7.1	Conclusions	282
7.2	Future Works	284
	References	287
	Appendix A	327
	Appendix B	329

List of figures

1.1	Population share by degree of urbanization and Sustainable Development Goals region (1950–2070) ordered by city population share in 1950. Source: World Cities Report 2022 (UN-Habitat, 2022)	36
1.2	Aerial LiDAR 3D point cloud of the 6 th arrondissement of Lyon, acquired in 2015 with a density of 12 points/m ² . The different colors correspond to the point classifications (i.e. vegetation in yellow, roofs in orange, façades in blue). Source: Métropole de Lyon website ²	42
1.3	Typical workflow for the calculation of solar radiation on roofs (R) and facades (F) in the urban environment from LiDAR data. Source: Desthieux et al. (2018a)	43
1.4	Land Surface Temperature (LST) of Paris, France from NASA's ECOSTRESS on July 15 th , 2022 at 11:21 PM CET. Credits: NASA/JPL-Caltech. Source: NASA website ³	44
1.5	Typical sunny summer day rural (left) and urban (right) energy balance for a location near Houston (Texas, USA). Numerical values refer to kWh/m ² /day. Adapted from source ⁴	47
1.6	LF-11 Linear Fresnel Collectors built by the company Industrial Solar at RAM Pharma, Amman (Jordan). Source: DLR Institute of Solar Research website ⁵	53
1.7	Linear Fresnel Collectors installed at the Cyprus Institute (CyI). Source: Cyprus Institute (CyI) website ⁶	54
2.1	List of the UN SDGs partially or fully addressed by the current study.	63
2.2	Visualization of the ten areas concerning solar neighborhood planning and design strategies treated in this article.	64
2.3	Interaction between solar neighborhoods and other neighborhood concepts, such as zero-emission neighborhoods and positive energy districts, existing in the literature (Baker et al., 2022; Brozovsky et al., 2021; Lund et al., 2011).	65
2.4	Taxonomy of metrics in solar neighborhood planning divided into the four categories identified by Czachura et al. (2022)	68
2.5	Passive solar strategies applied to the planning and design at the neighborhood scale	70
2.6	Passive solar strategies applied to the planning and design at the neighborhood scale	71

2.7	Other passive solar strategies applied to the planning and design at the neighborhood and building scale	73
2.8	Active solar strategies applied to the planning and design at the neighborhood and building scale	74
2.9	Project scales and phases of the planning and design process for solar neighborhoods. Solar planning and design strategies applied at different spatial scales. Description of the tools and norms used in the different project stages. Modified from Kanters and Wall (2016) and Nault et al. (2018)	76
2.10	Summary of the case studies with the main active and passive solar strategies applied	79
2.11	Example of the digital environment of the whole process of solar modeling on roofs and facades for the solar cadaster on the scale of Greater Geneva (about 2,000 km ²). Modified from Stendardo et al. (2020)	88
2.12	Solar strategies implemented in solar neighborhoods and their impacts on the ‘total environment’ (i.e., environmental impact, economy and energy impact, social impact)	92
3.1	Schematic representation of the developed methodological steps applied to the Canton of Geneva	110
3.2	1 st and 2 nd order cells (yellow and green respectively) determined through spatial weights with respect to a reference building (red). The operation is repeated for all the buildings	116
3.3	BIC and AIC scores per number of clusters	119
3.4	Ten homogeneous microclimatic clusters of the Geneva Canton identified through GMM clustering. Each cluster is represented by a different colour and white parts represent the surrounding rural areas.	121
3.5	Probability density functions of rural and urban temperatures. The representative months are February (left) and August (right).	123
3.6	Average monthly urban heat island intensity among the urban clusters.	124
3.7	Spatial variability of the monthly average UHII in August within the Canton of Geneva.	125
3.8	Maximum monthly urban heat island intensity among the urban clusters.	126
3.9	Average hourly urban heat island intensity among the urban clusters.	127
3.10	Boxplots of UHII during daytime (left) and nighttime (right).	128
3.11	Average monthly UHII (markers) and standard deviation (bars) arising from UWG simulations (UHII _{UWG}) and from real measurements (UHII _{real}) for two selected urban weather stations.	129
3.12	Average hourly UHII (markers) and standard deviation (bars) arising from UWG simulations (UHII _{UWG}) and from real measurements (UHII _{real}) for two selected urban weather stations	130
3.13	District plan with the reference building.	135

3.14	Sectioned axonometric view of the reference building with a typical floorplan. The red line represents a single flat.	136
3.15	3D view of the district in OpenStudio environment. The reference building is the central one and the surrounding dark constructions are “shading objects”.	138
3.16	Efficiency curve of the inverter.	142
3.17	Scheme of reference building façades. Numbering starts from the most irradiated floors and orientations.	144
3.18	Sequence of PV installation for attaining the given percentage of façade coverage PV areas do not include the glazed parts of the building.	145
3.19	Urban air temperature excess. Four-day long profile of rural and urban temperatures. Reference (case R) and Enhanced (case E) district design in the month of July.	146
3.20	Monthly mean, maximum and minimum air temperatures related to rural and UWG data, case E.	147
3.21	Monthly energy consumption for air conditioning of the reference building calculated with rural and urban EPW files. COP are provided in Table 3.4.	148
3.22	Estimated solar energy production per façade unit area evaluated by the TCSTC and Sandia methods.	150
3.23	Percent loss of PV energy production per surface unit [kWh/m ² July] for each façade orientation due to the decrease of surrounding buildings average albedo.	151
3.24	Façade PV energy production as a function of the PV percentage coverage on façades.	151
3.25	Monthly energy demand and photovoltaic production. PV modules are installed on 60% of the overall available surface of the reference building (rooftop and façades).	152
4.1	Schematic representation of the developed methodological steps applied to the Canton of Geneva.	160
4.2	Insight of the two shapefiles, <i>Cad.batiment.hors.sol</i> and <i>Ocen.solaire.irr.surface.utile</i> , and the related main attributes. Zoom on a specific area of Geneva.	161
4.3	$I_{theo-max}$ (left), $I_{roof-max}$ (centre), and the relative error Δ (right) as a function of the surface slope (β) and azimuth (γ).	163
4.4	Building footprints and related tessellation cells of a specific area of Geneva. The color scale is related to the building Coverage Area Ratio (CAR).	165
4.5	Schematics representation of a building (red) and its neighbours identified by the spatial weights.	166
4.6	Distribution of I^* on buildings.	168
4.7	Cumulative distribution function of I^* on buildings.	169
4.8	Boxplots of Q_{10} (light blue) and Q_{90} (red). Boxplots show the minimum (lower cap), maximum (upper cap), median (box middle line), 25 th percentile (lower box limit), and 75 th percentile (upper box limit).	170

4.9	Scatterplot representing the detection of outliers in footprint areas (m^2) in red triangles, and the inliers in grey points.	171
4.10	Scatterplot between $\log(I^*)$ and $\log(V)$. The black line represents the linear regression line and the red line is related to the linear quantile regression line based on 0.01 quantiles (red points).	173
4.11	Boxplots of V and FAR of the 48 municipalities of the Canton of Geneva. The city centre districts are highlighted with red boxes.	174
4.12	Scatterplot between I^* and $\overline{\Delta H}$ after the square root transformation. The black line represents the linear regression line.	175
4.13	Map of building footprints of the Liguria region (black). Architectural, archaeological, and landscape constraints are represented in colors.	181
4.14	Percentage of the number of buildings relative to the total, subdivided according to the category of use.	183
4.15	Percentage of available roof surface compared to the total, subdivided according to the category of use.	184
5.1	Analysed weather stations across the greater Sydney region.	195
5.2	Probability density function (PDF) of the air temperature (left) and wind speed (right) across the weather stations.	207
5.3	Probability density function (PDF) of the air temperature (left) and wind speed (right) across the weather stations.	208
5.4	PV cell operating temperatures across the weather stations and mounting configurations. Each graph represents a different mounting configuration whereas each weather station has a different color.	209
5.5	Mean PV cell operating temperatures across the weather stations as a function of the distance from the coast. Each graph represents a different mounting configuration.	210
5.6	Average (solid line) and maximum (dotted line) standard deviation of PV operating cell temperatures across the weather stations for each hour of the day during summer (January) and winter (July).	211
5.7	Monthly Performance Ratio (PR) across the weather stations and mounting configurations.	212
5.8	Exponential relationship between daily performance ratio (PR) and cumulative daily Cooling Degree Hours (CDH) across all weather stations during the summer months (December to February). Each diagram represents a different mounting configuration and the colour bar displays the daily total solar energy reaching the PV surface.	213
5.9	Average hourly values of PV efficiency across the weather stations during November (left) and July (right). Solid and dashed lines are referred to ORgp and IBgp configurations respectively.	214
5.10	Normalized efficiency and PV cell operating temperature for Penrith Lakes (PL) weather station. Each diagram represents a different mounting configuration.	215

5.11	Yearly average $P_{\text{loss},T}^*$ across the considered weather stations and mounting configurations identified by different colors.	216
5.12	Daily average $P_{\text{loss},T}^*$ (average values across all weather stations) across the mounting configurations identified by different colors.	216
5.13	Hourly $P_{\text{loss},T}^*$ and PV output power of insulated back PV modules under Penrith Lakes (PL) weather conditions.	217
5.14	Monthly PV power production (average across weather stations) as a function of the mounting configuration identified by the different colors. Error bars represent the maximum percentage difference of PV energy production across the weather stations.	218
5.15	Histogram of the convective heat fluxes across all weather stations during the warm (left) and the cool (right) periods for the two considered mounting configurations (open rack, OR, and close roof mount, CM). Mean, median, and standard deviation values are represented by the red, green, and black lines respectively.	219
5.16	Radiative and convective heat transfers as a percentage of total heat transfer at various wind speeds. The results are referred to close roof mount under Penrith Lakes (PL) climate conditions.	221
6.1	FresnelSim computational flowchart.	230
6.2	FresnelSim computational flowchart.	232
6.3	Sun position (\vec{S}), mirror normal (\vec{n}), and reflected ray (\vec{R}) vectors with respect to a generic N-S oriented mirror at $x_{m,i}$ distance from the axis origin (O).	235
6.4	Curved cylindrical mirror geometric parameters.	236
6.5	Determination of the shaded area from sun ray projection onto the vertical East-West plane.	238
6.6	Determination of blocked rays as a projection onto the vertical East-West plane.	239
6.7	Centesimal comparator and in-situ measurements of the mirror curvature at GEP facility during Authors' visiting period.	244
6.8	Percentage difference between optical efficiency (η_{opt}^I) as calculated by Fresnel-Sim and Tonatiuh (flat mirrors).	246
6.9	Percentage difference between optical efficiency (η_{opt}^I) considering perfect reflection and tracking and by introducing angular reflection error ($\lambda_{surf}=2$ mrad) and tracking error ($\sigma_{te}=1$ mrad).	247
6.10	Instantaneous optical efficiencies η_{opt}^I and η_{opt}^{II} during the reference days. Timestep is 10 minutes.	248
6.11	Instantaneous blocking, shading by adjacent mirrors, and shading by receiver efficiencies during day 355. Timestep is 10 minutes.	249
6.12	Mirror by mirror optical efficiency (η_{opt}^I) during day 355. Timestep is 10 minutes.	249
6.13	DNI distribution comparison between FresnelSim calculation (DNI_{FS}) and Meteonorm software (DNI_{MN}). The reference day is n°91.	250

6.14	Variation of LFC efficiencies as a function of the spacing between adjacent mirrors (gap). The reference day is n°79.	251
6.15	Energy arriving at the receiver aperture area (Ap_{CPC}) in a day by varying the receiver height.	252
6.16	Energy arriving at the absorber tube in a day by varying the receiver height. . .	253
6.17	Variation of LFC efficiencies (η_{opt} and $\eta_{opt-ene}$) with the spacing between adjacent mirrors (gap) for day n°79 (Ben Guerir, Morocco).	260
6.18	Schematics of the transversal (θ_T), and longitudinal (θ_L) angles in a LFC where the primary mirror aperture plane is horizontal.	261
6.19	Scatter plot of the IAM_{RT} as a function of the declination angle for the reference days (in legend the day number) and considering configuration C0.	265
6.20	Scatter plot of the IAM_{RT} as a function of the azimuth angle for the reference days (in legend the day number) and considering configuration C0.	266
6.21	Scatter plot of the IAM_{RT} as a function of the profile angle for the reference days (in legend the day number) and considering configuration C0.	267
6.22	Scatter plot of the IAM_{RT} as a function of the azimuth angle for the reference days (in legend the day number) and considering configuration C0.	268
6.23	Scatter plot of the IAM_{RT} as a function of the cosine of the zenith angle for the reference days (in legend the day number) and considering configuration C0. . .	269
6.24	Variation of the transversal and longitudinal IAM components with the related projected angle. Comparison between the ray-tracing (RT) and analytical (B) approaches when blocking is disabled.	271
6.25	Variation of the transversal and longitudinal IAM components with the related projected angle. Comparison between the ray-tracing (RT) and analytical (B) approaches when blocking is included.	272
6.26	Variation of the transversal and longitudinal IAM components with the related projected angle. Comparison between ray-tracing results for configuration C0 and C1.	273
6.27	Comparison between the instantaneous non-approximated IAM_{RT} and the bi-axial factored approximation $IAM_{RT,FA}$ over a time horizon of 25 days for configuration C0.	274
6.28	Comparison between the instantaneous non-approximated IAM_{RT} and the declination-zenith regression model IAM_{dzm} over a time horizon of 25 days for configuration C0.	275
6.29	Comparison between the instantaneous non-approximated IAM_{RT} and the declination-zenith regression model IAM_{dzm} over a time horizon of 25 days for configuration C1.	276
6.30	Comparison between the instantaneous non approximated IAM_{RT} and the declination-zenith regression model IAM_{dzm} based on a 3-day-long reduced database (days are n°171, 355, and 79) for plant configuration C0.	278

List of tables

2.1	Summary of the challenges to adopt passive solar strategies in solar neighborhoods	81
2.2	Summary of the challenges to adopt active solar strategies in solar neighborhoods	84
3.1	UWG main input parameters for UHI simulation	112
3.2	Reference values of building characteristics based on different construction periods	117
3.3	$U_{cluster}$ related to the ten clusters identified through GMM algorithm	122
3.4	Input parameters for the definition of the district and building characteristics within the Urban Weather Generator tool	137
3.5	PV module specifications for the performance evaluation	141
3.6	Values of surrounding surface and ground reflectivity adopted for the simulations	143
3.7	Monthly (July) irradiance of façades with respect to their floor and orientation	144
3.8	PV energy production per vertical surface unit in July evaluated through the Sandia method considering both rural and urban surface temperatures	149
4.1	Pearson correlation coefficients considering the whole building dataset. (†) represents square root transformation, whereas (††) is for log-log transformation.	172
4.2	Pearson correlation coefficients considering the four city-center districts. (†) represents square root transformation, whereas (††) is for log-log transformation.	174
4.3	Total available rooftop area [m ²] by building category	184
4.4	Reduction coefficients and usable rooftop surface [m ²] by building category	185
4.5	Estimated annual PV potential [GWh _{el} /year] by building category	185
5.1	Weather Station Information	196
5.2	Specifications of Canadian Solar 300 Watt Solar Module	199
5.3	Module performance parameters for different mounting configurations	199
5.4	Assumptions for the calculation of the convective heat flux as a function of the PV side and mounting configuration	203
5.5	Summary statistics of air temperature and wind speed values for each weather station	205

5.6	Total Convective Energy released by open rack (OR) and close roof (CM) installed PV modules across the selected weather stations (WS) during the warm and the cool periods	220
6.1	Geometric parameters of the GEP linear Fresnel plant used for simulations . . .	244
6.2	Optical properties of the GEP linear Fresnel plant components used for simulations	245
6.3	Regression constants based on all ray-tracing data (25-day-long database) for configuration C0	275
6.4	Regression constants calculated from the reduced 3-day-long database for configuration C0. The considered days are day n° 171, 355, and 79.	277
A.1	Meteorological and site parameters	328
B.1	Building Parameters and Descriptions	329

Nomenclature

Roman Symbols

A	Area [m^2]
AMa	Air mass coefficient for solar altitude angle
A_{PC}	Aperture width of the secondary LF reflector [m]
d	Distance [m]
E, G	Solar Irradiance [Wm^{-2}]
$f_1(AMa)$	Correction factor for air mass coefficient
$f_2(AOI)$	Correction factor for angle of incidence
g	Spacing between adjacent mirrors [m]
H	Height [m]
$h_{c, glass}$	Forced Convection heat transfer coefficient over a smooth surface [$Wm^{-2}K^{-1}$]
h_c	Convective heat transfer coefficient [$Wm^{-2}K^{-1}$]
h_n	Natural Convection heat transfer coefficient [$Wm^{-2}K^{-1}$]
HW	Height to width ratio [-]
I	Current [A]
i	Building infiltration rate [ach]
I^*	Scaled Solar Insolation [-]
K	Total number of clusters [-]
L	Length [m]
P	Building Perimeter [m] or PV power [W]
P_{25}	Theoretical DC Power of the PV array [Wm^{-2}]
$P_{loss, T}^*$	PV power losses due to temperature [%]
P_{mp}	Power at maximum power point [W]

PR	PV Performance Ratio [-]
Q	Heat flux [Wm^{-2}]
$Q_{10,90}$	0.1 and 0.9 quantiles
r, R^2	R-Pearson coefficient
S_{tot}	Total (rooftop) surface area for PV installations [m^2]
S_u	Useful (rooftop) surface area for PV installations [m^2]
T	Temperature [$^{\circ}C$]
U	Thermal transmittance [$Wm^{-2}K^{-1}$]
V	Voltage [V]
VH	Vertical to horizontal ratio [-]
W	Width [m]
w	Inverse of the distance [m^{-1}]
ws	Wind Speed [$m s^{-1}$]
x	x coordinate
Y	PV yield [Wh]
y	y coordinate
z	z coordinate

Greek Symbols

α	Absorptivity [-]
α_{Imp}	Temperature coefficient for maximum power current [$\% \text{ } ^{\circ}C^{-1}$]
α_{Isc}	Temperature coefficient for short-circuit current [$\% \text{ } ^{\circ}C^{-1}$]
α_p	Profile Angle [deg]
α_s	Solar Altitude Angle [deg]
β	Surface slope [deg]
β_{ref}	Temperature coefficient of power [$\% \text{ } ^{\circ}C^{-1}$]
β_{Vmp}	Temperature coefficient for maximum power voltage [$\% \text{ } ^{\circ}C^{-1}$]
β_{Voc}	Temperature coefficient for open-circuit voltage [$\% \text{ } ^{\circ}C^{-1}$]
Δ	Relative Error [$\%$]
δ	Sun Declination Angle [deg]
ΔT	Temperature difference [$^{\circ}C$]

Δt	Timestep [s]
η	Efficiency
γ	Surface azimuth [deg]
γ_s	Solar Azimuth Angle [deg]
λ	Angular deviation due to non perfect surface [mrad]
ω	Solar hour angle [deg]
ϕ	Latitude [deg]
ρ	Plan density or materials' reflectivity/albedo [-]
σ	Angular deviation of the tracking system [mrad]
τ	Time interval [s] or surface transmittance [-]

Subscripts

0	Reference
<i>a</i>	Ambient air
<i>b</i>	Beam/Direct solar irradiance
<i>bld</i>	Building
<i>Block</i>	Blocking effect
<i>c</i>	PV cell
<i>c, i</i>	Center coordinates of the i^{th} mirror
<i>cond</i>	Conduction
<i>conv</i>	Convective
<i>cos</i>	Cosine
<i>diff</i>	Diffuse solar irradiance
<i>distr</i>	District
<i>e</i>	Effective solar irradiance
<i>elec</i>	Electrical
<i>en</i>	Energetic
<i>f</i>	Front (or field)
FS	FresnelSim tool
<i>gg</i>	Glass/cell/glass
<i>gp</i>	Glass/cell/polymer

<i>gr</i>	Ground
<i>gross</i>	Gross land area of the mirror field
<i>m</i>	PV module
<i>max</i>	Maximum
<i>mean</i>	Mean
<i>min</i>	Minimum
<i>mir</i>	Mirror
<i>mp</i>	Maximum Power
<i>N</i>	Normalized
<i>tess</i>	Neighbouring building
<i>oc</i>	Open Circuit
<i>opt</i>	Optical
<i>p, proj</i>	Projection
<i>rad</i>	Radiative
<i>r, rays</i>	Rays
<i>ref</i>	Reference
<i>refl</i>	Reflected solar irradiance
<i>rur</i>	Rural
<i>sc</i>	Short Circuit
<i>sens</i>	Sensible heat flux
<i>Shad</i>	Shading effect from adjacent mirrors
<i>Shad, CPC</i>	Shading effect from secondary reflector (CPC type)
<i>t</i>	Receiver tube
<i>te</i>	Tracking error
<i>tess</i>	Tessellation
<i>theo – max</i>	Theoretical Maximum
<i>tot</i>	Total
<i>urb</i>	Urban

Acronyms / Abbreviations

AEMO Australian Energy Market Operator

AHP	Analytic Hierarchy Process
AI	Artificial Intelligence
AIC	Akaike Information Criterion
AOI	Angle of Incidence
BEM	Building Energy Model
BES	Building Energy Simulation
BIC	Bayesian Information Criterion
BIM	Building information modeling
BIPV	Building Integrated Photovoltaic
BPV	Bifacial photovoltaic
BREEAM	Building Research Establishment Environmental Assessment Method
CAT	Canyon Air Temperature
CBD	Central Business District
CDH	Cooling Degree Hours
CFD	Computational Fluid Dynamics
CLFC	Compact Linear Fresnel Collector
CM	Close roof PV mount
COP	Coefficient of Performance
CPC	Compound Parabolic Collector
CR	Concentration Ratio
CSP	Concentrating Solar Power
CWS	Crowdsourced Weather Station
DALE	Department of Planning, Housing, and Energy (Switzerland)
DBSCAN	Density Based Spatial Clustering of Applications with Noise
DEM	Digital Elevation Model
DHI	Diffuse Horizontal Irradiance
DNI	Direct Normal Irradiance
EM	Expectation Maximization
EPBD	Energy Performance of Buildings Directive
EPW	EnergyPlus Weather file

EV	Electric Vehicles
GDP	Gross Domestic Product
GHI	Global Horizontal Irradiance
GIS	Geographic Information System
GMM	Gaussian Mixture Model
HTF	Heat Transfer Fluid
HVAC	Heating Ventilation and Air Conditioning
IAM	Incidence Angle Modifier
IB	Insulated back PV mount
ICT	Information and Communication Technologies
IEA	International Energy Agency
KPI	Key Performance Indicators
LCOE	Levelized Cost of Electricity
LCZ	Local Climate Zone
LFC	Linear Fresnel Collector
LF	Linear Fresnel
LFR	Linear Fresnel Reflector
LiDAR	Light Detection and Ranging
LST	Land Surface Temperature
MCDA	Multi-Criteria Decision Analysis
MCDS	Multi-Criteria Decision-Support
MCRT	Monte Carlo Ray Tracing
NDVI	Normalized Difference Vegetation Index
NOCT	Nominal Operating PV Cell Temperature
NREL	National Renewable Energy Laboratory
nZEB	Nearly Zero Energy Buildings
nZED	Nearly Zero Energy Districts
OR	Open rack PV mount
PDF	Probability Density Function
PED	Positive energy district

PET	Physiological Equivalent Temperature
POA	Plane of Array
PTC	Parabolica Trough Collector
PV	Photovoltaic
PVSD	Photovoltaic shading devices
RMSE	Root Mean Squared Error
RSM	Rural Station Model (UWG)
RS	Remote Sensing
SAPM	Sandia PV Array Performance Model
SITG	Geneva Territory Information System
SN	Solar Neighborhood
SPT	Solar Power Tower
STC	Standard Test Conditions
SUHI	Surface Urban Heat Island
SVF	Sky View Factor
TEB	Town Energy Balance
TIR	Thermal Infrared
TMY	Typical Meteorological Year
UC-BEM	Urban Canopy-Building Energy Model (UWG)
UCM	Urban Canopy Model
UHII	Urban Heat Island Intensity
UHI	Urban Heat Island (atmospheric)
UWG	Urban Weather Generator
VDM	Vertical Diffusion Model (UWG)
VUWG	Vertical Urban Weather Generator
WMO	World Meteorological Organization
WRF	Weather Research Forecast
WS	Weather Station
XML	Extensible Markup Language

Chapter 1

Introduction

1.1 Background and Motivation

Urbanization is a dynamic and transformative process characterized by the concentration of the human population in cities and the subsequent increase in urban settlement density within specific regions. This process has undergone an unprecedented surge over the past five decades, resulting in a fourfold increase in the number of urban inhabitants since 1961. Currently, urban areas accommodate 55% of the world's population, and projections indicate that by 2050, approximately 68% of the global population, roughly 6.7 billion individuals, will reside in urban areas (UN-Habitat, 2022). The majority of this urban population growth, up to 90%, is expected to be concentrated in the regions of Asia and Africa (United Nations, 2018) as shown in Figure 1.1.

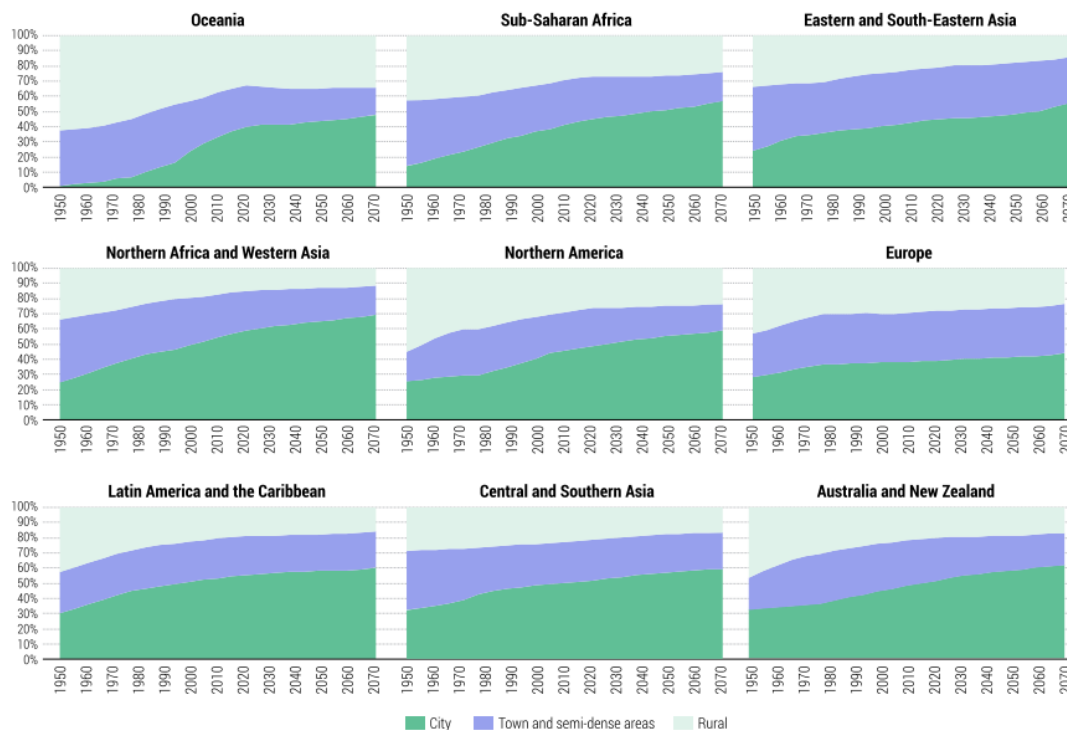


Fig. 1.1 Population share by degree of urbanization and Sustainable Development Goals region (1950–2070) ordered by city population share in 1950. Source: World Cities Report 2022 (UN-Habitat, 2022)

As urbanization, also the impact of climate change is unevenly distributed, with urban communities, especially those who are economically and socially marginalized, experiencing the greatest effects (Guerreiro et al., 2018). Developing countries, undergoing rapid urbanization, face additional challenges in the context of climate change due to their geographical disadvantages, such as inherent warmth and increased rainfall variability. Moreover, their economies heavily rely on agriculture, which is highly sensitive to climate fluctuations (Thornton et al., 2014). The combination of lower incomes and heightened climate vulnerabilities further complicates their ability to adapt, disproportionately impacting their development. Despite their

minimal historical greenhouse gas emissions, the poorest developing countries bear the heaviest burden of climate change consequences (Friedlingstein et al., 2022).

The interplay between urbanization and climate change gives rise to complex and dynamic relationships that necessitate in-depth investigation. Climate change directly affects the functioning of urban systems, while the characteristics of these systems also play a substantial role in shaping the impacts of climate change. The urban heat island effect serves as a noteworthy example, illustrating the intricate connection between urban systems and climate. This effect occurs when urban areas experience higher temperatures compared to surrounding rural areas due to several factors related to human activities and to the built environment (Oke, 1982).

Conducting comprehensive assessments of the interrelationships between various systems and a wide range of hazards is crucial, as many cities are already exposed to multiple climate-related risks (Guerreiro et al., 2018). Among the alarming consequences of climate change, extreme weather events, particularly heatwaves, pose significant challenges in the urban context (Perkins et al., 2012). Projections indicate that urban areas will face hotter and drier summers, leading to an increased demand for air conditioning (Pyrgou et al., 2017). This, in turn, exacerbates the urban heat island effect and raises temperatures within cities. The compounded effects of heatwaves and the urban heat island effect have substantial implications for energy systems, human health, and economy (Nadeem et al., 2022). The exposure to extreme heat can lead to heat-related illnesses and increased mortality rates. The economic consequences of these climate-related impacts on cities are substantial. Estimates suggest that by the end of the 21st century, cities may face potential losses of up to 10.9% in GDP due to the adverse effects of climate change (Dodman et al., 2023).

However, despite these challenges, urban areas continue to play a crucial role as vital economic hubs on a global scale, contributing approximately 80% of the world's GDP (United Nations and of Economic and Social Affairs, 2018). Nevertheless, the unprecedented growth of urbanization has resulted in environmental degradation, necessitating the implementation of effective mitigation strategies. Nowadays, cities heavily rely on fossil fuels, making them significant contributors to global carbon dioxide (CO₂) emissions from energy-related sources, accounting for an estimated 71-76% of these emissions. Additionally, urban centers account for a substantial proportion of global final energy consumption, ranging from 67-76% (IPCC, 2022).

To tackle the multifaceted challenges arising from the interplay between urbanization and climate change, the transition to renewable and low-carbon alternatives assumes a crucial role. Energy transition entails shifting away from fossil fuel-based energy systems towards renewable alternatives which are essential to reduce greenhouse gas emissions, mitigate the impacts of climate change, and foster sustainable urban development. Moreover, this transition enhances energy security by reducing dependence on fossil fuels, which exposes cities to price fluctuations, supply disruptions, and geopolitical tensions.

In the aforementioned context, strategic decisions pertaining to key energy infrastructure systems play a key role in shaping risks and enabling effective responses to climate change. The choices made in urban planning and development exert substantial influence over the creation and mitigation of climate change-related risks. The rapid and unplanned expansion of urban areas, including peri-urban development, as well as the degradation of green infrastructure and ecosystems, reduce adaptive capacity and potentially amplify risks. Therefore, thoughtful and well-informed urban planning, encompassing the design, construction, and maintenance of urban environments and critical infrastructure systems, assumes a crucial role in determining patterns of exposure. Furthermore, urban decision-making processes significantly impact the capacity of low- and zero-carbon development to address societal needs, promote well-being, and concurrently facilitate climate change mitigation, thereby advancing the Sustainable Development Goals (Sofeska, 2016).

In the present-day scenario, planners and policymakers face a multitude of intricate urban challenges that require careful consideration, as these challenges rapidly evolve over time. Shorter timeframes for addressing demands compared to previous decades add complexity to the task at hand. This changing landscape necessitates a shift in focus, moving beyond the physical structure of cities, towards comprehending and effectively managing the dynamic interactions among the diverse components coexisting within urban systems.

1.2 Cities and City-Scale

European countries have set ambitious decarbonization goals, with the aim of achieving climate neutrality by 2050 (International Energy Agency, 2021). In this process, cities assume a crucial role due to the rising global energy demand, depletion of fossil fuels, and the urgent challenge of climate change associated with their usage. Urbanization leads to a concentration of energy demand and subsequent emissions in high density urban areas, highlighting the necessity of transitioning from a centralized conventional grid to a distributed urban energy system for enhancing the resilience and reliability of power supply.

Traditional approaches to city planning and building design have been guided by city zoning and building codes, with the primary objective of addressing concerns related to energy efficiency, public health, and sustainability. However, these regulations have often led to a disconnect between the design of individual buildings and the comprehensive planning of urban environments. Designing a single, standalone low-carbon building is distinct from the complex task of planning an entire urban area (Mauree et al., 2019). This lack of integration has resulted in inadequate consideration of the impact of urban morphology and microclimate on energy demand and the potential for integrated energy production at the building scale (Boccalatte et al., 2020a,b). While building certifications and standards, such as the European Union's Nearly Zero Energy Buildings (nZEBs) standard (Grözinger et al., 2014), aim to promote the adoption of renewable energy sources, the optimization of energy demand and the implementation of

building-integrated systems often occur without adequate regard for the intricate interactions within the urban environment.

In light of these challenges and the significant role of cities in the energy transition, this thesis focuses primarily on cities and on the city scale as they play a critical role in achieving decarbonization goals and addressing the challenges of climate change.

1.3 Integrating Solar Energy into the Urban Environment

Solar energy represents one of the most prominent renewable resource due to its abundance, versatility, and technological maturity. Achieving the goals of the International Energy Agency's (IEA) Net Zero by 2050 Scenario requires a rapid expansion of solar photovoltaic (PV) installations in the next decade. To align with these objectives, the global average annual number of solar PV installations must increase nearly fourfold within the next ten years. By 2050, solar PV is projected to contribute one-third of the world's total electricity generation, a substantial increase from its 3% share in 2021 ([International Energy Agency, 2022b](#)). Unlike other renewable energy systems, solar technology, including both photovoltaics and solar thermal collectors, can be widely integrated into built environments, even in densely populated urban areas, through building elements (rooftop, facades, windows, shading systems, etc). This approach offers the advantage of localized electricity production, which has become a requirement for all new buildings in Europe since 2020 as specified by the Energy Performance of Buildings Directive ([European Commission for Energy, 2015](#)). Consequently, the integration of PV systems into buildings holds significant potential to meet a substantial portion of electricity demand, with over half of the necessary global PV capacity to achieve the 2050 goals potentially being installed on buildings ([International Energy Agency, 2022b](#)). The widespread adoption of photovoltaic systems in urban areas will provide a long term solution to meet energy demands ([Amado et al., 2017](#)). These trends are primarily driven by the decreasing costs of solar technologies ([International Energy Agency, 2022a](#)), advancements in efficiency through new technologies ([Singh et al., 2021](#)), and the environmental and economic benefits associated with distributed energy generation networks compared to centralized grids ([Nadeem et al., 2023](#)).

Challenges and Issues

The pursuit of maximizing solar power generation in urban areas may introduce challenges when considering other urban planning criteria, such as urban density or compactness. For instance, the integration of photovoltaics within the urban environment can lead to shading or reduced exposure due to surrounding constructions ([Desthieux et al., 2018a](#)). Furthermore, the increasing occurrence of heatwaves and the intensification of urban overheating can further decrease the efficiency of integrated solar systems within the urban environment ([Berardi and Graham, 2020](#)). Despite the promising prospects of integrating solar systems into urban surfaces, several challenges must be addressed.

The first obstacle is of a scientific nature and revolves around the physical modeling of the urban system. Due to its heterogeneous and complex dynamics, there is a limited understanding of the urban physical system (Masson et al., 2020). Characterizing the boundary and operational conditions of photovoltaic modules necessitates a profound comprehension of the intricate physical interactions within the city. This includes phenomena like the urban heat island effect and the distribution of irradiance on urban surfaces, which are influenced by the morphological characteristics of the city and determine shading and inter-reflection factors among urban surfaces.

In this particular context, alongside scientific and modeling challenges, practical obstacles also arise. The first practical challenge pertains to computational times. Urban-scale physical models need to process a vast number of elements, and employing complex microclimate or solar radiation models results in excessively long computation times. Consequently, simplifications become necessary for the spatial extrapolation of essential information (Lipson et al., 2022). Commonly employed qualitative techniques include the classification of Local Climate Zones (LCZ) (Leconte et al., 2015) for microclimate studies, or the determination of available areas for photovoltaics using averaged coefficients when dealing with large-scale solar potential estimations (Melius et al., 2013). These simplifications are driven by the complexity of the problem as well as practical considerations.

The second major practical obstacle is the lack of comprehensive and detailed data at the urban scale (Biljecki et al., 2021). Accurate data pertaining to the building stock, urban solar irradiance levels, energy consumption patterns, building characteristics, and infrastructure capacity play a crucial role in making informed decisions and achieving effective integration of solar systems within urban areas. This data is instrumental in comprehending the intricate physics of the urban system.

Hence, there exists an urgent requirement to digitalize the urban system, enabling the generation of urban-scale data that supports data-driven methodologies, optimization, and monitoring of solar systems in urban settings.

These aspects and challenges related to the integration of solar energy into urban environments are extensively explored and analyzed in Chapter 2 (Paper 1) providing a comprehensive understanding of solar neighborhood planning strategies and guidelines.

1.4 Digitalization of the Urban Environment

“There is a rich history of data being generated about cities concerning their form, their citizens, the activities that take place, and their connections with other locales. These data have been generated in a plethora of different ways, including audits, cartographic surveying, interviews, questionnaires, observations, photography and remote sensing, and are quantitative and qualitative in nature, stored in ledgers, notebooks, albums, files, databases and other media.”

Data about cities provide a wealth of facts, figures, snapshots and opinions that can be converted into various forms of derived data, transposed into visualizations, such as graphs, maps and infographics, analysed statistically or discursively, and interpreted and turned into information and knowledge. As such, urban data form a key input for understanding city life, solving urban problems, formulating policy and plans, guiding operational governance, modelling possible futures and tackling a diverse set of other issues. For as long as data have been generated about cities then, various kinds of data-informed urbanism have been occurring” (Kitchin, 2015)

As emphasized by Kitchin, urban data plays a crucial role in modeling, planning, and studying the urban environment. The integration of Information and Communication Technologies (ICTs) in the digitalization of the urban environment facilitates the collection and analysis of urban data (Wang et al., 2021a). The foundation for generating urban datasets lies in the ICT infrastructure, but its applications extend to validating simulation data, monitoring and optimizing energy systems, and more.

One fundamental application of digital technologies in the urban context is the ability to accurately map the geometric features of the urban environment. This process is essential for conducting solar radiation and microclimate studies at the city scale. Solar radiation in urban areas is influenced by various factors, with urban geometry playing a significant role in determining shading and inter-reflections between buildings. To accurately calculate solar radiation in large-scale urban areas, radiation models based on Geographic Information System (GIS) data provide the most suitable approach (Freitas et al., 2015).

Similarly, for conducting microclimate analyses on a large scale, it is crucial to gather information regarding urban geometry, such as building heights, building density, canyon height-to-width ratio, main orientation of the streets, Sky View Factor, and more (Maiullari et al., 2021; Mutani et al., 2019; Salvati et al., 2017c). Additionally, incorporating data on the presence of vegetation, which can be assessed using the Normalized Difference Vegetation Index (NDVI), is also vital for conducting simulations with parametric microclimate models and mesoscale models (Bernard et al., 2017).

Acquiring the necessary data for these models involves a series of data collection processes. Mapping the urban environment typically entails the creation of a Digital Elevation Model (DEM) that captures relevant surface features and their surroundings (Allegrini et al., 2015b). Various digital techniques can be employed for this purpose, including the utilization of aerial or satellite imagery. A common technique involves active remote sensing systems as Light Detection and Ranging (LiDAR) technology, which captures geometric information as a 3D point cloud (Brito et al., 2017). As shown in Figure 1.2 the points of a LiDAR acquisition can also contain information that can assist in their classification during post-processing. Additionally, stereo imagery, utilizing pairs of geo-referenced photographs, can be used to create a 3D model of the city through photogrammetry (Masson et al., 2020). Cadastre data, although more commonly used in 2D applications such as evaluating rooftop solar potential based on building

footprints, height, and slope information, can also be utilized to generate a 3D city model (Biljecki et al., 2015).



Fig. 1.2 Aerial LiDAR 3D point cloud of the 6th arrondissement of Lyon, acquired in 2015 with a density of 12 points/m². The different colors correspond to the point classifications (i.e. vegetation in yellow, roofs in orange, façades in blue). Source: Métropole de Lyon website¹

The second fundamental application of digital technologies for urban studies involves the physical characterization of the built environment.

One crucial aspect in the early stages of designing urban surfaces for solar energy potential is the calculation of solar radiation reaching those surfaces. While accurate solar radiation data can be obtained through in-situ measurements using pyranometers, their coverage is limited and time-consuming, particularly for large-scale applications such as cities. Solar radiation in urban areas is influenced not only by urban morphology but also by meteorological conditions, microclimatic phenomena, and atmospheric characteristics. Ground-based meteorological stations or satellite-derived climate measurements are able to provide the necessary inputs to calculate the solar irradiance levels at different tilt angles using geometric approaches to determine the sun's position (Romero Rodríguez et al., 2017). Then, a solar radiation model and a shadow casting routine are necessary for a comprehensive large-scale solar potential analysis (Desthieux et al., 2018a; Stendardo et al., 2020). This enables the creation of solar maps (or solar cadasters) providing annual irradiation levels for densely populated urban areas worldwide (Kanters et al., 2014) as schematically represented in Figure 1.3.

¹<https://data.grandlyon.com/jeux-de-donnees?q=lidar>

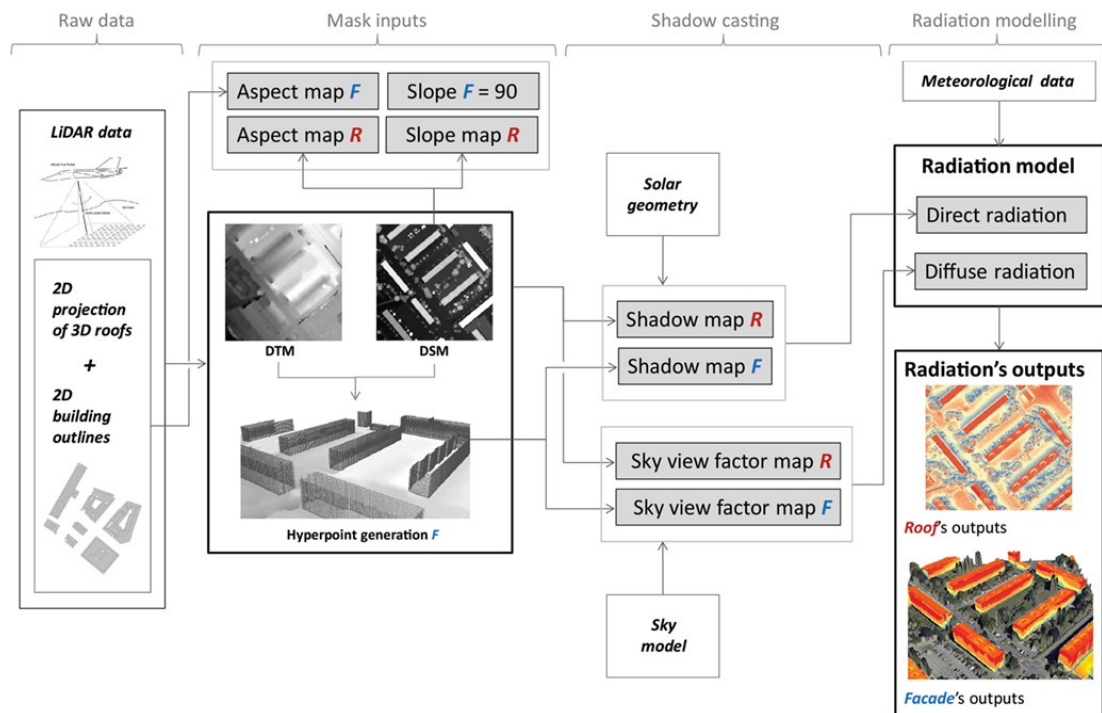


Fig. 1.3 Typical workflow for the calculation of solar radiation on roofs (R) and facades (F) in the urban environment from LiDAR data. Source: Desthieux et al. (2018a)

Regarding the characterization of urban microclimate, several digital techniques can be employed. These techniques include ground-based meteorological stations, Remote Sensing (RS), crowdsourced data (Varentsov et al., 2020), and in-situ campaigns using portable thermal cameras (Venter et al., 2020). This variety of sources allows for investigating both the atmospheric and surface-level urban heat island (UHI and SUHI, respectively) phenomena using diurnal and/or nocturnal data across different seasons of the year. At a large-scale, remote sensing serves at several purposes, providing spectral, thermal, and morphological information about the urban landscape (de Almeida et al., 2021). It can be employed to generate land cover maps, enabling the implementation of the Local Climate Zones (LCZ) classification (Lehnert et al., 2021). Additionally, Thermal Infrared (TIR) remote sensing data allows for the computation of Land Surface Temperature (LST), a critical parameter for assessing the radiative load on the Earth's surface (Figure 1.4). Analyzing LST provides a more detailed level of analysis, enabling the extraction of pertinent climate variables such as evapotranspiration, water-stressed vegetation, soil moisture, and thermal inertia. The application of both LCZ and LST analyses is extensive in UHI research (Unal Cilek and Cilek, 2021; Yan et al., 2021).

Beyond urban mapping and the physical characterization of the urban environment, digital technologies play a crucial role in monitoring, validating simulated data, and optimizing processes. For example, when optimizing the placement of solar systems in urban areas, Multi-Criteria Decision-Support (MCDS) systems assist local authorities in establishing design guidelines and criteria. These decision-making methodologies help evaluate and select alterna-

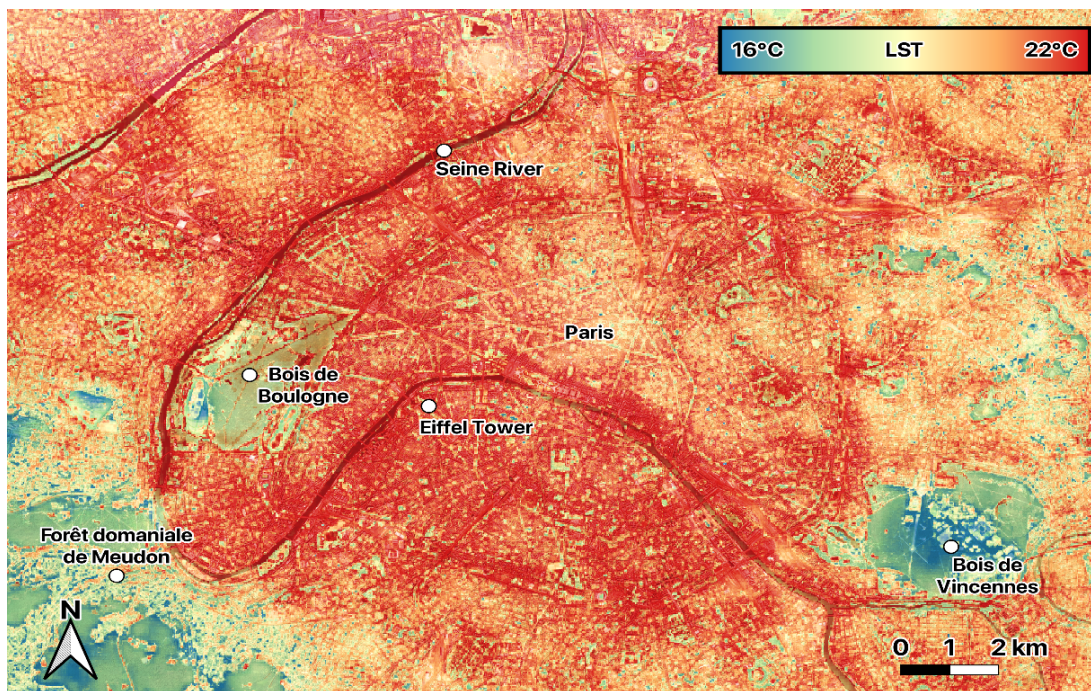


Fig. 1.4 Land Surface Temperature (LST) of Paris, France from NASA's ECOSTRESS on July 15th, 2022 at 11:21 PM CET. Credits: NASA/JPL-Caltech. Source: NASA website²

tives based on multiple criteria or objectives. In the context of large-scale photovoltaic (PV) array site selection, carrying capacity models that integrate Multi-Criteria Decision Analysis (MCDA) and the Analytic Hierarchy Process (AHP) with GIS technology can provide guidance (Thebault et al., 2020; Yang et al., 2011).

In addition to decision-making methodologies, machine learning, as a sub-field of artificial intelligence, finds applications in studying urban systems for various objectives (Wang and Biljecki, 2022). By employing both supervised and unsupervised machine learning techniques, it becomes possible to develop predictive models that can estimate unknown values and uncover relationships among phenomena. Machine learning methods, such as clustering, signal decomposition techniques, and neural networks, have the capability to identify and extract discriminative information from extensive data collections. This enables typological studies, spatial aggregation profiling, automatic extraction of relevant features, and many other applications.

In conclusion, the digitalization of the urban environment is of paramount importance in urban studies, enabling comprehensive data collection, advanced analysis, and informed decision-making. This overview of the various applications of digital technologies in urban studies highlights their capabilities in acquiring valuable insights into the complex dynamics of urban systems.

²<https://ecostress.jpl.nasa.gov/gallery/urbanheat/>

1.5 Urban Morphology

Urban morphology refers to the study of the physical characteristics of a city, including its geometric attributes, functional aspects, and patterns of development. Unlike the term *geometry*, which focuses primarily on spatial dimensions, *morphology* encompasses a broader and more dynamic understanding of urban forms and their evolutionary processes. It is defined as the study of "*the spatial structure, character of urban forms as well as the process of their development*" (Schirmer and Axhausen, 2015).

The field of urban morphology explores the interaction between urban form and various climate variables, which influence the microclimate of urban areas. Elements of urban morphology, such as building density, layout, and height, significantly impact air temperature, wind patterns, humidity levels, and solar radiation distribution (Adolphe, 2001). These morphological elements strongly determine shading and solar exposure in urban areas (Morganti et al., 2017; Poon et al., 2020; Robinson, 2006) potentially increasing the reliance on air conditioning systems for thermal comfort and the electricity needed for lighting (Kamal et al., 2021). Consequently, the increase in energy consumption by buildings further exacerbates anthropogenic heat emissions, contributing to the intensification of the Urban Heat Island (UHI) phenomenon (Hwang et al., 2020). This creates a vicious cycle.

Recognizing the interplay between urban morphology, urban microclimate, and urban solar potential underscores the significance of integrating urban form into energy-efficient urban planning. Spatial indicators or urban morphological parameters are employed by researchers to analyze the morphological characteristics of a given area (Carneiro et al., 2010; Fleischmann et al., 2022b; Xu et al., 2021). These quantitative measures assist in comprehending the intricate physical components that constitute urban environments. Moreover, they contribute to conceptualizing cities as complex adaptive systems and offer valuable insights for urban planners. In this regard, urban morphology provides evidence-based support for contemporary urban design theory and practice.

While qualitative approaches have traditionally dominated the field, recent advances in digitalization have facilitated the adoption of quantitative methods. Geographic Information System (GIS) spatial analysis (Fleischmann et al., 2020), statistical analysis, and machine learning techniques are increasingly being employed for processing urban data and deriving quantitative indicators (Cai et al., 2021; Schirmer and Axhausen, 2019).

In the context of data-driven urban design, learning from the reality of urban morphology enables decision-makers to make comprehensive design choices, considering social, environmental, and economic factors. These suggestions serve as valuable references and guidance. Researchers, on the other hand, can utilize insights from urban morphology to study the functionality and performance of urban systems.

In this dissertation, the focus has been on studying quantitative approaches to derive urban morphological indicators, specifically in relation to urban microclimate (Chapter 3, **Paper 2**) and urban solar potential (Chapter 4, **Paper 4**). By employing these quantitative methods, the research aims to provide a better understanding of the relationship between urban form and specific aspects of urban environments.

1.5.1 Urban Microclimate

The morphological characteristics of urban exert a significant influence on Urban Heat Island Intensity (UHII) (Allegri et al., 2015a). Cities, consisting predominantly of artificial materials, give rise to distinct urban weather conditions that result from the intricate interplay between urban morphology and atmospheric dynamics. Various attributes, such as building height and density, vertical-to-horizontal ratio, vegetation cover, are commonly employed to analyze the impact of urban morphology on overheating processes (Salvati et al., 2017c). Due to their diverse morphological features, cities introduce modifications to atmospheric phenomena, generating localized effects.

The concept of *microclimate* initially emerged within the field of meteorology in the first half of the 20th century and subsequently gained recognition among other disciplines related to urban studies in the latter half. *Microclimatology* was established by investigating the relevance and independent behavior of air layers within the boundary layer, the physical zone where global climate and local urban conditions overlap and mutually influence each other.

Early meteorological comparisons between urban and rural areas provided the first evidence of the disruption caused by the urban climate. Kratzer emphasized that “*the density of built-up areas, the heights of the houses, their distance from one another, the width of the streets and squares, their orientation and their plant life - all of these have their effect on the temperature picture of a city*”. Microclimates “*differ especially in the daily temperature curve, the vertical roughness (wind field disturbances), the topographic position and exposure and above all in the type of actual land use*”. Cities generate a variety of microclimates, subsequently “*One may now speak not only of a specific city climate, but also of a specific climate of broad streets, avenues and squares, and narrow alleyways*” (Kratzer, 1956).

The disruption caused by the urban climate has been defined as Urban Heat Island (UHI) effect, i.e. the air temperature difference between urban and rural areas. As observed by Kratzer, the intensity of the UHI effect exhibits significant variability, with peak temperature differences reaching up to 12°C, and its spatial and temporal distribution also varies (Santamouris et al., 2017). The UHI effect is not uniform throughout a city or during the day and seasons; instead, it encompasses diverse modifications to the urban climate influenced by various factors such as urban morphology, prevailing weather conditions, topography, and specific site characteristics (Salvati et al., 2020).

Oke identified three primary factors contributing to microclimatic changes within urban areas: (1) the interception of short- and long-wave radiation by buildings, (2) reduced long-wave heat emissions due to diminished sky visibility, and (3) increased storage of sensible heat within urban structures (Oke, 1982). Urban climatology extensively investigates the consequences of urban morphology on the alteration of radiative energy balance and the attenuation of heat dissipation through wind-driven turbulence in urban environments. The presence of urban structures and their surfaces facilitates radiative interactions that are absent in rural areas, where radiation is emitted into the atmosphere.

A crucial distinction between the surface energy budgets of rural and urban sites lies in the ratio of latent to sensible heat fluxes. Rural areas predominantly consist of vegetation-dominated surfaces that promote water evaporation, resulting in an increased latent heat flux (Smith and Levermore, 2008). Conversely, a significant proportion of urban surfaces is impermeable due to the prevalent use of non-porous materials, leading to a reduction in the latent heat flux (Grimmond et al., 2010). Figure 1.5 illustrates a comparison of daily energy balances between a representative rural landscape and an urban setting. The land use changes associated with urbanization contribute to increased solar absorption, heat trapping, and anthropogenic heat from human activities, while decreasing evapotranspiration from vegetation.

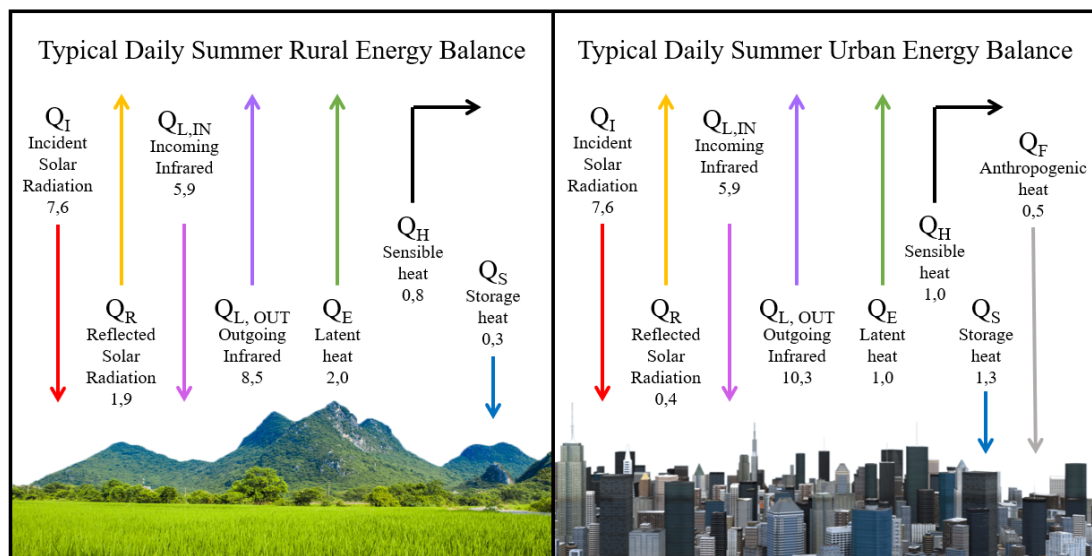


Fig. 1.5 Typical sunny summer day rural (left) and urban (right) energy balance for a location near Houston (Texas, USA). Numerical values refer to kWh/m²/day. Adapted from source³

Investigating urban overheating phenomena presents significant challenges due to the interconnected nature of climate processes across various scales, including meso-climate, local climate, and microclimate. A comprehensive assessment requires a multiscale approach that encompasses (1) analyzing the geographical and topographical features of the city and its surroundings, (2) examining the characteristics of the urban fabric in terms of local climate

³<http://www.ruf.rice.edu/~sass/UHI.html>

zones (Palme and Salvati, 2018; Stewart and Oke, 2012), (3) Evaluating the three-dimensional shape and arrangement of buildings within street canyons, the thermal and optical properties of urban and building materials, and the thermal performance and functionality of buildings (Kolokotroni et al., 2012).

The intricate interplay of these interactions and factors makes it challenging to establish physical models and universally applicable climate guidelines, as each city and its districts possess unique features.

1.5.1.1 Microclimate Models

Researchers employ various simulation approaches to simulate the urban heat island (UHI) effect (Jänicke et al., 2021; Mirzaei, 2015). However, most existing models are not designed to handle the horizontal and vertical complexity of cities.

Microscale Computational Fluid Dynamics (CFD) models offer a detailed representation of urban spaces at a spatial scale of 1 meter and a temporal scale of 1 second. These models solve fluid dynamics equations and capture eddies but require high computational costs (Lauzet et al., 2019).

Meso-scale atmospheric models operate at larger scales of 100 meters to 1 kilometer and rely on parameterizations for eddies. They often utilize information from larger-scale atmospheric models, such as numerical weather prediction models, to define lateral boundary conditions. Meso-scale models can also be coupled with urban canopy models (UCM), which simplify the representation of urban areas and typically treat streets as canyons. The characteristic size in these models is typically around 100 meters (Lauzet et al., 2019).

Another more recent approach involves statistical and machine learning regression models (Venter et al., 2020), which utilize observations (or crowdsourced weather data) from city centers and rural areas to characterize the UHI (Benjamin et al., 2021; Potgieter et al., 2021).

Several literature reviews have examined the benefits and drawbacks of various modeling approaches (Jänicke et al., 2021; Zhou et al., 2022). Nevertheless, no single method has yet achieved both highly accurate results on a broad scale and extended timeframes, all within computationally feasible limits.

1.5.1.2 Climate Change

In addition to the challenges posed by urban microclimate modeling, the escalating effects of climate change further complicate the understanding of UHI dynamics. Land-use changes associated with urbanization have been identified responsible of a mean surface warming rate of 0.27 °C per century (Kalnay and Cai, 2003). Furthermore, the projected increase in summer temperatures due to climate change may further exacerbate the UHI effect in the

near future (Burgstall, 2019). Nevertheless, despite the increasing severity and occurrence of heatwaves (Perkins et al., 2012), there remains a dearth of research concerning the extent of urban overheating variations during these periods and the potential interplay between heatwaves and the Urban Heat Island (UHI) effect. Although studies conducted in Sydney, Australia, demonstrate that heatwave periods can potentially elevate the peak average urban overheating magnitude by 8°C the precise interplay between these two phenomena warrants further investigation (Khan et al., 2020; Nadeem et al., 2022). Such understanding is vital for addressing heat-related mortality in urban areas.

1.5.1.3 Building Energy Simulation

Despite its complexity, understanding the UHI dynamics is essential. Building energy simulation (BES) plays a crucial role in assessing the performance of buildings, particularly in the context of urban environments. However, current approaches mostly rely on historical weather data obtained from historical records of the nearest weather station, typically situated in peri-urban areas (such as airports) or rural regions.

Nevertheless, this approach largely disregards the influence of urban microclimate phenomena (Lauzet et al., 2019). Recent studies have emphasized the inadequacy of solely relying on Typical Meteorological Year (TMY) data from rural weather stations for BES (Palme et al., 2017; Ren et al., 2014). TMY data is typically smoothed and averaged over multiple years, thus failing to capture the impact of the urban environment on local climate dynamics. This oversight becomes particularly problematic when addressing the Urban Heat Island (UHI) effect which significantly impact indoor thermal conditions, leading to increased energy demands for cooling and ventilation in buildings (Boccalatte et al., 2020a; Li et al., 2019b; Santamouris et al., 2015).

These aspects are further examined in Chapter 3 of this dissertation, specifically in **Paper 3**, where the influence of urban microclimate phenomena and the Urban Heat Island (UHI) effect on indoor thermal conditions and energy demands for cooling and ventilation in buildings is thoroughly investigated.

1.5.2 Implications of Urban Morphology and Microclimate on Integrated Solar Systems

Understanding the intricate interrelationship between urban morphology and microclimate (Chapter 3, **Paper 2**) is crucial for accurately characterizing the urban environment and designing energy-efficient urban areas with integrated solar energy systems (Wang et al., 2006). Urban morphological features, including building height, density, orientation, and spatial arrangement, play a pivotal role in shaping the thermal response of urban areas and directly impacting the availability and distribution of solar energy resources (Chapter 4, **Paper 4**).

The influence of urban morphology on solar energy extends beyond simple considerations of geometry and solar access. The geometry and surface characteristics of buildings and urban elements significantly affect the reflection, absorption, and dissipation of solar radiation. Utilizing materials with high reflectivity and low emissivity on roofs and facades can minimize heat gain from solar radiation, contributing to enhanced energy efficiency. Conversely, darker surfaces with higher absorption properties can reduce the reflected component of solar radiation in urban areas, potentially leading to lower power production from solar systems, as discussed in detail in Chapter 3 of **Paper 3**.

Moreover, the Urban Heat Island (UHI) effect has a profound impact on building energy consumption, adding complexity to the accurate prediction of energy demand without considering microclimatic conditions and consequently introducing uncertainties in sizing integrated PV systems.

Urban microclimates serve as critical boundary conditions for the operation of photovoltaic (PV) systems, necessitating precise modeling to forecast PV power output. The susceptibility of PV systems to extreme hot conditions induced by the UHI effect, further exacerbated by heatwaves, is an important aspect that will be extensively explored in Chapter 5 (**Paper 5**) of this dissertation.

In addition to solar energy integration, various urban mitigation strategies, such as implementing green roofs, facades, and utilizing highly reflective and emissive materials, can be employed to mitigate the risk of overheating (Akbari et al., 2001; Alexandri and Jones, 2008; Santamouris et al., 2018, 2011). However, simultaneously considering these mitigation strategies alongside the integration of active solar systems can lead to conflicting demands for urban surfaces. Thus, the development of accurate decision-making strategies becomes crucial to determine the optimal allocation of resources, carefully weighing the prioritization of mitigation strategies against active solar systems or exploring their synergistic integration (Sattler et al., 2017).

1.6 Alternative Solutions Based on Solar Concentration for Urban Industrial Applications

In light of the limited availability of space and the challenges associated with distributed solar power generation systems, a logical solution is to explore centralized solar power generation, specifically by leveraging the expansive surfaces of large commercial and industrial buildings. The integration of solar technologies on building rooftops, while promising, presents inherent complexities due to variations in height, orientation, and shading effects, along with legal considerations related to historical and architectural constraints.

To maximize the utilization of available surfaces in densely populated urban areas, a strategic approach involves the deployment of solar concentration systems. These centralized systems,

particularly well-suited for large commercial and industrial buildings with substantial rooftop surfaces, offer an efficient means of overcoming spatial constraints and increasing the overall efficiency of solar energy utilization.

Solar thermal systems can be categorized into two types: non-concentrating collectors and concentrating collectors (Lovegrove and Stein, 2012). Non-concentrating collectors have an absorber area that intercepts and absorbs solar radiation directly. Concentrating collectors can employ both mirrors and lenses to focus solar radiation onto a smaller absorber area, achieving solar concentration through specular reflection. This process concentrates only the direct solar irradiance if the concentration ratio exceeds 5; otherwise, a portion of diffuse radiation is also concentrated. The concentration ratio is inversely proportional to the angle at which the collector is oriented relative to the sky and the solar disk (Blanco and Santigosa, 2016; Chemisana and Ibáñez, 2010). This approach offers a promising opportunity to optimize the use of urban surfaces and reduce costs. While these systems are highly efficient, they exhibit significant differences concerning installation flexibility (as they can only be integrated onto flat or minimally sloped roof surfaces) and temperature range, which is notably higher than that of conventional flat plate solar collectors used in residential applications. These characteristics make them particularly suitable for commercial and industrial applications (Barbón et al., 2019).

Large commercial and industrial buildings, often located in peripheral regions, have substantial rooftop surfaces and low building heights. These features ensure minimal overshadowing by surrounding structures and a higher incidence of direct solar radiation compared to central urban districts. Therefore, rooftop areas of industrial buildings provide suitable space for accommodating concentrating solar collectors, overcoming the challenges posed by urban density and compactness, as well as the scarcity of large open areas in urban settings (Mekhilef et al., 2011). Moreover, placing these structures in peripheral areas, where buildings are less likely to be subject to architectural heritage protection, appears to be a logical choice, considering their potential significant impact on the landscape (Chemisana and Ibáñez, 2010).

Solar concentration technologies can be broadly classified into two main types: point focus and linear focus systems. Point focus technologies, such as solar power towers and Dish-Stirling systems, work by concentrating solar radiation onto a single focal point. On the other hand, linear focus technologies, like Parabolic Trough Collectors (PTCs) and Linear Fresnel Collectors (LFCs), concentrate solar radiation onto a linear receiver.

1.6.1 Linear Fresnel Collectors (LFCs)

Linear Fresnel Collectors (LFCs) offer several advantages over Parabolic Trough Collectors (PTCs), despite being slightly less efficient due to higher optical losses (Karathanasis, 2019). LFCs have a simpler and lightweight structure, reducing mechanical loads on supporting structures and providing better resistance to wind loads (El Gharbi et al., 2011). Their use of flat or low curvature mirrors significantly lowers manufacturing costs (Montes et al., 2014).

Moreover, LFCs require less energy for tracking, as only the mirrors need to rotate. The separation between the concentrator and the heat transfer fluid (HTF) line eliminates issues related to flexible or rotating connections between concentrators, simplifying maintenance procedures (Sahoo et al., 2012).

One crucial aspect where LFCs excel is in land use efficiency. They have a small aspect ratio, offering the most efficient land use per unit of electric nominal power among all Concentrating Solar Power (CSP) technologies (Chaitanya Prasad et al., 2017; Fossa et al., 2021).

Industrial processes generally require higher temperature ranges than residential applications, making CSP systems like Linear Fresnel Collectors an effective option. Unlike traditional solar systems, such as flat-plate collectors used in residential solar water-heating and space heating, which typically operate below 80°C, LFCs can achieve medium to medium-high temperatures ranging from 100°C to 250°C (Karathanasis, 2019), meeting the demands of various industrial processes (Tasmin et al., 2022). Some of the industrial applications that benefit from these medium-high temperature levels include solar drying, evaporation, distillation, pasteurization, sterilization, seawater desalination, and distributed power generation via the Organic Rankine Cycle (Hongn et al., 2015; Kalogirou, 2003). However, apart from industrial processes, LFCs have demonstrated versatility in other contexts related to non-industrial building integrated applications as domestic water heating (Sultana et al., 2012), absorption air-cooled Solar-GAX cycles (Velázquez et al., 2010), and solar space heating and cooling (Bermejo et al., 2010; Montenon et al., 2017, 2019).

1.6.2 Rooftop-Integrated LFCs Applications

Currently, the integration of Linear Fresnel Collectors (LFCs) into buildings is not widespread, but there are a few notable applications. One significant design within this category is the Compact Linear Fresnel Reflector (CLFC), introduced in 1997 by Mills and Morrison (Mills and Morrison, 2000). The CLFC system is specifically tailored for small to medium-sized applications and is used for direct steam generation. Similar systems have also been developed, such as the Solarmundo LFC (Haeberle et al., 2002) and the commercialized Mirroxx Fresnel reflector by Mirroxx GMBH (Zahler and Iglauer, 2012). The University of Sevilla has also employed a linear Fresnel reflector on a building rooftop as part of a solar/gas cooling plant (Bermejo et al., 2010). Another example is the LF-11 Fresnel collector from Industrial Solar (Industrial Solar, 2023). This LFC is characterized by a conventional primary mirror field, 7.5 m wide, with 11 rows of mirrors, each 0.5 m wide and a receiver composed of a single-tube design with a secondary Compound Parabolic Concentrator (CPC). One specific project involved the installation of LF-11 Fresnel modules at RAM Pharma, a pharmaceutical manufacturing company in Sahab, Jordan. In 2015, 18 LF-11 Fresnel modules were installed to harness solar energy for various applications (Haagen et al., 2015) (Figure 1.6). Another operating rooftop Fresnel plant was installed in July 2016 by the Cyprus Institute (CyI) on a roof in the outskirts of

Nicosia (1.7) (Montenon et al., 2017, 2019). In this instance, the Fresnel collector supplied part of the cooling demand using an absorption chiller and met the heating demand for the Novel Technologies Laboratory (NTL). Air-conditioning was directly supplied using the local solar resource with minimal electric consumption. The primary reflector for this system comprised 288 mirrors, tracking the sun's rays to concentrate them onto the absorber, which collected the heat for further use. The total reflective area covered 184.32 m², deployed on a gross surface of 9 m x 32 m.



Fig. 1.6 LF-11 Linear Fresnel Collectors built by the company Industrial Solar at RAM Pharma, Amman (Jordan). Source: DLR Institute of Solar Research website⁴

⁴https://www.dlr.de/sf/en/desktopdefault.aspx/tabid-9315/16078_read-39375/

⁵<https://energy.cyi.ac.cy/facilities/fresnel/>



Fig. 1.7 Linear Fresnel Collectors installed at the Cyprus Institute (CyI). Source: Cyprus Institute (CyI) website⁵

1.6.3 LFCs Modelling and Geometrical Optimization

However, the integration of Linear Fresnel Collectors (LFCs) on building roofs poses specific challenges. The available roof area is limited, and the presence of building components further restricts the space available for LFC installations. This reduction in available area typically ranges from 21% to 30% of the actual roof area, which has been identified as a significant limiting factor (Barbón et al., 2018; Bryan et al., 2010). The number of LFCs that can be installed on a roof depends on the mirror field area, which can be described in terms of the mirror length, receiver height, and mirror width.

Accurate solar tracking and precise ray tracing modeling are crucial for achieving optimal performance in Linear Fresnel Reflector (LFR) devices. Monte Carlo Ray Tracing (MCRT) simulations are commonly used in the majority of optical performance studies (Rungasamy et al., 2021). These simulations can be performed using in-house developed codes (Fossa et al., 2021) or commercial software such as SolTrace (Wendelin, 2003), Tonatiuh (Blanco et al., 2005), OTSUn (Cardona and Pujol-Nadal, 2020), and Tracer (WANG and LI, 2020).

Geometrical optimization of LFCs plays a fundamental role, especially in applications where minimal land use is essential. This optimization depends on various parameters, including the spacing between mirrors, the receiver height, and the design of the secondary reflector if present. In the context of this thesis, (Chapter 6, Paper 6) focuses on studying the optical performance of an existing Fresnel plant in Morocco in detail. It includes a parametric analysis that varies the spacing between mirrors and the receiver height to investigate their impact on the system's performance. On the other hand, (Chapter 6, Paper 7) proposes new correlations for calculating the Incidence Angle Modifier (IAM), necessary for determining the energy output of the LFC

system. These correlations aim to optimize the computational times of ray-tracing simulations, as year-long hourly analyses can result in large datasets that require extensive post-processing and significantly long computation times.

In conclusion, integrating solar systems on building rooftops in complex urban environments poses challenges, but carefully designed solar concentrating technologies like Linear Fresnel Collectors (LFCs) offer promising opportunities. LFCs exhibit advantages such as improved land use efficiency and cost-effectiveness. They can be successfully integrated into various applications, including industrial processes and large surface buildings such as commercial or academic facilities. Accurate geometrical and optical plant optimization, along with precise ray tracing modeling, are crucial for achieving optimal LFC performance. In this thesis, these topics related to the modeling and optimization of such systems are discussed in the concluding part of the manuscript within the context of alternative solutions for harnessing solar resources in urban environments. This opens up possibilities for future discussions regarding the practical challenges of integrating CSP technologies in urban settings.

Chapter 2

Key Principles of Solar Energy Integration in the Urban Environment

This chapter is based on the publication:

- **Paper 1.** Manni, M., Formolli, M., **Boccalatte, A.**, Croce, S., Desthieux, G., Hachem Vermette, C., Kanters, J., Ménézo, C., Snow, M., Thebault, M., Wall, M., Lobaccaro, G. (2023). Ten questions concerning planning strategies and design principles for solar neighborhoods. *Building and Environment* (submitted)

This publication represents an outcome of active participation throughout my doctoral period as a member of the IEA Task 63 "Solar Neighborhood Planning". This experience significantly enriched my scientific knowledge through collaboration with various experts in the field. Choosing this rather comprehensive publication for the initial chapter was deliberate, as it comprehensively addresses key issues related to solar neighborhood design. Some of the themes mentioned here will be further explored in a more specific and technical manner in the research papers included in subsequent chapters.

Contents

3.1	Mapping the Urban Heat Island at the Territory Scale: an Unsupervised Learning Approach for Urban Planning Applied to the Canton of Geneva	105
3.1.1	Introduction	105
3.1.1.1	Experimental Measurements of Urban Heat Island (UHI)	106
3.1.1.2	Modelling the Urban Heat Island (UHI) at Different Spatial Scales	107
3.1.1.3	Definition of Representative Districts for Microclimate Studies	108
3.1.2	Data Sources, Models and Methods	109
3.1.2.1	The Choice of the Urban Microclimate Model: The Urban Weather Generator	111
3.1.2.2	Validation and Limitations of the Urban Weather Generator Model for Urban Microclimate Analysis	113
3.1.2.3	Urban Data Sources for Urban Parameter Derivation in the Geneva Canton Case Study	113
3.1.2.4	Data Pre-Processing: Calculating the Average Urban Parameters with Tessellation and Spatial Weights	114
3.1.2.5	Inference of Human Activity Levels and Building Characteristics	116
3.1.2.6	Gaussian Mixture Model (GMM) Clustering	117
3.1.2.7	UHII Calculation and Mapping through the Urban Weather Generator and Validation towards Real Data	119
3.1.3	Results	120
3.1.3.1	Clustering Results	121
3.1.3.2	Comparison of Rural and Urban Temperatures using Probability Density Functions	122
3.1.3.3	Average and Maximum Monthly UHI Intensity Comparison among the Identified Clusters	123
3.1.3.4	Average Daily Variation of the UHI Intensity among the Identified Urban Clusters	126
3.1.3.5	Comparison between Predicted and Measured Average UHII Monthly Values	128
3.1.4	Discussion	130
3.1.5	Limitations and Future Perspectives	131
3.2	Best Arrangement of BIPV Surfaces for Future NZEB Districts while considering Urban Heat Island Effects and the Reduction of Reflected Radiation from Solar Façades	132
3.2.1	Introduction	132
3.2.2	Modelling a Solar Urban District	135
3.2.2.1	Building Energy Demand and Solar Radiation Availability: EnergyPlus and the Urban Weather Generator Coupled Approach	136
3.2.2.2	District Photovoltaic Production: Modelling the Temperature and Irradiance Effect on PV Module Performance	139
3.2.3	The Reference BIPV District Test Case	143

3.2.4	Towards the Nearly Zero Energy District: Results and Discussion	145
3.2.5	Conclusions	153

Paper 1

2.1 Ten Questions Concerning Planning and Design Strategies for Solar Neighborhoods

Abstract

Planning of neighborhoods that efficiently implement active solar systems (e.g., solar thermal technologies, photovoltaics) and passive solar strategies (e.g., daylight control, sunlight access through optimized buildings' morphology, cool pavements, greeneries) is increasingly important to achieve positive energy and carbon neutrality targets, as well as to create livable urban spaces. In that regard, solar neighborhoods represent a virtuous series of solutions for communities that prioritize the exploitation of solar energy, with limited energy management systems. The ten questions answered in this article provide a critical overview of the technical, legislative, and environmental aspects to be considered in the planning and design of solar neighborhoods. The article moves from the categorization of "Solar Neighborhood" and the analysis of the state-of-the-art passive and active solar strategies to the identification of challenges and opportunities for solar solutions' deployment. Insights into legislative aspects and lessons learned from case studies are also provided. Ongoing trends in solar energy digitalization, competing use of urban surfaces, and multi-criteria design workflows for optimal use of solar energy are outlined, emphasizing how they generate new opportunities for urban planners, authorities, and citizens. A framework is introduced to guide the potential evolution of solar neighborhoods in the next decade and to support the design of urban areas and landscapes with architecturally integrated solar energy solutions.

Keywords

Solar neighborhood; Active and Passive solar strategies; Urban planning; Solar design, Digitalization.

2.1.1 Introduction

Climate and energy crises have accelerated the urgency to identify and implement tailored solutions to ensure energy security on a larger scale. Clean energy investments and energy efficiency are recommended in the guidelines included in the World Energy Outlook 2022 ([International Renewable Energy Agency, 2022](#)). Nonetheless, existing buildings and neighborhoods have untapped potential for energy efficiency, while the availability of Renewable Energy Sources (RES) in the built environment, and among them the potential of solar energy, is far from being optimally exploited by both public and private investors. Globally, the Sustainable Develop-

ment Goals (SDGs) (United Nations, 2015) and various energy concepts (e.g., zero energy, positive energy) are set up to reduce the environmental impact of anthropogenic activities as well as to secure future energy supply from RES. Making buildings and neighborhoods more energy-efficient through refurbishment and/or new interventions by intensifying the use of RES is therefore fundamental to reduce greenhouse gas (GHG) emissions, towards positive energy districts (PED) and zero emission neighborhoods (ZEN). In that regard, an increased use of solar energy is one of the most effective strategies, as highlighted by the Sixth Intergovernmental Panel on Climate Change Assessment Report (Intergovernmental Panel on Climate Change, 2023).

Interactive platforms (i.e., Mapdwell¹ and Google sunroof²) for rooftop solar yield estimation, which cover most of the national building stock, have been developed in the United States of America. Conversely, in Europe and China, similar tools are spotted or ad-hoc initiatives from virtuous municipalities and regions (Cheng et al., 2020; Thebault et al., 2022). In some cases, these platforms (e.g., Helsinki³ and the Swiss solar cadaster⁴) are capable of extending the mapping of the solar energy potential to the facades. This is especially important at high-latitude locations, where vertical surfaces can harvest high amounts of solar irradiation. Such instruments allow urban planners and architects to support the integration of active solar systems (e.g., photovoltaics, solar thermal) into the urban surfaces (e.g., ground, facades, roofs, street furniture, infrastructures), contributing to increasing the share of the energy production from RES (Jouttijärvi et al., 2022; Lobaccaro et al., 2018a,b; Manni et al., 2020b). In addition, these platforms can also provide useful information on the implementation of passive solar strategies (Fabiani et al., 2019; Konis et al., 2016; Santamouris and Feng, 2018) such as solar gains and daylight access to reduce the energy use in buildings, as well as to improve the inhabitants' indoor and outdoor thermal and visual comfort.

Although the optimal and extensive use of passive and active solar strategies can pave the way towards a more sustainable model of urban development (United Nations, 2022), the rapid growth of cities and urban densification happening in many countries often lacks specific standards regulating the right-to-light (i.e., a legally enforceable right to a reasonable proportion of the natural unobstructed flow of direct solar radiation) at neighborhood level (Kanters et al., 2021; Li et al., 2019a), resulting in reduced efficiency of solar strategies and solar energy potential. In fact, codes and standards that exist about right-to-light in numerous countries primarily regulate sunlight and the insolation of building interiors (Darula et al., 2015; De Luca and Dogan, 2019). Similarly, the right-to-shade (i.e., a right to access shade in public spaces or to shield building portions from direct sunlight) is not legally recognized (Aleksandrowicz et al., 2020; Natanian et al., 2020; Vartholomaios, 2021), and it is rarely mentioned in the literature

¹mapdwell.com

²sunroof.withgoogle.com

³kartta.hel.fi

⁴uvek-gis.admin.ch

despite its importance in hot climates and in connection to the raising frequency of extreme events such as heat waves (Santamouris, 2020).

Achieving a tradeoff between the right-to-light and right-to-shade for a specific combination of location and surface use is among the most complex tasks for urban planners and architects, especially since solar irradiation varies markedly during the day and the year. Such a task has impacts on solar accessibility of outdoor and indoor spaces as well as on performance levels of active and passive solar strategies. On the one hand, right-to-light is usually prioritized in temperate, continental, and polar climate zones, where the energy demand for heating is predominant. On the other hand, the right-to-shade is demonstrated to be more important in zones where the energy demand for cooling is dominant, such as the tropical and dry climate zones. Moreover, planning for shaded areas is fundamental to creating a more livable built environment and mitigating the urban heat island (UHI) effects (i.e., overheating of the urban surfaces). However, there are cases where both optimal exposure to sunlight (resulting from right-to-light) and low surface temperature (resulting from right-to-shade) are required, such as for building integrated photovoltaic (BIPV) systems. BIPV systems need high solar accessibility to efficiently generate electricity, but the absence of shading in the surroundings contributes to increasing the air temperature, thus worsening performances. Therefore, it becomes more and more important to provide country-specific standards for the application of active and passive solar design strategies, as well as to find a balance of right-to-light and right-to-shade already in the early urban planning phases to avoid pitfalls and common mistakes (i.e., complex overshadowing effect in the built environment and uncontrolled mutual solar reflections among buildings and the ground) in the development of existing and/or new neighborhoods. Finally, long-term temporal fluctuations of solar energy due to climate changes are also to be considered. In fact, extreme weather events are expected to increase in both frequency and intensity, by impacting the identification of the tradeoff between the right-to-light and right-to-shade. For example, heat waves can result in higher solar irradiance due to the low presence of clouds, on the one hand; while increasing the air temperature and accelerating the aging rate of solar active systems (Oka et al., 2020), on the other hand.

In this framework, among the scientific studies on solar energy planning and design, the outcomes from the International Energy Agency (IEA) Solar Heating and Cooling (SHC) Task 51 “Solar Energy in Urban Planning” (2013-2017)⁵ and the ongoing SHC Task 63 “Solar Neighborhood Planning”⁶ underline the need to investigate the neighborhood scale by looking at multiple solar-related aspects ranging from active and passive solar strategies, design concepts, and energy systems, to economic aspects, societal and environmental impacts, stakeholder and researchers’ engagement and citizens participation. The ambition is to support key actors (e.g., developers, property owners/associations, architects, urban planners, municipalities, institutions)

⁵task51.iea-shc.org

⁶task63.iea-shc.org

towards the implementation of long-term planning and design solutions for neighborhoods that prioritize the exploitation of solar energy, with limited energy management systems.

The hereby ten questions article aims to identify the existing barriers and challenges in solar energy planning and to present the most common strategies, methods, and approaches for solar neighborhood planning and design through the insights from developers, architects, consultants, researchers, urban planners, municipalities, and other institutions. In addition, case studies and lessons learned are documented to show practices of successful implementations in solar neighborhoods. The research objectives of the study are: (i) to provide a clear definition of the solar neighborhood concept with respect to other existing neighborhood classifications (i.e., ZEN, PED), (ii) to outline recommendations and practices to design solar neighborhoods by identifying solar related variables, constrains and potential solutions, and (iii) to shape the future research trajectories and technical aspects to take into account for solar neighborhood planning and design, based on identified challenges and opportunities, with insights on the legislative agenda. The hereby presented study has a large impact on the SDGs from the United Nations (UN) (United Nations, 2015) by contributing to the advancement of the ones listed in Figure 2.1.








	SDG1 - No Poverty Active solar strategies for energy production that are proposed in this study for solar neighborhoods contribute to reducing fuel poverty, thus advancing SDG1.
	SDG2 - Zero Hunger Initiatives concerning urban farming and local food production within solar neighborhoods permit improving access to food resources for everyone, contributing to SDG2.
	SDG3 - Good Health and Wellbeing Achievements from this study allow for enhancing human indoor and outdoor comfort conditions within the solar neighborhood environment, improving human health and wellbeing.
	SDG7 - Affordable and Clean Energy Clean energy production and energy self-sufficiency are two important aspects in the design of solar neighborhoods, as well as to accomplish the SDG7.
	SDG9 - Industry Innovation and Infrastructure The present study can impact industry, innovation, and infrastructure, particularly with regard to active and passive solar solutions.
	SDG10 - Reduced Inequalities The study proposes a wide range of solutions that can be implemented in solar neighborhoods in relation to the climate context. Therefore, every country can apply solar neighborhood design principles to achieve carbon neutrality and energy self-sufficiency, regardless of the economic context, thus reducing inequalities.
	SDG11 - Sustainable Cities and Communities The multi-criteria analysis for solar neighborhood design, which is outlined in this study considers economy, environmental, energy, and social variables through specific performance indicators. This approach to neighborhood planning enables more sustainable cities and communities.
	SDG13 - Climate Action Design and technology solutions identified in this work can contribute to (i) mitigating urban overheating; (ii) decreasing the amount of carbon emissions in the atmosphere, and (iii) compensating the carbon footprint of the neighborhood by generating clean energy from RES.
	SDG15 - Life on Land The design principles characterizing the solar neighborhood positively impact biodiversity, reintroducing animal species in areas they used to inhabit before human-induced transformations.

Fig. 2.1 List of the UN SDGs partially or fully addressed by the current study.

The article is structured around ten questions concerning solar neighborhood planning and design (Figure 2.2).

It moves from the definition of the solar neighborhood concept (section 2.1.2.1) to the identification of the aspects to consider in a multi-criteria analysis for neighborhood design (section 2.1.2.2). Then, the active and passive strategies used to exploit the solar energy potential are described (section 2.1.2.3) besides representative and successful solar neighborhood design experiences at various latitudes (section 2.1.2.4). A focus on challenges in deploying and implementing passive (section 2.1.2.5) and active (section 2.1.2.6) solar strategies follows. The digitalization of the built environment and its potential to support the planning of solar neighborhoods is discussed (section 2.1.2.7), while the impact of solar neighborhoods on the total environment, here defined as the built, natural, and social environments where a community grows, lives, works, and ages, is also assessed (section 2.1.2.8). The last two questions look into the future of solar neighborhoods by identifying the needs in the legislative agenda (section 2.1.2.9) and the main aspects (e.g., architectural integration of solar systems, energy flexibility, digitalization techniques) to be developed in the future (section 2.1.2.10).



Fig. 2.2 Visualization of the ten areas concerning solar neighborhood planning and design strategies treated in this article.

2.1.2 Ten questions (and answers) concerning solar neighborhoods

2.1.2.1 What are Solar Neighborhoods?

While the main neighborhoods' definitions currently in use are based on the achieved emission and energy targets (i.e., zero emission neighborhood, positive energy district), the categorization of neighborhoods proposed in this study is identified with respect to the exploited RES. Such a definition is determined by upscaling (i.e., from the building to the neighborhood scale) and adapting the classification proposed by [Lund et al. \(2011\)](#) for zero-emission buildings (ZEBs), which distinguishes four types of ZEBs in reference to energy demand and installed RES typology (e.g., a Wind-ZEB is a ZEB with relatively low electricity demand and on-site active exploitation of wind). Following this, a solar neighborhood is primarily a neighborhood, hence an urbanized area either with a single function (e.g., residential neighborhood, commercial district) or with a mix of human activities and interactions (e.g., dwellings, workplaces, shops,

civic buildings, parks), in which the full and optimal exploitation of the sun is prioritized. It can be part of a high-, medium-, or low-density urban area, a remote rural development, or it can represent an isolated community (Formolli et al., 2022). Further, solar neighborhoods exist as virtual entities in which datasets of monitored solar and energy variables (e.g., solar energy production, solar energy gains, solar energy potential, level of illuminance, and sunlight exposure) are stored (Manni et al., 2023; Øgaard et al., 2021) and processed with specific decision-making tools (e.g., energy district distribution, energy price) to predict short-, medium-, and long-term scenarios and to identify efficient management strategies for active and passive solar solutions (Jouttijärvi et al., 2023; Lorenz and Heinemann, 2012).

Planning and design strategies for a solar neighborhood can be applied to both new and existing urban development areas and can contribute to achieving positive energy budgets and carbon neutrality in cities. In this regard, the interactions between solar neighborhoods (SN), zero-emission neighborhoods (ZEN), and positive energy districts (PED) are paramount (Figure 2.3). This study exclusively focuses on the SN and its sub-domains, which are numbered from 1 to 4 in Figure 2.3 while the other neighborhood types, such as ZEN and PED, are out of the scope of this work.

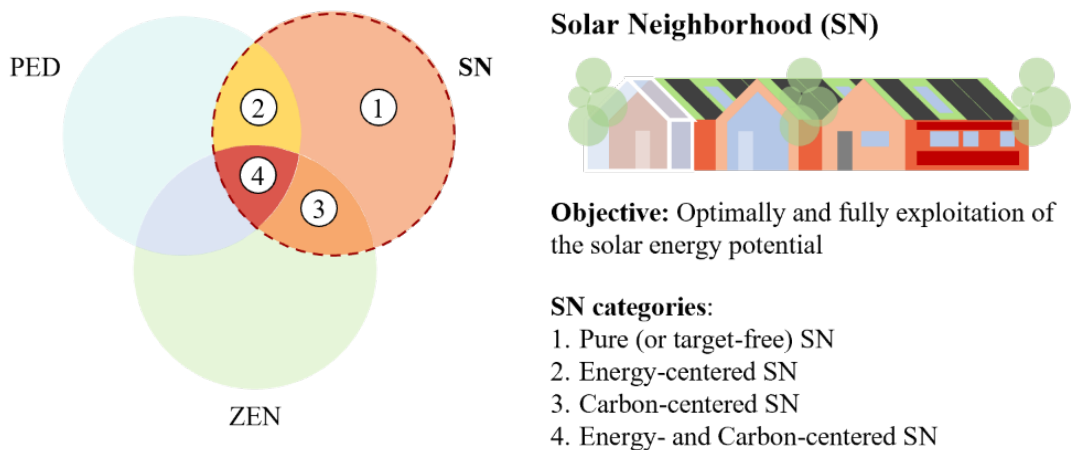


Fig. 2.3 Interaction between solar neighborhoods and other neighborhood concepts, such as zero-emission neighborhoods and positive energy districts, existing in the literature (Baker et al., 2022; Brozovsky et al., 2021; Lund et al., 2011).

Therefore, the following categorization is proposed for the solar neighborhoods:

- **Pure (or target-free) solar neighborhoods** (i.e., category 1 in Figure 2.3) are communities that prioritize the exploitation of solar energy, with limited energy management systems. Buildings' morphology and relations as well as building envelope and technological/material features are designed to maximize the efficiency of passive and active solar strategies. Furthermore, these solar neighborhoods are characterized by a microclimate that enables adequate thermal and visual comfort, and high life standards, both indoors and outdoors.

- **Energy-centered solar neighborhoods** (i.e., category 2 in Figure 2.3) implement the use of active solar strategies through advanced energy storage and management systems to enhance energy flexibility, resilience to energy price fluctuations, and independence on energy imports. The low energy demand of these neighborhoods is entirely met by on-site renewable energy mix, in which solar energy plays a major role along with the other RES such as wind and geothermal.
- **Carbon-centered solar neighborhoods** (i.e., category 3 in Figure 2.3) prioritize the application of passive solar strategies and the use of low-carbon technologies/materials to improve the energy efficiency of the building stock while reducing its carbon footprint. Additionally, active solar systems are implemented in these neighborhoods to minimize the reliance on fossil fuels and achieve carbon neutrality.
- **Energy- and Carbon-centered solar neighborhoods** (i.e., category 4 in Figure 2.3), present characteristics proper of both energy- and carbon-centered solar neighborhoods achieving energy and carbon targets.

Measurable criteria or thresholds for solar neighborhoods are still to be defined and represent a knowledge gap. Nonetheless, several criteria are worth further investigation to differentiate between a solar neighborhood and other neighborhood typologies. For example, the share of energy generated from the solar source, the amount of self-consumed energy from photovoltaics (PVs), and the improvement in visual/thermal comfort achieved through passive solar strategies.

In solar neighborhoods, buildings' morphological forms and relations (i.e., building height - H, distance between buildings or width of the street - W) are firstly optimized by guaranteeing either access to or shading from sunlight, accordingly to the specific needs (e.g., direct access to sunlight is preferable for PV modules, not always for pedestrians (Melnikov et al., 2022; Natanian et al., 2020) and climate context (e.g., right-to-shade can be more relevant than right-to-light in extremely hot climate zones). Besides the neighborhood's layout, the application of passive solar design solutions and the optimal localization and installation of active solar systems integrated (e.g., BIPV) or added (i.e., building added photovoltaics) into urban surfaces (e.g., building envelope, shelters, ad-hoc structures, etc.) are prioritized aspects in solar neighborhood planning. Active and passive solar strategies and technology-oriented solutions implemented at multiple scales, ranging from building to neighborhood and urban development scale, are beneficial for outdoor and indoor thermal and visual comfort, air quality, energy demand, and reduction of GHG in the atmosphere. This approach guarantees future-proof cities, independent of energy imports and fossil fuels (Ritchie et al., 2022). In addition, it pursues long-term solar accessibility for creating a more sustainable, livable, and healthy built environment. In solar neighborhoods, challenges arise around the competing uses of urban surfaces (see section 2.1.2.2) and around the implementation of solar strategies in high-density settlements.

Another key aspect in planning solar neighborhoods, particularly in mixed-use districts, is the identification of synergies among the human activities' schedule and the energy management strategies to minimize the energy consumption through 'peak shaving' (i.e., coupling residential and office buildings lead to more homogenous distribution of the energy consumption throughout the day) (Natanian, 2023). Besides this, energy storage technologies (e.g., phase change materials, electric batteries, seasonal thermal energy storage) (Finck et al., 2018; Gupta et al., 2021; Schill, 2014), energy distribution (e.g., smart grid, flexibility grid) (Mathiesen et al., 2015; Paatero and Lund, 2007), and sector coupling concepts (e.g., power-to-heat, power-to-mobility, power-to-hydrogen) (Manni and Nicolini, 2022; Mendoza et al., 2015) represent important solutions to enhance the energy flexibility of solar neighborhoods towards a match between energy delivered and the energy load profiles in terms of place, time, and quantity. However, such energy management characteristics are more peculiar to both energy-centered solar neighborhoods and energy- and carbon-centered solar neighborhoods than pure solar neighborhoods and carbon-centered solar neighborhoods. The latter, on the contrary, are primarily characterized by limited energy management systems.

2.1.2.2 Which aspects should be considered in the planning and design process of a solar neighborhood?

Solar neighborhoods are complex built environments to plan and design. Numerous design variables (e.g., urban morphology, installation/integration of PVs, location of passive heating/cooling systems) involving different spatial domains (e.g., indoor, building envelope, and outdoor) require to be addressed simultaneously due to their impact on a wide range of aspects (e.g., energy, economy, environment, society, microclimate, user comfort) and related metrics (Formolli et al., 2023). The main metrics to consider in solar neighborhood planning and design are presented in Figure 2.4 and grouped into four categories - geometrical, latitudinal, external climatic, and internal climatic - depending on the complexity of the input data, as in Czachura et al. (2022). Figure 2.4 highlights that the metrics are not limited to solar. In fact, several studies on multi-criteria approaches to solar planning (Delgarm et al., 2016; Naboni et al., 2019; Stamatakis et al., 2016; Yu et al., 2015) showed that focusing exclusively on solar-related metrics (e.g., solar potential, daylight accessibility, solar heat gains), often provides a partial view.

In this regard, the competing uses of an urban surface in a solar neighborhood are exemplary. The competing use of surfaces arises when defining the way to exploit the solar energy potential of the available urban surfaces (Croce and Vettorato, 2021). Indeed, the same surface can have multiple potential usages (e.g., green surface, PV surface, highly reflective surface), and the same strategy can impact different metrics at different scales (e.g., indoor daylighting, solar heat gains, energy generation). For example, solutions to enhance access to daylight also increase solar thermal stress, worsening the users' thermal comfort on hot days if the solar radiation

	Geometrical	Latitudinal	External Climatic	Internal Climatic
Input data	- Urban layout - Site and buildings' orientations - Site layout and form - Urban density	- Urban layout - Site layout and form - Latitude location	- Urban layout - Site layout and form - Latitude location - Local weather	- Urban layout - Site layout and form - Latitude location - Local weather - Buildings' geometry - Materials' properties - Buildings' functions
Metrics	<u>Solar</u> - Sky view factor - Sky exposure factor - Vertical sky component <u>Morphology</u> - Floor-to-area ratio - Volume-to-area ratio - Surface-to-volume ratio - Height-to-width ratio - Window-to-wall ratio - Open space ratio - Floor space index <u>User comfort</u> - Biophilia factor <u>Society</u> - Visual impact	<u>Solar</u> - Area of permanent shadow - Two-hour area - Direct sunlight - Shading mask - Daylight factor <u>Energy</u> - Grid capacity	<u>Solar</u> - Annual sunlight hours - Solar potential <u>Energy</u> - Energy generation - Storage capacity <u>Environment</u> - Biodiversity <u>Climate</u> - Urban heat intensity - Microclimate variations	<u>Solar</u> - Daylight autonomy - Illuminance - Solar heat gains - Spatial distributing glare <u>Energy</u> - Energy use for heating and cooling - Energy use for lighting - Energy self-consumption - Energy coverage - Specific yield <u>Environment</u> - Carbon emissions - Emission balance <u>Economy</u> - Capital expenditures - Operating expenditures - Payback period - Profitability - Net present value <u>User comfort</u> - Thermal comfort - Visual comfort - Air quality <u>Society</u> - Fuel poverty

Fig. 2.4 Taxonomy of metrics in solar neighborhood planning divided into the four categories identified by Czachura et al. (2022)

is uncontrolled through solar shading devices. Similarly, installing solar panels on roofs or facades to implement solar energy generation may cause unwilling solar reflections in the built environment and alter the radiative properties of urban surfaces, thus influencing both the visual comfort at the pedestrian level and the microclimate (Brito, 2020; De Luca et al., 2021). Furthermore, competing uses could arise between solar strategies and other interventions. In this regard, the key urban actors usually opt for solutions that enable the direct and immediate increase of the economic value of buildings and neighborhoods' properties (e.g., new additional volumes/stories, terraces, balconies). However, they neglect that such actions contribute to generating high-density settlements where a large portion of building façades, pedestrian paths, or public spaces may be partially or totally shaded from direct sunlight, compromising the performance of the urban surfaces, single or group of buildings, and the quality of private and public spaces. Therefore, when it comes to solar neighborhood planning and design, there is a need for a holistic approach (Florio, 2018; Gupta et al., 2021; Strzalka et al., 2012; Thebault et al., 2020, 2022) to address several aspects simultaneously by taking into account the following criteria:

- **Energy criteria:** e.g., energy production, energy demand for heating/cooling, energy demand for lighting, storage capacity, grid capacity;

- **Economy criteria:** e.g., capital expenditures, operating expenditures, payback period of the investments for the implemented solar strategies;
- **Environmental criteria:** e.g., carbon emissions, emissions balance (i.e., trade-off between compensated/offset emissions and emissions that are directly or indirectly caused by the neighborhood);
- **Social criteria:** e.g., visual impact, accessibility, stakeholder engagement, community participation, affordability, and equity;
- **User comfort criteria:** e.g., air quality, visual and thermal indoor and outdoor comfort.

This list of criteria is not exhaustive and depends on the constructive dialogue between stakeholders (e.g., public authorities, sociologists, social scientists, urban planners, architects, and engineers) and researchers; and how they are able, through a holistic approach, to converge their interests and objectives by prioritizing some aspects against others. For example, a private investor would mainly focus on economic indicators, whereas a municipality would rather find a balance between environmental, social, economic, and energy benefits.

It is crucial to determine the design objectives and to identify potential competing uses of urban surfaces from the early stage of the planning process (Croce et al., 2022; Croce and Vettorato, 2021). As proposed by Formolli et al. (2023), this leads to include multiple spatial domains (e.g., indoor, building envelope, and outdoor) as well as multiple scales (e.g., building, neighborhood, urban development) in the solar neighborhood design workflow. In fact, design solutions and technologies applied at different spatial domains and/or scales can influence each other, not necessarily in a negative way. For example, indoor daylight accessibility is influenced by the mutual inter-building solar reflections and/or shadowing effects from the surrounding built environment. Similarly, the energy production from a BIPV façade (building scale) is determined by its solar potential (neighborhood scale). Also, the coatings applied to the building envelope contribute to determining both the indoor and outdoor environment, with impacts, among others, on both the microclimate and the building energy demand (Formolli et al., 2021; Lobaccaro et al., 2017, 2019a). In the planning and design process of a mixed-use solar neighborhood, activities taking place within the buildings are defined based on solar availability. In this regard, buildings with good exposure to direct sunlight during the morning hours are selected to be schools and offices, while buildings that are well-exposed to sunlight during the afternoon hours are suitable for housing. In that regard, Natanian (2023) has developed a two-phase workflow that aims to optimize mixed-use district designs in hot climate zones to reach energy balance and environmental performance. Such workflow allows supporting diverse morphological configurations by optimizing solar accessibility towards zero energy and liveable districts.

Therefore, implementing an inter-disciplinary, holistic, and multi-criteria approach, which addresses the different competing uses of urban surfaces and their impacts on the total environ-

ment (see section 2.1.2.8) by operating at multiple scales and spatial domains, represents the key-approach of the solar neighborhood planning and design. Furthermore, such an approach facilitates repeatability and avoids common urban planning mistakes encountered by others in an urban densification process (Good et al., 2014) while fostering interaction between researchers and city authorities (Lindkvist et al., 2019; Xue et al., 2021) as well as citizens' engagement (Collins and Lindkvist, 2022).

2.1.2.3 Which are the passive and active solar strategies in solar neighborhoods?

In solar neighborhoods, passive and active solar strategies are implemented at different scales to develop climate-responsive settlements able to face the current and future short-, mid- and long-term climate conditions. At the neighborhood scale, the passive solar strategies leverage the inherent properties of sunlight and the neighborhood's design to improve thermal and visual comfort, while reducing energy consumption for heating, cooling, and lighting (Stevanović, 2013).

The **passive solar strategies** applied at the **neighborhood scale** contribute to shaping the district morphology and massing (PS1 in Figure 2.5), determining, among the others, buildings height (H), inter-building distance (i.e., width of the street – W), aspects ratio H/W (PS2), and district orientation (PS6). These together with the layout and pattern (PS5) of a solar neighborhood are influenced by the latitude and local climate, and they determine the solar energy potential of the urban surfaces (Figure 2.5).

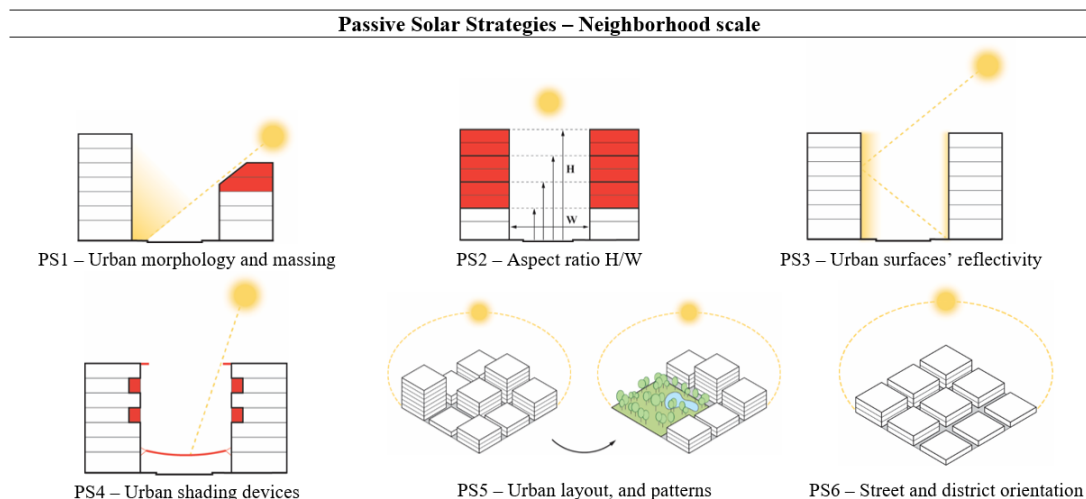


Fig. 2.5 Passive solar strategies applied to the planning and design at the neighborhood scale

At the **building scale**, several **passive solar strategies** can be applied (Figure 2.6). Building form, morphological type (e.g., courtyard, high-rise), and thermal mass (PS7 in Figure 2.6) alongside room depth and window-to-wall ratio (PS9) determine the penetration of natural light into the building's interiors. In those cases where the building morphology is particularly

constrained (e.g., existing and historical neighborhoods) as well as in high-rise neighborhoods, which constitute the common tendency of the urban growth happening today in cities, technological solutions such as light chimneys and tubular skylights (PS8) can be implemented for passive daylight control indoors (Zaręba et al., 2022).

Among the passive solar strategies applied at the building scale, there are the use of windows and glazed walls (PS9), massive walls (PS7) (e.g., Trombe walls) (Hu et al., 2017; Saadatian et al., 2012), and sunspaces or solar greenhouses (PS10). These can act as direct-gain passive systems while allowing – in the case of windows and glazed surfaces – appropriate levels of daylight to be achieved. Especially sunspaces and solar greenhouses represent valuable solutions in high-density settlements, by enabling the creation of additional covered spaces, although exposed to high levels of solar radiation and a wide temperature range (Asdrubali et al., 2012).

All these strategies as well as the distribution of functions and program (PS11) require a proper design, that considers the local climate (e.g., air and surface temperature, humidity, air pressure), urban complex phenomena (e.g., inter-building reflections, overshadowing), and urban surfaces' thermal properties, to avoid indoor overheating and outdoor thermal stress (Cuce and Riffat, 2015; De Luca et al., 2021; Gupta and Tiwari, 2016). In solar neighborhoods, municipalities should support the design process by providing house-owners with guidelines and recommendations about surface uses.

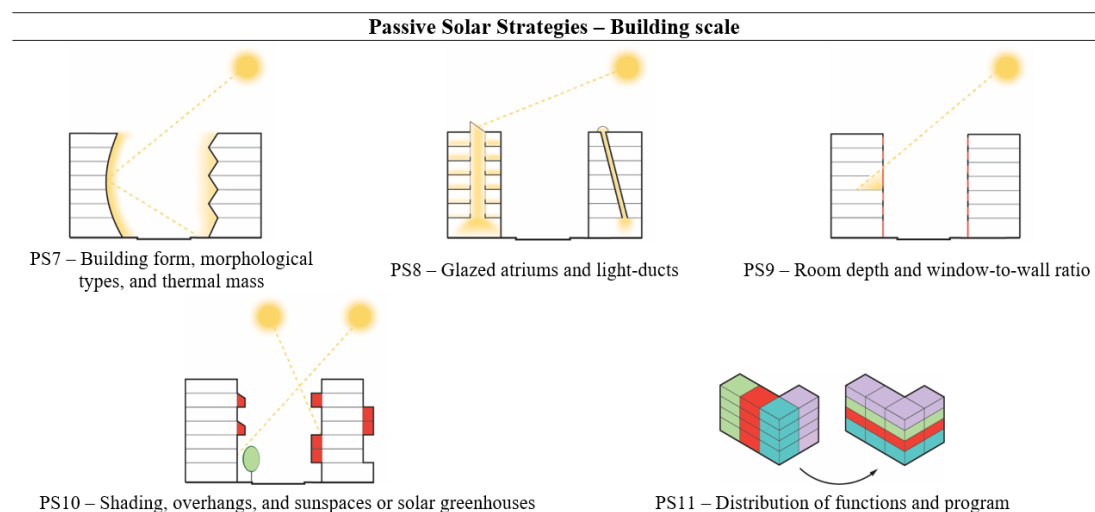


Fig. 2.6 Passive solar strategies applied to the planning and design at the neighborhood scale

Shading systems (PS10) are often coupled to the glazed areas as heat avoidance systems, aiming at protecting from direct solar radiation and reducing cooling energy use and peak loads. These solutions permit enhancing the buildings' energy efficiency and indoor thermal comfort while lowering carbon emissions (Bhamare et al., 2019). Shading devices can also be installed within neighborhoods (PS4 in Figure 2.5) (e.g., projecting roofs, lodges, shade sails) to avoid the thermal stress of pedestrians. This is particularly important in climate change hotspots with an enhanced warming trend like the Mediterranean region (Cos et al., 2022).

The use of **other passive strategies** includes materials and solutions that interact with solar radiation to control surface temperature and the related impacts on the outdoor and indoor environment (Figure 2.7). This is the case, for example, of conventional cool materials (light-colored and colored cool materials (Santamouris et al., 2011)), thermochromic pigments (Hu and Yu, 2019), retroreflective materials (Castellani et al., 2017; Fabiani et al., 2019; Morini et al., 2017; Rossi et al., 2015), photocatalytic materials (Kyriakodis and Santamouris, 2018), phase change materials (Lu et al., 2016; Pisello et al., 2017), photoluminescent paints (Levinson et al., 2017; Rosso et al., 2019), and supercool materials (i.e., engineered surfaces exploiting Passive Daytime Radiative Cooling (Lim, 2020; Santamouris and Feng, 2018)). These solutions can be used on pavements (PS12N in Figure 2.7) or building envelopes (PS12B) and are increasingly important in hot arid regions where urban greeneries might struggle. In solar neighborhoods, the most suitable surfaces are identified through simulations by considering complex phenomena that can either limit the materials' effectiveness or cause undesired drawbacks (e.g., glaring, excessive cooling in winter, etc.).

Another relevant element interacting with solar radiation within solar neighborhoods is urban greening. The vegetation can be located both on ground spaces (PS14N) (e.g., private and public parks, tree-lined streets) and on the building envelope (PS14B) (e.g., green roofs, vertical greening systems, balcony gardens) (Raji et al., 2015). Urban greening contributes as a passive technique for energy saving, through (i) evaporative cooling, (ii) thermal insulation, and (iii) shadow provided by the vegetation layer [65]. A green façade/roof can reduce the indoor temperature by absorbing solar radiation, leading to energy savings for cooling in summer conditions. However, these solutions should be designed in such a way that solar heat gains through the building envelope are not hindered in winter to avoid increasing the heating demand (Aleksandrowicz et al., 2017; Bowler et al., 2010; Vuckovic et al., 2017). Urban greening can also aim at the provision of food within the neighborhood boundaries, as in the case of urban agriculture (Azunre et al., 2019).

Finally, solar radiation influences the cooling capacity of water bodies (PS13), both natural and artificial, and evaporative techniques (e.g., mist spraying, water curtains, watering techniques) (Santamouris et al., 2016). This also applies to evaporative pavements (e.g., permeable, porous, pervious, and water-retaining pavements), designed to be applied on ground surfaces to retain water for evaporative cooling purposes and prevent storm-water runoff (Qin, 2015).

Active solar strategies are implemented at **neighborhood** and **building scale** (Figure 2.8) to exploit solar irradiation to generate either electricity or thermal energy through solar active systems (AS1B and AS1N in Figure 2.8) such as PV, solar thermal (ST), and hybrid photovoltaic/thermal systems (PV/T). Heliostat and sun-tracking reflector systems (AS2) for active daylight control and for concentrating and directing sunlight onto surfaces that would otherwise be shaded are also labeled as active solar strategies, requiring electric power to function. These systems are particularly useful in highly dense built environments (Fernández-Ahumada et al., 2022).

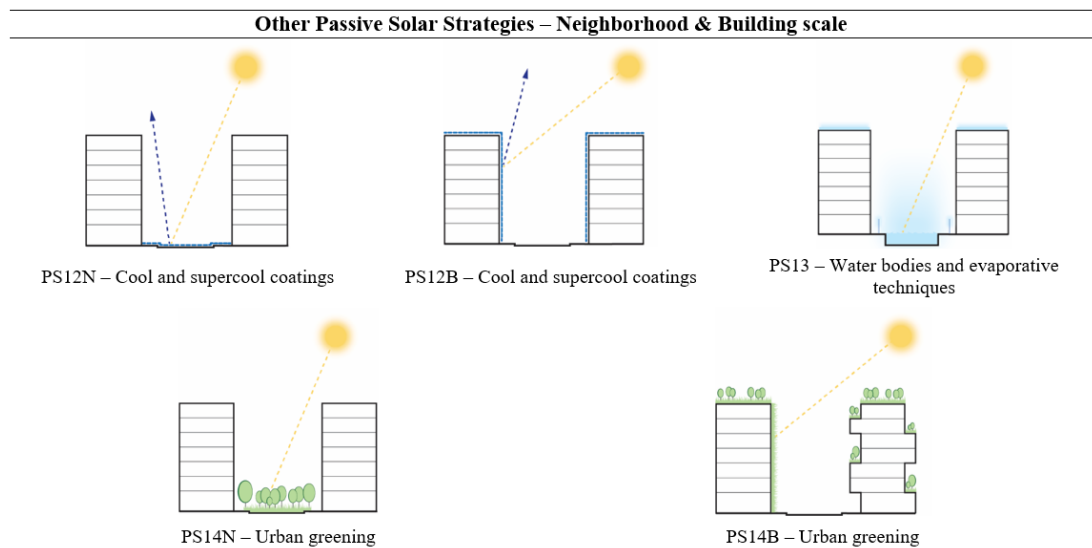


Fig. 2.7 Other passive solar strategies applied to the planning and design at the neighborhood and building scale

Inter-building areas, pavement and roads, barriers, and urban furniture represent suitable surfaces for solar energy generation at neighborhood scale (AS1N). PV modules can be added to pavements and roads, while asphalt solar collectors are being developed to employ the solar energy absorbed by the pavement for heating/cooling applications (e.g., melting snow on roads (Mirzanamadi et al., 2020), building heating, pavement cooling (Ahmad et al., 2019; Johnsson and Adl-Zarrabi, 2020)). In addition, PV road barriers, PV carports, PV-integrated urban furniture (e.g., street lighting, bus shelters, benches (Premier et al., 2022)), and solar-powered urban artworks are being tested to exploit the energy generation potential within the urban fabric (Ahmad et al., 2019).

Furthermore, active solar strategies include solutions for individual buildings. In fact, solar panels can be exploited in buildings (AS1B) as an additional external layer, or integrated into the envelope as specific architectural systems, like BIPV (Jelle and Breivik, 2012; Maurer et al., 2017) and building-integrated solar thermal systems (Buker and Riffat, 2015). On façades, these might be added as a cladding element on opaque surfaces, integrated into curtain wall systems, or integrated into windows (Sun et al., 2019) and other transparent architectural elements (Maturi and Adami, 2018; Shukla et al., 2017). On roofs, PV modules and ST collectors can be added to the outer surface (Maturi and Adami, 2018) or substitute the entire technological system, while PV-enhanced roof tiles and shingles allow replacing the external layer. Semi-transparent solutions can also be used on roof covering (Li et al., 2009). Among the PV technologies, the deployment of bifacial PV (BPV) and PV-integrated shading devices (PVSD) (Palmero-Marrero and Oliveira, 2006; Taveres-Cachat et al., 2019) is gaining more and more attention. The former is applied in both built environments and landscapes, especially at high latitudes where the sun geometry represents an advantage for the optimal exploitation of vertical BPV. The latter

has a twofold function, combining energy generation with the advantages of a shading device (e.g., protecting from natural light in summer, enabling solar heat gains in winter) (Zhang et al., 2018).

PV/T systems⁷ enable energy generation and active heat recovery with liquid (i.e., water-cooled PV/T) or forced air (i.e., air-cooled PV/T), in either a closed or open loop respectively (Al-Waeli et al., 2017). These systems are particularly suitable for applications with limited roof space (i.e., high-rise buildings), as their energy production per unit surface area is higher than that of side-by-side PV and ST, and the manufacturing and installation costs are lower (Abdelrazik et al., 2022). In solar neighborhoods, the share of PV, ST, and PV/T is determined at the neighborhood level depending on grid capacity and the exploited heating fuel, among the others.

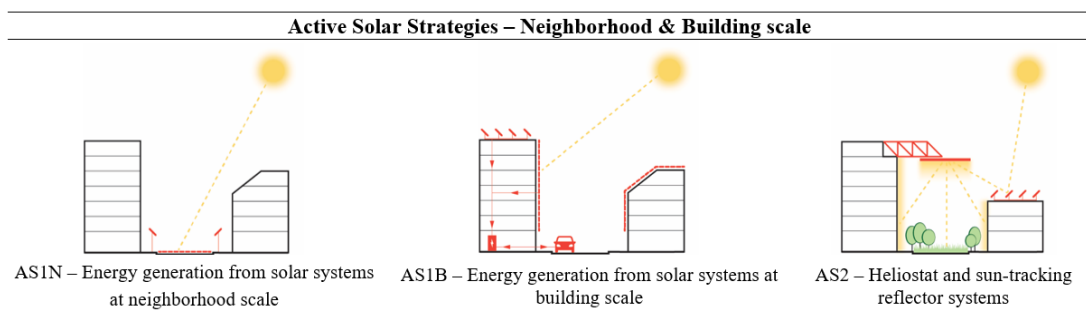


Fig. 2.8 Active solar strategies applied to the planning and design at the neighborhood and building scale

When it comes to densified urban areas, solutions that **integrate active and passive solar strategies** on the same surface should be prioritized. In this regard, solar panels and greening - often in competition - can work in synergy, as in the case of bio-solar or multifunctional solar-green roofs (Ciriminna et al., 2019; Shafique et al., 2020) and façade (Penaranda Moren and Korjenic, 2017). These solutions can, on one side, provide potential habitats for certain plant and insect species and increase plant diversity, and, on the other side, increase the efficiency and useful lifetime of solar panels thanks to the localized reduction of air temperature caused by vegetation (Gasparatos et al., 2017; Schindler et al., 2016). Several other solutions are also being developed: vertically mounted BPV can be combined either with green roofs (Baumann et al., 2019) or highly reflective materials (Altan et al., 2019), while solar panels are being coupled to vertical farming through the novel concept of productive façades (Tablada et al., 2018).

2.1.2.4 How are the passive and active solar strategies applied in solar neighborhoods?

The optimal implementation of passive and active solar strategies is fundamental in solar neighborhoods. This process requires considering all spatial scales, ranging from urban regional and urban development scale, down to neighborhood and building scale, and their inter-dependency (Figure 2.9). For example, the optimized solar accessibility of buildings' facades and the indoor

⁷task60.iea-shc.org

daylighting distribution (i.e., building scale) can be achieved only if the site plan allows natural light penetration into the urban canyon (i.e., neighborhood scale). The implementation of solar strategies determines, among others, (i) the urban layout and morphology at the urban development scale, (ii) the buildings' block configuration, orientation, volume, and form at the neighborhood scale, (iii) the facade exposure, the room depth, and the window-to-wall ratio at the building scale. Consequently, there is a wide range of factors to be considered during the planning process (see section 2.1.2.2). This sets energy planning apart from conventional urban planning, which typically begins with assessing the spatial characteristics of an area and later addresses energy-related issues. Given the complexity of this process, it necessitates the integration of various technical and non-technical perspectives, particularly considering the lengthy timeline associated with the planning process (Lindkvist et al., 2019; Nielsen et al., 2019).

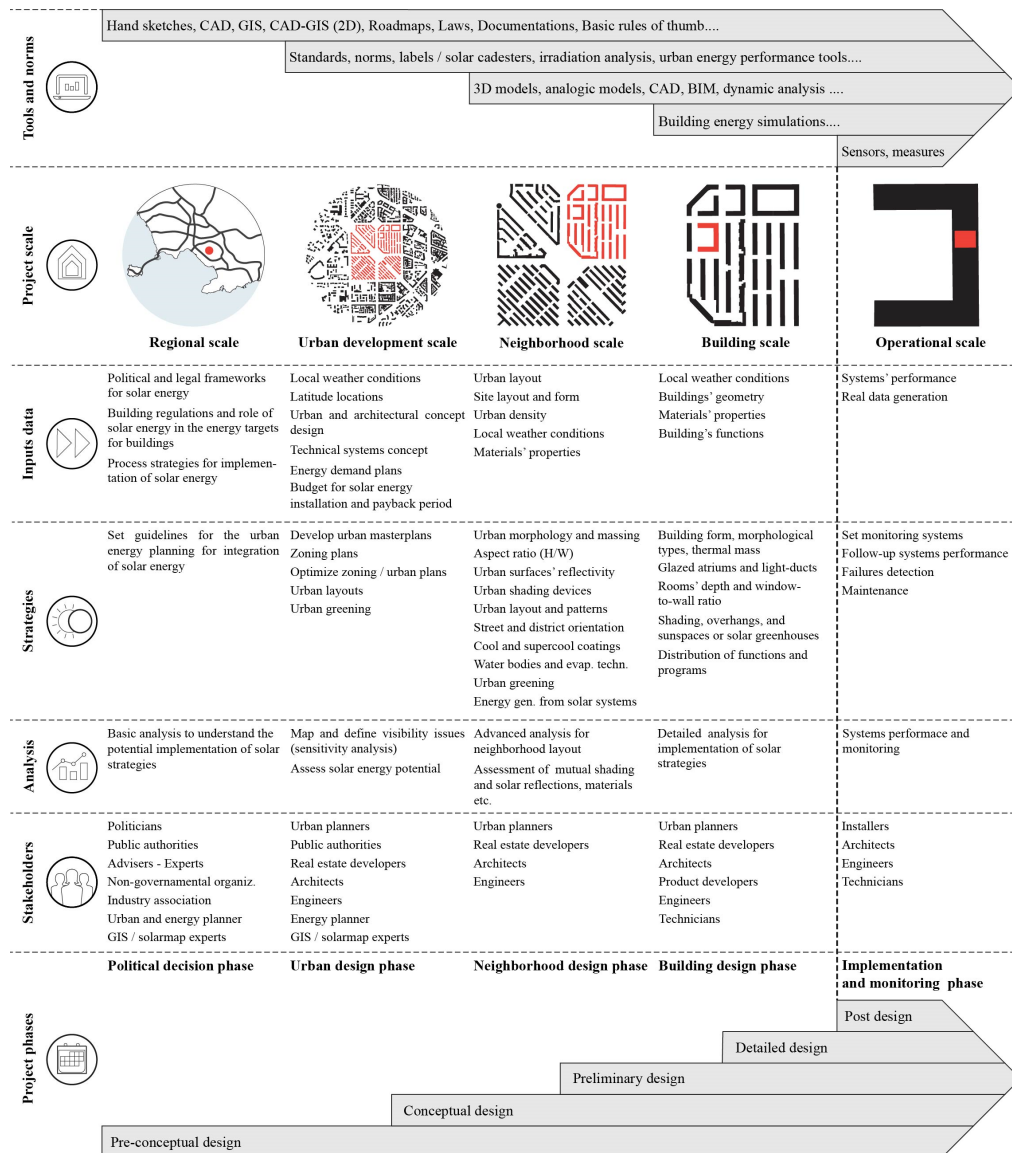


Fig. 2.9 Project scales and phases of the planning and design process for solar neighborhoods. Solar planning and design strategies applied at different spatial scales. Description of the tools and norms used in the different project stages. Modified from [Kanters and Wall \(2016\)](#) and [Nault et al. \(2018\)](#)

Five case studies, virtuous applications of planning and design strategies for solar neighborhoods in different climates and locations, are briefly presented and described in Figure 2.10.

One Central Park, in Sydney, Australia (Lat. 33.9° S), is a dual high-rise mixed-use development (5.6 ha). In 2006, the New South Wales Planning Minister called the site under state control with a revised masterplan approved in 2007. The precinct aimed to provide appropriate street and block connectivity whilst achieving good solar access in a highly densified urban landscape (PS6) that also promotes sustainable living and public community spaces. It is an exemplary case study of daylight enhancement at a large scale using an active solar strategy. 40 dual-axis tracking heliostats (each 6.5 m²) mounted on the East Tower redirect the light (AS2) to the underside of a cantilevered reflector frame composed of 320 fixed mirrors (each 1.25 m²) mounted on the West Tower. Approximately 800 W/m² are delivered under clear sky conditions to the underlying atrium commercial space, lap pool, and park (PS5, PS14N), which would otherwise be in the shade. Over 30,000 m² of the site has green plantings (PS14B), with also a large vertical living façade. This encompasses 5 km of linear planter boxes accommodating over 85,000 plants with over 250 different species. The façade itself reduces the heat load of the buildings by 15-20%. The urban renew project objective was to deliver approximately 2,200 apartments and 925 student dwellings, accommodating around 5,300 residents. Additionally, some 25,000 m² of premium commercial office space and 20,000 m² of retail space caters for 1,750 people to also work within the Central Park precinct.

West5 is a mixed-use community in London, Canada (Lat. 43.0° N). At the beginning of the project, the province of Ontario had in place the 'Green Energy Act' (repealed in 2019) that regulated building energy efficiency and RES generation. The local government supported the realization of the project through incentives related to energy efficiency, green buildings, electric vehicles (EV), on-site renewables, and cool roofs (PS12B). Also, at the federal level, energy-efficient building and community incentives were applied to the development of this net-zero energy mixed-use high-rise settlement. Initially, a feasibility study was carried out to demonstrate the impact of various solar technologies and energy efficiency measures in a new urban development area (PS5). This feasibility study and the related measures were adopted later in the actual project. Besides building envelopes (AS1B), PV systems are integrated into several urban elements such as parking lots and shelters (AS1N). The size of the PV plant in West5 is 1.7 MW_p, with an annual yield of 900 kWh/kW_p (in 2021). Even without considering the carbon offset from rooftop PV, the project compensates approximately 200 tCO₂-eq per year. Passive heating is guaranteed through optimal orientation of the whole neighborhood (PS6) and buildings (PS7), position of windows (PS9), and thermal massing (PS7). Buildings within this solar neighborhood are characterized by energy use intensity ranging from 91 kWh/m² for residential buildings to 92 kWh/m² for health and institutional buildings, and 124 kWh/m² for office buildings.

Norwegian University of Science and Technology (NTNU) Gløshaugen is a university campus in Trondheim, Norway (Lat. 63.4° N). In 2015, the Norwegian Government initiated a large redevelopment process for the site with the vision of establishing a ZEN through the refurbishment of the existing building stocks, the realization of new up-to-standard and plus

energy buildings, and the extensive implementation of passive and active strategies in the whole precinct. The recently constructed and under-development buildings posed attention to the surrounding urban layout and patterns (PS5), and their shapes and volume distribution (PS7) are modified throughout the design process to preserve existing recreational and historical heritage areas. Glass-covered connections between buildings create luminous informal meeting spaces and enhance visual comfort, while the use of glazed atriums acts as light wells for offices and classrooms overlooking them (PS8). About the active solar strategies, the largest installation is found in the ZEB Laboratory: a total of 963 m² BIPV (184 kW_p) are installed on the tilted roof, facades, and solar pergola (AS1B). Other active solar installations include (i) a system of 62 PV panels (20 kW_p) with 11 different angles and azimuth orientations installed on a rooftop, (ii) a 12.5 kW_p system integrated into the ZEB Living Laboratory, (iii) and PV, ST, and PV/T panels added on the roof of the ZEB Test Cell. The PV power and energy production of the campus is 4,956 kW_p and 3,477 MWh/yr, respectively.

Violino district is a residential social-housing neighborhood in Brescia, Italy (Lat. 45.5° N), designed according to bioclimatic principles. The municipality was heavily involved in the planning process by purchasing the land and setting energy and sustainability targets in the call for tenders. Architects, installers, and consultants collaborated in the urban and neighborhood design phases, providing solutions to meet the targets. The terraced house typology, the main building typology in the neighborhood (112 units), was adapted to the street layout by a partial rotation of the buildings' masses (PS1) to ensure solar accessibility. Two five-story multi-family houses are positioned on the north side of the settlement to avoid overshadowing (PS5). The distribution of volumes and functions at the building level (PS7, PS11) was also designed considering right-to-light principles, with the most used spaces (i.e., living room, kitchen, and bedrooms) placed on the south and west sides of the habitation units. Moreover, most of the terraced houses feature south-facing solar greenhouses (PS10), internally painted in dark-hues to maximize solar heat gains. Regarding active solar strategies, each terraced house is equipped with a 1.3 kW_p PV system, while the two multi-family houses have 5 to 20 kW_p PV systems (AS1B). PV modules' orientation is either horizontal or tilted 30° southwest. The project was also subjected to two monitoring campaigns in its post-design phase to (i) evaluate the performance of the PV systems and (ii) test smart energy management systems to minimize electricity costs.

The Science and Technology Park Adlershof, is a mixed-use development area located in Berlin, Germany (Lat. 52.4° N), encompassing offices, a university campus, research institutes, industries, residential and commercial buildings, and green areas. The City of Berlin has the goal to be climate neutral by 2050. In this framework, the Park Adlershof was subjected to a 35-year planning process aiming to reduce energy demand to 30% by 2020. The first PV system in Adlershof was a façade integrated semi-transparent system, installed in 1998. Nowadays, many examples of active solar systems are present in the area. Among them, a research center characterized by a slight curve façade (PS7) entirely covered by PV panels (AS1B), and the

headquarter of a PV manufacturer, whose façade is equipped with a demonstrative 210 kW_p system of PVSD (PS10). In Park Adlershof, green roofs are obligatory to retain storm water and to minimize the UHI effect (PS14B). Nonetheless, PV systems are accepted as an alternative measure, resulting in an installed PV power of more than 2 MW_p. Finally, energy flexibility was another focus of the project. Buildings are connected to the district heating network and the local grid is planned to support additional ST energy production in the future.






Case study	Which?	How?	Who?	When?
One Central Park 	<u>Passive strategies</u> PS5; PS6; PS14N; PS14B. <u>Active strategies</u> AS2 <u>Type of SN</u> Pure SN (new)	The light from tracking heliostats and fixed mirrors is redirected into indoor and outdoor space. Application of solar design, the use of irrigated green façades, and Low-E glazing to limit energy demand and promote indoor climatic.	Urban planners Real estate developers Architects Engineers	Urban design phase Neighborhood design phase
West5 	<u>Passive strategies</u> PS1; PS5; PS6; PS7; PS9, PS12B <u>Active strategies</u> AS1N; AS1B <u>Type of SN</u> Energy- and Carbon-centered SN (new)	Use of extensive green areas, solar passive heating through optimally oriented windows and thermal massing. Solar streetlights, solar parkades, and PV panels on different surfaces are monitored to evaluate the buildings' operation. Daylighting control systems to reduce the need for artificial lighting and overheating.	Land owner Urban planners Architects Researchers Installers Product producers	Urban design phase Neighborhood design phase Implementation-Monitoring phase
NTNU Gleshaugen 	<u>Passive strategies</u> PS5; PS7; PS8 <u>Active strategies</u> AS1B <u>Type of SN</u> Carbon-centered SN (existing)	Glass-covered connections and large glazed courtyards to bring natural daylight to offices and classrooms. PV and BIPV of roofs and facades of several buildings.	Government Contractors User groups Academic cluster user groups	Political decision phase Neighborhood design phase
Violino district 	<u>Passive strategies</u> PS1; PS5; PS7; PS10; PS11 <u>Active strategies</u> AS1B <u>Type of SN</u> Pure SN (new)	Competition initiated by the Municipality for realizing a social housing project through a holistic sustainable approach. Request for quantifiable requirements to assess the project's quality and sustainability.	Municipality Urban and energy planners Architects Engineers	Political decision phase Neighborhood design phase Implementation-Monitoring phase
Park Adlershof 	<u>Passive strategies</u> PS7; P10; PS14B <u>Active strategies</u> AS1B <u>Type of SN</u> Pure SN (existing)	Defined as an urban development area since 1994. The master plan is adapted to the functional diverse needs and mixed functions.	Municipalities Urban decision-makers Architects Operators of Technology Parks	Political decision phase Neighborhood design phase Implementation-Monitoring phase

Fig. 2.10 Summary of the case studies with the main active and passive solar strategies applied

The case studies presented above illustrate the possibilities offered by solar neighborhood planning and design strategies that bring together daylight provision and on-site energy generation. The implementation of passive and active solar solutions in these case studies highlights the importance of performing ad-hoc analyses (e.g. solar potential, daylighting, energy) that consider different scales and their inter-dependency, throughout the urban planning process. Also, routines built into the planning process are demonstrated to determine the successful development of solar strategies. However, due to the involvement of many different stakeholders with

different competences, priorities and interests, the overall duration and targets of the planning process may vary considerably. It is therefore important to involve all the relevant urban actors from the early stages of the design process to embed innovative concepts and technologies from research into real applications.

2.1.2.5 What are the challenges of implementing passive solar strategies into solar neighborhoods?

Integrating passive solar strategies into solar neighborhoods presents various challenges at both building and neighborhood scales, concerning the design aspects and regulatory compliance requirements. These challenges range from the building components and materials to the building typologies, and from neighborhood layout to urban development planning (Table 2.1).

Table 2.1 Summary of the challenges to adopt passive solar strategies in solar neighborhoods

Critical Aspects	Challenges
Social	<ul style="list-style-type: none"> • Balancing building uses with passive strategies that are optimal for those uses, evaluate the tradeoffs between conflicting uses of solar gain and between scales. • Increase user acceptance and impact of passive solar strategies in highly sensitive/constrained urban areas.
Layout	<ul style="list-style-type: none"> • Guarantee daylight and visual comfort in narrow street canyons and dense areas. • Mitigate UHI effects and inter-building reflections. • Design effective technological solutions in relation to building shape, orientation, and interior layout. • Apply building form and massing which guarantee right-to-light or right-to-shade according to the building uses.
Material	<ul style="list-style-type: none"> • Improve indoor/outdoor thermal comfort. • Adoption of new materials to improve daylight and visual comfort.
Modeling	<ul style="list-style-type: none"> • Develop form-finding optimization workflows for solar neighborhoods. • Reduce computational time for solar energy-related simulations. • Include the model of natural elements (e.g., trees, vegetation). • Develop digital clones of non-conventional materials and technologies.

Social. Human activity and user interaction within the neighborhood determine the potential for the implementation of passive solar strategies. The main challenge consists of balancing building uses with passive strategies that are optimal for those uses, evaluating the tradeoffs between conflicting uses of solar gain (e.g., self-shading to avoid glare phenomena vs. solar exposure to avoid poor visibility and visual discomfort) and between scales (solar passive strategies vary depending on the scale, encompassing buildings, neighborhoods, and urban

developments), considering a possible presence of active systems (e.g., large windows might be easily preferred to passively cooling surfaces treated with highly reflective materials, if an efficient district cooling system is present). Additional challenges concern increasing user acceptance of passive strategies to enhance visual (e.g., photoluminescent treatments, light chimneys) and thermal comfort (e.g., greeneries, supercool materials, greenhouses) in neighborhoods with high constraints (e.g., geometric, climatic, legal, economic, historical) that prohibit, or significantly limit, interventions in size, location, and design (Devetaković et al., 2020; Eder et al., 2019; Soman and Antony, 2019).

Layout. At the neighborhood level, narrow streets and high-density development can generate unsought inter-building effects (e.g., mutual and complex shading, multiple solar inter-building reflections) with an impact on solar accessibility within the neighborhood environment (Kanters and Wall, 2014). The main challenges associated with the neighborhood configuration concern (i) the optimal exploitation of solar accessibility to enhance visual comfort in narrow urban canyons and in densely built areas, and (ii) the mitigation of UHI effects and solar inter-building reflections to guarantee adequate indoor and outdoor thermal comfort. At the building level, shape, orientation, and interior layout influence the implementation of passive solar technologies. In that regard, the main challenge is the optimal design of building form and massing which guarantee right-to-light or right-to-shade according to the building uses, enabling to regulate the penetration of natural light through light shelves and shading systems, as well as controlling the indoor environment through solar chimneys and double-skin façades (Jankovic and Goia, 2021; Manni et al., 2022).

Materials. Retro-reflective, supercool, and photoluminescent materials are proposed in solar neighborhoods to address these main challenges: (i) decreasing the temperature of the urban surfaces (i.e., reducing UHI effects); (ii) improving users' outdoor thermal comfort in summer; (iii) increasing the impact on passive heating in winter and cooling in summer; and (iv) guaranteeing visual comfort and energy saving for artificial lighting. However, these materials present some drawbacks such as glare to neighboring buildings, reduced solar gains in winter, and aging issues (Manni et al., 2020a, 2018; Mastrapostoli et al., 2016). Although building finishes and claddings are usually covered at the building level, the multi-scale approach applied to the design of solar neighborhoods aims at defining materials applied to urban surfaces, avoiding the drawbacks mentioned above as well as the occurrence of shading phenomena that can reduce their efficiency.

Modeling. Estimating the impact of passive solar strategies is fundamental for decision-making within the solar neighborhood planning process. The main challenge regards the implementation of a form-finding optimization workflow for solar neighborhoods capable of (i) modeling natural elements (e.g., trees and vegetation), (ii) integrating multiple spatial scales (i.e., component, building, neighborhood, and city) and urban domains (i.e., outdoor, envelope, indoor) with (iii) low computational time. Alongside this, there is a need to (iv) develop digital clones of materials and technologies such as coatings with angular-dependent properties,

radiative coolers, electro-chromic windows, and photoluminescent pigments, which behave and perform differently from conventional materials.

2.1.2.6 What are the challenges of implementing active solar strategies into solar neighborhoods?

The challenges of increasing solar energy production in the solar neighborhoods can be grouped around the following seven aspects (Table [2.2](#)).

Table 2.2 Summary of the challenges to adopt active solar strategies in solar neighborhoods

Critical Aspects	Challenges
Location	<ul style="list-style-type: none"> • Balance the competing uses of surfaces by implementing multi-functional solutions.
Urban Planning	<ul style="list-style-type: none"> • Couple solar access and urban planning with respect to the type of interventions. • Electrification of heating and cooling systems, often linked to solar energy generation, but particularly constrained in high-density neighborhoods.
Modeling	<ul style="list-style-type: none"> • Develop simple approaches to process inter-building reflections. • Make data available from the early-design stages of the project. • Develop key performance indicators (KPIs) to effectively visualize and communicate results. • Develop urban canopy models to assess the impact of BIPV on the urban microclimate.
Architectural Integration	<ul style="list-style-type: none"> • Achieve high quality of integration through colored panels, layout, and sustainable materials. • Adapting urban regulations for heritage protected areas.
Energy Management	<ul style="list-style-type: none"> • Implement peak shaving strategies (e.g., batteries, smart devices). • Increase self-consumption of energy produced on-site.
Social Acceptance	<ul style="list-style-type: none"> • Increase end-user acceptance of active solar strategies through a structured legislative agenda.
Economy	<ul style="list-style-type: none"> • Reduce the cost of investment for certain complex solar installations.

Location. In buildings, active solar systems are usually preferred to opaque parts of the roofs and façades, particularly when these show a high solar energy potential. However, such surfaces are often also suitable for the implementation of passive solar strategies (e.g., green surfaces, windows, etc.). Similarly, in outdoor areas, the competing uses of the inter-building surfaces result in the exploitation of available parts of the areas for other purposes than solar energy production (e.g., mobility and transportation, pedestrian paths, parks, and squares). The major challenge related to the location of active solar systems concerns the development of multi-functional solutions, combining the capability to produce energy with other purposes, which permits to extend the applicability of such systems to other infrastructures (e.g., solar anti-noise barriers) or uses (e.g., hybrid solar green roofs, active solar windows, etc.).

Urban planning. On-site renewable energy production is becoming more frequently addressed in legal frameworks and building codes, and installing PV can be considered a standard practice. Nonetheless, developers are still reluctant to integrate PV into building envelopes due to the higher costs compared to traditional claddings as well as the challenges concerning architectural integration and fire safety. BIPV on the roof and façade present constraints like the conditions of the elements and their ability to support the weight of solar panels, the clutter of the roof, and the economic profitability (Thebault et al., 2022). Integration of PV into urban surfaces requires coupling the solar access analysis to urban planning, differentiating between new developments and retrofitting interventions. Challenges arise about self-shading within the district, as well as the absence of solar potential data to detect suitable areas for solar panels. In this regard, multi-layer cadasters (combining information layers about solar potential, shadow casting, heritage, open spaces to be covered, etc.) can play a key role in a holistic approach to designing solar neighborhoods and support the decision process to prioritize investments. Another challenge is the electrification of heating and cooling systems, often linked to solar energy generation, but particularly constrained in high-density neighborhoods. Indeed, such urban environments provide limited ground space for geothermal heat pumps or roof space on high buildings for air-source heat pumps, which compete with the surface areas required for solar panels. This necessitates planning global energy supply strategies that centralize energy production at the neighborhood scale, such as district thermal networks based on centralized geothermal heat pumps and solar energy (Calise et al., 2022).

Modeling. Several municipalities and public authorities have supported the development of solar cadasters of buildings' roofs as support instruments to inform owners of areas with solar potential, through various key performance indicators that allow to identify urban areas suitable for installing solar systems early in the planning process. Processing shadow casting and solar potential at the neighborhood scale based on Light Detection and Ranging (LiDAR) data is rather straightforward (Jakubiec and Reinhart, 2013; Stendaro et al., 2020), but estimating the building's potential for solar energy production is much more complex, particularly when considering vertical façades and inter-building reflections (Blaise and Gilles, 2022). The main challenges related to solar energy production concern (i) the development of simplified and

reliable modeling approaches to process solar inter-building reflections at neighborhood scale, (ii) data availability for decision-making generally limited in the beginning of the urban planning process, (iii) key performance indicators (KPIs) to visualize and communicate results in more user-friendly ways, and (iv) the development of an urban canopy model to assess the impact of BIPV on both the local climate and microclimate (Elhabodi et al., 2023).

Architectural integration. Increasing the solar energy production and the density of active solar systems while maintaining the visual aesthetics of the neighborhood is challenging and requires a particular effort on architectural integration. The next generation of active solar systems is expected to overcome this issue by (i) developing solar panel solutions that are more visually integrated (e.g., colored panels, solar tiles) (Couty and Simon, 2017; Xiang et al., 2021), while (ii) selecting sustainable materials to reduce their carbon footprint (Mehedi et al., 2022) and (iii) defining guidelines concerning the layout of solar modules when integrated on roofs and façades (e.g., multiple and isolated solar patches, unique and continuous area with solar panels). Furthermore, achieving the architectural integration of PV or ST systems and their visual harmonization with the urban surface poses a further challenge regarding (iv) urban regulations, particularly in historical zones where the use of active solar systems is often forbidden or subject to very strict regulations.

Energy management. There is a general agreement among national and local governments to boost solar energy production through distributed solar energy systems in urban areas. However, the peak demand on the grid is rarely solved by solar energy, and a massive infusion of energy into the grid without a significant demand for it may result in local low-voltage grid collapse. The main challenge related to energy management concerns the implementation of peak-shaving measures such as energy storage systems and sector coupling concepts (e.g., power-to-X concepts) (Nastasi et al., 2021), smart devices that work when the sun is shining, and the promotion of self-consumption strategies towards a better autonomy from the grid (Gallego-Castillo et al., 2021; Swens and Diestelmeier, 2022).

Social acceptance. The aspects presented above raised the issues of managing many conflicts of interest of the competing uses of urban surfaces, dealing with the complexity of initiating solar design projects, and achieving autonomy from the grid. Therefore, social acceptance of solar projects by end-users is the major issue to trigger solar projects. Simplification of legal frameworks and authorization procedures for installation, information, and communication are important drivers to boost the solar market in this regard.

Economic issues. Active solar installations can often be expensive, which may discourage property owners from investing in them, and make the cost of renting or selling buildings prohibitive. However, solar installations are typically subsidized by national or local governments (see section 2.1.2.9). For example, in Switzerland, the Federal Government provides non-recurrent remuneration that covers up to 30% of the investment costs for reference systems. This remuneration is higher for integrated solar systems, as well as for vertical installations on fa-

acades. Furthermore, given the context of rising electricity prices in Europe, the self-consumption of solar energy helps to reduce electricity bills and expedite the return on investment.

2.1.2.7 How can the digitalization of the built environment support the planning of solar neighborhoods?

The effective design of solar neighborhoods within the heterogeneous and complex dynamics of the urban system poses several challenges related to the physical characterization of the urban environment. This involves various complex phenomena (e.g., dynamic overshadowing, inter-building reflections, alteration of microclimate conditions), as well as technical aspects primarily associated with the complexity of numerical simulation models, which may require significant computational time depending on the scale and the desired level of detail (Masson et al., 2020).

In this regard, the process of digitalizing the built environment is imperative and it involves a series of actions aimed at acquiring, modeling, simulating, monitoring, and analyzing urban data through digital tools (Wang et al., 2021a). This data encompasses, among others, information about geometry, technical features of urban surfaces, construction standards, microclimate, energy grid, usage schedules, electricity infrastructure, or socio-economic aspects. Utilizing digital workflows is crucial to facilitate decision-making across the production of various KPIs (see section 2.1.2.2). Such KPIs extend beyond building energy efficiency and solar power generation potential, encompassing aspects like daylight access, biophilia and biodiversity, visual impact, outdoor thermal comfort, and social and economic factors (Naboni et al., 2019). Moreover, given the urge to implement solar energy strategies, digital built environments are necessary to test, deploy, and implement solutions at a wide scale. An overview of existing workflows and tools for solar neighborhood planning, as well as the KPIs commonly used by researchers, urban planners, and stakeholders to communicate the technical outcomes and data in a user-friendly way to both public authorities and citizens is presented in (Baker et al., 2022).

An illustration of a digital workflow for the estimation of the rooftop solar irradiance of the Greater Geneva region is depicted in Figure 2.11. The solar cadaster is made accessible through two channels: (i) a comprehensive database containing detailed information on roofs and buildings, available for download from the geoportal of the State of Geneva, and (ii) a web application that presents essential indicators to the public (see Social impacts in section 2.1.2.8). The current version of the solar cadaster exclusively offers data on solar potential for roofs and other surfaces like existing or potential carports. Consequently, it primarily focuses on facilitating active solar energy strategies by identifying the best-irradiated surfaces for solar panel installations (see challenges identified in section 2.1.2.6). Besides that, it encompasses irradiation and shading raster maps for the entire regional territory, available at various time scales (e.g., hourly, daily, monthly, yearly), which can support passive solar strategies (see challenges identified in section 2.1.2.5). The simulation engine has been designed to also

analyze solar radiation on facades, with a specific emphasis on solar reflection in urban canyons at a large scale, as initially introduced in (Blaise and Gilles, 2022). Consequently, the solar cadaster is slated for a forthcoming update that will include the facade component, providing a more comprehensive analysis of solar potential in the region.

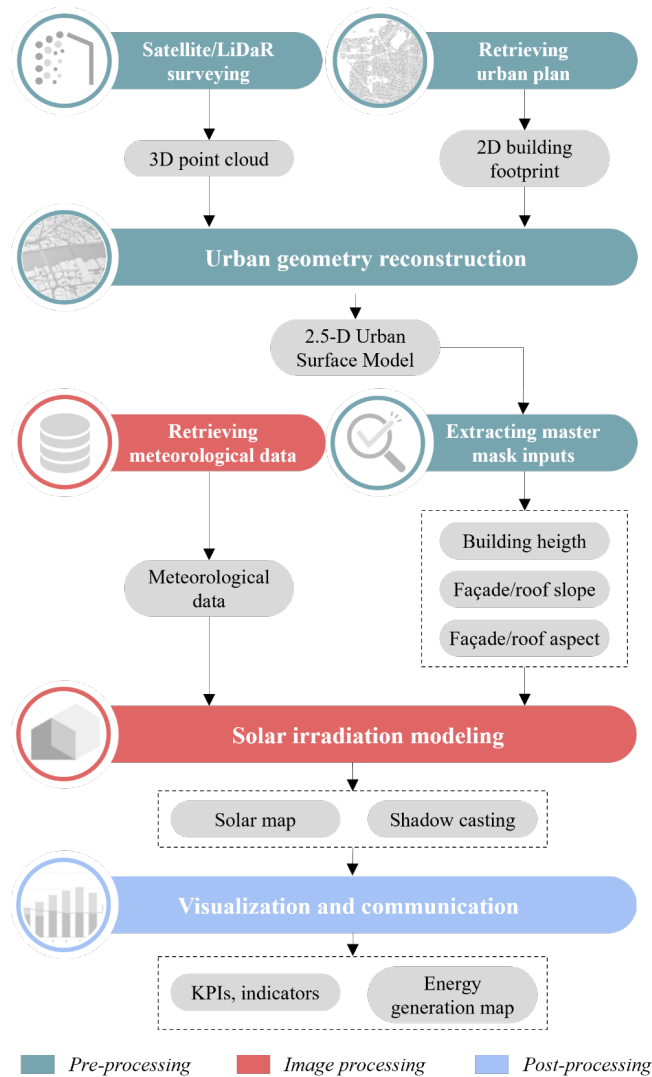


Fig. 2.11 Example of the digital environment of the whole process of solar modeling on roofs and facades for the solar cadaster on the scale of Greater Geneva (about 2,000 km²). Modified from Stendardo et al. (2020)

A digital built environment aims to provide a holistic environment. Nevertheless, there are different levels of complexity and accuracy. These levels of detail are similar to the classification of the KPIs described in section 2.1.2.2 and, as they increased in complexity, they allow the computation of more and more complex and/or diverse indicators.

Handling and modeling geometry. One fundamental application of digital technologies in solar neighborhood design involves creating a digital geometrical representation of the built environment. This can be achieved using established approaches such as computer-aided design

(CAD), Building Information Modeling (BIM), and Geographic Information System (GIS). The difference between these approaches lies in the scale and level of detail (LoD) required, which significantly impacts the quality of simulation outputs (Peronato et al., 2016). CAD is commonly used for detailed modeling of individual buildings or small groups with a high level of detail (LoD 3), including features like window placements and façade details. BIM encompasses and extends CAD capabilities by managing digital representations of physical and functional characteristics, fostering collaboration and interoperability among stakeholders (Abanda et al., 2021; Heffernan et al., 2017). For city-level representations, GIS-based tools are utilized but may necessitate lower detail due to computational constraints (Allegrini et al., 2015a). As the extent of the model increases, a decrease in detail is necessary. Nevertheless, more and more detailed models are handled through GIS tools, thanks to improvements in data handling as well as the increasing quality of available data (e.g., detailed LiDAR or photogrammetry data). Many cities already have such LoD models available for existing buildings, but the level of detail can vary significantly from simple 2D footprints to high-fidelity and textured three-dimensional models (Biljecki et al., 2015). Hybrid models combining GIS/LiDAR with CAD allow comprehensive urban environment representation. This first step allows for the calculation of the morphological indicators as presented in section 2.1.2.2.

Weather conditions and Solar Radiation. Another key element when dealing with the modeling of the physics of solar neighborhoods is the weather data, allowing the simulation of specific meteorological conditions. A weather data file is a dataset linked to a spatial localization, that provides climatic data with a specific time step (from minutes to hours), usually for a whole year. These data could either correspond to past recordings or to ‘Typical Meteorological Years’ (i.e., a ‘statistical’ year that is representative of the weather observed in the previous decade or more). Such data can be obtained through weather agencies or databases such as the EpwMap from the Ladybug Tools⁸, the National Solar Radiation Database from the National Renewable Energy Laboratory⁹, and the Meteonorm¹⁰ software. Recently, a certain number of future climate models have also been developed to modify weather datasets to account for climate changes (Jiang et al., 2019; Sørland et al., 2020). This weather data and the geometry are necessary to calculate solar radiation received on roofs and façades as well as all sorts of solar metrics (see section 2.1.2.2). One of the main challenges remains here the modeling of the façades and the related solar radiation exchanges. Indeed, unlike roofs, existing façades are more difficult to cartography from aerial imagery and more complex in terms of texture (e.g., presence of windows, balconies, superstructure elements, etc.) and physics (inter-reflections with surrounding buildings, specular reflections from the windows).

Energy usage modeling. While there are differences in models and approaches for simulating solar radiation, current tools handle these calculations well, when the geometry is sufficiently detailed and reasonable in size. On the contrary, modeling the usage of solar energy (both

⁸ladybug.tools/epwmap

⁹nsrdb.nrel.gov/data-viewer

¹⁰meteonorm.com

active and passive) in solar neighborhoods is more complex. A similar holistic digital workflow should account for both energy consumption and usage of each building while assessing the energy self-consumption potential (Ang et al., 2023). This requires detailed knowledge of the thermal properties of building components and involves the use of Urban Building Energy Modeling (UBEM), a physics-based approach that enables simulating thermal performances, space conditioning loads, and energy usage of multiple buildings at the urban scale (Reinhart and Cerezo Davila, 2016). Non-geometric building properties such as construction characteristics, age, and heating, ventilation, and air conditioning systems are essential inputs for UBEM. The choice of UBEM type depends on the level of detail and scale, with some using physics-based simulation engines and others relying on reduced-order models. Most UBEM tools integrate GIS-based datasets or use CityGML-based virtual city models (Hong et al., 2020).

Urban Microclimate. In urban areas, the microclimate strongly influences building energy use (Boccalatte et al., 2020a; Santamouris, 2014) and solar systems' performances (Berardi and Graham, 2020; Sailor et al., 2021). A solar neighborhood is rarely an isolated entity, and it should account for the energy exchanges with the surrounding areas and the energy infrastructures already in place (e.g., district heating plant, energy storage systems) which may drastically redefine the design and planning strategies to be implemented. When considering relatively small and/or new neighborhoods, electric and thermal needs, as well as outdoor and indoor thermal conditions can be easily modeled since the building geometry and thermal properties of each component are known. For example, microclimate conditions and users' thermal comfort can be evaluated through computational fluid dynamics models that are able to assess the impact of wind and thermal stratification (e.g., ENVI-met, Solene Microclimat). However, when considering large and/or existing urban areas, it is more difficult to reliably represent the neighborhood microclimate due to the scarcity of information about the thermal properties of the buildings' components and the need to apply some simplification to reduce the computational time. To that aim, parametric microclimate models are preferred, such as the Urban Weather Generator (UWG) (Boccalatte et al., 2020a, 2023), which modifies rural weather station temperature data based on the geometrical and thermal characteristics of the neighborhood.

In conclusion, the digitalization of the built environment is a complex operation that allows many actors to acquire useful data, carry out performance predictions with various time horizons, analyze and compare different strategies and solutions in the early urban design phase, and assess the impact of other factors such as climate change on the urban environment. The choice of digital tools and workflows is highly dependent on the required level of detail and scale. Digitalization is also key for the visualization of relevant solar data which, together with understandable KPIs and a user-friendly interface, can facilitate the stakeholders' involvement in the design process, promote the social acceptability of solar applications, and support municipalities in the development of roadmaps for solar energy implementation (see section 2.1.2.8). However, despite the numerous tools available nowadays, many of them still fall

short of interoperability. Solar design workflows mostly consist of a model chain (i.e., a chain of tools) and only a few of them provide the sufficient level of integration that is sought by building and urban design practitioners. The availability of data is another common barrier in the digitalization of the built environment. In fact, municipalities rarely have the time and infrastructure resources (e.g., sensors, data acquisition systems) needed for data acquisition and digitalization activities. Therefore, private parties usually perform such tasks providing limited access to the data.

2.1.2.8 How can the planning strategies and design solutions for solar neighborhoods impact on the 'total environment'?

The 'total environment' benefits from the creation of solar neighborhoods through a global enhancement of the life quality of its inhabitants, thus boosting the social acceptability of solar energy. As discussed in section 2.1.2.2, the active and passive solar strategies affect metrics concerning various disciplines besides solar, such as local climate and microclimate, users' comfort, energy, and carbon emissions. In this answer, the multiple impacts of solar neighborhoods are quantified and presented in three main groups: (i) environmental, (ii) economy and energy, and (iii) social impacts (Figure 2.12).

Environmental impact. When it comes to the impacts of solar neighborhoods on microclimate and emissions released in the atmosphere, low-carbon materials (e.g., local timber constructive elements, recycled materials) and solutions that reduce the exploitation of fossil fuel (e.g., transportation of raw materials through EV) can be applied to directly decrease the GHG emissions. One example is the ZEB Laboratory in the NTNU Gløshaugen campus case study (see section 2.1.2.4), where bio-diesel trucks were specifically selected to transport the timber structure elements. Besides these solutions, the envelope of the ZEB Laboratory is covered by around 960 m² of BIPVs (184 kW_p) to achieve the zero-emission target. The whole BIPV system has compensated for more than 38,000 kgCO₂-eq since it was opened in 2020, and around 15,000 kgCO₂-eq throughout 2022. Indeed, counterbalancing GHG emissions by implementing active solar systems (e.g., photovoltaic panels, solar thermal panels, hybrid panels) is a common practice (Lobaccaro et al., 2018b; Manni et al., 2020c), although the compensation potential varies in space and time depending on the composition of the national electricity mix (Gielen et al., 2019). Moreover, urban greeneries (e.g., green roofs and façades, parks, streets trees) can be exploited to sequester carbon dioxide such as in the One Central Park case study in Sydney, Australia (see section 2.1.2.4). A square meter of green roof or façade can absorb from 0.143 to 2.070 kgCO₂-eq per year through its bioactivity (Seyedabadi et al., 2021), while an adult plant can absorb between 10 kgCO₂-eq per year and 50 kgCO₂-eq per year (Cameron and Blanuša, 2016).

Treating urban surfaces with cool (e.g., retro-reflective materials, highly reflective materials) and supercool materials (e.g., radiative cool materials) creates a favorable microclimate in the

built environment that reduces both the concentration of pollutants and the urban overheating (Santamouris and Yun, 2020). In this regard, the replacement of conventional pavements with reflective and evaporative surfaces in (Croce et al., 2021) resulted in a reduction of the ground surface temperatures up to 14.0°C and a consequent decrease of the air temperature at pedestrian level between 0.6 and 1.2°C, during summer.

Permeable surfaces, water bodies, and vegetation can similarly contribute to mitigating UHI effects, with a positive impact on biodiversity. In the West5 case study from Canada, (see section 2.1.2.4) the natural surfaces designed within the solar neighborhood have permitted the reintroduction of animal species such as bees in areas they used to inhabit before human-induced transformations. Similarly, the green roof studied in Fleck et al. (2022); Irga et al. (2021) could support four times the avian, and nine times the insect diversity when compared to a conventional roof.

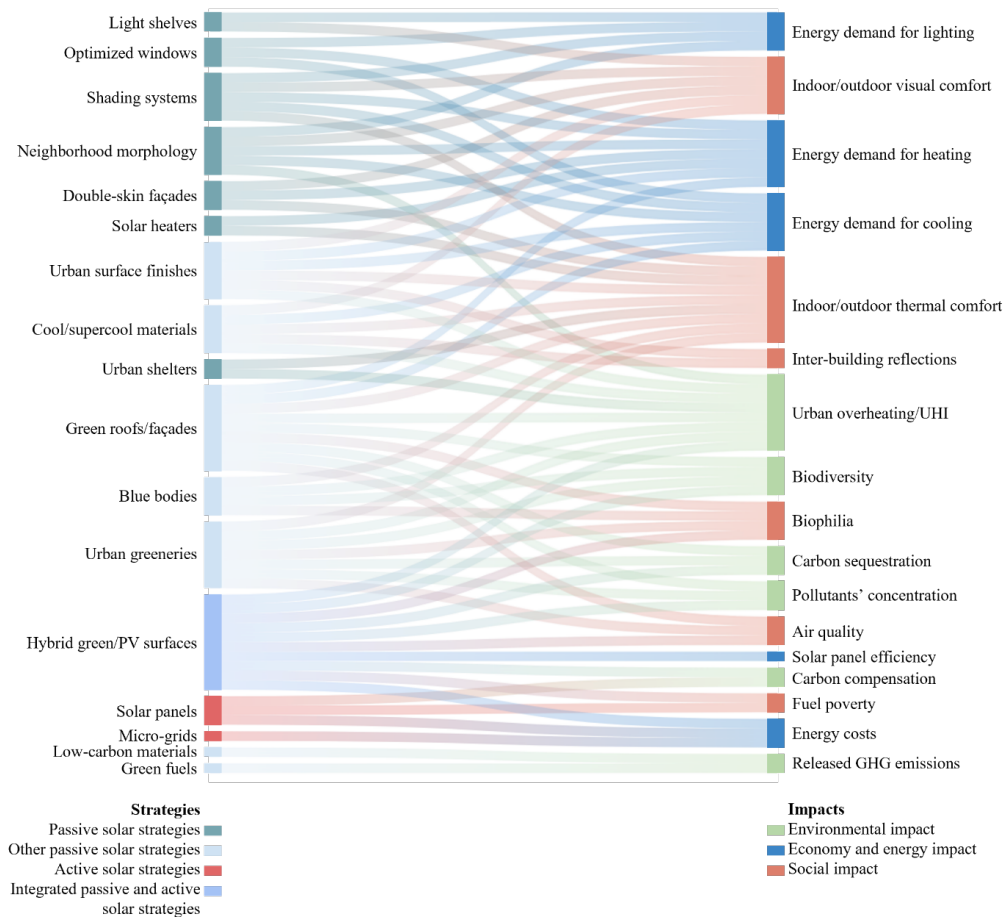


Fig. 2.12 Solar strategies implemented in solar neighborhoods and their impacts on the ‘total environment’ (i.e., environmental impact, economy and energy impact, social impact)

Economy and energy impact. Solar neighborhoods impact the economy and energy sectors. In general, the economic impact of the integration of solar strategies in a neighborhood lays in the revitalization of the areas, with new housing and economic activities, and in strengthening

business opportunities with new employment alternatives. This is best exemplified by the case studies of Science and Technology Park Adlershof (Germany) and West5 (Canada) where today a mix of new companies, scientific organizations, and single-family houses are located.

On the other hand, the energy impact is demonstrated through the active solar systems integrated within the urban fabric of the Violino district (Italy) and NTNU Gløshaugen (Norway) case studies (see section 2.1.2.4). The latitude and orientation (i.e., azimuthal and zenithal angle), and also the efficiency of the PV module determine the energy output. For example, the PV installation in the Violino district demonstrates a comparable annual energy output to that in the ZEB Living Laboratory at NTNU Gløshaugen (130 kWh/m² per year). This discrepancy is attributable, in part, to the different efficiency values of the PV cells, as well as the orientation of the panels in the Violino district, which is not optimized for the specific latitude (see section 2.1.2.4).

Furthermore, synergies between active solar strategies and passive cooling create better conditions for energy production by stabilizing temperatures on hot days and increasing the efficiency of PV systems by up to 5-10% in summer (Arenandan et al., 2022; Shafique et al., 2020). In fact, when temperatures rise above 25°C, the efficiency of PV panels decreases (Hoffmann and Koehl, 2014; Polo-Labarríos et al., 2020). In that sense, it is valuable to highlight the work performed within the IEA SHC Task 63 on the use of surfaces (Croce et al., 2022) and the contribution of other researchers worldwide such as the technological solutions combining PV shading devices and green surfaces developed by Tablada et al. (2018).

At the grid level, on-site energy generation and self-consumption lead to the decentralization of the energy grid by reducing transmission and distribution losses, and the need for expensive transmission and distribution infrastructure. The implementation of micro-grids, peer-to-peer energy trading, and sector coupling concepts have the potential to reduce energy costs for consumers. In the study by Long et al. (2018), this reduction for a residential community was quantified at 30% compared to a conventional peer-to-grid energy trading scheme.

Finally, passive solar design solutions such as solar air heaters and double-skin façades permit to reduce the energy demand for heating and cooling in the range of 30-50%, depending on the building's design and microclimate (Pelletier et al., 2023; Qahtan, 2019). Moreover, the optimal design of openings to exploit natural light coupled with energy-efficient lighting technologies permits to decrease the energy consumption for lighting by around 30%, even though it is strictly correlated to location, orientation, and design, as well as to lighting fixtures and controls strategies used (Omar et al., 2018).

Social impact. Impacts on society and quality of life are achieved in solar neighborhoods by reducing fuel poverty through active solar systems (Andreadis et al., 2013), as well as by empowering citizens with direct control over energy production, supply, and solar accessibility (Gómez-Navarro et al., 2021). The digitalization of the built environment is a crucial aspect in that sense, enabling extensive monitoring activities and direct access to data, as well as the social

acceptability of solar strategies and gamification strategies to enhance citizens' involvement. In that regard, the solar cadaster of Geneva, Switzerland, as well as the Solar City program in Halifax¹¹, Canada, offer a collaborative platform and innovative solar energy options for homeowners to boost economic activities around the solar sector and engage citizens through community planning and information sessions.

The creation of solar neighborhoods might also potentially result in socio and spatial injustices within urban areas and become a vehicle for gentrification. Indeed, a growing body of literature is analyzing the contribution of new green infrastructure to gentrification (Anguelovski et al., 2022), and the concept is recently being connected and expanded to other urban interventions, such as the energy rehabilitation of neighborhoods (Bouzarovski et al., 2018), the implementation of climate resilience and sustainability policies (Checker, 2011; Gould and Lewis, 2021), and the transition to the use of RES (Sander and Weißermel, 2023). In this framework, it is important to design and implement solar neighborhoods thoroughly considering, besides technical and aesthetical criteria, environmental and climate justice principles, avoiding any social inequality in the access to all the benefits produced by such neighborhoods.

Indoor and outdoor visual and thermal comfort of users within solar neighborhoods is determined by buildings' geometry, urban furniture, and technological/material features. Building shape and orientation as well as the design of windows and shading devices can enhance daylighting exploitation by ranges of 30–100%, depending on the location and the baseline scenario (Baghoolizadeh et al., 2023; De Luca et al., 2022). Urban shading structures move the perceived temperature level of a person to a less strong thermal stress, reducing the mean radiant temperature, Physiological Equivalent Temperature (PET), and Universal Thermal Climate Index (UTCI) up to 24.8°C, 12.0°C, and 5.9°C, respectively (Lam et al., 2023).

On the contrary, cool pavements can slightly worsen the level of thermal stress during the central hours of the day, due to the increased pedestrian exposure to shortwave radiation reflected from pavements and walls (Erell et al., 2014), as observed for cool pavements in Padua, Italy, through simulations (i.e., UTCI increases up to 0.6 °C in areas directly exposed to sunlight) (Croce et al., 2021). Nonetheless, their capability to enhance indoor thermal comfort is universally recognized (Santamouris et al., 2011). Compared to a conventional envelope, light-colored paint materials reduce discomfort hours by around 75%, in a hot-dry climate (Rawat and Singh, 2022), while a Trombe wall enhanced with phase-change materials achieves a 7% reduction in a hot summer and cold winter region (Li et al., 2022). It is worth mentioning that some cool materials (e.g., high- and retro-reflective materials) tend to reduce the passive heat gains throughout the year by negatively impacting indoor thermal comfort during winter. The unplanned use of highly reflective materials within solar neighborhoods may potentially cause uncontrolled concentration of solar irradiance at the pedestrian level. Diffusely reflective façades increase the solar irradiance at the pedestrian level by approximately 30%, while specular reflective façades can triple that amount (Speroni et al., 2022). Conversely, retro-reflective

¹¹halifax.ca

coatings can reduce the daily glare probability by around 5% compared to highly reflective coatings (Castellani et al., 2020).

The presence of trees and vegetation elements is fundamental to improving the quality of life and thermal comfort of persons by lowering urban surface temperatures, reducing micro-pollutant concentration, and making nature more accessible to people, enhancing their biophilia. In the One Central Park case study, over 30,000 m² of the site has been green planted, with a large vertical living façade that grows and changes color with the seasons. The façade itself reduces the heat load of the building by 15-20%, with a positive contribution to reducing undesirable UHI effects.

2.1.2.9 What legislative agenda is needed to support solar neighborhoods?

The legislative agenda together with policymakers' initiatives plays a key role in the adoption of solar neighborhoods. Their influence extends across multiple dimensions (e.g., regulatory frameworks, incentives, guidelines), emphasizing their importance in shaping sustainable urban development. By offering financial support and overseeing collaborations among the different stakeholders, policymakers can contribute to reducing barriers to entry and driving market transformation, accelerating the development and uptake of solar neighborhood solutions. This question focuses on the essential attributes of the legislative agenda to support solar neighborhoods, moving from the assessment of existing building regulations concerning solar energy to standards and certifications about broader themes such as energy efficiency and environmental sustainability, at building and neighborhood levels. Through this analysis, the key components required to create an effective and comprehensive legislative framework to promote the advancement of solar neighborhoods are identified.

In a global context, most countries have established standards to ensure access to sunlight at the individual building level. However, a gap persists in terms of codes and guidelines for regulating sunlight access and the application of active and passive solar strategies at the neighborhood scale. In the Canadian context, each province and sometimes cities have different approaches to solar access. The City of Toronto Official Plan¹² states that new developments in existing neighborhoods must allow for the provision of sunlight and views of the sky for the residents of new and existing buildings. In Europe, various regulations directly or indirectly related to solar access can be distinguished. For instance, in Italy, the Integrated National Energy and Climate Plan sets some growth targets for power and thermal energy from renewable sources at the national level, including solar energy. Regarding passive solar, some Italian regional laws require ensuring an appropriate level of visual comfort through daylighting and its integration with artificial lighting sources (Kunel et al., 2015). In Norway, the national regulation TEK 17 used to specified requirements to enhance direct solar access, including a minimum threshold to guarantee a satisfactory level of sun exposure for housing units and

¹²toronto.ca/city-government/planning-development/official-plan-guidelines/official-plan

communal outdoor areas (e.g., at least 5 hours in spring and autumn equinoxes). However, this guidance was repealed from TEK17 in 2021, allowing local municipalities to set specific requirements based on local conditions, while some guidelines have been provided by the Norwegian Association of Consulting Engineers¹³. In Sweden, detailed development plans are required to include description of the geometry of buildings such as building height, ridge height, total building height and roof inclination. The described geometry could have a direct effect on the performance of future solar energy systems installed in the area, as well as passive strategies implemented in the neighborhood. Legal judgments on solar access in Australia have also highlighted inconsistent interpretations of ‘nuisance’ in common law (Bradbrook, 2011). Similarly, solar access protection through easements or covenants can be overruled through jurisdictional state law (Clarke, 2019). This reinforces the importance of overarching legislative reform that promotes and protects solar neighborhood planning now and into the future.

Regarding solar technology implementation in the built environment, many countries have established building codes and permitting requirements that are mostly related to installation, safety, and structural considerations of active solar technologies, related to different types of buildings (Economidou et al., 2020). For example, the integration of PV modules into building envelopes or other surfaces within urban environments often encounters restrictions linked to considerations of visual aesthetics and structural and fire safety. Besides this, various policy mechanisms for solar modules have been adopted, which include feed-in tariffs, net metering, portfolio standards, project and tendering applications, tax exemptions, and research and development incentives (Kılıç and Kekezoğlu, 2022). In particular, Germany, France, and Canada employ financial support measures like subsidies, feed-in tariffs, premium feed-in tariffs, and loans. Similarly, China offers subsidies for small-scale projects, significantly reducing the total investment costs. In India, income tax reduction, accelerated depreciation, customs tax exemptions, production-based incentives, and obligation to purchase renewable energy have been established (Kılıç and Kekezoğlu, 2022). The USA primarily implements tax exemptions to incentivize private investments in a liberal market. In this regard, the effectiveness of incentives that directly lower consumer prices without imposing administrative burdens should be highlighted (Matisoff and Johnson, 2017). On the contrary, incentives that are extended over prolonged periods, demand administrative participation, or necessitate tax payment prior to collection are not advisable.

Furthermore, numerous voluntary standards and certificates address aspects beyond solar accessibility yet remaining pertinent within solar neighborhood planning. These include energy efficiency, sustainability within the built environment, and renewable energy production. Standards such as the ASHRAE/ICC/USGBC/IES Standard 189.1-2017¹⁴ provide guidelines regarding sustainability, energy efficiency, indoor environmental quality, material and resources, and construction and plans for operation, by also setting minimum requirements for on-site re-

¹³rif.no/wp-content

¹⁴ashrae.org

newable energy production. Besides this, the Green Globes Assessment Protocol for Commercial Buildings¹⁵, the Passive House Institute US (Asd, 2019), the Building Research Establishment Environmental Assessment Method (BREEAM) (Davda et al., 2010), and the Green Globes Certification (Díaz-López et al., 2021) provide different methods for evaluating various aspects (e.g., energy, indoor environment, site, water, resources, emissions, project and environmental management) of both residential and commercial buildings. At the neighborhood level, the Leadership in Energy and Environmental Design for Neighborhood Development (LEED-ND) (Talen et al., 2013), the SITES from the Green Business Certification Inc. (Small and Mazrooei, 2016), the Living Building Challenge (Wijesooriya et al., 2023), and the Net ZEB Certification from the International Living Future Institute (Satola et al., 2022) constitute third party verified rating system covering a range of sustainability issues, including, among the others, healthy environment, pollution and risks, energy efficiency, ecology, sustainable sites, management and quality of service, economic aspects, and community.

As the initiatives to achieve positive energy and carbon neutrality targets increase, the integration of high-energy performance criteria and the deployment of solar energy is becoming an integral part of the planning and design process (Akrofi and Okitasari, 2022). To support that, legislation on solar measures must be considered at early stages. Greater coherence between planning instruments and energy-related measures is also necessary to better calibrate energy demand and supply. This involves recognizing that passive and active solar solutions require different approaches depending on geo-locational and energy usage characteristics. Therefore, developing national codes that regulate long-term solar access at the neighborhood scale, particularly in high-density contexts, is needed to significantly improve the energy performance and sustainability of cities and communities. Finally, it is worth highlighting the importance of a legislative response to innovative approaches such as the one applied in the One Central Park case study, where light is redirected through heliostats and mirrors to brighten spaces that would otherwise be in full shade.

In conclusion, to establish a robust framework for supporting solar neighborhoods, a comprehensive legislative agenda should be developed based on the following points:

- **Incentives and subsidies** to promote the economic viability and adoption of solar technologies, particularly the passive ones, in communities aiming at significantly reducing energy consumption, and potentially achieving net zero energy status;
- **Regulations** to streamline the process of obtaining permits for the installation of active and passive solar solutions in residential and commercial areas, as well as in public and private spaces;
- **Guidelines** for architectural design that balance aesthetics with solar technology deployment;

¹⁵thegbi.org

- **Collaboration** between local governments, businesses, and communities to collectively drive solar neighborhood initiatives;
- **Standards for measuring and certifying** the performance levels achieved within solar neighborhoods based on a group of KPIs which are not limited to solar (see section 2.1.2.2).

2.1.2.10 What is next in planning and design strategies for solar neighborhoods?

Future trends in the research and implementation of solar neighborhoods can be identified. To begin with, two fundamental aspects of energy-centered solar neighborhood planning would be: (i) substantial breakthroughs in electricity storage capabilities and development of more efficient and economically affordable systems and (ii) development of smart grids allowing a seamless share of onsite electricity production within the neighborhood's boundaries. Legislative barriers currently in place worldwide will need to be overcome in that sense, while vehicle-to-grid technologies, implying a bidirectional flow of electricity between EV and the grid, are one promising solution to modulate energy demand and supply in those markets with a large share of EV (Bibak and Tekiner-Moğulkoç, 2021). Solar neighborhoods are expected to accelerate the penetration of distributed solar systems in the built environment, making these technologies more visible, affordable, and acceptable to citizens. However, despite the increased visibility of solar technologies proven to be an effective solution to foster social acceptability and adoption (Hai et al., 2017; Parkins et al., 2018), it often clashes with the need to limit visual exposure in sensitive urban areas (Legnér and Femenías, 2022; Munari Probst and Roecker, 2019). The challenge to combine these two diverging aspects will have to be addressed through a higher quality of architectural integration of solar systems and a wider availability of products (i.e., different colors, hues, sizes, and patterns) in the market to enable greater flexibility in the design.

As in the energy sector, self-sufficiency in terms of food supply is another important aspect in the planning of solar neighborhoods, particularly when it comes to carbon-centered solar neighborhoods. The increment of permeable surfaces can boost the implementation of urban farming techniques. Parasitic architectural elements in the form of greenhouses and cultivated surfaces coupled with PV systems should be integrated into the buildings' envelope, guaranteeing direct access to local food sources. In the planning and design of solar neighborhoods, more attention should be placed on the "total environment", through the development of a framework to evaluate conflicts and synergies of different surface uses. This will require the integration of vegetation models in the workflows (Balakrishnan and Jakubiec, 2022) and high LoD three-dimensional models to perform the planning and the design of solar neighborhoods. In fact, the presence of vegetation elements is often neglected due to the inherent complexity of modeling them. The development of novel methodologies for high LoD three-dimensional models should consider both the modeling of trees and urban furniture, building envelopes and architectural elements (e.g., balconies, louvers, overhang parts), and the detection of surface materials and

their optical properties, without overly affecting the computational time. This has a pivotal role in improving the accuracy of the analysis and the reliability of the results. In addition, developing workflows to simulate the emerging surface treatments and coatings (e.g., icephobic layers, retro-reflective coatings, radiative coolers, electrochromic windows, etc.) with optical and thermal properties determined by parameters different than of traditional materials (e.g., reflectivity, absorption, transparency, specularity, roughness) will be important to be considered in the future urban planning process of solar neighborhoods. Moreover, the inclusion of dynamic behaviors of the urban environment (e.g., seasonal variability of deciduous trees, variable reflectance of the terrain due to the presence of snow) should become standard practice when performing simulations spanning different seasons under current and future climate scenarios.

Solar assessments and optimizations combining different spatial domains of the urban environment (i.e., outdoor, building envelopes, indoor) as well as different uses of buildings are rare (Formolli et al., 2023). The development of multi-domain approaches able to weigh various solar KPIs within the same workflow can be seen as an objective to better discretize the complexity of the built environment in the future. To achieve the “total environment”, greater emphasis should be placed on environmental quality factors (e.g., comfort, daylight, air quality) during the selection of the KPIs to trade-off. Nowadays, the predominant holistic methodologies prioritize the optimization of energy and economic KPIs, relegating the evaluation of environmental impact and quality factors to a secondary position.

All these aspects are expected to be facilitated in the years to come by a broader digitalization of the building environment, supported by an extensive application of the Internet of Things (IoT), co-simulation approaches, advanced computer techniques (e.g., machine/deep learning, Artificial Intelligence - AI), and orchestration of real monitored data to realize more reliable and detailed digital twin of the built environment. In that regard, the combination of high LoD models of urban surfaces and high-resolution data can pave the way for digital twin platforms to conduct real-time solar analysis (i.e., solar maps) with multiple goals (e.g., optimal localization/integration of solar systems, optimize energy management strategies, detection of failures) and monitoring data that can provide valuable insights into the performance and optimization of solar energy systems. Moreover, advanced visualization techniques and indicators will make solar neighborhood planning instruments more accessible to the generic public. Finally, while the full potential of digital twin platforms is far from being fully exploited, the integration of deep learning techniques into holistic workflows (Manni and Nicolini, 2022) is fundamentally reshaping the simulation, analysis, and optimization of complex systems. This approach not only unlocks unparalleled levels of accuracy, efficiency, and adaptability, but also adeptly manages disconnected spatial scales (e.g., component, building, neighborhood, city) and diverse temporal domains, spanning short-, mid-, and long-term horizons.

2.1.3 Conclusions and further developments

Ten questions concerning planning and design strategies for solar neighborhoods have been addressed in this paper by discussing a wide range of aspects and related topics. For the first time, a classification is proposed for solar neighborhoods, which consist of neighborhoods primarily utilizing solar energy as RES. Four types of solar neighborhoods have been identified in section 2.1.2.1: the pure (or target-free) solar neighborhoods, the energy-centered solar neighborhoods, the carbon-centered solar neighborhoods, and the energy- and carbon-centered solar neighborhoods.

The workflow for planning solar neighborhoods is outlined after a comprehensive description of the design variables. In this regard, an overview of the passive and active solar strategies was provided together with examples of successful applications under different climatic conditions and urban contexts. The present study highlights the need for an inter-disciplinary and multi-criteria approach that can operate at multiple scales, ranging from building to neighborhood and city, and spatial domains (i.e., outdoor, building envelopes, and indoor), addressing the different competing uses of urban surfaces, along with their impacts on the total environment. Moreover, challenges, barriers, and drivers of solar neighborhoods are addressed. Driving forces that encourage the implementation of active and passive solar strategies in existing and new neighborhoods concern financial, environmental, and health incentives. Increasing energy efficiency, reducing energy consumption, reinstating a natural landscape to mitigate the effects of climate change-induced hazards, tackling UHI phenomena, enhancing air quality and comfort conditions within the cities, and assuring the right to light/shade and access to urban natural areas are some of the drivers identified in the ten answers. Nonetheless, significant challenges and barriers still exist. These are related to the social acceptability of solar strategies, the competing uses of urban surfaces, the drawbacks of some technologies (e.g., the impact of cool materials on energy demand for heating, solar energy production not correlated to energy demand), the lack of regulations about the exploitation of sunlight and access to shade, and the low profitability of most of the passive solar interventions.

Finally, the ten questions answered allowed to identify the knowledge gaps about solar neighborhood design and determine future research trends in this field. Future developments in solar neighborhood design concern:

- Identifying enhanced solutions for architectural integration of solar systems (i.e., different colors, hues, sizes, and patterns) to enable greater flexibility in the design.
- Integrating permeable surfaces in the built environment (i) to increase resilience to climate change effects and extreme weather events, and (ii) to enable direct food supply and urban farming.

- Implementing high LoD models for vegetation elements, urban furniture, and architectural features of buildings and neighborhoods without overly affecting the computational time of the analyses.
- Making a common practice to include the dynamic behaviors of the urban environment (e.g., the variation in transparency of deciduous trees, and the variable reflectance levels for the terrain due to the presence of snow) into the simulation process.
- Simulating the behavior of emerging surface treatments and technologies, such as icephobic layers, retroreflective coatings, thermochromic substrate, photoluminescent pigments, radiative coolers, electrochromic windows and their implications within the complex urban phenomena such as overshadowing effects and solar inter-building reflections.
- Boosting the digitalization of the built environment, supported by an extensive application of the IoT, co-simulation approach and advanced computer techniques (e.g., machine/deep learning, AI), and orchestration of data to realize more reliable and detailed digital twins of buildings and cities.
- Promoting legal reforms to solar access protection and improved planning approval processes where informed decisions can be made.
- Defining business models for solar neighborhoods to ensure the long-term viability, scalability, and financial sustainability of solar initiatives, facilitating their widespread adoption and maximizing their impact on energy transition and environmental goals.

Chapter 3

Characterizing the Urban Environment for Solar Energy Integration

As observed in the previous chapter, designing solar neighborhoods is a complex task that involves numerous physical factors, which are further complicated by the heterogeneity of the urban fabric. Consequently, the papers presented in this chapter delve deeply into topics related to understanding the urban microclimate and the intricate interactions between solar radiation and various elements of the urban environment. This chapter is based on the two publications:

- **Paper 2.** Boccalatte, A., Fossa, M., Thebault, M., Ramousse, J., Ménézo, C. (2023). Mapping the urban heat island at the territory scale: An unsupervised learning approach for urban planning applied to the Canton of Geneva. *Sustainable Cities and Society*, 96(February), 104677. <https://doi.org/10.1016/j.scs.2023.104677>
- **Paper 3¹.** Boccalatte, A., Fossa, M., Ménézo, C. (2020). Best arrangement of BIPV surfaces for future NZEB districts while considering urban heat island effects and the reduction of reflected radiation from solar façades. *Renewable Energy*, 160, 686–697. <https://doi.org/10.1016/j.renene.2020.07.057>

It is essential to underline that the scale of analysis differs between the two papers. Paper 2 refers to a large-scale analysis, while Paper 3 focuses on the district scale. Consequently, the simulation methodologies employed exhibit significant differences. In the case of the first paper, techniques oriented towards reducing computational times were adopted through automatic classification and machine learning. On the other hand, the second paper utilized a coupled approach to enhance the accuracy of Building Energy Models' (BEMs) results, taking into account the characteristics of urban surfaces and the microclimate.

¹The findings of this article were featured in an informative publication in PV Magazine available at <https://www.pv-magazine.com/2020/07/28/how-much-vertical-bipv-is-too-much/>

Contents

4.1	Evaluating the Impact of Urban Morphology on Rooftop Solar Radiation: a New City-Scale Approach based on Geneva GIS Data	157
4.1.1	Introduction	157
4.1.2	Data and Methods	159
4.1.2.1	GIS Data Sources and Case Study	160
4.1.3	Definition of I^* , the Scaled Solar Insolation	161
4.1.4	Morphological Tessellation and Calculation of Urban Form Features	164
4.1.5	Data Pre-processing	167
4.1.6	Results and Discussion	167
4.1.6.1	I^* distribution over the Canton of Geneva	168
4.1.6.2	Statistical Analysis of the Shading Conditions as a Function of the Urban Morphology	169
4.1.6.3	Correlation Study	171
4.1.6.4	Correlation Analysis by Municipality	173
4.1.7	Conclusions and Perspectives	176
4.2	Preliminary Estimation of the Solar Potential in the Liguria Region (Italy)	178
4.2.1	Executive Summary	178
4.2.1.1	Methodology and Data Sources	179
4.2.1.2	Results	183
4.2.1.3	Conclusions	185

Paper 2

3.1 Mapping the Urban Heat Island at the Territory Scale: an Unsupervised Learning Approach for Urban Planning Applied to the Canton of Geneva

Abstract

This study presents a fully reproducible clustering based methodology for the assessment of the urban heat island intensity (UHII) at the territory scale, using parametric microclimate models and limited computational resources. In large-scale climate modelling, a common preliminary operation is to utilize the well-established Local Climate Zone classification to characterize the thermal response of urban areas based on morphology. With the increasing availability of urban datasets, data-driven approaches can be implemented to quantitatively derive meaningful urban features without relying on a standardized classification. The proposed methodology employs a Gaussian Mixture Model clustering algorithm to partition the urban territory into a suitable number of homogeneous microclimate zones, enabling the calculation and mapping of the UHII for each zone through the Urban Weather Generator (UWG) tool. The developed approach is applied to the Canton of Geneva, Switzerland, identifying ten microclimatic areas and analyzing the spatiotemporal variation of UHII. Results show yearly average values of UHII ranging from 1.7°C to 2.2°C, depending on urban morphology. The simulated values are partially validated by comparison with on-site measurements from two urban weather stations, yielding a satisfactory agreement. The methodology can support urban planning with the goal of avoid overheating through a large-scale mapping.

Keywords

Urban Heat Island; Local Climate Zones; Urban Clustering; GIS-data; Urban Microclimate

3.1.1 Introduction

The urban heat island (UHI) phenomenon, i.e. the local increase of the urban air temperature compared to the rural surrounding areas, is a major issue for global climate disruption (Palme and Salvati, 2021). In addition to the global temperature rise of about 1.5°C and the ever more frequent climate anomalies such as heatwaves (IEA, 2021; IPCC, 2022; Pielke et al., 2022; Pyrgou et al., 2017), urbanization is responsible for an air temperature increase that may reach up to 12°C at peak in cities (Oke, 1982). This condition strongly increases the vulnerability of modern cities (Grimmond et al., 2010; Rajagopal et al., 2023) especially in Europe, which is particularly affected by global warming. Urban overheating negatively impact building energy

consumption (He, 2019; Hwang et al., 2020), public health (Tong et al., 2021), air pollution (Wang et al., 2021b), thermal comfort (Alvarez et al., 2021), ecosystems (Dissanayake et al., 2020), economics and productivity (AECOM Australia Pty Ltd et al., 2012; Memme and Fossa, 2022). In the literature, numerous field studies have been presented for more than 450 worldwide major cities including London, U.K. (Kolokotroni et al., 2012), Barcelona, Spain (Salvati et al., 2017a), Basel, Switzerland (Parlow et al., 2014), Sydney, Australia (Santamouris et al., 2018), Singapore (Bueno et al., 2015a), Wuhan, China (Huang et al., 2020), Los Angeles, United States (Vahmani and Ban-Weiss, 2016), Toronto, Canada (Wang et al., 2016).

Despite the evidence of this phenomenon, most research related to building energy performance evaluation still fails to integrate UHI into energy demand and thermal comfort analyses (Lauzet et al., 2019; Mirzaei and Haghghat, 2010; Santamouris, 2014). The majority of building energy-related studies exploit non-local weather data from reference weather station measurements located outside the cities (e.g. airports). As demonstrated in previous research by the Authors (Boccalatte et al., 2020a) and other studies (Li et al., 2019b; Lima et al., 2019; Palme et al., 2017; Salvati et al., 2017b), this affects to a great extent the building energy-use predictions. The UHI strongly modifies the energy demand related to building HVAC systems and buildings, in turn, negatively impact urban air temperature and thermal comfort through heat losses. In this sense, microclimate models are becoming essential for both building design and urban planning to adequately consider local climate conditions and plan mitigation strategies.

3.1.1.1 Experimental Measurements of Urban Heat Island (UHI)

Given the relevance of the Urban Heat Island (UHI) phenomenon, substantial research has been conducted to investigate its magnitude and the characteristics through experimental observations. Remote Sensing (RS) data acquired through satellites (e.g. Landsat, MODIS, ASTER), drones, aircrafts have been extensively used to map the urban heat at the city scale (Venter et al., 2020). By utilizing thermal images from RS, land use and land surface temperature (LST) data can be derived to investigate the spatiotemporal variation of urban heat (AIDousari et al., 2022; Chen et al., 2023; Unal Cilek and Cilek, 2021). Most of the large-scale Urban Heat Island (UHI) estimates derived from Land Surface Temperature (LST) data refers to the Surface Urban Heat Island (SUHI), which measures the temperature of the surface of the built environment. Nevertheless, for thermal comfort studies and Building Energy Modeling (BEM), it is crucial to consider the air temperature instead of the surface temperature.

In recent years, the use of sensors to measure air temperature in urban areas has become increasingly popular (de Almeida et al., 2021). Besides the traditional urban meteorological networks, various techniques exist for crowdsourcing, citizen science weather stations (CWS), and mobile data (Chàfer et al., 2022; Muller et al., 2015; Romero Rodríguez et al., 2020). For instance, Netatmo urban weather stations provide small, flexible, and affordable sensors that can be autonomously installed by citizens at multiple locations throughout a city, offering a good

level of spatial coverage for experimental data measurements (Benjamin et al., 2021; Brousse et al., 2022; Meier et al., 2015). Despite their value in UHI studies, sensors are subject to limitations related to device accuracy, placement, and maintenance, which may hinder capturing all the relevant information for comprehending the UHI effect. The data generated by these sensors provide uncertified observations, which may be misrepresentative. Several studies have reported significant daytime biases mainly resulting from improper shading of outdoor sensors (Varentsov et al., 2020). Additionally, while sensors may provide valuable insights, their usage is limited to providing point data, limiting the ability to evaluate the impact of mitigation strategies, changes in urban texture, or even projections with future weather scenarios. In this context, numerical simulation and modeling is still indispensable for decision-making procedures. To obtain a comprehensive understanding of the UHI effect, it is thus essential to combine sensors with modeling approaches, such as street scale, local scale, and city scale microclimate models.

3.1.1.2 Modelling the Urban Heat Island (UHI) at Different Spatial Scales

In recent decades, several modeling approaches have been proposed to investigate the Urban Heat Island (UHI) phenomenon at different spatial scales, ranging from the street scale to the city scale. However, a primary research gap still exists, which relates to the differences between microscale (street and local scale) and macroscale (city scale) models (Lauzet et al., 2019; Masson et al., 2020). Microscale models, while providing higher resolution and accuracy, are more computationally expensive and often limited to small areas (a street or a district), while macroscale models, although more computationally efficient, lack the necessary spatial resolution to capture the fine-grained features of urban environments. To overcome this gap, the main objective of this study is to implement a data-driven approach based on local scale parametric models that can bridge the gap between spatial resolution and computational efficiency. Reviews related to urban climate simulation and modeling tools illustrate the main differences across the urban scales and can be used as a reference to identify the most appropriate modeling approach for a given research question (Johari et al., 2020; Kumar et al., 2021; Lauzet et al., 2019; Lobaccaro et al., 2021; Lun et al., 2009; Mutani and Todeschi, 2020; Sola et al., 2020).

City Scale Models

Regarding city scale models, several limitations have been identified and discussed in the literature (Mirzaei, 2015). The simulation domain is often up to several kilometers, encompassing an entire city and its surroundings. Urban morphological features can be estimated through approximated values of roughness length or parametrized using Urban Canopy Models (UCM), such as the popular Town Energy Balance (TEB) model (Afshari and Ramirez, 2021; Lemonsu et al., 2012; Masson, 2000). However, mesoscale models, such as MESO-NH (Lac et al., 2018) and the Weather Research and Forecast (WRF) model (Grimmond, 2017), have inherent

limitations in terms of resolution making it challenging to observe local phenomena and capture differences among various urban morphologies.

Street and local scale models

Street scale models only cover the volume of air within the urban canyon, including local phenomena and detailed modeling of 3D geometry, heat transfers, and airflow regimes (Jänicke et al., 2021). Local scale models can be categorized into two types: detailed models and parametric models. Detailed models, such as Envi-met (ENVI-met, 2021), SOLENE-microclimat (Morille et al., 2015), take into consideration both fluid mechanics equations and 3D radiation equations, while SOLWEIG/UMEP (Lindberg et al., 2018) solves the detailed 3D radiations equations in real geometries. These models provide the most accurate representation of the urban environment, as they rely on a detailed representation of the area. However, due to the complex calculations involved, particularly those related to fluid mechanics (as in the case of ENVI-met or SOLENE-microclimat), performing year-long simulations over large spatial areas can be challenging.

In contrast, parametric models, including the Canyon Air Temperature (CAT) model (Erell and Williamson, 2006) and the Urban Weather Generator (UWG) (Bueno et al., 2013a, 2015a, 2013b, 2012, 2014) define urban morphological features through a set of urban parameters that characterize the thermal properties of the district, making them computationally efficient even for year long simulations. Despite their computational efficiency, they are typically limited to simulating a single district and cannot be directly applied at the city scale comprising multiple districts. This can be overcome if the whole studied area can be represented by a limited set of representative districts on which these parametric models can be applied.

3.1.1.3 Definition of Representative Districts for Microclimate Studies

The identification of representative urban morphologies within a city can be achieved through different approaches. Some studies rely on expert knowledge or on the administrative boundaries to identify homogeneous district morphologies within a city and calculate the related urban parameters for simulation purposes (Litardo et al., 2020; Salvati et al., 2020). Another “top-down” approach is the Local Climate Zone (LCZ) classification, originally introduced by Stewart and Oke (Oke, 1982; Stewart and Oke, 2012). The LCZ is used to categorize the landscape into 17 representative local climate zone typologies that are assumed to have a unique air temperature regime under similar atmospheric conditions (Stewart and Oke, 2012). A typical range of urban parameter values that describe the urban shape, the characteristics of the vegetation, the human activity levels, the land cover is associated with each LCZ. If some data are lacking, the scheme also allows deriving the values of unknown parameters from look-up tables for the parameters of the other categories (e.g., for mean building height and density, aspect ratio, sky view factor,

anthropogenic heat emissions, etc.). LCZs have been extensively applied to city-scale UHI studies based on both numerical simulations and field measurements (Brousse et al., 2022; Dimitrov et al., 2021; Fenner et al., 2014; Hashemi, 2020; Houet and Pigeon, 2011; Huang et al., 2020; Leconte et al., 2015; O'Malley and Kikumoto, 2022; Richard et al., 2018). Despite the advantages of this qualitative approach, as recently highlighted by Lipson et al. (Lipson et al., 2022), the growing availability of high resolution urban datasets (Biljecki et al., 2021; Milojevic-Dupont et al., 2023) and unsupervised machine learning classification techniques enables a transition to quantitative “bottom-up” approaches (Boccalatte et al., 2022).

This research aims to develop a data-driven approach that utilizes clustering techniques to quantitatively identify representative urban morphologies based on microclimate-related parameters. The proposed approach aims to bypass the subjectivity of expert knowledge as well as the abstraction of LCZs.

Unsupervised learning methods have been applied to a few urban studies (D'Acci and Batty, 2019; Wang and Biljecki, 2022), for example to identify representative building groups and predict the energy use at the city scale (Tardioli et al., 2018), to derive a detailed morphological classification of the urban form (Fleischmann et al., 2022a, 2020), to identify typo-morphologies and perform thermal comfort simulations with Envi-met (Maiullari et al., 2021).

However, the use of unsupervised learning for investigating Urban Heat Island (UHI) at the city scale remains relatively unexplored. While previous studies have utilized clustering techniques to investigate the Surface Urban Heat Island (SUHI) at the city scale (Kwak et al., 2020), the coupling of such approaches with parametric models for large scale UHI mapping is still unexplored, making it the original contribution of this study. Specifically, this research aims at identifying representative microclimate zones within the Canton of Geneva (whose area is approximately 300 km²) through GIS data and clustering. Subsequently, the microclimate-related parameters of each zone are fed into the Urban Weather Generator (UWG) tool (Bueno et al., 2013a, 2015a, 2013b, 2012, 2014), a parametric microclimate model that allows predicting the urban air temperatures at the district level based on urban parameters. The resulting workflow enables the simulation of the spatiotemporal variation of the UHI at the city scale with comparable accuracy to a local scale model but with much lower computational time. The simulated results have been partially validated against experimental measurements from two urban weather stations located in the city of Geneva yielding a satisfactory agreement.

3.1.2 Data Sources, Models and Methods

As briefly introduced in Section 3.1.1, this study aims to evaluate and map the Urban Heat Island intensity (UHII) at the city scale. Given the vast extent, using a parametric model is the most effective way to achieve the objective due to computational limitations that hinder the use of detailed 3D modeling. The starting point of the presented methodology is the determination of the urban parameters required for numerical simulations. These parameters, primarily related

to urban shape, vegetation, human activity levels, and building characteristics, serve as inputs for the simulations. In this study, the Urban Weather Generator tool is selected because of its validated accuracy and fast computational time (Section 3.1.2.1 and Section 3.1.2.2). Once the model is chosen, the following step is GIS data collection and pre-processing. At this stage, the urban parameters required for the selected model (in this case, the UWG tool) are extracted from GIS urban datasets (Section 3.1.2.3). Since GIS data can be either at the level of individual buildings or at a bigger scale (e.g. district), a certain number of pre-processing operations are performed to uniform data and obtain the averaged values of the urban parameters within a spatial area that is coherent with the selected simulation tool. This step is fundamental since a single building do not determine the urban microclimate, but a group of them does. To this end, the morphological tessellation technique is applied (Section 3.1.2.4) avoiding rough data averaging by means of a fixed grid. Then, starting from the averaged parameter values, an advanced clustering algorithm based on Gaussian Mixture Models (GMM) is employed to classify urban areas with similar characteristics, under the assumption of a similar impact on the microclimate (Section 3.1.2.6). Finally, the UWG tool is used to numerically simulate the intensity of the UHI phenomenon in each urban zone, resulting in a map of the entire city that accounts for the local urban characteristics.

The developed workflow is schematically represented in Figure 3.1. The total area under consideration in this study corresponds to the administrative boundaries of the Canton of Geneva, which are depicted in the figure (boxes 4 and 5) by the black line.

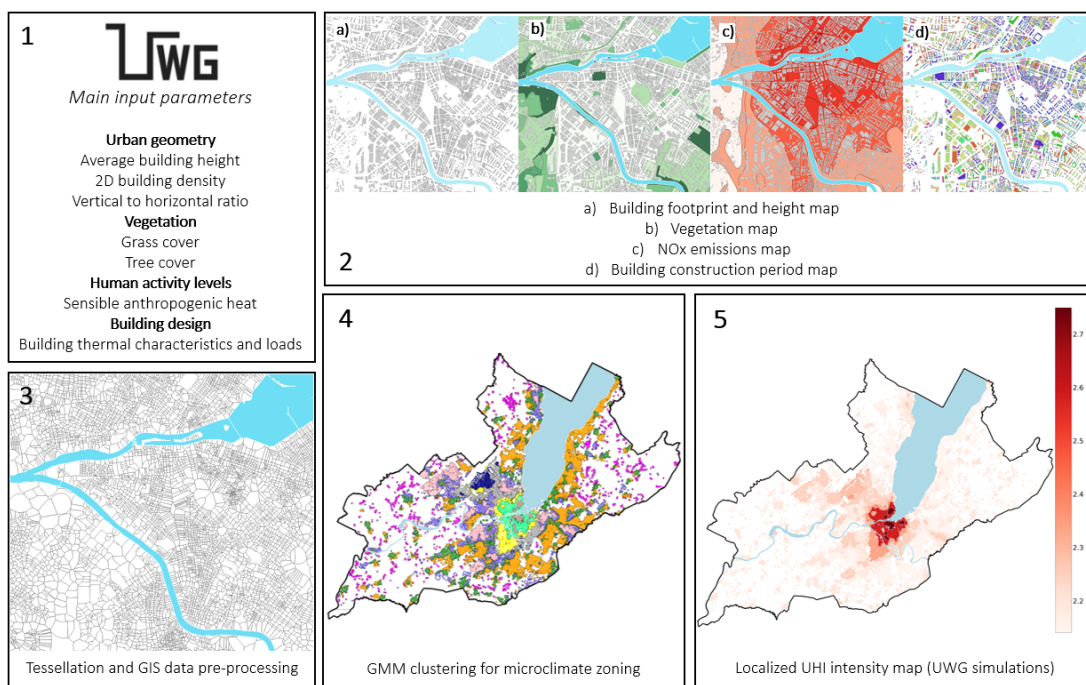


Fig. 3.1 Schematic representation of the developed methodological steps applied to the Canton of Geneva

3.1.2.1 The Choice of the Urban Microclimate Model: The Urban Weather Generator

The UHI intensity (UHII) is calculated through the Urban Weather Generator (UWG) model (Bueno et al., 2013a, 2015a, 2013b, 2012, 2014). The UWG is a parametric microclimate model that uses the principles of energy transfer and heat balance equations within the urban canopy to account for various physical processes such as solar radiation, thermal radiation, conduction, and convection. It is built upon the well-established Town Energy Balance (TEB) scheme (Masson, 2000), which is a two-dimensional representation of an urban canyon consisting of three surfaces: a wall, a road, and a roof. The TEB scheme calculates the climate conditions, drag force, and heat fluxes of a district composed of identical urban canyons. To improve the representation of the interactions between buildings and the urban climate, the UWG integrates the original TEB scheme with a detailed Building Energy Model (BEM) derived from EnergyPlus algorithms². The UWG comprises four calculation components, including the Rural Station Model (RSM), Vertical Diffusion Model (VDM), Urban Boundary-layer Model (UBL), and Urban Canopy and Building Energy Model (UC-BEM), which are fully described in (Bueno et al., 2015a). The UWG structure allows to predict urban canopy air temperature based on rural weather data and a parametric description of the urban area. The UWG tool is freely available to download³. Originally written in MATLAB in 2013⁴, the tool has been continuously updated and is now available into a Python library and as a grasshopper plugin. This study utilizes the latest Python version of the tool (V5). To run the simulations the UWG takes two inputs: a meteorological file in a .epw format from the nearest rural weather station and an .xml format file (Extensible Markup Language) describing the urban parameters. The output is a modified .epw format weather file in which air temperatures have been adjusted based on the local urban characteristics. The main input urban parameters can be subdivided into four main categories: urban geometry, vegetation, human activity levels, and building characteristics (including thermal properties of construction elements and building loads). Table 3.1 summarizes the most relevant parameters required for this study. These parameters have a significant impact on local microclimate changes and can vary widely across different areas of the city. It's worth noting that a certain number of other parameters related to general simulation settings (such as latitude and longitude of the city, day and night boundary layer height, road materials albedo and conductivity, etc.), or to specific building-related variables (such as wall and roof albedo, glazing ratio, solar heat gains from windows, etc.), are also needed, as fully described in (Bueno et al., 2014), but for sake of brevity they are reported in Appendix A.

²<https://energyplus.net/>

⁴<https://github.com/ladybug-tools/uwg.git>

⁴https://github.com/Jiachen-Mao/UWG_Matlab

Table 3.1 UWG main input parameters for UHI simulation

Symbol	Description
Urban geometry	
\bar{H}	Average height of buildings [m]
ρ_{urb}	Urban area building plan density [-]
VH	Vertical to horizontal ratio [-]
Vegetation¹	
ρ_{grass}	Grass coverage [-]
ρ_{trees}	Tree coverage [-]
Human activity levels	
Q_{sens}	Non-building sensible heat at street level [W/m^2]
Building characteristics²	
U_{wall}	Thermal transmittance of walls [$\text{W}/\text{m}^2\text{K}$]
U_{roof}	Thermal transmittance of roof [$\text{W}/\text{m}^2\text{K}$]
U_{window}	Thermal transmittance of windows [$\text{W}/\text{m}^2\text{K}$]
i	Building infiltration rate [ach]

¹ Since in the reference vegetation map the vegetation coverage is not differentiated between grass and trees, the vegetation coverage value is split in half between ρ_{grass} and ρ_{trees} resulting in $\rho_{\text{grass}} = \rho_{\text{trees}}$.

² Building characteristics are derived from the building construction period.

Several studies have conducted sensitivity analyses on the input parameters of the UWG model to determine their significance (Alchapar et al., 2019; Litardo et al., 2020; Mao et al., 2017; Salvati et al., 2017c). The results indicated that the most influential parameters are those related to urban geometry and sensible heat from traffic. In contrast, the impact of vegetation parameters in some cases is lower due to the simplified modeling of vegetation in the UWG model (Salvati et al., 2017c). The model assumes that a fraction of absorbed solar radiation is transformed into latent heat and does not contribute to the temperature increase in the urban canyon and it neglects the impact of tree shading on building walls and roofs, considering only its effect on the road. Regarding building characteristics, the sensitivity analysis performed by (İsmet Berke, 2010) showed that the thermal transmittance of walls and infiltration rate are among the most influential building characteristics. However, the model shows a low sensitivity to building albedo values. Overall the parameters considered for this study (Table 3.1) are deemed relevant for conducting the simulations.

3.1.2.2 Validation and Limitations of the Urban Weather Generator Model for Urban Microclimate Analysis

The accuracy of the UWG has been extensively validated using both field measurements and simulations in different urban environments including Basel (Switzerland), Toulouse (France) (Bueno et al., 2013b), Singapore (Bueno et al., 2015a), Boston (USA) (Street et al., 2013), Abu Dhabi (UAE) (Mao et al., 2017), Rome (Italy), Barcelona (Spain) (Salvati et al., 2016). The validation results show an average RMSE error of about 1-2K with respect to hourly temperature predictions.

However, it is crucial to recognize that the UWG model is based on a simplified computational model that may not fully capture site-specific microclimate effects beyond spatially averaged results. Nonetheless, these simplifications are necessary for computational efficiency, enabling large-scale simulations over extended periods which is the main objective of this study. The limitations of the model in simulating vegetation and advection from rural to urban boundary layers are considered acceptable due to the computational efficiency required for such simulations. Additionally, the UWG model does not account for the effects of large water bodies, which have been excluded from the study to date, leading to the assumption that the air above Lake Geneva has similar characteristics to rural air.

Despite these limitations, the UWG model has been extensively validated and shown to be suitable for a variety of urban environments. The UWG limitations are considered acceptable for this case study bearing in consideration that the UWG model performs best for urban sites characterized by low wind conditions, where the UHI intensity is primarily due to urban features and anthropogenic heat release.

3.1.2.3 Urban Data Sources for Urban Parameter Derivation in the Geneva Canton Case Study

The case study is the whole Canton of Geneva (46°13'05" N, 6°09'58" E, Switzerland), sizing about 300 km² and comprising about 60,000 buildings. The reference urban dataset is the Geneva Territory Information System (SITG)⁵ which is an open-source repository of hundred geodata sets related to town planning, mobility, energy, nature, and even climatic analyses. Data are stored into geospatial vector data or into raster data.

Here, a set of SITG vector data in shapefile format are used to derive the urban parameters required for simulations. The shapefile format is used to store the geometric location and one or multiple attributes of a geographic feature, which can be a point, a line, or a polygon (area). The reference geographic feature can be represented by individual buildings (e.g. building height data) or a portion of space delimited by predefined boundaries that fit the stored information (e.g. vegetation data). In this study, three shapefiles are used to derive the urban parameters.

⁵<https://ge.ch/sitg/>

Cad.batiment.hors.sol stores several data about each of the 60,000 buildings. Among them, the building height data are used to calculate the urban parameters related to building geometry and the building construction year data are used to derive the building element thermal characteristics, as explained in more detail in Section 3.1.2.4. *Ecopot.za* includes data related to biodiversity and vegetation for each district of the city, and it is used to derive the vegetation parameters. Finally, *Immissions.no2.moyenne* is a map of the yearly average NO₂ concentration within the city and it is used to derive the anthropogenic heat emissions, as explained in more detail in Section 3.1.2.5. Indeed, NO₂ emissions is related to vehicle exhausts, which account for the largest part of the anthropogenic heat emissions.

It is important to note that the reliability and accuracy of data obtained from large open source urban datasets are critical, particularly with respect to data frequency and updates. While sources like OpenStreetMap provides a comprehensive and accessible source of urban data, the accuracy and reliability of the data may not always be sufficient. In the present study, building height data were obtained from a high-precision LIDAR survey conducted by swisstopo in 2019, while the other data (building construction period, vegetation, and NO₂ emissions) were updated less than one year ago.

3.1.2.4 Data Pre-Processing: Calculating the Average Urban Parameters with Tessellation and Spatial Weights

The key point for the calculation of the urban parameters is to define the reference area that fits the microclimate model used for numerical simulation. The Urban Weather Generator is a district scale model able to simulate the urban temperatures within a 200/300 m radius reference area. This value aligns with the definition of a district in the Local Climate Zone (LCZ) framework. This framework considers a district to be a 300 m radius urban area with similar land use, ground cover, and building density. The most straightforward approach to quantify the average urban parameters within a coherent reference area is through a squared grid defining a certain number of cells measuring about 500 m each. Although the use of a fixed regular grid is a fast technique for data averaging, it represents an arbitrary segmentation that is not consistent with the complexity of the urban texture. Furthermore, since the UWG has to be fed with ‘average’ urban parameters of the site, using a square grid may lead to a loss of complexity and local specificities. In what follows an alternative approach is proposed to partition the city into homogeneous areas with respect to the input parameters needed for simulations. To this aim, a polygon-based adaptation of Voronoi tessellation is applied to this study. In particular, a recently developed Python toolkit named *momepy* (Fleischmann, 2017; Fleischmann et al., 2022a, 2020) is employed to define morphological cells based on building footprints. The morphological tessellation function aims to derive the “surface of influence” of a building, i.e. the smallest spatial unit that delineates the portion of space around each building (tessellation cell). In a first phase, the tessellation cell is used to calculate the building area plan

density (ρ_{bld}) and the vertical-to-horizontal ratio (VH_{bld}) of each building through Eq. 3.1 and 3.2:

$$\rho_{bld} = \frac{A_{bld}}{A_{tess}} \quad (3.1)$$

$$VH_{bld} = \frac{P_{bld} \cdot H_{bld}}{A_{tess}} \quad (3.2)$$

where A_{bld} , P_{bld} , and H_{bld} are respectively the footprint area, the perimeter, and the height of each building and A_{tess} is the area of the related tessellation cell.

As briefly introduced in Section 3.1.2.3, urban datasets collect GIS data that can be related to different geometrical entities based on the type of information described. In particular, building height (as well as the derived ρ_{bld} and VH_{bld}) and construction period data are related to individual buildings, whereas vegetation and NO₂ data relate to coherent portions of land. In the first case, where data are related to each building, the value assigned to each tessellation cell is the one of the building itself, whereas in the second case, the value assigned is obtained by superimposing the vegetation and NO₂ maps.

At this stage, the raw GIS data has undergone processing to compute the required urban parameters pertaining to each building/tessellation cell. As a result, a series of values relating to urban geometry, vegetation, human activity levels, and building characteristics are associated to each individual element (building/tessellation cell). However, measuring individual characters is insufficient to capture the impact on microclimate, as it is necessary to calculate the average values of these parameters within a defined area that corresponds to the extent of the UWG simulations (200/300 m radius). This is because the urban microclimate is altered by a group of buildings rather than by a single isolated building. To this aim *spatial weights* are used to calculate the contextual tendency of each urban parameter. Spatial weights are mathematical structures that identify the neighbouring buildings of a given building, i.e. the buildings whose tessellation cells are adjacent to the building in question. As depicted in Figure 3.2, it is possible to define n orders of spatial weights depending the number of times adjacency has been verified. For instance, if a generic reference building (shown in red in Figure 3.2) is considered, the 1st order spatial weights are the buildings (shown in yellow) whose tessellation cells touch the reference. This can be seen as the first ‘belt’ of the buildings (in yellow) around the reference one. The 2nd order spatial weights refer to the buildings (shown in green), whose tessellation cells are adjacent to the first order cells. This process is repeated for all the buildings and till an nth order level corresponding to the radius (from reference building) required by the UWG model.

In the present study, 3rd order spatial weights are chosen to calculate the averaged urban parameters so that a group of approximately 50 adjacent buildings are included, coherently with the extent of the UWG simulation (200/300 m radius). The averaged urban parameters,

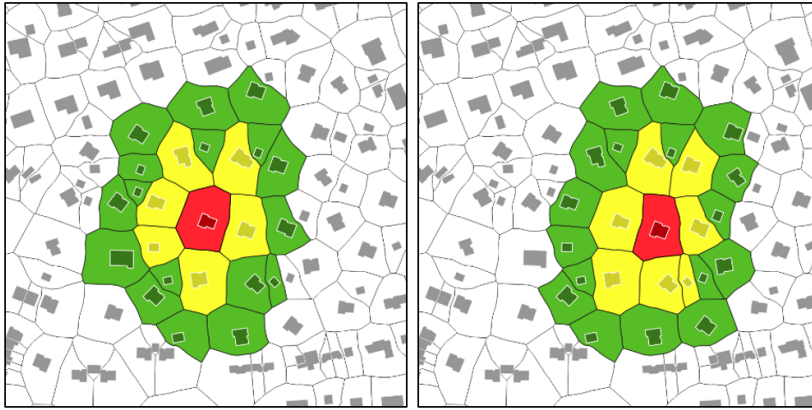


Fig. 3.2 1st and 2nd order cells (yellow and green respectively) determined through spatial weights with respect to a reference building (red). The operation is repeated for all the buildings

noted $U_{dist,j}$, replace the individual urban parameters for the j^{th} building, $U_{bld,j}$, and they are representative of the district immediately surrounding the considered building. In more detail, $U_{dist,j}$ are calculated as in Eq 3.3

$$U_{dist,j} = \frac{U_{bld,j} + \sum_{i=0}^{N_{neigh,3}} U_{bld,i}}{1 + N_{neigh,3}} \quad (3.3)$$

where $N_{neigh,3}$ is the number of 3rd order neighbouring buildings (i) around the reference j^{th} building, and $U_{bld,i}$ are the parameter values associated with each of them. In this way, for each building it is possible to calculate averaged urban parameters, that are representative of the district composed of this building and the surroundings 3rd order neighbours. This approach allows for the input to the UWG model to be representative of a district rather than just a single building. Therefore, it results in values that are not significantly different for neighbouring buildings, which are likely to be part of the same microclimate. This approach also allows for the consideration of morphological transition zones between the high-density city centre and the sparsely built rural areas.

3.1.2.5 Inference of Human Activity Levels and Building Characteristics

Unlike urban geometry and vegetation parameters, which can be directly derived from GIS pre-processing operations on shapefiles (respectively *Cad.batiment.hors.sol* and *Ecopot.za*), the non building sensible heat at street level (Q_{sens}) and building characteristics (U_{wall} , U_{roof} , U_{window} , i) need to be inferred from other data.

In order to determine the value of non-building sensible heat (Q_{sens}) at ground level, a maximum value of 20 W/m² is assumed based on literature studies (Mao et al., 2017). This value represents the highest heat emissions in the densest and busiest areas of the Canton according to similar studies. To determine the values for the other areas, a linear relationship is

established between Q_{sens} and the yearly average NO_2 concentration (whose maximum value is $38 \mu\text{g}/\text{m}^3$ for the Canton of Geneva), according to the *Immissions.no2.moyenne* shapefile. The reasoning behind this is that NO_2 emissions are related to vehicle exhausts, which can be considered proportional to the anthropogenic heat emissions. By scaling the maximum value with the maximum NO_2 concentration, a range of Q_{sens} values is obtained, representing the non-building sensible heat for the different areas of the Canton. However, it should be noted that in future scenarios where a significant increase in electric vehicle usage is expected, this assumption may need to be re-evaluated, taking into account the heat emission rates associated with electric vehicles (Mussetti et al., 2022).

The building characteristics are inferred based on their construction period contained in *Cad.batiment.hors.sol* shapefile. The reference values are obtained from a study by Tardioli et al. (Tardioli et al., 2020), which derived the main building characteristics based on building energy modelling standards in Switzerland (SIA 380/4, SIA 382/1, SIA 385/2) and on the expertise of the Department of Planning, Housing and Energy (DALE). The UWG tool allows for consideration of three different construction periods, i.e. before 1980, between 1980 and 2000, and after 2000. In this study, the building characteristics from Tardioli et al. is averaged to align with the required construction periods, as reported in Table 3.2. It should be noted that it would have been technically feasible to include building refurbishment in the analysis but this aspect is not considered due to the lack of available data and the relatively low refurbishment rate in the Canton of Geneva (Flourentzou, 2019). The other building related parameters which are assumed to be equal across the three construction periods, are detailed in Appendix A.

Table 3.2 Reference values of building characteristics based on different construction periods

Name	Units	Before 1980	Between 1980-2000	After 2000
U_{wall}	[W/m ² K]	1.28	0.47	0.21
U_{roof}	[W/m ² K]	1.01	0.38	0.21
U_{window}	[W/m ² K]	3.22	1.95	1.40
i	[ach]	1.10	0.60	0.45

3.1.2.6 Gaussian Mixture Model (GMM) Clustering

Clustering is a common unsupervised learning method that groups data based on their similarities. In this study, clustering is used to group portions of land that are expected to have similar microclimatic conditions. This is achieved by normalizing and using as inputs for the clustering algorithm the average urban parameters that are considered representative of the thermal response of a group of buildings.

The choice of the clustering method depends on the type of data, the purpose of the study, and the assumptions made about the data distribution. The selected clustering algorithm is

the Gaussian Mixture Model (GMM) clustering due to its suitability to handle complex and varied data distributions such as similar urban applications (Fleischmann et al., 2022b; Ma et al., 2021; Quan, 2020; Wang and Biljecki, 2022). Other popular methods for clustering include k-means, hierarchical clustering, and Density-Based Spatial Clustering of Applications with Noise (DBSCAN), but they may not always be optimal for urban studies with similar purposes, as they have certain limitations. For example, k-means assumes that clusters are spherical and equally sized, which may not hold for this type of urban data. DBSCAN is a density-based algorithm and could not achieve satisfactory results with multi density data distributions (Cesario et al., 2020). Hierarchical clustering is computationally expensive for large datasets as in this case. GMM, unlike other unsupervised algorithms, assumes that each cluster corresponds to a multi-dimensional Gaussian probability distribution, that is often used in statistical modeling as it provides a suitable way to represent complex data distributions. GMM uses the Expectation-Maximization (EM) approach (Reynolds, 2015) to fit data points to a mixture of K multi-dimensional Gaussian distributions (one for each cluster) which are randomly generated starting from a set of means and a covariance matrices. The EM algorithm iterates over the Expectation (E-step) and the Maximization (M-step) until it converges. Once the total number of clusters (K) is determined, each k^{th} component can be defined through a mean of μ_k and a covariance matrix Σ_k . The mixing coefficients for the k^{th} cluster are defined as π_k , with the constraint that $\sum_{k=1}^K \pi_k = 1$, so that the total probability distribution is 1. The probability density function of point x is calculated as in Eq 3.4

$$f(x) = \sum_{k=1}^K \pi_k N\left(x \mid \mu_k, \Sigma_k\right) \quad (3.4)$$

Where x is the data point being evaluated, $N(x \mid \mu_k, \Sigma_k)$ is the Gaussian distribution with mean μ_k and covariance Σ_k , and π_k is the mixing coefficient for the k^{th} cluster. Then, the M-step is used to determine the maximum value of the log-likelihood function. In this study, the GMM clustering algorithm is implemented through a Python script by means of the *scikit-learn* library (Pedregosa et al., 2011). To identify the optimal number of clusters, the Bayesian Information Criterion (BIC) and the Akaike Information Criterion (AIC) scores (Schwarz, 2007) are calculated and plotted for a range of potential cluster numbers, from 2 to 15, as shown in Figure 3.3. The selection of 15 clusters as the maximum limit is made to ensure that each cluster represented a sufficient number of buildings. Choosing more clusters would have added unnecessary complexity without significantly identifying representative clusters. Lower BIC and AIC scores indicate a higher quality of clustering performance. In this study, two distinct plateaux are identified in the results, at 8 and 10 clusters. Both options are carefully evaluated and it is determined that 10 clusters provide a more fine-grained classification of the urban textures in the Geneva Canton, effectively capturing the required diversity. On the other hand, 8 clusters offered a simpler, more generalized representation, but failed to distinguish between the old medieval area and the high-density city center.

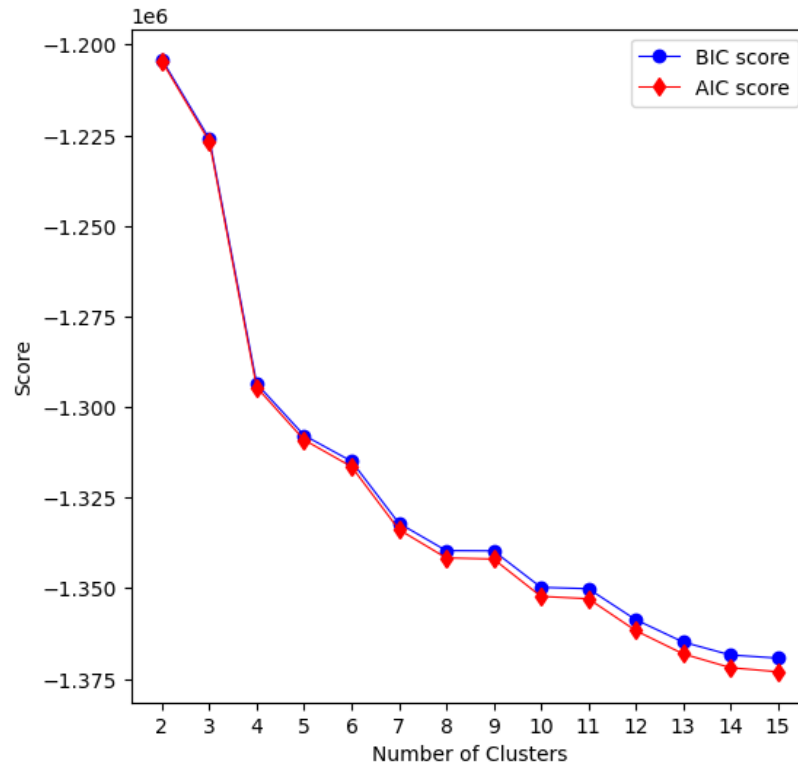


Fig. 3.3 BIC and AIC scores per number of clusters

Once the cluster are formed, the average urban parameters of each cluster ($U_{cluster}$) are calculated and used as inputs to the UWG simulations.

3.1.2.7 UHII Calculation and Mapping through the Urban Weather Generator and Validation towards Real Data

The systematic approach developed in this study allow the classification of urban textures in the Geneva Canton. In brief, the first step involves the determination of the building urban parameters (U_{bld}) for each of the 60,000 buildings in the study area using GIS data (Section 3.1.2.3). Next, the district urban parameters (U_{distr}) associated with each building are calculated through tessellation and spatial weights (Section 3.1.2.4). Finally, a Gaussian Mixture Model (GMM) is applied to classify the buildings into representative microclimatic clusters, reducing the number of alternatives from 60,000 to 10 (Section 3.1.2.6). From these clusters, the average cluster urban parameters ($U_{cluster}$) are calculated. This three-step approach is critical in gaining a comprehensive understanding of the representative microclimate zones within the Canton and classifying them effectively.

The $U_{cluster}$ parameters are then used as inputs to perform hourly microclimate simulations (10 simulations, one for each cluster) over the course of a typical meteorological year. The Urban Weather Generator (UWG) modifies the rural weather station data file (.epw format) to

create a new urban weather file with adjusted air temperatures based on the predetermined urban parameters. The source rural weather station data is obtained from the reference EnergyPlus weather file for the Canton of Geneva⁶(Geneva 067000 IWEC). The latter arises from the TMY (Typical Meteorological Year) weather file which was built based on more than ten years of real measurements recorded at the Geneva International Airport weather station (MeteoSwiss). The station is located on the city boundaries and it is officially recognised by the World Meteorological Organization (WMO). As a result of the UWG simulations, the spatiotemporal variation of the Urban Heat Island Intensity (UHII) is analysed and a UHII map of the whole Canton is created. The UHII is here defined as the positive difference between the urban and the rural air temperature as in Eq 3.5

$$UHII = (T_{urb} - T_{rur}) \quad \text{if } T_{urb} > T_{rur} \quad (3.5)$$

In order to verify the accuracy of the spatiotemporal variation of the Urban Heat Island intensity (UHII), a partial validation is carried out. Since the Typical Meteorological Year (TMY) file used in the simulation is a standard weather file and does not represent actual measurements, real data was necessary for validation. As a result, measurements from a rural weather station located in Brenex (used as the input rural weather file for UWG simulations) and two urban weather stations in the Canton of Geneva (situated in the Battelle and Prairie areas) were used for validation. The urban weather stations were monitored by the University of Geneva throughout 2019, and the measured data were compared with simulated data obtained from the UWG. It is important to note that this validation using real data is only partial, as only two out of the ten total clusters (i.e., Battelle and Prairie areas) could be compared to actual data due to the lack of supplementary reliable urban weather stations. The Results section presents the outcomes of this partial validation.

3.1.3 Results

The following sections present the results of the previously outlined methodology. Section 3.1.3.1 presents the classification of the Canton of Geneva into representative microclimate zones using the Gaussian Mixture Model (GMM) clustering. In Section 3.1.3.2 the temperature distribution of the rural and urban areas is analysed as a result of the UWG simulations. Section 3.1.3.3 focuses on the spatiotemporal variation of the Urban Heat Island Intensity (UHII) among the identified urban clusters. This section evaluates the microclimatic impact of the different urban clusters in terms of average and maximum monthly values ($UHII_{ave,month}$ and $UHII_{max,month}$ respectively). Section 3.1.3.4, explores the temporal variation of the UHII through the analysis of average hourly intensity values ($UHII_{ave,hour}$), highlighting the differences between nighttime and daytime. Finally, Section 3.1.3.5 is dedicated to the comparison between the UWG simulated values and on-site measurements.

⁶<https://energyplus.net/weather>

3.1.3.1 Clustering Results

As a result of the GMM clustering algorithm the 10 different homogeneous microclimatic zones have been identified and a map of them is shown in Figure 3.4. Each cluster C_j (with j ranging from 1 to 10) is represented by a different colour and the map shows that the clusters are well-defined and compact, effectively showcasing the morphological variations within the urban environment. White areas in the map represent unbuilt areas where the local conditions are thus expected to pertain the rural ones.

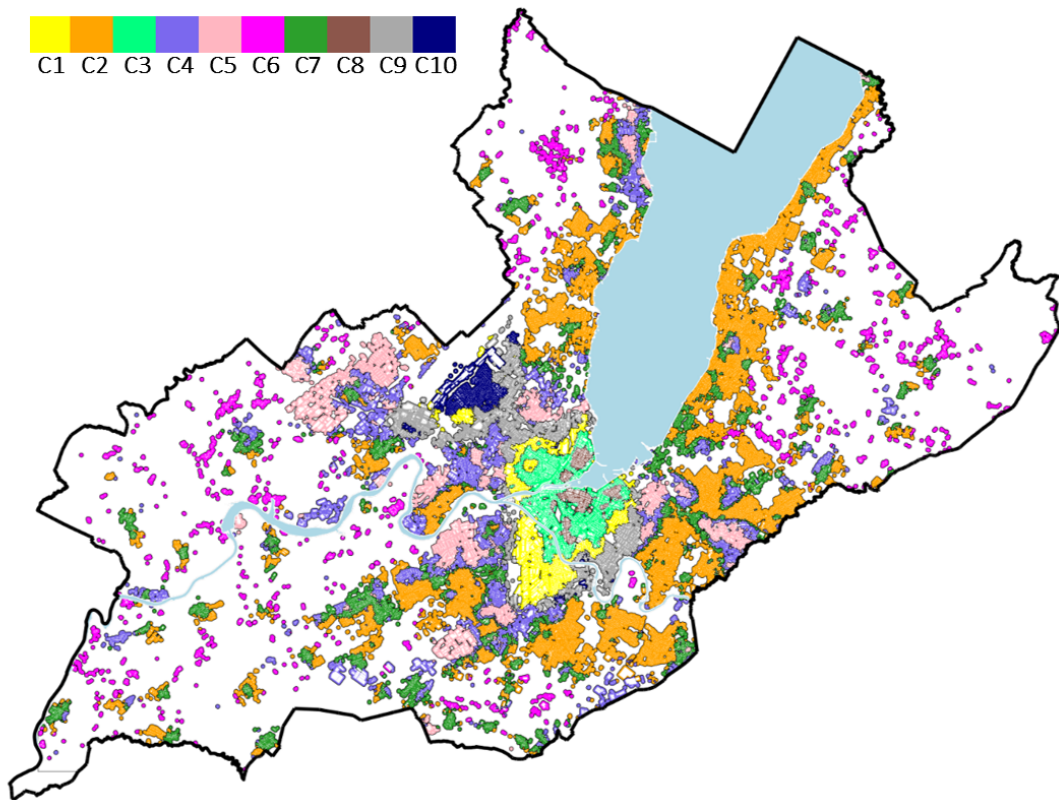


Fig. 3.4 Ten homogeneous microclimatic clusters of the Geneva Canton identified through GMM clustering. Each cluster is represented by a different colour and white parts represent the surrounding rural areas.

Table 3.3 lists the number of buildings and the average urban parameters for each cluster ($U_{cluster}$), which served as inputs for the Urban Weather Generator. From a morphological perspective, clusters C2, C4, C6, and C7 can be categorized as low-density urban areas, with the highest number of buildings and low impact of sensible anthropogenic heat. These areas generally feature well-spaced, low-rise buildings. On the other side, C1, C3, C8, and C9 are high-density and poorly vegetated urban areas. Here the impact of sensible anthropogenic heat is higher and the building construction period is typically before the year 1980. Clusters C5 and C10 can be considered intermediate urban typologies. Cluster C5 consists of medium/high-rise buildings in a compact urban texture, with a significant share of vegetation, low impact of human

activities, and more recent building constructions. On the other hand, cluster C10 represents recent low-rise building areas that are significantly impacted by nearby human activities.

Table 3.3 $U_{cluster}$ related to the ten clusters identified through GMM algorithm

ID	N° bldgs	\bar{H} [m]	ρ_{urb} [-]	VH [-]	$\rho_{grass/trees}$ [-]	Q_{sens} [W/m ²]	Construction period ¹ [%]		
							Pre1980	1980/2000	Post2000
C1	2856	17.8	0.31	1.5	0.13	8.3	70	15	15
C2	21676	7.5	0.11	0.4	0.33	< 1.5	47	32	21
C3	3916	21.6	0.39	2.1	0.06	16.5	77	13	10
C4	6826	11.3	0.15	0.5	0.27	< 1.5	51	23	27
C5	4195	16.81	0.22	1.0	0.21	< 1.5	60	23	17
C6	3135	7.7	0.08	0.3	0.47	< 1.5	58	27	16
C7	10402	9.5	0.18	0.7	0.29	< 1.5	52	29	19
C8	1827	20.6	0.55	3.2	0.03	20.0	75	10	15
C9	2767	16.3	0.17	0.8	0.22	4.0	64	20	16
C10	1234	9.5	0.14	0.5	0.28	11.7	46	30	24

¹The building construction period is expressed as percentage with respect to the total number of buildings within each cluster.

3.1.3.2 Comparison of Rural and Urban Temperatures using Probability Density Functions

In order to compare the simulated urban temperatures from the UWG with rural conditions, the probability density functions (PDFs) are calculated for each month of the year. The PDFs provide a smoothed representation of data that is useful to estimate and visualize the distribution of temperatures evidencing their density (probability of observing a specific temperature value) and distribution among rural areas and the ten identified urban clusters. To provide a more concise representation of the results, two representative months are selected to show the temperature distribution in the coldest and hottest periods of the year. February is chosen to represent the coldest months (September to April) while August represents the hottest months (April to September). Figure 3.5 shows the PDFs for February (left) and August (right). The black line represents the rural conditions, whereas the different colored lines (coherent with the map shown in Figure 3.4) are related to the ten urban clusters. In February, the distribution of urban temperatures has the typical bell shape, with values uniformly distributed around the maximum value which is between 0°C and 5°C. The distribution of the urban temperatures is similar in the shape but the curves are shifted upward and slightly to the right, indicating a higher frequency of higher temperatures. It can be also noticed that cluster C8 shows an inflection point between 5°C and 10°C, indicating higher temperatures compared to the other urban clusters. In August, the temperature distribution has a different and asymmetrical shape, with both rural and urban distributions having two peaks (of which one has an intensity equal to about half of the highest value). The rural temperature has its maximum peak reached between 15°C and 20°C and the

lower one between 25°C and 30°C. The pattern for all urban temperature distributions is exactly the same, with the two peaks of the rural temperatures being inverted in comparison to the urban temperatures.

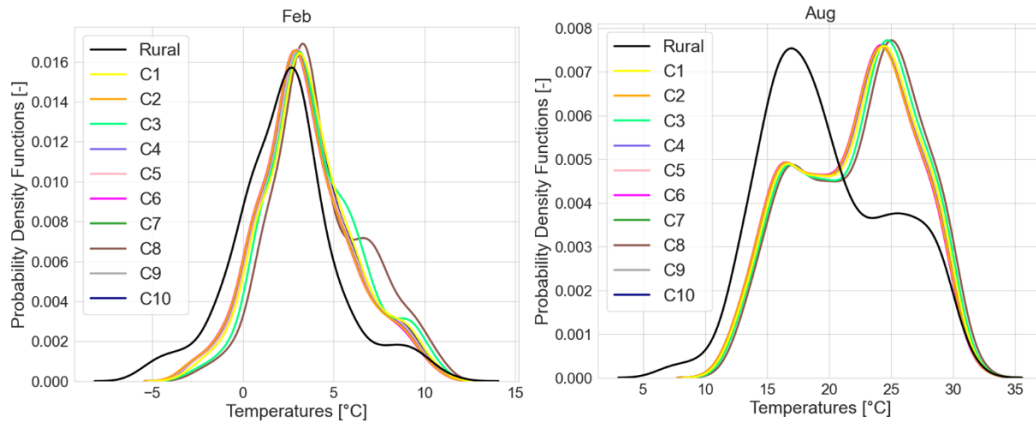


Fig. 3.5 Probability density functions of rural and urban temperatures. The representative months are February (left) and August (right).

3.1.3.3 Average and Maximum Monthly UHI Intensity Comparison among the Identified Clusters

In this section, the Urban Heat Island Intensity (UHII) for each urban cluster is investigated. As a yearly average the UHII ranges from a maximum value of 2.2°C for cluster C8 and a minimum value of 1.7°C for the low-density areas, namely clusters C2, C4 and C6, evidencing the impact of urban morphological features on overheating. To investigate the annual variability of the UHI the average monthly intensity ($UHII_{ave,month}$) is calculated for each cluster and shown in Figure 3.6. In general, it can be observed that the thermal behaviour of the identified urban clusters is clearly distinguishable. The ten clusters may be separated into four distinct groups according to their impact on microclimate. The groups, starting from the most impactful to the least, are clusters C3 and C8 (group 1), cluster C1 (group 2), clusters C5, C9, C10 (group 3), and clusters C2, C4, C6, C7 (group 4). The results align with the expectations based on the average urban characteristics of each group: group 1 represents the high-density historical city center, group 2 is a transition area near the city center, group 3 includes both medium-rise suburban areas (C5 and C9) and low-rise suburban areas with high anthropogenic impact (C10), and group 4 encompasses the peripheral open low-rise suburbs. The $UHII_{ave,month}$ difference between group 1 and 4 is considerable, ranging from about 0.4°C between April and September to 0.6°C between October and March. Considering all clusters, the minimum $UHII_{ave,month}$ value is of 0.73°C (cluster C6 in December), whereas the maximum value is of 3.13°C (cluster C8 in May). The months with the highest $UHII_{ave,month}$ are May, July, and August, with an overall overheating of 2.8°C, compared to the 0.9°C observed during November, December, and January. The results indicate that the UHII is not necessarily highest in the hottest months and

that the combination of solar radiation and morphological features such as vertical-to-horizontal ratios plays a role. In high-density urban areas (such as C8 and C3), the sun's lower angle during shoulder months leads to more heat accumulation on urban vertical surfaces (façades) and longer periods of elevated temperatures.

Finally, it is also important to note that although the UWG has been validated effectively for urban districts, its ability to predict the UHII in low-density suburban areas seems here limited. This is evident in cluster C6. This cluster is representative of very sparse building, with a very low density, and sometimes isolated building. Therefore, it would be expected, for this cluster to have temperatures closer to the rural ones. However, the UWG predicts a relatively significant UHII in these areas (Figure 3.5). Confrontation with experimental measurements would be necessary to fix this issue. But in case it would be likely linked to the assumption of the UWG model that the district being analyzed is surrounded by other urban districts rather than rural areas, potentially leading to an overestimation of overheating in boundary and suburban areas.

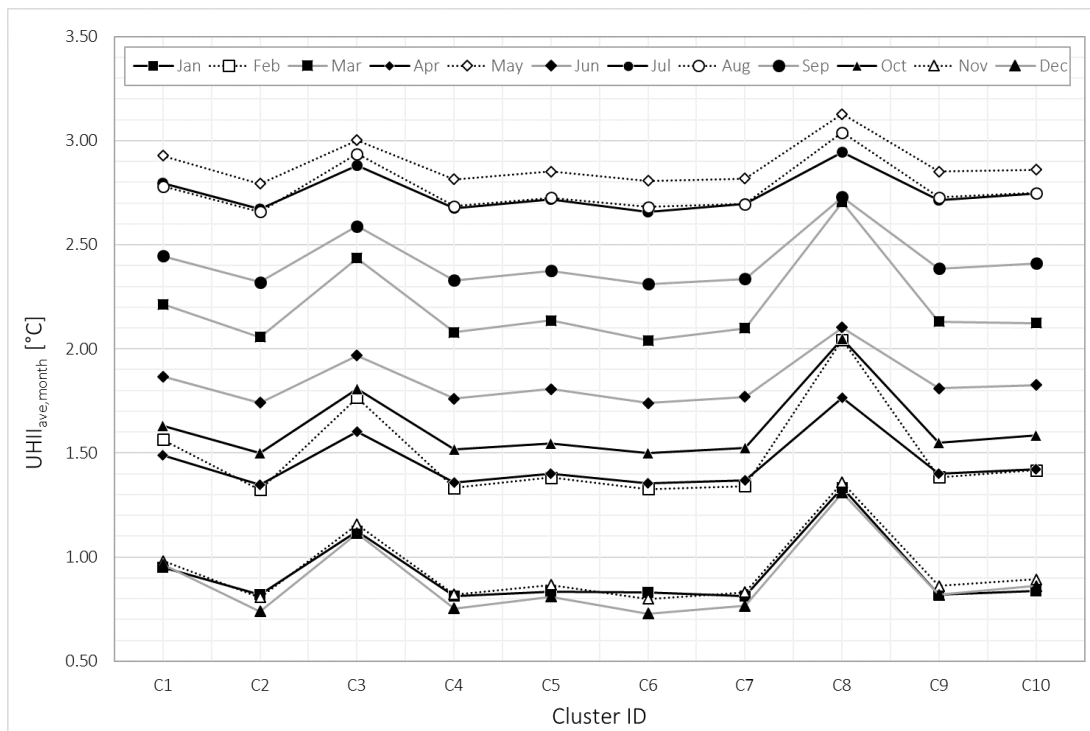


Fig. 3.6 Average monthly urban heat island intensity among the urban clusters.

The spatial variability of the $UHII_{ave,month}$ can be further elaborated through GIS tools to create a UHI map of the whole area visualizing the most impacted clusters. As an example, Figure 3.7 shows the $UHII_{ave,month}$ in August within the Geneva Canton. Consistent with previous numerical findings, the high-density urban areas (C8 and C3) closest to the lake experience the greatest UHII. While it is acknowledged that the absence of lake modeling represents a limitation of the UWG tool, it should be noted that the UHI phenomenon is most relevant in conditions of high irradiance and low wind speed. To address this, GEO-NET, a

bureau specializing in climatic analyses, conducted a detailed analysis of the current climate in the Canton of Geneva, identifying areas most affected by urban overheating (Gmbh, 2020). GEO-NET employed a mesoscale model, FITNAH 3D (Gross, 1992), to simulate the impact of wind and temperature on the entire Canton, generating UHII estimates for a single representative summer day under conditions of high irradiance and low wind speed. Although it is not possible to compare results directly due to the different temporal scales of the two studies (a single day compared to one year), detailed modeling results including are comparable to those obtained in the present study. In particular, they found that, despite the presence of the lake, the same high-density urban areas are the most impacted by overheating and that the air exchange is very limited due to the obstruction effect of buildings.

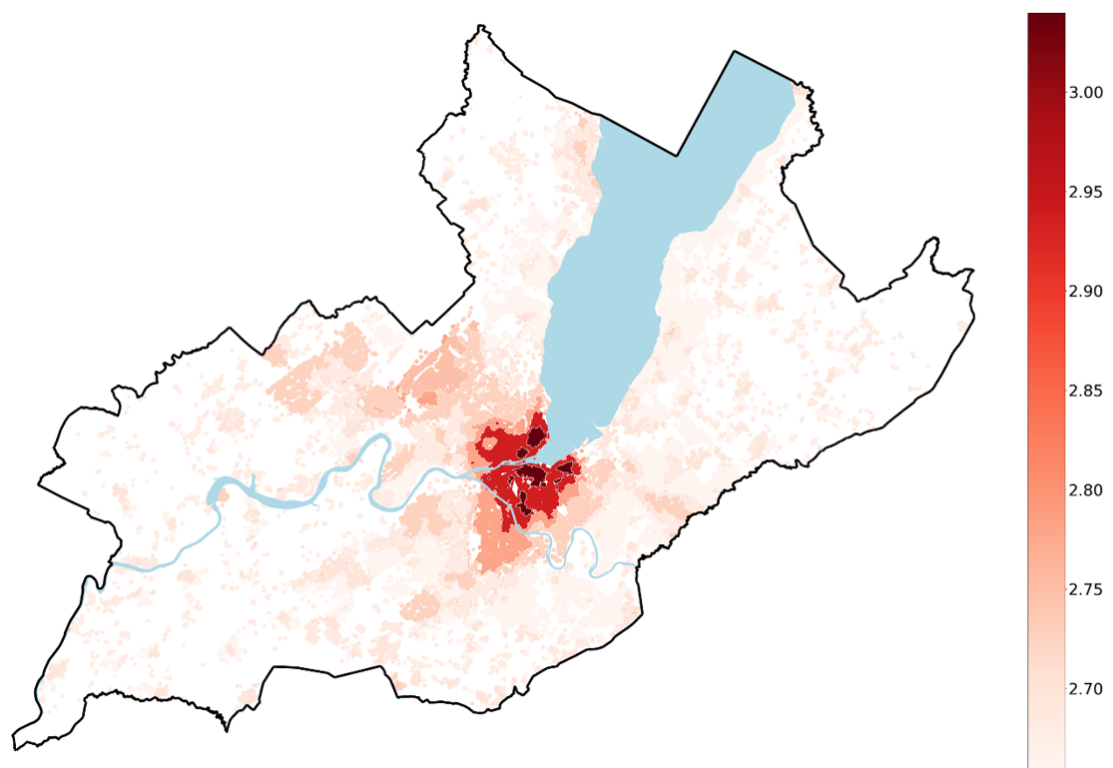


Fig. 3.7 Spatial variability of the monthly average UHII in August within the Canton of Geneva.

The peak hourly values of urban heat island intensity ($UHII_{max,month}$) for each month among the urban clusters are shown in Figure 3.8. During the colder months (October to February), the hourly peaks range from 5.1°C in clusters C2 and C6 to 8.6°C in cluster C8. However, during the warmer months (March to September), the calculated values are much higher, with a minimum of 7.9°C in cluster C6 and a maximum of 11.5°C in cluster C8. In general, the differences among the clusters are less evident compared to the average values, except for the two high density clusters C3 and C8, whose maximum values in some months are considerably higher. This is an effect of the non-simultaneous between nocturnal and diurnal conditions in rural and urban areas. At sunrise, when incoming solar radiation starts warming the urban

surfaces, high-density clusters experience a faster warming process due to their significantly higher thermal mass, resulting in a larger $\text{UHII}_{\text{max,month}}$ compared to low-density areas. This phenomenon is explained in more detail in Section 3.1.3.4.

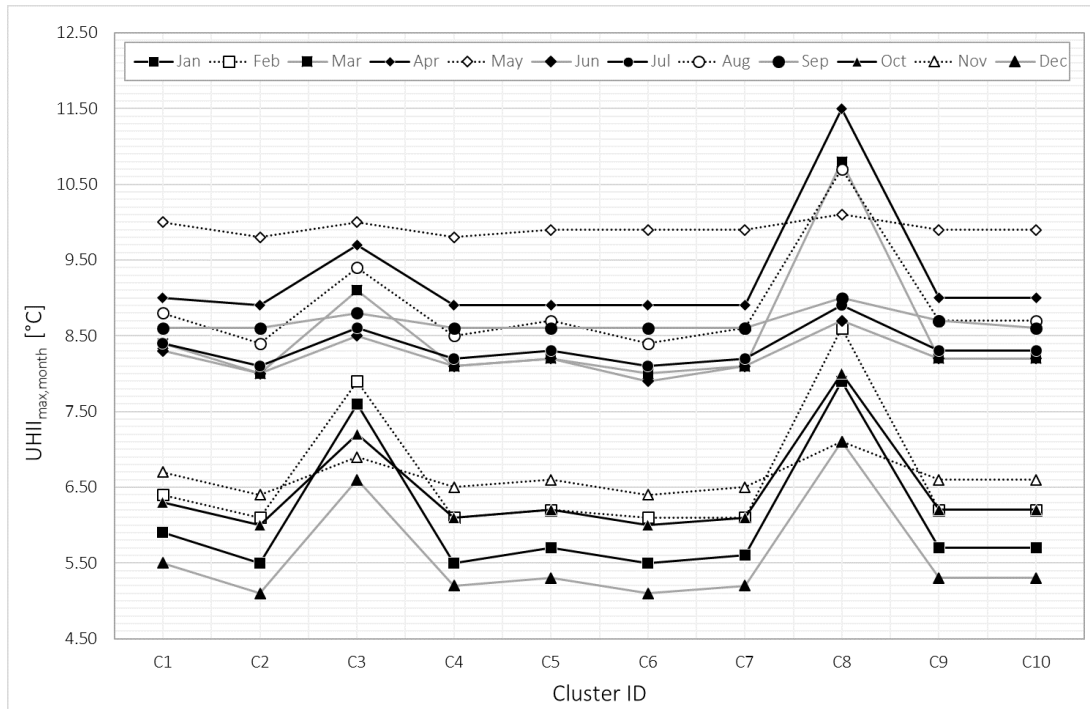


Fig. 3.8 Maximum monthly urban heat island intensity among the urban clusters.

3.1.3.4 Average Daily Variation of the UHI Intensity among the Identified Urban Clusters

This section is dedicated to the analysis of the diurnal cycle of the UHII. As shown in Figure 3.9 the average hourly urban heat island intensity ($\text{UHII}_{\text{ave,hour}}$) among the urban clusters is higher during nighttime, reaching a minimum between 11:00 h and 14:00 h, with values lower than 0.5°C . During the late afternoon, both the $\text{UHII}_{\text{ave,hour}}$ and the differences among the urban clusters increase, reaching values ranging from 2.5°C to 3.5°C , depending on the urban morphology. As observed in the previous Section 3.1.3.3, the high-density urban clusters (C3 and C8) exhibit the highest UHII peak values which are generally observed at sunrise (around 6:00 h). As previously anticipated, at this time, the atmosphere is transitioning between nocturnal and diurnal conditions, and the incoming solar radiation is beginning to warm the urban surfaces (Oke, 1982). Observing the UWG simulation process (which is based on an hourly timestep) it can be noticed that generally when sun rises the rural temperature is still at its minimum value (nighttime conditions), whereas the high-density urban clusters have already started the warming process. For the urban clusters with lower density this warming process is generally delayed by 1 hour, when the rural temperatures have also started to rise, resulting in a considerably lower $\text{UHII}_{\text{max,month}}$ compared to high density clusters. These results evidence that

the UWG predictions are strongly influenced by the input geometric parameters (in particular the vertical-to-horizontal ratio), which has been also highlighted in previous literature studies where the same behaviour has been observed (Alchapar et al., 2019; Salvati et al., 2017a).

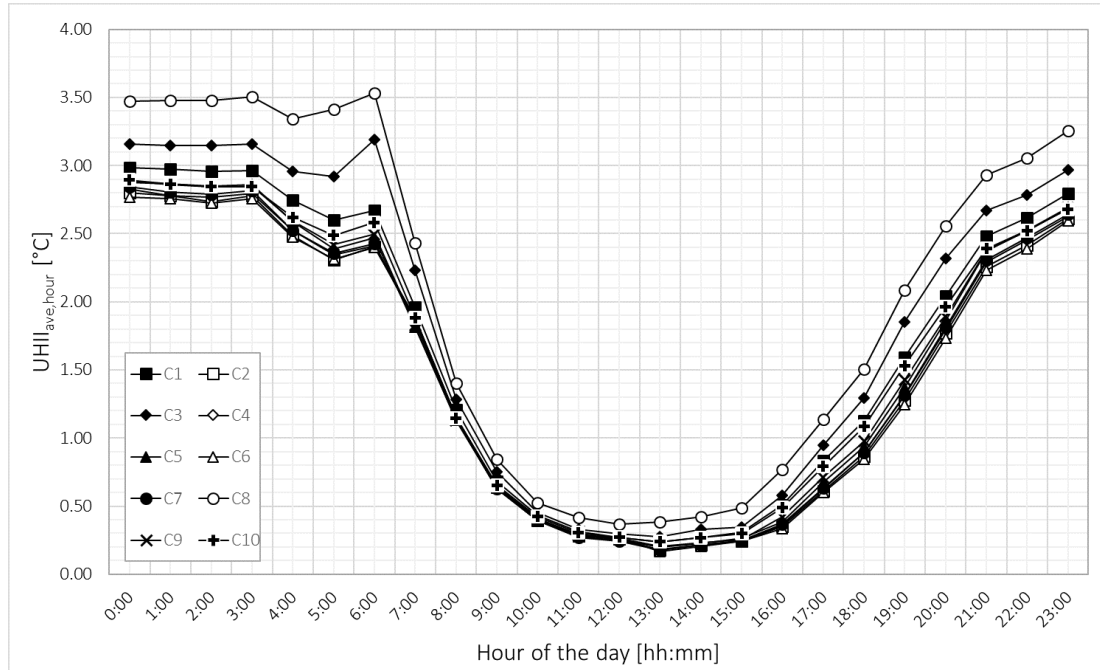


Fig. 3.9 Average hourly urban heat island intensity among the urban clusters.

The boxplots of the UHII during daytime and nighttime are plotted for each cluster and shown in Figure 3.10, left for daytime and right for nighttime. Each whisker represents the interquartile range (the 25th percentile for the lower quarter of the values, and the 75th for the upper quarter) of the yearly UHII data, with the median value represented by the line inside the box. Outliers are represented as individual points outside the whiskers. Daytime and nighttime periods have been determined based on solar radiation. It can be observed, as expected, that the median values of UHII during daytime is about 0.5°C for all the clusters, whereas the nighttime values range between 1.5°C and 2.2°C depending on urban morphology. It can be also observed that during nighttime the UHII experience a higher variability and that the differences between the clusters are more evident compared to daytime. Peak values reaching up to 10°C are also more likely to be observed during the night than during the day.

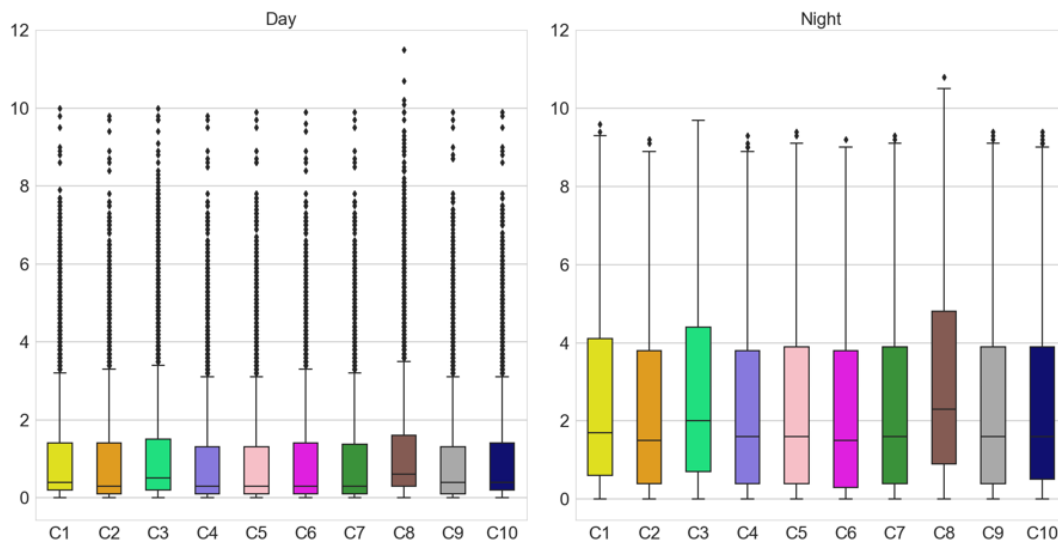


Fig. 3.10 Boxplots of UHII during daytime (left) and nighttime (right).

3.1.3.5 Comparison between Predicted and Measured Average UHII Monthly Values

This section includes the results of two additional simulations using the Urban Weather Generator (UWG) to validate the developed workflow and the simulated urban heat island intensity (UHII) values with metered data. Real temperature measurements from a rural site (Bernex, used as input weather file for UWG simulations) and two urban weather stations (Battelle and Prairie, used for comparison). The meteorological data from Bernex were recorded and provided by Agrométéo (suisse, 2022), while the data from Battelle and Prairie were monitored by the University of Geneva during the same year (University of Geneva, 2022). The recorded UHII of 2019 ($UHII_{real}$) is calculated for both Battelle and Prairie sites as the positive temperature difference with the rural site of Brenex. $UHII_{real}$ is then compared with the UWG simulated values ($UHII_{UWG}$) from two additional UWG simulations performed using Bernex data as the source rural weather file and the urban parameters of Battelle and Prairie areas derived from clustering. Based on the clustering results (Section 3.1.3.1), the Prairie weather station is located within the high-density cluster C3, whereas Battelle falls into the suburban cluster C4. Thus, the urban parameters used as an input to the UWG simulations are the ones of the related clusters (C3 and C4). The results are shown in Figure 3.11 in terms of average monthly values (markers) and related standard deviation (bars). Two different colors are used for Prairie and Battelle, and the different markers identify the simulated and the metered data. It can be observed that, overall, the simulated values follow the same yearly trend as the measured values while overestimating them in some cases. It should be noted that the standard deviation of the simulated data is generally larger than that of the measured data. With the exception of the months of February and June, where the simulated values are about 0.6°C higher than the measured ones, the average absolute difference in all other cases is around 0.15°C . The substantial discrepancy in the results of February and June could be due to the presence of various sources of error and uncertainty

which may have occurred in real-world conditions, in contrast to simulated values which are based on model assumptions and parameterizations.

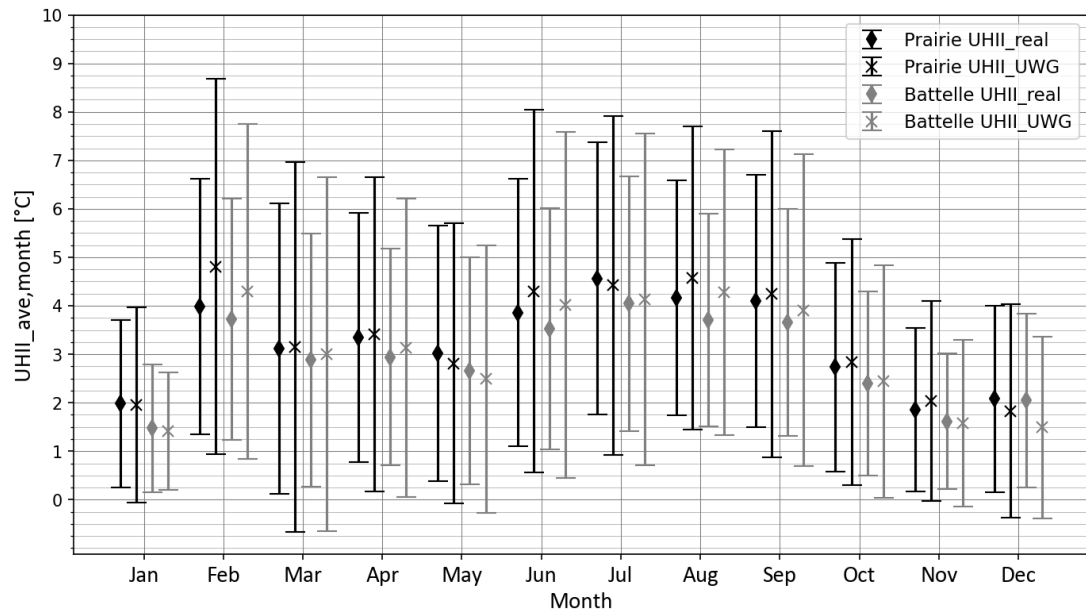


Fig. 3.11 Average monthly UHII (markers) and standard deviation (bars) arising from UWG simulations ($UHII_{UWG}$) and from real measurements ($UHII_{real}$) for two selected urban weather stations.

A comparison of the average hourly values and their related standard deviations is also conducted and shown in Figure 3.12. The results indicate that the UWG tool tends to overestimate the UHII during nighttime and underestimate it during daytime, which may be attributed to various factors such as model assumptions and input parameter quality. While improving the model is not within the scope of this article, these findings provide valuable insight for future improvements and refinement of the model accuracy, and highlight its potential limitations.

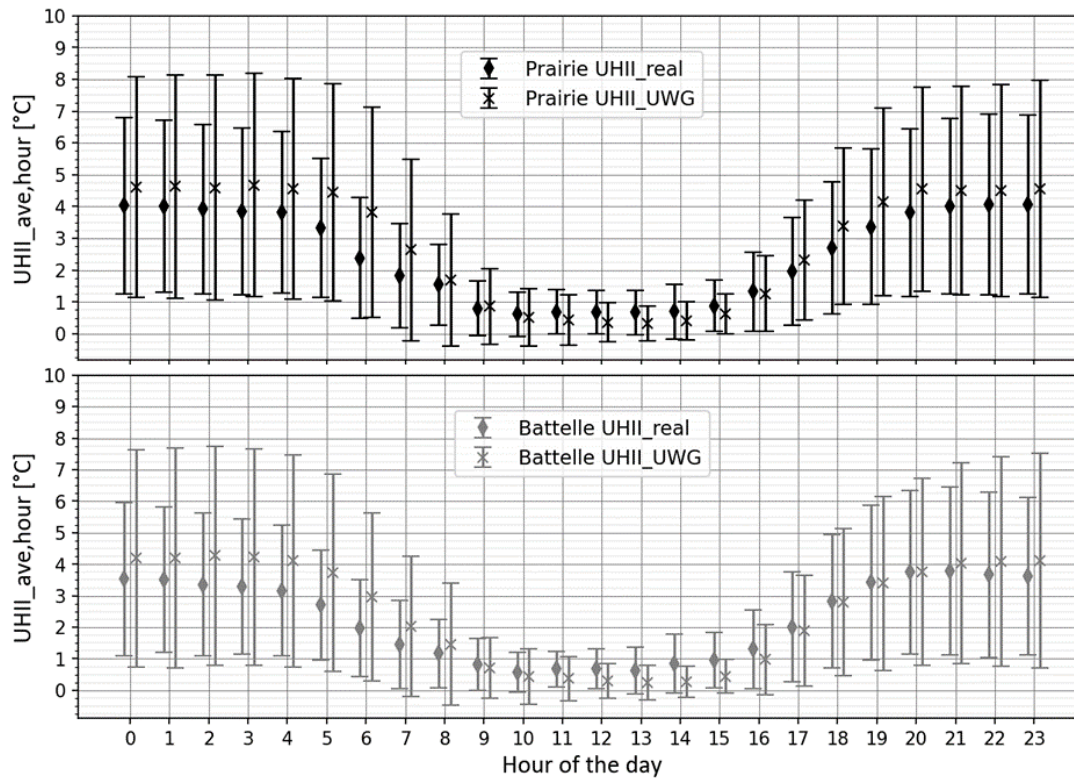


Fig. 3.12 Average hourly UHII (markers) and standard deviation (bars) arising from UWG simulations ($UHII_{UWG}$) and from real measurements ($UHII_{real}$) for two selected urban weather stations

3.1.4 Discussion

This study proposes a data-driven and machine learning-based approach to perform computationally efficient year-long Urban Heat Island (UHI) analyses at the city scale. The developed workflow aims to derive meaningful urban parameters and to identify representative microclimatic clusters within a city. The urban parameters are quantitatively obtained from detailed urban datasets, GIS pre-processing operations, and Gaussian Mixture Models (GMM) for clustering. The results are then used as inputs to the Urban Weather Generator (UWG), a well-established microclimate parametric model, to simulate urban weather conditions from rural weather station data. The methodology is applied to the Canton of Geneva and results in the identification of ten representative microclimatic clusters.

The simulated urban heat island intensity (UHII) has a considerable variability over the year and among the urban clusters, with a range of values from 0.7°C to 3.1°C and differences up to 0.6°C depending on the urban morphology. The results also show that the UHII monthly peak values range from 5.1°C up to 11.5°C . The daily variation of the UHII is also found to be much higher during nighttime (about 2.5°C) than during daytime (about 0.5°C), consistent with similar literature studies. Finally, the accuracy of the simulated values is compared towards

real measured data of two urban weather stations during 2019. In general, the accuracy of the simulated values is effective in capturing the average monthly UHI intensity and the differences between the two reference urban weather stations. However, for two months (February and June), the simulated values are significantly higher (about 0.6°C) than the measured ones, compared to an average difference of only 0.15°C for the other months. The model also slightly overestimates nighttime values while underestimating them during daytime.

3.1.5 Limitations and Future Perspectives

The proposed approach has some limitations that should be noted. Firstly, the approach is data-driven, and reproducing it in other cities is possible provided that a detailed urban dataset like the one used in this study is available. Secondly, as discussed in Section 2.2, the UWG model presents some simplifications mainly related to the modelling of advection, vegetation, and the presence of large water bodies. These simplifications may prevent from capturing site-specific phenomena and seems to overestimate the UHII in peri-urban areas. Nevertheless, the proposed workflow enables the simulation of one year on a large scale, making it suitable for city-wide analyses. Precise temperature time series in specific areas of the city would require more accurate simulations, not a parametric model.

However, despite these limitations, the proposed approach has several strengths. It offers a computationally efficient way to perform city-scale UHI analyses, providing valuable insights for urban planners to accurately plan UHI mitigation strategies, identify areas at the greatest risk of overheating, and plan energy-related interventions.

Future improvements to the Urban Weather Generator (UWG) model offer promising prospects for achieving even higher accuracy in simulating urban microclimates. Recent studies, such as the Vertical Urban Weather Generator (VUWG) (Moradi et al., 2021) and the improvements introduced by Xu et al. (Xu et al., 2022), are refining the capabilities of the UWG. The VUWG resolves vertical profiles of climate variables, including temperature, wind, specific humidity, and turbulence kinetic energy, in relation to urban design parameters. The improvements by Xu et al. enhance the radiation, vegetation, and convective heat transfer calculation processes, better matching the physical representation of urban districts.

In the future, the integration of Internet of Things (IoT) sensors for weather data, crowd-sourcing, satellite data, and other data sources could potentially enhance the accuracy of the proposed approach. These future prospects hold the potential for more reliable data and more precise modeling of urban microclimates.

Paper 3

3.2 Best Arrangement of BIPV Surfaces for Future NZEB Districts while considering Urban Heat Island Effects and the Reduction of Reflected Radiation from Solar Façades

Abstract

Building Integrated Photovoltaics (BIPV) constitute the way to reach Nearly Zero Energy Buildings and even zero energy districts (NZED). BIPV surfaces can operate on roofs and façades and their efficiency and productivity are related to orientation, shading, reflections from surrounding surfaces. The novelty of the present investigation relies on a chained model also able to account for the Urban Heat Island conditions. The building performance are analysed as EnergyPlus simulations, considering a multi thermal zone reference building located inside a district of similar characteristics. The PV power generation, from hourly to yearly values, is calculated accounting for PV module temperature, irradiance intensity and solar incident angles, by further developing the well known Sandia model. The whole model, applied to a particular city (41.9°N, 12.5°E), shows how the progressive increase of vertical PV surfaces on both the reference and surrounding buildings yields to a reduction of the energy production per PV unit area. The yearly NZED requirements is reached, in the present case, harvesting solar energy on 60% of rooftops and on 60% of the total area of the façades, with a 11% decrease in energy production per PV unit area due to "darkening" effects induced by PV surrounding buildings.

Keywords

Urban Heat Island; Building Integrated Photovoltaics; Nearly Zero Energy Buildings; Nearly Zero Energy District; PV efficiency; Reflected Solar Radiation

3.2.1 Introduction

Building Integrated Photovoltaics (BIPV) is one of the most suitable technologies to comply with the European Nearly Zero Energy Building (NZEB) requirements of on-site renewable energy production (Jelle and Breivik, 2012). The nearly zero-energy target can be reached when the energy yield balances the annual building energy demand. The success in the exploitation of BIPV within the urban environment is related to a proper evaluation of both building energy demand and photovoltaic performance.

In the last decades, several software and tools have been developed to help engineers in estimating the building energy needs. These physical models are called Building Energy

Models (BEMs). Through a series of inputs, including site and weather characteristics, building envelope and geometry specifications, thermal loads, occupancy schedules, these models are intended to provide a detailed building energy assessment. Building energy modelling is a straightforward and useful approach to investigate building physics. On the other hand, the results are strongly influenced by the user's assumptions on occupants behaviour, thermal loads conditions, HVAC systems characteristics. The inaccuracy of predictions might increase when the reference building is studied within the complex urban environment which is subjected, in turn, to variability depending on construction features. In this case, it is fundamental to account for local climate phenomena for realistic estimations (Allegri et al., 2015a; Pisello et al., 2014). This approach is often neglected by using the weather data recorded by rural weather stations for energy simulations.

One of the main urban climate distortions in cities is the Urban Heat Island UHI (Oke, 1982; Santamouris, 2014; Zhou et al., 2013), whose primary consequence is the increase in urban air and surface temperatures. This condition affects the building thermal balance altering the energy demand for air conditioning (Li et al., 2019b; Lima et al., 2019; Salvati et al., 2017a). Many studies deal with the development of tools able to tackle and integrate the UHI phenomenon in building energy simulations (Liu et al., 2017; Ren et al., 2014; Sun and Augenbroe, 2014). Among these, the Urban Weather Generator (UWG) (Bueno et al., 2013b) has been conceived to generate an EnergyPlus Weather file (EPW) defining local air temperatures based on the peculiar district morphology and characteristics. By coupling the UWG with the EnergyPlus simulations, a detailed assessment of building energy demand for air conditioning can be performed.

Another research issue concerns the evaluation of the PV power output, which is often challenging due to the several factors influencing module efficiency (Wijeratne et al., 2019). Firstly, a realistic PV model is fundamental to predict power output (Bücher et al., 1998; Dolara et al., 2015; Ma et al., 2014). Models have different levels of complexity, depending on the number of parameters involved. Previous studies investigated the reliability of various predictive methods based on different electric and thermal models (Cameron et al., 2008; Ciulla et al., 2014; De Blas et al., 2002). As for building energy demand estimations, the urban morphology and microclimate might also affect BIPV performance. Higher operating cell temperatures, caused by the increase in urban air temperatures (UHI), can decrease module performance due to aging acceleration, while dense and compact urban districts reduce solar radiation due to the inter-building shading effect (Lee et al., 2016). Hence, the integration of PV surfaces in cities is becoming increasingly challenging, and not best-oriented surfaces, such as façades, are gaining importance. Although the annual solar irradiance on vertical surfaces is remarkably lower than the horizontal one, many studies on BIPV installed on urban façades demonstrate that they considerably contribute to energy production (Redweik et al., 2013; Sánchez and Izard, 2015). Generally, façades of multiple storey buildings feature larger areas compared to rooftops (Molin et al., 2016), Esclapés et al. (Esclapés et al., 2014) report that they constitute the 60-80% of urban available surfaces. Besides, rooftops might be used as privately owned surfaces or green roofs

or even contain building mechanical and electrical components (elevators, air conditioning units, tanks). Moreover, vertical PV plants have a more stable annual production compared to the roof installed modules and they achieve higher peak irradiance shifted from noon, thus diminishing the mismatch between energy production and demand (Waibel et al., 2018). However, BIPV on façades are more sensitive to the variations of the solar indirect components (i.e. surrounding reflected energy) (Fouad et al., 2017). As it is well known, the total solar radiation reaching a surface is composed of beam, which arises directly from the sun disk, and indirect radiation, consisting of a diffuse and a reflected component. In particular, the reflected radiation is the part reflected by the other surfaces, including surrounding constructions and ground (Liu and Jordan, 1960; Pavlovic, 2020). The indirect components also reach shadowed surfaces, and their intensity depends on solar radiation intensity, on the Sky View Factor (SVF) for the diffuse component (Johnson and Watson, 1984; Redweik et al., 2013) and on surrounding surface reflectivity for the reflected part. In the urban environment, where the direct radiation, particularly on façades, is strongly reduced (Mohajeri et al., 2019), the indirect parts constitute a considerable contribution to the total radiative budget of vertical surfaces (Siddiqi, 1985). Therefore, façades are extremely sensitive to how urban materials react to solar radiation. Many studies in the literature were addressed to investigate the effects of solar radiation and reflectivity on vertical PV surface efficiency. Kotak et al. (Kotak et al., 2015) investigated the effect on a PV façade related to the application of high-reflective paint on surrounding rooftops, recording an increase of 48% on energy gain. Many other studies focused on the augmented reflectivity caused by the snow on module performance (Andrews et al., 2013; Thevenard and Haddad, 2006). Regarding solar radiation intensity in the urban environment, Wang et al. (Wang et al., 2005) highlighted that city pollution may reduce the shortwave input by 10-20% compared to the countryside. An integrated approach to PV production in urban areas was presented by Lobaccaro et al. (Lobaccaro et al., 2018a), which examined the solar potential of the façades of two buildings located in Bolzano (Italy) by comparing different interventions on surroundings. However, these studies are extremely case-specific or, in the case of Lobaccaro et al. (2018a), imply high computational cost and complex systems.

In a recent investigation by the Authors (Boccalatte et al., 2020a) the UWG analysis has been chained with EnergyPlus calculations aimed at assessing the impact of the UHI effect on cooling and heating demands of different district morphologies and building types in a selection of European capital cities. This chain approach in the present investigation is addressed to evaluate the influence of the urban morphology on the PV production of photovoltaic districts.

The present study aims to provide a simple approach to account for the urban environment in energy demand and supply predictions through the integration of common design tools and predictive models. The optimized design for BIPV installation based on the maximum exploitation of the solar potential of façades within an urban district is here presented with a view to NZED conversion on a yearly basis as in the definition of the reference European Directive (EPBD, (E. European Commission, 2005)). The methodological approach is based

on both the definition of the urban district climate conditions (Urban Heat Island analysis) and EnergyPlus simulations considering a multi thermal zone reference building located in a district, also modelled. An overview of several factors affecting building energy consumption and photovoltaic production is here presented, quantifying their influence on the study case and providing some guidelines to plan a nearly zero energy district.

3.2.2 Modelling a Solar Urban District

This study concerns the conversion of a whole district composed of 11 residential blocks, ideally settled in Rome, Italy (41.9° N, 12.5° E), into a self-energy sufficient suburb exploiting BIPV solutions. In the present investigation, where all constructions are equal except for small variations in their horizontal surface, a reference building is included. The latter is a four-storey residential apartment block with a 25% glazing ratio, containing four identical flats per floor, whose size on the horizontal is about 630 m^2 . Figure 3.13 shows the district plan with the reference building in the middle. Figure 3.14 represents a sectioned axonometric view of the facility with a typical floorplan. The letters specify the arrangement of the internal spaces (L=living room, R=bedroom, C=corridor, K=kitchen, B=bathroom) of a single flat.

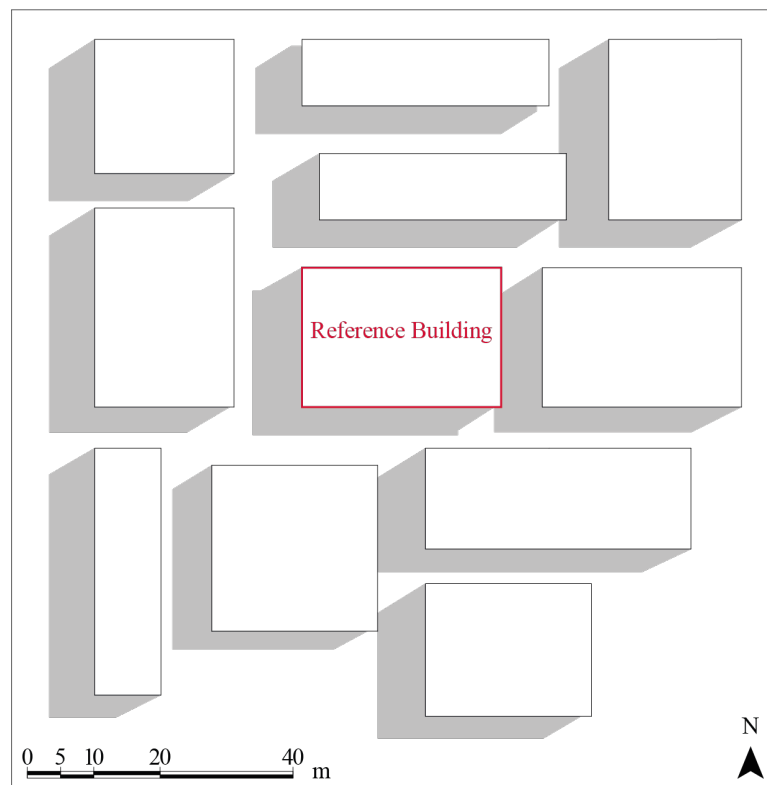


Fig. 3.13 District plan with the reference building.

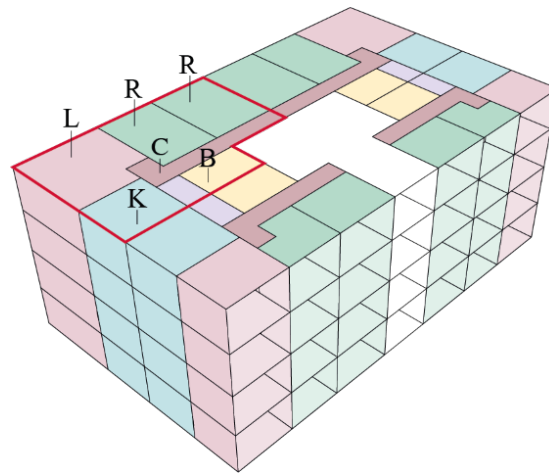


Fig. 3.14 Sectioned axonometric view of the reference building with a typical floorplan. The red line represents a single flat.

3.2.2.1 Building Energy Demand and Solar Radiation Availability: EnergyPlus and the Urban Weather Generator Coupled Approach

The first step of the developed methodology is to couple a detailed EnergyPlus model (implemented with OpenStudio plug-in) and the Urban Weather Generator (UWG) (Bueno et al., 2013b) tool to evaluate the reference building energy demand accounting for the Urban Heat Island (UHI) phenomenon. The Urban Weather Generator defines local air temperatures based on the district morphology and characteristics. The model is composed of four coupled physical models, fully described in (Bueno et al., 2013a, 2015b), simulating the energy transfers between the buildings and the urban environment. The inputs are the site-related rural station data (rural weather file, EPW), which often correspond to airport weather data (most of the time far from the city center), and a user-defined Extensible Markup Language (XML) file where the urban district characteristics are specified. The only output is an EnergyPlus Weather file (urban weather file, EPW) reporting the hourly UHI-influenced air temperatures. As stated in Section 3.2.1, a recent paper by the Authors (Boccalatte et al., 2020a) deeply investigated how to chain UWG and EnergyPlus calculations in a “quasi-feedback” approach where building heat release (together with district morphology) contributes to the local climate variation with respect to the rural conditions. A detailed description of input and output flow in the UWG/EnergyPlus chained analysis is provided in (Boccalatte et al., 2020a) and just summarized in the present paper for the sake of brevity.

In the present study, two district design scenarios are considered and their urban EPW file is generated through the UWG. The two cases are defined respectively to represent a reference (R=reference) and an enhanced (E=enhanced) design choice, referring to current country standards. In the first case, minimum energy efficiency targets are considered, in the second case, a series of UHI mitigation strategies are adopted. The reference scenario

(case R) is characterized by low reflectivity materials, simulating dark asphalt for roads and dark plaster cladding for the envelope of the buildings, high glazing ratios, worsening the UHI temperature excess because of the multiple reflections of short wave radiation, and high non-building sensible heat at street level (representing traffic or other heat sources). Concerning district E, high reflectivity asphalt and cladding, a suitable glazing ratio, a shading system preventing from indoor warming, lower anthropogenic heat flux from traffic are assumed. In all cases, constructions elements (walls, roofs and windows) fulfill the minimum transmittance requirements, imposed by the Italian building standard (zone D, Rome), with a further decrease of the limit value of 35% in case E. Table 3.4 reports main input parameters to the Urban Weather Generator for the two cases.

Table 3.4 Input parameters for the definition of the district and building characteristics within the Urban Weather Generator tool

Parameter	Case R	Case E
District Design		
Road albedo [-]	0.05	0.2
Road material [-]	Dark asphalt	Light asphalt
Sensible heat streets [W/m ²]	10	5
Glazing ratio of buildings [-]	0.6	0.25
Building Units		
Walls thermal resistance [m ² K/W]	2.9	5.3
Roof thermal resistance [m ² K/W]	3.3	5.9
Wall albedo (ext layer) [-]	0.1	0.5
Roof albedo (ext layer) [-]	0.1	0.7
Windows U-factor [W/m ² K]	2.0	1.1
HVAC System		
COP _{Cooling} [-]	3	4
COP _{Heating} [-]	2	3

The two UWG-generated urban weather files with the site-specific air temperatures are used as input to a detailed EnergyPlus model, which includes the inter-building shading effect: surrounding buildings are here modelled as “shading geometries” in OpenStudio, as represented in Figure 3.15. The energy simulations are run with a subhourly timestep (5 minutes) and along one year. The yearly building energy demand of the reference building is thus estimated including both urban microclimate and morphology. In a further step, the energy analysis has been extended to the whole district scale. The yearly energy balance between energy demand and production through BIPV installations has been examined on the assumption that the 11 residential blocks are equally energy-consuming.

A point of clarification is needed concerning the adopted methodology. The considered definition of NZEB (and NZED at the district scale) is consistent with the Article 2.2. of the

Energy Performance of Buildings Directive (EPBD) (European Commission, 2018). However, considering the yearly energy balance between energy demand and PV production is in a certain way limiting. NZEB/NZED definition as it stands does not provide any information about the interaction with the electric grid or about battery storage systems aimed at reducing the mismatch between energy demand and supply. On the other hand, as will be demonstrated also in the present paper, the electric energy balance at building level cannot be reached in any month of the year due to the large variation in available solar energy resource, typically 3 to 5 times comparing January with June at latitudes typical to Europe or North America, just as quick example.

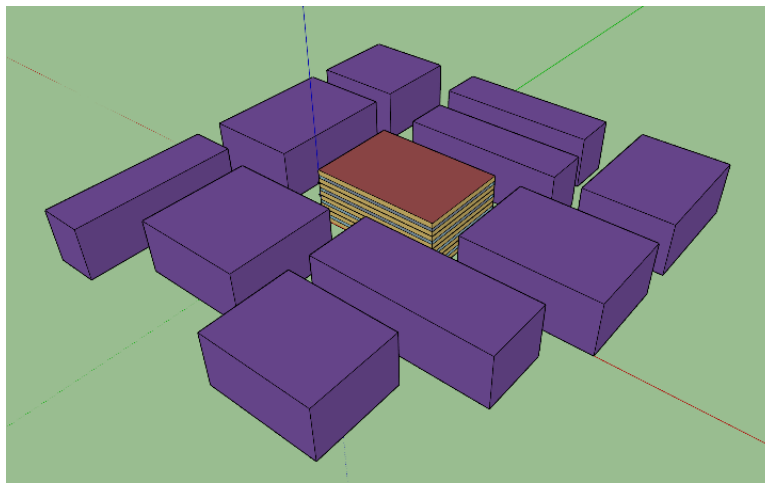


Fig. 3.15 3D view of the district in OpenStudio environment. The reference building is the central one and the surrounding dark constructions are “shading objects”.

To design the BIPV installations required for the NZEB task, the solar potential of the envelope, with a particular interest to the façades of the reference building, has been evaluated by coupling EnergyPlus simulations with several postprocessing calculations. Two physical models for PV performance have been implemented to predict PV power output. The Sandia method for the photovoltaic array performance (King et al., 2004), has been selected to investigate the façade power generation per PV surface unit, by accounting for microclimate and morphology effects. In particular, concerning the local climate, the Urban Heat Island temperature excess (ΔUHI) is defined as the hourly positive difference between the air temperature recorded at the rural weather station and the urban air temperature generated by the Urban Weather generator, as reported in Eq 3.6

$$\Delta UHI = T_{urb} - T_{rur} \text{ if and only if } T_{urb} > T_{rur} \quad (3.6)$$

The UHI temperature excess (ΔUHI) arising from the reference district design choice (case R), whose main characteristics are reported in Table 3.4, is calculated through Eq 3.6. To include the effect of ΔUHI within the PV array post-processing calculations, two EnergyPlus simulations

are run in the UHI-free (using the rural meteorological data as input) and UHI-influenced (using the urban EPW, related to case R) condition. The values of the irradiance per surface unit and the surface temperatures resulting from the EnergyPlus simulations are used as input parameters to the Sandia model to predict the PV output of the façades of the reference building.

3.2.2.2 District Photovoltaic Production: Modelling the Temperature and Irradiance Effect on PV Module Performance

The prediction of PV module performance is always a challenging task due to the parameters affecting the energy output (Wijeratne et al., 2019). A large amount of PV design tools (Klise and Stein, 2009) and physical models, with different levels of complexity, have been developed over the years. Dolara et al. outline that, in some cases, the advantage of using multi-parameter models is scarce (Dolara et al., 2015).

In the present study, the traditional linear expression for PV efficiency, accounting only for the cell temperature influence, is compared to the Sandia model, including optical, thermal and electrical effects on modules. The first model, named here Temperature Corrected Standard Test Condition (TCSTC) method, estimates the PV module efficiency (η) at a given operating temperature (T_c) starting from module efficiency ($\eta_{T_{ref}}$) at the reference temperature (T_{ref}) and the temperature coefficient of power (β_{ref}) usually provided by the manufacturer. The reference temperature and the temperature coefficient of power refer to the Standard Test Conditions (STC), namely the laboratory conditions at which, on the contrary, module temperature is kept at 25°C, irradiance is 1000 W/m² and radiation spectrum is related to AMa=1.5. The linear relation can be expressed through Eq 3.7 (Evans, 1981)

$$\eta = \eta_{T_{ref}} [1 - \beta_{ref} (T_c - T_{ref})] \quad (3.7)$$

This method is largely employed in PV design but it only accounts for the effect of temperature on the efficiency of a PV cell/module. Sandia National Laboratories developed a physically based performance model (King et al., 2004). The Sandia model is based on of a set of equations involving different types of parameters based on irradiance (E_e , C_0 , C_1 , C_2 , C_3), solar source characteristics (E_b , E_{diff} , f_d , E_e , E_0 , AMa, AOI, f_1 (AMa), f_2 (AOI)), cell temperature (α_{Isc} , α_{Imp} , β_{Voc} , β_{Vmp}), empirically determined coefficients and STC parameters (T_0 , E_0 , I_{sco} , I_{mpo} , V_{oco} , V_{mpo}). The model calculates the I_{sc} , I_{mp} , V_{mp} , V_{oc} and P_{mp} as reported in Eq 3.8 to 3.12

$$I_{sc} = I_{sco} \cdot f_1(AM_a) \cdot (E_b \cdot f_2(AOI) + f_d \cdot E_{diff}/E_0) \cdot (1 + \alpha_{Isc} \cdot (T_c - T_0)) \quad (3.8)$$

$$I_{mp} = I_{mpo} \cdot (C_0 \cdot E_e + C_1 \cdot E_e^2) \cdot (1 + \alpha_{Imp} \cdot (T_c - T_0)) \quad (3.9)$$

$$V_{oc} = V_{oco} + N_s \cdot \delta(T_c) \cdot \ln(E_e) + \beta_{Voc}(E_e) \cdot (T_c - T_0) \quad (3.10)$$

$$V_{mp} = V_{mpo} + C_2 \cdot N_s \cdot \delta(T_c) \cdot \ln(E_e) + C_3 \cdot N_s \cdot (\delta(T_c) \cdot \ln(E_e))^2 + \beta_{Vmp}(E_e) \cdot (T_c - T_0) \quad (3.11)$$

$$P_{mp} = I_{mp} \cdot V_{mp} \quad (3.12)$$

The symbols above represent currents (I), voltages (V) and temperatures (T) and they are fully described in the nomenclature. Short circuit current, open circuit voltage, and the maximum power point current and voltage are included in equations 3.8 to 3.12. Other equations, fully described in (King et al., 2004) provide some additional quantities (I_x , I_{xx} , $\delta(T_c)$ and E_e) not reported here for the sake of brevity. Concerning the operating temperature (T_c) which is a key driver of standard crystalline PV performance, the Sandia model provides an empirically based thermal model to evaluate the cell temperature through Eq 3.13

$$T_c = T_m + \left(\frac{E}{E_0} \right) \cdot \Delta T \quad (3.13)$$

where T_m is the back surface PV module temperature. It is determined with an empirical correlation based on air temperature, irradiance, wind speed and empirical coefficients. ΔT is the temperature difference between the cell and the back surface at E_0 irradiance level (1000 W/m^2). In the present study, Eq 3.13 is not employed and the cell temperature T_c is inferred directly from EnergyPlus output values to be consistent with the thermal model adopted for the other surfaces of the built environment.

The comparison between the two methods has been performed by subdividing the reference building façades into 16 surfaces (the four floors of the four orientations, on the same axis with the cardinal directions). EnergyPlus outside surface incident solar radiation and the outside surface temperature values are exported to perform postprocessing calculations, based on equations 3.7 to 3.12, for each surface. Table 3.5 contains some of the specifications of the c-Si PV modules considered in the present study.

Table 3.5 PV module specifications for the performance evaluation

Parameter	Value	Unit
General Specifications		
Model	Silevo Triex U300 B	-
Year	2014	-
Area	1.68	m ²
Material	c-Si	-
Cells in series	96	-
Parallel strings	1	-
TCSTC related parameters		
$\eta_{T,ref}$	0.179	-
T_{ref}	25	°C
β_{ref}	-0.27	%/K
STC Power Rating	300	W
Sandia related parameters		
I_{sco}	5.77	A
V_{oco}	68.59	V
I_{mpo}	5.38	A
V_{mpo}	55.45	V

The PV system is here conceived to be connected to a solar inverter whose efficiency varies as a function of the input DC power and voltage. The rated efficiency of the device is 95% and it works according to the efficiency curve, displayed in Figure 3.16. The efficiency curve shows the variation of the selected inverter efficiency as a function of the inverter power ratio for the nominal working conditions.

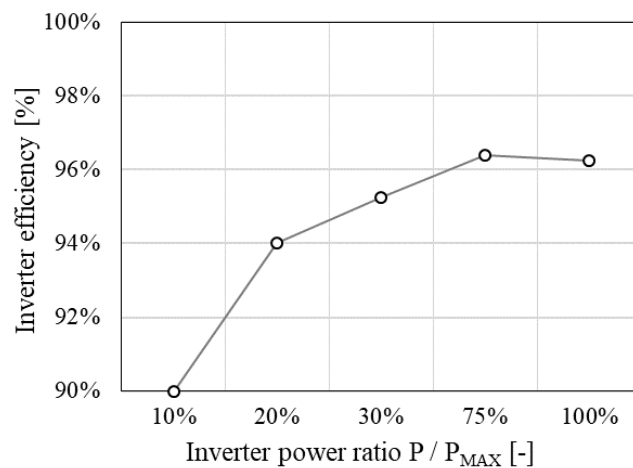


Fig. 3.16 Efficiency curve of the inverter.

In a further step, the impact of the optical properties of surrounding surfaces on the photovoltaic production of the reference building façades has been investigated. In EnergyPlus the overall surface incident solar radiation is calculated as the sum of the direct (beam solar), the diffuse (sky diffuse and ground diffuse) and the reflected (sky diffuse reflected, beam to beam surface reflected, sky diffuse surface reflected) solar radiation rate per area. Concerning vertical surfaces, in the present case study where adjacent constructions obstruct the direct solar beam, they are significantly irradiated through the indirect components of solar radiation. The reflected portion is strictly dependent on the reflectivity of materials. Within the EnergyPlus model, the reflectivity (ρ) of the envelope of the adjacent buildings has been varied from a maximum value of 0.50 (simulating light plaster) to a minimum of 0.10 (simulating dark colors). A total of six cases have been considered, by reducing the reflectivity by steps as reported in Table 3.6. The solar potential of the reference building façades has been calculated with the Sandia method and considering the surface incident solar radiation and temperature of the EnergyPlus simulations. The results show that lower reflectivity values yield a decrease in PV module productivity due to the reduced amount of solar reflected radiation from the surroundings. Likewise, the process has been repeated with the ground reflectivity (ρ_{gr}), considering two cases: dark asphalt (case A) and lighter material (case B), and obtaining the above overall behavior in terms of PV production (Table 3.6).

Table 3.6 Values of surrounding surface and ground reflectivity adopted for the simulations

Case	Reflectivity
Surrounding building reflectivity (ρ)	
Case 0	0.50
Case 1	0.42
Case 2	0.34
Case 3	0.26
Case 4	0.18
Case 5	0.10
Ground reflectivity (ρ_{gr})	
Case A	0.05
Case B	0.23

3.2.3 The Reference BIPV District Test Case

Low surrounding surface reflectivity negatively affects the vertical BIPV production. Considering that photovoltaic modules themselves are dark surfaces, optimizing the harvest of solar energy in fully PV districts can result in a difficult task. This section aims to find the best BIPV area at the district level as a trade off between maximizing the overall collecting area and maintaining high levels of reflected solar energy. A progressive increase of PV modules on vertical surfaces has been considered: at every addition, 20% of the whole district total available façade area is turned into PV while respecting the constraints on existing glazed parts. As the PV surface is increased, the EnergyPlus model has been modified in terms of decreasing reflectivity of building surfaces (from 0.5 to 0.1). A specific sequence has been here conceived for the increase. Based on the irradiance values arising from EnergyPlus, the modules have been first “mounted” on best irradiated surfaces, as depicted in Figure 3.17 where every surface is associated with its order number.

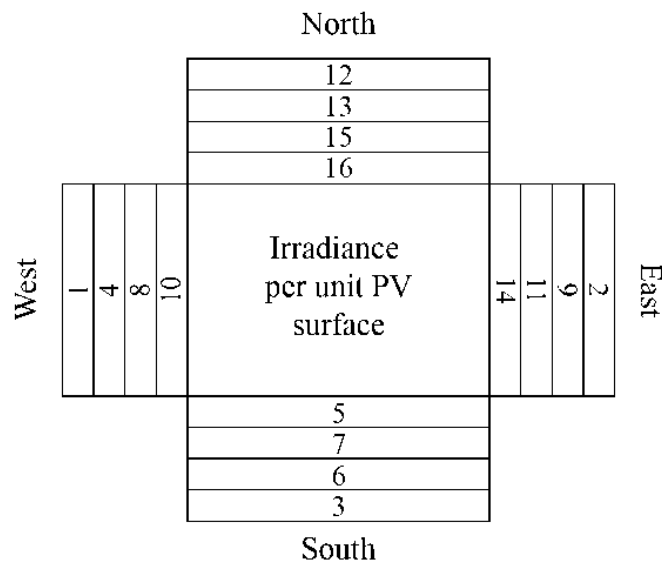


Fig. 3.17 Scheme of reference building façades. Numbering starts from the most irradiated floors and orientations.

As an example, the irradiance values on each floor and orientation are reported in Table 3.6 for July.

Table 3.7 Monthly (July) irradiance of façades with respect to their floor and orientation

N°	Floor and Orientation	kWh/m ² July
1	4 th floor - West	13.9
2	4 th floor - East	12.7
3	4 th floor - South	11.5
4	3 rd floor - West	11.3
5	1 st floor - South	10.4
6	3 rd floor - South	10.1
7	2 nd floor - South	9.9
8	2 nd floor - West	9.4
9	3 rd floor - East	8.9
10	1 st floor - West	7.5
11	2 nd floor - East	6.2
12	4 th floor - North	6.1
13	3 rd floor - North	4.8
14	1 st floor - East	4.5
15	2 nd floor - North	4.3
16	1 st floor - North	3.6

The sequence assumed for the present analysis is best shown in Figure 3.18 where lighter colors represent the added PV surface corresponding to the reported percentage, whereas, darker

colors represent the BIPV already installed. The PV production has been calculated with the Sandia method for a series of PV coverage values (20%, 40%, 60%, 80%, 100%).

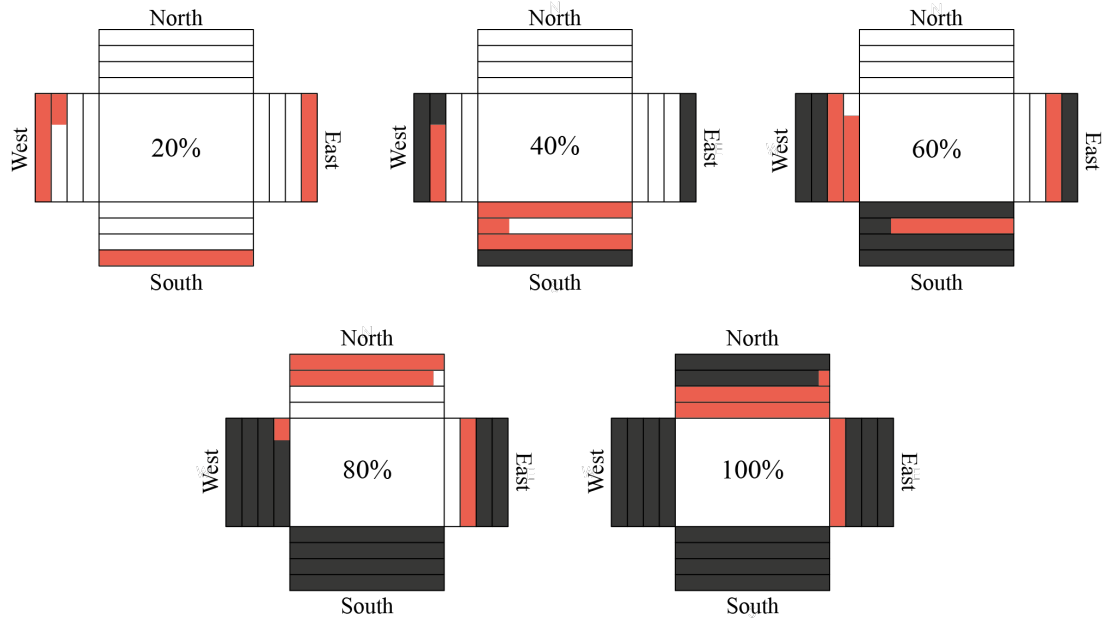


Fig. 3.18 Sequence of PV installation for attaining the given percentage of façade coverage PV areas do not include the glazed parts of the building.

The annual energy production of PV façades, related to the best BIPV area at the district level, has been evaluated through the implementation of the traditional linear expression for PV efficiency (TCSTC method) and by further refining the calculations with the inverter efficiency curve, the latter reported in Figure 3.16. The BIPV yearly production has been compared with the annual building energy demand arising from EnergyPlus, by employing the UWG weather file for predicting the performance of the enhanced district (Table 3.4).

The PV production of the rooftop is finally employed for filling the gap between the district energy demand and the PV production on a suitable portion of façades to completely attain the Nearly Zero Energy District (NZED) goal at the yearly base. Worth stressing again, no analysis is provided in terms of time matching of electricity demand and production, since as demonstrated later on, the available building surface (the present one but also any building conceived as a parallelepiped block) does not allow any possibility of suitable energy production during the low insolation months.

3.2.4 Towards the Nearly Zero Energy District: Results and Discussion

The urban air temperature excess (ΔUHI) has been defined as the hourly positive difference between the air temperature recorded at a reference rural weather station and the urban air temperature (Eq 3.6). The reference rural weather station considered in the present study is

located near the Roma Ciampino airport which is about 14 km away from the city center, where is ideally located the study district. The reference rural weather file (.epw) containing the hourly values of the different environmental quantities such as air temperature, humidity, solar radiation, to name but a few, has been downloaded from the EnergyPlus Weather Data database⁷ (Rome 162420 (IWEC)). The urban air temperature has been determined through the UWG simulations. Figure 3.19 shows the profile of the ΔUHI during a four-day long period in July. The blue and the red colors represent respectively the enhanced (E) and the reference (R) district design scenarios (Table 3.4). In general, it can be observed that urban air temperature is significantly higher than the rural one in particular during the night and in the morning. On the contrary, the ΔUHI is zero or nearly zero around noon. Concerning the peak values, a maximum temperature excess of 9.7°C is reached in the reference district and of 8.5°C in the enhanced one. In July, the monthly mean value of ΔUHI is 3.15°C and 2.64°C for the R and E case respectively (red and blue dashed lines). Thus, mitigation strategies adopted for case E yield to a decrease in the average ΔUHI of July of about 0.5°C .

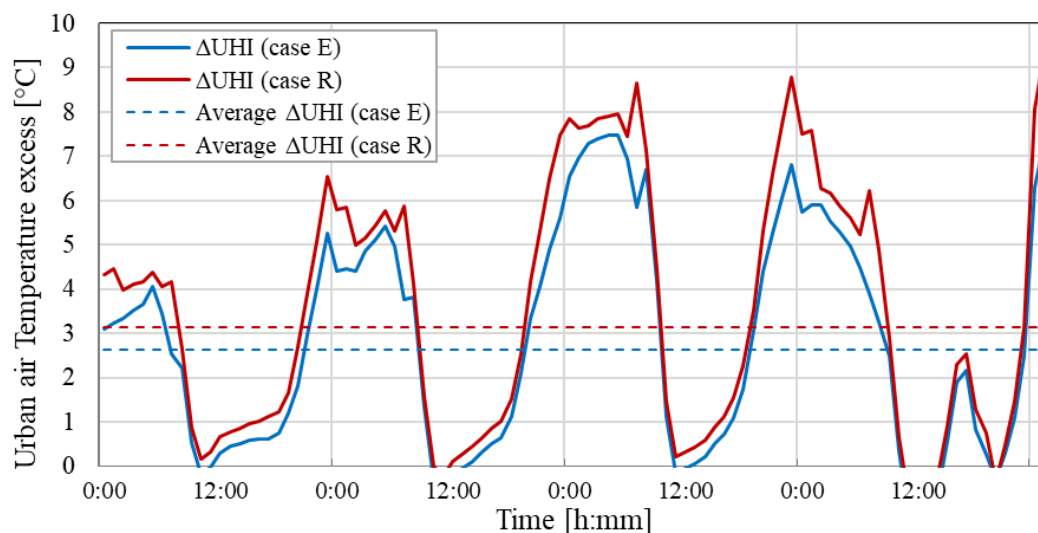


Fig. 3.19 Urban air temperature excess. Four-day long profile of rural and urban temperatures. Reference (case R) and Enhanced (case E) district design in the month of July.

For a reliable evaluation of the reference building energy demand associated with the E district, the UWG model is employed for yearly simulations too. Figure 3.20 shows the rural and urban air temperatures (case E) as monthly mean, maximum and minimum values. The results show that the yearly mean value of ΔUHI is about 0.75°C , with a peak occurring in September (3°C as monthly mean value).

⁷<https://energyplus.net/weather>

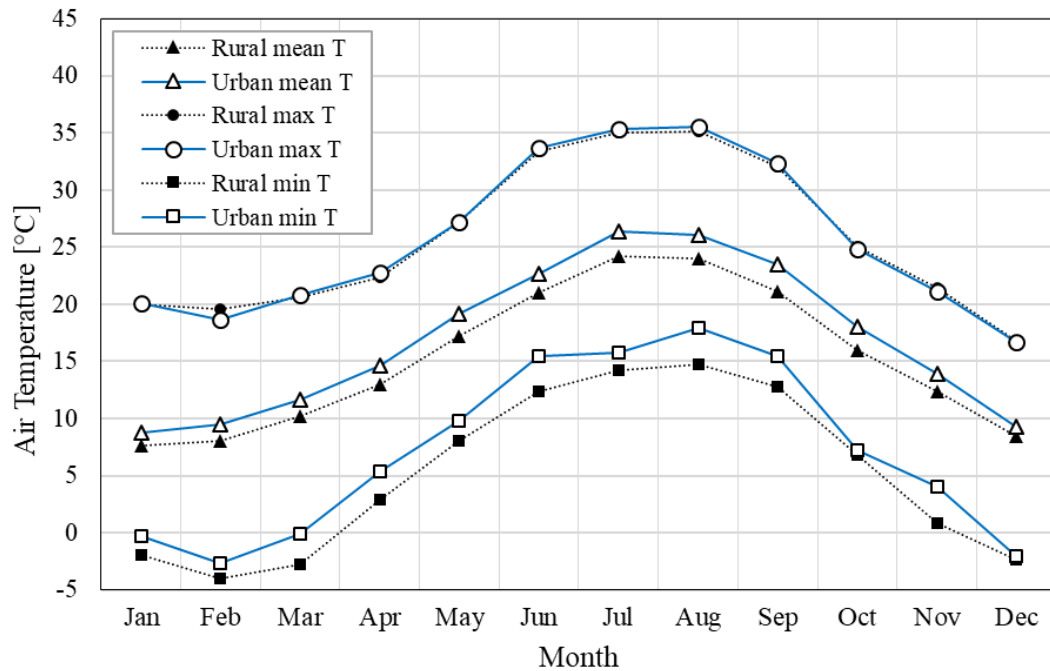


Fig. 3.20 Monthly mean, maximum and minimum air temperatures related to rural and UWG data, case E.

The urban air temperatures affect the air conditioning load of the reference building according to EnergyPlus calculations. Figure 3.21 refers to the enhanced district case study and it shows the monthly heating and cooling loads, in terms of electric energy (assuming an electric heat pump for air conditioning at given COP, Table 3.4), evaluated by using respectively the rural and the urban weather files. It can be observed that the HVAC energy demand shows wide monthly variations, with peaks of discrepancies until 1365 kWh_{el}/month occurring in August. The yearly energy demand for air conditioning has been estimated of 30680 kWh_{el}/year in the UHI-free condition and of 33256 kWh_{el}/year in the UHI-influenced one, thus obtaining an overall underestimation of 8% when the rural weather file is used. As the effect of the urban heat island phenomenon is opposite in relation to the heating and cooling demand the annual difference is less impactful than in a single month. Considering separately the total amount of energy required for heating and for cooling over a year, it can be remarked an increase of the heating duty of 30% and a decrease of the cooling demand of 29% when the rural weather file is used.

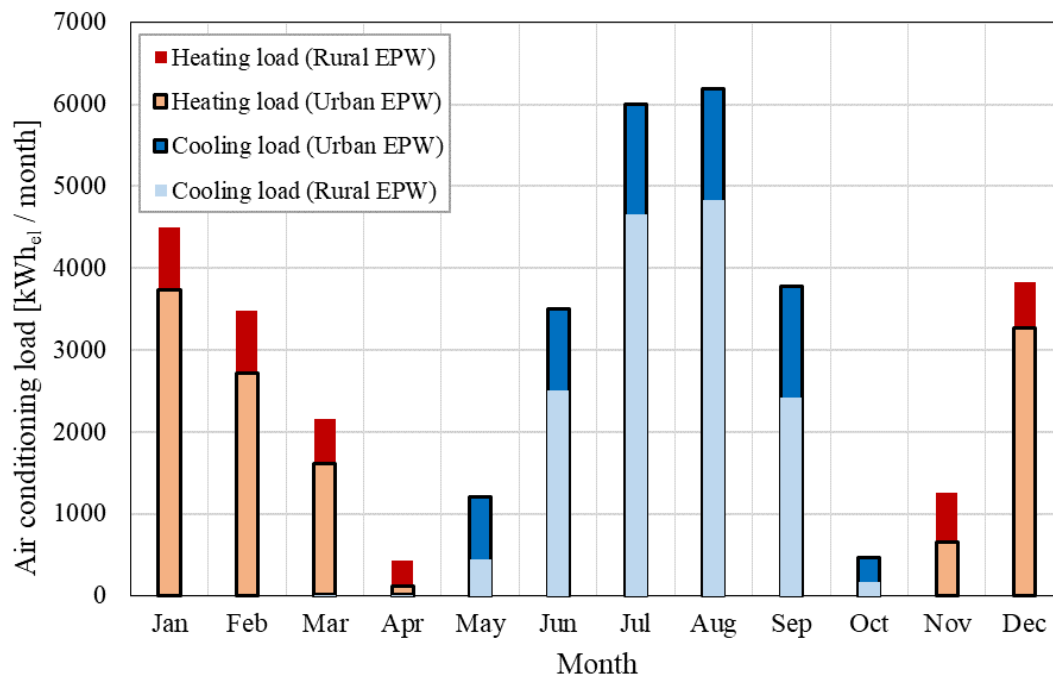


Fig. 3.21 Monthly energy consumption for air conditioning of the reference building calculated with rural and urban EPW files. COP are provided in Table 3.4.

The numerical results provided by the present models show that the influence of the UHI temperature excess (ΔUHI) related to the E district does not significantly affect the productivity of vertical PV installed on the reference building façades. The Sandia method predicts a decrease in PV energy production per surface unit on façades, as it is reported in Table 3.8. As an average on all walls and related orientations, the percent loss of PV power generation potential per PV surface unit, as an effect of the UHI conditions in July, is only about 0.3%. It can be noticed that the maximum UHI related loss is reached at the 4th floor of the north oriented façade and it is by 0.5%. The limited influence of ΔUHI on PV power generation can be explained by pointing out that most of the solar conversion occurs during the central hours of the day, while the ΔUHI peaks are reached at nighttime and in the morning, as evidenced from Figure 3.19.

Table 3.8 PV energy production per vertical surface unit in July evaluated through the Sandia method considering both rural and urban surface temperatures

Floor and Orientation	Rural T (kWh/m ² July)	Urban T (kWh/m ² July)	% Loss in PV Energy
1 st floor - North	3.86	3.84	0.41%
2 nd floor - North	4.73	4.71	0.40%
3 rd floor - North	5.27	5.25	0.45%
4 th floor - North	6.45	6.42	0.49%
1 st floor - South	10.30	10.28	0.20%
2 nd floor - South	10.00	9.98	0.21%
3 rd floor - South	10.24	10.22	0.23%
4 th floor - South	11.46	11.43	0.25%
1 st floor - West	7.67	7.65	0.34%
2 nd floor - West	9.73	9.70	0.36%
3 rd floor - West	11.81	11.76	0.38%
4 th floor - West	14.25	14.19	0.41%
1 st floor - East	4.68	4.67	0.18%
2 nd floor - East	6.53	6.52	0.19%
3 rd floor - East	9.33	9.30	0.26%
4 th floor - East	13.07	13.00	0.46%

The comparison between the traditional linear expression for PV efficiency (TCSTC method) and the Sandia model provides significant differences in BIPV solar potential per surface unit. Figure 3.22 shows the variation of solar energy production (per façade area unit) between the two methods as a function of floor and façade orientation. The reference month is here July. As a general consideration, the TCSTC method overestimates the PV energy production compared to the Sandia algorithm and, on average, the overestimation is about +6.6%, with peaks up to +11.2% occurring in the 1st floor North oriented, and a minimum of +3.4% for the 4th floor facing East. As it could be expected, the Sandia method, accounting for several optical, thermal and electrical effects, provides lower values of PV efficiency.

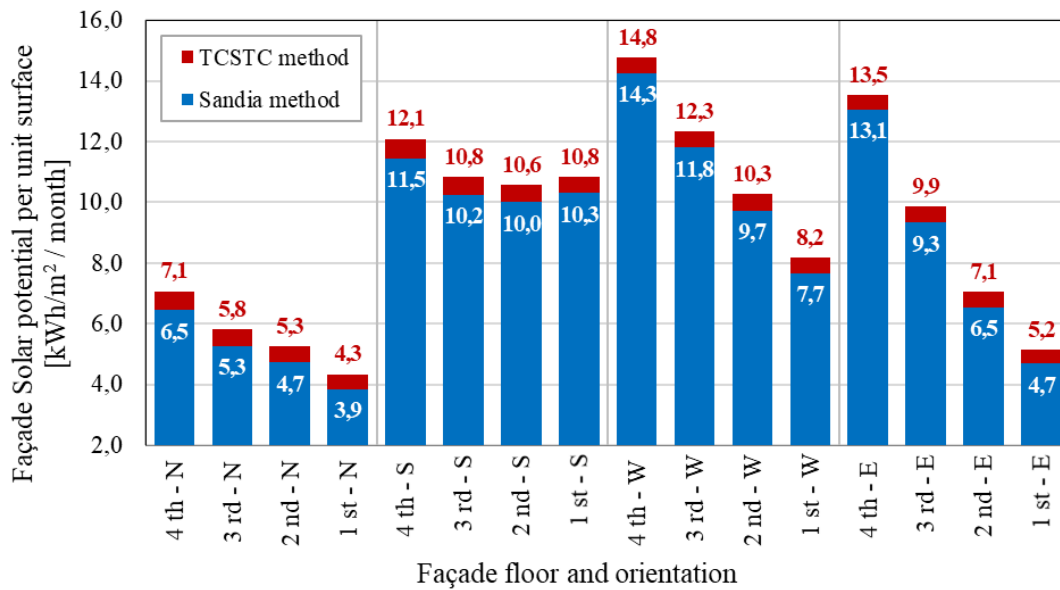


Fig. 3.22 Estimated solar energy production per façade unit area evaluated by the TCSTC and Sandia methods.

By varying the reflectivity of surrounding surfaces and ground, the solar energy production per PV unit surface (on the reference building) results to be significantly affected. Figure 3.23 shows the percent loss of the energy output per PV unit surface for each façade orientation compared to the baseline condition, in which the reflectivity (albedo) of surrounding buildings is set to 0.5 (case 0), to the lowest value of 0.1 (case 5), according to the sequence reported in Table 3.6. The energy production per surface unit refers to the average amount of the four floors and for each of the four orientations. This productivity decreases linearly with district albedo and the slope of the function is indicative of the sensitivity of each façade to the optical variations of the surroundings. It can be observed that the reduction is greater for the less irradiated surfaces: in North façade, the percent loss of case $\rho=0.1$, compared to case $\rho=0.5$, is -37%, in East direction is -16%, in West is -14% and in South is -8%. As an average of all the orientations, the percent loss is represented by the dashed line and it is by -3%, -6%, -9%, -13%, -16% respectively from $\rho=0.1$ to $\rho=0.5$. Similarly, concerning ground reflectivity (ρ_{gr}), by diminishing its value from 0.23 to 0.05, as reported in Table 3.6, the percent loss of solar energy productivity per PV unit surface of façades, as an average of all floors and orientations, is by -7%.

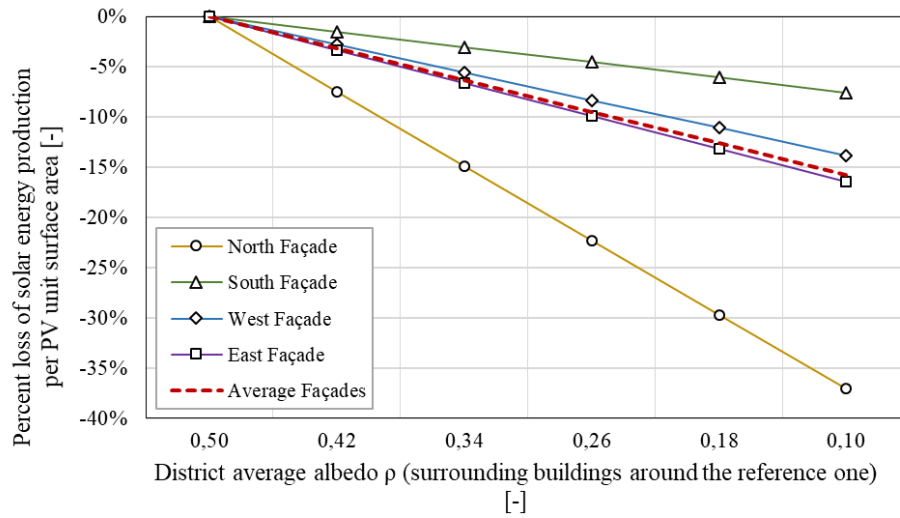


Fig. 3.23 Percent loss of PV energy production per surface unit [kWh/m² July] for each façade orientation due to the decrease of surrounding buildings average albedo.

Adding gradually (sequence of Figure 3.18) PV surfaces on both the reference and the adjacent buildings reduces the conversion capacity of PV surfaces because of the darkening effect associated to the low reflectivity of photovoltaic modules, which in turn reduces the available reflected solar radiation. Figure 3.24 shows the increase in the photovoltaic energy production from all the vertical surfaces, starting from the condition with no BIPV installations on façades (0%) until the final condition at which all the façades of the district are photovoltaic (100%), assuming a +20% BIPV area increase at each step. The PV energy production increases significantly until 60% of PV coverage, whereas, for further additions, a lower further increase can be observed as an effect of global “darkening” at the district level. The above considerations suggest that the best productivity of vertical PV surfaces on the building is related to façade PV coverage up to 40%-60% of the whole available district surface.

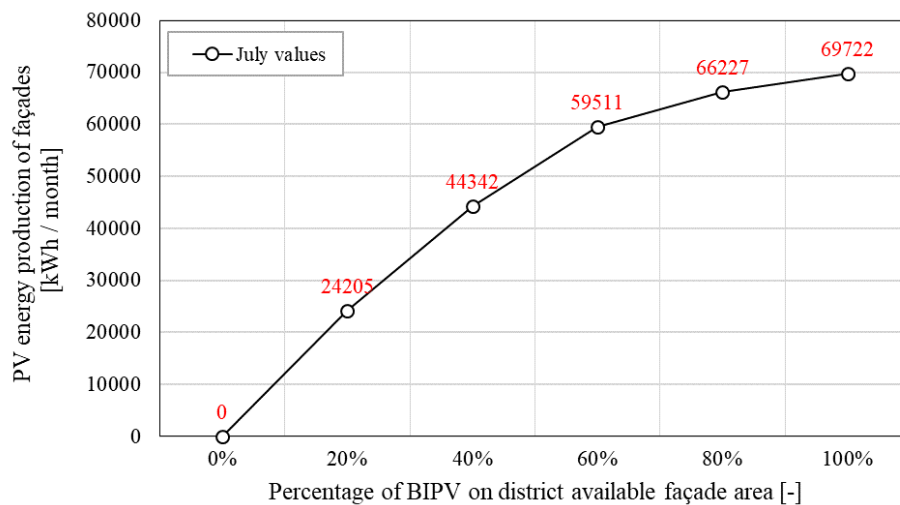


Fig. 3.24 Façade PV energy production as a function of the PV percentage coverage on façades.

Assuming a 60% coverage as the best condition (based on PV energy productivity), further calculations have been made by simulating the presence of PV modules on the rooftop too.

The yearly electric energy demand of the reference building (case E), including the UWG predictions, is about 105 MWh_{el} per year. Meanwhile, the annual photovoltaic production related to one building with 60% of BIPV on façades is 41 MWh_{el} (TCSTC method). By further integrating the effect of the inverter efficiency (Figure 3.16), the production drops to 39 MWh_{el} year. To convert the building into an NZEB the façade PV system is implemented with further rooftop photovoltaic installations. By coupling EnergyPlus and the TCSTC method, it has been evaluated the solar energy production per rooftop PV unit area (including the inverter effect). The area required to supply the remaining 66 MWh_{el}/year is about 520 m², corresponding to 60% of the overall roof surface. Since all the buildings are assumed to be equivalent in terms of energy demand and solar productivity, it is possible to attain the nearly zero energy goal for the whole district (NZED) through the harvesting of solar energy on 60% of the total area of façades and on about the same percentage area of rooftops.

Figure 3.25 shows the monthly amount of required electric energy and the corresponding PV production by assuming a 60% PV coverage on the whole building. It is apparent from the Figure that the NZED target is attained only at the yearly level, since from November to February included the electric production is lower than the needed one. Taking into consideration the month of January, the required PV surface for full coverage of the monthly demand would be almost 3 times the selected one, say exceeding twice the overall building surface. On the other hand, in spring, summer and autumn months there is a meaningful extra production able to completely cover the yearly electricity demand.

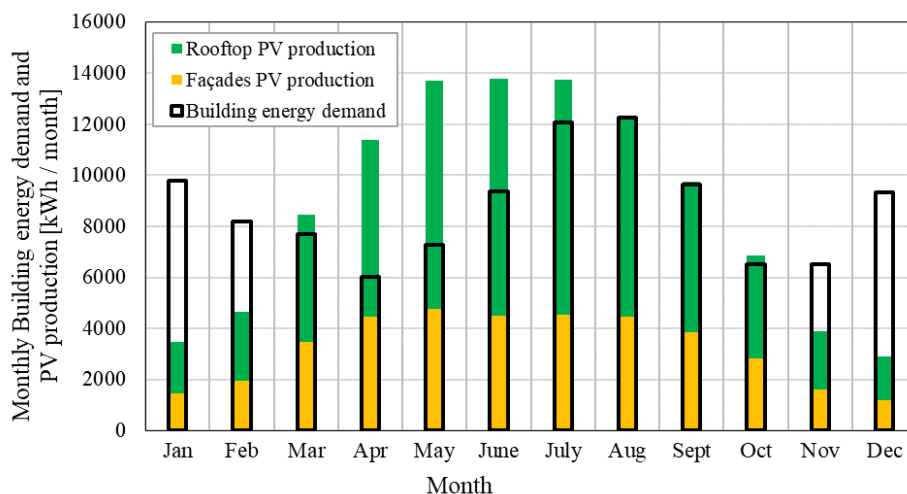


Fig. 3.25 Monthly energy demand and photovoltaic production. PV modules are installed on 60% of the overall available surface of the reference building (rooftop and façades).

3.2.5 Conclusions

This study aims at showing the need to include urban climatic and radiation conditions for the analysis of both building energy demand and supply with integrated solar power technologies. However, taking into account the geometry complexity as well of interrelated physical phenomena must nevertheless be able to achieve through a compromise between computation means and precision on prediction at such large spatial and temporal scales.

In this paper, a comprehensive approach, based on the integration of existing physical models and design tools with post-processing calculations, has been applied to urban district PV production estimations. The whole model includes the Urban Weather Generator tool, EnergyPlus reference building and whole district hourly simulation, and post-processing analyses for a detailed prediction of PV module energy production.

The exploitation of the UWG tool allowed to demonstrate that the Urban Heat Island effects in the test case district can affect building energy demand for air conditioning by 30% because of urban air temperature excess. Concerning the supply side, photovoltaic production, with a particular focus on vertical BIPV installations on façades, was investigated within a realistic urban environment. It was found that PV productivity (energy per surface unit) related to façades is strongly influenced by solar reflected energy and characterized by high incident angles. These conditions, that can be properly addressed by comprehensive PV models like the Sandia one, here compared to a simple temperature based efficiency model (TCSTC) whose yield estimations resulted to be 6.6% higher than the first, in both cases taking into account the inverter efficiency as a function of the power level.

The increase in urban air temperatures due to the UHI effects resulted to weakly decrease (-0.33%) the PV energy production since the air temperature excess is typically associated with hours of low or nil insolation.

On the other hand, the present study reveals that a progressive increase of the PV surfaces at the district level severely affects the PV productivity on façades, due to a “darkening” of the suburb, which causes less availability of reflected solar energy. In particular, by decreasing the reflectivity of surrounding surfaces and ground, the energy output of the façades of the reference building can drop down to -37% in the worst case.

A final part of the investigation is devoted to the goal of converting the whole district into an NZED one by optimising the BIPV installations on building façades. It has been found that by installing PV on 60% of the whole district façade area causes a decrease of PV module productivity (energy per surface unit) of 11%. The gap between solar energy production of façades and building energy consumption is filled by further rooftop BIPV installations, covering a net surface corresponding to the 60% of the total roof area.

Chapter 4

Influence of Urban Morphology on City-Scale Solar Resource Distribution

After addressing the urban microclimate topic at a large scale and analyzing the interactions between the physical properties of urban elements and solar radiation at the district scale, this chapter focuses on investigating the influence of urban morphology on solar radiation distribution at a large scale. This chapter is based on the publication:

- **Paper 4. Boccalatte, A.,** Thebault, M., Ménézo, C., Ramousse, J., Fossa, M. (2022). Evaluating the impact of urban morphology on rooftop solar radiation: A new city-scale approach based on Geneva GIS data. *Energy and Buildings*, 260, 111919. <https://doi.org/10.1016/j.enbuild.2022.111919>

Additionally, the chapter draws insights from the technical report conducted for the **Preliminary Estimation of the Solar Potential in the Liguria Region (Italy)** as part of the Regional Energy Environmental Plan of the Liguria Region (PEAR 2030).

In Paper 4, statistical analysis techniques are employed on extensive urban datasets. The results of this analysis enable the definition of a simplified approach to achieve the objectives outlined in the subsequent technical report.

Contents

5.1	Assessing the Combined Effects of Local Climate and Mounting Configuration on the Electrical and Thermal Performance of PV Systems. Application to Greater Sydney	189
5.1.1	Introduction	189
5.1.1.1	Insights from Previous Research on Urban Overheating in Sydney	190
5.1.1.2	Research Gap and Aim of the Study	191
5.1.1.3	PV Temperature Models and Effect of Local Climate Conditions on PV Performance	192
5.1.1.4	Indirect Effects of PVs on Urban Climate	193
5.1.2	Materials and Methods	194
5.1.2.1	Measured Data from Local Weather Stations	194
5.1.2.2	Study Area and Territorial Partitioning	196
5.1.2.3	The Sandia Array Performance Model (SAPM)	197
5.1.2.4	Figures of Merit of PV Performance Assessment	200
5.1.2.5	Daytime Convective and Radiative Heat Fluxes	201
5.1.3	Results and Discussion	204
5.1.3.1	Local Climate Conditions across the Weather Stations	205
5.1.3.2	PV Operating Cell Temperatures and Performance Metrics	208
5.1.3.3	Daytime Convection and Radiation	218
5.1.4	Conclusions and Future Perspectives	221

Paper 4

4.1 Evaluating the Impact of Urban Morphology on Rooftop Solar Radiation: a New City-Scale Approach based on Geneva GIS Data

Abstract

Building rooftops represent one of the most valuable resources to harvest solar energy in cities. Nevertheless, this potential is limited by the urban morphology impacting the shading conditions. This study suggests a general methodology to assess the impact of urban form on solar harvesting. To this aim, a new GIS-based approach is developed to extract meaningful morphological parameters at a very large scale. The rooftop overall shading rate is here defined as a benchmark, and it is measured through a scaled insolation representing the ratio between the insolation of a surface within the urban context and its unshaded theoretical maximum. A set of 40 morphological features is calculated for 60,000 buildings in the Canton of Geneva (Switzerland), and the scaled solar insolation of about 350,000 roof pieces is derived from the Solar Cadaster of Geneva. The results outline the insolation distribution within the city and as a function of urban morphology. The rooftop overall shading rate shows moderate Pearson coefficients ($r=0.2/0.4$) towards some parameters, namely building height, volume, and height difference with surroundings, while others seem irrelevant. Analysing the 48 Geneva municipalities one at a time, the denser downtown areas reach higher correlation levels ($r=0.4/0.6$) compared to the suburban ones.

Keywords

Urban Morphology; Rooftop Solar Radiation; Solar Cadaster; GIS; Correlation Analysis

4.1.1 Introduction

The decrease of building energy consumption and the exploitation of renewable resources are key goals of the current EU regulation toward energy transition in urban areas ([European Commission, 2018](#)). In Europe, the buildings and the building construction sector combined account for 35% of the total global final energy consumption but new constructions are expected to reduce considerably their energy use thanks to the more stringent policies ([Güneralp et al., 2017](#)). However, if we take into account the growth of the world's population, urbanization and the low rate of renewal of the building stock (less than 1% per year), efforts have to be accentuated and ensure that buildings also produce energy. The relatively recent concept of Nearly Zero Energy Buildings (NZEB) and Districts (NZED), has helped to develop more

awareness on on-site energy production issues (Boccalatte et al., 2020b; Brozovsky et al., 2021). In this context, solar energy stands out among renewable sources for its ease of adaptation to urban surfaces. Based on the International Energy Agency (IEA) projections more than 50% of the overall photovoltaic capacity will be installed on residential and commercial buildings by 2050 (IEA, 2014). Thus, cities play a central role to boost renewable energy production at a larger scale than standalone building or district installations.

The solar resource varies to a great extent with the time scale and location, and efficient exploitation requires a high level of knowledge on the actual resource. In the last decades, thanks to the great improvement in large scale simulation, open-source geographic datasets, and Light Detection and Ranging (LiDAR) data acquisition, it has been possible to assess the solar energy potential of a city at a macroscale, resulting in a solar map or solar cadaster (Freitas et al., 2015). However, as it emerges from the study by Kanters et al. (Kanters et al., 2014), there is still a restricted number of accurate city-scale solar cadasters. These solar cadasters give access to an average annual irradiation on the roofs or even an average annual energy production depending on the solar technology selected. Nevertheless, the main limiting factors are the complex shadowing conditions and building radiation interreflections (Lobaccaro et al., 2019b) having an impact on computation time, and the high level of expertise required to set up radiation models and large scale simulations. Given the difficulty of computing the solar potential at an urban territory scale, another key issue regarding the distribution of solar radiation within the urban environment is to analyse the effects of the urban form, or morphology, on solar availability. This could contribute to create guidelines for urban planners at the early design stage and help municipalities to identify the most suitable areas to harvest solar energy.

In the last decade, there has been a significant interest in investigating the effect of the urban form on both building energy performance (Chen et al., 2020; Martins et al., 2013; Shi et al., 2021; Tardioli et al., 2020) and solar power potential analyses (Carneiro et al., 2010; Mohajeri et al., 2019; Montavon et al., 2004; Robinson, 2006; Sarralde et al., 2015). Some parametric studies on elementary and ideal urban archetypes evidence strong correlations between morphological features and irradiance levels (Poon et al., 2020). Despite being a very useful reference for designers and planners, this level of accuracy in the results cannot be expected when dealing with real and highly heterogeneous systems such as real cities. In the last few years, also thanks to the growing availability of 3D (or 2.5D) information about cities, there has been significant progress in managing real urban data. Chatzipoulka et al. (2016) investigated the relationship between urban geometry and solar availability on building façades and open spaces of 24 neighborhoods of London of the size of 500 m x 500 m. (Mohajeri et al., 2016) studied the effects of 6 relevant urban compactness indicators on the solar potential of 16 districts (11,418 buildings) of the city of Geneva (Switzerland). Also, Morganti et al. (2017) evaluated the impact of 7 morphological features on the façade solar irradiance of 14 urban textures of Rome (Italy) and Barcelona (Spain). While these studies outline the relationship between solar potential and the urban texture, they are mostly focused on façades and the calculation of the

morphological features is generally done at the neighborhood level, averaging the building characteristics within a certain administrative border or cell of a squared grid. Additionally, the considered sample of buildings is often limited to a few thousand and the selection of the morphological features does not follow a rigorous methodology, being considerably variable depending on the research objectives.

In the meantime, substantial advances have been done in the so-called Urban Morphometrics (UMM) (Araldi and Fusco, 2019; Boeing, 2020; Dibble et al., 2017), a branch of urban morphology study aiming at developing objective and reproducible methodologies to compute rigorously the geometrical attributes of a city to support scientific researches. In particular, Fleischmann et al. (Fleischmann, 2017, 2019; Fleischmann et al., 2022a, 2020, 2022b) developed a new approach to derive a meaningful spatial unit of analysis at the building scale (in other words the “surface of influence” of a building), allowing the calculation of several morphological attributes related to the buildings themselves and the adjacent surroundings. This process has been also implemented in a python library called Momepy (Fleischmann, 2019), thus enabling automatization and reproducibility.

The present study is intended to fill three main research gaps. Firstly, despite the recent improvements in solar cadasters, a lack of statistical analyses related to the solar radiation distribution within the urban context can be highlighted. These studies mainly concern the solar radiation model and computational issues, without any interpretation of the results with a view to urban morphology. Secondly, it has been pointed out the necessity to establish a systematic in-depth analysis to assess meaningful morphological features at the building scale and to investigate the correlations with insolation without averaging the urban characters. Finally, the use of very large building datasets seems to be still very restricted.

The present research is related to calculating and analysing 40 morphological features (including building geometry, shape, density, spatial distribution) on each of the 60,000 buildings of the Canton of Geneva through GIS data and the Momepy library (Fleischmann, 2019). The yearly rooftop insolation data from the Solar Cadaster of Geneva (Desthieux et al., 2018a,b) have been analysed in relation to urban morphology. Finally, Pearson correlation analysis has been performed without averaging the features at the neighborhood level. The results provide interesting statistical findings regarding the potentially most influential parameters for solar urban planning, but also the city related morphological specificities and their impact on solar harvesting.

4.1.2 Data and Methods

The following sections include an outline of the data sources and methods. The methodology is schematically represented in Figure 4.1. The workflow highlights the three main phases of the developed approach, i. e. the computation of the scaled solar insolation (I^* , as defined in Eq 4.1) derived by the Solar Cadaster of Geneva, the morphological tessellation and the consequent

calculation of the 40 selected parameters for each building, and finally the analysis of the results arising from the statistical correlations.

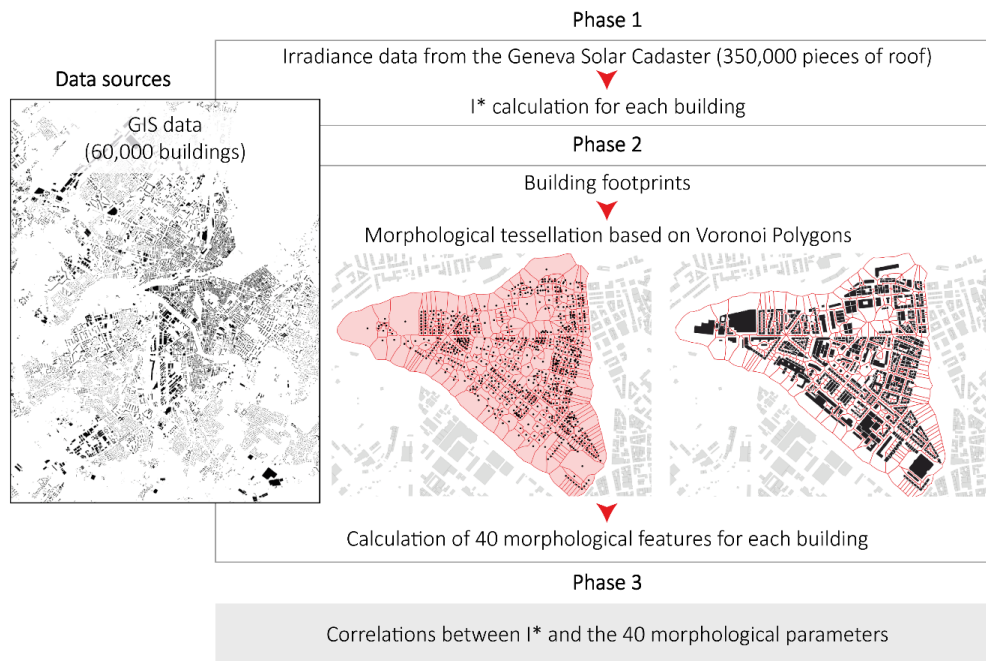


Fig. 4.1 Schematic representation of the developed methodological steps applied to the Canton of Geneva.

4.1.2.1 GIS Data Sources and Case Study

The present paper proposes a general methodology to evaluate the impact of urban morphology on the rooftop solar potential for large city-scale studies. Worth noting, the developed approach is general and it applies to any urban area and considering any benchmark in addition to rooftop insolation.

This methodology is then applied to a case study: the Canton of Geneva ($46^{\circ} 13' 05''$ N, $6^{\circ} 09' 5''$ E, Switzerland). Its total surface is 282 km^2 and it comprises about 60,000 buildings subdivided into 48 municipalities.

The input data to the present GIS-based analysis comprise building geometry and solar radiation information in the form of geospatial vector data for Geographic Information Systems. One of the most common format to handle vector data is the shapefile, which stores a set of geo-referenced attributes for each element (here the buildings), depending on the information needed. This study involves two shapefiles retrieved from the on-line repository of the Geneva territory (SITG: Le système d'information du territoire à Genève¹), namely *Cad.batiment.hors.sol* and *Ocen.solaire.irr.surface.utile*. The first gathers general information about the building, such as period of construction, belonging municipality, final use and, most important here, the building height. The second concerns solar radiation and geometrical information (slope and azimuth)

of each piece of roof. Figure 4.2 shows the two shapefiles within the QGIS environment with a non-exhaustive attribute table of the most important information stored in each. The color scale of *Ocen.solaire.irr.surface.utile* refers to the yearly average solar insolation (kWh/m² year) received by each piece of the rooftop as computed in (Desthieux et al., 2018a,b) to build the Solar Cadaster of Geneva. One can note that the size of the two shapefiles is different: *Cad.batiment.hors.sol* stores a set of information for each building (about 60,000 elements), whereas *Ocen.solaire.irr.surface.utile* is related to each piece of roof (about 350,000 elements).

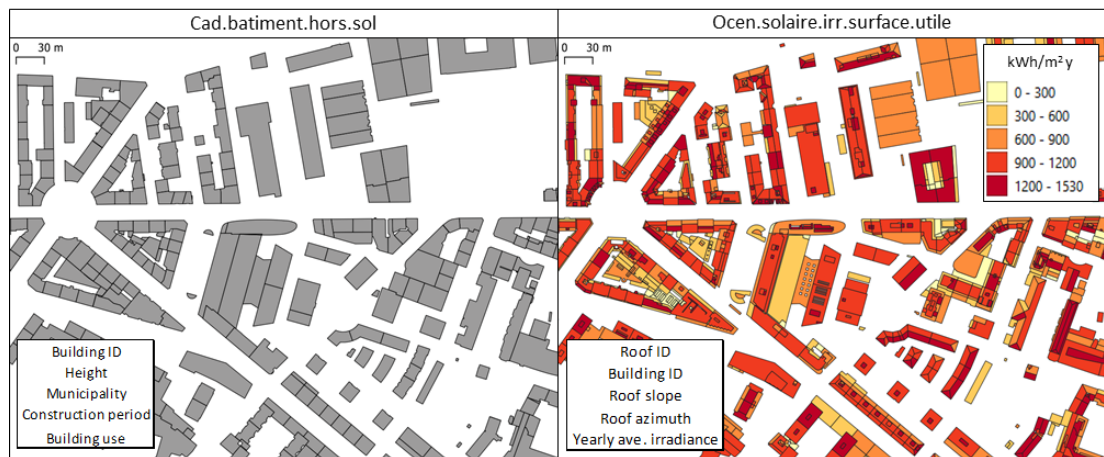


Fig. 4.2 Insight of the two shapefiles, *Cad.batiment.hors.sol* and *Ocen.solaire.irr.surface.utile*, and the related main attributes. Zoom on a specific area of Geneva.

4.1.3 Definition of I^* , the Scaled Solar Insolation

As briefly outlined in the Introduction section, the key issue of the developed approach relates to the investigation of the relationship between the building rooftop overall shading rate and the morphological parameters. A scaled solar insolation (I^*) has been introduced as a measure of the shading level of a building rooftop. I^* has been defined as the ratio between the insolation of a roof surface within the urban context and its unshaded theoretical maximum, as a function of its slope (β) and azimuth (γ). I^* is a dimensionless parameter, ranging from 0 to 1, which represents the share of theoretical maximum insolation (without any shading) that can be attained by a rooftop surface within the urban context. The closer I^* gets to 1, the lower is the building rooftop overall shading rate, approaching the unshaded condition.

For the calculation of I^* , the yearly average solar insolation (in kWh/m² year) received by each piece of rooftop (about 350,000 elements) within the Canton of Geneva has been retrieved from the open-access Geneva Geoportail (SITG) in the Energy section²(shapefile *Ocen.solaire.irr.surface.utile*). The city-scale insolation computation was carried out in the

¹<https://ge.ch/sitg/>

framework of the development of the Solar Cadaster of Geneva (Desthieux et al., 2018a,b; Thebault et al., 2020). The latter is a powerful integrated tool involving the use of LiDAR, 2D and 3D cadastral data. The solar radiation modelling was implemented through GIS in combination with Matlab, using the Hay anisotropic model for sky-diffuse radiation (Hay, 1979) and accounting for the shading coefficients on the direct and diffuse components (Ratti and Richens, 2004). For each piece of rooftop (i), having a certain slope (β) and azimuth (γ), the dimensionless scaled solar insolation (I_{roof}^*) has been calculated as in Eq 4.1

$$I_{roof}^*(i) = \frac{I_{roof}(i)}{I_{theo-max}(\beta, \gamma)} \quad (4.1)$$

where I_{roof} is the surface yearly average solar radiation (in kWh/m² year) of the i^{th} surface extracted from the Solar Cadaster of Geneva and $I_{theo-max}$ is the unshaded theoretical maximum insolation that corresponds to the i^{th} surface, calculated from its slope ($\beta(i)$) and azimuth ($\gamma(i)$). In other words, considering a specific piece of rooftop (i), $I_{theo-max}(\beta(i), \gamma(i))$ can be seen as the yearly solar radiation that would be received by this roof if it were not shaded by surroundings elements (buildings, elements on the roof etc). Therefore, a I_{roof}^* value of 1 corresponds to a roof that is not shaded at all.

The calculation of $I_{theo-max}$ is based on the well-known plane-of-array (POA) solar radiation formulation, evaluating the incident insolation on a tilted surface (β, γ) from horizontal radiation data (transposition model) as in Eq 4.2

$$I_{theo-max}(\beta, \gamma) = I_{dir}(\beta, \gamma) + I_{diff}(\beta, \gamma) + I_{refl}(\beta) \quad (4.2)$$

where I_{dir} , I_{diff} , I_{refl} are respectively the direct, the diffuse, and the reflected solar radiation components. To be consistent with the calculations of the Solar Cadaster of Geneva, the Hay model has been chosen for diffuse radiation, and the same (with respect to the Cadaster) horizontal monthly average insolation data have been used as the input for the maximum unshaded insolation calculation. A heuristic approach has been adopted for further validation: $I_{theo-max}$ has been compared with the maximum insolation value ($I_{roof-max}$) extracted from the Cadaster for each possible combination of slope and azimuth (β, γ) as in Eq 4.3

$$I_{roof-max}(\beta, \gamma) = \max(I_{roof}(i), (\beta(i), \gamma(i)) = (\beta, \gamma)) \quad (4.3)$$

The main idea behind the calculation of $I_{roof-max}$ is that, considering the large number of roof surfaces in the dataset, it could be expected that, for each possible combination of slope and azimuth, there is at least one roof that should be unshaded so that $I_{roof-max}(\beta, \gamma) = I_{theo-max}(\beta, \gamma)$. The relative error (Δ) between the two quantities is calculated in percentage as in Eq 4.4

²<https://map.sitg.ch/app/>

$$\Delta(\beta, \gamma) = \left(\frac{I_{theo-max}(\beta, \gamma) - I_{roof-max}(\beta, \gamma)}{I_{theo-max}(\beta, \gamma)} \right) \cdot 100 \quad (4.4)$$

Worth noting, to be consistent with the abovementioned assumption, $I_{roof-max}$ can be compared to the unshaded condition ($I_{theo-max}$) only when the number of surfaces (having the same slope and azimuth values) is sufficient to assume that at least one among them is not shaded. This condition is not always met, typically when $\beta > 40^\circ$, since highly inclined roof surfaces are less common and more likely to be shaded from surroundings. Here, the minimum number of roof surfaces that is considered statistically significant, and thus allowing the calculation of the error Δ , is set to 30. Despite the heuristic validation has been carried out for a reduced dataset, being the calculation of $I_{theo-max}$ identical for all the surfaces, the validation process can be extended to the whole dataset. Figure 4.3 shows the values of $I_{theo-max}$ (left), $I_{roof-max}$ (centre), and Δ (right), as a function of the surface slope (β) and azimuth (γ). It can be observed that the general appearance of $I_{theo-max}$ and $I_{roof-max}$ is very similar, with some punctual differences and a greater disagreement for $\beta > 40^\circ$ due to the scarcity (less than 30) of comparable surfaces. The mean Δ is 3.26%, with some localized peaks of 10%, which is considered acceptable. As expected, Δ is mostly positive meaning that $I_{theo-max}$ is generally higher than $I_{roof-max}$ due to the not-perfect unshaded conditions within the urban environment (despite the limitation set to 30 buildings).

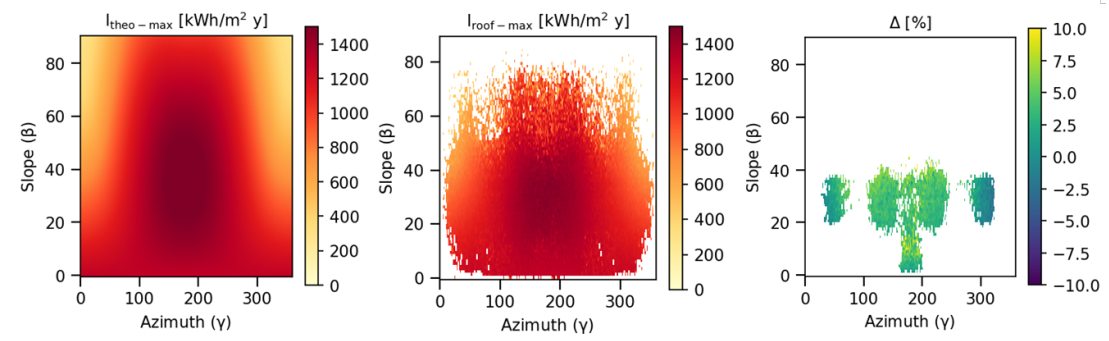


Fig. 4.3 $I_{theo-max}$ (left), $I_{roof-max}$ (centre), and the relative error Δ (right) as a function of the surface slope (β) and azimuth (γ).

Since the evaluation of the morphological parameters is made for each building and not for each roof, I_{bld}^* is introduced. It corresponds to the average area-weighted value of I_{roof}^* for each building and it is calculated as in Eq 4.5

$$I_{bld}^* = \frac{\sum_{i \in bld} I_{roof}^*(i) \cdot A_{roof}(i)}{\sum_{i \in bld} A_{roof}(i)} \quad (4.5)$$

where A_{roof} is the area of each roof surface. As all the following analyses are related to the building elements, from now on, I_{bld}^* will be simply denoted as I^* for the sake of brevity. At this point it is worth mentioning that the proposed methodology is perfectly suitable for the

study of insolation received by façades. However, this information is still not available yet at the scale of the Canton of Geneva.

4.1.4 Morphological Tessellation and Calculation of Urban Form Features

This study aims at evaluating the relationship between the building rooftop overall shading rate, measured through I^* , and the characteristics of the urban environment. A set of 40 meaningful morphological features have been selected and calculated for each building of the Canton of Geneva. Differently from previous studies (Chatzipoulka et al., 2016; Mohajeri et al., 2016; Morganti et al., 2017), where the urban morphological parameters were related to average values within a predefined reference boundary (grid or municipality), here the objective is to obtain a non-averaged unique value for each building. Indeed, meaningful indicators should capture not only simple geometrical attributes of one building (namely the height, surface, volume, ...) but also its relationship with the surroundings (namely the inter building distance, density, height difference with neighbours, and more).

From the 60,000 building footprints and the building height information stored in the shapefile *Cad.batiment.hors.sol*, a python script has been implemented to extract the selected urban metrics. To this aim, a package named Momepy (Fleischmann, 2019) has been exploited. The Momepy library is based on the other hand on well-known python packages for GIS data analysis as GeoPandas (Jordahl et al., 2019), PySAL (Rey and Anselin, 2007), and networkX (Hagberg et al., 2008). It provides several algorithms measuring six categories of features: *dimension*, *shape*, *intensity*, *spatial distribution*, *connectivity*, and *diversity*, identified by the developers through detailed literature research (Fleischmann, 2017). In the present study, 40 among the attributes measuring building *dimension*, *shape*, *intensity*, and *spatial distribution* have been selected. The list of features, as well as the related equations and description, is reported in Appendix B for the sake of conciseness. The categories of *connectivity* and *diversity* (as defined in (Fleischmann, 2019)) are not included in this research as they are mainly related to network analysis and they are not representative for solar studies related to the resource spatial distribution.

The *dimension* category concerns the basic geometrical attributes of a building (perimeter, footprint and total floor areas, volume, longest axis length, and more), whereas the *shape* group includes some shape descriptors (e. g. degree of elongation, compactness, squareness, shape index). Contrarily to the previous categories, which are strictly related to the building geometry, the *intensity* category is more related to the urban fabric, comprising the calculation of the density. In urban studies, density is generally defined as the ratio between the footprint area (or the total floor area) and the unbuilt space. The calculation of the density requires the definition of a reference boundary that is often established using a grid or by simply considering the administrative limits of a district. However, this approach results in averaged values of a space portion, and it fails in capturing site-specific and building-related density information. To

overcome this limitation, the Momepy *morphological tessellation* function is used to evaluate the “surface of influence” of each building. The tessellation cell is a geometric derivative of Voronoi polygons obtained from building footprints. It represents the smallest spatial unit that delineates the portion of land around each building. Through the morphological tessellation, it is thus possible to capture the influence that each building exerts on the surrounding space as well as the building-related density information. Figure 4.4 shows the building footprints and the space subdivision into tessellation cells in a selected portion of the city of Geneva. The color scale shows the *intensity* of the built environment in terms of building Coverage Area Ratio (CAR) expressed as the ratio between the building footprint area and the area of the related tessellation cell. As it can be observed from the figure, the darker is the color the greater is the proportion of the tessellation cell covered by the building footprint, thus mapping precisely the densest areas within the urban fabric.

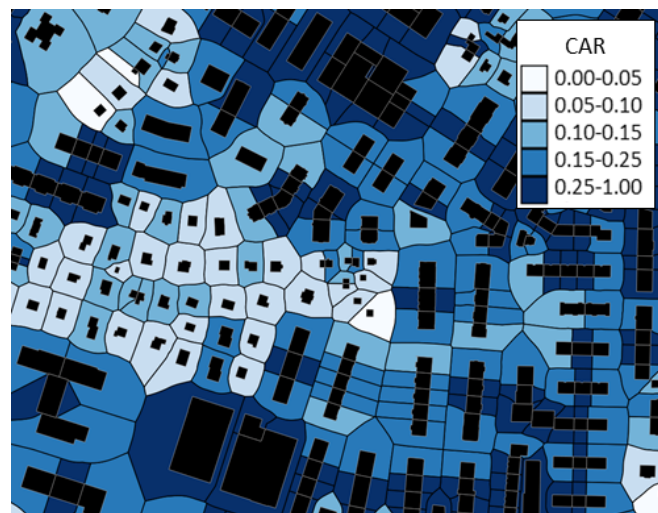


Fig. 4.4 Building footprints and related tessellation cells of a specific area of Geneva. The color scale is related to the building Coverage Area Ratio (CAR).

The *spatial distribution* aims at capturing the spatial relationships among buildings. Each building is influenced by its surroundings and it must be analysed within a spatial context, accounting for the neighbouring elements. This is possible using the *spatial weights*, i. e. mathematical structures used to detect the relationship between elements in the form of a binary matrix (1 = neighbours, 0 = not neighbours). In a few words, a building neighbour is a building whose tessellation cell is adjacent to the one under consideration as it is schematically represented in Figure 4.5.

Once the neighbours are defined, some morphological features, such as the mean distance to neighbouring constructions or averaged characters of the surroundings (average building height, surface, volume, and many others on adjacent cells), have been calculated. Finally, a set of additional morphological parameters that are not included in the Momepy library has been considered for this specific solar-related analysis. In more detail, the area-weighted average rooftop slope ($\bar{\beta}$) is calculated as in Eq 4.6

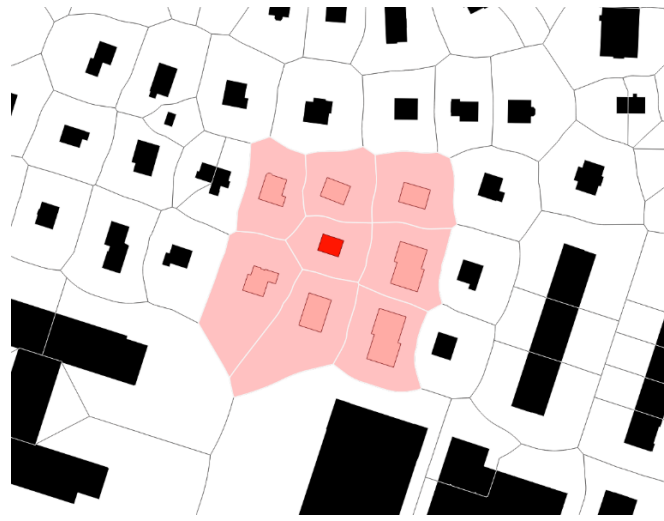


Fig. 4.5 Schematics representation of a building (red) and its neighbours identified by the spatial weights.

$$\bar{\beta} = \frac{\sum_{i \in \text{bld}} \beta_{\text{roof}}(i) \cdot A_{\text{roof}}(i)}{\sum_{i \in \text{bld}} A_{\text{roof}}(i)} \quad (4.6)$$

where β_{roof} , and A_{roof} are respectively the slope and the area of each piece of roof (i). The average Height to Width (HW) ratio, a useful measure for urban street canyon analyses, is evaluated through Eq 4.7

$$HW = \frac{1}{N_{\text{neigh}}} \sum_{j \in \text{neigh}} \frac{H}{d(j)} \quad (4.7)$$

where H is the height of the reference building and the subscript 'neigh' refers here to the set of neighboring buildings. N_{neigh} is the number of neighbors and $d(j)$ is the distance between the reference building and its j^{th} neighbor. The distance weighted average height difference ($\overline{\Delta H}$) has been also introduced as in Eq 4.8

$$\overline{\Delta H} = \frac{\sum_{j \in \text{neigh}} (H(j) - H) \cdot w(j)}{\sum_{j \in \text{neigh}} w(j)} \quad (4.8)$$

where $H(j)$ is the height of the j^{th} neighbor, and $w(j)$ are the distance weights for the average. Here, $w(j)$ is the inverse of the distances between the reference building and its neighbors ($w(j)=1/d(j)$), thus giving more weight to the nearest constructions as they are expected to have a greater impact on solar potential. Likewise, also the positive distance weighted average height difference ($\overline{\Delta H^+}$) is defined, including in the calculation only the neighbors that are higher than the building itself ($H(j) > H$). Finally, the angle α , the average neighborhood shading angle, is expressed through Eq 4.9

$$\alpha = \arctan \left(\frac{1}{N_{\text{neigh}}} \sum_{j \in \text{neigh}} \frac{H(j) - H}{d(j)} \right) \quad (4.9)$$

As for $\overline{\Delta H}$, the positive α ($\alpha+$) is also included considering only the neighboring buildings that are higher than the considered one ($H(j) > H$).

4.1.5 Data Pre-processing

A series of pre-processing operations have been performed to set up the statistical analysis and the correlations between I^* and the morphological parameters (M_n , with n ranging from 1 to 40). First, missing values have been checked and removed. The building dataset has been cleaned from not significant elements, i. e. buildings having a footprint area below 20 m² and/or a height lower than 3 m, representing approximately the 0.03% of the total elements. In addition, when investigating the correlations between I^* and the morphological features, the outlier buildings, having height, footprint area or tessellation area values significantly higher than the rest of the dataset, have been removed using an Isolation Forest method implemented in a scikit-learn python package (Buitinck et al., 2013). Finally, the data related to both the scaled insolation and the urban morphology have been merged using the building ID (named *EGID* in the shapefiles) thus obtaining a table of attributes, composed by the 40 morphological features plus one value of I^* , for each building.

4.1.6 Results and Discussion

In the following sections, the results are presented. The first two parts are related to the statistical analysis on the distribution of I^* (Section 4.1.6.1) and the morphological differences between the buildings with respectively the lowest and highest values of I^* (Section 4.1.6.2). To this aim, two groups of buildings have been identified within the dataset through quantiles. The first one (Q_{10}) comprises all the buildings having a I^* value lower than the 0.1 quantile, whereas the second (Q_{90}) is related to the ones with I^* higher than the 0.9 quantile. The morphological features of Q_{10} (lowest I^*) and Q_{90} (highest I^*) have been analysed and compared interpreting boxplots.

Sections 4.1.6.3 and 4.1.6.4 investigate the correlations between I^* and the morphological features. The Pearson Correlation coefficients (R^2) and the scatter plots between I^* and each morphological feature (M_n) have been calculated and analysed to investigate the correlation between the dependent variable y (I^*) and the independent variable x (M_n). In some cases, M_n resulted in a non-normal distribution and, to reduce the skewness of data and get a more linear relationship, different types of mathematical transformations on the original dataset have been tested. Following Rosenblad (2009), the logarithmic and square root transformations in some cases proved to be more effective to represent the relationship between I^* and M_n . The

correlation study has been carried out in the first instance on the whole building dataset (Section 4.1.6.3), and then within the different 48 municipalities of the Canton of Geneva evidencing the differences as a function of the urban characteristics (Section 4.1.6.4).

4.1.6.1 I^* distribution over the Canton of Geneva

Figure 4.6 shows the histogram of the I^* distribution over the 60,000 buildings. The I^* values on the x-axis have been subdivided into 50 homogeneous intervals and the y-axis represents the related percentage of buildings with respect to the total number. As it can be observed, the I^* distribution is characterized by a negative skewness, i.e. the mass of the distribution is concentrated on relatively high I^* values.

It can be also noticed that buildings with an I^* value of 1.0 are also infrequent. This means that the urban morphology affects most of the time the building rooftop irradiance, either by affecting the whole building or by affecting one piece of roof of the building since I^* is an average value (see Eq 4.5). Nevertheless, it is worth considering that there could be slight discrepancies between the calculation of $I_{theo-max}$ and the insolation values as computed by the Solar Cadaster of Geneva. Indeed, even if, in the present paper, same hypothesis regarding reflections and diffusion model were made, considering the complexity of the calculation, the results might be affected by some minor differences. However, even by considering an uncertainty of 10% (which corresponds to a rather conservative value of uncertainty with regards to the validation conducted in Section 4.1.3) it appears that more than 75% of the buildings have a I^* below 0.9 and can therefore be considered as partly shaded.

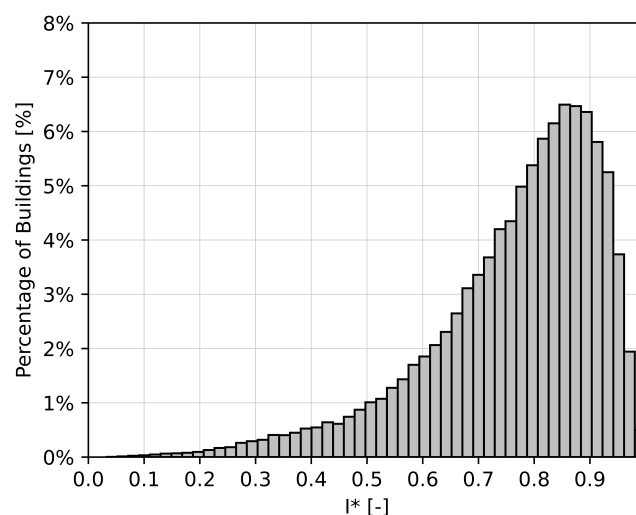


Fig. 4.6 Distribution of I^* on buildings.

The related cumulative distribution function of I^* is shown in Figure 4.7. The mean I^* value is 0.77 and the 25th percentile is 0.69 meaning that in general, despite the overall influence of the urban morphology on the solar resource, the shading levels are quite low.

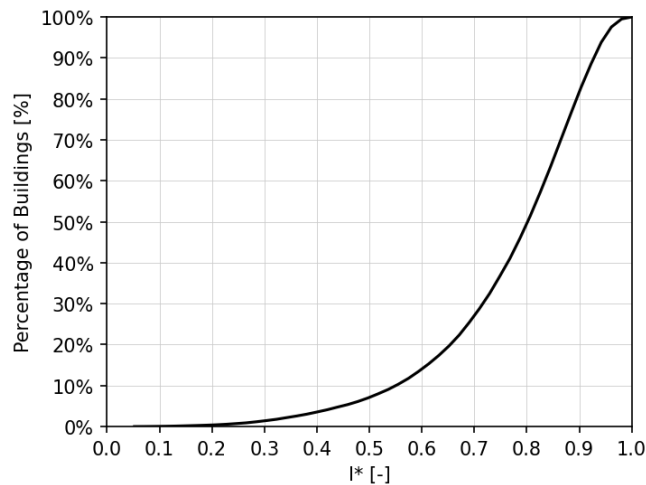


Fig. 4.7 Cumulative distribution function of I^* on buildings.

4.1.6.2 Statistical Analysis of the Shading Conditions as a Function of the Urban Morphology

Figure 4.8 outlines a summary statistic (median and interquartile range) of the selected lower (Q_{10}) and the upper (Q_{90}) quantiles of I^* with respect to the main meaningful morphological features, whose values are reported into the y-axis. In more detail, the size of the two groups is identical (both represent the 10% of the total number of buildings) but Q_{10} comprises all the buildings having an I^* lower than 0.55, whereas Q_{90} includes the ones with an I^* higher than 0.93. The analysis is aimed at evidencing the main morphological differences between more shaded buildings (light blue, Q_{10}) and the less shaded ones (red, Q_{90}). Boxplots show the minimum (lower cap), maximum (upper cap), median (box middle line), 25th percentile (lower box limit), and 75th percentile (upper box limit) value of the selected morphological features for the two groups. Concerning the height (H), the footprint area (A), and the total floor area (fA), the boxplots representing the group Q_{90} are comparatively higher than the ones that represent Q_{10} , meaning that taller and bigger (in terms of areas) constructions are more likely to be less shaded. The spread of the boxplots represents the variability of a parameter. Observing the total floor area (fA), the variability is much lower for Q_{10} , meaning that in general the rooftop shading mainly affects small constructions, with a fA typically lower than 250 m².

The boxplots of the Volume to Façade Ratio (VFR) evidence that Q_{90} mainly comprises constructions that have a big volume compared to the façade area. In other words, low-rise large buildings (with higher VFR) are generally less shaded than the high-rise/tower-like ones. In terms of urban density, if we refer to the building Floor Area Ratio (FAR), i. e. the ratio

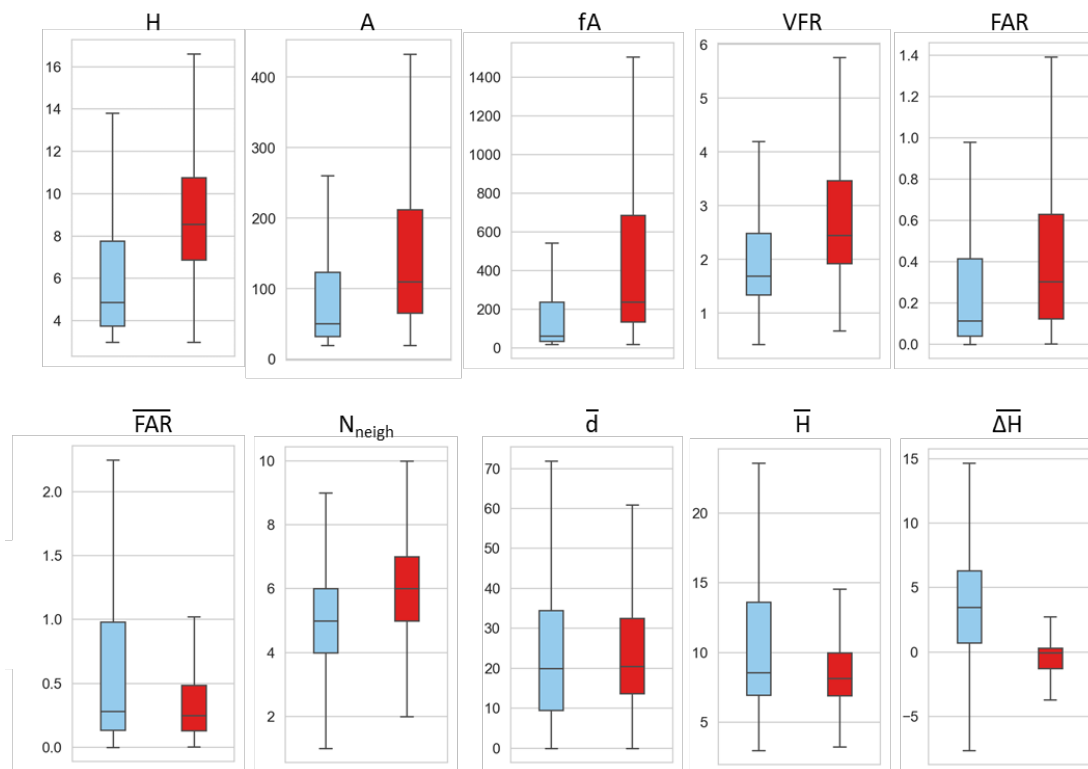


Fig. 4.8 Boxplots of Q_{10} (light blue) and Q_{90} (red). Boxplots show the minimum (lower cap), maximum (upper cap), median (box middle line), 25^{th} percentile (lower box limit), and 75^{th} percentile (upper box limit).

between the building total floor area and the area of the related tessellation cell, it is possible to notice higher density values for less shaded buildings (Q_{90}). This is apparently in contrast with previous studies that evidence a negative correlation between solar radiation and density. However, as highlighted in the Introduction, thanks to the tessellation, here the calculation of the FAR density is not averaged within a selected area, but it is computed within each tessellation cell, thus resulting in a building-related parameter independent from the characteristics of the surroundings. Contrarily, referring to the urban density as the average Floor Area Ratio of neighboring constructions (\overline{FAR}), lower \overline{FAR} values are associated to a lower shading rate, evidencing that less shadowed buildings are mostly surrounded by low-density areas. The tendency that identifies large-surface buildings being significantly less shaded, is also confirmed by the number of neighbors (N_{neigh}). One could expect that a weaker shading may be related to buildings that have a few neighbors. However, observing the boxplot of N_{neigh} the results show the opposite for this case study. This can be explained by the fact that large-surface buildings are more likely to have more neighboring constructions compared to tower-like or small constructions.

The average distance with neighboring constructions (\bar{d}) seems not significant to detect the differences between Q_{10} and Q_{90} , as it fails in capturing any information about the size (both in terms of height and area) of the surrounding building. In contrast, as expected, the average

height of the building neighbors (\bar{H}) shows a small variability and comparatively lower values for less shaded building (Q_{90}).

Finally, as expected, the height difference with surrounding constructions ($\overline{\Delta H}$) is mostly positive for more shaded buildings, i. e. neighbors are higher than the building itself, whereas it is negative or near to zero for the less shaded ones.

4.1.6.3 Correlation Study

As briefly outlined in Section 4.1.5 a series of data cleaning and pre-processing operations have been performed before investigating the correlations between I^* and the morphological features (M_n). Figure 4.9 shows the detection, through the Isolation Forest method, of the removed outliers for the footprint area values. Each marker represents one building, labeled through its ID number (ranging from 0 to 60,000) on the x-axis and the colors identify the inliers (grey points) and the outliers (red triangles). The same procedure has been applied also for the height and the area of the tessellation cell, the diagrams are not displayed for the sake of conciseness. As a result, a total of about 150 outlier buildings have been removed from the dataset before performing the correlation analysis. The aim of such a pre-treatment operation is to exclude specific buildings with uncommon characteristics in the statistical analysis in order to reduce the induced bias.

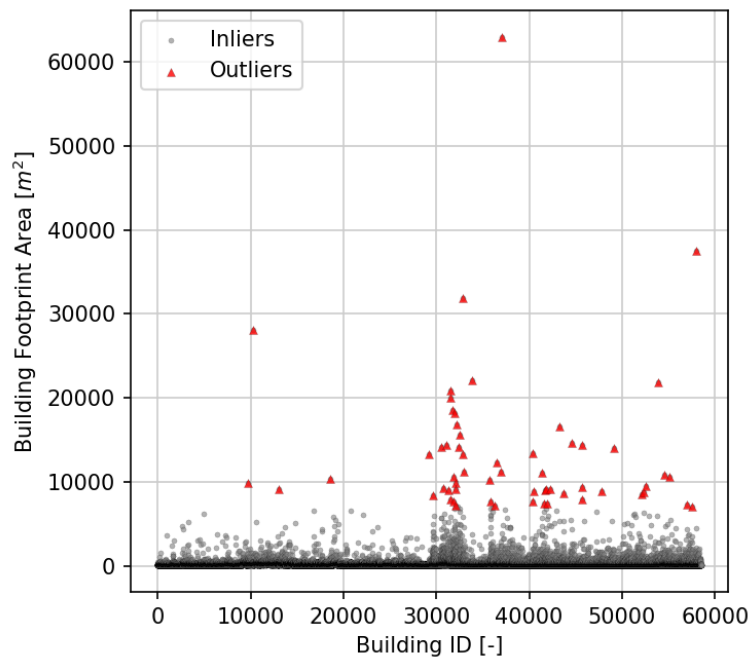


Fig. 4.9 Scatterplot representing the detection of outliers in footprint areas (m^2) in red triangles, and the inliers in grey points.

As a preliminary analysis to investigate the relationship between I^* and the 40 morphological features (M_n) here considered (see Appendix B), the calculation of the Pearson correlation coefficients (R^2) has been performed on the whole dataset. Table 4.1 shows the R^2 values between I^* and each morphological feature of the present study. The results are sorted in descending order of R^2 absolute value with rows and columns. The markers next to the parameter name specify if the R^2 value is the result of a log-log ($\dagger\dagger$) or square root (\dagger) transformation, in case one of the two provided higher correlation coefficients in absolute value compared to the non-transformed data. The parameters related to the height difference between buildings ($\overline{\Delta H}$, $\overline{\Delta H}^+$, α , α^+) and the building rooftop average slope ($\bar{\beta}$) shows moderate correlation coefficient absolute values (ranging from 0.39 and 0.45). On the contrary, all the other spatial metrics related to dimension, shape, density, and spatial distribution have very low or no significant correlations with I^* . As a general comment, the parameters related to the building shape are the ones that exhibit the worst correlation coefficients at it was expected.

Table 4.1 Pearson correlation coefficients considering the whole building dataset. (\dagger) represents square root transformation, whereas ($\dagger\dagger$) is for log-log transformation.

Symbol	R^2	Symbol	R^2	Symbol	R^2	Symbol	R^2
$\overline{\Delta H}$	-0.45	\overline{FAR}	-0.17	$Cco(\dagger\dagger)$	0.09	$A_{tess}(\dagger\dagger)$	0.07
$\overline{\Delta H}^+(\dagger)$	-0.43	$P(\dagger\dagger)$	0.16	$FrD(\dagger)$	-0.09	$\bar{d}(\dagger\dagger)$	0.06
$\bar{\beta}$	-0.39	$LaL(\dagger\dagger)$	0.15	$\overline{fA}(\dagger\dagger)$	-0.09	Ali	-0.06
α^+	-0.25	$FAR(\dagger\dagger)$	0.14	$LaL_{tess}(\dagger\dagger)$	0.09	$Sqco$	0.05
α	-0.25	$Rug(\dagger\dagger)$	0.14	$\bar{V}(\dagger\dagger)$	-0.08	$\bar{A}(\dagger\dagger)$	-0.04
$V(\dagger\dagger)$	0.21	\bar{H}	-0.12	$Elo(\dagger\dagger)$	0.08	Rec	0.04
$fA(\dagger\dagger)$	0.20	\overline{CAR}	-0.11	$Squ(\dagger\dagger)$	-0.08	$CovA(\dagger\dagger)$	0.03
$VFR(\dagger\dagger)$	0.20	$N_{neigh}(\dagger\dagger)$	0.11	$FoF(\dagger\dagger)$	-0.08	$\overline{SWR}(\dagger\dagger)$	0.03
$H(\dagger\dagger)$	0.20	$Adj(\dagger\dagger)$	0.11	$CAR(\dagger\dagger)$	0.08	$\overline{A}_{tess}(\dagger)$	-0.01
$A(\dagger\dagger)$	0.18	$ShIdx(\dagger\dagger)$	0.09	$HW(\dagger\dagger)$	0.07	ERI	0.01

Despite the low correlation values, observing the scatterplots representing the relationship between I^* and the morphological parameters, in some cases a “triangular” pattern can be noticed. More precisely, for the parameters related to the building dimension (namely A, H, V, P, fA , VFR, LaL), called $M_{n,dim}$ for brevity, it is possible to define a relationship of the type $I^* > a \cdot M_{n,dim} + b$ (or $\log(I^*) > a \cdot \log(M_{n,dim}) + b$ in case of log-log transformation) through a quantile regression. Figure 4.10 shows the scatterplot between I^* (y-axis) and V (x-axis) after the log-log transformation. As it can be noticed, the variability of $\log(I^*)$ is so high for lower $\log(V)$ values, that the linear correlation between the two, represented by the black regression line, is unsuitable to describe the data. On the other hand, performing a quantile linear regression by considering the 0.01 quantiles of data (red points) it is possible to define a regression line (red line) with $R^2=0.87$. Despite it is not possible to predict I^* based on $M_{n,dim}$, using a quantile linear regression it is possible to define the most probable range of I^* values corresponding to a

selected Mn,dim value. Worth noting that the same considerations presented for V apply to the other dimensional features of the building (A, H, P, fA, VFR, LaL).

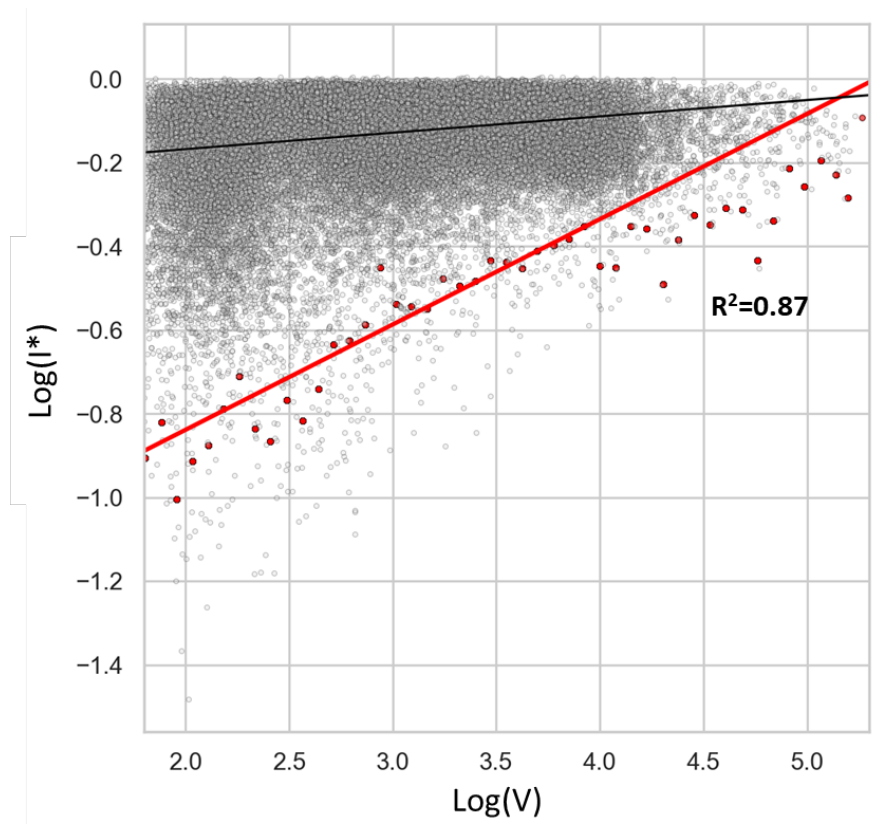


Fig. 4.10 Scatterplot between $\log(I^*)$ and $\log(V)$. The black line represents the linear regression line and the red line is related to the linear quantile regression line based on 0.01 quantiles (red points).

4.1.6.4 Correlation Analysis by Municipality

The Canton of Geneva is a rather heterogeneous territory, composed of 48 municipalities, some being small rural municipalities, others being part of the urban area of the Geneva city itself. By analysing the average morphological features characterising each of the 48 municipalities of the Canton of Geneva, some evident differences can be noticed. In particular, four out of the 48 municipalities appear over scale both in terms of building size and of built density. The four municipalities correspond to the city center district, having a denser urban morphology compared to the more open residential suburbs. Figure 4.11 shows the boxplots related to the building volume (V) and the building Floor Area Ratio (FAR) for each municipality, evidencing in red the four municipalities that correspond to the Geneva city center.

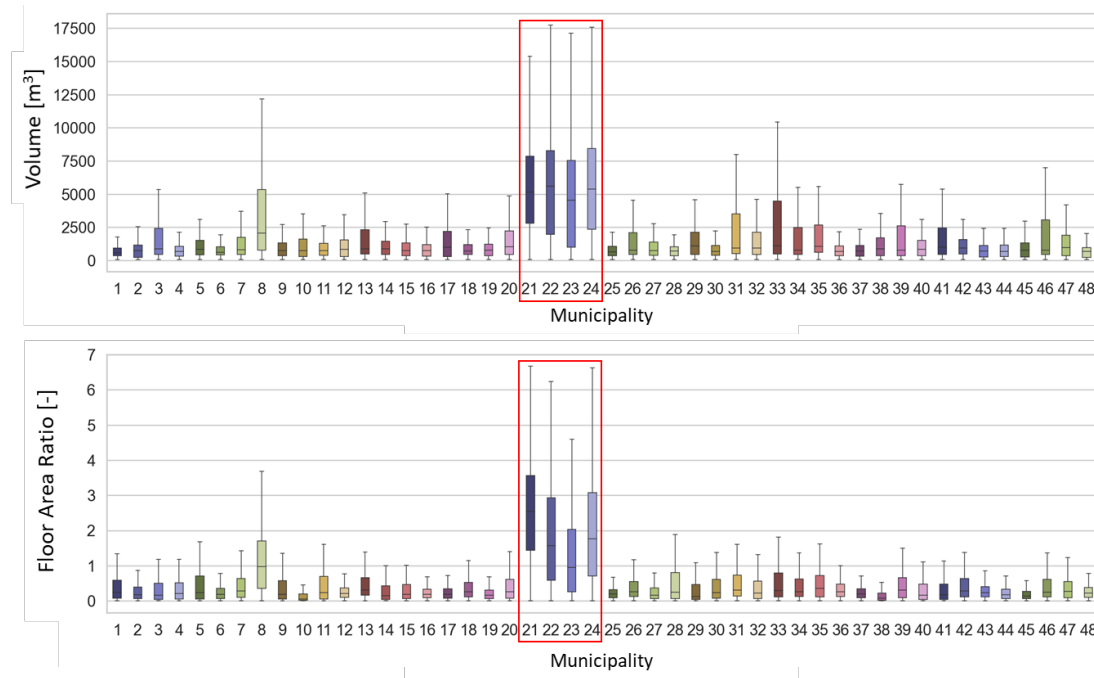


Fig. 4.11 Boxplots of V and FAR of the 48 municipalities of the Canton of Geneva. The city centre districts are highlighted with red boxes.

The linear Pearson correlation coefficients have been calculated considering a reduced dataset of buildings, including only the four city center municipalities. The results are reported in Table 4.2. As it can be observed, in this case, the correlations between I^* and the morphological parameters are higher. As in the previous case, the most relevant parameters to describe I^* are the ones related to the height difference with surrounding buildings (R^2 about 0.6). Additionally, also some building dimension features (namely H , fA , V , FoF , VFR , A) show moderate correlation coefficient absolute values towards I^* (ranging from 0.32 to 0.53).

Table 4.2 Pearson correlation coefficients considering the four city-center districts. (\dagger) represents square root transformation, whereas ($\dagger\dagger$) is for log-log transformation.

Symbol	R^2	Symbol	R^2	Symbol	R^2	Symbol	R^2
$\overline{\Delta H}(\dagger)$	-0.60	$A_{tess}(\dagger\dagger)$	0.29	$ShIdx(\dagger)$	0.22	$\overline{H}(\dagger)$	0.12
$\overline{\Delta H}^+(\dagger)$	-0.58	$LaL_{tess}(\dagger\dagger)$	0.28	$FrD(\dagger\dagger)$	-0.21	\overline{FAR}	0.11
$H(\dagger\dagger)$	0.53	$\overline{d}(\dagger\dagger)$	0.27	$Elo(\dagger\dagger)$	0.20	Rec	0.09
$fA(\dagger\dagger)$	0.47	$FAR(\dagger\dagger)$	0.27	$HW(\dagger)$	0.20	$Squ(\dagger\dagger)$	-0.09
$V(\dagger\dagger)$	0.47	$P(\dagger\dagger)$	0.26	$CovA(\dagger\dagger)$	0.20	$\overline{A}(\dagger\dagger)$	0.08
$FoF(\dagger\dagger)$	-0.38	$Adj(\dagger\dagger)$	0.25	$\overline{A}_{tess}(\dagger\dagger)$	0.17	$\overline{V}(\dagger\dagger)$	0.07
$VFR(\dagger\dagger)$	0.35	$Rug(\dagger\dagger)$	0.25	\overline{CAR}	0.17	$\overline{fA}(\dagger\dagger)$	0.07
α	-0.32	$\overline{\beta}$	-0.25	CAR	0.15	ERI	0.03
$A(\dagger\dagger)$	0.32	$LaL(\dagger\dagger)$	0.24	$Sqco$	0.15	$SWR(\dagger)$	0.03
α^+	-0.31	$Cco(\dagger)$	0.23	$N_{neigh}(\dagger\dagger)$	0.12	$Ali(\dagger)$	0.02

The most meaningful correlation is shown in Figure 4.12, representing the scatterplot between I^* and the building average height difference with surrounding ($\overline{\Delta H}$), after the square root transformation, as well as the regression line with the related equation. In general, the greater is the height difference with the surroundings, the lower is the I^* value, meaning that the buildings are more likely to be shaded by the neighboring constructions.

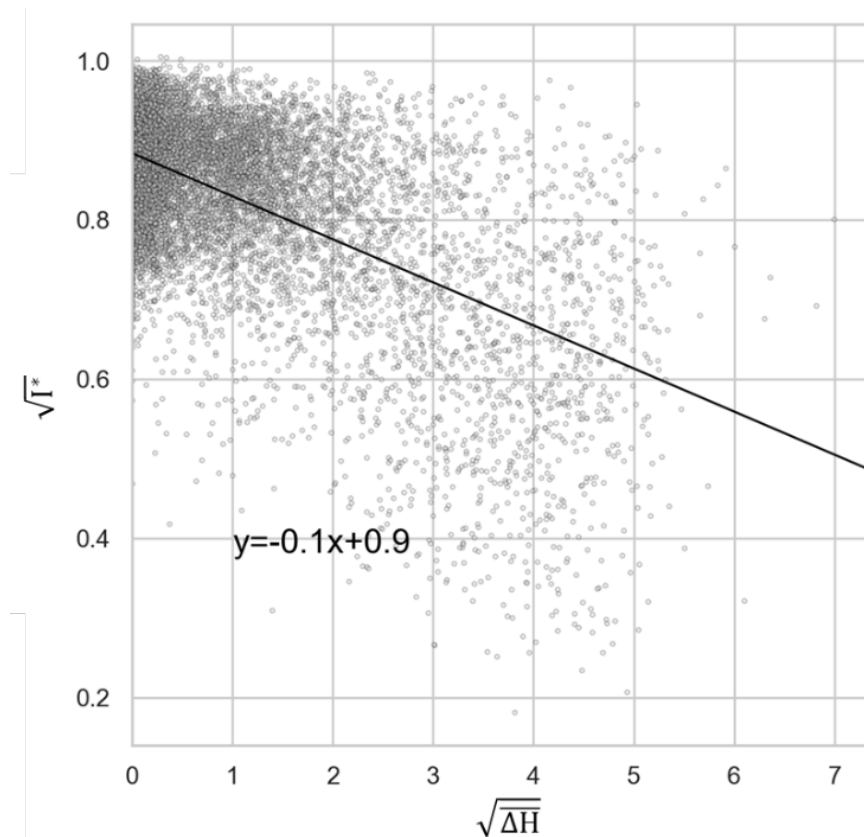


Fig. 4.12 Scatterplot between I^* and $\overline{\Delta H}$ after the square root transformation. The black line represents the linear regression line.

The results arising from this correlation study evidence that some tendencies and meaningful information about rooftop shading conditions, and more in general on solar radiation analyses, can be extracted through detailed urban morphological studies. However, for most of the selected parameters the correlation coefficients are not sufficient to suggest accurate predictive models. The features related to the building dimension and the height difference with the surrounding constructions are the most useful to investigate the overall rooftop shading rate and they provide interesting qualitative considerations both for researchers and planners. Contrarily to solar radiation on façades (Chatzipoulka et al., 2016; Mohajeri et al., 2016; Morganti et al., 2017), the analysed density-related parameters do not show meaningful relationship towards solar radiation conditions. On the other hand, as it has been presented for the four downtown municipalities, the density is a meaningful measure of the impact level of urban morphology on shading conditions.

The higher is the built density, the greater is the effect of surrounding constructions of rooftop solar radiation.

4.1.7 Conclusions and Perspectives

In this paper we propose a new general methodology to investigate the relationship between rooftop insolation and urban morphology. A comprehensive statistical analysis has been performed with respect to rooftop solar producibility related to the Canton of Geneva, Switzerland. About 60 thousand buildings have been considered for a detailed analysis based on 40 urban morphological parameters. The selected morphological features refer to building dimension, shape, interbuilding geometrical parameters as differences in height, distance, land area occupancy whose values have been calculated thanks to a Python Authors' code able to process GIS-data. The independent variables (the urban morphological parameters) have been statistically processed versus the dimensionless insolation, defined in the present study as the ratio of the Solar Cadaster previously calculated insolation values and the unshaded insolation per roof portion. In the present studies it is showed that:

- Within the studied area, more than 75% of the buildings is partly shaded. On the other hand, 75% of the buildings receive more than 69% of the solar insolation that they would receive if they were not shaded.
- The most shaded buildings (0.1 quantile) and least shaded (0.9 quantile) feature significantly different morphological characteristics. The least shaded ones are more likely to be low rise large buildings (with big surfaces) rather than high-rise/tower-like constructions, as it could be expected.
- At the scale of the Canton of Geneva, correlations between the scaled irradiance and the morphological are rather low, reaching a maximum R^2 of 0.45 for $\overline{\Delta H}$. However, analysing the municipalities, correlations are significantly improved for dense urban patterns (city centre), with R^2 coefficient that can reach up to 0.60.
- In general, the morphological parameters that exhibit the best correlations are the ones related to building dimension and interbuilding height difference, in particular referring to the city centre municipalities. On the contrary, the features related to density and building shape have low or irrelevant correlation coefficients.
- In some cases, according to the heterogeneity of the large dataset, correlation coefficient may not appear as the most relevant indicator. Instead, a correlation of the lowest quantiles can appear to well represent the dataset with correlation coefficient by up to 0.87.

In order to pursue the proposed approach, it would be interesting to apply it to other territories with different weather, latitude as well as urban morphology. However, this requires the access to large data set of rooftop irradiance, which unfortunately is not common to find in open-access.

As mentioned earlier, it is also worth mentioning that the proposed methodology can be applied to any type of urban surface, including vertical façades. The latter would be extremely interesting since these surfaces are more likely to be sensitive to shadings from surroundings.

Finally, the proposed approach is not limited to solar analysis. Indeed, it can be applied to any type of variable related to the urban microclimate such as, for example pollution, or temperature.

Technical Report

4.2 Preliminary Estimation of the Solar Potential in the Liguria Region (Italy)

This study was carried out within the framework of the Liguria Region's newly established Regional Environmental Energy Plan 2030 (PEAR 2030). The investigations pertaining to PEAR 2030 were undertaken at the DIME Department of the University of Genoa, with Marco Fossa as the designated reference person. These analyses involved an extensive evaluation of renewable energy potentials within the Liguria Region, encompassing diverse sources including hydro, solar, wind, aerothermal, geothermal, and biomass. The part dedicated to assessing the solar potential associated with building surfaces in Liguria was conducted as an integral part of the ongoing research activities within the current Ph.D. thesis.

4.2.1 Executive Summary

The primary objective of this investigation is to provide a preliminary and approximate estimation of the photovoltaic (PV) generation potential from building rooftops within the region. The estimation is based on two main parameters: the total roof area data obtained from Geographic Information System (GIS) and the average solar insolation levels within the geographic area under consideration.

The present estimation of the rooftop PV potential considers various factors, including landscape and architectural characteristics, technical and engineering factors, and productive factors related to shading caused by surrounding constructions. A comparative study is being conducted concerning this last aspect using the results from Paper 4, considering the similar morphological characteristics of the Canton of Geneva and the Municipality of Genoa. The results from this study are presented in an aggregate form for regional policy-making, and the PV potential is not georeferenced. The obtained results present a comparison between the power and energy outputs derived from the estimated PV potential and the regional energy demand. These previously undisclosed figures are intended to foster the development of photovoltaics in the Liguria Region, as the adoption of solar energy technologies remains relatively limited in the area, despite the presence of favorable solar irradiation levels, approximately 3.8-4.1 kWh/m²/day in Liguria.

As of the year 2020, the installed capacity of photovoltaic solar energy in the Liguria Region stands at 119 MW, representing roughly 54% of the target set by the previous regional energy plan (PEAR 2020), which aimed to achieve 220 MW by 2020. With the introduction of the new PEAR 2030, more ambitious objectives have been set, striving to reach an installed photovoltaic capacity exceeding 700 MW. Therefore, the primary focus of this current analysis is to provide

an initial estimation of the photovoltaic potential from building rooftops in the region, aiming to align with and fulfill the targets established in PEAR 2030.

4.2.1.1 Methodology and Data Sources

To provide a preliminary estimation of the photovoltaic solar potential of building rooftops, various methodologies can be employed to assess the usable surface suitable for PV installations based on the total available rooftop area in the region (Melius et al., 2013). The usable surface refers to the portion of available surface with characteristics conducive to installing photovoltaic systems, considering architectural, technical, and productive aspects. The following methodologies can be used, depending on data quality and availability:

- **Constant-value Methods:** This approach involves determining coefficients to derive the usable surface from the total available rooftop surface (Eiffert, 2003; Wiginton et al., 2010). These coefficients can be obtained from literature data or expert assumptions. The constant-value method is effective for providing a preliminary estimation of the solar potential using only a GIS building footprint database, as adopted in this analysis. The advantages of this methodology include its simplicity of calculation and the requirement of only the total roof surface area as input data. However, it may yield generalized results that do not consider specific characteristics of individual rooftops, providing only a rough preliminary estimate.
- **Manual Selection Methods:** This method involves manually selecting rooftops from sources such as aerial photography, offering a more refined but more time-intensive approach to identifying suitable rooftop space compared to constant-value methods (Ordóñez et al., 2010; T. Nguyen and M. Pearce, 2013). These studies manually select rooftops from aerial imagery with characteristics that appear suitable for rooftop PV, such as flat and south-facing roofs, and that appear to have minimal shade from building components, trees, or nearby buildings.
- **GIS-based Methods:** Similar to manual selection methods, this approach also requires detailed data and sophisticated algorithms for accurate estimations (Compagnon, 2004; Santos et al., 2011). The key distinction is that rooftop suitability decisions are not based on predetermined constant values or manual selection but are determined through a computer model using ideal values for rooftop characteristics. GIS software then identifies areas of high suitability, resulting in a quicker, more objective, and more accurate method for identifying rooftop availability. GIS-based methods primarily use 3D models to determine solar resource or shadow effects on buildings. These models are typically generated from orthophotography or light detection and ranging (LiDAR) data and are combined with slope, orientation, and building structure data to estimate total solar energy

generation potential. The availability of high-resolution LiDAR data in recent years has made this method more desirable for estimating rooftop area.

For this preliminary study of Ligurian photovoltaic potential, only the GIS building footprint data are available, thus the constant-value method is chosen. The GIS building footprint data is retrieved from the Liguria Region's geoportal, specifically the "Buildings and Structures - C.T.R. scale 1:5000 - 2007/2013 - II Edition 3D/DB Topographic" map³. This mapping, conducted between 2007 and 2013, includes a census of all Ligurian buildings and their respective categories of use.

By processing the GIS data, the total rooftop area of all the buildings is obtained. However, it is necessary to reduce this area to account for factors influencing the fraction of available roof area for solar photovoltaic applications. These factors include landscape and architectural constraints, the use of roof space for other purposes such as ventilation or heating/air conditioning, and the presence of shading from neighboring buildings and trees.

In the current analysis, three reduction coefficients (c_1 , c_2 , and c_3) are introduced to account for the reduction in the total available rooftop surface area based on landscape and architectural factors, technical and engineering factors, and productive factors, respectively. These coefficients are unitless and have values between 0 and 1, depending on specific conditions.

- Landscape and architectural factors: to protect the Ligurian Region's landscape and architectural heritage, all surfaces belonging to particularly valuable buildings (protected or under heritage restrictions) or located in protected areas from a landscape perspective are excluded.
- Technical and engineering factors: the portion of the available roof surface where it is not technically feasible to install a photovoltaic system must be excluded. Particularly for flat roofs, these surfaces often accommodate superstructures (e.g., elevators, technical rooms, rooftop air conditioning systems, etc.) that prevent the exploitation of the entire available surface. It is also necessary to allow an adequate distance between the photovoltaic modules (if installed in parallel rows of inclined modules, as in the case of flat roofs) to prevent mutual shading between the rows.
- Productive factors: for effective design of the photovoltaic system, ensuring an adequate return on investment, surfaces with suitable exposure (generally referred to in the literature as receiving rooftop surfaces $> 1000 \text{ kWh/m}^2/\text{year}$) and optimal orientation must be selected, minimizing shading caused by surrounding structures (Walch et al., 2019).

Therefore, to accurately estimate the usable surface area, three coefficients are introduced in this analysis, taking into account all the factors mentioned. Specifically, the usable surface area (S_u) is calculated using Eq 4.10

³Liguria Region, Geoportal: <https://geoportal.regione.liguria.it/>

$$S_u = c_1 \cdot c_2 \cdot c_3 \cdot S_{tot} \quad (4.10)$$

where S_{tot} is the total available roof area in m^2 , and c_1 , c_2 , and c_3 are the dimensionless reduction coefficients related to landscape and architectural factors (c_1), technical and engineering factors (c_2), and productive factors (c_3), respectively.

Landscape and Architectural Factors and Calculation of Coefficient c_1

The first coefficient (c_1) takes into account considerations related to land and building use. Industrial buildings, which are generally not of significant architectural importance and are rarely situated in protected areas, are assigned a coefficient value of 1. On the other hand, for all other building categories (residential, public services, commercial, agricultural and administrative), a coefficient value of 0.7 is adopted. The selection of this value has been carefully evaluated by overlaying the built-up areas of the Region with the protected areas under landscape constraints, which include zones of architectural, archaeological, and landscape significance⁴. These protected areas are indicated with colors in Figure 4.13.

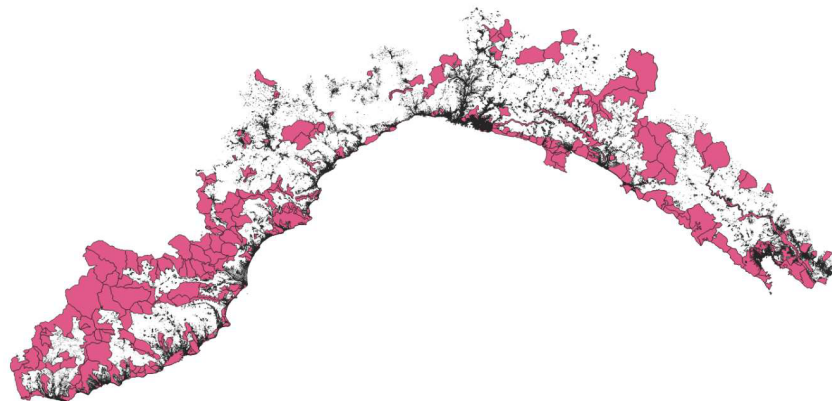


Fig. 4.13 Map of building footprints of the Liguria region (black). Architectural, archaeological, and landscape constraints are represented in colors.

The analysis revealed that approximately 70% of buildings are situated outside these protected areas, hence justifying the use of the coefficient value of 0.7 for the majority of building categories. It is important to note that specific point-based archaeological and architectural constraints, which pertain to individual buildings, are not considered in this initial analysis due to their negligible impact on the overall results. The focus is primarily on broader landscape and architectural considerations that affect a significant portion of the buildings in the region.

⁴Map of architectural, archaeological, and landscape constraints: <https://geoportal.regione.liguria.it/>

Technical and Engineering Factors and Calculation of Coefficient c_2

The coefficient c_2 relates to technical and engineering factors, and its value is derived mainly from scientific literature. Key results from various studies worldwide are summarized in a report of the National Renewable Energy Laboratory (NREL) (Melius et al., 2013). For the Liguria Region, a value of c_2 equal to 0.5 is considered, aligning with assumptions made in several similar studies (Ghaleb and Asif, 2022; Koch et al., 2022; Scartezzini et al., 2002).

Productive Factors, Solar Cadasters, and Calculation of Coefficient c_3

The coefficient c_3 is associated with productive factors and aims to quantify surfaces that receive good solar exposure, typically exceeding 1,000 kWh/m²/year, while also considering shading from surrounding structures. To conduct a thorough analysis for these factors, comprehensive and detailed building data (i.e. individual building heights, roof types, and slope angles) are required. Obtaining such detailed data can be achieved through a Solar Cadaster, an essential tool in planning large-scale solar energy development. The Solar Cadaster facilitates the calculation of direct, diffuse, and reflected solar radiation on all urban surfaces, helping identify suitable areas for photovoltaic installations.

For this study, data derived from the Solar Cadaster of Geneva city⁵, developed within the Interreg project "G2Solaire" between France and Switzerland. The analysis of the Geneva Solar Cadaster and the results obtained from Paper 4 lead to a conservative estimate of the coefficient c_3 at 0.5, indicating that approximately 50% of the available rooftop surfaces in Liguria is estimated to experience an average annual solar irradiation greater than 1,000 kWh/m²/year.

It is essential to highlight that this estimate is conservative for two reasons. Firstly, the comparison between the Canton of Geneva and the City of Genoa, which is the capital city of Liguria Region, is facilitated by their relatively similar morphological density, both around 2,000 inhabitants/km². However, the overall density of the whole Liguria Region is significantly lower (approximately 300 inhabitants/km²) than that of Genoa City, potentially resulting in better solar irradiation conditions due to reduced mutual shading among buildings. Secondly, Liguria experiences a higher global average annual solar irradiation on a horizontal surface (around 1,420 kWh/m²/year) compared to the Canton of Geneva (1,350 kWh/m²/year)⁶.

Finally, after obtaining the usable surface area (S_u) through the coefficient-based formula, the estimation of the annual photovoltaic potential (E_{PV}) in terms of cumulative electricity produced in a reference solar year (kWh_{el}/year) is calculated, considering the solar irradiation and photovoltaic conversion efficiency through Eq 4.11

$$E_{PV} = S_u \cdot E_{tot} \cdot \eta_{PV} \quad (4.11)$$

⁵Geneva Solar Cadaster: <https://apps.sitg-lab.ch/solaire/>

⁶Solargis, Global Solar Atlas 2.0: <https://globalsolaratlas.info/map>

where S_u (m^2) represents the usable surface area, E_{tot} (kWh/m^2) is the average annual global solar radiation value at a specific location on a unit surface, and η_{PV} (%) is the photovoltaic conversion efficiency of the considered module. Regarding E_{tot} , in the present analysis, it refers to the average annual global solar radiation value on a surface optimally oriented (South) and inclined at approximately 30° , localized in Liguria. Based on estimates from ENEA⁷ and in alignment with experimental data collected in recent years at the University of Genoa (Savona Campus), a typical solar radiation value of about $1,500 kWh/m^2/year$ is obtained. Lastly, for the photovoltaic conversion efficiency (η_{PV}), a conservative value of 15% is considered, taking into account not only the efficiency of commercial modules but also the efficiency of inverters and accounting for losses due to temperature, shading, and fouling.

4.2.1.2 Results

From the data processing phase, it emerges that the total number of buildings in the region amounts to 447,329 units (excluding underground buildings and those under construction). As represented in Figure 4.14, the majority of Ligurian real estate is composed of buildings for residential use, accounting for 92.4%. The remaining 7.6% consists of industrial buildings (2.9%), public structures such as hospitals and educational facilities (1.0%), buildings used for agriculture (0.9%), commercial buildings (0.6%), and administrative buildings (0.1%). The remaining 2.9%, referred to as "Other," includes all buildings intended for specific purposes (places of worship, military buildings, etc.) that, due to their particular designation, will be excluded from the subsequent analysis of usable surfaces.

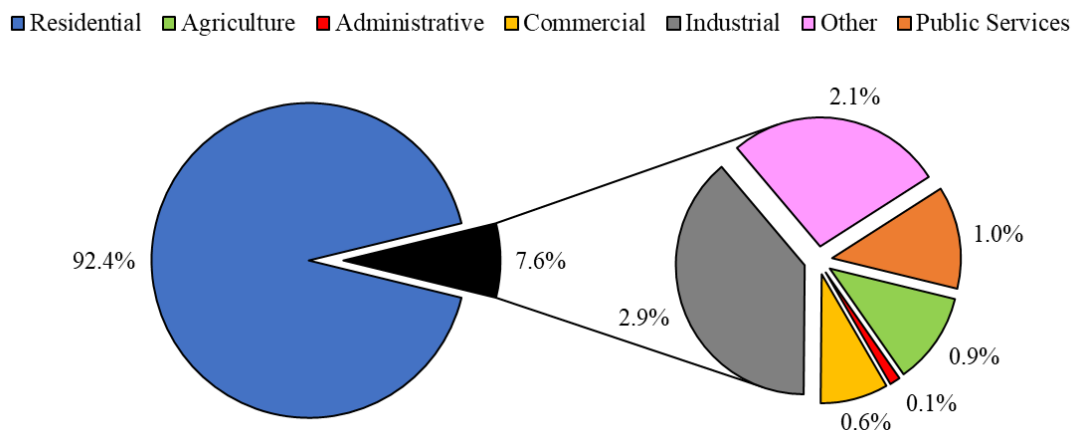


Fig. 4.14 Percentage of the number of buildings relative to the total, subdivided according to the category of use.

⁷ENEA: <http://www.solaritaly.enea.it/CalcComune/Calcola.php>

Focusing on the total roof surface, it is found that the available roof surface throughout the Region amounts to 66,170,224 m², subdivided according to the quantities described in Table 4.3.

Table 4.3 Total available rooftop area [m²] by building category

Category	Total Area [m ²]
Residential	51,183,091
Industrial	9,900,511
Other	1,763,655
Public Services	1,597,900
Commercial	1,251,756
Agricultural	348,083
Administrative	125,227
Total Roof Area	66,170,224

The data reveals that, despite the portion of industrial buildings constituting only 2.9% of the Ligurian real estate, the total roof surface available in this category accounts for 15% of the overall roof area in the Region. Figure 4.15 illustrates the percentage breakdown of available surfaces in relation to the total roof area, categorized by use.

■ Residential ■ Agriculture ■ Administrative ■ Commercial ■ Industrial ■ Other ■ Public Services

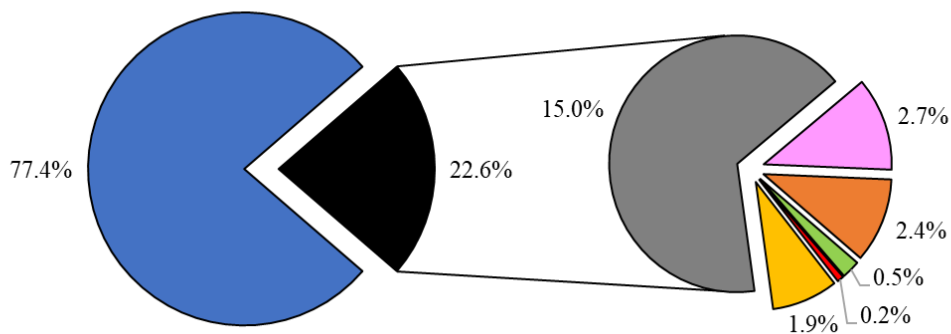


Fig. 4.15 Percentage of available roof surface compared to the total, subdivided according to the category of use.

According to the analysis, the total usable rooftop surface evaluated for Liguria amounts to about 12 km², with the usable surface for the residential category amounting to about 9 km². Table 4.4 presents the values adopted for each coefficient and the resulting usable surface in m² derived for each building category.

Table 4.4 Reduction coefficients and usable rooftop surface [m²] by building category

Category	c_1	c_2	c_3	S_u [m ²]
Residential	0.7	0.5	0.5	8,957,041
Industrial	1.0	0.5	0.5	2,475,128
Public Services	0.7	0.5	0.5	279,632
Commercial	0.7	0.5	0.5	219,057
Agricultural	0.7	0.5	0.5	60,915
Administrative	0.7	0.5	0.5	125,227
Total Usable Surface [m ²]				12,117,000

The results show that, according to this preliminary estimation of the photovoltaic potential of building rooftops in Liguria, the total production of electricity from PV is around 2,700 GWh_{el}/year, which, when compared with the Region's annual electricity consumption of about 5,400 GWh_{el}/year, would account for 50% of the total demand. This potential corresponds to an installed capacity of 1,818 MW_p. Table 4.5 presents the results divided by building categories.

Table 4.5 Estimated annual PV potential [GWh_{el}/year] by building category

Category	E_{PV} [GWh _{el} /year]
Residential	2,015
Industrial	557
Public Service	63
Commercial	49
Agricultural	14
Administrative	28
Total PV Potential [GWh _{el} /year]	2,726
Corresponding PV Capacity [MW _p]	1,818

4.2.1.3 Conclusions

The objective of this analysis is to provide a preliminary and approximate estimation of the photovoltaic potential from the building stock in the Liguria Region, aiming to assess its feasibility in relation to the targets set in the Regional Energy Plan PEAR 2030. Considering the results and the goal to achieve a total installed capacity able to exceed 700 MW_p by 2030, this objective corresponds to 40% of the estimated photovoltaic potential from building rooftops as determined in this study.

The total estimated potential production is around 2,700 GWh_{el}/year, which can be achieved by utilizing a roof surface area of approximately 12 km². This corresponds to occupying less than 20% of the total available roof area in the region with photovoltaic modules. The results indicate that the photovoltaic potential from building rooftops has the capability to cover nearly half of the region's total annual electricity demand.

It is important to note that the estimations provided in this study are preliminary and based on a simplified methodology using the constant-value method. This approach only requires knowledge of the total roof area and typical regional solar insolation values. The reduction coefficients applied are based on existing literature and previous comparative studies. A conservative approach was adopted in determining these coefficients, which should be validated in the future through more detailed analyses supported by increased data availability.

Nevertheless, the outcomes are highly promising, underscoring the considerable potential of photovoltaic energy generation in the Liguria Region. The results suggest that, given proper planning and execution, the photovoltaic potential from building rooftops has the capacity to satisfy approximately 50% of the region's total annual electricity demand. Such an accomplishment would represent a significant stride towards realizing the targets outlined in the PEAR 2030 and fostering the widespread adoption of solar systems throughout the Liguria Region.

Chapter 5

Performance of Photovoltaic Systems in Urban Environments

This chapter is the result of the visiting period at the University of New South Wales (UNSW) in Sydney, Australia. It is based on the following publication:

- **Paper 5. Boccalatte, A.,** Thebault, M., Paolini, R., Fossa, M., Ramousse, J., Ménézo, C., Santamouris M. (2023). Assessing the Combined Effects of Local Climate and Mounting Configuration on the Electrical and Thermal Performance of Photovoltaic Systems. Application to the Greater Sydney Area. *Renewable Energy* (revised version submitted)

Similar to the previous papers, this study also focuses on a large-scale analysis. However, the main objective here is not solar radiation; instead, the focus shifts to photovoltaic (PV) system performance and how it is influenced by local and/or extreme climatic factors that currently characterize several urban sites and may affect an ever-increasing number of sites in the future.

Contents

6.1	Solar Fresnel Modelling, Geometry Enhancement and 3D Ray Tracing Analysis devoted to Different Energy Efficiency Definitions and applied to a Real Facility	225
6.1.1	Introduction	225
6.1.2	Modelling a Linear Fresnel Concentrator based on a Ray-tracing Technique	229
6.1.2.1	Linear Fresnel Geometrical and Optical Parameters	231
6.1.2.2	The 3D Ray-tracing Modeling and Assumptions	232
6.1.3	Optical Optimization Methodology	241
6.1.3.1	Optical and Energy Efficiencies Definition	241
6.1.3.2	Parametric Analysis	243
6.1.3.3	The Reference LFC at Green Energy Park(GEP) Solar Facility, Morocco	243
6.1.3.4	Validation and Verification of Previous Assumptions of the Model	245
6.1.4	Results and Discussion	247
6.1.4.1	Model Results related to GEP Geometry	247
6.1.4.2	Optimization of Mirrors' Gap and Receiver Height	250
6.1.5	Conclusions	253
6.2	Calculation of the Incidence Angle Modifier of a Linear Fresnel Collector: the Proposed Declination and Zenith Angle Model compared to the biaxial factored approach	255
6.2.1	Introduction	255
6.2.2	Modelling the Linear Fresnel System and Define its Figures of Merit	257
6.2.3	The 3D Optical Model of a Linear Fresnel Concentrator and Efficiency Definitions	258
6.2.4	The Case Study and the Geometry Optimization	259
6.2.5	The Incidence Angle Modifier in LFC and the Biaxial Factored Approach	260
6.2.6	The Present Model for Sun Angle-Based Incidence Angle Modifier	263
6.2.7	Results	270
6.2.7.1	The Biaxial Factored Approach	270
6.2.7.2	The Proposed Declination-Zenith Regression Model	273
6.2.8	Conclusions	278

Paper 5

5.1 Assessing the Combined Effects of Local Climate and Mounting Configuration on the Electrical and Thermal Performance of Photovoltaic Systems. Application to the Greater Sydney Area

Abstract

Extremely high urban temperatures adversely affect photovoltaic (PV) system performance. Accurate PV cell temperature assessment relies on local weather conditions, exacerbated by urban overheating, often overlooked by inadequate temperature models and non-local data. This study investigates the electrical and thermal PV performance, considering mounting configurations and local conditions. Data from ten local weather stations in Greater Sydney (NSW) during 2016-2017, including a hot summer, are used. The Sandia model is used to predict cell temperatures and power output for four mounting configurations, from open rack to building-integrated (BIPV). A PV thermal model is implemented to analyse daytime convection, crucial for understanding PV impact on local climate. Results show peak cell temperatures of 60°C (open rack) to over 90°C (BIPV), causing up to 50% power loss and an 11% reduction in monthly performance ratio. Local climate variations impact PV energy output up to 6%, with mounting configuration effects up to 11%. Daytime convective flux averages 150-180 W/m², peaking at 700 W/m². Convective release varies up to 22% based on local climate, generally higher for open racks than close roof mounts, with potential reversals under low wind speed conditions. These findings can support PV design in urban areas facing increasingly extreme temperatures.

Keywords

Urban Overheating; Photovoltaic (PV) system performance; Mounting configurations; Daytime convective flux

5.1.1 Introduction

The impact of climate change on air temperature trends and the rise of heatwaves in cities warrants careful attention. Urban overheating, a significant research topic worldwide, results in higher temperatures in cities compared to surrounding rural areas (Kumar et al., 2021; Mirzaei, 2015; Oke, 1982; Santamouris et al., 2015). Unlike regional heatwaves, urban overheating is a local phenomenon influenced by complex factors, including urban morphology (Boccalatte et al., 2020a, 2023), prevailing weather conditions (Khan et al., 2021a), and the extreme weather events (Habeeb et al., 2015; Khan et al., 2021b; Nadeem et al., 2022).

In various regions, including Australia, high air temperatures in urban areas adversely affect PV system performance (Principe and Takeuchi, 2019), with projections indicating potential unprecedented temperatures of 50°C in major Australian cities under a 2°C global warming scenario (Lewis et al., 2017). Comparative studies show that Australia experiences higher PV degradation rates, ranging from -1.35% to -1.46% per year, compared to the UK's rate of -1.05% to -1.16% per year (Dhimish and Alrashidi, 2020). A previous investigation conducted by EnergyAustralia (Outhred and Retnanestri, 2015) examined the performance of rooftop PV systems installed for the Sydney Olympic Games in 2000 and found that nearly 20% of the analysed systems underperformed.

The PV market has experienced substantial growth in grid-connected photovoltaic systems, with significant integration on rooftops. In 2021, the Australian market saw a surge in solar installations, with 4.9 GW of new capacity, of which over 3 GW consisted of rooftop PV systems. Residential roofs accounted for 1.7 GW, while commercial and industrial roofs contributed 1.3 GW (Chapman et al., 2016; Koschier and Egan, 2021).

Despite the annual mean daily solar irradiation in Australia ranges from 16 MJ/m² day in southern regions to 22 MJ/m² day in northern areas (Ma et al., 2017), PV system performance and reliability are significantly impacted by high air temperatures and extreme climatic conditions (Ma et al., 2016; Perkins et al., 2012), raising concerns about long-term efficiency (Dhoke and Mengede, 2018; Principe and Takeuchi, 2019).

In light of this global scenario, comprehensive analyses are critical to realistically predict PV system performance and optimize their deployment in urban areas, where heat mitigation strategies are vital. Urban overheating is an escalating worldwide concern, necessitating attention and appropriate strategies for adequate PV development in urban settings.

5.1.1.1 Insights from Previous Research on Urban Overheating in Sydney

Previous research on urban overheating has highlighted the significance of this phenomenon as a global concern. In coastal cities like Sydney, intricate interactions between synoptic climatology and local factors can impact overheating dynamics (Potgieter et al., 2021). Sydney's geographical location along the eastern coastline of the South Pacific Ocean exposes the city to coastal and desert winds, presenting challenges in understanding urban heat islands (UHI) resulting from coastal-inland airflows (Livada et al., 2019; Yun et al., 2020).

Previous research by Santamouris et al. (Santamouris et al., 2017) analysed a 10-year climatic dataset from six meteorological stations in the Greater Sydney, revealing significant variations in UHI intensity ranging from 0 to 11°C. These variations arise from the interaction between the cooling mechanism of sea breezes and the heating mechanism of westerly winds, leading to a pronounced divergence in the UHI effect between eastern and western parts of the city. Despite higher tree canopy cover and lower built density, western areas of Sydney exhibit

stronger UHI effects due to reduced influence from sea breezes. [Yun et al. \(2020\)](#) investigated urban overheating in Sydney using hourly temperature measurements collected over an 18-year period from eight different sites within a 50 km radius from the coastline. They found that Urban Heat Island Intensity (UHII) was negative during the night and evening hours and positive during the central hours of the day (between 10 am and 4 pm), peaking around 3 pm. The highest UHII values occurred during summer (November to February), with peak values ranging from 3.7°C to 8.5°C, proportional to the distance from the coast. [Khan et al. \(2020\)](#) examined the interaction between urban overheating and heatwave periods in the Greater Sydney region, finding that the average peak difference between the urban overheating magnitude during heatwave periods and non-heatwave periods was 8°C in western Sydney, and 4-4.5°C in inner Sydney.

Regarding the effects of urban overheating in Sydney, [Vaneckova et al. \(2008\)](#) reported a 4.5-12% increase in mortality rate in Sydney, due to a 10°C rise in daily maximum temperatures and high concentrations of ozone and particulate matter. Previous studies also investigated the impact of overheating on building cooling demand, finding that western Sydney suburbs have considerably higher Cooling Degree Days (approximately three times higher than those observed in the eastern part), thus leading an increase of cooling demand [Garshasbi et al. \(2023\)](#); [Santamouris et al. \(2015\)](#).

5.1.1.2 Research Gap and Aim of the Study

Previous literature has explored urban overheating dynamics in Greater Sydney, emphasizing its negative effects on building energy consumption ([Santamouris and Feng, 2018](#)) and mortality ([Vaneckova et al., 2008](#)). However, despite the substantial increase of roof-mounted PV systems, no study has specifically the impact of high temperatures on their performance. Existing findings indicate that urban overheating peaks during the central hours and summer, exacerbated by the increasing frequency of heatwaves. Future projections indicate substantial temperature rises in newly developed western and southwestern urban areas ([Matthew Adams and Trieu, 2015](#)), particularly vulnerable to overheating due to desert winds' heating mechanism. Consequently, high temperatures negatively impact PV performance, particularly during peak production periods and anticipated urban development in overheating-prone regions. A comprehensive analysis of PV system performance, considering local climate variability and integration into buildings, is crucial.

Therefore, the primary objective of this study is to analyse the thermal and electrical performance of PV systems under diverse local climatic conditions and mounting configurations in the Greater Sydney region to enhance the understanding of how local climatic conditions and system design choices impact the overall effectiveness of PV system operation.

Unlike similar studies focusing on PV performance variations across different climatic regions, this study specifically addresses the impact of complex local climate patterns at the metropolitan scale. To achieve this, one year of experimental weather data from ten local weather

stations in the Greater Sydney region (2016-2017) is utilized. The study employs the detailed Sandia Array Performance Model (SAPM) to uncover significant differences in mounting configurations, often overlooked in conventional models. Additionally, a PV thermal model is developed to analyse daytime heat fluxes. This aspect is crucial for urban PV installations, as simulations have shown that integrating PV systems on building roofs may increase local air temperatures by 0.6-2.3°C in Sydney during summer (Garshasbi et al., 2023).

The findings of this study extend beyond the Greater Sydney region, stressing the need to consider local climate data and mounting configurations in PV system planning to account for relevant dynamics affecting performance.

The subsequent sections outline key aspects of PV performance models and the indirect impact of PV systems on the urban microclimate, providing the necessary background for framing the research and its objectives.

5.1.1.3 PV Temperature Models and Effect of Local Climate Conditions on PV Performance

The performance of PV modules is greatly affected by cell temperatures, which directly determine energy output and heat dissipation. Cell efficiency is typically rated under Standard Test Conditions (STC) at 25°C cell temperature, 1,000 W/m² irradiance, and air mass of 1.5. Nevertheless, real-world outdoor installations experience non-STC conditions, resulting in varying cell temperatures influenced by local weather (Atsu et al., 2020; Chumpolrat et al., 2014; Gaglia et al., 2017; Hassan Daher et al., 2022; Mehdi et al., 2023; Obiwulu et al., 2020; Tebibel and Labeled, 2013). Operating temperatures often exceed 25°C, leading to reduced efficiency compared to the rated value. The temperature coefficient for crystalline silicon cells indicates approximately 0.4% efficiency reduction per 1°C increase above the STC reference temperature, resulting in up to 30% lower power production compared to STC conditions (Berardi and Graham, 2020). Furthermore, PV overheating can cause delamination, hot spots, and damage adhesive seals (Dhimish et al., 2022; Solheim et al., 2013).

Accurate PV cell temperature prediction is crucial for evaluating installation efficiency and converting module performance from standard rating temperature (25°C) to actual operating temperatures. In absence of direct measurements, PV models are used to estimate cell temperature. Many proposed models for PV cell temperature prediction have been extensively validated against experimental data. Skoplaki and Palyvos (Skoplaki and Palyvos, 2009) reviewed approximately 40 correlations, implicit and explicit, for calculating operating temperatures. These correlations involve environmental variables and numerical parameters, which are material and/or system dependent. Therefore, careful selection of a suitable expression considering specific climate conditions, mounting configuration, and integration level with the building is necessary.

Correlations commonly used in the field estimate cell temperature by utilizing the Nominal Operating Cell Temperature (NOCT). The NOCT represents the average temperature of a PV module in open rack installations under Standard Operating Conditions (irradiance: 800 W/m², ambient temperature: 20°C, tilt angle: 45°, wind speed: 1 m/s, open circuit operation). However, several studies evidence the sensitivity of PV temperature predictions to wind speed conditions (Gökmen et al., 2016; Kaldellis et al., 2014). Using correlations based on NOCT, wind speed is not accounted for, and the method is limited to open rack applications leading to an underestimation of PV cell operating temperatures by up to 20°C in integrated systems (Davis et al., 2001).

To address the limitations of the NOCT model, various empirical and semi-empirical models have been proposed, including the Sandia PV Array Performance Model (SAPM) by King et al. (King et al., 2004), the Faiman model (Faiman, 2008), the model proposed by Muzathik (Muzathik, 2014), the Skoplaki model (Skoplaki et al., 2008), the Fuentes model (Fuentes et al., 1987), the Ross model (Ross, 1976). The SAPM has shown better performance compared to the abovementioned models under different climatic conditions (D’Orazio et al., 2014; Trinuruk et al., 2009), notably when wind speed exceeds 6 m/s, and under hot desert climate conditions (Aoun, 2022).

The Sandia model is used for the present analyses as it offers greater flexibility than the other models as it allows considering three different mounting setups (open rack, close roof mount, and insulated back) and two module types (glass/cell/glass and glass/cell/polymer sheet). The influence of mounting configuration on PV cell temperatures has been deeply analysed since, as shown in several studies, it represents a critical parameter for PV performance assessment (Kaldellis et al., 2014; Kempe et al., 2021; Kurnik et al., 2011).

5.1.1.4 Indirect Effects of PVs on Urban Climate

PV modules, having lower thermal inertia than other surfaces, quickly heat up and release absorbed solar energy through radiation and convection (Sailor et al., 2021). The convective heat flux between modules and surrounding air is crucial, influenced by factors such as temperature difference, local wind speed, and PV mounting configuration. Experimental studies show that when PV modules are exposed to hot climate conditions like Arizona (US) and Libya (Africa), the PV cell temperatures can reach up to 90°C and 125°C, respectively (Hasan et al., 2016; Nassar and Salem, 2007; Oh et al., 2010). Beyond the reduced efficiency and power generation, the thermal effects of urban PV installations may have implications for the overall urban energy balance (Garshasbi et al., 2023; Sailor et al., 2021).

Previous studies on urban PV system impacts on air temperatures have yielded conflicting results, often due to errors and inappropriate assumptions (Barron-gafford et al., 2016; Berardi and Graham, 2020; Heusinger et al., 2021, 2020; Pham et al., 2019; Pokhrel et al., 2020; Sailor et al., 2021). Common limitations of existing approaches include the use of the "effective albedo"

and the neglect of convective heat released by the back PV surface in rooftop applications (Taha, 2013). To understand the indirect effects on the microclimate, empirical studies and accurate modelling of convective and radiative heat transfer are crucial. Recent literature studies have shown advancements in this area by including the modelling of the surfaces shaded by PV modules (Cavadini and Cook, 2021; Heusinger et al., 2020; Pham et al., 2019; Scherba et al., 2011). Tools like *UCR-Solar_{roof}* have been recently developed to accurately represent the sensible heat transfers of rooftop PV installations (Heusinger et al., 2021).

This study further develops a PV thermal model to explore daytime heat released through convection and radiation. Note that it does not assess PV systems' impact on the urban microclimate, which would require more complex modelling. The focus remains on quantifying electrical performance and understanding the influence of climatic conditions and mounting configurations on daytime heat fluxes.

5.1.2 Materials and Methods

Section 5.1.2 is devoted to describing the data and models employed in this analysis. It is organized as follows: Section 5.1.2.1 provides an overview of the meteorological data obtained from ten selected weather stations in the Greater Sydney region. In Section 5.1.2.2, the primary geomorphological characteristics and local climate influences of the study area are presented, highlighting the distinctions between the western and eastern suburbs. Section 5.1.2.3 outlines the Sandia Array Performance model (SAPM), which is employed to conduct precise calculations on various selected figures of merit, further explained in Section 5.1.2.4. Lastly, Section 5.1.2.5 details the developed thermal PV model, specifically designed for calculating the daytime sensible heat based on the PV mounting configuration.

5.1.2.1 Measured Data from Local Weather Stations

The objective of this study is to evaluate the performance of photovoltaic systems installed in various locations within the Greater Sydney, located in New South Wales, Australia. The Greater Sydney area encompasses the city of Sydney and its surroundings, including the local government areas of Sydney, Parramatta, Blacktown, Penrith, Liverpool, Campbelltown, and Sutherland. The region covers an approximate land area of 12,368 km², extending from the coastline in the east to the Blue Mountains in the west, spanning about 70 km. The climate in the region is classified as a humid subtropical climate (Köppen Geiger climate classification, type Cfa).

Hourly meteorological data from ten different weather stations have been utilized in this research. These data were collected by the Australian Bureau of Meteorology¹ (BoM) between May 2016 and April 2017. The Greater Sydney region and the geographical distribution of the selected weather stations is illustrated in Figure 5.1. The different colors attributed to each

weather station refers to the territorial partitioning which is further detailed in the following Section 5.1.2.2.

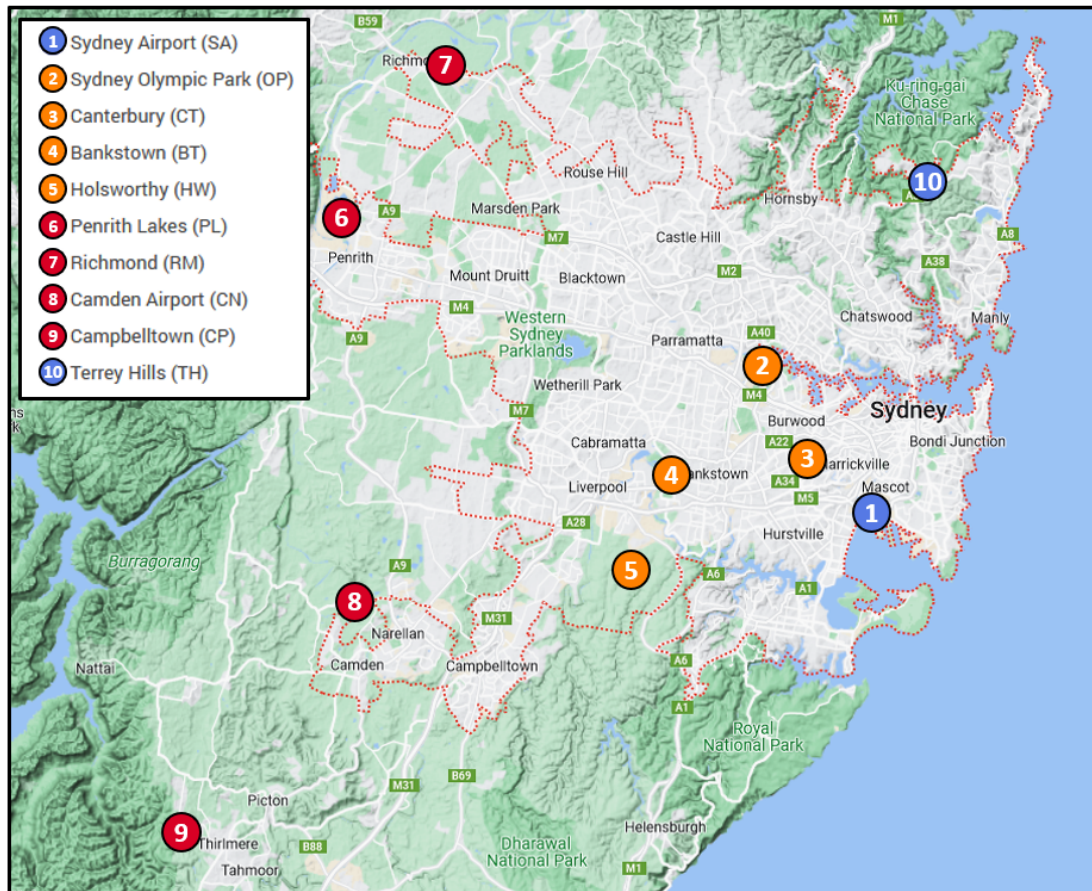


Fig. 5.1 Analysed weather stations across the greater Sydney region.

The station ID assigned by the Bureau of meteorology (BoM), the geographical coordinates, and the elevation of the selected weather stations are presented in Table 5.1.

The measured meteorological variables include dry-bulb and wet-bulb air temperature, which have been used to compute relative humidity, as well as wind speed and direction, air pressure, and daily cumulative rainfall from 9 am. Global horizontal solar radiation data have been obtained from Macquarie University (latitude: -33.7748, longitude: 151.1111, elevation: 66.8 m), assuming it to be equal for all weather stations due to the low spatial variability of irradiance intensity within the study area (Wilcox and Gueymard, 2010). The Reindl et al. (1990) model is used to derive diffuse radiation whereas the variant of the Prata model proposed by Lindberg et al. (2008) is used for infrared radiation. To ensure data quality, all raw data underwent filtering, validation, and gap filling using artificial intelligence techniques, as fully detailed in Yun et al. (2020).

¹Australian Government Bureau of Meteorology <http://www.bom.gov.au/>

Table 5.1 Weather Station Information

Weather Station	Station ID	Latitude (°S)	Longitude (°E)	Elevation (m)
Sydney Airport AMO (SA)	66037	-33.9465	151.1731	6.0
Sydney Olympic Park AWS (OP)	66212	-33.8338	151.0718	4.0
Canterbury Racecourse AWS (CT)	66194	-33.9057	151.1134	3.0
Bankstown Airport AWS (BT)	66137	-33.9181	150.9864	6.5
Holsworthy Aerodrome AWS (HW)	66161	-33.9925	150.9489	68.2
Penrith Lakes AWS (PL)	67113	-33.7195	150.6783	24.7
Richmond RAAF (RM)	67105	-33.6004	150.7761	19.0
Camden Airport AWS (CN)	68192	-34.0157	150.6910	73.9
Campbelltown – Mount Annan (CP)	68257	-34.0615	150.7735	112.0
Terrey Hills AWS (TH)	66059	-33.6908	151.2253	199.0

5.1.2.2 Study Area and Territorial Partitioning

Based on the latest census of the Australian Bureau of Statistics², the Greater Sydney region had a total population of 5.2 million people in 2021, with a total site area of 12,368 km². This translates to a population density of approximately 428 persons per square kilometer. The region is surrounded by several national parks to the north and south, and the estimated total built area is approximately 4,196 km². In the last years, urban expansion has predominantly occurred in western suburbs, which are projected to accommodate more than 50% of the population of the Greater Sydney region by 2036 (Matthew Adams and Trieu, 2015). For the purposes of this study, the Greater Sydney area is subdivided into three zones: eastern (coastal), inner, and western areas, based on their proximity to the coastline, as previously shown through different colors in Figure 5.1.

The Sydney Airport (SA) weather station in eastern Sydney is located on the coast in proximity to Botany Bay and it is surrounded by Sydney inner suburbs on its non coastal boundaries. The land surrounding Sydney Airport is a mixed-use development with aviation purposes, and residential, commercial, and industrial areas.

Inner Sydney comprises of Olympic Park (OP), Canterbury (CT), Bankstown (BT), and Holsworthy (HW). The distance of the inner suburbs from the nearest coast ranges from 7 km (CT) to about 16 km (BT and HW). Sydney Olympic Park, located approximately 14 km west of the Sydney Central Business District (CBD), is in close proximity to significant water features such as the Parramatta River, wetlands, and scattered waterways. The surrounding areas are predominantly sparsely built mixed-use areas with some commercial, recreational, and parkland

²Australian Government Bureau of Statistics <https://www.abs.gov.au/>

land uses. Canterbury and Bankstown are inner suburbs characterized by open, low-rise-mixed use and residential buildings, with high built and population density in Canterbury. Holsworthy Aerodrome is situated far from the Sydney CBD, near the district of Liverpool, within a densely vegetated area.

Western Sydney includes the Penrith Lakes (PL), Richmond (RM), Camden Airport (CN), and Campbelltown (CP) weather stations. These stations are the farthest from both the CBD and the coastline and are generally characterized by low-density built areas, multiple bodies of water, wetlands, and extensive tree canopy. Camden Airport (CN) and Campbelltown (CP) are more peripheral compared to Penrith Lakes (PL) and Richmond (RM), with Campbelltown (CP) weather station being slightly outside the administrative boundaries of Greater Sydney.

Terrey Hills (TH) weather station deviates slightly from the defined territorial partitioning as it is located in the northern forest district at an elevation of 199 m above sea level. It is positioned 25 km north of Sydney CBD and 7.5 km from the nearest coastline, encompassing a large area of dense greenery, including national parks, bushland, and reserves, with a total tree canopy cover of approximately 58%.

The tree canopy cover is higher for the Western Sydney sites (25-35%), compared to inner and eastern Sydney where it is around 15-17% (Jacobos et al., 2014). The distance from the nearest coast increases in Western Sydney, with Penrith Lakes situated 50 km away, while other Western Sydney sites are approximately 30 km from the nearest coast. Inner Sydney sites are located 8-12 km from the coast, and the Sydney CBD is situated near the coastline.

In this study, the local climate conditions of the ten weather stations are analyzed, focusing on yearly summary statistics of air temperature and wind speed values. Additionally, the impact of local climate conditions on electricity demand for cooling purposes is assessed through the calculation of Cooling Degree Hours (CDH). CDH is calculated as the sum of positive hourly differences between outdoor air temperature and a base temperature, which in this case is set at 19.5°C based on the Australian Energy Market Operator (AEMO) guidelines for New South Wales (Australian Energy Market Operator (AEMO), 2019). The formula for calculating CDH is described in Eq 5.1

$$CDH = \sum_{i=1}^N (T_{\text{air}} - T_{\text{ref}}) \quad \text{for } T_{\text{air}} > T_{\text{ref}} \quad (5.1)$$

here, N is the number of hours over a selected time period (day, month, year), T_{air} is the hourly air temperature, and T_{ref} is the reference base temperature.

5.1.2.3 The Sandia Array Performance Model (SAPM)

Several photovoltaic (PV) performance models have been developed and documented in the literature to assess the power production of PV systems (Klise and Stein, 2009). These models vary

in complexity, with some based on generalized system assumptions, while others incorporate manufacturer parameters, derived quantities, and empirically derived data. For this study, the Sandia Array Performance Model (SAPM) developed by the US Sandia National Laboratories (SNL) has been chosen due to its proven accuracy in relation to field measurements (King et al., 2004).

The SAPM is an empirically formulated model that employs a steady-state approach and relies on empirically derived module parameters obtained from day-long I-V measurements conducted on modules from various manufacturers. Through testing PV modules under non standard conditions, the SAPM accounts for the influences of cell temperature, spectral variations, and angle of incidence, and thus enables linearization of most elements of its five-equation model. In its general form, the calculation of the DC power output of the module can be expressed through Eq 3.8 to 3.12, which have been previously reported in **Paper 3** and are not repeated here for brevity. For a comprehensive understanding of the model, the interested reader is referred to the original source (King et al., 2004) for a more detailed description.

The SAPM model has recently been integrated into the pvlib Python library (Laboratories, 2021), which is used to calculate PV power output. The primary inputs for the model include the plane of array solar irradiance incident on the module surface, as well as wind speed and ambient air temperature, which are required for estimating the PV cell temperature through the Sandia thermal model.

The plane of array irradiance (G_{POA}) represents the combined contribution of beam component, sky diffuse component, and ground-reflected component incident on a tilted module surface. The calculation of the plane of array irradiance is performed using the GHI (Global Horizontal Irradiance), DNI (Direct Normal Irradiance), and DHI (Diffuse Horizontal Irradiance) values, which are processed with the solar position calculator and transposition model from the pvlib library. To determine the diffuse component, the Perez diffuse radiation model (Perez et al., 1992) is selected and applied within the transposition model.

In this analysis, the focus is on c-Si modules, specifically the Canadian Solar 300 Watt Solar Module, which is assumed to be inclined at a tilt angle of 28 degrees and oriented towards the north. This tilt angle is chosen to be close to both the optimal angle for maximizing yearly energy yield and the typical slope of roofs in the Sydney area (Memme and Fossa, 2022). The technical specifications of the Canadian Solar 300 Watt Solar Module are summarized in Table 5.2.

Table 5.2 Specifications of Canadian Solar 300 Watt Solar Module

Name	Canadian Solar 300 Watt Solar Module
Model	CS6X-300M
Manufacturer	Canadian Solar
Year	2013
Material	Monocrystalline Silicon
Cells in series	72
STC Power Rating	300 W
Peak Efficiency	15.63%
Impo	8.22 A
Vmpo	36.5 V
Isco	8.74 A
Voco	45 V
Temp. Coefficient of Power	-0.45%/K

The SAPM operating PV cell temperature (T_c) is defined through Eq 5.2

$$T_c = T_m + \left(\frac{G_{POA}}{G_{STC}} \right) \cdot \Delta T \quad (5.2)$$

where G_{POA} is the plane of array (POA) irradiance incident on module surface [W/m^2], G_{STC} is the irradiance at Standard Test Conditions (STC), namely $1000 W/m^2$, ΔT is the temperature difference [$^{\circ}C$] between the PV cell and the back surface of the module at G_{STC} irradiance level, and T_m is the back surface module temperature [$^{\circ}C$] which can be calculated based on Eq 5.3

$$T_m = G_{POA} \cdot \left\{ e^{a+b \cdot ws} \right\} + T_a \quad (5.3)$$

where ws is the wind speed [m/s], T_a is the ambient air temperature [$^{\circ}C$], and a and b are empirically determined coefficients depending on the module type and the mounting configuration. ΔT , a , and b can be derived from Table 5.3 (King et al., 2004).

Table 5.3 Module performance parameters for different mounting configurations

Module type	Mount	a	b	ΔT ($^{\circ}C$)
Glass/cell/glass	Open rack	-3.47	-0.0594	3
Glass/cell/glass	Close roof mount	-2.98	-0.0471	1
Glass/cell/polymer sheet	Open rack	-3.56	-0.0750	3
Glass/cell/polymer sheet	Insulated back	-2.81	-0.0455	0

The configurations include "Glass/Cell/Glass" module type with an open rack or close roof mount, as well as "Glass/Cell/Polymer Sheet" module type with an open rack or insulated back. These configurations represent different scenarios with varying degrees of air flow and heat transfer behind the PV modules, ranging from maximum air flow (open rack) to limited air flow (close roof mount) to insulated back surfaces representing building-integrated applications (BIPV). These four configurations, along with local air temperature and wind speed data from ten selected weather stations, are utilized to compute the PV cell temperatures and power production.

5.1.2.4 Figures of Merit of PV Performance Assessment

Based on the previous section discussing the calculation of PV power production using the SAPM model, various figures of merit are selected to analyse the impact of local climate, PV configuration, and high temperature conditions on the electrical performance of PV installations. These figures of merit include efficiency, normalized efficiency, temperature losses, performance ratio, and photovoltaic production, which provide valuable insights into the performance of the PV system.

The PV module efficiency (η_{PV}) quantifies the electrical efficiency of the PV module. It is calculated as the ratio of the DC power generated by the PV array system to the plane of array irradiance received by the module as in Eq 5.4

$$\eta_{PV}(t) = \frac{P(t)}{G_{POA}(t)} \quad (5.4)$$

where P is the DC power generated by the PV array system per unit surface [W/m^2] and G_{POA} is the plane of array (POA) irradiance received by the module per unit surface [W/m^2].

The normalized efficiency (η_N) is another important parameter that considers the rated PV power at Standard Test Conditions and normalizes the DC power and irradiance based on their respective values at STC. It provides a useful metric that facilitates performance comparisons under different operating conditions and it can be calculated as in Eq 5.5

$$\eta_N(t) = \frac{P(t) \cdot \frac{1}{P_{STC}}}{G_{POA}(t) \cdot \frac{1}{G_{STC}}} \quad (5.5)$$

where P_{STC} is the rated PV power at Standard Test Conditions (STC) of $G_{STC}=1000 W/m^2$, $T_c=25^\circ C$, and air mass of 1.5. To quantify the impact of high temperatures on PV production, the power losses due to temperature ($P_{loss,T}^*$) are evaluated. This metric compares the actual DC power generated by the PV array system at a given temperature to the theoretical DC power at STC cell temperature ($T_c=25^\circ C$). The power losses due to temperature represent the percentage reduction in power output caused by higher cell temperatures than the reference one and it is

defined as in Eq 5.6

$$P_{\text{loss},T}^* = \frac{P(t) - P_{25}(t)}{P(t)} \cdot 100\% \quad (5.6)$$

where P_{25} is the theoretical DC power of the PV array system [W/m^2] at STC cell temperature, namely $T_c=25^\circ\text{C}$. The Performance Ratio (PR) is an important parameter defined in the IEC 61724 standard for assessing the overall performance of a PV system (Klise et al., 2017). The PR represents the ratio of the actual electricity generated by the PV system to the electricity that would have been generated if the system consistently converted sunlight to electricity at the level expected from its DC nameplate rating (Dierauf et al., 2013). The PR can be calculated over a specific time interval τ (typically a day) as the ratio between the Final Yield $Y_{f,\tau}$ and the Reference Yield $Y_{r,\tau}$ as in Eq 5.7

$$PR_\tau = \frac{Y_{f,\tau}}{Y_{r,\tau}} = \frac{1}{P_{\text{STC}}} \cdot \sum_\tau P(t) \cdot \Delta t \cdot \frac{1}{G_{\text{STC}}} \cdot \sum_\tau G_{\text{POA}}(t) \cdot \Delta t \quad (5.7)$$

where P_{STC} is the rated PV power at Standard Test Conditions (STC) of $G_{\text{STC}}=1000 \text{ W}/\text{m}^2$, $T_c=25^\circ\text{C}$, and air mass of 1.5, $P_{mp}(t)$ is the DC power generated by the PV array system [W/m^2] and $G_{\text{POA}}(t)$ is the plane of array (POA) irradiance received by the module [W/m^2] at time t , and Δt represents the time step.

5.1.2.5 Daytime Convective and Radiative Heat Fluxes

In this section, the impact of PV configuration and local climate conditions on the daytime convective and radiative heat fluxes is analysed by introducing the developed thermal PV model.

The Sandia model is effective in predicting the temperatures of photovoltaic (PV) cells during daytime conditions. However, night time temperature predictions are not provided. In this study, the convective and radiative heat fluxes are calculated exclusively during daytime operation when the PV temperature is always higher than the ambient air temperature. Only two out of the three previously considered mounting configurations are analysed: open rack glass/polymer, which exhibits lower temperatures, and close roof mount glass/glass. Insulated back glass/polymer configuration is not considered since their thermal modelling depends on the thermal properties of the roof, whose modelling is beyond the scope of this study. Here, the calculation of the released heat fluxes is exclusively related to the PV module and does not consider the combined effect of PV and the roof. Therefore, the impact of PV on the urban microclimate is not intended to be assessed, as that would require more accurate models and precise information about the roof structure and configuration (Heusinger et al., 2020; Scherba et al., 2011). Instead, the objective is to compare the influence of local climate factors and PV mounting configuration on urban heat transfers.

During daytime operation, the conversion of incident shortwave radiation on the PV module results in the generation of both electrical and thermal energies. Some of this radiation is

dissipated as thermal losses through longwave radiation and convection, while the remaining energy is converted into electrical power.

The steady-state heat balance over the PV cell layer (disregarding thermal capacitance) is determined through Eq 5.8 (Driesse et al., 2022)

$$G_{POA}(1 - \rho) - Q_{elec} - Q_{rad} - Q_{conv} - Q_{cond} = 0 \quad (5.8)$$

here, G_{POA} represents the incident is the plane of array (POA) irradiance on module surface, ρ is the reflectivity of the front glass which is assumed equal to 0.1, Q_{elec} is the energy flux extracted as electrical power, and the remaining terms account for heat losses through radiation (Q_{rad}), convection (Q_{conv}), and conduction (Q_{cond}), all in W/m^2 . Conduction is neglected due to the small contact area between the PV module frame and mounting structure.

The convection model used in this study is based on the DOE-2 algorithm (Booten et al., 2012), which considers natural and forced convection, as well as surface orientation. The key input parameters for the convection model are wind speed, surface tilt angle, surface temperature, ambient temperature, and roughness coefficients. The convective heat flux [W/m^2] is calculated through Eq 5.9

$$Q_{conv} = h_c \cdot (T_{surface} - T_{ambient}) \quad (5.9)$$

where $T_{surface}$ represents the temperature of the PV front/back surfaces, and $T_{ambient}$ is the temperature of the air in contact with them. Distinctions are made to account for different physical conditions and mounting configurations. For the open rack mounting, the back surface temperature (T_{back}) can be calculated using the equation for the calculation of T_m (Eq 5.3) according to the Sandia thermal model. The front surface temperature (T_{front}) is assumed to be equal to the Sandia PV cell temperature T_c (Eq 5.2), which ranges from 0 to 3°C higher than the back surface temperature depending on the irradiance levels and mounting configuration. As for $T_{ambient}$, it is assumed to be equal to the air temperature on both PV sides for the open rack configuration. For the back PV side of the close roof mount configuration, $T_{ambient}$ represents the temperature of the air in the gap between the PV module and the roof and thus it is calculated as the film temperature (T_{film}), which is the average of T_{back} and T_{air} , as in Eq 5.10

$$T_{film} = \frac{T_{back} + T_{air}}{2} \quad (5.10)$$

The convective heat transfer coefficient h_c , according to the DOE-2 convection model (Booten et al., 2012), is a combination of the natural convection coefficient (h_n) and the forced convection coefficient over a smooth surface ($h_{c,glass}$). The equations used to calculate h_c are Eq 5.11 and 5.12

$$h_c = h_n + R_f \cdot (h_{c,glass} - h_n) \quad (5.11)$$

$$h_{c,glass} = \sqrt{h_n^2 + (a \cdot [ws]^b)^2} \quad (5.12)$$

the constants a and b depend on the surface position with respect to the wind direction, where $a=3.26$ and $b=0.89$ for windward surfaces, and $a=3.55$ and $b=0.617$ for leeward surfaces. A simplifying assumption that the front PV surface is windward, and the bottom is leeward is used based on [Scherba et al. \(2011\)](#). R_f represents the surface roughness coefficient, which is assumed to be equal to 1 (very smooth), and w_s is the wind speed.

For the close roof mount configuration, the same theoretical model proposed for the open rack PV system applies to the front PV side, considering both natural and forced convection. However, for the back PV side, only natural convection is considered ([Kaplani and Kaplanis, 2020](#); [Silva et al., 2022](#)). The natural convection component for an upward-facing surface (front PV side) is given by Eq 5.13

$$h_n = \frac{9.842 \cdot |\Delta T|^{1/3}}{7.283 - |\cos(\beta)|} \quad (5.13)$$

and for a downward facing surface (back PV side) is given by Eq 5.14

$$h_n = \frac{1.810 \cdot |\Delta T|^{1/3}}{1.382 + |\cos(\beta)|} \quad (5.14)$$

in these equations, β represents the PV surface tilt angle, and ΔT is the temperature difference between the PV surface and the air temperature.

A summary of the assumptions made for the front and back PV surfaces, as well as the two different mounting configurations, is provided in Table 5.4

Table 5.4 Assumptions for the calculation of the convective heat flux as a function of the PV side and mounting configuration

	T_{surface} (Eq 5.9)	T_{ambient} (Eq 5.9)	h_c (Eq 5.11)	a, b (Eq 5.12)
Open rack (front PV side)	T_c (Eq 5.2)	T_{air}	DOE 2 algorithm (natural + forced)	Windward ($a = 3.26, b = 0.89$)
Open rack (back PV side)	T_m (Eq 5.3)	T_{air}	DOE 2 algorithm (natural + forced)	Leeward ($a = 3.55, b = 0.617$)
Close roof (front PV side)	T_c (Eq 5.2)	T_{air}	DOE 2 algorithm (natural + forced)	Windward ($a = 3.26, b = 0.89$)
Close roof (back PV side)	T_m (Eq 5.3)	T_{film} (Eq. 15)	DOE 2 algorithm (only natural)	Leeward ($a = 3.55, b = 0.617$)

Concerning the radiation heat transfer rate, it could be theoretically calculated for both the front and back surfaces of the PV module as the summation of the long-wave radiation emitted to the sky ($Q_{rad,sky}$) and to the ground ($Q_{rad,ground}$), with some modifications for the close roof mount whose back surface is facing only the roof. The expressions for these components are Eq 5.15 to 5.17

$$Q_{rad,f} = Q_{rad,sky} + Q_{rad,ground} \quad (5.15)$$

$$Q_{rad,sky} = F_{pv,sky} \cdot \epsilon_{pv} \cdot \sigma \cdot (T_{pv}^4 - T_{sky}^4) \quad (5.16)$$

$$Q_{rad,ground} = F_{pv,ground} \cdot \epsilon_{pv} \cdot \sigma \cdot (T_{pv}^4 - T_{ground}^4) \quad (5.17)$$

where ϵ_{pv} is the front/back emissivity, $F_{pv,sky}$ and $F_{pv,ground}$ are the view factors of the front/back PV surface with the sky and the ground respectively, T_{pv} is the front/back surface temperature of the PV module, T_{sky} is the effective sky temperature, T_{ground} is the ground temperature (assumed to be equal to T_{air}), and σ is the Stefan-Boltzmann constant.

The effective sky temperature T_{sky} is a straightforward indirect way to calculate the net radiative exchange with the atmosphere. There are many correlations in the literature with air temperature, humidity, time of day, and/or other parameters to estimate sky temperature (Aigarni and Nutter, 2015; Karn et al., 2019). The most commonly used one is given by Eq 5.18 (Swinbank, 1963)

$$T_{sky} = 0.0552 \cdot T_{air}^{1.5} \quad (5.18)$$

However, this correlation applies to clear night time conditions (Nowak, 1989) and also the other correlations in the literature are specifically for cloud-free conditions. As recently highlighted by (Driesse et al., 2022) when this correlation is applied to PV temperature models such as in Fuentes model (Fuentes et al., 1987) daytime PV temperatures can fall below ambient in particular when irradiance is low. Based on the above considerations, the radiation heat transfer rate is derived after calculating the convective one based on the PV heat balance equation (Eq 5.8).

5.1.3 Results and Discussion

The present section (Section 5.1.3) outlines and discuss the results obtained through the present research. The section is subdivided as follows: Section 5.1.3.1 provides an analysis of the different local climate conditions at the ten considered weather stations, with a particular focus on air temperature, wind speed, and Cooling Degree Hours (CDH). Section 5.1.3.2 is dedicated to the analysis of PV operating cell temperatures and performance metrics across the weather station and mounting configurations. It further focuses on the impact of high temperatures on a series of selected figures of merit, on temperature-induced power losses, and on PV production. Finally, the results related to daytime convective and radiative heat fluxes are presented in Section 5.1.3.3.

5.1.3.1 Local Climate Conditions across the Weather Stations

Table 5.5 provides summary statistics, including mean, standard deviation, minimum, and maximum values, of the measured air temperature and wind speed for each of the ten weather stations during the analyzed period (from May 2016 to April 2017). The weather stations are identified by abbreviations: SA (Sydney Airport), OP (Olympic Park), CT (Canterbury), BT (Bankstown), HW (Holsworthy), PL (Penrith Lakes), RM (Richmond), CN (Camden Airport), CP (Campbelltown), and TH (Terrey Hills). The table also includes the distance from the nearest coastline (including Sydney Harbour and Botany Bay) and the distance from Sydney Central Business District (CBD), which are measured using GIS tools.

Table 5.5 Summary statistics of air temperature and wind speed values for each weather station

Weather Station										
	SA	OP	CT	BT	HW	PL	RM	CN	CP	TH
Distance from the nearest coast [km]										
	0.1	12.9	6.9	16.3	16.5	47.3	34.5	35.0	39.2	5.6
Distance from Sydney CBD [km]										
	8.7	13.2	9.5	21.0	27.4	51.8	50.1	50.3	72.0	20.1
Air Temperature [°C]										
mean	19.2	18.5	18.1	18.4	17.6	18.5	18.1	17.3	17.1	17.5
std	5.2	6.2	6.0	6.4	6.4	6.8	7.2	7.0	6.8	5.4
min	5.7	2.3	1.2	1.4	0.1	1.5	-1.4	-1.7	-0.4	3.0
max	40.8	43.5	42.9	43.8	44.1	46.4	46.0	44.9	44.7	39.6
Wind speed [m/s]										
mean	5.7	2.4	3.1	3.3	3.2	2.2	2.8	2.5	2.1	2.8
std	2.7	1.8	2.2	2.3	1.8	1.7	2.2	2.2	1.5	1.2
min	0.0	0.0	0.0	0.0	0.0	0.0	0.0	0.0	0.0	0.0
max	16.0	10.0	11.1	12.1	11.8	11.0	12.1	11.7	8.2	11.2

The mean air temperature varies among the weather stations, ranging from 17.1°C to 19.2°C. Station SA, located on the coast in eastern Sydney, records the highest mean temperature of 19.2°C, while station CP, in the western area, has the lowest mean temperature of 17.1°C. This suggests that the proximity to dense urban areas around SA may contribute to higher mean temperatures in that area due to urban overheating. On the other hand, stations CP and CN, which are more peripheral and farther from both the CBD and the coast, experience a mean

air temperature that is about 2°C lower. Worth noticing also that CP and CN weather stations, together with TH, have the highest elevation above sea level (Table 5.1), which can contribute to a faster release of absorbed heat. Focusing on the inner suburbs, HW exhibits lower mean air temperature values compared to other inner stations (OP, CT, BT), potentially influenced by the surrounding densely vegetated areas.

The standard deviation values of air temperature range from 5.2°C to 7.2°C, indicating varying degrees of temperature variability across the stations. Station RM exhibits the highest standard deviation, implying greater temperature fluctuations. This could be attributed to the distance from the coast, as western stations farther from the coast generally experience greater temperature variations (around 6.8°C) compared to eastern/coastal stations such as SA and TH, where the standard deviation of air temperatures is lower (around 5.3°C). Moreover, as observed in prior research (Yun et al., 2020), Richmond (RM) features extensive woodlands and a scattered built environment, enabling unimpeded flow of the prevailing north-eastern wind and resulting in diminished heat entrapment mechanisms, thereby leading to the noticeable variability.

Analyzing the minimum air temperatures, station CN reports the lowest minimum temperature of -1.7°C, whereas SA and TH, which are nearest to the coast, reach a minimum temperature of about 5.3°C. This observation suggests that coastal locations benefit from the moderating influence of the nearby ocean. Regarding maximum temperatures, the trend appears to be the opposite, with areas farthest from the coast exhibiting higher maximum temperatures. For instance, station PL, located in inner western Sydney, records the highest maximum temperature of 46.4°C. In contrast, stations closer to the coast, such as TH, do not exceed 39.6°C, and station SA reaches a maximum temperature of 40.8°C.

The mean wind speed across the weather stations near Sydney ranges from 2.1 m/s to 5.7 m/s. Station SA experiences the highest mean wind speed of 5.7 m/s, while station CP has the lowest mean wind speed of 2.1 m/s. In general, wind speed values hover around 3 m/s across most weather stations, except for SA, where the wind speed is almost two times higher. The standard deviation values of wind speed range from 1.2 m/s in TH to 2.7 m/s in SA, indicating that variations in wind speed are not solely dependent on the distance from the coast but may be influenced by specific wind patterns associated with each station.

Examining the maximum wind speeds, they range from 8.2 m/s to 16.0 m/s, with station SA reporting again the highest value and station CP reporting the lowest one.

Figure 5.2 illustrates the estimated probability density functions (PDF) of air temperature (left) and wind speed (right) across the weather stations. Each distribution represents the normalized frequency of occurrence of the respective variable. Each Greater Sydney area (east/coast, inner, west) is represented by a different color and different linestyles differentiate the weather stations. The Gaussian kernel density estimation method is employed to calculate the density of the distribution, with a kernel covariance of 0.2 to control the smoothness of the

distribution. Analyzing the air temperature distributions reveals a correlation with the territorial partitioning of weather stations. The western suburbs (PL, RM, CN, CP) are represented in red, the inner suburbs (OP, CT, BT, HW) in orange, and the eastern/coastal locations (SA, TH) in blue. Within each group, temperature distributions exhibit similar patterns with slight variations. The western suburbs exhibit lower frequencies of the peak/modal value, which typically falls between 20°C and 25°C, compared to the inner and eastern/coastal stations. Notably, SA and TH display distinct patterns compared to the inner and western suburbs. SA exhibits a higher occurrence of higher temperatures, with a distribution shifted towards higher values. On the other hand, TH has a lower modal value that does not exceed 20°C, and its bell-shaped distribution is narrower, indicating less variability. Focusing on wind speed distributions, greater variability and no clear correlation with territorial partitioning are observed. Station SA demonstrates higher values and greater variability in wind speeds, while station PL exhibits lower values and reduced variability.

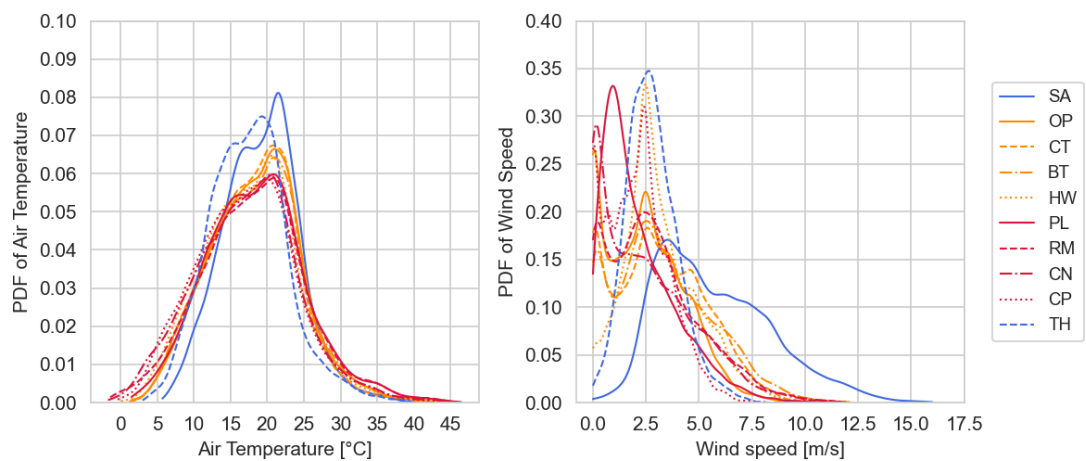


Fig. 5.2 Probability density function (PDF) of the air temperature (left) and wind speed (right) across the weather stations.

Figure 5.3 illustrates the annual Cooling Degree Hours (CDH) calculated using a base temperature of 19.5°C. CDH represents the cumulative sum of hourly (positive) temperature differences from the base temperature over the course of the year. The resulting cooling degree hours (CDHs) range from a minimum of 11,054 at TH to a maximum of 19,568 in PL for the period 2016-2017. There is no discernible pattern related to territorial partitioning, and the spatial variation of CDHs is likely influenced by topographic factors (urban form, vegetation, proximity to water bodies). However, as , the western stations of RM and PL exhibit the highest CDH values, while the eastern TH station shows nearly half of the CDH values. These findings align with previous studies conducted during the period 2016-2017 (Santamouris et al., 2017).

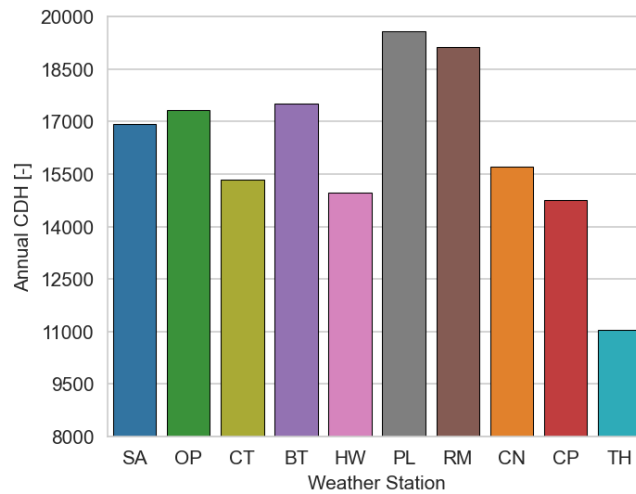


Fig. 5.3 Probability density function (PDF) of the air temperature (left) and wind speed (right) across the weather stations.

5.1.3.2 PV Operating Cell Temperatures and Performance Metrics

This section focuses on photovoltaic (PV) operating cell temperatures predictions and the associated performance metrics. It investigates the influence of mounting configurations and local climate conditions on PV cell temperatures, highlighting the adverse impact of high temperature conditions on PV electrical performance.

PV Operating Cell Temperatures across Weather Stations and Mounting Configurations

Figure 5.4 presents the boxplot depicting the distribution of PV cell operating temperature estimations across different weather stations and mounting configurations, namely open rack glass/cell/polymer (ORgp), open rack glass/cell/glass (ORgg), close roof mount glass/cell/glass (CMgg), and insulated back glass/cell/polymer (IBgp). The median value of PV cell operating temperature varies across configurations, ranging from approximately 30°C for open rack configurations to about 35°C for close roof and insulated back configurations. Nevertheless, close roof and insulated back configurations exhibit higher variability compared to the two open rack configurations, with the 75th percentile reaching up to 50°C, approximately 10°C higher than open rack.

The maximum values for the open rack configurations fall within the range of 65°C to 70°C, while close roof mount ranges between 80°C and 90°C. The insulated back configuration can reach even higher temperatures, ranging from 90°C to 100°C.

Across weather stations, no significant differences are observed, except for station SA, which exhibits lower variability and a lower frequency of extremely high temperatures. This can be attributed to the beneficial effect of substantially higher wind speeds at that particular site.

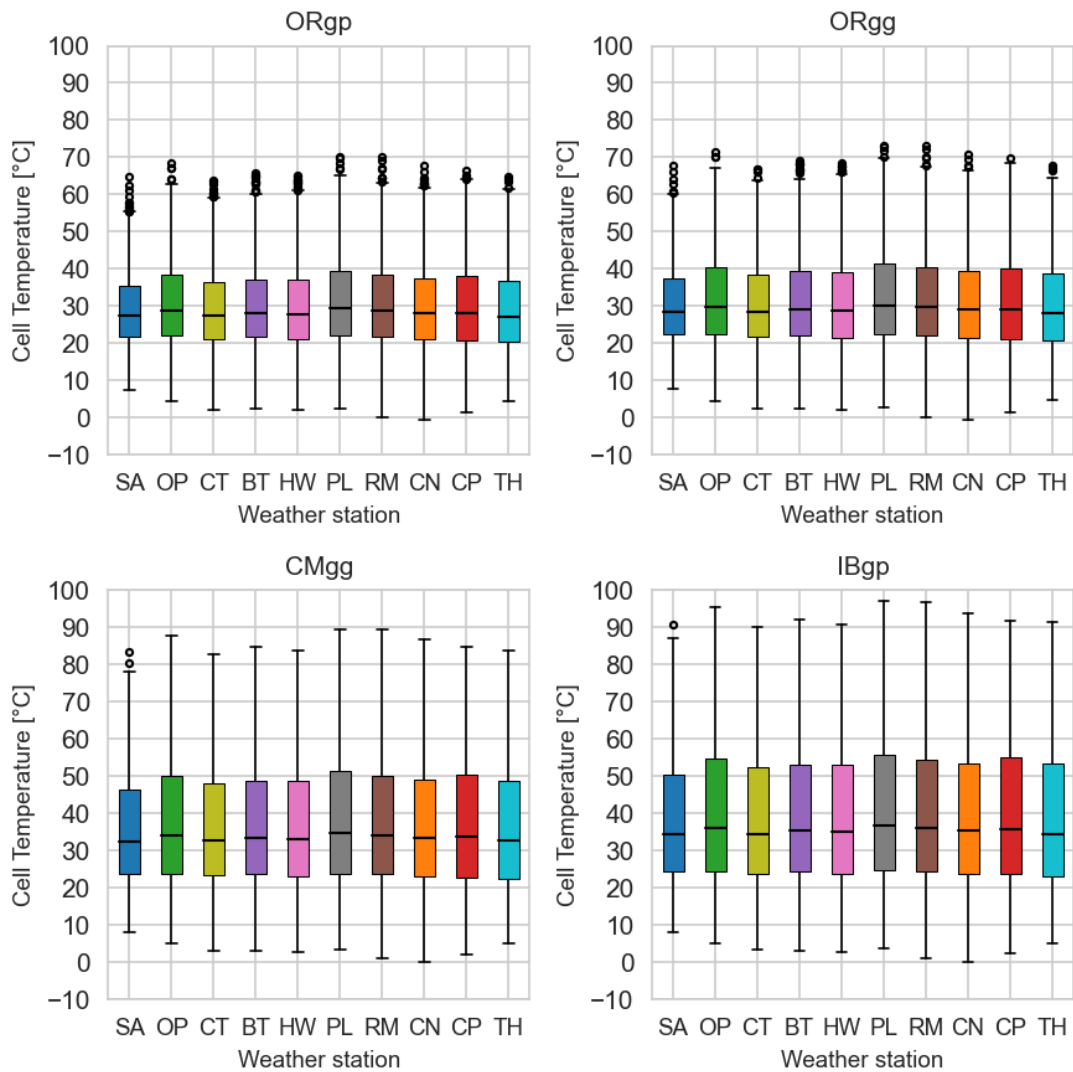


Fig. 5.4 PV cell operating temperatures across the weather stations and mounting configurations. Each graph represents a different mounting configuration whereas each weather station has a different color.

Observing the mean PV cell temperatures across the stations over the entire period, relatively small variations of approximately 2-3°C are observed. However, a significant positive linear relationship (R-Pearson ranging from 0.76 to 0.79) emerges between the mean values and the distance from the nearest coast, as depicted in Figure 5.5. This relationship suggests that as the distance from the coast increases, the mean PV cell temperatures tend to rise.

It is worth noting that station OP deviates from this trend. Despite having similar air temperatures to other inner stations such as CT, BT, and HW, station OP exhibits higher PV operating cell temperatures. This anomaly may be attributed to lower wind speed values at station OP, aligning it more closely with the western stations (PL, RM, CN, and CP).

Conversely, the positive influence of sea breeze is once again highlighted by the lower PV cell temperatures observed at stations SA and TH. These stations benefit from the cooling effect of the sea breeze, resulting in lower mean PV cell temperatures compared to other locations.

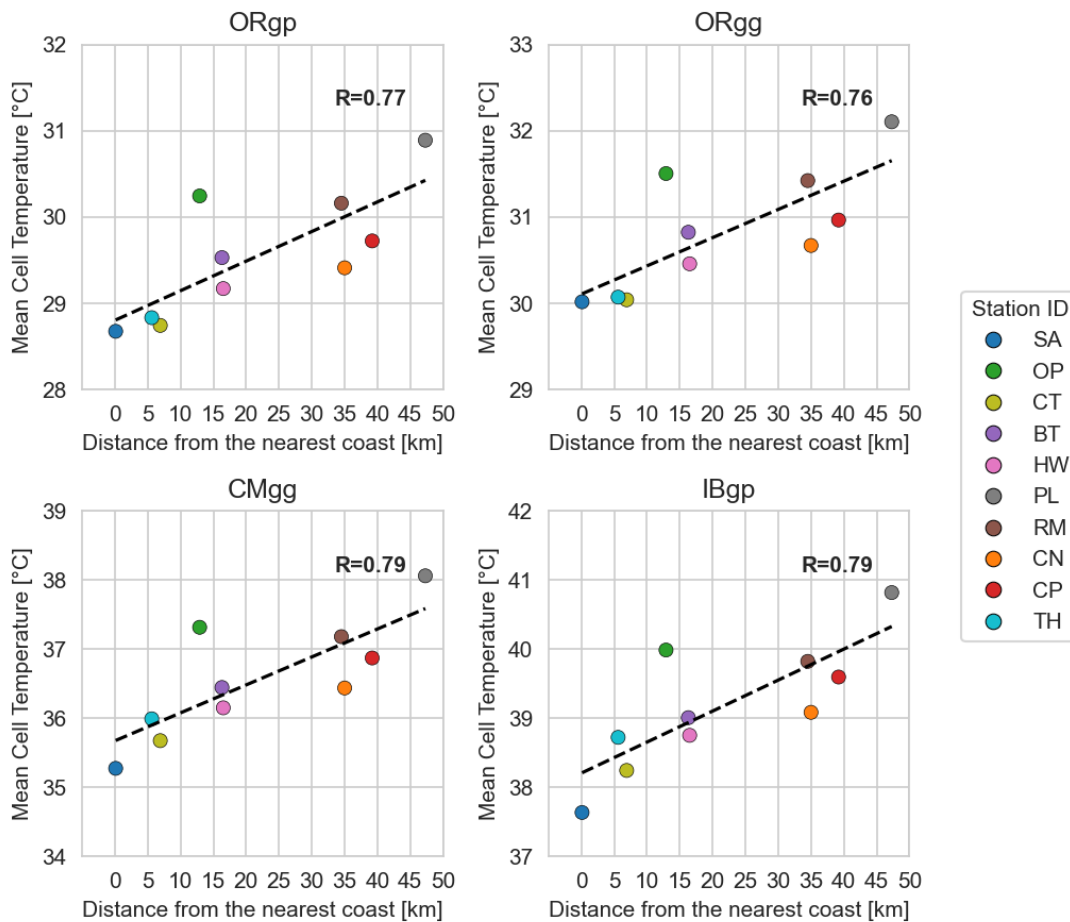


Fig. 5.5 Mean PV cell operating temperatures across the weather stations as a function of the distance from the coast. Each graph represents a different mounting configuration.

Despite overall slight variations in PV operating cell temperatures across the stations over the entire period, analyzing the hourly and monthly patterns reveals more significant differences. In Figure 5.6, the average (solid line) and maximum (dotted line) standard deviation across the ten weather stations are plotted for each hour of the day. The months of January (representing the summer period, shown in red) and July (representing the winter period, shown in blue) are shown for the sake of clarity.

It is observed that PV operating cell temperature variability is minimal in winter but becomes more pronounced during the central hours of the day in summer when solar radiation values are higher. The maximum standard deviation values range from 7 to over 8°C around midday, with average standard deviation values between 3 and 4°C. This demonstrates the significant impact of solar radiation on PV cell temperature variability.

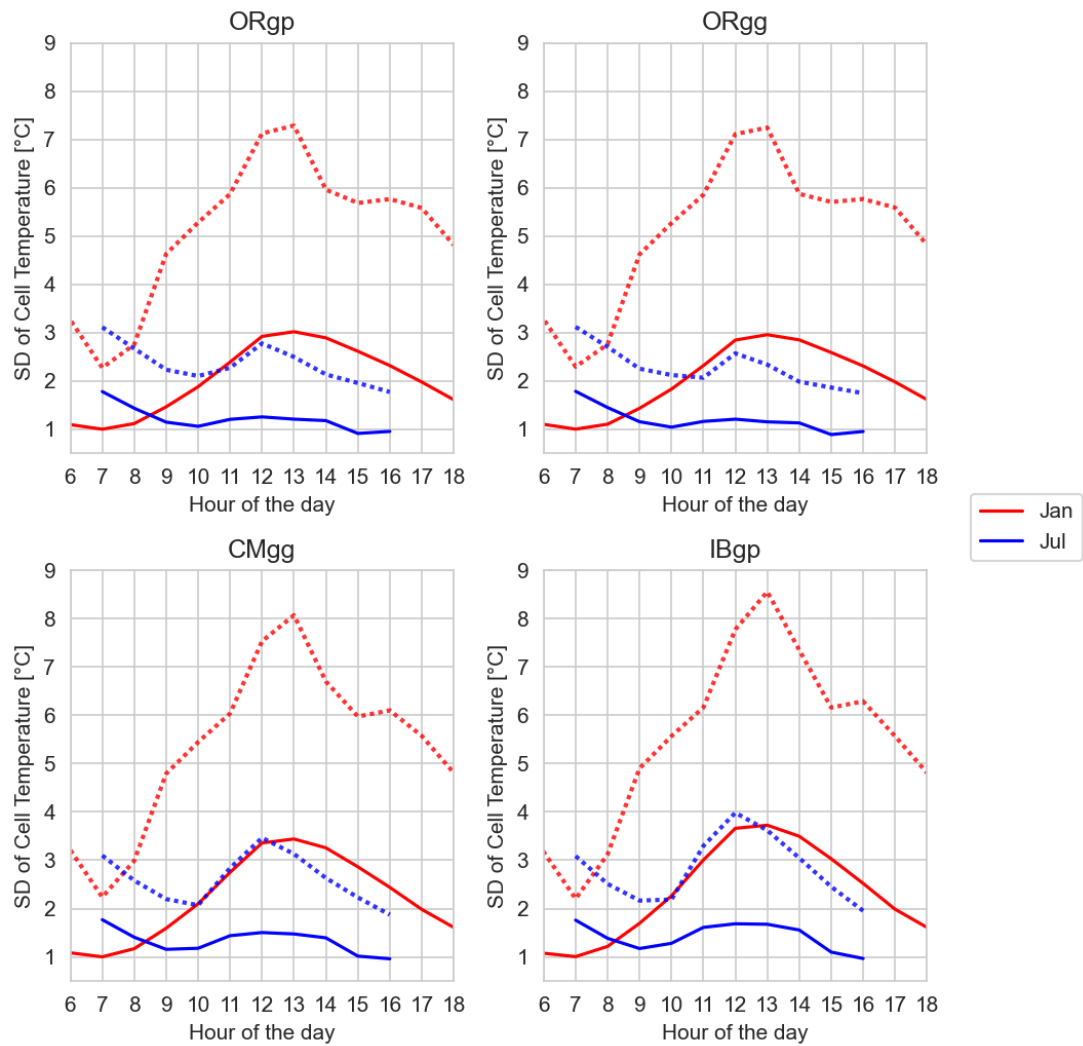


Fig. 5.6 Average (solid line) and maximum (dotted line) standard deviation of PV operating cell temperatures across the weather stations for each hour of the day during summer (January) and winter (July).

The temperature analysis revealed variations in PV cell operating temperatures across weather stations and mounting configurations, with close roof and insulated back mount configurations exhibiting significantly higher temperatures and greater variability compared to open rack configurations. Additionally, meaningful variations in PV cell operating temperatures among weather stations are observed particularly during summer. Based on these findings, the next section is dedicated to the the impact of high cell operating temperatures on the selected PV performance metrics.

Effects of High Temperatures on Performance Metrics

Figure 5.7 shows the monthly Performance Ratio (PR) for the four different mounting configurations, namely open rack glass/cell/polymer (ORgp), open rack glass/cell/glass (ORgg), close roof mount glass/cell/glass (CMgg), and insulated back glass/cell/polymer (IBgp), across the ten weather stations. Each diagram represents a specific mounting configuration, while each weather station is indicated by a distinct colour. The highest PR values are observed in July (winter), with average values across all weather stations ranging from 0.93 for the two open rack configurations (ORgg and ORgp) to 0.89 for the close roof mount (CMgg) and 0.88 for the insulated back (IBgp). During the winter months, the differences in PR across the weather stations are minimal, with variances of around 1%. In contrast, the lowest PR values are recorded in November (summer). On average, across all weather stations, the PR values in November range from 0.88 and 0.87 for ORgp and ORgg respectively, to 0.82 for CMgg and 0.80 for IBgp. Notably, the variations across the weather stations are more substantial during this period, with differences ranging from 3.5% for the open rack configurations to 5.0% for the insulated back, comparing the best site (Sydney Airport, SA) to the worst one (Penrith Lakes, PL).

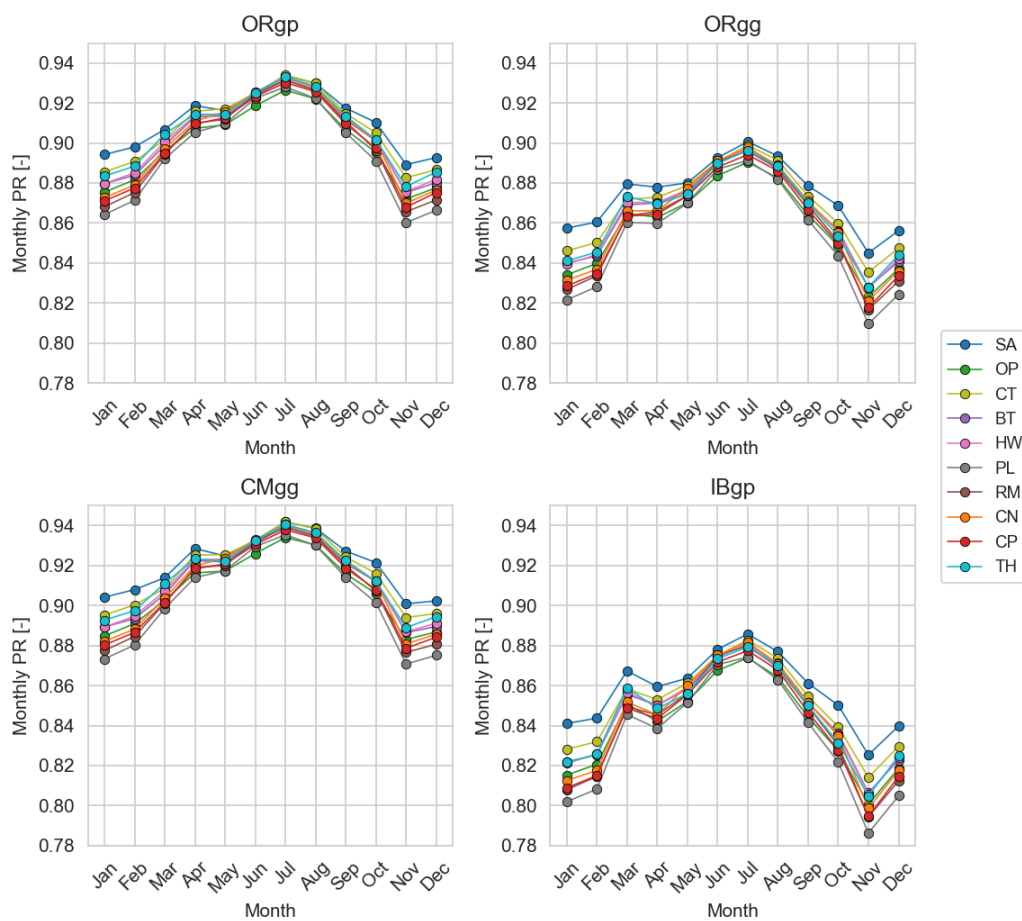


Fig. 5.7 Monthly Performance Ratio (PR) across the weather stations and mounting configurations.

To further investigate the impact of high temperatures on both PV system performance and cooling demand during the summer months (December to February), the daily performance ratio (PR) is calculated for all the weather stations. The calculated daily PR values are then plotted against the cumulated daily values of Cooling Degree Hours (CDH), with a colour gradient used to represent the levels of daily total solar radiation reaching the PV surface expressed in Wh/(m²day). The results are shown in Figure 5.8, with each scatterplot representing a different mounting configuration. The black line in the figure evidence a negative exponential relationship between the two variables, with a coefficient of correlation (R^2) ranging from 0.49 for the IBgp configuration to 0.67 for the ORgp configuration. Higher CDH, indicating a greater cooling demand, correspond to a decrease in the PV performance ratio. The PR varies from a minimum value of about 0.80 for the open rack configurations to about 0.70 for the insulated back configuration. This decrease is particularly evident on days with high irradiances, where the potential for energy conversion is high, but the PV performance is significantly reduced, leading to a maximum decrease of PR values up to 0.20-0.30.

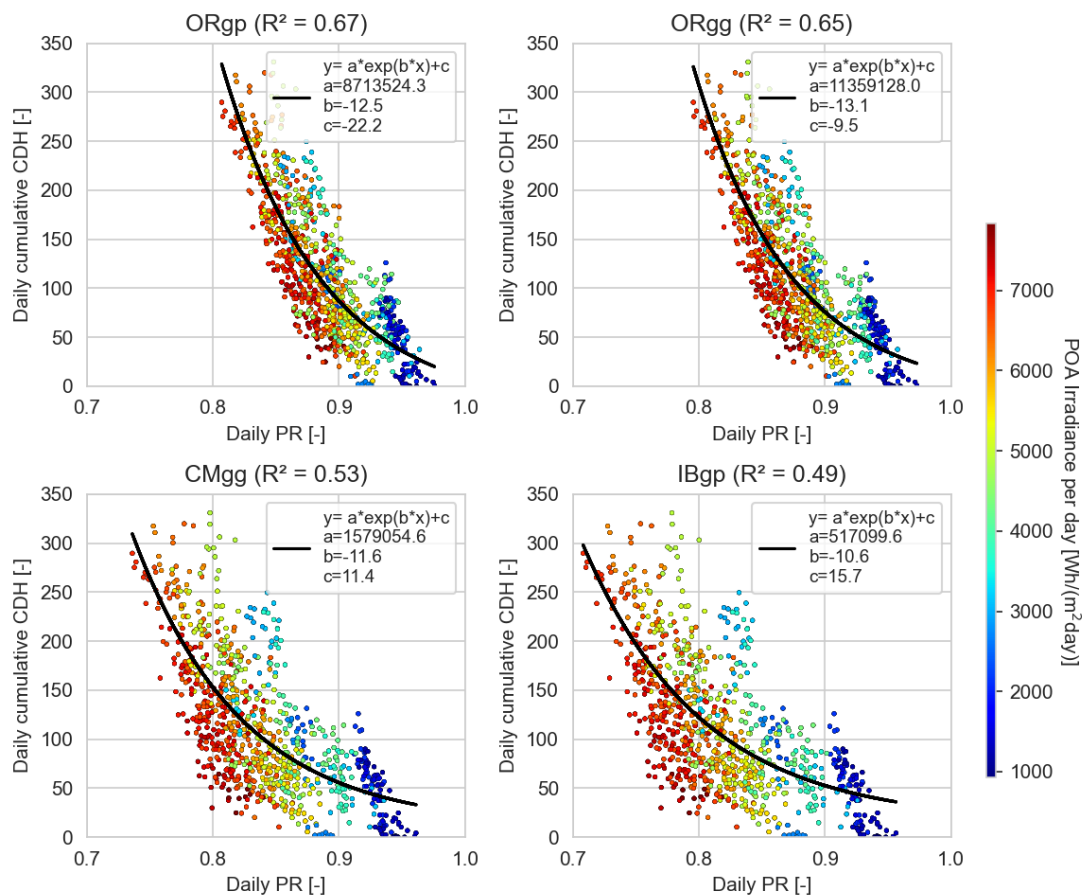


Fig. 5.8 Exponential relationship between daily performance ratio (PR) and cumulative daily Cooling Degree Hours (CDH) across all weather stations during the summer months (December to February). Each diagram represents a different mounting configuration and the colour bar displays the daily total solar energy reaching the PV surface.

Figure 5.9 presents the average hourly values of photovoltaic (PV) efficiency in November (left) and July (right) across all weather stations. These two months were chosen to represent the best and worst PV performance periods. The plots compare the performance of the best-case scenario (open rack glass/cell/polymer, ORgp) and the worst-case scenario (insulated back glass/cell/polymer, IBgp), indicated by solid and dashed lines, respectively.

As observed from both graphs, there is a substantial difference in efficiency between the two analysed months, with November exhibiting significantly lower values compared to July. The influence of the mounting configuration is evident in both graphs, with efficiency values lower by approximately 1-2% for the insulated back configuration. Conversely, the impact of local climatic conditions becomes apparent only in November, particularly during the central hours of the day, where efficiency differences of approximately 1% exist between different weather stations. During the central hours in November, the minimum efficiency values can drop as low as about 11% compared to the rated efficiency at Standard Test Conditions (STC) of 15.63%.

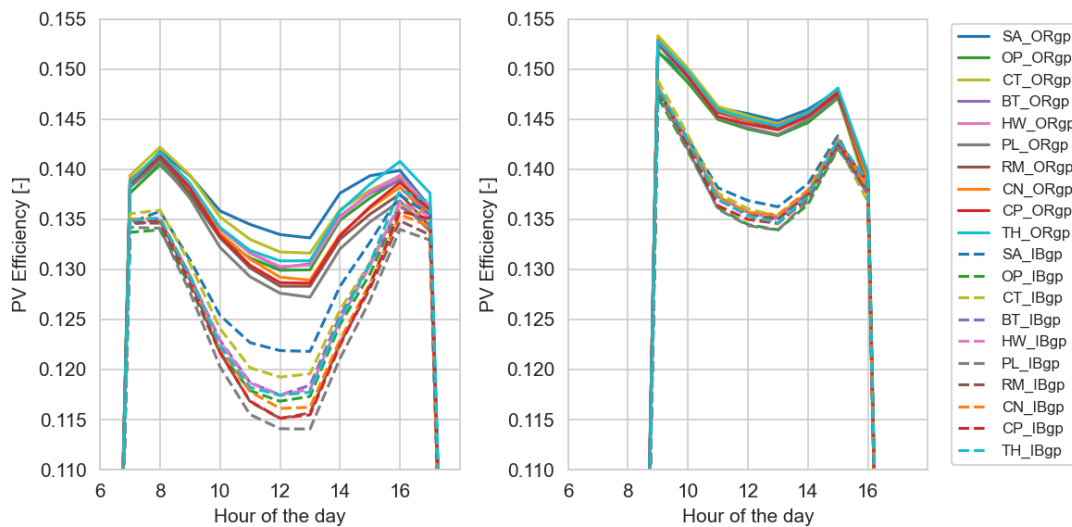


Fig. 5.9 Average hourly values of PV efficiency across the weather stations during November (left) and July (right). Solid and dashed lines are referred to ORgp and IBgp configurations respectively.

Figure 5.10 shows the relationship between hourly values of normalized efficiency and PV cell operating temperatures. To illustrate the results concisely, only the data for Penrith Lakes (PL) weather station, which experiences the highest temperatures, is presented. For open rack configurations, the cell temperature can reach up to 70°C, resulting in a decline in normalized efficiency to approximately 0.75. In contrast, close roof mount and insulated back configurations exhibit higher cell temperatures, reaching around 90°C and 100°C, respectively, leading to a further reduction in normalized efficiency, to less than 0.65.

The diagram also reveals that at an operating cell temperature of approximately 25°C, which corresponds to the standard test temperature, and during periods of low irradiance levels (<250

W/m^2), the normalized efficiency shows greater variability. This variability is primarily related to the angular effect, which is most prominent during sunrise and sunset hours.

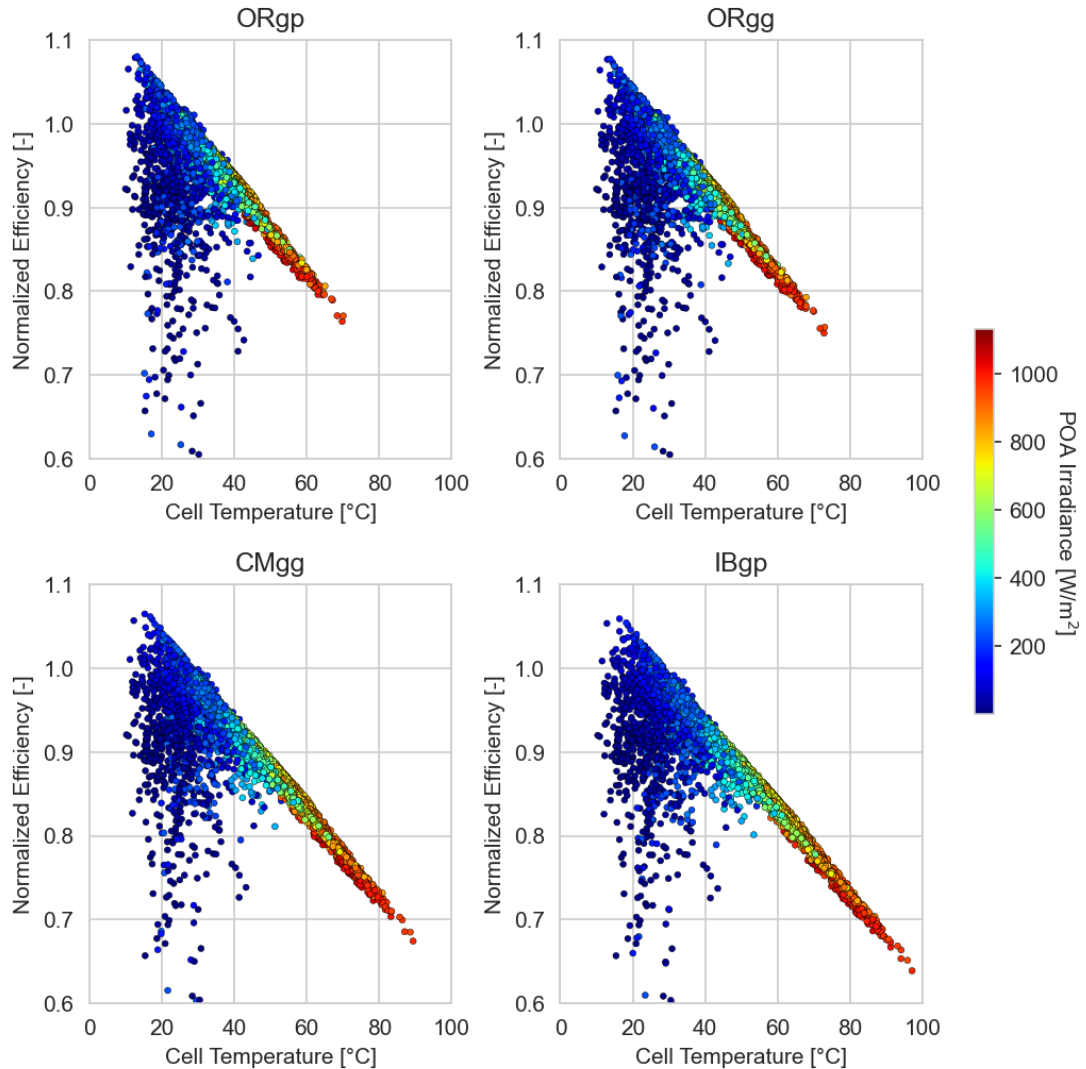


Fig. 5.10 Normalized efficiency and PV cell operating temperature for Penrith Lakes (PL) weather station. Each diagram represents a different mounting configuration.

Power Losses due to Temperature

The power losses due to temperature ($P_{\text{loss},T}^*$) quantify the deviation of PV power output from the standard test cell temperature conditions ($T_c=25^\circ\text{C}$). Figure 5.11 illustrates the yearly average $P_{\text{loss},T}^*$ for each weather station (x-axis) and mounting configuration (represented by different colors). As anticipated, the insulated back configuration (IBgp) exhibits the highest temperature losses, with a value of approximately -10%, compared to -8% for the close roof mount configuration (CMgg). In contrast, the open rack configurations (ORgp and ORgg) demonstrate significantly lower temperature losses, generally below -5%. Among the weather

stations, the impact of temperature is more pronounced in the western stations of PL, RM, and CP, as well as in the inner station of OP, which experiences lower wind speeds compared to other inner stations. Conversely, station SA, located on the coast, is the least affected, despite higher ambient temperatures, due to the beneficial effect of the sea breeze.

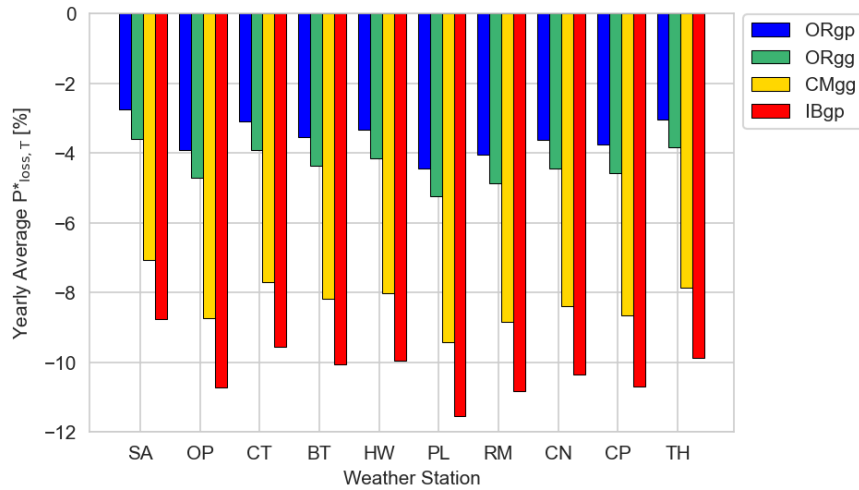


Fig. 5.11 Yearly average $P^*_{loss,T}$ across the considered weather stations and mounting configurations identified by different colors.

Observing the daily average $P^*_{loss,T}$ (averaged across all weather stations), which are plotted in Figure 5.12, it is evident that during extremely hot days from November to February, $P^*_{loss,T}$ can reach values as low as approximately -35

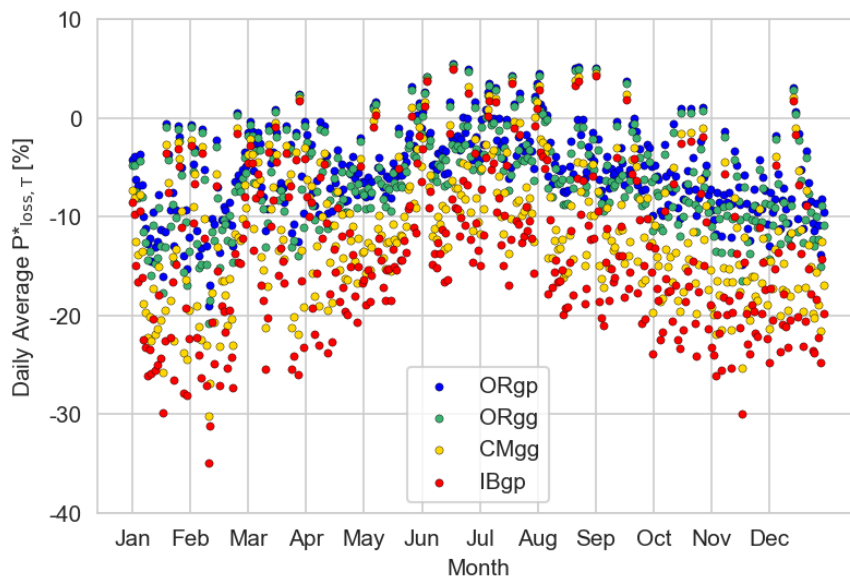


Fig. 5.12 Daily average $P^*_{loss,T}$ (average values across all weather stations) across the mounting configurations identified by different colors.

Considering a threshold value of -20%, the number of hours where $P_{loss,T}^*$ falls below this threshold is 2, 11, 392, and 884 for ORgp, ORgg, CMgg, and IBgp configurations, respectively. Taking into account the total number of operating hours for PV systems, which is approximately 3700, this implies that power loss due to temperature significantly affects PV production for 0.1%, 0.3%, 10.7%, and 24.0% of the time for ORgp, ORgg, CMgg, and IBgp configurations, respectively.

Focusing on the worst case scenario, specifically the insulated back configuration under Penrith Lakes (PL) local climate conditions, Figure 5.13 shows the hourly values of $P_{loss,T}^*$ and the corresponding PV output power (W/m^2). The highest temperature derating can reach up to -50%. This phenomenon is predominantly observed during the summer months and the central hours of the day when PV output power reaches its peak.

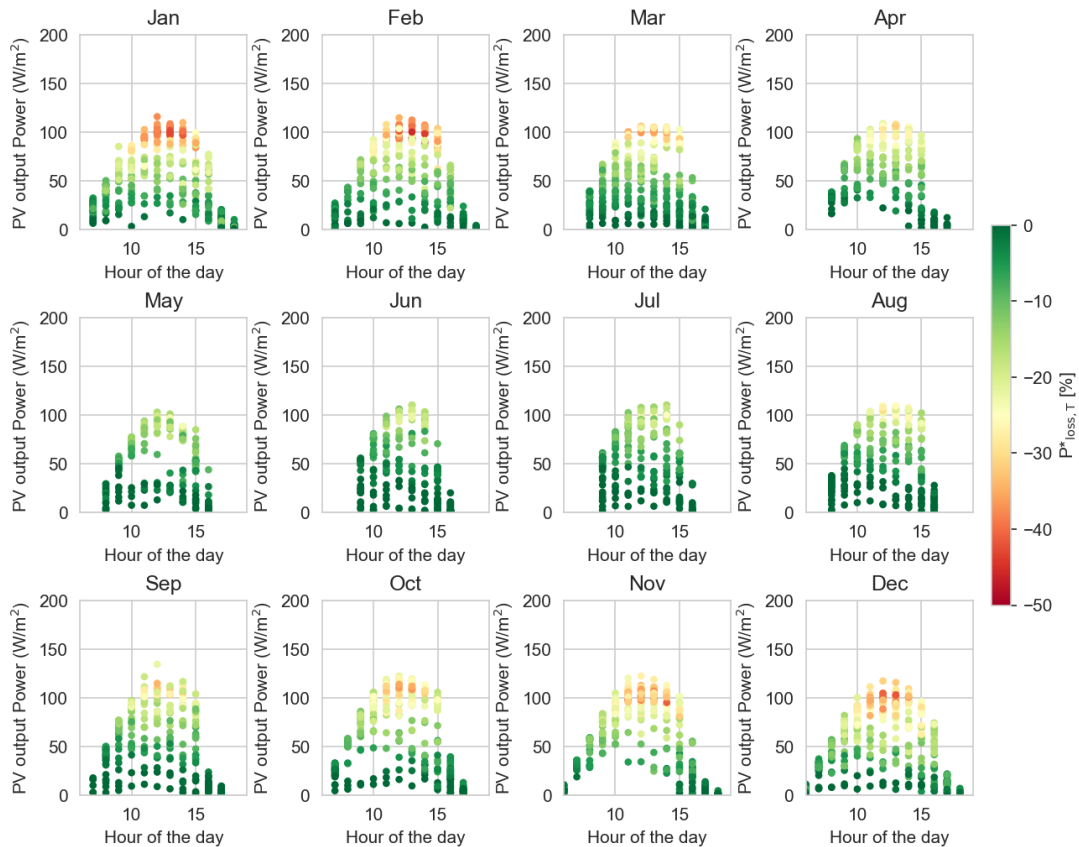


Fig. 5.13 Hourly $P_{loss,T}^*$ and PV output power of insulated back PV modules under Penrith Lakes (PL) weather conditions.

Impact of Local Climate and Mounting Configuration on PV Production

Figure 5.14 presents the average monthly PV energy production in $kWh/(m^2 \text{ month})$ across all weather stations for different mounting configurations, distinguished by different colors. Error bars are included to illustrate the percentage difference in average monthly PV energy

production between the least and most productive weather station. The impact of local climate conditions is particularly evident from November to February and for the close roof mount and insulated back configurations, as indicated by the error bars. The highest percentage difference is observed in January for the insulated back configuration, reaching a maximum value of 5.7%. Conversely, the lowest values are observed from May to July, where the impact of local climate conditions is minimal (approximately 1% in July). The mounting configuration also plays a significant role, especially during the hottest months. Across all weather stations, the ORgp configuration exhibits the highest power production, benefiting from lower temperatures. On the other hand, the least productive configuration is IBgp, which experiences a monthly power production decrease compared to ORgp ranging from a minimum of 7.6% in March to a maximum of 10.6% in November.

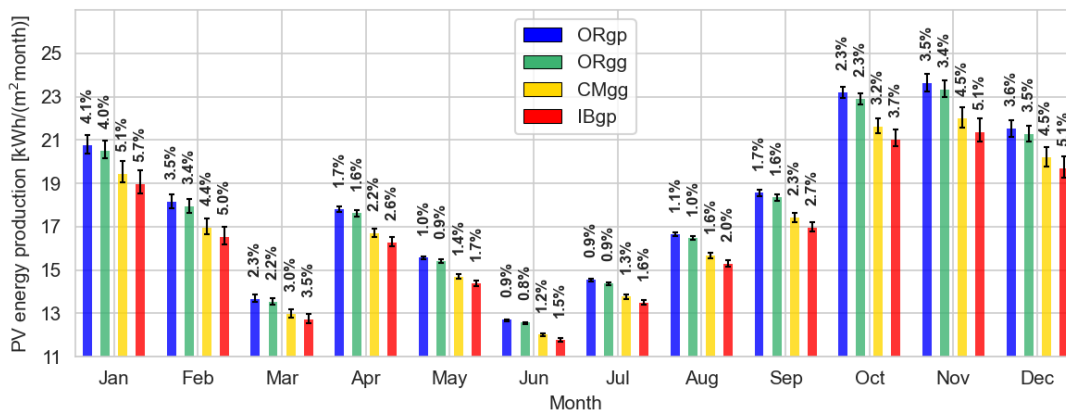


Fig. 5.14 Monthly PV power production (average across weather stations) as a function of the mounting configuration identified by the different colors. Error bars represent the maximum percentage difference of PV energy production across the weather stations.

5.1.3.3 Daytime Convection and Radiation

This section presents the results regarding the daytime convective and radiative heat fluxes released by PV modules for the open rack glass/cell/polymer and close roof mount glass/cell/glass configurations. The aim is to analyse the impact of local climatic conditions on these fluxes.

Figure 5.15 shows the histograms of the convective flux values across all weather stations for the two analysed configurations (open rack, OR, and close roof mount, CM), along with the mean, median, and standard deviation values for the warm period (left), which spans from October to March, and the cool period (right), from April to September.

As observed from the graphs, despite the temperature differences in the PV cells highlighted in the previous sections, the differences between the two configurations are slight. The open rack configuration exhibits, according to the present model, slightly higher values compared to CM, especially for higher flux values. The mean, median, and standard deviation values are very similar for both configurations. During the warm period, the average convective flux is

slightly higher (around 170-180 W/m²) compared to the cool period, which hovers around 150 W/m². In the warm period, the maximum values for the CM configuration do not exceed 550 W/m², while for the OR configuration, they reach peaks of approximately 700 W/m².

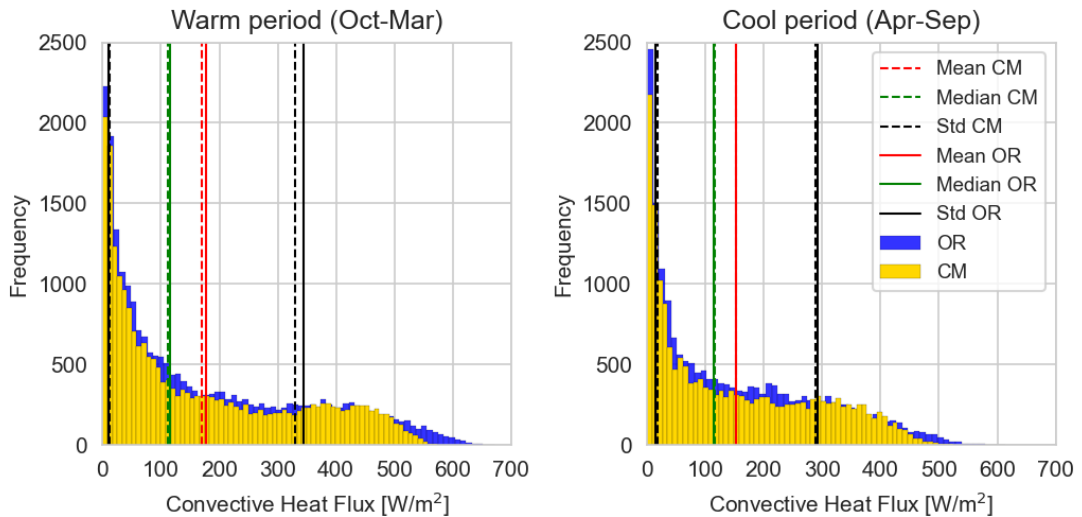


Fig. 5.15 Histogram of the convective heat fluxes across all weather stations during the warm (left) and the cool (right) periods for the two considered mounting configurations (open rack, OR, and close roof mount, CM). Mean, median, and standard deviation values are represented by the red, green, and black lines respectively.

Table 5.6 summarizes the total convective energy in kWh/m² released by open rack (OR) and close roof (CM) installed PV modules over the warm and the cool periods across all ten weather stations. The table also includes the percentage difference calculated between the CM and OR configuration values. The data reveals noticeable variations among the weather stations. In both periods, the highest values are observed at Sydney Airport (SA) station, with average values ranging from 480 kWh/m² during the warm period to around 340 kWh/m² during the cool period. On the other hand, the lowest values are observed at Penrith Lakes (PL) station, ranging from 380 kWh/m² in the warm period to 260 kWh/m² in the cool period, resulting in a percentage difference of approximately -22% compared to SA.

Interestingly, during the warm period, in most weather stations the present model exhibits a negative percentage difference between the CM and OR configurations, indicating a decrease in the total convective energy released by the close roof mount configuration. However, this trend does not hold for the PL, CP, and TH stations. This trend becomes even more pronounced during the cool period, particularly at the PL station, where the total convective energy released by the close roof mount configuration is 8.4% higher than the open rack configuration. This observation can be attributed to local climatic conditions, particularly wind speed. As seen in previous sections, the PL station experiences higher PV cell temperatures primarily due to lower wind speeds at the site (which is located in the western part of the Greater Sydney area), which hinder effective cooling compared to areas closer to the coast. The reduced air circulation

around the modules diminishes the convective heat flux, impeding module cooling. As a result, the higher PV cell temperatures in the close roof mount configuration lead to an increased convective heat flux compared to the open rack configuration due to the larger temperature difference between the cells and the surrounding air. In most other weather stations, where wind speed values are higher, air circulation is favored, especially in the open rack configuration, resulting in greater convective heat release compared to CM, despite lower cell temperatures.

Table 5.6 Total Convective Energy released by open rack (OR) and close roof (CM) installed PV modules across the selected weather stations (WS) during the warm and the cool periods

WS	Total Convective Energy [kWh/m ²]					
	Warm (Oct-Mar)			Cool (Apr-Sept)		
	OR	CM	% diff	OR	CM	% diff
SA	512.1	454.2	-11.3%	357.8	328.1	-8.3%
OP	419.1	406.4	-3.0%	282.5	288.1	2.0%
CT	459.5	427.7	-6.9%	312.0	303.7	-2.6%
BT	454.8	425.1	-6.5%	312.8	304.2	-2.7%
HW	445.6	420.5	-5.6%	306.1	300.5	-1.8%
PL	376.0	384.9	2.3%	249.0	270.0	8.4%
RM	421.4	408.4	-3.1%	289.8	291.7	0.6%
CN	416.0	404.0	-2.9%	287.1	289.5	0.8%
CP	390.9	392.4	0.4%	279.2	286.6	2.6%
TH	392.1	392.9	0.2%	270.4	282.2	4.4%

The variation of wind speed values has a discernible impact on the relative significance of changes in radiative and convective heat transfer, as shown in Figure 5.16. The graph presents the proportional contributions of radiative and convective heat transfer to the overall heat transfer, as a function of wind speed and net irradiance incident on the PV surface (i.e., total irradiance minus the reflected component from the front PV glass). For conciseness, the results are specifically displayed for the close roof mount configuration in the Penrith Lakes (PL) local climate conditions, although similar patterns are observed across other weather stations and mounting configurations. At low wind speeds (<2 m/s), convection accounts for only 30-40% of the total heat transfer, while at 10 m/s, its contribution increases to approximately 60%. Beyond approximately 3-6 m/s, the convective heat transfer process is the dominant mode.

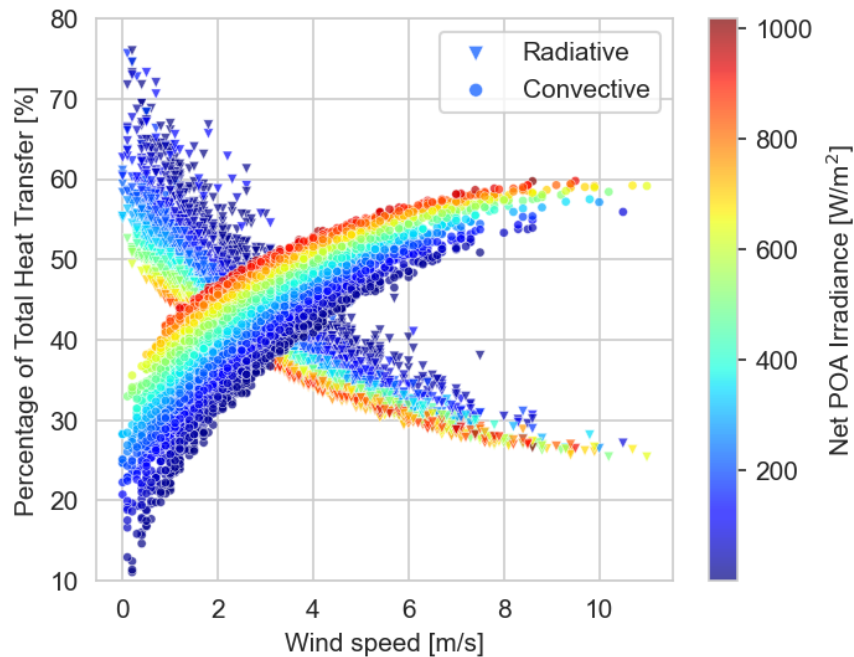


Fig. 5.16 Radiative and convective heat transfers as a percentage of total heat transfer at various wind speeds. The results are referred to close roof mount under Penrith Lakes (PL) climate conditions.

The analysis of convective and radiative heat fluxes in PV modules under different local climate conditions and mounting configurations provides valuable insights into the thermal behavior of PV systems. Open rack PV modules generally exhibit higher convective heat release compared to close roof mount. This difference is primarily due to lower convective heat transfer at the lower side of tilted roofs, as opposed to open rack systems with free air flow on both sides. The higher convective heat flux in open rack configurations corresponds to lower PV cell temperatures and increased power output. Conversely, close roof installations experience lower convective heat flux due to limited air circulation, resulting in higher PV cell temperatures. Nonetheless, the impact of wind speed is critical in this context. At sites characterized by low wind speeds (<2 m/s), the relative contribution of convective heat transfer to the overall heat transfer is approximately half that observed at wind speeds around 10 m/s. Consequently, this circumstance may cause higher convective heat transfer in close roof mount configurations, primarily due to high PV cell temperatures.

5.1.4 Conclusions and Future Perspectives

Given the growing importance of urban-integrated PV systems, accurate electrical and thermal models are essential for predicting their performance under local climate conditions characterized by high temperatures and exacerbated by urban overheating and extreme climate events. The study analysed the electrical and thermal performance of four PV configurations (open rack

glass/cell/polymer, open rack glass/cell/glass, close roof mount glass/cell/glass, and insulated back glass/cell/polymer) using local climatic data recorded between 2016 and 2017 from ten weather stations in Greater Sydney. The present study relies on dedicated modelling based also on Sandia set of equations. Variations in mounting configurations resulted in significant differences in PV operating cell temperature, with up to 30°C variation between open rack and insulated back setups. Cell temperature variations of approximately 8°C were observed across weather stations, particularly during midday hours and summer months. High temperatures negatively affected performance metrics, leading to power losses of up to -50% compared to standard test temperatures. Local climate conditions and mounting configurations caused variations of approximately 6% and 11% in PV energy output, respectively. Daytime convective and radiative heat flux analysis highlighted the influence of wind, with higher convective heat flux in open rack configurations but a potential reversal under low wind speed conditions.

Based on the findings, it is evident that the decline in PV performance is directly related to the level of PV system integration. Furthermore, under low wind speed conditions, roof-mounted systems exhibited lower electrical performance and potentially higher convective heat release.

This study provides valuable insights into the thermal behavior of PV systems in urban contexts exhibiting substantial local climate variations due to overheating. Significant variations are observed within the same metropolitan area, emphasizing the importance of acquiring local data, especially in European cities often characterized by a limited number of weather stations which are located far from urban centers. Concerning Sydney case study, the results show that PV performance in western suburbs is significantly affected by power losses due to temperature, highlighting the need of prioritizing the implementation of adequate urban planning and development strategies (cooling techniques for PV systems, climate mitigation strategies as cool roofs, green roofs).

Limitations of this study include the use of local climate data from non-urban weather stations, potentially underestimating the impact of urban overheating on PV performance, and the exclusion of other meteorological parameters like rainfall that can cool PV modules. The study focused on daytime heat fluxes and did not consider the impact of PVs on rooftop heat balance, highlighting the need for rooftop modelling to accurately quantify the influence of PVs in the urban environment. Additionally, while the King's temperature model used in this study is valuable for predicting PV cell temperatures during daytime, it is not able to account for cooling below ambient air temperatures at night, which is relevant for urban heat island studies.

In conclusion, accurate modelling incorporating local climate conditions and mounting configurations is crucial for understanding the electrical and thermal behavior of urban-integrated PV systems. The results emphasize their effects on PV operating cell temperature, power production, and convective heat flux. Future research should address these limitations by incorporating rooftop modelling, improving temperature models, and evaluating PVs' actual impact on urban overheating.

Chapter 6

Modeling and Optimization of Linear Fresnel Solar Concentration Systems

This final chapter explores a complementary theme compared to the previous topics, considering both the solar energy production modelling techniques and the methodologies employed, as well as the scale of the analyzed system. Specifically, this chapter is related to solar concentration and energy production through Linear Fresnel Collectors (LFCs). This chapter is based on the two following publications:

- **Paper 6.** Fossa, M., **Boccalatte, A.**, Memme, S. (2021). Solar Fresnel modeling, geometry enhancement, and 3D ray-tracing analysis devoted to different energy efficiency definitions and applied to a real facility. *Solar Energy*, 216, 75–89. <https://doi.org/10.1016>
- **Paper 7**¹. **Boccalatte, A.**, Fossa, M., Ménézo, C. (2021). Calculation of the incidence angle modifier of a Linear Fresnel Collector: The proposed declination and zenith angle model compared to the biaxial factored approach. *Renewable Energy*. <https://doi.org/10.1016/j.renene.2021.12.017>

In contrast to the earlier papers, which focused on different aspects of solar energy and urban environments, this chapter examines solar concentration technology, particularly the utilization of LFCs for energy generation. The methodologies utilized in this studies differ from the previous ones due to the unique characteristics of solar concentration systems, requiring specific ray-tracing techniques to assess their performance accurately.

¹Please note that in the current manuscript, certain sections of the published version of this article have been slightly reduced to avoid repetitions, as it was designed as a continuation of **Paper 6**

Contents

7.1	Conclusions	282
7.2	Future Works	284

Paper 6

6.1 Solar Fresnel Modelling, Geometry Enhancement and 3D Ray Tracing Analysis devoted to Different Energy Efficiency Definitions and applied to a Real Facility

Abstract

Despite their few installations, Linear Fresnel Collectors (LFC) represent a very promising technology for efficient solar energy exploitation at medium to high temperatures thanks to their lowest land area per electric energy ratio. Their first appearance was in the '60, thanks to Professor Giovanni Francia realizations at the University of Genova, Italy. This research aims to determine the performance of a LFC and perform parametric studies through 3D ray-tracing simulations. The in-house developed code accounts for all geometrical parameters of the mirrors and receiver assembly, including mirror dimensions, curvature and distance, primary mirror optical errors, receiver aperture area and elevation, secondary mirror compound parabolic shape. The present study includes a detailed investigation on shading, blocking and end effect issues while introducing 6 different different optical and energy efficiency definitions. A parametric analysis is applied to the distance between mirrors and the receiver height. After the code validation against Tonatiuh, the calculations are performed to analyse in details the performance of a real LFC plant in Morocco. The peak optical efficiency of the test case plant has been estimated up to 87% but it is demonstrated the selection of the efficiency definition is crucial for performing successful geometry optimizations.

Keywords

Linear Fresnel Collector; Optical and Energy efficiency; Raytracing simulations; Fresnel plant optimization; Parametric study

6.1.1 Introduction

Increasing the exploitation of solar energy availability will be a key factor for a next fully sustainable development in many countries of the tropical and subtropical regions. These Countries include North Africa nations (e.g. Morocco), Australia, and Andean regions.

Renewable energy conversion at high shares, on the local and global scale, requires a mix of technologies and solar thermal can offer opportunities of energy storage for peak shaving and fulfilling the variability of demand and production (Kalogirou, 2004; Schnatbaum, 2009). As it is well-known, solar concentration relies on three main technologies: solar tower systems (SPT), parabolic through collectors (PTC), linear Fresnel collectors (LFC). Each technology boasts

specific advantages. The solar towers allow higher concentration ratios (CR), up to 1000, (as in Noor III plant (Relloso and Gutiérrez, 2017), in Ouarazate, Morocco) and generally ranging between 300 and 1500 (Breeze, 2016). This optical performance allows the highest temperatures and best first and second law conversion efficiencies compared to linear focusing systems. On the other hand, the LCOE (Levelized Cost of Electricity) of SPT is still high (0.15 €/kWh_{el} (García-Barberena et al., 2014)). Parabolic through is, by far, the most mature technology, accounting for more than 80% of the currently installed CSP capacity (International Renewable Energy Agency, 2011), its typical CR values are much lower than solar tower plants (usually in the range 70-100 (Fuqiang et al., 2017)) and the LCOE is similar (0.18 €/kWh_{el} (Salgado Conrado et al., 2017)) to STP. Fresnel mirror systems can account for few realizations worldwide: the main commercial plants based on Linear Fresnel (LF) technology are Puerto Errado 1 (1.4 MW_{el}) and Puerto Errado 2 (30 MW_{el}) in Spain, Kimberlina (5 MW_{el}) in California (USA), Liddell Power Station (9.3 MW_{el}) in New South Wales (Australia), Dhursar (125 MW_{el}) in Rajasthan (India), Augustin Fresnel 1 (250 kW_{el}) and eLLO (9 MW_{el}) in France (Areva Solar, 2013; Morin et al., 2012b, 2011; Novatec Solar, 2014; SolarPACES, 2019; SUNCNIM, 2017). The concentration ratio of LFC is often quoted from manufacturers as the ratio of mirror aperture to the absorber tube diameter and it typically ranges between 50 and 80 (Blanco and Santigosa, 2016) compared to 80-90 of PTC. However, this definition is misleading since optical collection and thermal losses come from the full perimeter, which should be used as denominator. Although the concentration ratio is not among the highest, Linear Fresnel plants feature the best land use per unit electric nominal power. In this study, it has been calculated the ratio between the gross mirror area and the nominal power of 40 main operating CSP plants all over the world. The results extrapolated from the Global Energy Observatory² and NREL-SolarPaces (SolarPACES, 2019) databases show that LF collectors reach 20 m²/kWh_{el} (ENEA, 2020), compared to 30 m²/kWh_{el} of parabolic through and 43 m²/kWh_{el} of solar towers. Furthermore, the intrinsic simplicity of Fresnel structure and its easy maintenance (e.g. mirror cleaning,) offer great margins for further engineering development and hence reduction of final costs (Zhu et al., 2014).

Linear Fresnel Collector (LFC) systems, conceived and realized for the first time by the Italian Giovanni Francia in 1963 at the University of Genova (Silvi, 2009, 2011), is a concentrated solar technology based on flat or nearly flat mirrors arranged on a horizontal surface and redirecting the sun rays to a linear absorber, often equipped by a secondary mirror acting as refocusing unit (Abbas et al., 2012, 2013; Mills and Morrison, 2000). As noticed before, Fresnel systems are characterized by optical performance lower than those of PTC collectors (Montes et al., 2014; Morin et al., 2009, 2012a; Nixon et al., 2010) but they allow lower investment costs due to structure simplicity (Sait et al., 2015). Many literature studies have investigated the geometric and optical performance of LFR collectors with different mirror patterns. The geometric parameters such as number, positions, widths, curvatures, and focal distances of

²Global Energy Observatory https://globalenergyobservatory.org/list.php?db=PowerPlants&type=Solar_Thermal&utm_content=cmp-true

the mirrors, shape of the secondary reflector, plant dimensions can be varied independently to achieve the best arrangement. Mills and Morrison (2000) investigated a new plant design, named Compact Linear Fresnel Reflector (CLFR), aimed at minimizing cosine losses as well as shading and blocking effects through the exploitation of two alternative receivers. Non-uniform configurations with variable sizes, spacing, receiver height have been analyzed in Abbas and Martínez-Val (2015); Chaves and Collares-Pereira (2010). The comparison between the performance of flat and curved mirrors is also an important issue. Different studies have been devoted to demonstrating the increase of efficiency when using curved primary reflectors (Benyakhlef et al., 2016). A very large amount of research has been devoted to the optimum shape of the secondary reflector and the absorber type (Abbas et al., 2018; Bellos et al., 2018; Benyakhlef et al., 2016; Chaitanya Prasad et al., 2017; Zhu, 2017). The optical performance is influenced by several factors such as shading and blocking effects (Sharma et al., 2015), solar incidence angle (Bellos and Tzivanidis, 2018; Hertel et al., 2015; McIntire, 1982), end effects (Buie, Damien, Christopher Dey and Mills., 2002; Heimsath et al., 2014; Pu and Xia, 2011), tracking, and manufacturing errors (Zheng et al., 2014), shape and efficiency of the secondary receiver (Duffie and Beckman, 2013). In Literature, several studies have been carried out to find the best design and working conditions with respect to different criteria. (Mathur et al., 1991) proposed an optimization method based on minimizing the shading and blocking effects at solar noon. Other authors proposed approaches based on the Levelized Cost Of Electricity (Mertins et al., 2004; Morin et al., 2008). Boito and Grena (2016) provided a specific cost function, considering only the geometric optical collection, to find the optimal plant geometry and, in another study (Boito and Grena, 2017), they optimized the focal length of mirrors considering an average optical efficiency over the year. Chaitanya Prasad et al. (2017) proposed an optimization method of the mirror tilt and radii to obtain uniform flux distribution over the absorber tube. González-Mora and Dolores Durán García (2020) proposed an opto-geometric optimization of the FRESDEMO Fresnel field (Bernhard et al., 2008) to find the best receiver height and secondary reflector (CPC type) geometry considering the intercept factor at the solar noon during summer solstice for a specific location. However, due to the relatively low amount of operating Linear Fresnel installations, only a few investigations are related to existing LFC. Eddhibi et al. (2017) analysed the optical performance of the NOVATEC plant (in Liege, Belgium), but under the Tunisian climate. Bellos et al. (2016) presented an experimental and numerical investigation of a linear Fresnel solar collector with a flat plate receiver located in Athens (Greece), but their objective was not optical optimization. Concerning the methodology, many analytical models have been developed to investigate LFC optical performance (Pino et al., 2013; Sharma et al., 2015; Zhu, 2013) but ray-tracing techniques are mostly used for their high accuracy and flexibility. The most used ray-tracing software tools are Tonatiuh (Blanco et al., 2005), OptiCAD (Di Lauro et al., 2008), OTSun (Cardona and Pujol-Nadal, 2020), SolTrace (Wendelin, 2003), TracePro (LAMBDA, 2019) to name but a few, but different researchers developed their own codes (Cheng et al., 2013; Kistler, 1986; Pulido-Iparraguirre et al., 2019).

The previous literature review highlights that there is a significant scientific interest in optical efficiency and LFC optimization strategies, but there is no uniformity in the methodology used, the parameters involved, and the optical efficiency definition. The most common approach for designing LFC is to define the best arrangement (receiver height, mirror width and number) based on geometrical considerations and attempting to minimize optical losses. However, the present study shows that a mere optical characterization cannot attempt to provide enough information about the real performance of the system.

This research presents a novel approach with regard to LFC performance evaluation and optimization strategies. Starting from model validation against Tonatiuh software and error analysis (non-perfect specularly and tracking errors), the study of the optical performance of LFC is applied to a real plant as a test case. A new model for describing the solar beam collection, reflection, and deflection on target has been developed at the University of Genova, Italy (Memme, 2018). The Matlab code, named FresnelSim, is based on a 3D ray-tracing technique that allows generating a series of parallel sun rays based on the time-varying sun position in the skydome (Memme, 2018).

Results are presented in terms of cumulative energy per selected days (e.g. solstices and equinoxes) and of optical and energy efficiencies. Six different efficiency definitions have been investigated depending on reflectors (primary and secondary) and reference areas (net primary mirrors and gross “land” area). A parametric analysis of the horizontal distance between adjacent mirrors (gap) and the receiver height is conducted to achieve the best energy collection in the selected test case, as a general approach about optical and “ray energy” optimization. Worth stressing that the present research is not related to customary LFC design methodology, but its objective is to assess the global performance of the reference real plant and to suggest some possible improvements based on the abovementioned considerations on efficiency.

6.1.2 Modelling a Linear Fresnel Concentrator based on a Ray-tracing Technique

The present model aims to assess the optical and radiative energy performance of a LFC where mirrors at the horizontal plane are addressing the sun rays to a secondary receiver shaped according to the Compound Parabolic (CPC) theory. A new in-house code, named FresnelSim, has been built to this aim. The code capabilities include the possibility to change a series of aperture and absorber geometric parameters: primary mirror dimensions, curvature, and gap, secondary reflector height, shape (in this case CPC profile), aperture and acceptance angle. An appropriate number of rays is generated and they are reflected by the primary and secondary reflectors according to Snell-Descartes law of reflection. The mirror law of motion is calculated for the best sun tracking and, starting to this condition, at hourly or sub-hourly time steps, it is calculated the number of rays on the absorber plane and even on the secondary mirror.

FresnelSim takes into account a series of phenomena, including cosine losses, blocking by adjacent mirrors, shading from other mirrors or from the receiver assembly, and end effect losses due to the finite length of both mirrors and absorber. As a result of each simulation, the solar irradiance on the receiver tube is obtained as well as the instantaneous, hourly, daily, or yearly amount of incident energy. Additionally, the heat losses from the absorber tube can be calculated through a steady-state heat transfer problem, but this part of the model is not discussed in the present paper. Figure 6.1 represents the complete computational flowchart of FresnelSim, namely a diagram that depicts the ray-tracing algorithm. The rectangular shaped boxes contain actions and processes, whereas the rhombus shaped ones are decision symbols, that indicate the question to be answered (usually with yes/no).

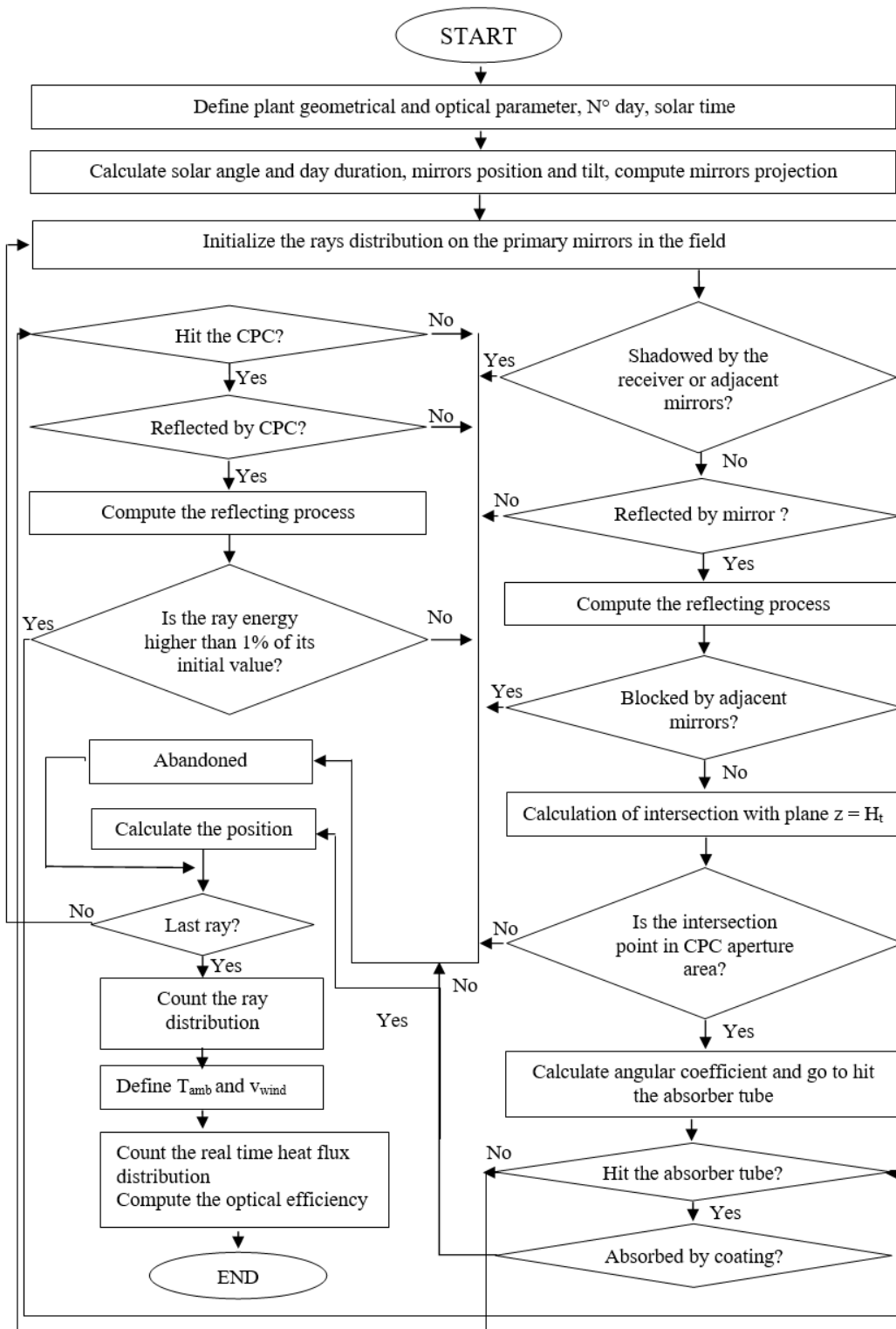


Fig. 6.1 FresnelSim computational flowchart.

6.1.2.1 Linear Fresnel Geometrical and Optical Parameters

A scheme of the reference linear Fresnel collector and its receiver assembly geometry is provided in Figure 6.2. Geometrically, a linear Fresnel collector is defined by a variety of parameters, including:

- Length of the field, L_f (which is equal to the single mirror length)
- Width of the field, W_f
- Number of mirror rows, N_{mir} (in Figure 6.2 mirrors are numbered from 1 to 10)
- Width of the single mirror, w
- Spacing between adjacent mirrors, g
- Radius of curvature of mirrors, r (in Figure 6.2 the curvature is imperceptible, a detailed scheme of mirror curvature is shown later in Figure 6.4)
- Position of the mirror centre line with respect to axis origin, x_m (in this case x values are assumed to be positive eastward)
- Height of the receiver tube, H_t
- Aperture width of the secondary reflector (CPC type), A_{pCPC}
- Acceptance angle of the secondary reflector, θ_a
- External and internal radius of the absorber tube, r_1 , and r_2 respectively

The tilt angle β is calculated for each mirror as a function of its location along the x -axis and the sun position as described in Section 6.1.2.2.

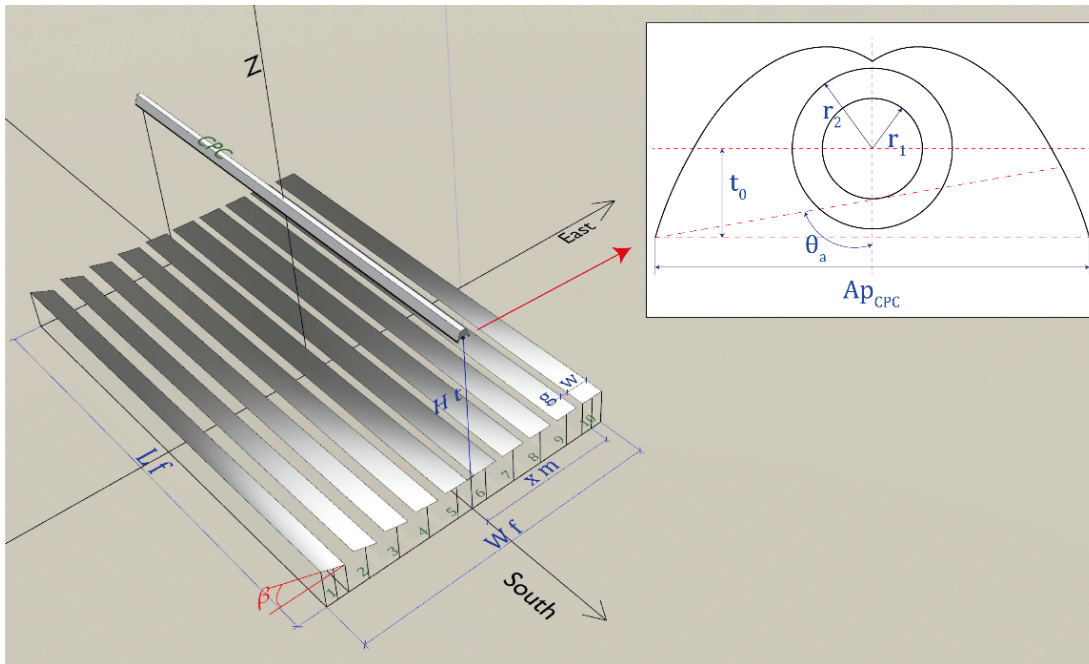


Fig. 6.2 FresnelSim computational flowchart.

Concerning optical parameters, they consist of absorptivity α , transmittance τ and reflectivity ρ of each component of the plant, namely primary mirrors, tube glass cover, absorber tube, and secondary reflector (CPC type) surface.

6.1.2.2 The 3D Ray-tracing Modeling and Assumptions

The proposed code performs an analysis based on some simplifying assumptions:

- only beam (direct) solar radiation is considered;
- direct solar radiation is assumed to be incident as parallel beams;
- reflected ray energy content depends on incoming ray DNI (Direct Normal Irradiance) and single mirror surface zenith angle ($\theta_{w,i}$);
- optical properties of reflecting surfaces are considered independent of beam direction (i.e., constant values for absorptivity, transmissivity, and reflectivity have been defined for each material);
- tracking error and misalignment of the receiver with respect to reflectors are not considered (except in the verification process where an angular tracking deviation is applied to the ideal mirror tilt angle);
- all reflective surfaces are treated as perfectly specular and free from deformations (except in the verification process where a given scattered direction is applied to reflected beams).

As a comment on the above assumptions, let us stress that the measured mirror curvatures along the mirror cords of the test case plant are within 2%, and the related aiming error is expected to be compensated by the acceptance angle of the secondary mirror. The same consideration applies to the non-perfect parallelism of the sun rays due to the real dimensions of the sun disk (as well known, about half of a degree). As in many similar studies and books (Barbón et al., 2020; Eddhibi et al., 2017; He et al., 2012; Karathanasis, 2019; Nixon and Davies, 2012; Sharma et al., 2015; Zheng et al., 2014; Zhu and Huang, 2014), the exact sun shape-related distribution of rays "makes little difference" in solar concentrator modelling when the concentration ratio is lower than 10000 suns, say orders of magnitude higher than the typical Fresnel applications. For this reason, the incoming rays have been considered perfectly parallel, as in the present case, the secondary reflector allows more tolerance in the angular deviation of rays, as later demonstrated in the validation section. Mirror surface error and tracking inaccuracy may affect the performance of the system, and a specifically devoted analysis is here applied to the present Fresnel modelling by introducing specular errors due to primary mirror non-ideal surface conditions and tracking errors.

The simulation must be defined in terms of time and space, i.e., latitude (ϕ), day number (N_{day}), and solar time (h). Sun position is determined according to Eq. 6.1. \vec{S} represents the sun vector, and S_x, S_y, S_z are the x, y, z components; x represents the East-West direction, y the North-South one, while z is the axis perpendicular to the xy plane.

$$\vec{S} = [S_x, S_y, S_z] = [\cos(\alpha_s) \cdot \cos(\gamma_s), \cos(\alpha_s) \cdot \sin(\gamma_s), \sin(\alpha_s)] \quad (6.1)$$

where α_s is the solar altitude angle, and γ_s is the solar azimuth angle, which are calculated starting from latitude (ϕ), sun declination (δ), and hour angle (ω) according to the well-known formulations for sun position (Duffie and Beckman, 2013). The solar azimuth angle γ_s is here assumed to be positive from South to East and negative from South to West. The sun declination angle is calculated through empirical approximations, and the Cooper one (Duffie and Beckman, 2013) is here used. Sun declination (δ) is assumed to be constant during the whole day, as its maximum daily change is 0.5° (occurring at the equinoxes), which is generally insignificant for practical purposes.

The mirror law of motion is defined for a North-South oriented plant, both in case of even or odd rows with uniform horizontal spacing. Based on Snell's Law of Reflection and following the approach proposed by Zheng et al. (Zheng et al., 2014), the vector \vec{R} , representing the reflected ray, is calculated. With elementary geometrical considerations, it is possible to determine the three components of the reflection unit vector \vec{r} as in Eq. 6.2:

$$\vec{r} = \left[\frac{-x_{m,i}}{R}, \frac{E}{R}, \frac{H_t}{R} \right] \quad (6.2)$$

where R is the magnitude of the reflection vector \vec{R} :

$$R = \sqrt{x_{m,i}^2 + E^2 + H_t^2} \quad (6.3)$$

$x_{m,i}$ indicates the x -coordinate of the i -th mirror (which is positive Eastward), H_t is the receiver height, and E represents the reflected ray projection along the y axis, which is calculated according to the law of reflection as in Eq. 6.4:

$$E = \frac{-S_y}{\sqrt{(1 - S_y^2)}} \cdot \sqrt{x_{m,i}^2 + H_t^2} \quad (6.4)$$

For each mirror row, starting from the incident sun rays, it is possible to determine the bunch of reflected rays and their intersection with the aperture plane at H_t height. The ideal tilt angle β_i is calculated as in Eq. 6.5:

$$\beta_i = \tan^{-1} \left[\frac{\left(\frac{x_{m,i}}{R} - S_x \right)}{\left(\frac{H_t}{R} - S_z \right)} \right] \quad (6.5)$$

As in real systems, the perfect functioning of the tracking mechanism may not be guaranteed, FresnelSim also comprises the calculation of a uniformly distributed random deviation of the ideal tilt angle of mirrors in both directions of rotation. The real tilt angle of mirrors ($\beta_{i,te}$) includes the tracking error (σ_{te}), as it is expressed in Eq. 6.6:

$$\beta_{i,te} = \beta_i + \sigma_{te} \quad (6.6)$$

When addressing reflection under realistic conditions, also non-perfect specularity of mirrors should be included. Manufacturing errors and surface non-uniformities may affect the optical efficiency by deviating the reflected rays out of the target. To model this phenomenon, the reflected vector \vec{r} (Eq. 6.2) is deviated by a particular angle. A uniformly distributed angular random deviation, λ_{surf} (in radians), redirects \vec{r} about its origin. This angular offset (applied point-to-point on the mirror surfaces) has been conceived as an effect of local surface non-uniformities (curvature, twisting, other irregularities). The coordinates $[x, y, z]$ of the point P_r , representing the intersection of the reflected ray with the plane $z = H_t$, can be expressed as in Eq. 6.7:

$$P_r = [x + \varepsilon_x, y + \varepsilon_y, z + \varepsilon_z] \quad (6.7)$$

where ε_x , ε_y , and ε_z represent the displacement introduced in the three directions by the angle λ_{surf} . The preliminary simulations include surface non-uniformity and tracking inaccuracies. In the Validation section, it is demonstrated that the secondary (non-imaging) mirror is able to collect the large majority of incoming rays even in case of reflection errors onto the primary

mirrors. Thus, for the sake of generality, the performance analysis has been carried out in ideal conditions, neglecting specularly and tracking errors.

Figure 6.3 shows the scheme of sun position (\vec{S}), mirror normal (\vec{n}), and reflected ray (\vec{R}) vectors with respect to a generic N-S oriented mirror at $x_{m,i}$ distance from the axis origin (O).

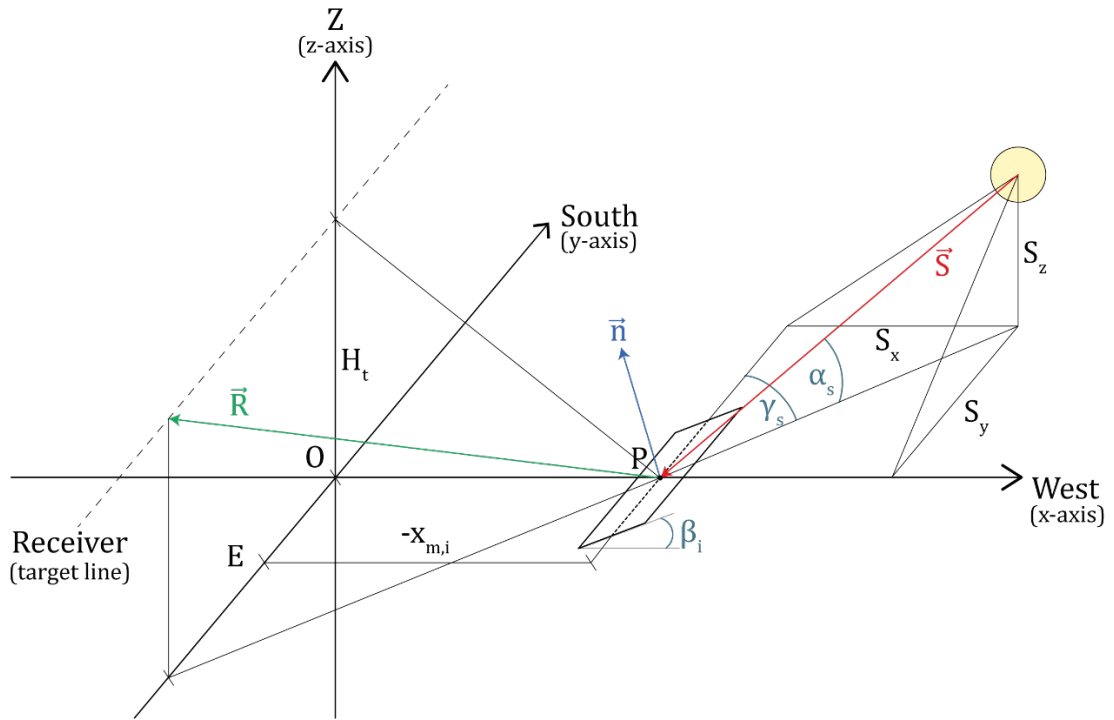


Fig. 6.3 Sun position (\vec{S}), mirror normal (\vec{n}), and reflected ray (\vec{R}) vectors with respect to a generic N-S oriented mirror at $x_{m,i}$ distance from the axis origin (O).

FresnelSim can run simulating both flat and curved mirrors of any shape. Regarding the mirror shape, this is defined through the radius of a cylinder to which they belong (r) and the value of the angle ϕ that subtends the corresponding chord (\widehat{AB}), as represented in Figure 6.4. The cylinder radius can be inferred by considering the maximum value assumed by the distance measured from the mirror arc \widehat{AB} to the corresponding chord \overline{AB} , indicated as “d” in Figure 6.4.

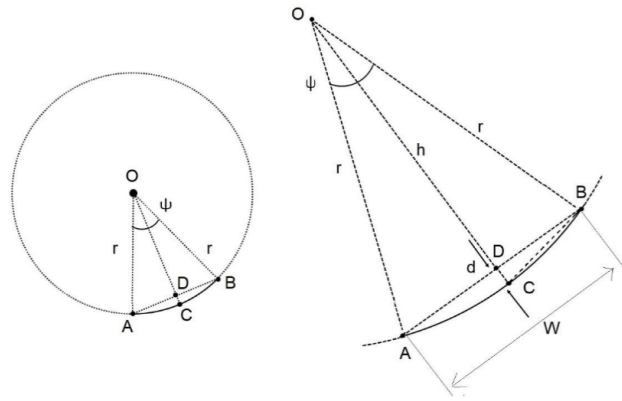


Fig. 6.4 Curved cylindrical mirror geometric parameters.

According to Eq. 6.8 and 6.9, it is possible to calculate r and φ :

$$r = \frac{w^2}{8d} + \frac{d}{2} \quad (6.8)$$

$$\varphi = 2 \sin^{-1} \left(\frac{w}{2r} \right) \quad (6.9)$$

Identifying the coordinates of each cylinder axis of symmetry (the straight lines parallel to the y -axis to which the centers of the mirrors belong) is crucial since the description of the rotation of the cylindrical mirrors is related to the change of cylinder axis coordinates in space. The $x_{c,i}$ and $z_{c,i}$ coordinates are calculated according to Eq. 6.10 and 6.11 as a function of the tilt angle β , the distance between the chord \overline{AB} and the center of the cylinder (h), and the x -coordinates of each mirror $x_{m,i}$:

$$x_{c,i} = x_{m,i} + h \sin(-\beta_i) \quad (6.10)$$

$$z_{c,i} = h \cdot \cos(\beta_i) \quad (6.11)$$

In the most common ray-tracing codes, an irradiating surface representing the sun is used to initialize rays, whereas, in FresnelSim, the rays are initialized directly on each mirror surface to significantly reduce the computational time. Accordingly to the geometrical constraints of the mirrors, a "rand" Matlab function ξ (which generates a random number between 0 and 1) is used to assign three randomly chosen coordinates to the sun rays according to Eq. 6.12, 6.13, and 6.14:

$$x_{i,j} = x_{m,i} + (\xi - 0.5) \cdot w \cdot \cos(\beta_i) \quad (6.12)$$

$$y_{i,j} = L_f \cdot (\xi - 0.5) \quad (6.13)$$

$$z_{i,j} = z_{c,i} - \sqrt{[r - (x_{i,j} - x_{c,i})] \cdot [r + (x_{i,j} - x_{c,i})]} \quad (6.14)$$

where i represents the mirror index, ranging from 1 to N_{mir} , and j is the progressive ray for each mirror, assuming values from 1 to N_{rays} (the number of generated rays, which is a user input value).

Once all the preliminary operations have been performed, the 3D ray-tracing algorithm is started to determine the path of sun rays reflected by the primary mirrors to an imaginary rectangle subtended to the CPC profile, at a height equal to H_t .

The first check involves the reflectivity ρ_1 of the primary mirrors. For each ray, a random number ξ between 0 and 1 is created and compared to ρ_1 ; if it is lower, the ray will be reflected, and further calculations will occur before moving to the subsequent ray. If instead ξ is higher than ρ_1 , the ray won't be reflected and thus neglected.

Secondly, FresnelSim evaluates if a mirror is subjected to shading and/or blocking. If the ray has been reflected, its position on the mirror surface is projected to the x-axis (x_{proj}) according to the sunbeam incoming direction through Eq. 6.15, to be compared to edge projections of the other mirrors and of the receiver:

$$x_{proj} = x_{m,i} \mp \sqrt{[x_{i,j} - x_{m,i}]^2 + z_{i,j}^2} \cdot \left[\sin \left(\frac{(\alpha_P \mp \beta_i)}{\alpha_P} \right) \right] \quad (6.15)$$

The mirror and the receiver edges projections must be defined starting from the tilt angle of each mirror (β_i) and the profile angle. The latter is the angle between the surface normal vector and the projection of sun rays on a vertical surface normal to the same surface. As it is defined, for North-South oriented plants, the profile angle coincides with the projection of solar altitude (α_s) on the transversal plane (transversal solar altitude angle, α_T). In the present study, the profile angle is named α_P and it is evaluated as in Eq. 6.16 (angles in degrees):

$$\alpha_P = \tan^{-1} \left[\frac{\tan(\alpha_s)}{\cos(90 - \gamma_s)} \right] \quad (6.16)$$

The analytical determination of the shadow coordinates of each object (mirrors and receiver) is achieved through the projection of each element edge on the x-axis according to incident sun rays direction (\vec{I}). A matrix of $[2 \times N_{mir}]$ dimension is created. The first row contains the x-coordinate of the i^{th} mirror edge projection to the West ($x_{p,w,i}$), and the second its East projection ($x_{p,e,i}$). The equations for the calculation of $x_{p,w,i}$ and $x_{p,w,e}$, according to Sharma et al. (2015), are Eq. 6.17 and 6.18:

$$x_{p,w,i} = \begin{cases} x_{m,i} - 0.5 \cdot w \cdot \sin \left[\frac{\alpha_p - \frac{\gamma}{|\gamma|} \cdot \beta_i}{\sin(\alpha_p)} \right] & \text{if } \gamma \neq 0 \\ x_{m,i} - 0.5 \cdot w \cdot \cos(\beta_i) & \text{if } \gamma = 0 \end{cases} \quad (6.17)$$

$$x_{p,e,i} = \begin{cases} x_{m,i} + 0.5 \cdot w \cdot \sin \left[\frac{\alpha_p - \frac{\gamma}{|\gamma|} \cdot \beta_i}{\sin(\alpha_p)} \right] & \text{if } \gamma \neq 0 \\ x_{m,i} + 0.5 \cdot w \cdot \cos(\beta_i) & \text{if } \gamma = 0 \end{cases} \quad (6.18)$$

Similarly, also the receiver assembly (named CPC in equations to abbreviate) shadow coordinates are determined as in Eq. 6.19 and 6.20:

$$x_{p,w,CPC} = \begin{cases} x_{p,e,CPC} - 0.5 \cdot A_{p,CPC} \cdot [\cos(\alpha_p) \cdot \cot(\alpha_p) + \sin(\alpha_p) + 1] & \text{if } \gamma > 0 \\ H_t \cdot \cot(\alpha_p) - 0.5 \cdot A_{p,CPC} & \text{if } \gamma < 0 \\ -0.5 \cdot A_{p,CPC} & \text{if } \gamma = 0 \end{cases} \quad (6.19)$$

$$x_{p,e,CPC} = \begin{cases} -[H_t \cdot \cot(\alpha_p) - 0.5 \cdot A_{p,CPC}] & \text{if } \gamma > 0 \\ x_{p,w,CPC} + 0.5 \cdot A_{p,CPC} \cdot [\cos(\alpha_p) \cdot \cot(\alpha_p) + \sin(\alpha_p) + 1] & \text{if } \gamma < 0 \\ 0.5 \cdot A_{p,CPC} & \text{if } \gamma = 0 \end{cases} \quad (6.20)$$

Figure 6.5 shows a scheme of the mirror edge projections and shading effect between two adjacent mirrors.

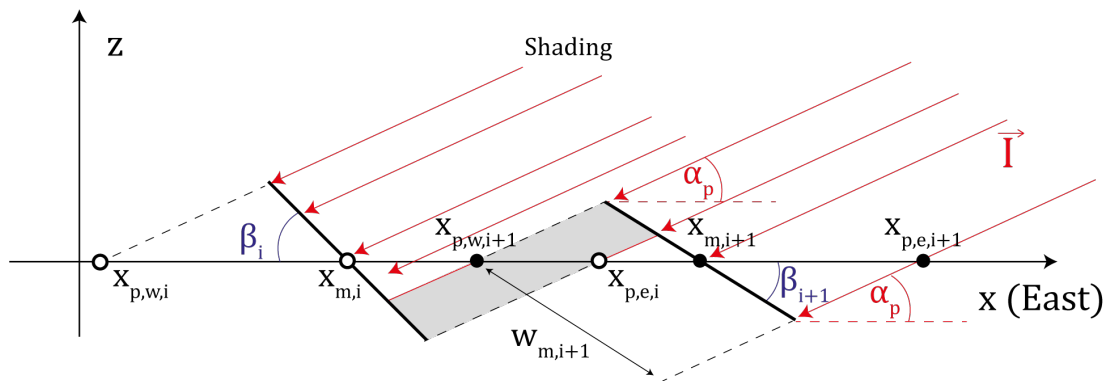


Fig. 6.5 Determination of the shaded area from sun ray projection onto the vertical East-West plane.

If the examined mirror is not subjected to shadow from the receiver or adjacent mirrors, the ray is reflected. The law of specular reflection expressed in Eq. 6.21 allows calculating the

reflection vector (\vec{R}) as a function of the incident direction of the incoming radiation vector (\vec{I}) and the normal surface vector (\vec{N}):

$$\vec{R} = 2 \cdot (\vec{I} \cdot \vec{N}) \cdot \vec{N} - \vec{I} \quad (6.21)$$

The projections of mirror edges are calculated according to the direction of the potentially reflected rays to check ray blocking. Figure 6.6 shows the blocking effect between two adjacent mirrors.

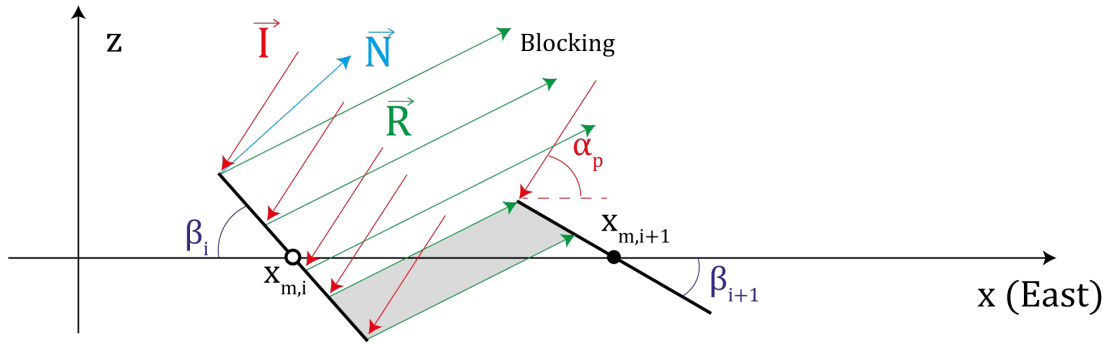


Fig. 6.6 Determination of blocked rays as a projection onto the vertical East-West plane.

When a ray has not been shaded or blocked it will intersect the plane $z = H_t$ in a point P_r , whose coordinates are analytically determined through a simple geometric problem. The $[x, y, z]$ coordinates of P_r are given by Eq. 6.22 as a function of the parameter t defined in Eq. 6.23:

$$P_r = [x + R_x \cdot t; y + R_y \cdot t; H_t] \quad (6.22)$$

$$t = \frac{H_t - z}{R_z} \quad (6.23)$$

where R_x, R_y, R_z are the x, y, z components of the reflection vector \vec{R} . A further check on P_r coordinates allows determining if the reflected ray is intercepted by the aperture area of the receiver (Ap_{CPC}). The final condition of each ray (not reflected, shaded by mirrors, shaded by the receiver, blocked, reflected out of the target, reflected on target) is determined.

The interactions between the sun rays which reached the flat (and horizontal) aperture area (Ap_{CPC}) and the secondary reflector itself are described in FresnelSim through a 2D simulation. The CPC profile shape is calculated as proposed by Qiu et al. (2015) through Eq. 6.24 and described in cylindrical coordinates θ_0 and ρ_0 :

$$\begin{cases} y_{CPC} = \rho_0 \cdot \cos(\theta_0) - r_1 \cdot \sin(\theta_0) \\ z_{CPC} = \rho_0 \cdot \sin(\theta_0) + r_1 \cdot \cos(\theta_0) \end{cases} \quad (6.24)$$

where:

$$\rho_0 = \begin{cases} r_1 \cdot (\theta_0 + \sigma), & \text{if } \cos^{-1}\left(\frac{r_1}{r_2}\right) \leq \theta_0 \leq \frac{\pi}{2} + \theta_a \\ \frac{r_1 \cdot [\theta_0 + \theta_a + \frac{\pi}{2} + 2 \cdot \sigma - \cos(\theta_0 - \theta_a)]}{1 + \sin(\theta_0 - \theta_a)}, & \text{if } \frac{\pi}{2} + \theta_a \leq \theta_0 \end{cases}$$

once coefficient σ has been preventively defined as:

$$\sigma = \sqrt{\left(\frac{r_2}{r_1}\right)^2 - 1} - \cos^{-1}\left(\frac{r_1}{r_2}\right) \quad (6.25)$$

It is useful to remind that r_1 and r_2 are the external and internal radius of the absorber tube respectively, and θ_a represents the CPC profile acceptance angle as previously shown in Figure 6.2.

The 2D ray-tracing algorithm consists in formulating an analytical geometrical problem to determine if the ray directly hits the absorber tube or if it undergoes further reflections. This check is performed by solving a simple second-degree equation $ax^2 + bx + c = 0$ resulting from the combination of the absorber tube equation, which is known, and the equation of a straight line (reflected ray) passing through a specified point P_r with a known angular coefficient “m” expressed as in Eq. 6.26.

$$m = \frac{H_t - z}{R_x - x} \quad (6.26)$$

The resulting equation is solved and admits two distinct, two coincident or no solutions depending on the sign of the discriminant Δ :

- if $\Delta = 0$ the path of the analysed ray is ideally tangent to the absorber tube;
- if $\Delta > 0$ two intersecting points exist between the straight line and the absorber tube profile, and a subsequent check allows to determine which one is feasible;
- if $\Delta < 0$ the problem doesn't have real solutions, which would mean that the ray is not directly intersecting the absorber tube.

In the first two cases, the loop is stopped, and the energy of the rays impinging on the tube is stored. On the contrary, if more reflections happen, the intersection point(s) between the ray path and CPC profile is analytically determined: the direction of the reflected ray as in Eq. 6.21 by including energy losses due to the reflectivity of CPC type surface (ρ_2). A number of

iterations are performed until the ray is abandoned because one of the following conditions is reached:

- the reflected ray intersects the absorber tube;
- the reflected ray has lost 95% of its initial energy, which is a typical condition of rays intersecting CPC profile with angular coefficients close to $\tan(\theta_a)$. It is worth mentioning that the 95% rule is related to the usual Confidence Band applied in typical engineering analyses, and a different value could be chosen.

At this point, the optical analysis is complete, and a database of rays interacting with surfaces has been created.

6.1.3 Optical Optimization Methodology

Modelling LFC to achieve the best performance is challenging task due to the large number of involved parameters (the receiver height, H_r , the horizontal spacing between adjacent mirrors, g , the mirror width, w , the field length L_f , the mirror radius of curvature, r). In the present study, a parametric analysis is conducted to find the best energy yield as a function of the spacing between adjacent mirrors and the receiver height. The following section describes the six different efficiency definitions used to evaluate the reference LFC performance.

6.1.3.1 Optical and Energy Efficiencies Definition

The efficiency of primary reflectors can be investigated, from a purely geometric point of view, by considering the number of incident rays to the target with respect to the overall number of generated rays (N_{rays}). Two optical efficiencies are introduced, through Eq. 6.27 and 6.28, to quantify the number of rays reaching the aperture area of the receiver (A_{PCPC}) and the absorber tube, respectively:

$$\eta_{opt}^I = \frac{\sum \text{Rays on } A_{PCPC}}{N_{rays} \cdot N_{mir}} \quad (6.27)$$

$$\eta_{opt}^{II} = \frac{\sum \text{Rays on tube}}{N_{rays} \cdot N_{mir}} \quad (6.28)$$

From the above expressions, it is also possible to define the secondary reflector (CPC type) optical efficiency as in Eq. 6.29:

$$\eta_{opt,CPC} = \frac{\eta_{opt}^{II}}{\eta_{opt}^I} \quad (6.29)$$

To apply the previous optical definitions to the energy analysis at the absorber tube, a given amount of energy has to be associated with each ray ($E_{r,j}$). This quantity is calculated as a function of the direct normal irradiance (E_{DNI}), depending on the day number (N_{day}) and solar time, of the single mirror area ($L_f \cdot w$), and of the well-known "cosine efficiency" ($\eta_{cos,i}$), which is the cosine of the solar zenith angle of the i^{th} mirror ($\theta_{w,i}$). $E_{r,j}$ is finally calculated as follows (Eq. 6.30):

$$E_{r,j} = \frac{E_{DNI} \cdot L_f \cdot w \cdot \eta_{cos,i}}{N_{rays}} \quad (6.30)$$

Due to the lack of reliable measured data (based on more than 10 years of measurements) for the selected location, E_{DNI} [W/m^2] can be calculated analytically as a function of the day number (N_{day}) and altitude solar angle (α_s), by a clear sky model (Duffie and Beckman, 2013) as expressed in Eq. 6.31:

$$E_{DNI} = 1367 \cdot \left[1 + 0.033 \cdot \cos\left(\frac{2\pi \cdot N_{day}}{365}\right) \cdot \frac{\sin(\alpha_s)}{[\sin(\alpha_s) + 0.33]} \right] \quad (6.31)$$

Since clear sky models are not able to account for the variability of the DNI under the same latitude, in order to verify the reliability of the values obtained through Eq. 6.31, they have been here compared with the DNI hourly values as provided by the Meteonorm software ($E_{DNI,MN}$) for the location under consideration.

Four different "opto-energy" efficiencies are introduced through Eq. 6.32 to 6.35 to estimate the energy flux to the target:

$$\eta_{en}^I = \frac{\sum_{n=1}^{N_{APCPC}} E_{r,j}}{E_{DNI} \cdot A_{tot,mirr}} \quad (6.32)$$

$$\eta_{en}^{II} = \frac{\sum_{i=1}^{N_{tube}} E_{r,j}}{E_{DNI} \cdot A_{tot,mirr}} \quad (6.33)$$

$$\eta_{en}^{III} = \frac{\sum_{i=1}^{N_{APCPC}} E_{r,j}}{E_{DNI} \cdot A_{gross}} \quad (6.34)$$

$$\eta_{en}^{IV} = \frac{\sum_{i=1}^{N_{tube}} E_{r,j}}{E_{DNI} \cdot A_{gross}} \quad (6.35)$$

η_{en}^I and η_{en}^{II} express the ratio between the energy flux onto the target (the first is related to the aperture area of the receiver, whereas the second to the absorber tube) and the incident energy flux on the net area of the mirrors ($A_{tot,mirr}$). On the contrary, η_{en}^{III} and η_{en}^{IV} are related to the gross area of the mirror field (A_{gross}).

6.1.3.2 Parametric Analysis

The objective of the parametric analysis is to study the energy yield variation as a function of the spacing between adjacent mirrors and receiver height. First, the two optical efficiencies η_{opt}^I and η_{opt}^{II} are used to analyse the optical performance of the actual geometry of the GEP Fresnel plant. It is worth noticing that η_{opt}^I and η_{opt}^{II} will be higher for very narrow and spaced rows since this configuration presents the lowest blocking and shading losses. However, this configuration does not necessarily maximize energy collection and it is the worst for land use. In the present study, the choice is to maximize the energy collection, even if the optical efficiency of primary reflectors will be affected by losses.

The parametric analysis has been carried out by varying the gap between mirrors from 0 to 0.5 m, with a step of 0.1 m (including 0.05 m, which is considered the first constructionally feasible value since 0 m is only an ideal case). Once the best spacing (according to our criteria) has been selected, the receiver height is varied from 2 to 6 m, with a step of 1 m.

6.1.3.3 The Reference LFC at Green Energy Park(GEP) Solar Facility, Morocco

The Green Energy Park (GEP) is a solar energy testing, research, and training platform located in the city of Ben Guerir (32.2359° N, 7.9538° W) in Morocco. It was developed by the Research Institute of Solar Energy and New Energies (IRESEN) with the support of the Ministry of Energy and the OCP Group. The optical performance of the GEP Fresnel plant is here investigated. The North-South oriented solar field has an overall capacity of 1 MW_{el}. The primary receiver field, measuring 11434 m², is constituted by ten identical mirror rows (produced by Soltigua company), whereas the receiver unit is composed of an encapsulated absorber tube (manufactured by Archimede Solar Energy) and a secondary concentrator of CPC type. All the geometric parameters used for FresnelSim simulations are described in Table 6.1.

Table 6.1 Geometric parameters of the GEP linear Fresnel plant used for simulations

Parameter	Value
Length of the field (which is equal to the mirror length)	$L_f = 12.34$ m
Width of the field	$W_f = 8.05$ m
Number of mirror rows	$N_{mir} = 10$
Width of mirrors	$W = 0.625$ m
Spacing between adjacent mirrors	$g = 0.20$ m
Radius of curvature of mirrors	$r = 9.05$ m
Height of the receiver tube	$H_t = 4$ m
Aperture width of the secondary reflector (CPC type)	$A_{PCPC} = 0.318$ m
Acceptance angle of the CPC profile	$\theta_a = 0.778$ rad (44.576°)
External radius of the absorber tube	$r_1 = 0.035$ m
Internal radius of the absorber tube	$r_2 = 0.0625$ m
Tracking error	$\sigma_{te} = 1$ mrad
Angular deviation of the reflection vector	$\lambda_{surf} = 2$ mrad

All these quantities were available and have been verified through in situ measurements except for the radius of curvature of the mirrors (r) that was not indicated in datasheets. During the visiting period of the authors at GEP, the exact value of mirror curvature (constant for each row) has been measured using a centesimal comparator (0.01 mm accuracy) as shown in the photo (Figure 6.7).

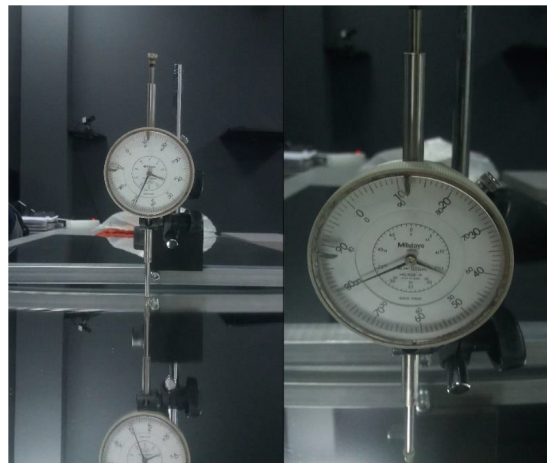


Fig. 6.7 Centesimal comparator and in-situ measurements of the mirror curvature at GEP facility during Authors' visiting period.

The optical properties of the reflective plant elements, i.e. absorptivity (α), transmissivity (τ), and reflectivity (ρ), are reported in Table 6.2. It is useful to remind that they are assumed constant

during simulations. The glass cover reflectivity is set to zero to simulate an anti-reflective coating; however, the reflectivity of the receiver (absorber tube + glass cover) is taken into account as only 95% of rays hit the tube (due to the absorber tube reflectivity).

Table 6.2 Optical properties of the GEP linear Fresnel plant components used for simulations

Component	Absorptivity (α)	Transmissivity (τ)	Reflectivity (ρ)
Primary reflectors	0.06	0.00	0.94
Glass Cover	0.04	0.96	0.00
Absorber tube	0.95	0.00	0.05
Secondary reflector (CPC type)	0.10	0.00	0.90

6.1.3.4 Validation and Verification of Previous Assumptions of the Model

FresnelSim model has been validated against ray-tracing results by Tonatiuh software, an open-source Monte Carlo ray trace for energetic and optical simulations of CSP plants (Blanco et al., 2005). Since FresnelSim works as a Monte Carlo simulation, a preliminary analysis of results accuracy as a function of the number of rays simulated (N_{rays}) is necessary. The most appropriate number of rays for simulations has been selected by comparing the instantaneous optical efficiency (η_{opt}^I), for three reference days (equinox and solstices) with a 15 min timestep. At each simulation run, η_{opt}^I has been calculated by simulating 100,000 rays per each mirror; then, starting from 10 rays per mirror and iteratively increasing this value at each simulation run. The relative difference between the exact value and the calculated one has been evaluated according to Eq. 6.36:

$$\varepsilon_j = \frac{|\eta_{opt, N_{rays}=j}^I - \eta_{opt, N_{rays}=100000}^I|}{\eta_{opt, N_{rays}=100000}^I} \quad (6.36)$$

As a result, $N_{rays} = 5000$ turned out to be a suitable trade-off between results accuracy and short computational times, being the relative difference ε_j less than 1%.

The software validation against Tonatiuh has been carried out by setting the same environment parameters except for sun shape. As it has been highlighted in the previous section, in FresnelSim the rays are initialized directly on the mirrors to reduce the computational time, thus neglecting the sun shape effects. On the contrary, the Tonatiuh simulations are performed assuming the Buie sun model. The comparison between FresnelSim and its benchmark is done for plane mirror geometry, and the figure of merit is the optical efficiency (η_{opt}^I). The simulations are run for three selected days: spring equinox ($N_{day} = 79$), summer solstice ($N_{day} = 171$), and winter solstice ($N_{day} = 355$). The discrepancy between η_{opt}^I obtained with FresnelSim and

Tonatiuh, respectively, is represented in Figure 9 in terms of percentage difference (Δ) during the three selected days. The dashed lines represent the average daily value of Δ . The results evidence that the daily average difference is less than 1.5%, with a peak of 3.5% occurring at 13 pm on day 171, which is largely acceptable. Furthermore, these results confirm that, in the present case, the angular sunshape errors do not impact significantly the optical efficiency calculations.

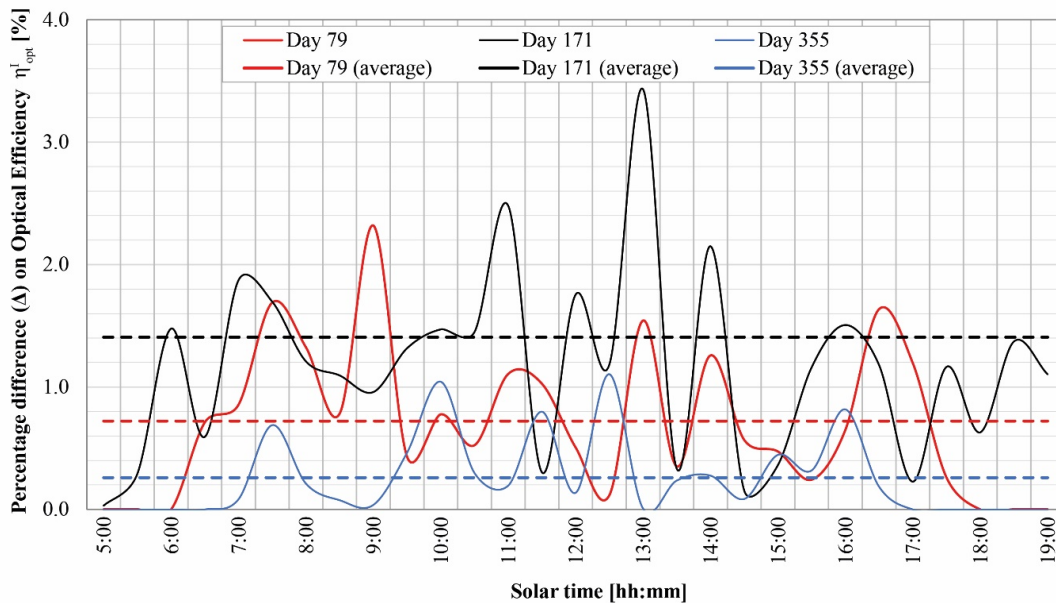


Fig. 6.8 Percentage difference between optical efficiency (η_{opt}^I) as calculated by FresnelSim and Tonatiuh (flat mirrors).

Finally, it has been performed a verification of the previously defined assumptions concerning tracking and mirror surface errors. A given primary reflection error (λ_{surf}) and a tracking error (σ_{te}) are defined. In this case, the GEP facility geometry is considered, including the curvature of primary mirrors. The aim is to check the validity of the FresnelSim main working mode (e.g. “perfect tracking and mirrors surface”) as compared to the efficiency results obtained for the non perfect case (random errors applied to the \vec{r} vector and to the ideal tilt angle of mirrors). The angular deviation λ_{surf} it is supposed to be of 2.0 mrad, coherently with recent studies (Abbas et al., 2018; Cumpston and Coventry, 2017; Tsekouras et al., 2018), whereas the tracking error σ_{te} has been set to 1.0 mrad according to Zhu (2013). The figure of merit is again the optical efficiency (η_{opt}^I) for three selected days, Nday=79, 171 and 355. The difference between η_{opt}^I obtained with the perfect reflection and tracking assumption with respect to the non-perfect condition is presented in Figure 6.9 in terms of percentage difference (Δ) during the three selected days. The results show that the daily average difference is less than 0.8%, thus demonstrating, in this study case, the capability of the secondary mirror to efficiently collect most rays irrespective of possible primary surface deformities.

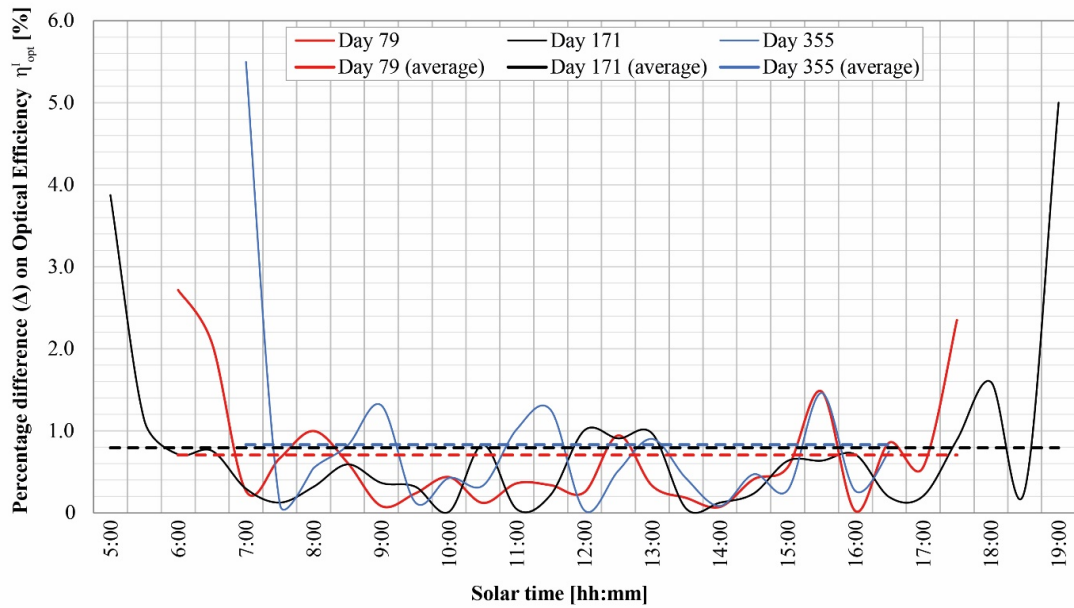


Fig. 6.9 Percentage difference between optical efficiency (η_{opt}^I) considering perfect reflection and tracking and by introducing angular reflection error ($\lambda_{surf}=2$ mrad) and tracking error ($\sigma_{te}=1$ mrad).

6.1.4 Results and Discussion

6.1.4.1 Model Results related to GEP Geometry

The performance of the Green Energy Park (GEP) Fresnel plant has been evaluated over a time horizon of one year. Concerning the optical efficiencies η_{opt}^I and η_{opt}^{II} , the results show a peak efficiency at day 171 (summer solstice) when their daily average value is of 0.72 and 0.67 respectively for receiver aperture area and absorber tube energy collection, on the other hand, during the winter solstice (day 355) the optical efficiencies do not exceed 0.38 and 0.35 respectively. The yearly optical efficiency of the plant, calculated by averaging the daily values, is equal to 0.51 for the receiver aperture area and 0.49 for the absorber tube. Figure 6.10 shows the daily trend of η_{opt}^I and η_{opt}^{II} during the three reference days (day 79, day 171, and day 355). Clearly, η_{opt}^{II} is always lower than η_{opt}^I due to multiple reflections inside the secondary reflector (whose reflectivity is lower than the unity) and rays arriving outside the acceptance angle. It can be observed that, in this case, the instantaneous peak efficiency (calculated with a 10 minutes timestep) η_{opt}^I is equal to 0.87 at the summer solstice, with three equivalent peaks at 9:00, 12:00 and 15:00. Concerning the other reference days, the maximum value is not reached at noon, when LFC are typically tested. The best efficiency, in days 79 and 355 is reached about 2-3 hours before and after noon as it is evidenced by the arrows. The peak value in day 355 is 0.51, which is 18% higher than the value at noon, whereas for day 79 is 0.73, exceeding by 7% the instantaneous optical efficiency at 12:00. This is mainly due to the secondary receiver shadow onto the mirrors below it.

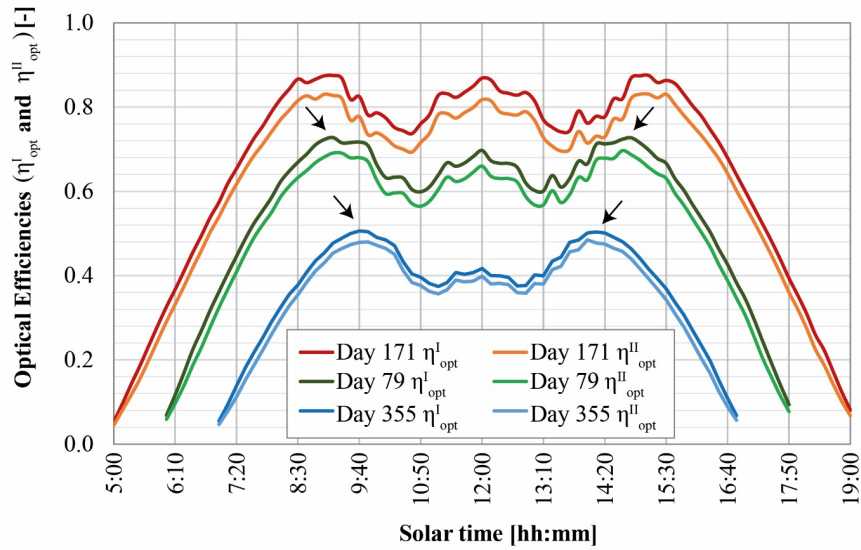


Fig. 6.10 Instantaneous optical efficiencies η_{opt}^I and η_{opt}^{II} during the reference days. Timestep is 10 minutes.

Three auxiliary efficiencies have been introduced to study separately the influence of blocking, shading from adjacent mirrors, and shading by the top receiver effects:

$$\eta_{Block} = 1 - \frac{N_{Block}}{N_{rays}} \quad (6.37)$$

$$\eta_{Shad} = 1 - \frac{N_{Shad}}{N_{rays}} \quad (6.38)$$

$$\eta_{Shad,CPC} = 1 - \frac{N_{Shad,CPC}}{N_{rays}} \quad (6.39)$$

where N_{Block} , N_{Shad} , and $N_{Shad,CPC}$ are respectively the numbers of abandoned rays due to blocking, shading from adjacent mirrors, and shading from the receiver structure. Figure 6.11 shows the three auxiliary efficiencies during day 355, when the optical losses are higher due to the lower inclination of sun rays.

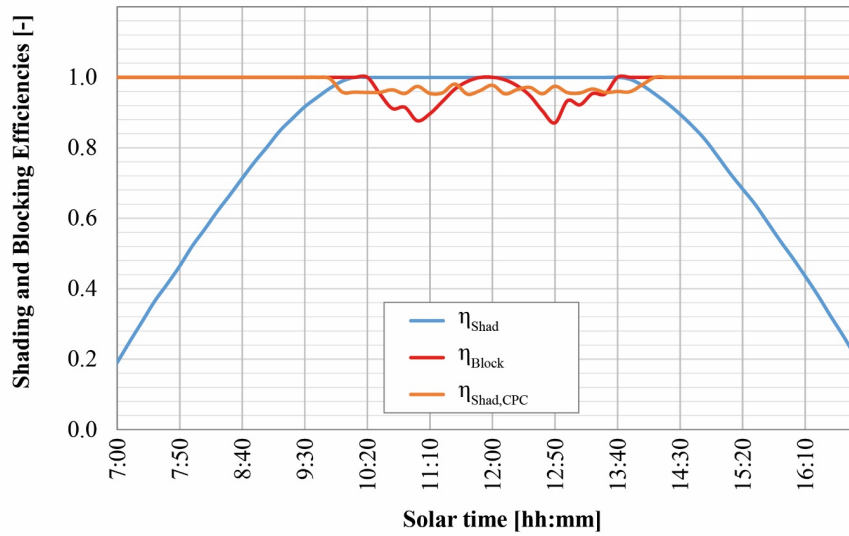


Fig. 6.11 Instantaneous blocking, shading by adjacent mirrors, and shading by receiver efficiencies during day 355. Timestep is 10 minutes.

This trend is also confirmed by the mirror-by-mirror analysis in Figure 6.12, where the optical efficiency η_{opt}^I is evaluated during day 355 for every single mirror. The numbering starts from the mirror under the receiver (Mirror 1, M1) to the easternmost one (Mirror 5, M5). It is useful to specify that the trend is exactly symmetrical for mirrors from 6 to 10, which are not displayed for the sake of clarity. In particular, every mirror shows a local minimum during the day, which is due to the receiver shadow.

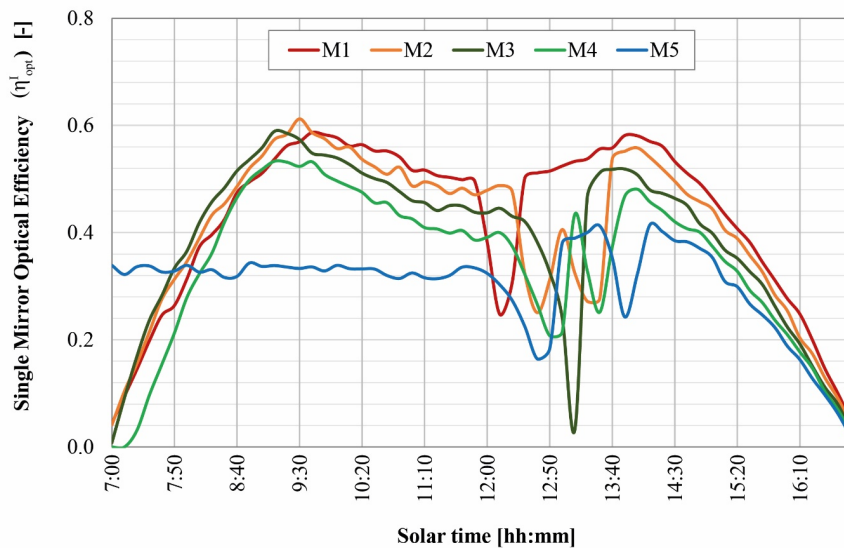


Fig. 6.12 Mirror by mirror optical efficiency (η_{opt}^I) during day 355. Timestep is 10 minutes.

6.1.4.2 Optimization of Mirrors' Gap and Receiver Height

In order to optimize the design of an LFC, it is not sufficient to account only for η_{opt}^I and η_{opt}^{II} , since they are not directly related to DNI. In this section, the results are presented considering not only η_{opt}^I and η_{opt}^{II} , but also η_{en}^I , η_{en}^{II} , η_{en}^{III} , and η_{en}^{IV} , which take into account the energy arriving at the aperture area of the receiver (Ap_{CPC}) and the absorber tube.

Firstly, it has been verified that the expression used for the DNI calculation (Eq. 6.31) was consistent with the hourly distribution of Direct Normal Irradiance provided by Meteonorm software as TMY (Typical Meteorological Year) data for the real plant location (Ben Guerir, Morocco, 32.2359° N, 7.9538° W). Six days over a year have been compared, analyzing the DNI hourly values from Meteonorm (DNI_{MN}) and the ones arising from Fresnelsim adopted correlation (DNI_{FS}). Figure 13 shows the comparison for day 91 (the same behavior is observed for the other days under consideration). In addition to DNI_{MN} and DNI_{FS} of day 91, also the maximum daily values of days near the reference one (the 5 previous and following days) are plotted. The choice of using Eq. 6.31 is related to the need of selecting representative sunny day conditions during the year. On the contrary, TMY data also include overcast conditions. Figure 6.13 shows that the selected clear sky model properly represents DNI distribution over a day, particularly considering the maximum daily value within the selected range.

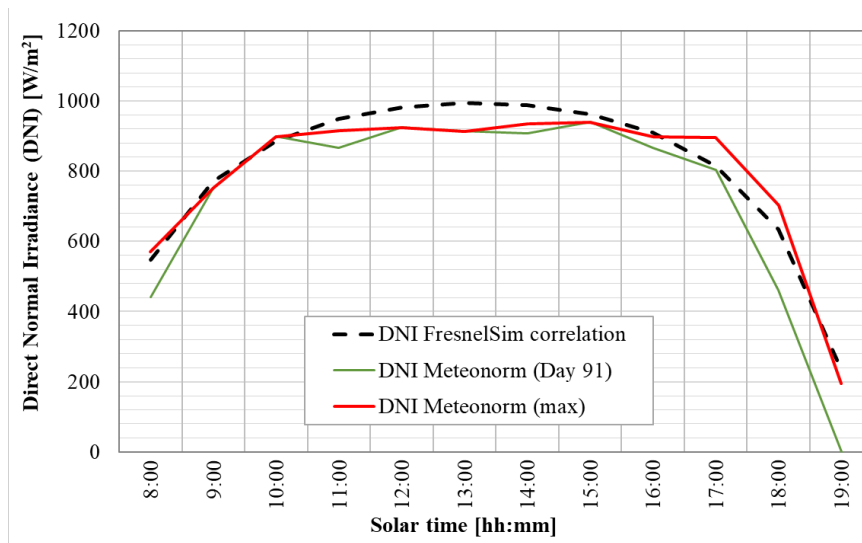


Fig. 6.13 DNI distribution comparison between FresnelSim calculation (DNI_{FS}) and Meteonorm software (DNI_{MN}). The reference day is n°91.

Concerning the gap variation, the spacing between adjacent mirrors has been varied from 0 to 0.5 m (with a step of 0.1 m, including 0.05 m as bottom value) while maintaining the receiver height equal to 4 m. The trend of the six defined efficiencies has been studied for the three selected reference days (day 79, day 171, and day 355), observing the same trend. The results are shown in terms of average daily efficiency in Figure 6.13 for day 79.

Concerning the aperture area of the receiver, to which η_{opt}^I and η_{en}^I are related, the average daily peak efficiency is reached for a gap equal to 0.3. This means that 0.3 m spacing is the best condition to minimize optical losses due to shading and blocking (mirrors are properly distanced), while maintaining a proper focal distance, and to maximize energy concentration per net mirror area. On the contrary, if we refer to the absorber tube the best value for η_{opt}^{II} and η_{en}^{II} is 0.1 m. This difference is due to the fact that increasing the mirror spacing it would be necessary to modify the acceptance angle of the compound reflector (θ_a) since for 0.3 m some rays are lost due to back reflection and they do not reach the absorber tube.

Finally, concerning η_{en}^{III} and η_{en}^{IV} , they are related to the gross area of the primary mirror field. The maximum efficiencies in terms of incident energy per gross area are reached when the gap is 0 m (which is only an ideal value since for constructive reasons the minimum spacing could be at least 0.05 m). This is an interesting point to be further explored especially for applications where the minimum land use is necessary as, for example, in building integration of Fresnel on roofs.

It is also useful to notice that gap variation primarily influences optical losses due to shading from adjacent mirrors. By comparing 0 m case with 0.5 m, the daily average number of rays affected by mirror shading halves (from 29% to 14% respectively). On the contrary, shading from the above secondary mirror remains within 2% and blocking varies only from 3% to 2% as the gap is changed in the selected range.

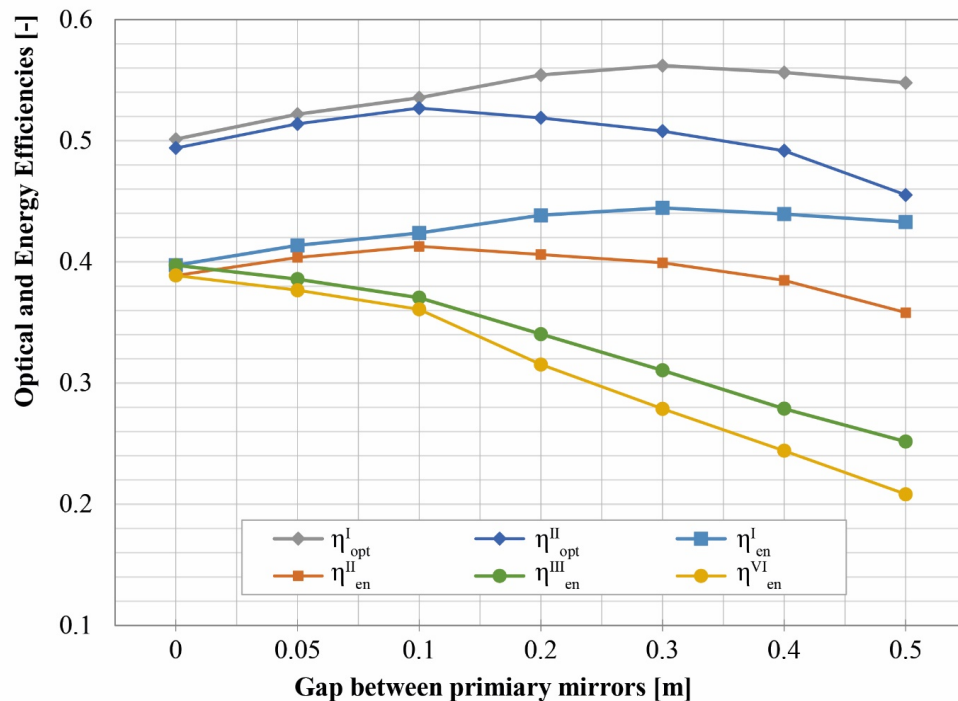


Fig. 6.14 Variation of LFC efficiencies as a function of the spacing between adjacent mirrors (gap). The reference day is n°79.

From the previous considerations, the best horizontal spacing for mirrors has been selected to be 0.3 m. It is worth noticing that this choice has been motivated by the fact that the optimization of the secondary reflector geometry is beyond the objectives of this paper, and land use minimization is assumed not crucial in this case. The receiver height has been varied from 2 m to 6 m (with a step of 1 m). By plotting the trend of the six defined efficiencies during reference days (day 79, day 171, and day 355), it can be observed that, differently from the gap variation, the maxima are not reached for the same height. The maximum value of energy arriving at the aperture of the Central Receiver (A_{pCPC}) and at the absorber tube varies from 3 m to 5 m depending on the day. Further simulations by varying Ht within this range (3, 4, and 5 m) have been conducted considering 25 days over a year (two per month plus the summer solstice). The results are shown in Figure 6.15 and 6.16 in terms of energy arriving at the aperture plane (A_{pCPC}) and at the tube, respectively. From Figure 6.15, it can be observed that the maximum energy is obtained with Ht=3 m, except for the days in between day n°105 and day n°244 (see arrows in the Figure), when the height 4 m performs better.

Figure 6.16 refers to the energy on the receiver tube: in this case, Ht=5 m maximizes the energy arriving at the tube during the central days of the year, whereas the height 3 m provides better performance during winter, late autumn, and early spring.

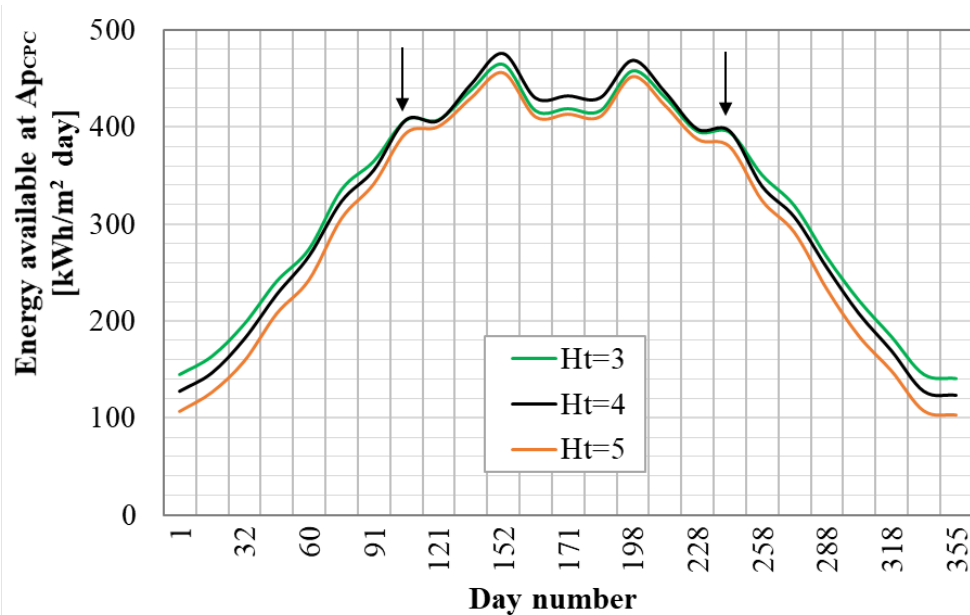


Fig. 6.15 Energy arriving at the receiver aperture area (A_{pCPC}) in a day by varying the receiver height.

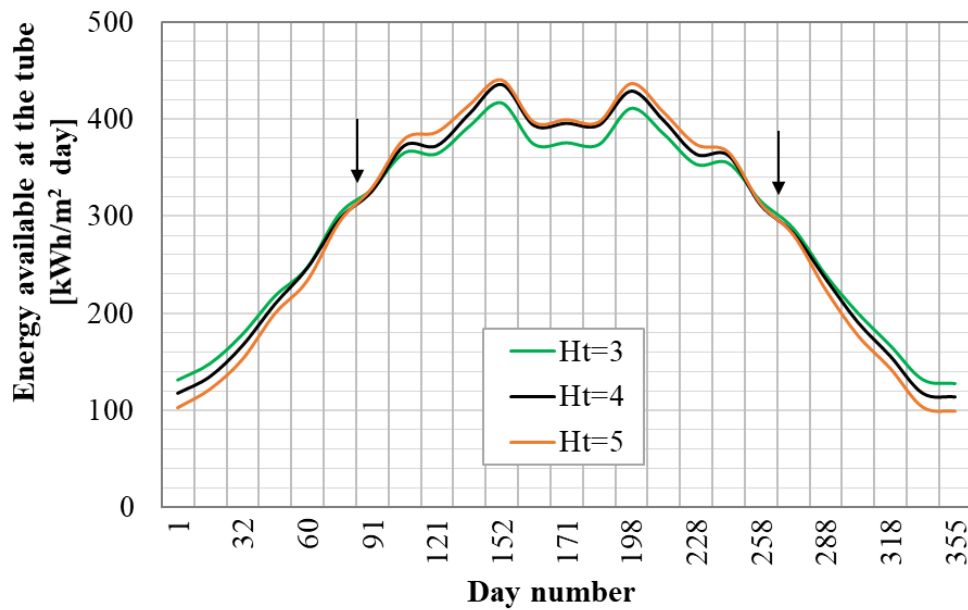


Fig. 6.16 Energy arriving at the absorber tube in a day by varying the receiver height.

Based on the above evidence, it can be concluded that depending on sun rays inclination, the optimum receiver height varies: lower heights maximize the picking up of more inclined rays, whereas a higher receiver is more efficient when the sun is closer to the zenith. Concerning the difference between the 4 and 5 m as an optimum condition related to the aperture area and to the tube, respectively, it can be noticed that the CPC type reflector better performs with less inclined rays due to the least amount of secondary reflections (energy is lost at any reflection). Finally, it can be noticed that by varying Ht from 2 to 6 m during the three reference days, the optical losses due to shading and blocking differ only by 1%.

6.1.5 Conclusions

In the present work, a new 3D model for ray-tracing analyses has been developed in order to investigate the optical and energy performance of Fresnel collectors. The in-house ray-tracing software (named FresnelSim) was conceived for taking into account the primary and secondary mirror curvatures and for precisely describing shading, blocking, and end effects. The validation of the model have been made against the well known Tonatiuh software and the agreement in terms of optical efficiency was, as an average, within 1.5%. The present analysis was firstly addressed at investigating the theoretical performance of a real Fresnel plant, located in Morocco at the Green Energy Park of Ben Guerir. It was found that the yearly average optical efficiency of the field is 0.51 and the average daily peak value is close to 0.70, occurring at the summer solstice. Then, a parametric analysis was performed on the reference geometry by acting on secondary mirror height and primary mirror gap. To this aim, six different optical and energy efficiencies were introduced to optimize LFC performance. The results highlighted the

importance of a proper plant efficiency definition, as some currently used formulations only give incomplete information. It was shown that less distanced mirrors allow the energy per gross area to be maximized, whereas a gap of 0.3 m (10 cm more than initial configuration) is the best arrangement to maximize the radiant energy impinging on the receiver aperture area, if we refer to the net area of mirrors. The variation of the receiver height has revealed that there is not a unique optimum value all over the year. Lower heights are generally more favorable with more inclined sunrays (autumn to spring), whereas a higher receiver position improves the LFC performance from spring to autumn, according to peculiar performance patterns that have been presented based on a 25 days per year resolution.

Paper 7³

6.2 Calculation of the Incidence Angle Modifier of a Linear Fresnel Collector: the Proposed Declination and Zenith Angle Model compared to the biaxial factored approach

Abstract

Since their first appearance as a contribution by Professor Francia at the University of Genova, Italy, the Linear Fresnel Collectors (LFC) demonstrated to be an engineering efficient technology for medium to high temperature solar applications. The strength of the LFC concept is related to the simple mirror motion law, to the compactness of the mirror fields (power to land surface ratios), to the lowest resistance to wind, to the system intrinsic scalability. To perform reliable LCOE analyses, robust performance simulation tools are needed. The Authors developed to this aim a 3D ray-tracing model, able to account for shading, blocking, and end effects as a function of LFC geometry, including primary and secondary mirror curvatures. In this paper, a new approach is implemented to reduce huge yearly ray-tracing datasets and provide very compact analytical equations for fast hourly performance simulations. The present model introduces new Incidence Angle Modifier (IAM) correlations based on the declination and zenith angles. The new model demonstrated to fit sub-hourly 3D ray-tracing data all year long with an overall error lower than 1.5%, well below the best IAM factored models here compared as a general criticism to the biaxial factored approach related to Fresnel applications.

Keywords

Linear Fresnel Collector; Optical and Energy efficiency; Incidence angle modifier; Ray-tracing simulation; Correlation Analysis

6.2.1 Introduction

Global utilization of fossil fuels is resulting in critical environmental problems and energy decarbonization is essential. Renewable energies play a key role to convert energy systems into net-zero-carbon. Among the different resources, solar energy represents a promising alternative to fossil fuel thanks to its abundance, cost-effectiveness, and multiple conversion technologies. Concentrating solar power (CSP) plants have recently gained interest for medium to high thermal processes (Calderón et al., 2021). Stationary non-concentrating collectors reach temperatures for domestic use, but for industrial processes, absorption chillers, and thermodynamic conversion

³Please note that in the current manuscript, certain sections of the published version of this article have been slightly reduced to avoid repetitions, as it was designed as a continuation of **Paper 6**

temperatures higher than 100-200°C (El Gharbi et al., 2011), concentration is necessary for working at high efficiencies (Beltagy et al., 2017). The International Energy Agency (IEA) reports that CSP generation grew by 34% in 2019, with an increase of the installed capacity by 600 MW_{el} (Price and Summers, 2004). Nevertheless, CSP worldwide are still a few, and further research is needed to make them competitive. The three main CSP technologies are parabolic trough (PT), solar tower (ST), and linear Fresnel (LF) systems (Santos et al., 2018). In the Literature, many comparative studies analyse advantages and disadvantages of each technology (Kuravi et al., 2013; Lovegrove and Stein, 2012; Raboaca et al., 2019; Siva Reddy et al., 2013). Parabolic trough and Linear Fresnel reflectors are linearly focusing systems as they reflect and concentrate solar radiation on a linear receiver (Desai and Bandyopadhyay, 2017). PT systems track the sun position with a parabolic mirror structure, whereas in LF collectors (LFC) the parabolic mirror shape is split up into mirror facets according to the non-imaging Fresnel lens principle. Nowadays, Linear Fresnel technology is underdeveloped compared to PT but, thanks to its low construction and maintenance costs, they are one of the most promising CSP systems (Barlev et al., 2011). Conversely, since Fresnel Reflectors cannot be constantly adjusted to point at Sun, they have lower optical efficiency, and their concentration factor (i. e. the ratio of mirror aperture to the absorber tube diameter) typically ranges between 40 and 80 compared to 80-90 of PTC (Manikandan et al., 2019).

The Optical Efficiency (η) of a Linear Fresnel Collector can be defined in different ways, as recently discussed by this research group (Fossa et al., 2021). LFCs typically have lower optical efficiencies compared to PTCs due to optical losses (cosine losses, shading and blocking, end effects). In Literature, significant research has been done on LF optimum design to improve optical efficiency and minimize losses (Abbas et al., 2017; Bellos et al., 2019; Elmaanaoui and Saifaoui, 2014; Mills and Morrison, 2000; Montes et al., 2012; Pu and Xia, 2011; Sharma et al., 2016, 2015). Singh et al. (1999) studied the optical efficiency of an LFC by varying the number of mirror rows, considering 10, 15, and 20 stripes, and the spacing between. The Authors studied in details the optical performance of an existing Fresnel plant in Morocco and performed a parametric analysis by varying the spacing between mirrors and the receiver height (Fossa et al., 2021). Boito and Grena (2016) optimized the plant geometry with respect to the focal length of primary mirrors.

The optical performance evaluation of a LF plant is a complex problem depending on geometry and many other parameters. The majority of these studies relies on ray-tracing software instead of analytical approaches. Some of the most used ray-tracing software tools are Tonatiuh (Blanco et al., 2005), OptiCAD (Di Lauro et al., 2008), OTSun (Cardona and Pujol-Nadal, 2020), SolTrace (Wendelin, 2003). However, many researchers developed their own codes to overcome possible limitations of commercial tools (Cheng et al., 2013; Pulido-Iparraquirre et al., 2019). The Authors themselves implemented a 3D ray-tracing model, named FresnelSim, specifically devoted to the optical performance of LFCs, which has been fully described in Fossa et al. (2021).

In general, ray-tracing techniques are very robust, but year-long hourly analyses require huge datasets to be post-processed, and computation time can be definitely long. To decrease computational time, the optical performance can be described through the Incidence Angle Modifier (IAM). The IAM is defined as the ratio between the optical efficiency at a certain sun position and the optical efficiency at normal incidence (Karathanasis, 2019). In collectors that are symmetrical about the collector normal, such as PTC, the IAM is usually expressed through a polynomial equation (Lovegrove and Stein, 2012). Contrarily, for non-imaging collectors as LFCs the IAM is a complex function depending on many factors (Horta and Osório, 2014). A commonly accepted approach is factorization, as it was proposed for the first time by McIntire (1982) with his semi-experimental study on a non-imaging cusp concentrator. The IAM function can be determined as the product of its transversal (IAM_T) and longitudinal (IAM_L) components. Instead of obtaining data (either experimentally or from ray-tracing) for the entire hemisphere above the collector aperture, it is expected to be sufficient to evaluate IAM_T and IAM_L at various incidence angles to obtain the factored approximation of the IAM. Many studies have been devoted to developing models that perform a good approximation of the transversal and longitudinal components of the Incidence Angle Modifier (Horta and Osório, 2014; Rönnelid et al., 1997). In particular, Bellos and Tzivanidis (2018) proposed a set of analytical expressions, based on simple geometric parameters, to predict the longitudinal and transversal IAM in LFC as an alternative ray-tracing. However, as Hertel et al. (2015) highlighted the traditional factored approach inherently introduces errors by factorizing non factorable phenomena such as cosine losses. In LFC, the shading, blocking, cosine and end losses, multiple reflections within the secondary reflector play a key role in the variation of the optical efficiency with the incidence angle. All these issues can be fully described by robust, but computationally intensive, ray-tracing tools, whereas the factored approach fails in the accuracy, especially when these effects are remarkable (e. g. very small spacing between adjacent mirrors).

The objective of this research is to present new Incidence Angle Modifier (IAM) correlations based on solar declination and zenith angles and to compare the results to the factored IAM values as a general criticism. The 3D ray-tracing software developed by the Authors (FresnelSim) is used to perform year-long subhourly analyses of the optical performance considering different LFC geometries. The factored IAM, obtained through ray-tracing along the transversal and longitudinal axes, is compared to the analytical approach proposed by Bellos and Tzivanidis (2018). Finally, based on yearly ray-tracing simulation data, the new model is proposed to reduce the computation effort through a simple analytic expression able to precisely provide efficiency estimations and energy yield predictions.

6.2.2 Modelling the Linear Fresnel System and Define its Figures of Merit

The following sections address the primary aspects related to the modeling and performance evaluation of Linear Fresnel Collectors (LFCs). Detailed explanations of LFC design, modeling,

and the operating principles of the developed in-house code (FresnelSim) can be found in the previous publication (Paper 6), specifically in sections 6.1.2, 6.1.2.1, and 6.1.2.2. To avoid redundancy within this manuscript, these aspects are not reiterated here. For further clarification, the reader is encouraged to refer to the original published version of the article at <https://doi.org/10.1016/j.renene.2021.12.017>.

6.2.3 The 3D Optical Model of a Linear Fresnel Concentrator and Efficiency Definitions

Before starting the discussion about the Incidence Angle Modifier (IAM), it is useful to clarify the definition of optical efficiency. Many studies related to field design optimization have attempted to minimize optical losses such as shading and blocking effects. However, this approach may not be the most appropriate. For example, very narrow and well-spaced mirrors show the lowest amount of blocking and shading phenomena, but this configuration does not necessarily maximize energy collection and is not ideal for land use.

The optical efficiency of the Linear Fresnel Collector (LFC) can be investigated, from a purely geometric point of view, by considering the ratio between the incident rays on the absorber tube with respect to the generated rays (N_{rays}) on the field of mirrors (where N_{mir} is the number of mirrors) as in Eq. 6.40:

$$\eta_{opt} = \frac{\sum \text{Rays on tube}}{N_{rays} \cdot N_{mir}} \quad (6.40)$$

Clearly, η_{opt} is higher when shading and blocking are minimized. However, since the daily energy distribution is variable, and these effects mainly occur when the rays are more inclined (i.e., in the morning and late afternoon), this only provides partial indications about the real plant performance. For introducing a more proper "opto-energy" efficiency, a given amount of energy has to be associated with each j^{th} ray ($E_{r,j}$). In FresnelSim, this quantity is calculated as in Eq. 6.41:

$$E_{r,j} = \frac{E_{DNI} \cdot A_{mir} \cdot \eta_{cos,i}}{N_{rays}} \quad (6.41)$$

where E_{DNI} is the direct normal irradiance, A_{mir} is the single mirror area, and $\eta_{cos,i}$ is the well-known "cosine efficiency" (i.e., the cosine of the i^{th} mirror zenith angle). According to the Authors, a more complete and useful optical efficiency definition is through Eq. 6.42:

$$\eta_{opt-ene} = \frac{\sum_{j=1}^{N_{tube}} E_{r,j}}{E_{DNI} \cdot A_{gross}} \quad (6.42)$$

where N_{tube} is the number of rays reaching the absorber tube, E_{DNI} is the direct normal irradiance, and A_{gross} is the gross area (including the gap between mirrors) of the mirror field. It is worth noticing, while referring to the Direct Normal Irradiance (DNI), that the system is compared to a full tracking receiver always facing the sun disk. Furthermore, it is important to stress that often optical efficiency is related to the net mirror area ($A_{mir,tot}$). Nevertheless, in such a way, the land-use issue, which may be very important in applications where minimum land use is required (for example, in building integration), is not included. As defined in Eq. 6.42, $\eta_{opt-ene}$ expresses the ratio between the energy flux to the absorber and the normal incidence energy flux on the gross area of the mirror field, which is the most suitable indicator to perform optimization studies.

6.2.4 The Case Study and the Geometry Optimization

The object of study of this research is an existing Linear Fresnel Collector located at the Green Energy Park (GEP) in Ben Guerir (32.2359° N, 7.9538° W), Morocco (for the detailed description please refer to Section 6.1.3.3 in Paper 6, or to the original publication).

The LFC optical performance assessment has been conducted over a time horizon of one year with FresnelSim ray-tracing. Furthermore, a parametric analysis by varying the gap between the mirrors as well as the height of the absorber tube has been performed to suggest an optimized plant geometry (C1) with respect to the current one (C0). The new design maximizes $\eta_{opt-ene}$ which is not the best in C0.

Figure 6.17 shows the variation of the optical-geometric efficiency, as defined in Eq. 6.40 (η_{opt}), and of the (more suitable) opto-energy efficiency, as defined in Eq. 6.42 ($\eta_{opt-ene}$), as a function of the gap between mirrors. The day shown in Figure 6.17 is day 79 for the sake of conciseness, but the same trend could be observed all over the year as it is described in Paper 6. The spacing of mirrors has been varied from 0 to 0.5 m with a step of 0.1 m, including 0.05 m as the minimum value due to cleaning and maintenance. As it can be noticed, in the current configuration (C0) the gap is 0.2 m which is very efficient in terms of η_{opt} . However, 0.05 m gap is better in terms of $\eta_{opt-ene}$, despite having more optical losses due to the reduced spacing between mirrors.

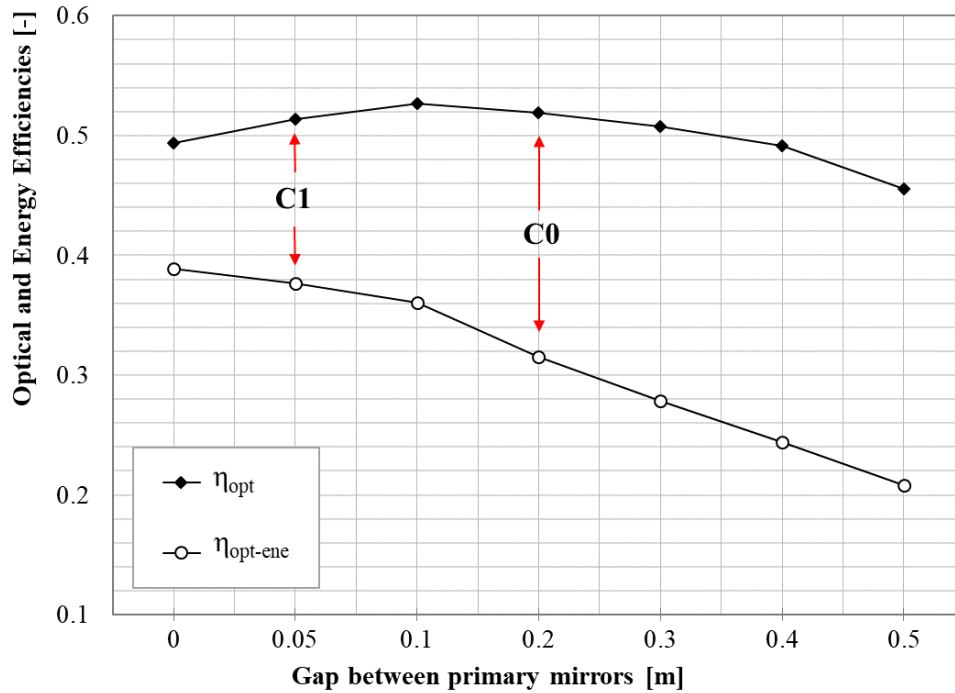


Fig. 6.17 Variation of LFC efficiencies (η_{opt} and $\eta_{opt-ene}$) with the spacing between adjacent mirrors (gap) for day n°79 (Ben Guerir, Morocco).

Once the gap has been set to 0.05 m also the receiver height is varied from 2 m to 6 m (4 m is the current value of C0). Through year long ray-tracing simulations, it was found that the best $\eta_{opt-ene}$ is reached for H=3 m.

The evaluation of the LFC optical performance and of the Incidence Angle Modifier, discussed in the next section, is related to configurations C0 and C1.

6.2.5 The Incidence Angle Modifier in LFC and the Biaxial Factored Approach

Besides optical efficiency, the varying performance of a solar collector with sun position can be described through the Incidence Angle Modifier (IAM). The IAM indicates the variation of the opto-energy efficiency with the solar incidence angle, i.e. the angle between the sun vector with respect to the normal to the collector aperture plane. This variation is expressed, as in Eq. 6.43, in relation to a specific reference solar angle (which can differ depending on the collector type and application).

$$IAM = \frac{\eta_{opt-ene}(\theta)}{\eta_{opt-ene}(\theta_{ref})} \quad (6.43)$$

where $\eta_{opt-ene}(\theta)$ is the opto-energy efficiency at an arbitrary angle of incidence, and $\eta_{opt-ene}(\theta_{ref})$ is the one with respect to the selected reference solar angle. Worth noticing, when

the field of primary mirrors lies on the horizontal plane (as in the present study and in most of existing LF plants), the angle of incidence coincides with the solar zenith angle (θ), depending in turn on declination and hour solar angles, δ and ω respectively. Secondly, the denominator represents the (expected) maximum opto-energy efficiency that is reached at a normal particular incidence angle (θ_{ref}) that in this case is 0° . This is why the IAM normally varies from 0 to 1.

Based on this definition of IAM (Eq. 6.43), it is possible to perform ray-tracing simulations to calculate the overall incidence angle modifier (IAM_{RT}) and to infer the energy yield at the receiver along the year. To this aim, it is sufficient (and necessary) to know the maximum opto-energy efficiency of the system and the corresponding values at given different sun positions. Besides ray-tracing, the opto-energy efficiency values could be also inferred through experimental data. Nevertheless, obtaining hourly datasets over a year through measurements or ray-tracing is extremely time consuming and, as a consequence, the factored approach is often adopted.

Unlike PTCs and flat plate collectors whose optical efficiency is symmetrical about the collector normal, the IAM of non-imaging LFCs shows a biaxial behavior that requires specification of proper transversal and longitudinal angle modifiers. These last are related to the transversal and longitudinal incidence angles, identified in Figure 6.18 as θ_T and θ_L , and representing the projection of the solar zenith angle in the transversal and longitudinal directions, respectively.

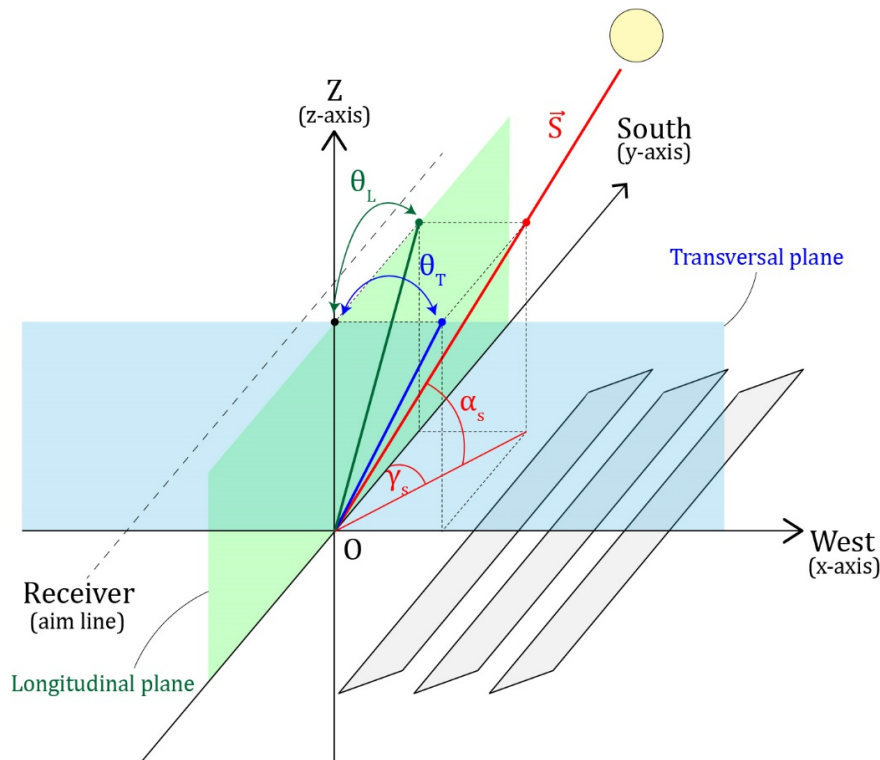


Fig. 6.18 Schematics of the transversal (θ_T), and longitudinal (θ_L) angles in a LFC where the primary mirror aperture plane is horizontal.

An accepted practice, despite intrinsically introducing an error (Hertel et al., 2015), is the factored approximation for biaxial incident angle modifiers proposed for the first time by McIntire (1982). The factored IAM (indicated from now on as IAM_{FA}) value at a specific incidence angle is the product of the corresponding transversal and longitudinal incidence angle modifiers, as in Eq. 6.44.

$$IAM_{FA}(\theta_T, \theta_L) = IAM_T(\theta_T, 0) \cdot IAM_L(0, \theta_L) \quad (6.44)$$

The main advantage of the factored approach is that the IAM is evaluated only for a limited number of incidence angles, inferring the other values through the factorization of the two components.

According to Pujol Nadal and Martínez Moll (2012), the transversal and longitudinal components of the IAM can be expressed through Eq. 6.45 and Eq. 6.46.

$$IAM_T(\theta_T, 0) = \frac{\eta_{opt-ene}(\theta_T, \theta_L = 0)}{\eta_{opt-ene}(\theta_{ref} = 0)} \quad (6.45)$$

$$IAM_L(0, \theta_L) = \frac{\eta_{opt-ene}(\theta_T = 0, \theta_L)}{\eta_{opt-ene}(\theta_{ref} = 0)} \quad (6.46)$$

$IAM_T(\theta_T, 0)$ and $IAM_L(0, \theta_L)$ can be both determined through ray-tracing and analytical expressions, as described in a recent paper by Bellos and Tzivanidis (2018). From now on we will denote the transversal and longitudinal angle modifiers obtained through ray-tracing as $IAM_{RT,T}$ and $IAM_{RT,L}$ respectively, and the ones obtained through the analytical approach presented in Bellos and Tzivanidis (2018) as $IAM_{B,T}$ and $IAM_{B,L}$.

For ray-tracing analyses (including the present FresnelSim one), two different simulations must be run. $IAM_{RT,T}$ is calculated by varying θ_T from 0° to 90° while maintaining $\theta_L = 0$. Likewise, $IAM_{RT,L}$ is calculated through the opposite process. In a few words, it is equivalent to run a simulation where the sun moves from East to West on the transversal plane and, in the opposite case, from South to North on the longitudinal plane. Once the opto-energy efficiency ($\eta_{opt-ene}$) is calculated for each transversal and longitudinal angle, its value is divided by the maximum opto-energy efficiency which is referred to the sun position at the zenith (i.e., in this case when $\theta_T = 0$ and $\theta_L = 0$). Then, through $IAM_{RT,T}$ and $IAM_{RT,L}$, it is possible to obtain the factored $IAM_{RT,FA}$ for each combination of (θ_T, θ_L) , namely for each sun position.

In the present study, the two series of ray-tracing simulations have been performed with FresnelSim for the two selected configurations of the Fresnel plant under consideration (C0 and C1). The ray-tracing results have been obtained by initializing 5000 rays on each mirror for each transversal and longitudinal angle from 0° to 90° with a step of 1° . The factored incidence angle modifier thus obtained ($IAM_{RT,FA}$) has been calculated as the product of the two components ($IAM_{RT,T}$, $IAM_{RT,L}$).

Besides ray-tracing, [Bellos and Tzivanidis \(2018\)](#) developed an interesting analytical model that allows the calculation of $IAM_T(\theta_T, 0)$ and $IAM_L(0, \theta_L)$ based on the main geometrical parameters of an LFC and trigonometric relationships. The strength of their model is related to the possibility of evaluating precisely the transversal and longitudinal component without relying on ray-tracing. For the sake of brevity, only the two main expressions for the calculation of $IAM_{B,T}$ (transversal) and $IAM_{B,L}$ (longitudinal) are provided here but the complete model is fully detailed in [Bellos and Tzivanidis \(2018\)](#). The two main phenomena affecting efficiency in the transversal direction are shading/blocking between mirrors and cosine effects. It is possible, again according to [Bellos and Tzivanidis \(2018\)](#), to express the transversal Incidence Angle Modifier ($IAM_{B,T}$) as in Eq. 6.47:

$$IAM_{B,T} = \eta_{rot} \cdot \eta_{shT} \quad (6.47)$$

where η_{rot} is the rotation optical loss and η_{shT} is the shading optical loss. Contrarily, the longitudinal component is influenced by the solar altitude angle γ_s , expressed as $\cos(\theta_L)$, and by the non-illuminated length of the receiver due to end effects. The longitudinal Incidence Angle Modifier ($IAM_{B,L}$) can be expressed as in Eq. 6.48 ([Bellos and Tzivanidis, 2018](#)):

$$IAM_{B,L} = \cos(\theta_L) - \frac{H}{L} \cdot 1 + \left(\frac{w}{4 \cdot H}\right)^2 \cdot \sin(\theta_L) \quad (6.48)$$

Worth noticing that to develop this analytical model, a series of assumptions have been made: primary mirrors are flat, primary mirror lies on the horizontal plane and rotates along the north to south direction, the secondary reflector shape is not considered, and blocking is not included in calculations.

Following the same approach as in ray-tracing, the factored IAM_{FA} surface deriving from the analytical model results $IAM_{B,FA}$ has been calculated for the two plant geometries (C0 and C1). The first part of the Results section is devoted to the comparison of the factored IAM resulting from the two different methodologies ($IAM_{RT,FA}$ and $IAM_{B,FA}$).

6.2.6 The Present Model for Sun Angle-Based Incidence Angle Modifier

As briefly noticed in the Introduction, the factored approach is very valuable to reduce yearly data collection despite introducing errors related to the factorization of non-factorable quantities ([Hertel et al., 2015](#)). The objective of this study is to provide an alternative interpretive scheme to reduce yearly datasets into a simple analytic expression. To this aim, the instantaneous opto-energy efficiency of the reference plant in both the configurations (C0 and C1) is evaluated through FresnelSim. The non approximated instantaneous value of the Incidence Angle Modifier (IAM_{RT}) is calculated based on Eq. 6.43. A total amount of 25 days, equally distributed along the year, have been chosen to perform daily simulations representing the yearly optical

performance. The timestep selected is 30 minutes and the number of rays initialized on each mirror is 5000. The main concept is to study the variation of the dependent variable of the problem (the instantaneous IAM_{RT}) with respect to a series of known “meaningful” variables (independent variables).

To find the correct independent variables, the daily variation of the instantaneous IAM_{RT} has been investigated towards a series of solar angles. The angles considered are the solar altitude (α_s), the azimuth (γ_s), the zenith (θ), the declination (δ) and the profile angle (α_p). The latter is the angle between the surface normal vector and the projection of the sun rays on a vertical surface normal to the same surface.

A scatter plot (with the angle on the x-axis and the IAM_{RT} on the y-axis) has been created to evaluate the correlation. The declination angle (δ) resulted the most appropriate one to represent the variation of the IAM_{RT} during the different days of the year. Indeed, the variation of the declination angle within a day is so small (about 0.4° per day maximum) that it can be assumed constant (Duffie and Beckman, 2013). Figure 6.19 shows the scatter plot of the IAM_{RT} and the declination angle (δ) for 8 days equally distributed all over the year. Worth noticing, the choice of showing only 8 days out of the 25 in the diagram is purely for the sake of visualization clarity, but the same trend could be observed for the other days. The legend of the graph indicates the day number. As it can be observed, the daily data assume a vertical trend, and the maximum value of the IAM_{RT} increases with declination angle (approaching to the summer solstice when δ is maximum and equal to $23^\circ 27'$). The summer and the winter solstices are day 171 and 355, respectively.

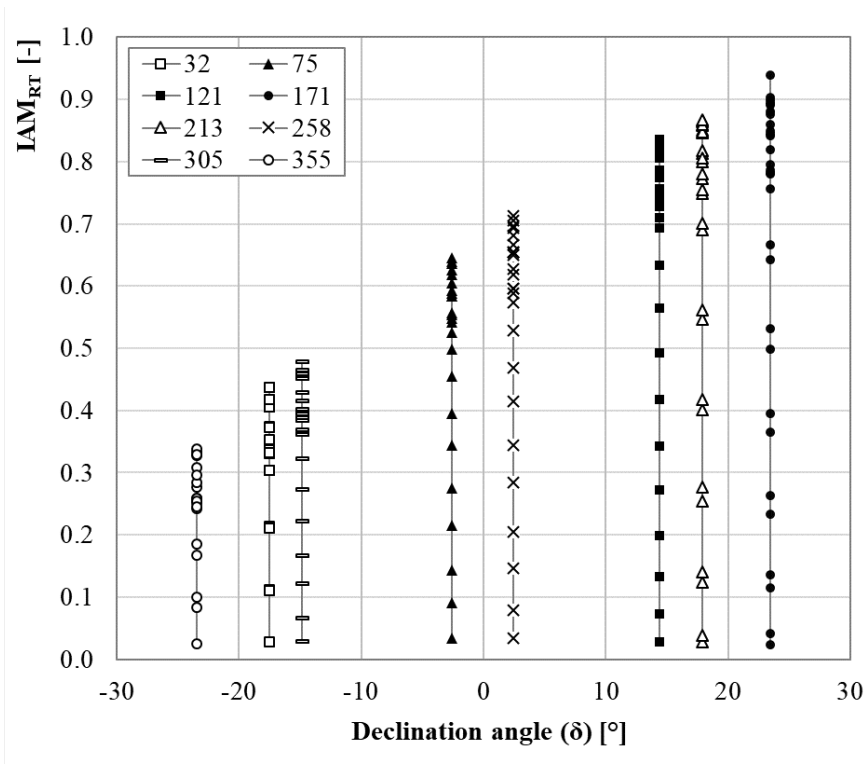


Fig. 6.19 Scatter plot of the IAM_{RT} as a function of the declination angle for the reference days (in legend the day number) and considering configuration C0.

Despite properly representing the variation of the IAM_{RT} during the different days, δ does not give any information about the hourly variation.

Figure 6.20 shows the variation of the IAM_{RT} with the azimuth angle (γ_s). The trend is quite different during the days of the year. Observing the values of γ_s between -30° and $+30^\circ$, a concave shape for day 355, opposing the convex shape of day 171, can be remarked.

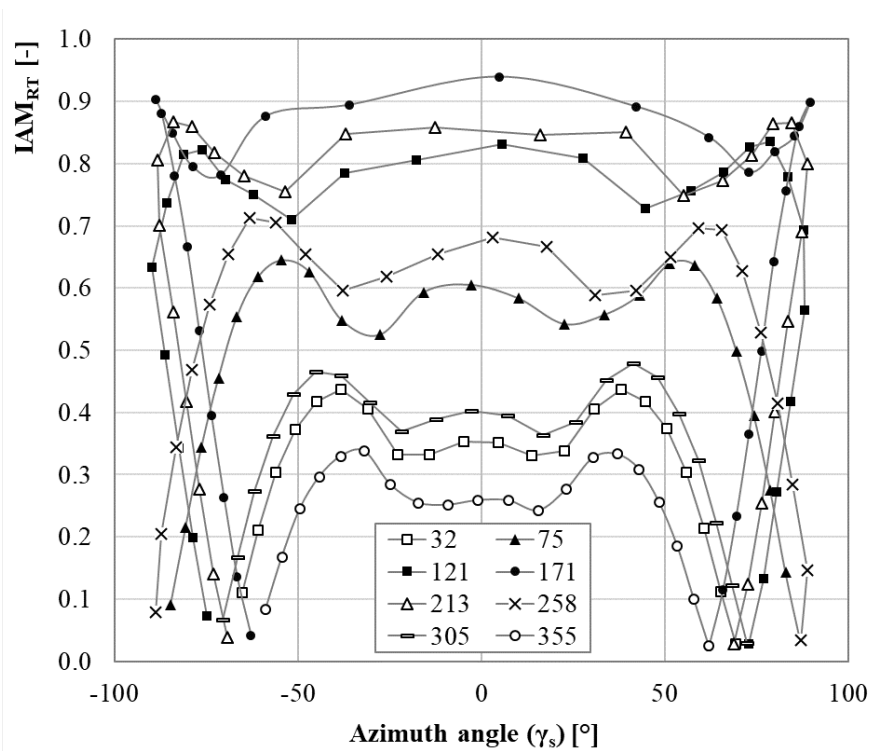


Fig. 6.20 Scatter plot of the IAM_{RT} as a function of the azimuth angle for the reference days (in legend the day number) and considering configuration C0.

The uneven trend during the days of the year, can be seen in Figure 6.21 that is related to the profile angle, α_p .

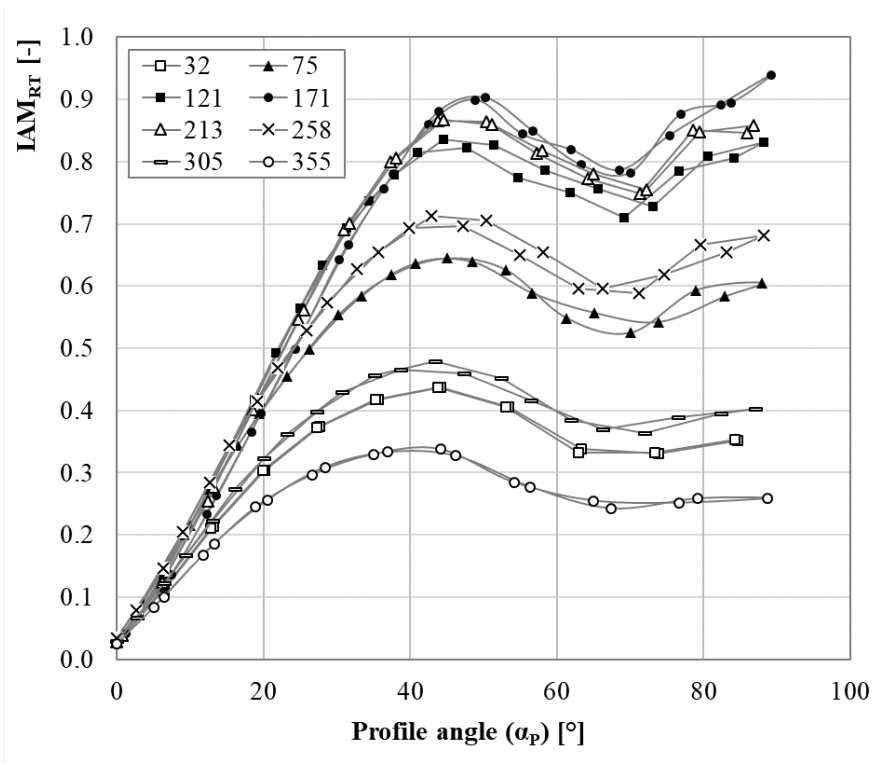


Fig. 6.21 Scatter plot of the IAM_{RT} as a function of the profile angle for the reference days (in legend the day number) and considering configuration C0.

Finally, the altitude and the zenith angles have been investigated. As they are complementary, only θ is considered but the same considerations (with the opposite trend) apply to α_s . In opposition to azimuth and profile angles, the trend is similar for the different days: a concave shape for lower values of θ and, subsequently, an almost linear decreasing trend with increasing θ . The diagram is represented in Figure 6.22.

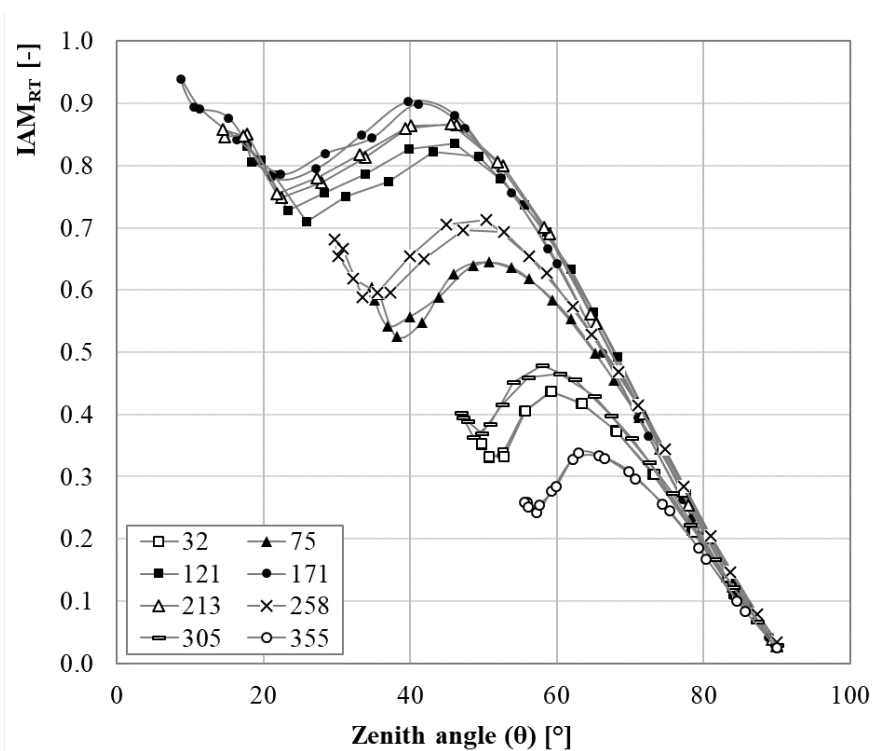


Fig. 6.22 Scatter plot of the IAM_{RT} as a function of the azimuth angle for the reference days (in legend the day number) and considering configuration C0.

Based on the above considerations, the solar declination (δ) and the solar zenith angle (θ) have been selected as proper independent variables to establish a multiple regression. Before testing different types of multiple regression models the two angles have been inserted in the appropriate functions of sine and cosine. Proceeding by trial and error, the sine has been found to be the most suitable for δ and the cosine for θ . Figure 6.23 shows the variation of the IAM_{RT} with respect to the cosine of the zenith angle ($\cos\theta$).

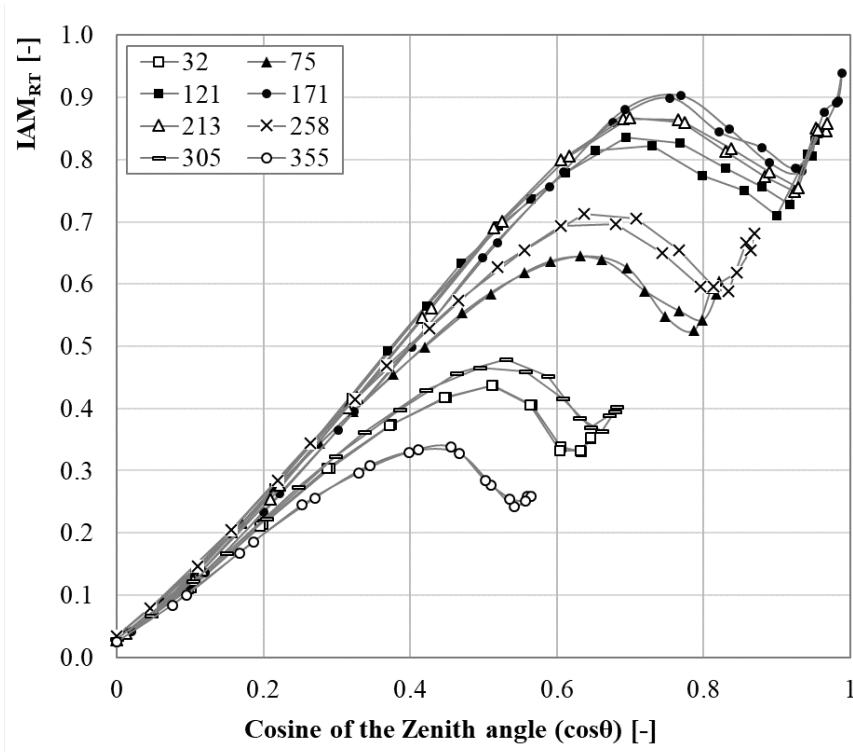


Fig. 6.23 Scatter plot of the IAM_{RT} as a function of the cosine of the zenith angle for the reference days (in legend the day number) and considering configuration C0.

Finally, using an application for curve fitting and data analysis (CurveExpert Professional, v.2.6.5 (Hyams, 2014)), different multiple regression models have been tested. In more details, a 3rd order (cubic) polynomial linear regression, as in Eq. 6.49, ended up giving the best results:

$$Y = a + b \cdot X_1 + c \cdot X_2 + d \cdot X_1^2 + e \cdot X_2^2 + f \cdot X_1^3 + g \cdot X_2^3 + h \cdot X_1 \cdot X_2 + i \cdot X_1^2 \cdot X_2 + j \cdot X_1 \cdot X_2^2 \quad (6.49)$$

where Y is the dependent variable (IAM_{RT}), X_1 is the first independent variable ($\cos \theta$), X_2 is the second independent variable ($\sin \delta$), and a, b, \dots, j are the regression constants after curve fitting.

Lastly, to demonstrate the robustness of the declination zenith regression model, the same approach has been applied to both the reference geometries (C0 and C1) and to a reduced dataset of the three most representative days of the year, i.e. the spring equinox and the summer and winter solstices (days n°79, 171, and 355, respectively).

6.2.7 Results

In the following sections, the results are presented first as a comparison with literature correlations (Bellos and Tzivanidis, 2018) (Section 6.2.7.1), and, in the second part, in terms of the new IAM scheme based on solar angles, compared to the factored approach (Section 6.2.7.2). The results obtained have been compared mainly in terms of mean absolute percentage error (Δ) and root mean square error (RMSE).

6.2.7.1 The Biaxial Factored Approach

As discussed above, FresnelSim ray-tracing simulations have been run for calculating the transversal and longitudinal angle modifiers, denoted as $IAM_{RT,T}$ and $IAM_{RT,L}$. The two projected modifiers have been also calculated based on the set of analytical expressions developed by Bellos and Tzivanidis (2018), denoted as $IAM_{B,T}$ and $IAM_{B,L}$. Then, the biaxial factored approach has been applied to evaluate the overall factored incidence angle modifier, arising from both ray-tracing ($IAM_{RT,FA}$) and analytical ($IAM_{B,FA}$) techniques.

The first part of the results is devoted to the comparison of $IAM_{RT,T}$, $IAM_{RT,L}$, $IAM_{RT,FA}$ with the corresponding $IAM_{B,T}$, $IAM_{B,L}$, $IAM_{B,FA}$.

Figure 6.24 shows the transversal and longitudinal components as a function of the corresponding projected incidence angles (θ_T for the transversal and θ_L for the longitudinal), related to the current plant configuration (C0). The longitudinal incidence angle shows a pronounced reduction with θ_L , becoming close to zero at $\theta_L = 70$. Contrarily, for the transversal component, the decrease with increasing θ_T is slighter. One can notice the uneven profile of the $IAM_{RT,T}$ curve: this is the shadow effect of the receiver assembly as it moves over the bottom mirrors and/or on the gaps among them. The lines are related to the analytical model by Bellos and Tzivanidis (2018), whereas the points represent the result of the ray-tracing simulations in 1° steps. Worth noticing, in the first instance, the ray-tracing simulations have been performed by disabling the blocking effect to be consistent with the analytical model that does not consider this phenomenon. In general, there is good agreement between the two models. The difference is more evident in the transversal components ($IAM_{RT,T}$ and $IAM_{B,T}$) with a RMSE of 0.0307 and a mean absolute error (Δ) of 5.84%. The major deviation is observed in the fluctuations characterizing $IAM_{RT,T}$ between 0° and 50° . Contrarily, the difference is imperceptible for the longitudinal components ($IAM_{RT,L}$ and $IAM_{B,L}$) with a RMSE of 0.0040 and a mean absolute error (Δ) of 1.60%.

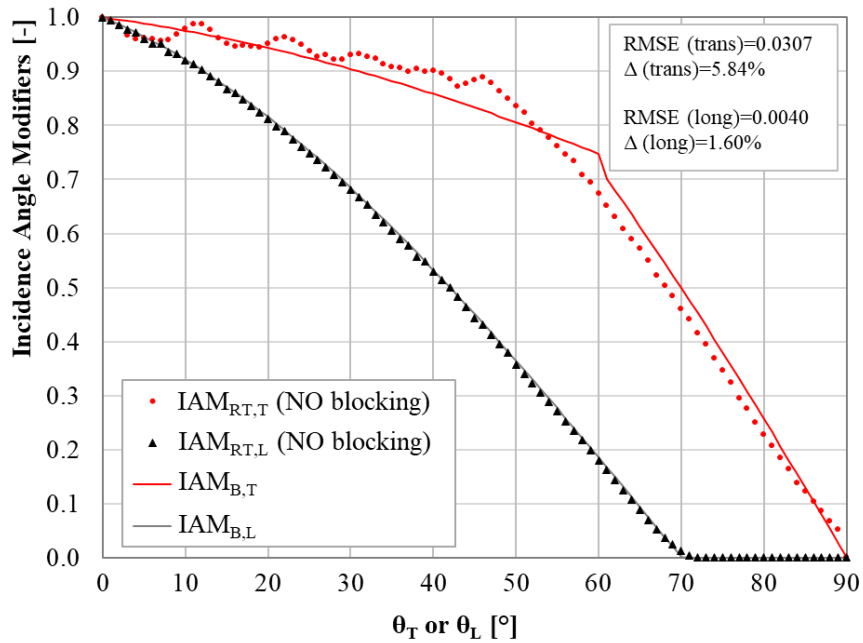


Fig. 6.24 Variation of the transversal and longitudinal IAM components with the related projected angle. Comparison between the ray-tracing (RT) and analytical (B) approaches when blocking is disabled.

Figure 6.25 shows the same condition described in Figure 6.24 but including the blocking effect. As expected, the blocking effect only affects the transversal component, and the difference with the analytical model increase, above all between 0° and 40°, with a RMSE of 0.0519 and a mean absolute error Δ of 7.58%.

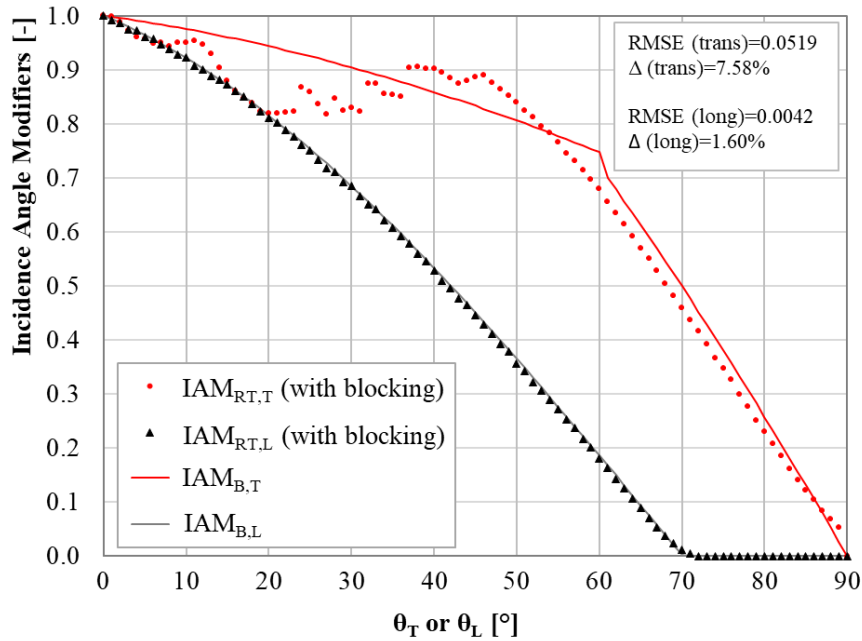


Fig. 6.25 Variation of the transversal and longitudinal IAM components with the related projected angle. Comparison between the ray-tracing (RT) and analytical (B) approaches when blocking is included.

The results evidence that, for the studied plant geometry (C0), where blocking largely occurs, the analytical model is unsuitable to represent the transversal modifier. In the other reference configuration (C1), where the mirrors are even narrower (0.05 m instead of 0.2 m of C0), the blocking effect is more pronounced as Figure 6.26 shows. In this case, the difference with the analytical model further increases to a mean absolute error Δ of 9.42% in the transversal and 3.03% in the longitudinal component.

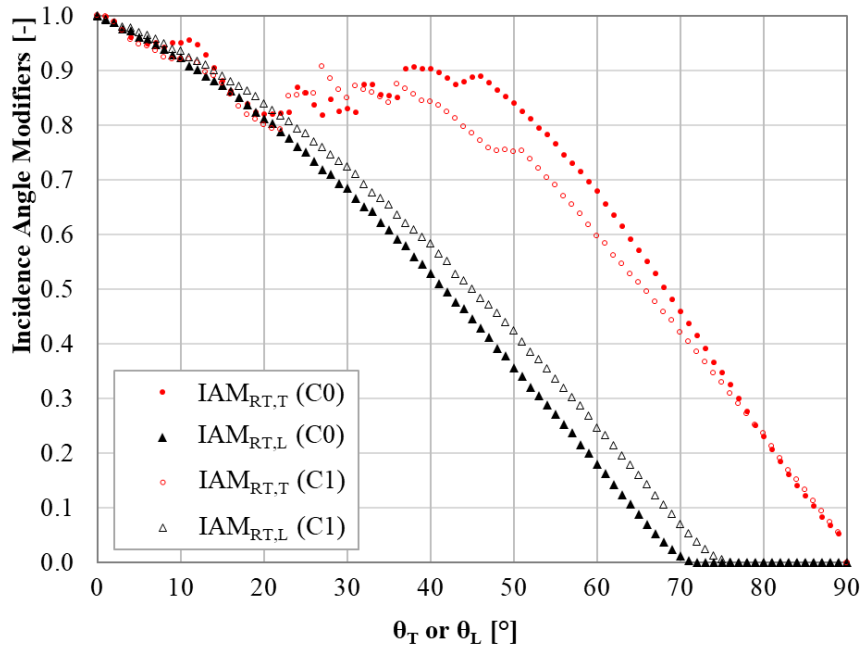


Fig. 6.26 Variation of the transversal and longitudinal IAM components with the related projected angle. Comparison between ray-tracing results for configuration C0 and C1.

6.2.7.2 The Proposed Declination-Zenith Regression Model

In a second stage, the biaxial factored approximation of the Incidence Angle Modifier obtained through the ray-tracing simulations ($IAM_{RT,FA}$) has been compared to the non-approximated instantaneous value (IAM_{RT}) arising from the FresnelSim simulations. The scatter plot represented in Figure 6.27 shows the results over a time horizon of 25 days (equally distributed along the year) with a 30-minute time-step and it is related to plant configuration C0. As it can be noticed, IAM_{RT} is remarkably higher than $IAM_{RT,FA}$, in particular for lower IAM values. This is due to the fact that the factored approach is less precise than ray-tracing simulations in accounting for optical losses. Contrarily, for values higher than 0.7, IAM_{RT} and $IAM_{RT,FA}$ are much closer, but the overall mean absolute error (Δ) of 32.2% and the root mean squared error (RMSE) of 0.1087 are still very high.

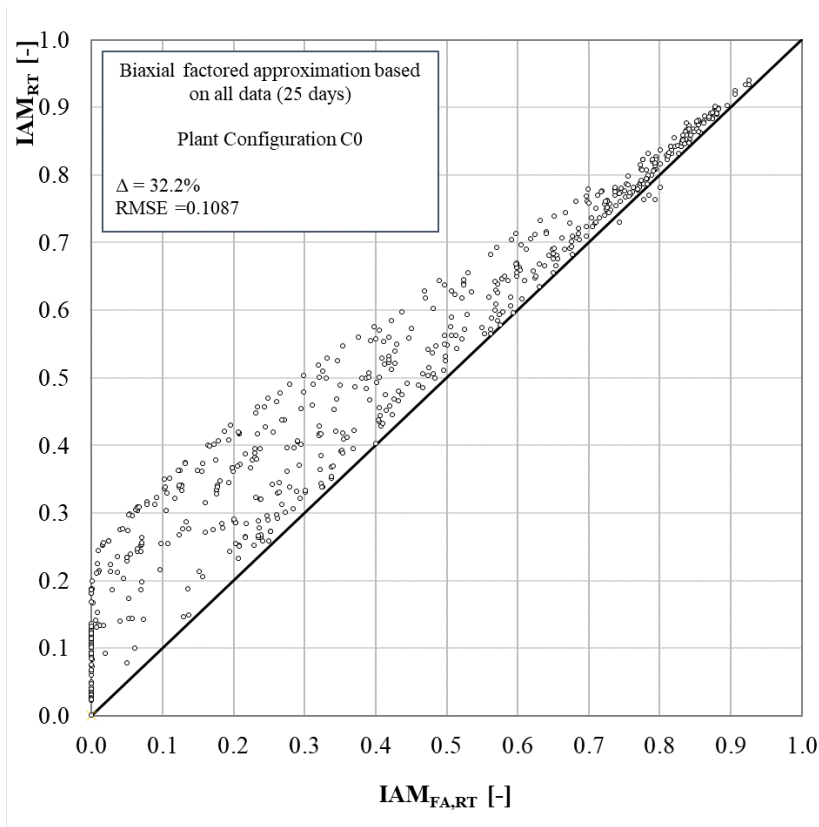


Fig. 6.27 Comparison between the instantaneous non-approximated IAM_{RT} and the biaxial factored approximation $IAM_{RT,FA}$ over a time horizon of 25 days for configuration C0.

Figure 6.28 shows the comparison between the non-approximated instantaneous value of the incidence angle modifier (IAM_{RT}) and the value obtained through the present regression model, named declination zenith model (IAM_{dzm}). At first, the 3rd order multiple polynomial regression has been based on all data (25 days) for plant configuration C0, inferring the regression constants provided in Table 6.3. The coefficient of correlation (r) resulted to be about 0.991 and the coefficient of determination (r^2) is equal to 0.983. As it can be observed, the declination zenith regression model is more suitable than the factored approach to approximate the IAM_{RT} , with a mean absolute error (Δ) of only 2.29%, a maximum Δ of about +/-10%, and a root mean squared error (RMSE) of about 0.0340.

Table 6.3 Regression constants based on all ray-tracing data (25-day-long database) for configuration C0

Regression constants	Value
A	0.0073
B	1.2535
C	-0.0277
D	0.6090
E	0.0360
F	-1.5299
G	0.2315
H	-0.1676
I	2.0067
J	-1.6333

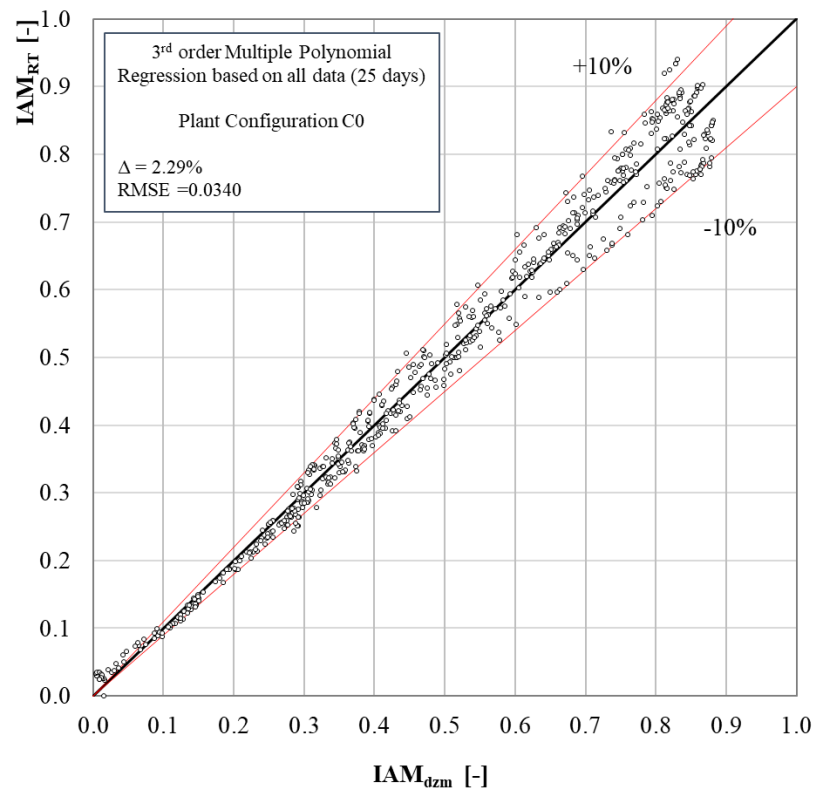


Fig. 6.28 Comparison between the instantaneous non-approximated IAM_{RT} and the declination-zenith regression model IAM_{dzm} over a time horizon of 25 days for configuration C0.

The same approach has been applied to configuration C1 to test the declination zenith model on other geometries. The results are shown in Figure 6.29. In this case, the model fits even

better the simulated data with a mean absolute error (Δ) of 1.32% and a root mean squared error (RMSE) of about 0.0248. The coefficient of correlation (r) in this case is 0.995, and the coefficient of determination (r^2) is 0.989.

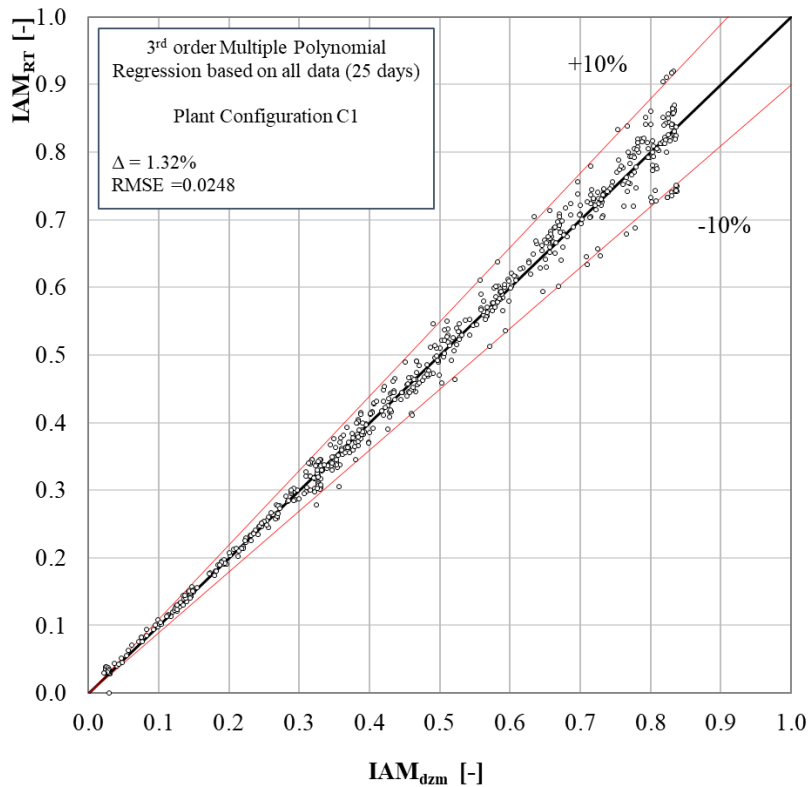


Fig. 6.29 Comparison between the instantaneous non-approximated IAM_{RT} and the declination-zenith regression model IAM_{dzm} over a time horizon of 25 days for configuration C1.

A comment arising from Figure 6.28 and 6.29 is that the declination-zenith regression model demonstrates robustness in reproducing the dataset from where it was “tuned”. This provides an important finding to Fresnel theory: a simple correlation, able to provide precise information about the hourly energy yield, for parametric analyses (e.g., site comparison) and/or economic/financial evaluations.

Additionally, the proposed approach results even more robust than expected when tested against a reduced database. New regression coefficients have been inferred starting from ray-tracing data of only 3 days along the year that are considered the most representatives (i.e., the summer and winter solstices and the spring equinox, days n° 171, 355, and 79, respectively). Figure 6.30 represents the results arising from the reduced database test for configuration C0, and Table 6.4 the related regression constants. Worth noticing that the results are presented only for configuration C0 for the sake of brevity, but the same considerations have been tested and apply to C1. Observing Figure 6.30, the markers are related to day n° 171, 355, and 79, as it is

described in the legend, whereas the smaller points are related to the yearly database. The model demonstrates to be very robust as the mean absolute error Δ is even slightly lower compared to the 25 days database (1.90% instead of 2.29%). Concerning the RMSE between the two cases it is roughly the same (0.0348 instead of 0.0340).

Table 6.4 Regression constants calculated from the reduced 3-day-long database for configuration C0. The considered days are day n° 171, 355, and 79.

Regression constants	Value
A	0.0007
B	1.2632
C	-0.0055
D	0.6073
E	0.1071
F	-1.5290
G	0.0047
H	-0.1761
I	2.0910
J	-1.8333

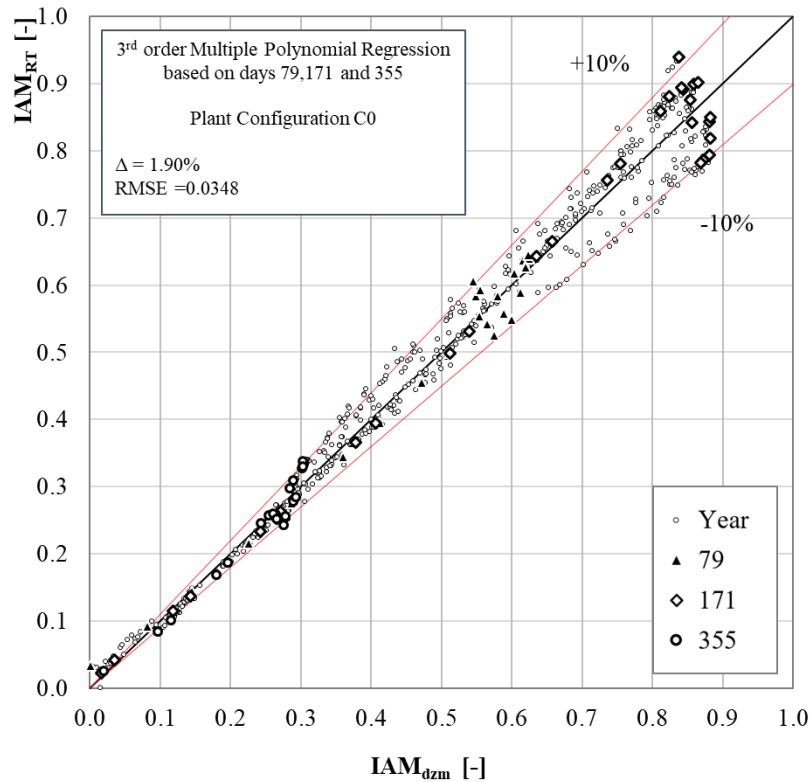


Fig. 6.30 Comparison between the instantaneous non approximated IAM_{RT} and the declination-zenith regression model IAM_{dzm} based on a 3-day-long reduced database (days are n° 171, 355, and 79) for plant configuration C0.

6.2.8 Conclusions

In the present work, new Incidence Angle Modifier (IAM) correlations based on the declination and zenith angles have been proposed to perform hourly energy simulations on Linear Fresnel (LF) Collectors. The constants involved in the present compact formula have been calculated through a regression analysis on year round, three dimensional, hourly ray-tracing simulations of given LFC geometries. The new model and its corresponding correlation, applied to a real LF plant located in Ben Guerir (Morocco), have been compared to the well known biaxial factored approach, based on the transversal and longitudinal IAM components.

Incidence angle modifier values as factored formula have been in turn calculated starting from both ray-tracing values (in-house code by the Authors) and analytic Literature equations. Agreement with Literature expressions was reasonably good (mean absolute percentage difference on IAM transversal and longitudinal, 8% and 2% respectively), considering that analytic expressions cannot completely take into considerations shadings, blocking and end effects as sources of “lost” sun rays on receiver. Nevertheless, even the most accurate and complete ray-tracing model, when employed for providing factored IAM series, fails in reproducing the

real energy yield of LF plants (present test cases, mean absolute error about 30% and RMSE about 0.11).

On the contrary, when the full dataset of ray-tracing simulations (25 days along the year with sub-hourly time steps) is employed for calculating in a regression analysis the constants of the proposed (solar angle based) correlation, the present model demonstrated to be able to fit the full 3D ray-tracing data with a mean absolute error of about 2% and a RMSE of about 0.03.

The robustness and reliability of the model has been also tested while calculating its constants just employing 3 days of ray-tracing simulations (equinox and solstices). The corresponding correlation provided very similar results (and similar constants) to the one based on the full yearly dataset of ray-tracing simulations, thus enabling energy and economic analyses with a very small computational (or experimental, if performance data is from measurements) effort.

Chapter 7

Conclusions and Future Perspectives

7.1 Conclusions

The various research efforts undertaken in this doctoral thesis encompass a comprehensive investigation into the key issues and challenges related to the integration and performance assessment of solar systems in urban environments.

Given the inherent complexity in modeling urban systems and the spatial distribution of solar resources within them, a primary objective of this doctoral thesis was to explore the potential of data-driven methodologies in analyzing large-scale urban datasets that encompass entire cities. These methodologies have demonstrated their effectiveness in conducting urban analyses, providing deeper insights into microclimatic aspects and solar energy production within urban settings.

The research outcomes have substantial relevance across various disciplines, including solar and energy engineering, urban planning, architecture, building performance simulation, and environmental design. Moreover, the findings serve as valuable support for decision-making processes focused on sustainable urban development and the efficient integration of solar technologies.

To achieve the thesis objectives, diverse methodologies were employed, chosen based on the specific research focus and the scale of analysis. These methodologies comprised urban microclimate analysis, solar radiation modeling, photovoltaic (PV) performance modeling, district-scale numerical simulation engines, and ray-tracing techniques. The significant differences among these methodologies underscore the necessity of adopting a holistic and comprehensive approach when conducting urban-related analyses.

The scale of the research subjects investigated in this thesis ranged from large scales, encompassing entire cities, to district-level and system-level analyses. This multi-scale approach was essential to capture the intricate interactions between urban morphology, microclimatic conditions, and solar energy utilization. Each scale of analysis provided crucial insights into different aspects of the integration of solar systems within urban environments, collectively contributing to a comprehensive understanding of the challenges and opportunities associated with solar energy production in cities.

One of the key contributions of this research is the development of a data-driven and machine learning-based approach for conducting computationally efficient year-long analyses of Urban Heat Islands (UHI) at the city scale (**Paper 2**). This approach successfully identified representative microclimatic clusters within cities, offering valuable insights into the spatial distribution of Urban Heat Island intensity (UHII) throughout the year and across various urban clusters. The results revealed significant variability in UHII, with peak values ranging from 5.1°C to 11.5°C, underscoring the importance of considering urban microclimate when addressing building energy demand and photovoltaic (PV) production modeling. These findings were further supported by the outcomes of **Paper 3**, which investigated the impact of Urban Heat

Island effects on building energy demand and PV productivity in realistic urban environments. The study demonstrated the substantial influence of UHI effects on building energy demand, leading to potential variations of up to 30% in air conditioning requirements. Additionally, the research highlighted that extensive deployment of PV systems on building facades could result in reduced PV productivity due to the "darkening" effect on the urban environment. This critical aspect emphasizes the paramount importance of optimizing the utilization of urban surfaces by considering both solar energy generation and the urban microclimate. Effective mitigation strategies for Urban Heat Islands must be thoughtfully integrated into urban planning and solar energy system design. Furthermore, the investigation into the electrical and thermal performance of PV systems in Greater Sydney (**Paper 5**) confirmed the significant influence of both local climate conditions and mounting configuration on PV performance within the urban environment. Local climate conditions, including extreme heat events, had a negative impact on PV performance, leading to power losses of up to 50% compared to standard test conditions. The study emphasized the importance of accurate models for predicting PV performance under local climate conditions.

Regarding the relationship between solar irradiance distribution and urban morphology, this thesis provides valuable insights into shading patterns and solar potential in various urban textures (**Paper 4**). The study identified certain morphological parameters, such as building dimensions and inter-building height differences, that exhibited stronger correlations with solar irradiance, particularly in dense urban patterns. One of the most significant outcomes of this analysis was the application of these results, made possible by accurate and large-scale urban data, in statistical analyses of urban fabric and comparative studies. These findings underscore the potential of digitizing the urban environment not only for specific site-related analyses but also for obtaining valuable information for other investigations.

Lastly, the thesis also explored the capabilities of 3D ray-tracing models for analyzing the optical and energy performance of Fresnel collectors (**Paper 6 and 7**). The developed methodologies not only enabled the optimization of collector geometry but also facilitated the reduction of computational effort required for extensive ray-tracing simulations. Both land use optimization and reduced computational times are essential for envisioning the future integration of these systems into building rooftops, a topic that was not extensively addressed in the present thesis due to time constraints.

Overall, the research findings contribute to a deeper understanding of the key issues related to the integration of solar energy production within the urban environment. They also underscore the challenges of effectively managing extensive urban datasets and the need for data-driven methodologies in large-scale urban energy planning.

Furthermore, the results reveal the need of a multidisciplinary planning approach in the integration of solar systems into urban environments. The massive deployment of PV systems in cities without due consideration of local microclimatic phenomena can have detrimental effects, both in terms of PV performance and urban thermal comfort. Additionally, the importance

of studying urban morphology has emerged, emphasizing that certain urban layouts are more favorable to effective solar energy harvesting than others.

In general, the findings do not allow for the delineation of an ideal urban morphology for solar energy integration in cities. However, they do highlight the feasibility of conducting morphological studies to identify the solar potential of specific city areas. This approach can guide development strategies, prioritizing areas with optimal solar exposure, thereby fostering sustainable urban development and advancing climate change mitigation and energy transition efforts.

7.2 Future Works

The effective integration of solar energy within urban environments remains a complex issue, and this doctoral thesis has provided valuable findings and guidelines. However, several avenues for future research and development can further advance the field:

- **Utilizing Machine Learning (ML) and Artificial Intelligence (AI) for Advanced Urban Modeling and Understanding:** The digitalization of urban environments has emerged as a fundamental aspect in this thesis manuscript, enabling comprehensive analysis at a large scale, encompassing various aspects such as urban microclimate, solar radiation distribution, and photovoltaic (PV) system performance in urban settings. The proposed approaches and workflows in this thesis contribute to a detailed understanding of the complex interactions within urban systems. However, the integration of Machine Learning (ML) and Artificial Intelligence (AI) techniques holds the potential to further enhance these aspects, especially regarding the generation of high-resolution, spatially explicit datasets. These datasets can capture crucial information not only related to microclimatic conditions and solar radiation but also other pertinent factors such as pollutant concentrations, which have not been explicitly addressed in this manuscript.

By integrating these datasets with solar radiation data, it becomes possible to more accurately assess the solar energy potential in cities and evaluate the dynamic potential of solar energy production within urban environments. Combining remote sensing and crowdsourced data with AI techniques allows for the generation of valuable insights into the spectral, thermal, and morphological characteristics of urban areas, complementing in-situ measurements. Furthermore, AI-driven analyses of urban morphology can facilitate the optimization of urban solar planning and the supervision of energy production capacities.

Through AI-driven analyses, optimal locations for solar installations can be identified, ensuring maximum solar exposure while minimizing shading effects from surrounding buildings. Additionally, AI can optimize the operation and maintenance of solar systems in urban areas by utilizing real-time data, including energy production, temperature, and

weather information. This improves the reliability, performance, and durability of PV systems, maximizing their operational efficiency and return on investment for stakeholders involved in solar energy within urban areas.

- **Enhancing Parametric Microclimate Simulation Models for Large-scale Urban Analysis:** While the data-driven approach developed in **Paper 2** has demonstrated its effectiveness in understanding general urban heat island patterns, there is still room for improvement in current parametric microclimate modeling tools. Future research should concentrate on refining these models to more accurately capture the complexity of urban microclimates. This involves incorporating a more comprehensive range of physical processes into the models, including sophisticated airflow modeling to better simulate urban ventilation and air movement. Additionally, improving the modeling of evapotranspiration processes is essential, as they significantly impact the microclimatic conditions in urban areas. Furthermore, the presence of water bodies within the urban environment, such as lakes, rivers, or ponds, can exert a considerable influence on local microclimates and their integration into microclimate models can lead to more realistic simulations. For advancing in large-scale microclimate simulations, it is imperative to address two critical aspects: the establishment of reliable urban datasets and the refinement of simulation techniques through a reduction of the computational time. Both of these challenges may be partially tackled through the application of AI.
- **Investigating Concentrated Solar Systems Integration on Building Rooftops:** The geometrical optimization of Linear Fresnel Collectors (LFCs) presented in **Paper 6** made a valuable contribution towards enhancing the efficiency of Fresnel concentration systems. To facilitate the widespread adoption of concentrated solar technologies, future research should extend this work to explore the practical implementation of these systems on building rooftops. Evaluating the feasibility and economic viability of LFCs and other concentrated solar technologies for industrial applications will be crucial in promoting their integration into urban environments. Conducting large-scale solar radiation analyses, similar to those presented in this manuscript, can play a pivotal role in identifying the optimal placement of concentrated solar systems on building rooftops. Such analyses would help avoid a reduction in the direct solar radiation component, thereby maximizing the energy capture potential of these systems. Moreover, by considering factors such as energy demand, available rooftop area, and system maintenance, Detailed Building Energy Modeling (BEM) can provide valuable insights into the seamless integration of concentrated solar technologies into existing building structures. Through comprehensive BEM simulations, researchers can assess the impact of concentrated solar systems on the overall energy demand of buildings, enabling the development of strategies for optimal system sizing and energy management.

References

- (2019). Chapter 3 - From Efficient to Sustainable and Zero Energy Consumption Buildings. pages 75–205. Butterworth-Heinemann.
- Abanda, F. H., Sibilla, M., Garstecki, P., and Anteneh, B. M. (2021). A literature review on BIM for cities Distributed Renewable and Interactive Energy Systems. *International Journal of Urban Sustainable Development*, 13(2):214–232.
- Abbas, R. and Martínez-Val, J. M. (2015). Analytic optical design of linear Fresnel collectors with variable widths and shifts of mirrors. *Renewable Energy*, 75:81–92.
- Abbas, R., Montes, M. J., Piera, M., and Martínez-Val, J. M. (2012). Solar radiation concentration features in Linear Fresnel Reflector arrays. *Energy Conversion and Management*, 54(1):133–144.
- Abbas, R., Muñoz-Antón, J., Valdés, M., and Martínez-Val, J. M. (2013). High concentration linear Fresnel reflectors. *Energy Conversion and Management*, 72:60–68.
- Abbas, R., Sebastián, A., Montes, M. J., and Valdés, M. (2018). Optical features of linear Fresnel collectors with different secondary reflector technologies. *Applied Energy*, 232:386–397.
- Abbas, R., Valdés, M., Montes, M. J., and Martínez-Val, J. M. (2017). Design of an innovative linear Fresnel collector by means of optical performance optimization: A comparison with parabolic trough collectors for different latitudes. *Solar Energy*, 153:459–470.
- Abdelrazik, A., Shboul, B., Elwardany, M., Zohny, R., and Osama, A. (2022). The recent advancements in the building integrated photovoltaic/thermal (BIPV/T) systems: An updated review. *Renewable and Sustainable Energy Reviews*, 170:112988.
- Adolphe, L. (2001). A simplified model of urban morphology: Application to an analysis of the environmental performance of cities. *Environment and Planning B: Planning and Design*, 28(2):183–200.
- AECOM Australia Pty Ltd, van Raalte, L., Nolan, M., Thakur, P., Xue, S., and Parker, N. (2012). Economic Assessment of the Urban Heat Island Effect. *City of Melbourne*, pages 1–71.
- Afshari, A. and Ramirez, N. (2021). Improving the accuracy of simplified urban canopy models for arid regions using site-specific prior information. *Urban Climate*, 35(October 2020):100722.
- Ahmad, S., Abdul Mujeebu, M., and Farooqi, M. A. (2019). Energy harvesting from pavements and roadways: A comprehensive review of technologies, materials, and challenges. *International Journal of Energy Research*, 43(6):1974–2015.
- Aigarni, S. and Nutter, D. (2015). Survey of sky effective temperature models applicable to building envelope radiant heat transfer. *ASHRAE Conference-Papers*, 121(July):351–363.

- Akbari, H., Pomerantz, M., and Taha, H. (2001). Cool surfaces and shade trees to reduce energy use and improve air quality in urban areas. *Solar Energy*, 70(3):295–310.
- Akrofi, M. M. and Okitasari, M. (2022). Integrating solar energy considerations into urban planning for low carbon cities: A systematic review of the state-of-the-art. *Urban Governance*, 2(1):157–172.
- Al-Waeli, A. H. A., Sopian, K., Kazem, H. A., and Chaichan, M. T. (2017). Photovoltaic/Thermal (PV/T) systems: Status and future prospects. *Renewable and Sustainable Energy Reviews*, 77:109–130.
- Alchapar, N. L., Pezzuto, C. C., Correa, E. N., and Salvati, A. (2019). Thermal Performance of the Urban Weather Generator Model as a Tool for Planning Sustainable Urban Development. *Geographica Pannonica*, 23(4):374–384.
- AlDousari, A. E., Kafy, A. A., Saha, M., Fattah, M. A., Almulhim, A. I., Faisal, A. A., Al Rakib, A., Jahir, D. M. A., Rahaman, Z. A., Bakshi, A., Shahrier, M., and Rahman, M. M. (2022). Modelling the impacts of land use/land cover changing pattern on urban thermal characteristics in Kuwait. *Sustainable Cities and Society*, 86(August):104107.
- Aleksandrowicz, O., Vuckovic, M., Kiesel, K., and Mahdavi, A. (2017). Current trends in urban heat island mitigation research: Observations based on a comprehensive research repository. *Urban Climate*, 21(February):1–26.
- Aleksandrowicz, O., Zur, S., Lebendiger, Y., and Lerman, Y. (2020). Shade maps for prioritizing municipal microclimatic action in hot climates: Learning from Tel Aviv-Yafo. *Sustainable Cities and Society*, 53:101931.
- Alexandri, E. and Jones, P. (2008). Temperature decreases in an urban canyon due to green walls and green roofs in diverse climates. *Building and Environment*, 43(4):480–493.
- Allegrini, J., Dorer, V., and Carmeliet, J. (2015a). Influence of morphologies on the microclimate in urban neighbourhoods. *Journal of Wind Engineering and Industrial Aerodynamics*, 144:108–117.
- Allegrini, J., Orehounig, K., Mavromatidis, G., Ruesch, F., Dorer, V., and Evins, R. (2015b). A review of modelling approaches and tools for the simulation of district-scale energy systems. *Renewable and Sustainable Energy Reviews*, 52:1391–1404.
- Altan, H., Alshikh, Z., Belpoliti, V., Kim, Y. K., Said, Z., and Al-chaderchi, M. (2019). An experimental study of the impact of cool roof on solar PV electricity generations on building rooftops in Sharjah, UAE. *International Journal of Low-Carbon Technologies*, 14(2):267–276.
- Alvarez, I., Quesada-Ganuza, L., Briz, E., and Garmendia, L. (2021). Urban heat islands and thermal comfort: A case study of zorrotzaurre island in Bilbao. *Sustainability (Switzerland)*, 13(11):1–13.
- Amado, M., Poggi, F., Amado, A. R., and Breu, S. (2017). A cellular approach to Net-Zero energy cities. *Energies*, 10(11).
- Andreadis, G., Roaf, S., and Mallick, T. (2013). Tackling fuel poverty with building-integrated solar technologies: The case of the city of Dundee in Scotland. *Energy and Buildings*, 59:310–320.
- Andrews, R. W., Pollard, A., and Pearce, J. M. (2013). The effects of snowfall on solar photovoltaic performance. *Solar Energy*, 92:84–97.

- Ang, Y. Q., Berzolla, Z. M., Letellier-Duchesne, S., and Reinhart, C. F. (2023). Carbon reduction technology pathways for existing buildings in eight cities. *Nature Communications*, 14(1).
- Anguelovski, I., Connolly, J. J. T., Cole, H., Garcia-Lamarca, M., Triguero-Mas, M., Baró, F., Martin, N., Conesa, D., Shokry, G., del Pulgar, C. P., Ramos, L. A., Matheney, A., Gallez, E., Oscilowicz, E., Máñez, J. L., Sarzo, B., Beltrán, M. A., and Minaya, J. M. (2022). Green gentrification in European and North American cities. *Nature Communications*, 13(1):3816.
- Aoun, N. (2022). Methodology for predicting the PV module temperature based on actual and estimated weather data. *Energy Conversion and Management: X*, 14(July 2021):100182.
- Araldi, A. and Fusco, G. (2019). From the street to the metropolitan region: Pedestrian perspective in urban fabric analysis. *EPB: Urban Analytics and City Science*, 46(7):1243–1263.
- Arenandan, V., Wong, J. K., Ahmed, A. N., and Chow, M. F. (2022). Efficiency enhancement in energy production of photovoltaic modules through green roof installation under tropical climates. *Ain Shams Engineering Journal*, 13(5):101741.
- Areva Solar (2013). AREVA SOLAR - Kogan Creek - AREVA.
- Asdrubali, F., Cotana, F., and Messineo, A. (2012). On the evaluation of solar greenhouse efficiency in building simulation during the heating period. *Energies*, 5(6):1864–1880.
- Atsu, D., Seres, I., Aghaei, M., and Farkas, I. (2020). Analysis of long-term performance and reliability of PV modules under tropical climatic conditions in sub-Saharan. *Renewable Energy*, 162:285–295.
- Australian Energy Market Operator (AEMO) (2019). Electricity Demand Forecasting Methodology Information Paper Important notice PURPOSE. (August).
- Azunre, G. A., Amponsah, O., Pephrah, C., Takyi, S. A., and Braimah, I. (2019). A review of the role of urban agriculture in the sustainable city discourse. *Cities*, 93(March 2018):104–119.
- Baghoolizadeh, M., Rostamzadeh-Renani, M., Rostamzadeh-Renani, R., and Toghraie, D. (2023). Multi-objective optimization of Venetian blinds in office buildings to reduce electricity consumption and improve visual and thermal comfort by NSGA-II. *Energy and Buildings*, 278:112639.
- Baker, N., Belmonte Monteiro, R., Boccalatte, A., Bouty, K., Brozovsky, J., Caliot, C., Campamà Pizarro, R., Compagnon, R., Czachura, A., Desthieux, G., Formolli, M., Giroux-Julien, S., Guillot, V., Govehovitch, B., Hachem-Vermette, C., Herman, E., Herrera, O. A., Kämpf, J. H., Lobaccaro, G., Ménéz, C., Musy, M., Peronato, G., Petersen, A. J., Rodler, A., Singh, K., Sjöberg, V., Snow, M., Tjetland, J., and Yupeng, W. (2022). Identification of existing tools and workflows for solar neighborhood planning. Technical report.
- Balakrishnan, P. and Jakubiec, J. A. (2022). Trees in Daylight Simulation – Measuring and Modelling Realistic Light Transmittance through Trees. *LEUKOS*, pages 1–28.
- Barbón, A., Barbón, N., Bayón, L., and Sánchez-Rodríguez, J. A. (2018). Optimization of the distribution of small scale linear Fresnel reflectors on roofs of urban buildings. *Applied Mathematical Modelling*, 59:233–250.
- Barbón, A., Bayón-Cueli, C., Bayón, L., and Ayuso, P. F. (2020). Influence of solar tracking error on the performance of a small-scale linear Fresnel reflector. *Renewable Energy*, 162:43–54.
- Barbón, A., Bayón-Cueli, C., Bayón, L., and Rodríguez, L. (2019). Investigating the influence of longitudinal tilt angles on the performance of small scale linear Fresnel reflectors for urban applications. *Renewable Energy*, 143:1581–1593.

- Barlev, D., Vidu, R., and Stroeve, P. (2011). Innovation in concentrated solar power.
- Barron-gafford, G. A., Minor, R. L., Alle, N. A., Cronin, A. D., Brooks, A. E., and Pavaozuckerman, M. A. (2016). The Photovoltaic Heat Island Effect : Larger solar power plants increase local temperatures. *Nature Publishing Group*, (May):1–7.
- Baumann, T., Nussbaumer, H., Klenk, M., Dreisiebner, A., Carigiet, F., and Baumgartner, F. (2019). Photovoltaic systems with vertically mounted bifacial PV modules in combination with green roofs. *Solar Energy*, 190:139–146.
- Bellos, E., Mathioulakis, E., Tzivanidis, C., Belessiotis, V., and Antonopoulos, K. A. (2016). Experimental and numerical investigation of a linear Fresnel solar collector with flat plate receiver. *Energy Conversion and Management*, 130:44–59.
- Bellos, E. and Tzivanidis, C. (2018). Development of analytical expressions for the incident angle modifiers of a linear Fresnel reflector. *Solar Energy*, 173:769–779.
- Bellos, E., Tzivanidis, C., and Moghimi, M. A. (2019). Reducing the optical end losses of a linear Fresnel reflector using novel techniques. *Solar Energy*, 186:247–256.
- Bellos, E., Tzivanidis, C., and Papadopoulos, A. (2018). Secondary concentrator optimization of a linear Fresnel reflector using Bezier polynomial parametrization. *Solar Energy*, 171:716–727.
- Beltagy, H., Semmar, D., Lehaut, C., and Said, N. (2017). Theoretical and experimental performance analysis of a Fresnel type solar concentrator. *Renewable Energy*, 101:782–793.
- Benjamin, K., Luo, Z., and Wang, X. (2021). Crowdsourcing urban air temperature data for estimating urban heat island and building heating/cooling load in london. *Energies*, 14(16).
- Benyakhlef, S., Al Mers, A., Merroun, O., Bouatem, A., Boutammachte, N., El Alj, S., Ajdad, H., Erregueragui, Z., and Zemouri, E. (2016). Impact of heliostat curvature on optical performance of Linear Fresnel solar concentrators. *Renewable Energy*, 89:463–474.
- Berardi, U. and Graham, J. (2020). Investigation of the impacts of microclimate on PV energy efficiency and outdoor thermal comfort. *Sustainable Cities and Society*, 62(July):102402.
- Bermejo, P., Pino, F. J., and Rosa, F. (2010). Solar absorption cooling plant in Seville. *Solar Energy*, 84(8):1503–1512.
- Bernard, J., Musy, M., Calmet, I., Bocher, E., and Keravec, P. (2017). Urban heat island temporal and spatial variations: Empirical modeling from geographical and meteorological data. *Building and Environment*, 125:423–438.
- Bernhard, R., Laabs, H., and Lalaing, J. D. (2008). Linear Fresnel collector demonstration on the PSA, Part I—design, construction and quality control. *SolarPaces . . .*, pages 1–10.
- Bhamare, D. K., Rathod, M. K., and Banerjee, J. (2019). Passive cooling techniques for building and their applicability in different climatic zones—The state of art. *Energy and Buildings*, 198:467–490.
- Bibak, B. and Tekiner-Moğulkoç, H. (2021). A comprehensive analysis of Vehicle to Grid (V2G) systems and scholarly literature on the application of such systems. *Renewable Energy Focus*, 36:1–20.
- Biljecki, F., Chew, L. Z. X., Milojevic-Dupont, N., and Creutzig, F. (2021). Open government geospatial data on buildings for planning sustainable and resilient cities.

- Biljecki, F., Stoter, J., Ledoux, H., Zlatanova, S., and Çöltekin, A. (2015). Applications of 3D city models: State of the art review. *ISPRS International Journal of Geo-Information*, 4(4):2842–2889.
- Blaise, R. and Gilles, D. (2022). Adapted strategy for large-scale assessment of solar potential on facades in urban areas focusing on the reflection component. *Solar Energy Advances*, 2:100030.
- Blanco, M. J., Amieva, J. M., and Mancilla, A. (2005). The tonatiuh software development project: AN open source approach to the simulation of solar concentrating systems. In *American Society of Mechanical Engineers, Computers and Information in Engineering Division, CED*, volume 10, pages 157–164.
- Blanco, M. J. and Santigosa, L. R. (2016). *Advances in concentrating solar thermal research and technology*.
- Boccalatte, A., Fossa, M., Gaillard, L., and Menezo, C. (2020a). Microclimate and urban morphology effects on building energy demand in different European cities. *Energy and Buildings*, 224:110129.
- Boccalatte, A., Fossa, M., and Ménézo, C. (2020b). Best arrangement of BIPV surfaces for future NZEB districts while considering urban heat island effects and the reduction of reflected radiation from solar façades. *Renewable Energy*, 160:686–697.
- Boccalatte, A., Fossa, M., Thebault, M., Ramousse, J., and Ménézo, C. (2023). Mapping the urban heat Island at the territory scale: An unsupervised learning approach for urban planning applied to the Canton of Geneva. *Sustainable Cities and Society*, 96(February):104677.
- Boccalatte, A., Thebault, M., Ménézo, C., Ramousse, J., and Fossa, M. (2022). Evaluating the impact of urban morphology on rooftop solar radiation: A new city-scale approach based on Geneva GIS data. *Energy and Buildings*, 260:111919.
- Boeing, G. (2020). Off the Grid... and Back Again? *Journal of the American Planning Association*, 87(1):123–137.
- Boito, P. and Grena, R. (2016). Optimization of the geometry of Fresnel linear collectors. *Solar Energy*, 135:479–486.
- Boito, P. and Grena, R. (2017). Optimal focal length of primary mirrors in Fresnel linear collectors. *Solar Energy*, 155:1313–1318.
- Booten, C., Kruis, N., and Christensen, C. (2012). Identifying and Resolving Issues in Energy-Plus and DOE-2 Window Heat Transfer Calculations. (August).
- Bouzarovski, S., Frankowski, J., and Tirado Herrero, S. (2018). Low-Carbon Gentrification: When Climate Change Encounters Residential Displacement. *International Journal of Urban and Regional Research*, 42(5):845–863.
- Bowler, D. E., Buyung-Ali, L., Knight, T. M., and Pullin, A. S. (2010). Urban greening to cool towns and cities: A systematic review of the empirical evidence. *Landscape and Urban Planning*, 97(3):147–155.
- Bradbrook, A. (2011). The Legal Right to Solar Access. *Environment Design Guide*, pages 1–9.
- Breeze, P. (2016). Solar Towers. In *Solar Power Generation*, pages 35–40.
- Brito, M. C. (2020). Assessing the Impact of Photovoltaics on Rooftops and Facades in the Urban Micro-Climate. *Energies*, 13(11):2717.

- Brito, M. C., Freitas, S., Guimarães, S., Catita, C., and Redweik, P. (2017). The importance of facades for the solar PV potential of a Mediterranean city using LiDAR data. *Renewable Energy*, 111:85–94.
- Brousse, O., Simpson, C., Walker, N., Fenner, D., Meier, F., Taylor, J., and Heaviside, C. (2022). Evidence of horizontal urban heat advection in London using six years of data from a citizen weather station network. *Environmental Research Letters*, 17(4):44041.
- Brozovsky, J., Gustavsen, A., and Gaitani, N. (2021). Zero emission neighbourhoods and positive energy districts – A state-of-the-art review. *Sustainable Cities and Society*, 72:103013.
- Bryan, H., Rallapalli, H., and Jin Ho, J. (2010). Designing a solar ready roof: EStablishing the conditions for a high-performing solar installation. In *39th ASES National Solar Conference 2010, SOLAR 2010*, volume 5, pages 4081 – 4110.
- Bücher, K., Kleiss, G., and Bätzner, D. (1998). Photovoltaic modules in buildings: Performance and safety. *Renewable Energy*, 15(1-4):545–551.
- Bueno, B., Hidalgo, J., Pigeon, G., Norford, L., and Masson, V. (2013a). Calculation of air temperatures above the urban canopy layer from measurements at a rural operational weather station. *Journal of Applied Meteorology and Climatology*, 52(2):472–483.
- Bueno, B., Nakano, A., and Norford, L. (2015a). Urban weather generator: a method to predict neighborhood-specific urban temperatures for use in building energy simulations. *ICUC9 - 9th International Conference on Urban Climate jointly with 12th Symposium on the Urban Environment*.
- Bueno, B., Nakano, A., and Norford, L. (2015b). Urban weather generator: a method to predict neighborhood-specific urban temperatures for use in building energy simulations. *ICUC9 - 9th International Conference on Urban Climate jointly with 12th Symposium on the Urban Environment*, i.
- Bueno, B., Norford, L., Hidalgo, J., and Pigeon, G. (2013b). The urban weather generator. *Journal of Building Performance Simulation*, 6(4):269–281.
- Bueno, B., Pigeon, G., Norford, L. K., Zibouche, K., and Marchadier, C. (2012). Development and evaluation of a building energy model integrated in the TEB scheme. *Geoscientific Model Development*, 5(2):433–448.
- Bueno, B., Roth, M., Norford, L., and Li, R. (2014). Computationally efficient prediction of canopy level urban air temperature at the neighbourhood scale. *Urban Climate*, 9:35–53.
- Buie, Damien, Christopher Dey and Mills., D. (2002). Optical considerations in line focus Fresnel concentrators. *11th Proceedings of the SolarPACES International Symposium on Solar Thermal Concentrating Technologies*.
- Buitinck, L., Louppe, G., Blondel, M., Pedregosa, F., Müller, A. C., Grisel, O., Niculae, V., Prettenhofer, P., Gramfort, A., Grobler, J., Layton, R., Vanderplas, J., Joly, A., Holt, B., and Varoquaux, G. (2013). API design for machine learning software: experiences from the scikit-learn project.
- Buker, M. S. and Riffat, S. B. (2015). Building integrated solar thermal collectors - A review. *Renewable and Sustainable Energy Reviews*, 51:327–346.
- Burgstall, A. (2019). Representing the Urban Heat Island Effect in Future Climates. (105):92.
- Cai, C., Guo, Z., Zhang, B., Wang, X., Li, B., and Tang, P. (2021). Urban morphological feature extraction and multi-dimensional similarity analysis based on deep learning approaches. *Sustainability (Switzerland)*, 13(12).

- Calderón, A., Barreneche, C., Prieto, C., Segarra, M., and Fernández, A. I. (2021). Concentrating Solar Power Technologies: A Bibliometric Study of Past, Present and Future Trends in Concentrating Solar Power Research. *Frontiers in Mechanical Engineering*, 7:45.
- Calise, F., Cappiello, F. L., Dentice d'Accadia, M., Petrakopoulou, F., and Vicidomini, M. (2022). A solar-driven 5th generation district heating and cooling network with ground-source heat pumps: a thermo-economic analysis. *Sustainable Cities and Society*, 76:103438.
- Cameron, C. P., Boyson, W. E., and Riley, D. M. (2008). Comparison of PV system performance-model predictions with measured PV system performance. In *Conference Record of the IEEE Photovoltaic Specialists Conference*.
- Cameron, R. W. F. and Blanuša, T. (2016). Green infrastructure and ecosystem services - is the devil in the detail? *Annals of botany*, 118(3):377–391.
- Cardona, G. and Pujol-Nadal, R. (2020). OTSsun, a python package for the optical analysis of solar-thermal collectors and photovoltaic cells with arbitrary geometry. *PLoS ONE*, 15(10 October).
- Carneiro, C., Morello, E., Desthieux, G., and Golay, F. (2010). Urban environment quality indicators: application to solar radiation and morphological analysis on built area. *Advances in visualization, imaging and simulation*.
- Castellani, B., Gambelli, A. M., Nicolini, A., and Rossi, F. (2020). Optic-energy and visual comfort analysis of retro-reflective building plasters. *Building and Environment*, 174:106781.
- Castellani, B., Morini, E., Anderini, E., Filipponi, M., and Rossi, F. (2017). Development and characterization of retro-reflective colored tiles for advanced building skins. *Energy and Buildings*, 154:513–522.
- Cavadini, G. B. and Cook, L. M. (2021). Green and cool roof choices integrated into rooftop solar energy modelling. *Applied Energy*, 296(May):117082.
- Cesario, E., Uchubilo, P. I., Vinci, A., and Zhu, X. (2020). Discovering Multi-density Urban Hotspots in a Smart City. *Proceedings - 2020 IEEE International Conference on Smart Computing, SMARTCOMP 2020*, pages 332–337.
- Chàfer, M., Tan, C. L., Hien, W. N., Pisello, A., and Cabeza, L. F. (2022). Mobile Measurements of Microclimatic Variables Through the Central Area of Singapore. *SSRN Electronic Journal*, 83(June).
- Chaitanya Prasad, G. S., Reddy, K. S., and Sundararajan, T. (2017). Optimization of solar linear Fresnel reflector system with secondary concentrator for uniform flux distribution over absorber tube. *Solar Energy*, 150:1–12.
- Chapman, A. J., McLellan, B., and Tezuka, T. (2016). Residential solar PV policy: An analysis of impacts, successes and failures in the Australian case. *Renewable Energy*, 86:1265–1279.
- Chatzipoulka, C., Compagnon, R., and Nikolopoulou, M. (2016). Urban geometry and solar availability on façades and ground of real urban forms: using London as a case study. *Solar Energy*, 138:53–66.
- Chaves, J. and Collares-Pereira, M. (2010). Etendue-matched two-stage concentrators with multiple receivers. *Solar Energy*, 84(2):196–207.
- Checker, M. (2011). Wiped Out by the “Greenwave”: Environmental Gentrification and the Paradoxical Politics of Urban Sustainability. *City & Society*, 23(2):210–229.

- Chemisana, D. and Ibáñez, M. (2010). Linear Fresnel concentrators for building integrated applications. *Energy Conversion and Management*, 51(7):1476–1480.
- Chen, H. C., Han, Q., and de Vries, B. (2020). Urban morphology indicator analyzes for urban energy modeling. *Sustainable Cities and Society*, 52(September).
- Chen, Y., Shu, B., Zhang, R., and Amani-Beni, M. (2023). LST determination of different urban growth patterns: A modeling procedure to identify the dominant spatial metrics. *Sustainable Cities and Society*, 92(February):104459.
- Cheng, L., Zhang, F., Li, S., Mao, J., Xu, H., Ju, W., Liu, X., Wu, J., Min, K., Zhang, X., and Li, M. (2020). Solar energy potential of urban buildings in 10 cities of China. *Energy*, 196:117038.
- Cheng, Z. D., He, Y. L., and Cui, F. Q. (2013). A new modelling method and unified code with MCRT for concentrating solar collectors and its applications. *Applied Energy*, 101:686–698.
- Chumpolrat, K., Sangsuwan, V., Udomdachanut, N., Kittisontirak, S., Songtraai, S., Chinnavorn-rungsee, P., Limmanee, A., Sritharathikhun, J., and Sriprapha, K. (2014). Effect of ambient temperature on performance of grid-connected inverter installed in Thailand. *International Journal of Photoenergy*, 2014(March 2010).
- Ciriminna, R., Meneguzzo, F., Pecoraino, M., and Pagliaro, M. (2019). Solar Green Roofs: A Unified Outlook 20 Years On. *Energy Technology*, 7(6):1900128.
- Ciulla, G., Lo Brano, V., Di Dio, V., and Cipriani, G. (2014). A comparison of different one-diode models for the representation of I-V characteristic of a PV cell.
- Clarke, P. (2019). The legal right to solar access. *Environment*, (3):1–15.
- Collins, D. and Lindkvist, C. (2022). Block by block: potential and challenges of the blockchain in the context of facilities management. *IOP Conference Series: Earth and Environmental Science*, 1101(6):62003.
- Compagnon, R. (2004). Solar and daylight availability in the urban fabric. In *Energy and Buildings*, volume 36, pages 321–328.
- Cos, J., Doblas-Reyes, F., Jury, M., Marcos, R., Bretonnière, P.-A., and Samsó, M. (2022). The Mediterranean climate change hotspot in the CMIP5 and CMIP6 projections. *Earth System Dynamics*, 13(1):321–340.
- Couty, P. and Simon, E. (2017). Solar Energy in retrofitting building: 10 case studies of integration in the residential heritage of the 20th century in Western Switzerland. *Energy Procedia*, 122:931–936.
- Croce, S., D’Agnolo, E., Caini, M., and Paparella, R. (2021). The Use of Cool Pavements for the Regeneration of Industrial Districts. *Sustainability*, 13(11).
- Croce, S., Hachem-Vermette, C., Formolli, M., Vettorato, D., and Snow, M. (2022). Surface Uses in Solar Neighborhoods. Technical report.
- Croce, S. and Vettorato, D. (2021). Urban surface uses for climate resilient and sustainable cities: A catalogue of solutions. *Sustainable Cities and Society*, 75:103313.
- Cuce, E. and Riffat, S. B. (2015). A state-of-the-art review on innovative glazing technologies. *Renewable and Sustainable Energy Reviews*, 41:695–714.
- Cumpston, J. and Coventry, J. (2017). Derivation of error sources for experimentally derived heliostat shapes. In *AIP Conference Proceedings*, volume 1850.

- Czachura, A., Kanters, J., Gentile, N., and Wall, M. (2022). Solar Performance Metrics in Urban Planning: A Review and Taxonomy. *Buildings*, 12(4).
- D'Acci, L. and Batty, M. (2019). *The Mathematics of Urban Morphology Foreword by Michael Batty*.
- Darula, S., Christoffersen, J., and Malikova, M. (2015). Sunlight and Insolation of Building Interiors. *Energy Procedia*, 78:1245–1250.
- Davda, P. C. J., Sex, G., and Broomfield, J. (2010). 24 - Materials for energy efficiency and thermal comfort in high performance buildings. In Hall, M. R. B. T. M. f. E. E. and in Buildings, T. C., editors, *Woodhead Publishing Series in Energy*, pages 589–630. Woodhead Publishing.
- Davis, M. W., Fanney, A. H., and Dougherty, B. P. (2001). Prediction of building integrated photovoltaic cell temperatures. *Journal of Solar Energy Engineering, Transactions of the ASME*, 123(3):200–210.
- de Almeida, C. R., Teodoro, A. C., and Gonçalves, A. (2021). Study of the urban heat island (Uhi) using remote sensing data/techniques: A systematic review.
- De Blas, M. A., Torres, J. L., Prieto, E., and García, A. (2002). Selecting a suitable model for characterizing photovoltaic devices. *Renewable Energy*, 25(3):371–380.
- De Luca, F. and Dogan, T. (2019). A novel solar envelope method based on solar ordinances for urban planning. *Building Simulation*, 12(5):817–834.
- De Luca, F., Naboni, E., and Lobaccaro, G. (2021). Tall buildings cluster form rationalization in a Nordic climate by factoring in indoor-outdoor comfort and energy. *Energy and Buildings*, 238:110831.
- De Luca, F., Sepúlveda, A., and Varjas, T. (2022). Multi-performance optimization of static shading devices for glare, daylight, view and energy consideration. *Building and Environment*, 217:109110.
- Delgarm, N., Sajadi, B., Delgarm, S., and Kowsary, F. (2016). A novel approach for the simulation-based optimization of the buildings energy consumption using NSGA-II: Case study in Iran. *Energy and Buildings*, 127:552–560.
- Desai, N. B. and Bandyopadhyay, S. (2017). Line-focusing concentrating solar collector-based power plants: a review.
- Desthieux, G., Carneiro, C., Camponovo, R., Ineichen, P., Morello, E., Boulmier, A., Abdennadher, N., Dervev, S., and Ellert, C. (2018a). Solar energy potential assessment on rooftops and facades in large built environments based on lidar data, image processing, and cloud computing. Methodological background, application, and validation in geneva (solar cadaster). *Frontiers in Built Environment*, 4(March).
- Desthieux, G., Carneiro, C., Susini, A., Abdennadher, N., Boulmier, A., Dubois, A., Camponovo, R., Beni, D., Bach, M., Leverington, P., and Morello, E. (2018b). Solar Cadaster of Geneva: A Decision Support System for Sustainable Energy Management. *From Science to Society*, (January):129–137.
- Devetaković, M., Djordjević, D., Radojević, M., Krstić-Furundžić, A., Burduhos, B.-G., Martinopoulos, G., Neagoe, M., and Lobaccaro, G. (2020). Photovoltaics on Landmark Buildings with Distinctive Geometries. *Applied Sciences*, 10(19):6696.

- Dhimish, M., Ahmad, A., and Tyrrell, A. M. (2022). Inequalities in photovoltaics modules reliability: From packaging to PV installation site. *Renewable Energy*, 192:805–814.
- Dhimish, M. and Alrashidi, A. (2020). Photovoltaic degradation rate affected by different weather conditions: A case study based on pv systems in the uk and australia. *Electronics (Switzerland)*, 9(4).
- Dhoke, A. and Mengede, A. (2018). Degradation analysis of PV modules operating in Australian environment. *2017 Australasian Universities Power Engineering Conference, AUPEC 2017*, 2017-Novem:1–5.
- Di Lauro, P., Heß, S., Rose, S., and Rommel, M. (2008). Characterisation of the Optical Properties of Solar Collectors by Ray-tracing Simulations.
- Díaz-López, C., Carpio, M., Martín-Morales, M., and Zamorano, M. (2021). Defining strategies to adopt Level(s) for bringing buildings into the circular economy. A case study of Spain. *Journal of Cleaner Production*, 287:125048.
- Dibble, J., Prelorndjos, A., Romice, O., Zanella, M., Strano, E., Pagel, M., and Porta, S. (2017). On the origin of spaces: Morphometric foundations of urban form evolution:. *EPB: Urban Analytics and City Science*, 46(4):707–730.
- Dierauf, T., Growitz, A., Kurtz, S., and Hansen, C. (2013). Weather-Corrected Performance Ratio. *NREL Technical Report NREL/TP-5200-57991*, (April):1–16.
- Dimitrov, S., Popov, A., and Iliev, M. (2021). An application of the LCZ approach in surface urban heat island mapping in Sofia, Bulgaria. *Atmosphere*, 12(11).
- Dissanayake, K., Kurugama, K., and Ruwanthi, C. (2020). Ecological Evaluation of Urban Heat Island Effect in Colombo City, Sri Lanka Based on Landsat 8 Satellite Data. In *2020 Moratuwa Engineering Research Conference (MERCon)*, pages 531–536.
- Dodman, D., Hayward, B., Pelling, M., Castan Broto, V., Chow, W. T. L., Chu, E., Dawson, R., Khirfan, L., McPhearson, T., Prakash, A., Zheng, Y., and Ziervogel, G. (2023). Cities, Settlements and Key Infrastructure. In *Climate Change 2022 – Impacts, Adaptation and Vulnerability*, pages 907–1040. Cambridge University Press.
- Dolara, A., Leva, S., and Manzolini, G. (2015). Comparison of different physical models for PV power output prediction. *Solar Energy*, 119:83–99.
- D’Orazio, M., Di Perna, C., and Di Giuseppe, E. (2014). Experimental operating cell temperature assessment of BIPV with different installation configurations on roofs under Mediterranean climate. *Renewable Energy*, 68:378–396.
- Driesse, A., Stein, J. S., and Theristis, M. (2022). Improving Common PV Module Temperature Models by Incorporating Radiative Losses to the Sky. (August).
- Duffie, J. A. and Beckman, W. A. (2013). *Solar Engineering of Thermal Processes: Fourth Edition*.
- E. European Commission (2005). Energy Performance of Buildings Directive.
- Economidou, M., Todeschi, V., Bertoldi, P., D’Agostino, D., Zangheri, P., and Castellazzi, L. (2020). Review of 50years of EU energy efficiency policies for buildings. *Energy and Buildings*, 225:110322.
- Eddhibi, F., Amara, M. B., Balghouthi, M., Qoaidar, L., and Guizani, A. A. (2017). Analytic optical design of a Linear Fresnel solar collector with variable parameters. *Journal of Materials and Environmental Science*, 8(11):4068–4084.

- Eder, G., Peharz, G., Trattinig, R., Bonomo, P., Saretta, E., Frontini, F., Polo López, C. S., Wilson, H. R., Eisenlohr, J., and Chivelet, N. M. (2019). Coloured bipv: Market, research and development.
- Eiffert, P. (2003). Non-Technical Barriers to the Commercialization of PV Power Systems in the Built Environment International Energy Agency PVPS Task 7 : Photovoltaic Power Systems in the Built Non-Technical Barriers to the Commercialization of PV Power Systems in the Built. (January).
- El Gharbi, N., Derbal, H., Bouaichaoui, S., and Said, N. (2011). A comparative study between parabolic trough collector and linear Fresnel reflector technologies. In *Energy Procedia*, volume 6, pages 565–572.
- Elhabodi, T. S., Yang, S., Parker, J., Khattak, S., He, B.-J., and Attia, S. (2023). A review on BIPV-induced temperature effects on urban heat islands. *Urban Climate*, 50:101592.
- Elmaanaoui, Y. and Saifaoui, D. (2014). Shading efficiency calculation for Linear Fresnel reflector. In *Proceedings of 2014 International Renewable and Sustainable Energy Conference, IRSEC 2014*, pages 100–103.
- ENEA (2020). Energia: solare, alleanza ENEA e industria per due nuove centrali termodinamiche in Sicilia.
- ENVI-met (2021). ENVI-met.
- Erell, E., Pearlmutter, D., Boneh, D., and Kutiel, P. B. (2014). Effect of high-albedo materials on pedestrian heat stress in urban street canyons. *Urban Climate*, 10(P2):367–386.
- Erell, E. and Williamson, T. (2006). Simulating air temperature in an urban street canyon in all weather conditions using measured data at a reference meteorological station. *International Journal of Climatology*, 26(12):1671–1694.
- Esclapés, J., Ferreira, I., Piera, J., and Teller, J. (2014). A method to evaluate the adaptability of photovoltaic energy on urban façades. *Solar Energy*, 105:414–427.
- European Commission (2018). Energy performance of buildings directive revision.
- European Commission for Energy (2015). *Energy Performance of Buildings Directive (EPBD) : compliance study : final report*. Publications Office.
- Evans, D. L. (1981). Simplified method for predicting photovoltaic array output. *Solar Energy*, 27(6):555–560.
- Fabiani, C., Pisello, A. L., Bou-Zeid, E., Yang, J., and Cotana, F. (2019). Adaptive measures for mitigating urban heat islands: The potential of thermochromic materials to control roofing energy balance. *Applied Energy*, 247(August 2018):155–170.
- Faiman, D. (2008). Assessing the outdoor operating temperature of photovoltaic modules. *Progress in Photovoltaics: Research and Applications*, 16(4):307–315.
- Fenner, D., Meier, F., Scherer, D., and Polze, A. (2014). Spatial and temporal air temperature variability in Berlin, Germany, during the years 2001-2010. *Urban Climate*, 10(P2):308–331.
- Fernández-Ahumada, L. M., Osuna-Mérida, M., López-Sánchez, J., Gómez-Uceda, F. J., López-Luque, R., and Varo-Martínez, M. (2022). Use of Polar Heliostats to Improve Levels of Natural Lighting inside Buildings with Little Access to Sunlight. *Sensors*, 22(16):5996.

- Finck, C., Li, R., Kramer, R., and Zeiler, W. (2018). Quantifying demand flexibility of power-to-heat and thermal energy storage in the control of building heating systems. *Applied Energy*, 209:409–425.
- Fleck, R., Gill, R. L., Saadeh, S., Pettit, T., Wooster, E., Torpy, F., and Irga, P. (2022). Urban green roofs to manage rooftop microclimates: A case study from Sydney, Australia. *Building and Environment*, 209:108673.
- Fleischmann, M. (2017). *A Systematisation of Attributes for Quantitative Urban Morphology Measuring Urban Form*. PhD thesis.
- Fleischmann, M. (2019). momepy: Urban Morphology Measuring Toolkit. *Journal of Open Source Software*, 4(43):1807.
- Fleischmann, M., Feliciotti, A., and Kerr, W. (2022a). Evolution of Urban Patterns: Urban Morphology as an Open Reproducible Data Science. *Geographical Analysis*, 54(3):536–558.
- Fleischmann, M., Feliciotti, A., Romice, O., and Porta, S. (2020). Morphological tessellation as a way of partitioning space: Improving consistency in urban morphology at the plot scale. *Computers, Environment and Urban Systems*, 80(November 2019):101441.
- Fleischmann, M., Feliciotti, A., Romice, O., and Porta, S. (2022b). Methodological foundation of a numerical taxonomy of urban form. *Environment and Planning B: Urban Analytics and City Science*, 49(4):1283–1299.
- Florio, P. (2018). Towards a GIS-based Multiscale Visibility Assessment Method for Solar Urban Planning THÈSE N O 8826 (2018) ÉCOLE POLYTECHNIQUE FÉDÉRALE DE LAUSANNE PRÉSENTÉE LE 14 SEPTEMBRE 2018 À LA FACULTÉ DE L'ENVIRONNEMENT NATUREL, ARCHITECTURAL ET CONSTRUIT LABORATO. 8826:247.
- Flourentzou, F. (2019). Possible strategies and obstacles in the pathway towards energy transition of residential building stocks in Switzerland. *IOP Conference Series: Earth and Environmental Science*, 323(1).
- Formolli, M., Croce, S., Vettorato, D., Paparella, R., Scognamiglio, A., Mainini, A. G., and Lobaccaro, G. (2022). Solar Energy in Urban Planning: Lesson Learned and Recommendations from Six Italian Case Studies. *Applied Sciences*, 12(6).
- Formolli, M., Kleiven, T., and Lobaccaro, G. (2023). Assessing solar energy accessibility at high latitudes: A systematic review of urban spatial domains, metrics, and parameters. *Renewable and Sustainable Energy Reviews*, 177:113231.
- Formolli, M., Lobaccaro, G., and Kanters, J. (2021). Solar energy in the nordic built environment: Challenges, opportunities and barriers. *Energies*, 14(24).
- Fossa, M., Boccalatte, A., and Memme, S. (2021). Solar Fresnel modelling, geometry enhancement and 3D ray tracing analysis devoted to different energy efficiency definitions and applied to a real facility. *Solar Energy*, 216:75–89.
- Fouad, M. M., Shihata, L. A., and Morgan, E. S. I. (2017). An integrated review of factors influencing the performance of photovoltaic panels.
- Freitas, S., Catita, C., Redweik, P., and Brito, M. C. (2015). Modelling solar potential in the urban environment: State-of-the-art review. *Renewable and Sustainable Energy Reviews*, 41:915–931.

- Friedlingstein, P., O'sullivan, M., Jones, M. W., Andrew, R. M., Gregor, L., Hauck, J., Le Quéré, C., Luijkx, I. T., Olsen, A., Peters, G. P., Peters, W., Pongratz, J., Schwingshackl, C., Sitch, S., Canadell, J. G., Ciais, P., Jackson, R. B., Alin, S. R., Alkama, R., Arneeth, A., Arora, V. K., Bates, N. R., Becker, M., Bellouin, N., Bittig, H. C., Bopp, L., Chevallier, F., Chini, L. P., Cronin, M., Evans, W., Falk, S., Feely, R. A., Gasser, T., Gehlen, M., Gkritzalis, T., Gloege, L., Grassi, G., Gruber, N., Gürses, Ö., Harris, I., Hefner, M., Houghton, R. A., Hurtt, G. C., Iida, Y., Ilyina, T., Jain, A. K., Jersild, A., Kadono, K., Kato, E., Kennedy, D., Klein Goldewijk, K., Knauer, J., Korsbakken, J. I., Landschützer, P., Lefèvre, N., Lindsay, K., Liu, J., Liu, Z., Marland, G., Mayot, N., Mcgrath, M. J., Metzl, N., Monacci, N. M., Munro, D. R., Nakaoka, S. I., Niwa, Y., O'brien, K., Ono, T., Palmer, P. I., Pan, N., Pierrot, D., Pocock, K., Poulter, B., Resplandy, L., Robertson, E., Rödenbeck, C., Rodriguez, C., Rosan, T. M., Schwinger, J., Séférian, R., Shutler, J. D., Skjelvan, I., Steinhoff, T., Sun, Q., Sutton, A. J., Sweeney, C., Takao, S., Tanhua, T., Tans, P. P., Tian, X., Tian, H., Tilbrook, B., Tsujino, H., Tubiello, F., Van Der Werf, G. R., Walker, A. P., Wanninkhof, R., Whitehead, C., Willstrand Wranne, A., Wright, R., Yuan, W., Yue, C., Yue, X., Zaehle, S., Zeng, J., and Zheng, B. (2022). Global Carbon Budget 2022. *Earth System Science Data*, 14(11):4811–4900.
- Fuentes, M. K., Laboratory, S., and of Energy, U. S. D. (1987). *A Simplified Thermal Model for Flat-plate Photovoltaic Arrays*. SAND (Series) (Albuquerque, N.M.). Sandia Laboratories, United States.
- Fuqiang, W., Ziming, C., Jianyu, T., Yuan, Y., Yong, S., and Linhua, L. (2017). Progress in concentrated solar power technology with parabolic trough collector system: A comprehensive review.
- Gaglia, A. G., Lykoudis, S., Argiriou, A. A., Balaras, C. A., and Dialynas, E. (2017). Energy efficiency of PV panels under real outdoor conditions—An experimental assessment in Athens, Greece. *Renewable Energy*, 101:236–243.
- Gallego-Castillo, C., Heleno, M., and Victoria, M. (2021). Self-consumption for energy communities in Spain: A regional analysis under the new legal framework. *Energy Policy*, 150:112144.
- García-Barberena, J., Monreal, A., Mutuberria, A., and Sánchez, M. (2014). Towards cost-competitive solar towers - Energy cost reductions based on decoupled solar combined cycles (DSCC). In *Energy Procedia*, volume 49, pages 1350–1360.
- Garshasbi, S., Khan, A., and Santamouris, M. (2023). On the cooling energy penalty of urban photovoltaics: a case study in Sydney, Australia. *Energy and Buildings*, 294(June):113259.
- Gasparatos, A., Doll, C. N. H., Esteban, M., Ahmed, A., and Olang, T. A. (2017). Renewable energy and biodiversity: Implications for transitioning to a Green Economy. *Renewable and Sustainable Energy Reviews*, 70:161–184.
- Ghaleb, B. and Asif, M. (2022). Application of solar PV in commercial buildings: Utilizability of rooftops. *Energy and Buildings*, 257:111774.
- Gielen, D., Boshell, F., Saygin, D., Bazilian, M. D., Wagner, N., and Gorini, R. (2019). The role of renewable energy in the global energy transformation. *Energy Strategy Reviews*, 24:38–50.
- Gmbh, G.-n. U. (2020). Situation climato-écologique du canton de Genève : Analyse climatique sur la base d'un modèle Décembre. Technical report.
- Gökmen, N., Hu, W., Hou, P., Chen, Z., Sera, D., and Spataru, S. (2016). Investigation of wind speed cooling effect on PV panels in windy locations. *Renewable Energy*, 90:283–290.

- Gómez-Navarro, T., Brazzini, T., Alfonso-Solar, D., and Vargas-Salgado, C. (2021). Analysis of the potential for PV rooftop prosumer production: Technical, economic and environmental assessment for the city of Valencia (Spain). *Renewable Energy*, 174:372–381.
- González-Mora, E. and Dolores Durán García, M. (2020). Methodology for an opto-geometric optimization of a linear Fresnel reflector for direct steam generation. *Energies*, 13(2).
- Good, C. S., Lobaccaro, G., and Hårklau, S. (2014). Optimization of Solar Energy Potential for Buildings in Urban Areas – A Norwegian Case Study. In *Energy Procedia*, volume 58, pages 166–171.
- Gould, K. A. and Lewis, T. L. (2021). Resilience Gentrification: Environmental Privilege in an Age of Coastal Climate Disasters. *Frontiers in Sustainable Cities*, 3.
- Grimmond, C. S., Roth, M., Oke, T. R., Au, Y. C., Best, M., Betts, R., Carmichael, G., Cleugh, H., Dabberdt, W., Emmanuel, R., Freitas, E., Fortuniak, K., Hanna, S., Klein, P., Kalkstein, L. S., Liu, C. H., Nickson, A., Pearlmutter, D., Sailor, D., and Voogt, J. (2010). Climate and more sustainable cities: Climate information for improved planning and management of cities (Producers/Capabilities Perspective). *Procedia Environmental Sciences*, 1(1):247–274.
- Grimmond, C. S. B. (2017). The integrated WRF / urban modelling system : Development , evaluation , and applications to urban environmental problems The integrated WRF / urban modelling system : development , evaluation , and applications to urban environmental. (March):1–38.
- Gross, G. (1992). Results of supercomputer simulations of meteorological mesoscale phenomena. *Fluid Dynamics Research*, 10(4-6):483–498.
- Grözinger, J., Boermans, T., Ashok, J., Wehringer, F., and Seehusen, J. (2014). Overview of Member States information on NZEBs Background paper – final report.
- Guerreiro, S. B., Dawson, R. J., Kilsby, C., Lewis, E., and Ford, A. (2018). Future heat-waves, droughts and floods in 571 European cities. *Environmental Research Letters*, 13(3).
- Güneralp, B., Zhou, Y., Ürge-Vorsatz, D., Gupta, M., Yu, S., Patel, P. L., Fragkias, M., Li, X., and Seto, K. C. (2017). Global scenarios of urban density and its impacts on building energy use through 2050. *Proceedings of the National Academy of Sciences of the United States of America*, 114(34):8945–8950.
- Gupta, N. and Tiwari, G. N. (2016). Review of passive heating/cooling systems of buildings. *Energy Science and Engineering*, 4(5):305–333.
- Gupta, R., Pena-Bello, A., Streicher, K. N., Roduner, C., Thöni, D., Patel, M. K., and Parra, D. (2021). Spatial analysis of distribution grid capacity and costs to enable massive deployment of PV, electric mobility and electric heating. *Applied Energy*, 287:116504.
- Haagen, M., Zahler, C., Zimmermann, E., and Al-Najami, M. M. (2015). Solar Process Steam for Pharmaceutical Industry in Jordan. *Energy Procedia*, 70:621–625.
- Habeeb, D., Vargo, J., and Stone, B. (2015). Rising heat wave trends in large US cities. *Natural Hazards*, 76(3):1651–1665.
- Haeberle, A., Zahler, C., Lerchenmueller, H., Mertins, M., Wittwer, C., Trieb, F., and Dersch, J. (2002). The Solarmundo line focussing Fresnel collector. Optical and thermal performance and cost calculations. *Proceedings of SolarPACES*, (January):1–11.
- Hagberg, A. A., Schult, D. A., and Swart, P. J. (2008). Proceedings of the Python in Science Conference (SciPy): Exploring Network Structure, Dynamics, and Function using NetworkX. In *Proceedings of the 7th python in science conference*, pages 11–15, Pasadena, CA USA.

- Hai, M. A., Moula, M. M. E., and Seppälä, U. (2017). Results of intention-behaviour gap for solar energy in regular residential buildings in Finland. *International Journal of Sustainable Built Environment*, 6(2):317–329.
- Hasan, A., Alnoman, H., and Rashid, Y. (2016). Impact of integrated photovoltaic-phase change material system on building energy efficiency in hot climate. *Energy and Buildings*, 130:495–505.
- Hashemi, F. (2020). A novel approach for investigating canopy heat island effects on building energy performance : A case study of Center City of Philadelphia , PA. (November):1–6.
- Hassan Daher, D., Gaillard, L., and Ménézo, C. (2022). Experimental assessment of long-term performance degradation for a PV power plant operating in a desert maritime climate. *Renewable Energy*, 187:44–55.
- Hay, J. E. (1979). Calculation of monthly mean solar radiation for horizontal and inclined surfaces. *Solar Energy*, 23(4):301–307.
- He, B.-J. (2019). Towards the next generation of green building for urban heat island mitigation: Zero UHI impact building. *Sustainable Cities and Society*, 50:101647.
- He, J., Qiu, Z., Li, Q., and Zhang, Y. (2012). Optical design of linear Fresnel reflector solar concentrators. In *Energy Procedia*, volume 14, pages 1960–1966.
- Heffernan, E., Sohel, M., Beazley, S., and McCarthy, T. (2017). From BIM (Building Information Modelling) to BEM (Building Energy Modelling): A collaborative approach. *Australasian Building Simulation 2017*, pages 1–11.
- Heimsath, A., Bern, G., Van Rooyen, D., and Nitz, P. (2014). Quantifying optical loss factors of small linear concentrating collectors for process heat application. In *Energy Procedia*, volume 48, pages 77–86.
- Hertel, J. D., Martinez-Moll, V., and Pujol-Nadal, R. (2015). Estimation of the influence of different incidence angle modifier models on the biaxial factorization approach. *Energy Conversion and Management*, 106:249–259.
- Heusinger, J., Broadbent, A. M., Krayenhoff, E. S., and Weber, S. (2021). Adaptation of a photovoltaic energy balance model for rooftop applications. *Building and Environment*, 192(September 2020):107628.
- Heusinger, J., Broadbent, A. M., Sailor, D. J., and Georgescu, M. (2020). Introduction, evaluation and application of an energy balance model for photovoltaic modules. *Solar Energy*, 195(November 2019):382–395.
- Hoffmann, S. and Koehl, M. (2014). Effect of humidity and temperature on the potential-induced degradation. *Progress in Photovoltaics: Research and Applications*, 22(2):173–179.
- Hong, T., Chen, Y., Luo, X., Luo, N., and Lee, S. H. (2020). Ten questions on urban building energy modeling. *Building and Environment*, 168(October 2019):106508.
- Hongn, M., Larsen, S. F., Gea, M., and Altamirano, M. (2015). Least square based method for the estimation of the optical end loss of linear Fresnel concentrators. *Solar Energy*, 111:264–276.
- Horta, P. and Osório, T. (2014). Optical characterization parameters for line-focusing solar concentrators: Measurement procedures and extended simulation results. In *Energy Procedia*, volume 49, pages 98–108.

- Houet, T. and Pigeon, G. (2011). Mapping urban climate zones and quantifying climate behaviors - An application on Toulouse urban area (France). *Environmental Pollution*, 159(8-9):2180–2192.
- Hu, J. and Yu, X. B. (2019). Adaptive thermochromic roof system: Assessment of performance under different climates. *Energy and Buildings*, 192:1–14.
- Hu, Z., He, W., Ji, J., and Zhang, S. (2017). A review on the application of Trombe wall system in buildings. *Renewable and Sustainable Energy Reviews*, 70(February 2016):976–987.
- Huang, J., Jones, P., Zhang, A., Peng, R., Li, X., and wai Chan, P. (2020). Urban Building Energy and Climate (UrBEC) simulation: Example application and field evaluation in Sai Ying Pun, Hong Kong. *Energy and Buildings*, 207(February 2020).
- Hwang, R. L., Lin, T. P., and Lin, F. Y. (2020). Evaluation and mapping of building overheating risk and air conditioning use due to the urban heat island effect. *Journal of Building Engineering*, 32(November):101726.
- Hyams, D. G. (2014). CurveExpert Professional Documentation Release 2.0.4 Daniel G. Hyams.
- IEA (2014). Technology Roadmap - Solar Photovoltaic Energy 2014. Technical report.
- IEA (2021). World Energy Outlook 2021 : Part of the World Energy Outlook. *International Energy Agency*, page 386.
- Industrial Solar (2023). Fresnel Collector LF-11: Concentrating sunlight for industrial process heat.
- Intergovernmental Panel on Climate Change (2023). Climate Change 2023: Synthesis Report. A Report of the Intergovernmental Panel on Climate Change. Contribution of Working Groups I, II and III to the Sixth Assessment Report of the Intergovernmental Panel on Climate Change IPCC. Technical report, Geneva.
- International Energy Agency (2021). Conditions and Requirements for the Technical Feasibility of a Power System with a High Share of Renewables in France Towards 2050. Technical report.
- International Energy Agency (2022a). Renewable Energy Market Update. *Renewable Energy Market Update*.
- International Energy Agency (2022b). Special Report on Solar PV Global Supply Chains. Technical report.
- International Renewable Energy Agency (2011). Technology Roadmap. Technical report.
- International Renewable Energy Agency (2022). World Energy Transition - Outlook 2022: 1.5°C Pathway. Technical report, Abu Dhabi.
- IPCC (2022). Climate Change 2022: Impacts, Adaptation, and Vulnerability. Contribution of Working Group II to the Sixth Assessment Report of the Intergovernmental Panel on Climate Change. Technical report, The Intergovernmental Panel on Climate Change.
- Irga, P., Fleck, R., Wooster, E., Torpy, F., Alameddine, H., and Sharman, L. (2021). Green roof and solar array. Technical report, Sidney.
- Jacos, B., Mikhailovich, N., and Delaney, C. (2014). Benchmarking Australia's Urban Tree Canopy: An i-Tree Assessment, Final Report 2014. page 47.

- Jakubiec, J. A. and Reinhart, C. F. (2013). A method for predicting city-wide electricity gains from photovoltaic panels based on LiDAR and GIS data combined with hourly Daysim simulations. *Solar Energy*, 93:127–143.
- Jänicke, B., Milošević, D., and Manavvi, S. (2021). Review of user-friendly models to improve the urban micro-climate. *Atmosphere*, 12(10):1–22.
- Jankovic, A. and Goia, F. (2021). Impact of double skin facade constructional features on heat transfer and fluid dynamic behaviour. *Building and Environment*, 196:107796.
- Jelle, B. P. and Breivik, C. (2012). State-of-the-art building integrated photovoltaics. In *Energy Procedia*, volume 20, pages 68–77.
- Jiang, A., Liu, X., Czarnecki, E., and Zhang, C. (2019). Hourly weather data projection due to climate change for impact assessment on building and infrastructure. *Sustainable Cities and Society*, 50:101688.
- Johari, F., Peronato, G., Sadeghian, P., Zhao, X., and Widén, J. (2020). Urban building energy modeling: State of the art and future prospects. *Renewable and Sustainable Energy Reviews*, 128.
- Johnson, G. T. and Watson, I. D. (1984). The determination of view-factors in urban canyons. *Journal of Climate & Applied Meteorology*, 23(2):329–335.
- Johnsson, J. and Adl-Zarrabi, B. (2020). A numerical and experimental study of a pavement solar collector for the northern hemisphere. *Applied Energy*, 260(June 2019):114286.
- Jordahl, K., den Bossche, J. V., Wasserman, J., McBride, J., Gerard, J., Fleischmann, M., Tratner, J., Perry, M., Farmer, C., Hjelle, G. A., Gillies, S., Cochran, M., Bartos, M., Culbertson, L., Eubank, N., Maxalbert, Rey, S., Bilogur, A., Arribas-Bel, D., Ren, C., Wilson, J., Journois, M., Wolf, L. J., Wasser, L., Özak, Ö., YuichiNotoya, Leblanc, F., Filipe, Holdgraf, C., and Greenhall, A. (2019). *geopandas/geopandas: v0.6.1*.
- Jouttijärvi, S., Lobaccaro, G., Kamppinen, A., and Miettunen, K. (2022). Benefits of bifacial solar cells combined with low voltage power grids at high latitudes. *Renewable and Sustainable Energy Reviews*, 161:112354.
- Jouttijärvi, S., Thorning, J., Manni, M., Huerta, H., Ranta, S., Di Sabatino, M., Lobaccaro, G., and Miettunen, K. (2023). A comprehensive methodological workflow to maximize solar energy in low-voltage grids: A case study of vertical bifacial panels in Nordic conditions. *Solar Energy*, 262:111819.
- Kaldellis, J. K., Kapsali, M., and Kavadias, K. A. (2014). Temperature and wind speed impact on the efficiency of PV installations. Experience obtained from outdoor measurements in Greece. *Renewable Energy*, 66:612–624.
- Kalnay, E. and Cai, M. (2003). Impact of urbanization and land-use change on climate. *Nature*, 423(6939):528–531.
- Kalogirou, S. (2003). The potential of solar industrial process heat applications. *Applied Energy*, 76(4):337–361.
- Kalogirou, S. A. (2004). *Solar thermal collectors and applications*.
- Kamal, A., Abidi, S. M. H., Mahfouz, A., Kadam, S., Rahman, A., Hassan, I. G., and Wang, L. L. (2021). Impact of urban morphology on urban microclimate and building energy loads. *Energy and Buildings*, 253:111499.

- Kanters, J., Gentile, N., and Bernardo, R. (2021). Planning for solar access in Sweden: routines, metrics, and tools. *Urban, Planning and Transport Research*, 9(1):347–367.
- Kanters, J. and Wall, M. (2014). The impact of urban design decisions on net zero energy solar buildings in Sweden. *Urban, Planning and Transport Research*, 2(1):312–332.
- Kanters, J. and Wall, M. (2016). A planning process map for solar buildings in urban environments. *Renewable and Sustainable Energy Reviews*, 57:173–185.
- Kanters, J., Wall, M., and Kjellsson, E. (2014). The Solar Map as a Knowledge Base for Solar Energy Use. *Energy Procedia*, 48:1597–1606.
- Kaplani, E. and Kaplanis, S. (2020). PV Module Temperature Prediction at Any Environmental Conditions and Mounting Configurations. pages 921–933.
- Karathanasis, S. (2019). *Linear Fresnel Reflector Systems for Solar Radiation Concentration*.
- Karn, A., Chintala, V., and Kumar, S. (2019). An investigation into sky temperature estimation, its variation, and significance in heat transfer calculations of solar cookers. *Heat Transfer - Asian Research*, 48(5):1830–1856.
- Kempe, M. D., Holsapple, D., Whitfield, K., and Shiradkar, N. (2021). Standards development for modules in high temperature micro-environments. *Progress in Photovoltaics: Research and Applications*, 29(4):445–460.
- Khan, H. S., Paolini, R., Santamouris, M., and Caccetta, P. (2020). Exploring the synergies between urban overheating and heatwaves (HWS) in western Sydney. *Energies*, 13(2):1–17.
- Khan, H. S., Santamouris, M., Kassomenos, P., Paolini, R., Caccetta, P., and Petrou, I. (2021a). Spatiotemporal variation in urban overheating magnitude and its association with synoptic air-masses in a coastal city. *Scientific Reports*, 11(1):1–15.
- Khan, H. S., Santamouris, M., Paolini, R., Caccetta, P., and Kassomenos, P. (2021b). Analyzing the local and climatic conditions affecting the urban overheating magnitude during the Heatwaves (HWs) in a coastal city: A case study of the greater Sydney region. *Science of the Total Environment*, 755:142515.
- King, D. L., Boyson, W. E., and Kratochvil, J. A. (2004). Photovoltaic array performance model. *Sandia Report No. 2004-3535*, 8:1–19.
- Kistler, B. L. (1986). A user's manual for DELSOL3: A computer code for calculating the optical performance and optimal system design for solar thermal central receiver plants. *Other Information: Portions of this document are illegible in microfiche products. Original copy available until stock is exhausted. Includes 5 sheets of 48x reduction microfiche*, page Medium: X; Size: Pages: 231.
- Kitchin, R. (2015). Data-Driven, Networked Urbanism. *SSRN Electronic Journal*.
- Klise, G. T. and Stein, J. S. (2009). Models used to assess the performance of photovoltaic systems. *Sandia National Laboratories*, (December):1–67.
- Klise, K. A., Stein, J. S., and Cunningham, J. (2017). Application of IEC 61724 Standards to Analyze PV System Performance in Different Climates. In *2017 IEEE 44th Photovoltaic Specialist Conference (PVSC)*, pages 3161–3166.
- Koch, H., Lechner, S., Erdmann, S., and Hofmann, M. (2022). Assessing the Potential of Rooftop Photovoltaics by Processing High-Resolution Irradiation Data, as Applied to Giessen, Germany. *Energies*, 15(19).

- Kolokotroni, M., Ren, X., Davies, M., and Mavrogianni, A. (2012). London's urban heat island: Impact on current and future energy consumption in office buildings. *Energy and Buildings*, 47:302–311.
- Konis, K., Gamas, A., and Kensek, K. (2016). Passive performance and building form: An optimization framework for early-stage design support. *Solar Energy*, 125:161–179.
- Koschier, L. and Egan, R. (2021). National Survey Report of PV Power Applications in Australia 2021. Technical report.
- Kotak, Y., Gul, M. S., and Muneer, T. (2015). Investigating the Impact of Ground Albedo on the Performance of PV Systems. *CIBSE Technical Symposium, London, UK*.
- Kratzer, A. (1956). *Das Stadtklima*. Die Wissenschaft. F. Vieweg.
- Kumar, M., Bhan, S. C., Tyagi, A., Magotra, R., and Sharma, Y. (2021). Review of Urban Heat Islands: Monitoring, Forecast and Impacts. *VayuMandal*, 47(2):2021.
- Kunel, S., Kontonasiou, E., Arcipowska, A., Mariottini, F., and Atanasiu, B. (2015). *Indoor air quality, thermal comfort and daylight. Analysis of residential building regulations in eight EU member states*. BPIE.
- Kuravi, S., Trahan, J., Goswami, D. Y., Rahman, M. M., and Stefanakos, E. K. (2013). Thermal energy storage technologies and systems for concentrating solar power plants.
- Kurnik, J., Jankovec, M., Brecl, K., and Topic, M. (2011). Outdoor testing of PV module temperature and performance under different mounting and operational conditions. *Solar Energy Materials and Solar Cells*, 95(1):373–376.
- Kwak, Y., Park, C., and Deal, B. (2020). Discerning the success of sustainable planning: A comparative analysis of urban heat island dynamics in Korean new towns. *Sustainable Cities and Society*, 61(January):102341.
- Kyriakodis, G. E. and Santamouris, M. (2018). Using reflective pavements to mitigate urban heat island in warm climates - Results from a large scale urban mitigation project. *Urban Climate*, 24:326–339.
- Kılıç, U. and Kekezoğlu, B. (2022). A review of solar photovoltaic incentives and Policy: Selected countries and Turkey. *Ain Shams Engineering Journal*, 13(5):101669.
- Laboratories, S. N. (2021). `pvl` _ python Documentation.
- Lac, C., Chaboureau, J.-P., Masson, V., Pinty, J.-P., Tulet, P., Escobar, J., Leriche, M., Barthe, C., Aouizerats, B., Augros, C., Aumond, P., Auguste, F., Bechtold, P., Berthet, S., Bielli, S., Bosseur, F., Caumont, O., Cohard, J.-M., Colin, J., Couvreur, F., Cuxart, J., Delautier, G., Dauhut, T., Ducrocq, V., Filippi, J.-B., Gazen, D., Geoffroy, O., Gheusi, F., Honnert, R., Lafore, J.-P., Lebeaupin Brossier, C., Libois, Q., Lunet, T., Mari, C., Maric, T., Mascart, P., Mogé, M., Molinié, G., Nuissier, O., Pantillon, F., Peyrillé, P., Pergaud, J., Perraud, E., Pianezze, J., Redelsperger, J.-L., Ricard, D., Richard, E., Riette, S., Rodier, Q., Schoetter, R., Seyfried, L., Stein, J., Suhre, K., Taufour, M., Thouron, O., Turner, S., Verrelle, A., Vié, B., Visentin, F., Vionnet, V., and Wautelet, P. (2018). Overview of the Meso-NH model version 5.4 and its applications. *Geoscientific Model Development*, 11(5):1929–1969.
- Lam, C. K. C., Weng, J., Liu, K., and Hang, J. (2023). The effects of shading devices on outdoor thermal and visual comfort in Southern China during summer. *Building and Environment*, 228:109743.
- LAMBDA (2019). TracePro.

- Lauzet, N., Rodler, A., Musy, M., Azam, M. H., Guernouti, S., Mauree, D., and Colinart, T. (2019). How building energy models take the local climate into account in an urban context – A review. *Renewable and Sustainable Energy Reviews*, 116(August):109390.
- Leconte, F., Bouyer, J., Claverie, R., and Pétrissans, M. (2015). Using Local Climate Zone scheme for UHI assessment: Evaluation of the method using mobile measurements. *Building and Environment*, 83:39–49.
- Lee, K. S., Lee, J. W., and Lee, J. S. (2016). Feasibility study on the relation between housing density and solar accessibility and potential uses. *Renewable Energy*, 85:749–758.
- Legnér, M. and Femenías, P. (2022). The Implementation of Conservation Policy and the Application of Solar Energy Technology in Small House Areas: Stockholm, Sweden. *The Historic Environment: Policy & Practice*, 13(2):171–195.
- Lehnert, M., Savić, S., Milošević, D., Dunjić, J., and Geletič, J. (2021). Mapping local climate zones and their applications in european urban environments: A systematic literature review and future development trends. *ISPRS International Journal of Geo-Information*, 10(4).
- Lemonsu, A., Masson, V., Shashua-Bar, L., Erell, E., and Pearlmutter, D. (2012). Inclusion of vegetation in the Town Energy Balance model for modelling urban green areas. *Geoscientific Model Development*, 5(6):1377–1393.
- Levinson, R., Chen, S., Ferrari, C., Berdahl, P., and Slack, J. (2017). Methods and instrumentation to measure the effective solar reflectance of fluorescent cool surfaces. *Energy and Buildings*, 152:752–765.
- Lewis, S. C., King, A. D., and Mitchell, D. M. (2017). Australia’s Unprecedented Future Temperature Extremes Under Paris Limits to Warming. *Geophysical Research Letters*, 44(19):9947–9956.
- Li, D. H., Lam, T. N., and Cheung, K. (2009). Energy and cost studies of semi-transparent photovoltaic skylight. *Energy Conversion and Management*, 50(8):1981–1990.
- Li, J., Zhang, Y., Zhu, Z., Zhu, J., Luo, J., Peng, F., and Sun, X. (2022). Thermal comfort in a building with Trombe wall integrated with phase change materials in hot summer and cold winter region without air conditioning. *Energy and Built Environment*.
- Li, L., Lei, Y., Tang, L., Yan, F., Luo, F., and Zhu, H. (2019a). A 3D spatial data model of the solar rights associated with individual residential properties. *Computers, Environment and Urban Systems*, 74:88–99.
- Li, X., Zhou, Y., Yu, S., Jia, G., Li, H., and Li, W. (2019b). Urban heat island impacts on building energy consumption: A review of approaches and findings.
- Lim, X. Z. (2020). The super-cool materials that send heat to space. *Nature*, 577(7788):18–20.
- Lima, I., Scalco, V., and Lamberts, R. (2019). Estimating the impact of urban densification on high-rise office building cooling loads in a hot and humid climate. *Energy and Buildings*, 182:30–44.
- Lindberg, F., Grimmond, C. S., Gabey, A., Huang, B., Kent, C. W., Sun, T., Theeuwes, N. E., Järvi, L., Ward, H. C., Capel-Timms, I., Chang, Y., Jonsson, P., Krave, N., Liu, D., Meyer, D., Olofson, K. F. G., Tan, J., Wästberg, D., Xue, L., and Zhang, Z. (2018). Urban Multi-scale Environmental Predictor (UMEP): An integrated tool for city-based climate services. *Environmental Modelling and Software*, 99:70–87.

- Lindberg, F., Holmer, B., and Thorsson, S. (2008). SOLWEIG 1.0 – Modelling spatial variations of 3D radiant fluxes and mean radiant temperature in complex urban settings. *International Journal of Biometeorology*, 52(7):697–713.
- Lindkvist, C., Juhasz-Nagy, E., Nielsen, B. F., Neumann, H. M., Lobaccaro, G., and Wyckmans, A. (2019). Intermediaries for knowledge transfer in integrated energy planning of urban districts. *Technological Forecasting and Social Change*, 142:354–363.
- Lipson, M., Nazarian, N., Hart, M. A., Nice, K. A., and Conroy, B. (2022). A transformation in city-descriptive input data for urban climate models. *Frontiers in Environmental Science*, 10(July):1–18.
- Litardo, J., Palme, M., Borbor-Cordova, M., Caiza, R., Macias, J., Hidalgo-Leon, R., and Soriano, G. (2020). Urban Heat Island intensity and buildings' energy needs in Duran, Ecuador: Simulation studies and proposal of mitigation strategies. *Sustainable Cities and Society*, 62(July):102387.
- Liu, B. Y. and Jordan, R. C. (1960). The interrelationship and characteristic distribution of direct, diffuse and total solar radiation. *Solar Energy*, 4(3):1–19.
- Liu, Y., Stouffs, R., Tablada, A., Wong, N. H., and Zhang, J. (2017). Comparing micro-scale weather data to building energy consumption in Singapore. *Energy and Buildings*, 152:776–791.
- Livada, I., Synnefa, A., Haddad, S., Paolini, R., Garshasbi, S., Ulpiani, G., Fiorito, F., Vassilakopoulou, K., Osmond, P., and Santamouris, M. (2019). Time series analysis of ambient air-temperature during the period 1970–2016 over Sydney, Australia. *Science of the Total Environment*, 648:1627–1638.
- Lobaccaro, G., Carlucci, S., Croce, S., Paparella, R., and Finocchiaro, L. (2017). Boosting solar accessibility and potential of urban districts in the Nordic climate: A case study in Trondheim. *Solar Energy*, 149:347–369.
- Lobaccaro, G., Croce, S., Vettorato, D., and Carlucci, S. (2018a). A holistic approach to assess the exploitation of renewable energy sources for design interventions in the early design phases. *Energy and Buildings*, 175:235–256.
- Lobaccaro, G., De Ridder, K., Acero, J. A., Hooyberghs, H., Lauwaet, D., Maiheu, B., Sharma, R., and Govehovitch, B. (2021). Applications of models and tools for mesoscale and microscale thermal analysis in mid-latitude climate regions—A review. *Sustainability (Switzerland)*, 13(22).
- Lobaccaro, G., Lisowska, M. M., Saretta, E., Bonomo, P., and Frontini, F. (2019a). A Methodological Analysis Approach to Assess Solar Energy Potential at the Neighborhood Scale. *Energies 2019, Vol. 12, Page 3554*, 12(18):3554.
- Lobaccaro, G., Lisowska, M. M., Saretta, E., Bonomo, P., and Frontini, F. (2019b). A methodological analysis approach to assess solar energy potential at the neighborhood scale. *Energies*, 12(18).
- Lobaccaro, G., Wiberg, A. H. A., Ceci, G., Manni, M., Lolli, N., and Berardi, U. (2018b). Parametric design to minimize the embodied GHG emissions in a ZEB. *Energy and Buildings*, 167:106–123.
- Long, C., Wu, J., Zhou, Y., and Jenkins, N. (2018). Peer-to-peer energy sharing through a two-stage aggregated battery control in a community Microgrid. *Applied Energy*, 226:261–276.

- Lorenz, E. and Heinemann, D. (2012). Prediction of Solar Irradiance and Photovoltaic Power. *Comprehensive Renewable Energy*, 1:239–292.
- Lovegrove, K. and Stein, W. (2012). *Concentrating Solar Power Technology: Principles, Developments and Applications*.
- Lu, S., Chen, Y., Liu, S., and Kong, X. (2016). Experimental research on a novel energy efficiency roof coupled with PCM and cool materials. *Energy and Buildings*, 127:159–169.
- Lun, I., Mochida, A., and Ooka, R. (2009). Progress in Numerical Modelling for Urban Thermal Environment Studies. *Advances in Building Energy Research*, 3:147–188.
- Lund, H., Marszal, A., and Heiselberg, P. (2011). Zero energy buildings and mismatch compensation factors. *Energy and Buildings*, 43(7):1646–1654.
- Ma, R., Li, X., and Chen, J. (2021). An elastic urban morpho-blocks (EUM) modeling method for urban building morphological analysis and feature clustering. *Building and Environment*, 192(January):107646.
- Ma, T., Yang, H., and Lu, L. (2014). Solar photovoltaic system modeling and performance prediction.
- Ma, W. W., Rasul, M. G., Liu, G., Li, M., and Tan, X. H. (2016). Climate change impacts on techno-economic performance of roof PV solar system in Australia. *Renewable Energy*, 88:430–438.
- Ma, Y., Saha, S. C., Miller, W., and Guan, L. (2017). Comparison of different solar-assisted air conditioning systems for Australian office buildings. *Energies*, 10(10).
- Maiullari, D., Pijpers-Van Esch, M., and van Timmeren, A. (2021). A quantitative morphological method for mapping local climate types. *Urban Planning*, 6(3):240–257.
- Manikandan, G. K., Iniyar, S., and Goic, R. (2019). Enhancing the optical and thermal efficiency of a parabolic trough collector – A review. *Applied Energy*, 235:1524–1540.
- Manni, M., Cardinali, M., Lobaccaro, G., Goia, F., Nicolini, A., and Rossi, F. (2020a). Effects of retro-reflective and angular-selective retro-reflective materials on solar energy in urban canyons. *Solar Energy*, 209:662–673.
- Manni, M., Kousis, I., Lobaccaro, G., Fiorito, F., Cannavale, A., and Santamouris, M. (2022). Urban overheating mitigation through facades: the role of new and innovative cool coatings. *Rethinking Building Skins: Transformative Technologies and Research Trajectories*, pages 61–87.
- Manni, M., Lobaccaro, G., Goia, F., and Nicolini, A. (2018). An inverse approach to identify selective angular properties of retro-reflective materials for urban heat island mitigation. *Solar Energy*, 176:194–210.
- Manni, M., Lobaccaro, G., Lolli, N., and Bohne, R. A. (2020b). Parametric Design to Maximize Solar Irradiation and Minimize the Embodied GHG Emissions for a ZEB in Nordic and Mediterranean Climate Zones. *Energies*, 13(18).
- Manni, M. and Nicolini, A. (2022). Multi-Objective Optimization Models to Design a Responsive Built Environment: A Synthetic Review. *Energies*, 15(2).
- Manni, M., Nocente, A., Bellmann, M., and Lobaccaro, G. (2023). Multi-Stage Validation of a Solar Irradiance Model Chain: An Application at High Latitudes. *Sustainability*, 15(4).

- Manni, M., Petrozzi, A., Coccia, V., Nicolini, A., and Cotana, F. (2020c). Investigating alternative development strategies for sport arenas based on active and passive systems. *Journal of Building Engineering*, 31:101340.
- Mao, J., Yang, J. H., Afshari, A., and Norford, L. K. (2017). Global sensitivity analysis of an urban microclimate system under uncertainty: Design and case study. *Building and Environment*, 124:153–170.
- Martins, T., Adolphe, L., and Bonhomme, M. (2013). Building Energy Demand Based on Urban Morphology Case Study in Maceió, Brazil. *PLEA 2013: Sustainable Architecture for a Renewable Future*, (September):1–6.
- Masson, V. (2000). A physically-based scheme for the urban energy budget in atmospheric models. *Boundary-Layer Meteorology*, 94(3):357–397.
- Masson, V., Heldens, W., Bocher, E., Bonhomme, M., Bucher, B., Burmeister, C., de Munck, C., Esch, T., Hidalgo, J., Kanani-Sühring, F., Kwok, Y. T., Lemonsu, A., Lévy, J. P., Maronga, B., Pavlik, D., Petit, G., See, L., Schoetter, R., Tornay, N., Votsis, A., and Zeidler, J. (2020). City-descriptive input data for urban climate models: Model requirements, data sources and challenges. *Urban Climate*, 31(August 2019):100536.
- Mastrapostoli, E., Santamouris, M., Kolokotsa, D., Vassilis, P., Venieri, D., and Gompakis, K. (2016). On the ageing of cool roofs: Measure of the optical degradation, chemical and biological analysis and assessment of the energy impact. *Energy and Buildings*, 114:191–199.
- Mathiesen, B. V., Lund, H., Connolly, D., Wenzel, H., Østergaard, P. A., Möller, B., Nielsen, S., Ridjan, I., Karnøe, P., Sperling, K., and Hvelplund, F. K. (2015). Smart Energy Systems for coherent 100% renewable energy and transport solutions. *Applied Energy*, 145:139–154.
- Mathur, S. S., Kandpal, T. C., and Negi, B. S. (1991). Optical design and concentration characteristics of linear Fresnel reflector solar concentrators-II. Mirror elements of equal width. *Energy Conversion and Management*, 31(3):221–232.
- Matisoff, D. C. and Johnson, E. P. (2017). The comparative effectiveness of residential solar incentives. *Energy Policy*, 108:44–54.
- Matthew Adams, H. D. and Trieu, T. (2015). Impacts of land-use change on Sydney's future temperatures. *Office of Environment and Heritage*,.
- Maturi, L. and Adami, J. (2018). BIPV architectural systems. In *Building Integrated Photovoltaic (BIPV) in Trentino Alto Adige*, number 9783319741154, pages 9–14. Springer Cham.
- Mauree, D., Naboni, E., Coccolo, S., Perera, A. T., Nik, V. M., and Scartezzini, J. L. (2019). A review of assessment methods for the urban environment and its energy sustainability to guarantee climate adaptation of future cities. *Renewable and Sustainable Energy Reviews*, 112(May):733–746.
- Maurer, C., Cappel, C., and Kuhn, T. E. (2017). Progress in building-integrated solar thermal systems. *Solar Energy*, 154:158–186.
- McIntire, W. R. (1982). Factored approximations for biaxial incident angle modifiers. *Solar Energy*, 29(4):315–322.
- Mehdi, M., Ammari, N., Alami Merrouni, A., El Gallassi, H., Dahmani, M., and Ghennioui, A. (2023). An experimental comparative analysis of different PV technologies performance including the influence of hot-arid climatic parameters: Toward a realistic yield assessment for desert locations. *Renewable Energy*, 205(July 2022):695–716.

- Mehedi, T. H., Gemechu, E., and Kumar, A. (2022). Life cycle greenhouse gas emissions and energy footprints of utility-scale solar energy systems. *Applied Energy*, 314:118918.
- Meier, F., Fenner, D., Grassmann, T., Jänicke, B., Otto, M., and Scherer, D. (2015). Challenges and benefits from crowdsourced atmospheric data for urban climate research using Berlin, Germany, as testbed. In *ICUC9 - 9th International Conference on Urban Climate jointly with 12th Symposium on the Urban Environment Challenges*, number September, page 6p.
- Mekhilef, S., Saidur, R., and Safari, A. (2011). A review on solar energy use in industries. *Renewable and Sustainable Energy Reviews*, 15(4):1777–1790.
- Melius, J., Margolis, R., and Ong, S. (2013). Estimating Rooftop Suitability for PV : A Review of Methods , Patents , and Validation Techniques. *NREL Technical Report*, (December):35.
- Melnikov, V. R., Christopoulos, G. I., Krzhizhanovskaya, V. V., Lees, M. H., and Sloom, P. M. A. (2022). Behavioural thermal regulation explains pedestrian path choices in hot urban environments. *Scientific Reports*, 12(1):2441.
- Memme, S. (2018). *Solar Energy Modelling with Fresnel Systems and Exploitation in Morocco Solar Facilities*. Msc, Università degli Studi di Genova.
- Memme, S. and Fossa, M. (2022). Maximum energy yield of PV surfaces in France and Italy from climate based equations for optimum tilt at different azimuth angles. *Renewable Energy*, 200(May):845–866.
- Mendoza, J. M. F., Sanyé-Mengual, E., Angrill, S., García-Lozano, R., Feijoo, G., Josa, A., Gabarrell, X., and Rieradevall, J. (2015). Development of urban solar infrastructure to support low-carbon mobility. *Energy Policy*, 85:102–114.
- Mertins, M., Lerchenmüller, H., and Häberle, A. (2004). Geometry optimization of Fresnel-collectors with economic assessment. *Conference Proceedings EuroSun*, pages 1–918.
- Mills, D. R. and Morrison, G. L. (2000). Compact linear fresnel reflector solar thermal powerplants. *Solar Energy*, 68(3):263–283.
- Milojevic-Dupont, N., Wagner, F., Nachtigall, F., Hu, J., Brüser, G. B., Zumwald, M., Biljecki, F., Heeren, N., Kaack, L. H., Pichler, P.-P., and Creutzig, F. (2023). EUBUCCO v0.1: European building stock characteristics in a common and open database for 200+ million individual buildings. *Scientific Data*, 10(1):147.
- Mirzaei, P. A. (2015). Recent challenges in modeling of urban heat island.
- Mirzaei, P. A. and Haghigat, F. (2010). Approaches to study Urban Heat Island - Abilities and limitations. *Building and Environment*.
- Mirzananadi, R., Hagentoft, C.-E., and Johansson, P. (2020). Coupling a Hydronic Heating Pavement to a Horizontal Ground Heat Exchanger for harvesting solar energy and heating road surfaces. *Renewable Energy*, 147:447–463.
- Mohajeri, N., Gudmundsson, A., Kunckler, T., Upadhyay, G., Assouline, D., Kämpf, J. H., and Scartezzini, J. L. (2019). A solar-based sustainable urban design: The effects of city-scale street-canyon geometry on solar access in Geneva, Switzerland. *Applied Energy*, 240(August 2018):173–190.
- Mohajeri, N., Upadhyay, G., Gudmundsson, A., Assouline, D., Kämpf, J., and Scartezzini, J. L. (2016). Effects of urban compactness on solar energy potential. *Renewable Energy*, 93:469–482.

- Molin, A., Schneider, S., Rohdin, P., and Moshfegh, B. (2016). Assessing a regional building applied PV potential - Spatial and dynamic analysis of supply and load matching. *Renewable Energy*, 91:261–274.
- Montavon, M., Compagnon, R., and Scartezzini, J.-L. (2004). Comparison of the solar energy utilisation potential of different urban environments. *Plea2004 - The 21th Conference on Passive and Low Energy Architecture*, (September):1–6.
- Montenon, A. C., Fylaktos, N., Montagnino, F., Paredes, F., and Papanicolas, C. N. (2017). Concentrated solar power in the built environment. *AIP Conference Proceedings*, 1850(June).
- Montenon, A. C., Tsekouras, P., Tzivanidis, C., Bibron, M., and Papanicolas, C. (2019). Thermo-optical modelling of the linear Fresnel collector at the Cyprus institute. *AIP Conference Proceedings*, 2126.
- Montes, M. J., Abbas, R., Rovira, A., Martínez-Val, J. M., and Muñoz-Antón, J. (2012). Analysis of Linear Fresnel Collectors Designs To Minimize Optical and Geometrical Losses. *SolarPaces Conference*, 1:8–9.
- Montes, M. J., Rubbia, C., Abbas, R., and Martínez-Val, J. M. (2014). A comparative analysis of configurations of linear fresnel collectors for concentrating solar power. *Energy*, 73:192–203.
- Moradi, M., Dyer, B., Nazem, A., Nambiar, M. K., Rafsan Nahian, M., Bueno, B., Mackey, C., Vasanthakumar, S., Nazarian, N., Scott Krayenhoff, E., Norford, L. K., and Aliabadi, A. A. (2021). The vertical city weather generator (vcwg v1.3.2). *Geoscientific Model Development*, 14(2):961–984.
- Morganti, M., Salvati, A., Coch, H., and Cecere, C. (2017). Urban morphology indicators for solar energy analysis. *Energy Procedia*, 134(October):807–814.
- Morille, B., Lauzet, N., and Musy, M. (2015). SOLENE-microclimate: A tool to evaluate envelopes efficiency on energy consumption at district scale. *Energy Procedia*, 78:1165–1170.
- Morin, G., Dersch, J., Eck, M., Häberle, A., and Platzer, W. (2009). Comparison of linear Fresnel and parabolic trough collector systems – Influence of linear Fresnel collector design variations on break even cost. In *Proc. 15th SolarPACES International Symposium*.
- Morin, G., Dersch, J., Platzer, W., Eck, M., and Häberle, A. (2012a). Comparison of Linear Fresnel and Parabolic Trough Collector power plants. *Solar Energy*, 86(1):1–12.
- Morin, G., Kirchberger, J., Lemmert, N., and Mertins, M. (2012b). Operational Results and Simulation. In *SolarPaces Conference*.
- Morin, G., Mertins, M., Kirchberger, J., and Selig, M. (2011). SUPERNOVA – Construction, control & performance of steam superheating Linear Fresnel collector. *SolarPACES Conference 2011*, pages 1–6.
- Morin, G., Platzer, W., Strelow, M., and Leithner, R. (2008). Techno-economic system simulation and optimization of solar thermal power plants. In *Proc. 14th SolarPACES International Symposium*.
- Morini, E., Castellani, B., Presciutti, A., Filipponi, M., Nicolini, A., and Rossi, F. (2017). Optic-energy performance improvement of exterior paints for buildings. *Energy and Buildings*, 139:690–701.
- Muller, C. L., Chapman, L., Johnston, S., Kidd, C., Illingworth, S., Foody, G., Overeem, A., and Leigh, R. R. (2015). Crowdsourcing for climate and atmospheric sciences: current status and future potential. *International Journal of Climatology*, 35(11):3185–3203.

- Munari Probst, M. C. and Roecker, C. (2019). Criteria and policies to master the visual impact of solar systems in urban environments: The LESO-QSV method. *Solar Energy*, 184:672–687.
- Mussetti, G., Davin, E. L., Schwaab, J., Acero, J. A., Ivanchev, J., Singh, V. K., Jin, L., and Seneviratne, S. I. (2022). Do Electric Vehicles Mitigate Urban Heat? The Case of a Tropical City. *Frontiers in Environmental Science*, 10(February):1–9.
- Mutani, G. and Todeschi, V. (2020). Building energy modeling at neighborhood scale. *Energy Efficiency*, 13(7):1353–1386.
- Mutani, G., Todeschi, V., and Matsuo, K. (2019). Urban heat island mitigation: A GIS-based Model for Hiroshima. *Instrumentation Measure Metrologie*, 18(4):323–335.
- Muzathik, A. M. (2014). Photovoltaic Modules Operating Temperature Estimation Using a Simple Correlation. *International Journal of Energy engineering*, 4:151–158.
- Naboni, E., Natanian, J., Brizzi, G., Florio, P., Chokhachian, A., Galanos, T., and Rastogi, P. (2019). A digital workflow to quantify regenerative urban design in the context of a changing climate. *Renewable and Sustainable Energy Reviews*, 113(February):109255.
- Nadeem, F., Tariq, S., Haq, Z. U., and Khan, H. S. (2022). Investigating the synergies between the Urban Heat Island (UHI) and Heatwaves (HWs). *Preprints- Environmental Science and Pollution Research*, pages 1–32.
- Nadeem, T. B., Siddiqui, M., Khalid, M., and Asif, M. (2023). Distributed energy systems: A review of classification, technologies, applications, and policies:. *Energy Strategy Reviews*, 48(April):101096.
- Nassar, Y. F. and Salem, A. A. (2007). The reliability of the photovoltaic utilization in southern cities of Libya. *Desalination*, 209(1-3 SPEC. ISS.):86–90.
- Nastasi, B., Mazzoni, S., Groppi, D., Romagnoli, A., and Astiaso Garcia, D. (2021). Solar power-to-gas application to an island energy system. *Renewable Energy*, 164:1005–1016.
- Natanian, J. (2023). Optimizing mixed-use district designs in hot climates: A two-phase computational workflow for energy balance and environmental performance. *Sustainable Cities and Society*, 98:104800.
- Natanian, J., Kastner, P., Dogan, T., and Auer, T. (2020). From energy performative to livable Mediterranean cities: An annual outdoor thermal comfort and energy balance cross-climatic typological study. *Energy and Buildings*, 224:110283.
- Nault, E., Waibel, C., Carmeliet, J., and Andersen, M. (2018). Development and test application of the UrbanSOLve decision-support prototype for early-stage neighborhood design. *Building and Environment*, 137:58–72.
- Nielsen, B. F., Baer, D., and Lindkvist, C. (2019). Identifying and supporting exploratory and exploitative models of innovation in municipal urban planning; key challenges from seven Norwegian energy ambitious neighborhood pilots. *Technological Forecasting and Social Change*, 142:142–153.
- Nixon, J. D. and Davies, P. A. (2012). Cost-exergy optimisation of linear Fresnel reflectors. *Solar Energy*, 86(1):147–156.
- Nixon, J. D., Dey, P. K., and Davies, P. A. (2010). Which is the best solar thermal collection technology for electricity generation in north-west India? Evaluation of options using the analytical hierarchy process. *Energy*, 35(12):5230–5240.

- Novatec Solar (2014). Novatec Solar.
- Nowak, H. (1989). The sky temperature in net radiant heat loss calculations from low-sloped roofs. *Infrared Physics*, 29(2-4):231–232.
- Obiwulu, A. U., Erusiafe, N., Olopade, M. A., and Nwokolo, S. C. (2020). Modeling and optimization of back temperature models of mono-crystalline silicon modules with special focus on the effect of meteorological and geographical parameters on PV performance. *Renewable Energy*, 154:404–431.
- Øgaard, M. B., Aarseth, B. L., Skomedal, Å. F., Riise, H. N., Sartori, S., and Selj, J. H. (2021). Identifying snow in photovoltaic monitoring data for improved snow loss modeling and snow detection. *Solar Energy*, 223:238–247.
- Oh, J., Samy, G., and Mani, T. (2010). Temperature testing and analysis of PV modules per ANSI/UL 1703 and IEC 61730 standards. *Conference Record of the IEEE Photovoltaic Specialists Conference*, pages 984–988.
- Oka, K., Mizutani, W., and Ashina, S. (2020). Climate change impacts on potential solar energy production: A study case in Fukushima, Japan. *Renewable Energy*, 153:249–260.
- Oke, T. R. (1982). The energetic basis of the urban heat island. *Quarterly Journal of the Royal Meteorological Society*, 108(455):1–24.
- O'Malley, C. and Kikumoto, H. (2022). An investigation into heat storage by adopting local climate zones and nocturnal-diurnal urban heat island differences in the Tokyo Prefecture. *Sustainable Cities and Society*, 83(March):103959.
- Omar, O., García-Fernández, B., Fernández-Balbuena, A. Á., and Vázquez-Moliní, D. (2018). Optimization of daylight utilization in energy saving application on the library in faculty of architecture, design and built environment, Beirut Arab University. *Alexandria Engineering Journal*, 57(4):3921–3930.
- Ordóñez, J., Jadraque, E., Alegre, J., and Martínez, G. (2010). Analysis of the photovoltaic solar energy capacity of residential rooftops in Andalusia (Spain). *Renewable and Sustainable Energy Reviews*, 14(7):2122–2130.
- Outhred, H. and Retnanestri, M. (2015). Insights from the Experience with Solar Photovoltaic Systems in Australia and Indonesia. *Energy Procedia*, 65:121–130.
- Paatero, J. V. and Lund, P. D. (2007). Effects of large-scale photovoltaic power integration on electricity distribution networks. *Renewable Energy*, 32(2):216–234.
- Palme, M., Inostroza, L., Villacreses, G., Lobato-Cordero, A., and Carrasco, C. (2017). From urban climate to energy consumption. Enhancing building performance simulation by including the urban heat island effect. *Energy and Buildings*, 145:107–120.
- Palme, M. and Salvati, A. (2018). UWG -TRNSYS Simulation Coupling for Urban Building Energy Modelling. *Proceedings of BSO 2018: 4th Building Simulation and Optimization Conference, Cambridge, UK: 11-12 September 2018*, pages 635–641.
- Palme, M. and Salvati, A. (2021). *Urban Microclimate Modelling for Comfort and Energy Studies*.
- Palmero-Marrero, A. I. and Oliveira, A. C. (2006). Evaluation of a solar thermal system using building louvre shading devices. *Solar Energy*, 80(5):545–554.

- Parkins, J. R., Rollins, C., Anders, S., and Comeau, L. (2018). Predicting intention to adopt solar technology in Canada: The role of knowledge, public engagement, and visibility. *Energy Policy*, 114:114–122.
- Parlow, E., Vogt, R., and Feigenwinter, C. (2014). The urban heat island of Basel - Seen from different perspectives. *Erde*, 145(1-2):96–110.
- Pavlovic, T. (2020). Solar energy. In *Green Energy and Technology*, pages 1–44.
- Pedregosa, F., Weiss, R., Brucher, M., Varoquaux, G., Gramfort, A., Michel, V., Thirion, B., Grisel, O., Blondel, M., Prettenhofer, P., Weiss, R., Dubourg, V., Vanderplas, J., Passos, A., Cournapeau, D., Brucher, M., Perrot, M., and Duchesnay, É. (2011). Scikit-learn: Machine Learning in Python. *Journal of Machine Learning Research*, 12(85):2825–2830.
- Pelletier, K., Wood, C., Calautit, J., and Wu, Y. (2023). The viability of double-skin façade systems in the 21st century: A systematic review and meta-analysis of the nexus of factors affecting ventilation and thermal performance, and building integration. *Building and Environment*, 228:109870.
- Penaranda Moren, M. S. and Korjenic, A. (2017). Hotter and colder – How Do Photovoltaics and Greening Impact Exterior Facade Temperatures: The synergies of a Multifunctional System. *Energy and Buildings*, 147:123–141.
- Perez, R. R., Ineichen, P., Maxwell, E. L., Seals, R. D., and Zelenka, A. (1992). Dynamic global-to-direct irradiance conversion models. In *ASHRAE Transactions*, volume 98, pages 354 – 369.
- Perkins, S. E., Alexander, L. V., and Nairn, J. R. (2012). Increasing frequency, intensity and duration of observed global heatwaves and warm spells. *Geophysical Research Letters*, 39(20):1–5.
- Peronato, G., Bonjour, S., Stoeckli, J., Rey, E., Andersen, M., and Lausanne, D. (2016). Sensitivity of calculated solar irradiation to the level of detail: insights from the simulation of four sample buildings in urban areas. *32rd PLEA Conference Proceedings*, pages 702–707.
- Pham, J. V., Baniassadi, A., Brown, K. E., Heusinger, J., and Sailor, D. J. (2019). Comparing photovoltaic and reflective shade surfaces in the urban environment: Effects on surface sensible heat flux and pedestrian thermal comfort. *Urban Climate*, 29(January).
- Pielke, R., Burgess, M. G., and Ritchie, J. (2022). Plausible 2005-2050 emissions scenarios project between 2 °c and 3 °c of warming by 2100. *Environmental Research Letters*, 17(2).
- Pino, F. J., Caro, R., Rosa, F., and Guerra, J. (2013). Experimental validation of an optical and thermal model of a linear Fresnel collector system. In *Applied Thermal Engineering*, volume 50, pages 1463–1471.
- Pisello, A. L., Castaldo, V. L., Poli, T., and Cotana, F. (2014). Simulating the Thermal-Energy Performance of Buildings at the Urban Scale: Evaluation of Inter-Building Effects in Different Urban Configurations. *Journal of Urban Technology*, 21(1):3–20.
- Pisello, A. L., Fortunati, E., Fabiani, C., Mattioli, S., Dominici, F., Torre, L., Cabeza, L. F., and Cotana, F. (2017). PCM for improving polyurethane-based cool roof membranes durability. *Solar Energy Materials and Solar Cells*, 160(July 2016):34–42.
- Pokhrel, R., Walker, A., and González, J. E. (2020). A New Methodology to Assess Building Integrated Roof Top Photovoltaic Installations at City Scales: The Tropical Coastal City Case. *ASME Journal of Engineering for Sustainable Buildings and Cities*, 1(1):1–11.

- Polo-Labarríos, M. A., Quezada-García, S., Sánchez-Mora, H., Escobedo-Izquierdo, M. A., and Espinosa-Paredes, G. (2020). Comparison of thermal performance between green roofs and conventional roofs. *Case Studies in Thermal Engineering*, 21:100697.
- Poon, K. H., Kämpf, J. H., Tay, S. E., Wong, N. H., and Reindl, T. G. (2020). Parametric study of URBAN morphology on building solar energy potential in Singapore context. *Urban Climate*, 33(February):100624.
- Potgieter, J., Nazarian, N., Lipson, M. J., Hart, M. A., Ulpiani, G., Morrison, W., and Benjamin, K. (2021). Combining High-Resolution Land Use Data With Crowdsourced Air Temperature to Investigate Intra-Urban Microclimate. *Frontiers in Environmental Science*, 9(September):1–19.
- Premier, A., GhaffarianHoseini, A., and GhaffarianHoseini, A. (2022). Solar-powered smart urban furniture: preliminary investigation on limits and potentials of current designs. *Smart and Sustainable Built Environment*, 11(2):334–345.
- Price, S. and Summers, R. (2004). A technology roadmap for rehabilitation engineering. *Annual International Conference of the IEEE Engineering in Medicine and Biology - Proceedings*, 26 V:3471–3473.
- Principe, J. A. and Takeuchi, W. (2019). Assessment of solar PV power potential in the Asia Pacific region with remote sensing considering the effects of high temperature, dust and snow. *International Archives of the Photogrammetry, Remote Sensing and Spatial Information Sciences - ISPRS Archives*, 42(4/W19):339–346.
- Pu, S. and Xia, C. (2011). End-effect of linear Fresnel collectors. In *Asia-Pacific Power and Energy Engineering Conference, APPEEC*.
- Pujol Nadal, R. and Martínez Moll, V. (2012). Optical analysis of the fixed mirror solar concentrator by forward ray-tracing procedure. *Journal of Solar Energy Engineering, Transactions of the ASME*, 134(3).
- Pulido-Iparraguirre, D., Valenzuela, L., Serrano-Aguilera, J. J., and Fernández-García, A. (2019). Optimized design of a Linear Fresnel reflector for solar process heat applications. *Renewable Energy*, 131:1089–1106.
- Pyrgou, A., Castaldo, V. L., Pisello, A. L., Cotana, F., and Santamouris, M. (2017). On the effect of summer heatwaves and urban overheating on building thermal-energy performance in central Italy. *Sustainable Cities and Society*, 28:187–200.
- Qahtan, A. M. (2019). Thermal performance of a double-skin façade exposed to direct solar radiation in the tropical climate of Malaysia: A case study. *Case Studies in Thermal Engineering*, 14:100419.
- Qin, Y. (2015). A review on the development of cool pavements to mitigate urban heat island effect. *Renewable and Sustainable Energy Reviews*, 52:445–459.
- Qiu, Y., He, Y. L., Cheng, Z. D., and Wang, K. (2015). Study on optical and thermal performance of a linear Fresnel solar reflector using molten salt as HTF with MCRT and FVM methods. *Applied Energy*, 146:162–173.
- Quan, S. J. (2020). Identifying Urban Form Typologies in Seoul with Mixture Model Based Identifying Urban Form Typologies in Seoul with Mixture Model Based Clustering. *ISUF 2020 Cities in the 21st Century*, (October).
- Raboaca, M. S., Badea, G., Enache, A., Filote, C., Rasoi, G., Rata, M., Lavric, A., and Felseghi, R. A. (2019). Concentrating solar power technologies.

- Rajagopal, P., Priya, R. S., and Senthil, R. (2023). A review of recent developments in the impact of environmental measures on urban heat island. *Sustainable Cities and Society*, 88(March 2022):104279.
- Raji, B., Tenpierik, M. J., and Van Den Dobbelsteen, A. (2015). The impact of greening systems on building energy performance: A literature review. *Renewable and Sustainable Energy Reviews*, 45:610–623.
- Ratti, C. and Richens, P. (2004). Raster analysis of urban form. *Environment and Planning B: Planning and Design*, 31(2):297–309.
- Rawat, M. and Singh, R. N. (2022). Impact of light-colored paint materials on discomfort in a building for hot-dry climate. *Materials Today: Proceedings*, 52:998–1005.
- Redweik, P., Catita, C., and Brito, M. (2013). Solar energy potential on roofs and facades in an urban landscape. *Solar Energy*, 97:332–341.
- Reindl, D. T., Beckman, W. A., and Duffie, J. A. (1990). Diffuse fraction correlations. *Solar Energy*, 45(1):1–7.
- Reinhart, C. F. and Cerezo Davila, C. (2016). Urban building energy modeling - A review of a nascent field. *Building and Environment*, 97:196–202.
- Relloso, S. and Gutiérrez, Y. (2017). SENER molten salt tower technology. Ouarzazate NOOR III case. In *AIP Conference Proceedings*, volume 1850.
- Ren, Z., Wang, X., Chen, D., Wang, C., and Thatcher, M. (2014). Constructing weather data for building simulation considering urban heat island. *Building Services Engineering Research and Technology*, 35(1):69–82.
- Rey, S. J. and Anselin, L. (2007). PySAL: A Python library of spatial analytical methods. *Review of Regional Studies*, 37(1):5–27.
- Reynolds, D. (2015). *Gaussian Mixture Models*, pages 827–832. Springer US, Boston, MA.
- Richard, Y., Emery, J., Dudek, J., Pergaud, J., Chateau-Smith, C., Zito, S., Rega, M., Vairet, T., Castel, T., Thévenin, T., and Pohl, B. (2018). How relevant are local climate zones and urban climate zones for urban climate research? Dijon (France) as a case study. *Urban Climate*, 26(October):258–274.
- Ritchie, H., Roser, M., and Rosado, P. (2022). Energy. *Our World in Data*.
- Robinson, D. (2006). Urban morphology and indicators of radiation availability. *Solar Energy*, 80(12):1643–1648.
- Romero Rodríguez, L., Duminil, E., Sánchez Ramos, J., and Eicker, U. (2017). Assessment of the photovoltaic potential at urban level based on 3D city models: A case study and new methodological approach. *Solar Energy*, 146:264–275.
- Romero Rodríguez, L., Sánchez Ramos, J., Sánchez de la Flor, F. J., and Álvarez Domínguez, S. (2020). Analyzing the urban heat Island: Comprehensive methodology for data gathering and optimal design of mobile transects. *Sustainable Cities and Society*, 55(January):102027.
- Rönnelid, M., Perers, B., and Karlsson, B. (1997). On the factorisation of incidence angle modifiers for CPC collectors. In *Solar Energy*, volume 59, pages 281–286.
- Rosenblad, A. (2009). *Applied Multivariate Statistics for the Social Sciences, Fifth Edition* by James P. Stevens, volume 77. John Wiley & Sons, Ltd.

- Ross, R. G. (1976). Interface design considerations for terrestrial solar cell modules.
- Rossi, F., Castellani, B., Presciutti, A., Morini, E., Filippini, M., Nicolini, A., and Santamouris, M. (2015). Retroreflective façades for urban heat island mitigation: Experimental investigation and energy evaluations. *Applied Energy*, 145:8–20.
- Rosso, F., Fabiani, C., Chiatti, C., and Pisello, A. L. (2019). Cool, photoluminescent paints towards energy consumption reductions in the built environment. *Journal of Physics: Conference Series*, 1343(1).
- Rungasamy, A. E., Craig, K. J., and Meyer, J. P. (2021). A review of linear Fresnel primary optical design methodologies. *Solar Energy*, 224(May):833–854.
- Saadatian, O., Sopian, K., Lim, C. H., Asim, N., and Sulaiman, M. Y. (2012). Trombe walls: A review of opportunities and challenges in research and development. *Renewable and Sustainable Energy Reviews*, 16(8):6340–6351.
- Sahoo, S., Singh, S., and Banerjee, R. (2012). Analysis of heat losses from a trapezoidal cavity used for Linear Fresnel Reflector system. *Solar Energy*, 86.
- Sailor, D. J., Anand, J., and King, R. R. (2021). Photovoltaics in the built environment: A critical review. *Energy and Buildings*, 253:111479.
- Sait, H. H., Martinez-Val, J. M., Abbas, R., and Munoz-Anton, J. (2015). Fresnel-based modular solar fields for performance/cost optimization in solar thermal power plants: A comparison with parabolic trough collectors. *Applied Energy*, 141:175–189.
- Salgado Conrado, L., Rodriguez-Pulido, A., and Calderón, G. (2017). Thermal performance of parabolic trough solar collectors.
- Salvati, A., Coch, H., and Morganti, M. (2017a). Effects of urban compactness on the building energy performance in Mediterranean climate. In *Energy Procedia*, volume 122, pages 499–504.
- Salvati, A., Coch Roura, H., and Cecere, C. (2016). Predicción urbana de la isla de calor en el contexto mediterráneo: Una evaluación del modelo generador de tiempo urbano. *Architecture, City and Environment*, 11(32):135–156.
- Salvati, A., Coch Roura, H., and Cecere, C. (2017b). Assessing the urban heat island and its energy impact on residential buildings in Mediterranean climate: Barcelona case study. *Energy and Buildings*, 146:38–54.
- Salvati, A., Palme, M., Chiesa, G., and Kolokotroni, M. (2020). Built form, urban climate and building energy modelling: case-studies in Rome and Antofagasta. *Journal of Building Performance Simulation*, 13(2):209–225.
- Salvati, A., Palme, M., and Inostroza, L. (2017c). Key Parameters for Urban Heat Island Assessment in A Mediterranean Context: A Sensitivity Analysis Using the Urban Weather Generator Model. *IOP Conference Series: Materials Science and Engineering*, 245(8).
- Sánchez, E. and Izard, J. (2015). Performance of photovoltaics in non-optimal orientations: An experimental study. *Energy and Buildings*, 87:211–219.
- Sander, H. and Weißermel, S. (2023). Urban Heat Transition in Berlin: Corporate Strategies, Political Conflicts, and Just Solutions. *Urban Planning; Vol 8, No 1 (2023): Social Justice in the Green CityDO - 10.17645/up.v8i1.6178*.
- Santamouris, M. (2014). On the energy impact of urban heat island and global warming on buildings. *Energy and Buildings*, 82:100–113.

- Santamouris, M. (2020). Recent progress on urban overheating and heat island research. Integrated assessment of the energy, environmental, vulnerability and health impact. Synergies with the global climate change. *Energy and Buildings*, 207:109482.
- Santamouris, M., Cartalis, C., Synnefa, A., and Kolokotsa, D. (2015). On the impact of urban heat island and global warming on the power demand and electricity consumption of buildings - A review. *Energy and Buildings*, 98:119–124.
- Santamouris, M., Ding, L., Fiorito, F., Oldfield, P., Osmond, P., Paolini, R., Prasad, D., and Synnefa, A. (2016). Passive and active cooling for the outdoor built environment - Analysis and assessment of the cooling potential of mitigation technologies using performance data from 220 large scale projects. *Solar Energy*.
- Santamouris, M. and Feng, J. (2018). Recent progress in daytime radiative cooling: Is it the air conditioner of the future? *Buildings*, 8(12).
- Santamouris, M., Haddad, S., Fiorito, F., Osmond, P., Ding, L., Prasad, D., Zhai, X., and Wang, R. (2017). Urban heat island and overheating characteristics in Sydney, Australia. An analysis of multiyear measurements. *Sustainability (Switzerland)*, 9(5).
- Santamouris, M., Haddad, S., Saliari, M., Vasilakopoulou, K., Synnefa, A., Paolini, R., Ulpiani, G., Garshasbi, S., and Fiorito, F. (2018). On the energy impact of urban heat island in Sydney: Climate and energy potential of mitigation technologies. *Energy and Buildings*, 166:154–164.
- Santamouris, M., Synnefa, A., and Karlessi, T. (2011). Using advanced cool materials in the urban built environment to mitigate heat islands and improve thermal comfort conditions.
- Santamouris, M. and Yun, G. Y. (2020). Recent development and research priorities on cool and super cool materials to mitigate urban heat island. *Renewable Energy*, 161:792–807.
- Santos, J. J., Palacio, J. C., Reyes, A. M., Carvalho, M., Freire, A. J., and Barone, M. A. (2018). Concentrating Solar Power. In *Advances in Renewable Energies and Power Technologies*, volume 1, pages 373–402.
- Santos, T., Gomes, N., Brito, M. C., Freire, S., Fonseca, A., and Tenedório, J. A. (2011). Solar potential analysis in Lisbon using LiDAR data. *Proceedings of the 31st EARSeL Symposium*, pages 13–19.
- Sarralde, J. J., Quinn, D. J., Wiesmann, D., and Steemers, K. (2015). Solar energy and urban morphology: Scenarios for increasing the renewable energy potential of neighbourhoods in London. *Renewable Energy*, 73:10–17.
- Satola, D., Wiberg, A. H., Singh, M., Babu, S., James, B., Dixit, M., Sharston, R., Grynberg, Y., and Gustavsen, A. (2022). Comparative review of international approaches to net-zero buildings: Knowledge-sharing initiative to develop design strategies for greenhouse gas emissions reduction. *Energy for Sustainable Development*, 71:291–306.
- Sattler, S., Österreicher, D., and Zluwa, I. (2017). Combining green roofs and renewable energy – the photovoltaic rooftop garden. In *International Multidisciplinary Scientific GeoConference Surveying Geology and Mining Ecology Management, SGEM*, volume 17, pages 803–810.
- Scartezzini, J.-L., Montavon, M., and Compagnon, R. (2002). Computer evaluation of the solar energy potential in an urban environment. *EuroSun 2002*, pages 1–8.
- Scherba, A., Sailor, D. J., Rosenstiel, T. N., and Wamser, C. C. (2011). Modeling impacts of roof reflectivity, integrated photovoltaic panels and green roof systems on sensible heat flux into the urban environment. *Building and Environment*, 46(12):2542–2551.

- Schill, W.-P. (2014). Residual load, renewable surplus generation and storage requirements in Germany. *Energy Policy*, 73:65–79.
- Schindler, B. Y., Blank, L., Levy, S., Kadas, G., Pearlmutter, D., and Blaustein, L. (2016). Integration of photovoltaic panels and green roofs: review and predictions of effects on electricity production and plant communities. *Israel Journal of Ecology and Evolution*, 62(1-2):68–73.
- Schirmer, P. M. and Axhausen, K. W. (2015). A multiscale classification of urban morphology. *Journal of Transport and Land Use*, 9.
- Schirmer, P. M. and Axhausen, K. W. (2019). *A multiscale clustering of the urban morphology for use in quantitative models*. Springer International Publishing.
- Schnatbaum, L. (2009). Solar thermal power plants. *European Physical Journal: Special Topics*, 176(1):127–140.
- Schwarz, G. (2007). Estimating the Dimension of a Model. *The Annals of Statistics*, 6(2):461–464.
- Seyedabadi, M. R., Eicker, U., and Karimi, S. (2021). Plant selection for green roofs and their impact on carbon sequestration and the building carbon footprint. *Environmental Challenges*, 4:100119.
- Shafique, M., Luo, X., and Zuo, J. (2020). Photovoltaic-green roofs: A review of benefits, limitations, and trends. *Solar Energy*, 202:485–497.
- Sharma, V., Khanna, S., Nayak, J. K., and Kedare, S. B. (2016). Effects of shading and blocking in compact linear fresnel reflector field. *Energy*, 94:633–653.
- Sharma, V., Nayak, J. K., and Kedare, S. B. (2015). Effects of shading and blocking in linear Fresnel reflector field. *Solar Energy*, 113:114–138.
- Shi, Z., Fonseca, J. A., and Schlueter, A. (2021). A parametric method using vernacular urban block typologies for investigating interactions between solar energy use and urban design. *Renewable Energy*, 165(March):823–841.
- Shukla, A. K., Sudhakar, K., and Baredar, P. (2017). Recent advancement in BIPV product technologies: A review. *Energy and Buildings*, 140:188–195.
- Siddiqi, A. A. (1985). Evaluation of the Effect of Choice of Materials on the Surface Temperatures of Buildings in Urban Built Up Areas. pages 899–907.
- Silva, D. D., Marson, V., de Souza, R. R., de Oliveira, J. D., Silva, J. B. C., and Cardoso, E. M. (2022). A new predictive model for a photovoltaic module's surface temperature. *Energy Reports*, 8:15206–15220.
- Silvi, C. (2009). The pioneering work on Linear Fresnel Reflector Concentrators (LFCs) in Italy. *SolarPaces Conference*, pages 1–8.
- Silvi, C. (2011). Italian contribution to CSP with flat or almost flat reflectors. In *30th ISES Biennial Solar World Congress 2011, SWC 2011*, volume 2, pages 952–962.
- Singh, B. P., Goyal, S. K., and Kumar, P. (2021). Solar pv cell materials and technologies: Analyzing the recent developments. *Materials Today: Proceedings*, 43:2843–2849.
- Singh, P. L., Ganesan, S., and Yàdav, G. C. (1999). Performance study of a linear Fresnel concentrating solar device. *Renewable Energy*, 18(3):409–416.

- Siva Reddy, V., Kaushik, S. C., Ranjan, K. R., and Tyagi, S. K. (2013). State-of-the-art of solar thermal power plants - A review.
- Skoplaki, E., Boudouvis, A. G., and Palyvos, J. A. (2008). A simple correlation for the operating temperature of photovoltaic modules of arbitrary mounting. *Solar Energy Materials and Solar Cells*, 92(11):1393–1402.
- Skoplaki, E. and Palyvos, J. A. (2009). On the temperature dependence of photovoltaic module electrical performance: A review of efficiency/power correlations. *Solar Energy*, 83(5):614–624.
- Small, E. P. and Mazrooei, M. A. (2016). Evaluation of Construction-specific Provisions of Sustainable Design Codes and Standards in the United Arab Emirates. *Procedia Engineering*, 145:1021–1028.
- Smith, C. and Levermore, G. (2008). Designing urban spaces and buildings to improve sustainability and quality of life in a warmer world. *Energy Policy*, 36(12):4558–4562.
- Sofeska, E. (2016). Relevant Factors in Sustainable Urban Development of Urban Planning Methodology and Implementation of Concepts for Sustainable Planning (Planning Documentation for the Master Plan Skopje 2001–2020). *Procedia Environmental Sciences*, 34:140–151.
- Sola, A., Corchero, C., Salom, J., and Sanmarti, M. (2020). Multi-domain urban-scale energy modelling tools: A review. *Sustainable Cities and Society*, 54(February 2019):101872.
- SolarPACES (2019). SolarPACES.
- Solheim, H. J., Fjær, H. G., Sørheim, E. A., and Foss, S. E. (2013). Measurement and simulation of hot spots in solar cells. *Energy Procedia*, 38(1876):183–189.
- Soman, A. and Antony, A. (2019). Colored solar cells with spectrally selective photonic crystal reflectors for application in building integrated photovoltaics. *Solar Energy*, 181:1–8.
- Sørland, S. L., Fischer, A. M., Kotlarski, S., Künsch, H. R., Liniger, M. A., Rajczak, J., Schär, C., Spirig, C., Strassmann, K., and Knutti, R. (2020). CH2018 – National climate scenarios for Switzerland: How to construct consistent multi-model projections from ensembles of opportunity. *Climate Services*, 20:100196.
- Speroni, A., Mainini, A. G., Zani, A., Paolini, R., Pagnacco, T., and Poli, T. (2022). Experimental Assessment of the Reflection of Solar Radiation from Facades of Tall Buildings to the Pedestrian Level. *Sustainability*, 14(10).
- Stamatakis, A., Mandalaki, M., and Tsoutsos, T. (2016). Multi-criteria analysis for PV integrated in shading devices for Mediterranean region. *Energy and Buildings*, 117:128–137.
- Stendardo, N., Desthieux, G., Abdennadher, N., and Gallinelli, P. (2020). GPU-enabled shadow casting for solar potential estimation in large urban areas. Application to the solar cadaster of Greater Geneva. *Applied Sciences (Switzerland)*, 10(15).
- Stevanović, S. (2013). Optimization of passive solar design strategies: A review. *Renewable and Sustainable Energy Reviews*, 25:177–196.
- Stewart, I. D. and Oke, T. R. (2012). Local climate zones for urban temperature studies. *Bulletin of the American Meteorological Society*, 93(12):1879–1900.

- Street, M., Reinhart, C., Norford, L., and Ochsendorf, J. (2013). Urban heat island in boston - An evaluation of urban airtemperature models for predicting building energy use. In *Proceedings of BS 2013: 13th Conference of the International Building Performance Simulation Association*, pages 1022–1029.
- Strzalka, A., Alam, N., Duminil, E., Coors, V., and Eicker, U. (2012). Large scale integration of photovoltaics in cities. *Applied Energy*, 93:413–421.
- suisse, C. (2022). Agrometeo.
- Sultana, T., Morrison, G. L., and Rosengarten, G. (2012). Thermal performance of a novel rooftop solar micro-concentrating collector. *Solar Energy*, 86(7):1992–2000.
- Sun, Y. and Augenbroe, G. (2014). Urban heat island effect on energy application studies of office buildings. *Energy and Buildings*, 77:171–179.
- Sun, Y., Liu, D., Flor, J.-F., Shank, K., Baig, H., Wilson, R., Liu, H., Sundaram, S., Mallick, T. K., and Wu, Y. (2019). Analysis of the daylight performance of window integrated photovoltaics systems. *Renewable Energy*, 145:153–163.
- SUNCNIM (2017). Mastering Solar Energy and Energy Storage.
- Swens, J. and Diestelmeier, L. (2022). Developing a legal framework for energy communities beyond energy law. *Energy Communities*, pages 59–71.
- Swinbank, W. C. (1963). Long-wave radiation from clear skies. *Quarterly Journal of the Royal Meteorological Society*, 89:339–348.
- T. Nguyen, H. and M. Pearce, J. (2013). Automated quantification of solar photovoltaic potential in cities. *International Review for Spatial Planning and Sustainable Development*, 1(1):49–60.
- Tablada, A., Kosorić, V., Huang, H., Chaplin, I. K., Lau, S.-K., Yuan, C., and Lau, S. S. (2018). Design Optimization of Productive Façades: Integrating Photovoltaic and Farming Systems at the Tropical Technologies Laboratory.
- Taha, H. (2013). The potential for air-temperature impact from large-scale deployment of solar photovoltaic arrays in urban areas. *Solar Energy*, 91:358–367.
- Talen, E., Allen, E., Bosse, A., Ahmann, J., Koschinsky, J., Wentz, E., and Anselin, L. (2013). LEED-ND as an urban metric. *Landscape and Urban Planning*, 119:20–34.
- Tardioli, G., Kerrigan, R., Oates, M., O'Donnell, J., and Finn, D. P. (2018). Identification of representative buildings and building groups in urban datasets using a novel pre-processing, classification, clustering and predictive modelling approach. *Building and Environment*, 140(May):90–106.
- Tardioli, G., Narayan, A., Kerrigan, R., Oates, M., O'Donnell, J., and Finn, D. P. (2020). A methodology for calibration of building energy models at district scale using clustering and surrogate techniques. *Energy and Buildings*, 226:110309.
- Tasmin, N., Farjana, S. H., Hossain, M. R., Golder, S., and Mahmud, M. A. (2022). Integration of Solar Process Heat in Industries: A Review. *Clean Technologies*, 4(1):97–131.
- Taveres-Cachat, E., Lobaccaro, G., Goia, F., and Chaudhary, G. (2019). A methodology to improve the performance of PV integrated shading devices using multi-objective optimization. *Applied Energy*, 247:731–744.
- Tebibel, H. and Labeled, S. (2013). Performance results and analysis of self-regulated PV system in algerian sahara. *Renewable Energy*, 60:691–700.

- Thebault, M., Clivillé, V., Berrah, L.-a., Gaillard, L., and Desthieux, G. (2020). Multi-criteria decision aiding for the integration of photovoltaic systems in the urban environment : the case of the Greater Geneva. (January 2021):9–30.
- Thebault, M., Desthieux, G., Castello, R., and Berrah, L. (2022). Large-scale evaluation of the suitability of buildings for photovoltaic integration: Case study in Greater Geneva. *Applied Energy*, 316:119127.
- Thevenard, D. and Haddad, K. (2006). Ground reflectivity in the context of building energy simulation. *Energy and Buildings*, 38(8):972–980.
- Thornton, P. K., Ericksen, P. J., Herrero, M., and Challinor, A. J. (2014). Climate variability and vulnerability to climate change: A review. *Global Change Biology*, 20(11):3313–3328.
- Tong, S., Prior, J., McGregor, G., Shi, X., and Kinney, P. (2021). Urban heat: An increasing threat to global health. *The BMJ*, 375:1–5.
- Trinuruk, P., Sorapipatana, C., and Chenvidhya, D. (2009). Estimating operating cell temperature of BIPV modules in Thailand. *Renewable Energy*, 34(11):2515–2523.
- Tsekouras, P., Tzivanidis, C., and Antonopoulos, K. (2018). Optical and thermal investigation of a linear Fresnel collector with trapezoidal cavity receiver. *Applied Thermal Engineering*, 135:379–388.
- UN-Habitat (2022). *Envisaging the Future of Cities*.
- Unal Cilek, M. and Cilek, A. (2021). Analyses of land surface temperature (LST) variability among local climate zones (LCZs) comparing Landsat-8 and ENVI-met model data. *Sustainable Cities and Society*, 69(March):102877.
- United Nations (2015). Transforming our world: the 2030 Agenda for Sustainable Development.
- United Nations (2018). *World Urbanization Prospects*, volume 12.
- United Nations (2022). *World cities report 2022: Envisaging the future of cities*.
- United Nations, D. and of Economic and Social Affairs, P. D. (2018). The World's Cities in 2018. *World Urbanization Prospects: The 2018 Revision*, page 34.
- University of Geneva (2022). Archives numériques.
- Vahmani, P. and Ban-Weiss, G. A. (2016). Impact of remotely sensed albedo and vegetation fraction on simulation of urban climate in WRF-urban canopy model: A case study of the urban heat island in Los Angeles. *Journal of Geophysical Research*, 121(4):1511–1531.
- Vaneckova, P., Beggs, P. J., de Dear, R. J., and McCracken, K. W. (2008). Effect of temperature on mortality during the six warmer months in Sydney, Australia, between 1993 and 2004. *Environmental Research*, 108(3):361–369.
- Varentsov, M. I., Samsonov, T. E., Kargashin, P. E., Korosteleva, P. A., Varentsov, A. I., Perkhurova, A. A., and Konstantinov, P. I. (2020). Citizen weather stations data for monitoring applications and urban climate research: An example of Moscow megacity. *IOP Conference Series: Earth and Environmental Science*, 611(1):0–11.
- Vartholomaios, A. (2021). Classification of the influence of urban canyon geometry and reflectance on seasonal solar irradiation in three European cities. *Sustainable Cities and Society*, 75:103379.

- Velázquez, N., García-Valladares, O., Saucedo, D., and Beltrán, R. (2010). Numerical simulation of a Linear Fresnel Reflector Concentrator used as direct generator in a Solar-GAX cycle. *Energy Conversion and Management*, 51(3):434–445.
- Venter, Z. S., Brousse, O., Esau, I., and Meier, F. (2020). Hyperlocal mapping of urban air temperature using remote sensing and crowdsourced weather data. *Remote Sensing of Environment*, 242(January):111791.
- Vuckovic, M., Kiesel, K., and Mahdavi, A. (2017). Studies in the assessment of vegetation impact in the urban context. *Energy and Buildings*, 145:331–341.
- Waibel, C., Mavromatidis, G., Bollinger, A., Evins, R., and Carmeliet, J. (2018). Sensitivity analysis on optimal placement of façade based photovoltaics. In *ECOS 2018 - Proceedings of the 31st International Conference on Efficiency, Cost, Optimization, Simulation and Environmental Impact of Energy Systems*.
- Walch, A., Mohajeri, N., and Scartezzini, J. L. (2019). A critical comparison of methods to estimate solar rooftop photovoltaic potential in Switzerland. *Journal of Physics: Conference Series*, 1343(1):0–6.
- Wang, D., Zhou, T., and Wang, M. (2021a). Information and communication technology (ICT), digital divide and urbanization: Evidence from Chinese cities. *Technology in Society*, 64(December 2020):101516.
- Wang, J. and Biljecki, F. (2022). Unsupervised machine learning in urban studies: A systematic review of applications. *Cities*, 129(December 2021):103925.
- Wang, Y., Berardi, U., and Akbari, H. (2016). Comparing the effects of urban heat island mitigation strategies for Toronto, Canada. *Energy and Buildings*, 114:2–19.
- Wang, Y., Guo, Z., and Han, J. (2021b). The relationship between urban heat island and air pollutants and them with influencing factors in the Yangtze River Delta, China. *Ecological Indicators*, 129:107976.
- WANG, Y. and LI, B. (2020). An optimized solar-air degree-day method to evaluate energy demand for poultry buildings in different climate zones. *Frontiers of Agricultural Science and Engineering*, 7(4):478–489.
- Wang, Y., Tian, W., Zhu, L., Ren, J., Liu, Y., Zhang, J., and Yuan, B. (2005). Interactions between Building Integrated Photovoltaics and microclimate in urban environments. In *International Solar Energy Conference*, pages 499–504.
- Wang, Y., Tian, W., Zhu, L., Ren, J., Liu, Y., Zhang, J., and Yuan, B. (2006). Interactions between building integrated photovoltaics and microclimate in urban environments. *Journal of Solar Energy Engineering, Transactions of the ASME*, 128(2):168–172.
- Wendelin, T. (2003). Soltrace: A new optical modeling tool for concentrating solar optics. In *International Solar Energy Conference*, pages 253–260.
- Wiginton, L. K., Nguyen, H. T., and Pearce, J. M. (2010). " Quantifying Solar Photovoltaic Potential on a Large Scale for Renewable Energy Regional Policy " Quantifying Rooftop Solar Photovoltaic Potential for Regional Renewable Energy Policy. *Computers, Environment and Urban Systems*, 34:345–357.
- Wijeratne, W. M. U., Yang, R. J., Too, E., and Wakefield, R. (2019). Design and development of distributed solar PV systems: Do the current tools work?

- Wijesooriya, N., Brambilla, A., and Markauskaite, L. (2023). Biophilic design frameworks: A review of structure, development techniques and their compatibility with LEED sustainable design criteria. *Cleaner Production Letters*, 4:100033.
- Wilcox, S. and Gueymard, C. A. (2010). Spatial and temporal variability of the solar resource in the united states. *39th ASES National Solar Conference 2010, SOLAR 2010*, 2:1389–1409.
- Xiang, C., Matusiak, B. S., Røyset, A., and Kolås, T. (2021). Pixelization approach for façade integrated coloured photovoltaics-with architectural proposals in city context of Trondheim, Norway. *Solar Energy*, 224:1222–1246.
- Xu, G., Li, J., Shi, Y., Feng, X., and Zhang, Y. (2022). Improvements, extensions, and validation of the Urban Weather Generator (UWG) for performance-oriented neighborhood planning. *Urban Climate*, 45(March):101247.
- Xu, S., Li, Z., Zhang, C., Huang, Z., Tian, J., Luo, Y., and Du, H. (2021). A method of calculating urban-scale solar potential by evaluating and quantifying the relationship between urban block typology and occlusion coefficient: A case study of Wuhan in Central China. *Sustainable Cities and Society*, 64(September 2019).
- Xue, Y., Lindkvist, C. M., and Temeljotov-Salaj, A. (2021). Barriers and potential solutions to the diffusion of solar photovoltaics from the public-private-people partnership perspective – Case study of Norway. *Renewable and Sustainable Energy Reviews*, 137:110636.
- Yan, H., Wang, K., Lin, T., Zhang, G., Sun, C., Hu, X., and Ye, H. (2021). The challenge of the urban compact form: Three-dimensional index construction and urban land surface temperature impacts. *Remote Sensing*, 13(6):1–23.
- Yang, B., Sun, Y., and Lin, Y. (2011). Decision-making on PV modules for very large scale photovoltaic systems using improved analytic hierarchy process. *Asia-Pacific Power and Energy Engineering Conference, APPEEC*, pages 1–5.
- Yu, W., Li, B., Jia, H., Zhang, M., and Wang, D. (2015). Application of multi-objective genetic algorithm to optimize energy efficiency and thermal comfort in building design. *Energy and Buildings*, 88:135–143.
- Yun, G. Y., Ngarambe, J., Duhirwe, P. N., Ulpiani, G., Paolini, R., Haddad, S., Vasilakopoulou, K., and Santamouris, M. (2020). Predicting the magnitude and the characteristics of the urban heat island in coastal cities in the proximity of desert landforms. The case of Sydney. *Science of the Total Environment*, 709:136068.
- Zahler, C. and Iglauer, O. (2012). Solar process heat for sustainable automobile manufacturing. *Energy Procedia*, 30:775–782.
- Zaręba, A., Krzemińska, A., Kozik, R., Adynkiewicz-Piragas, M., and Kristiánová, K. (2022). Passive and Active Solar Systems in Eco-Architecture and Eco-Urban Planning. *Applied Sciences*, 12(6):3095.
- Zhang, X., Lau, S.-K., Lau, S. S. Y., and Zhao, Y. (2018). Photovoltaic integrated shading devices (PVSDs): A review. *Solar Energy*, 170:947–968.
- Zheng, J., Yan, J., Pei, J., and Liu, G. (2014). Solar tracking error analysis of fresnel reflector. *Scientific World Journal*, 2014.
- Zhou, Y., An, N., and Yao, J. (2022). Characteristics, Progress and Trends of Urban Microclimate Research: A Systematic Literature Review and Bibliometric Analysis. *Buildings*, 12(7).

- Zhou, Y., Eom, J., and Clarke, L. (2013). The effect of global climate change, population distribution, and climate mitigation on building energy use in the U.S. and China. *Climatic Change*, 119(3-4):979–992.
- Zhu, G. (2013). Development of an analytical optical method for linear fresnel collectors. *Solar Energy*, 94:240–252.
- Zhu, G. (2017). New adaptive method to optimize the secondary reflector of linear Fresnel collectors. *Solar Energy*, 144:117–126.
- Zhu, G., Wendelin, T., Wagner, M. J., and Kutscher, C. (2014). History, current state, and future of linear Fresnel concentrating solar collectors. *Solar Energy*, 103:639–652.
- Zhu, J. and Huang, H. (2014). Design and thermal performances of Semi-Parabolic Linear Fresnel Reflector solar concentration collector. *Energy Conversion and Management*, 77:733–737.
- İsmet Berke, Ç. (2010). *Global Sensitivity Analysis for Urban Heat Island Effect: A Case Study in a Residential Neighbourhood in Ankara, Turkey*. PhD thesis.

Appendix A

In this Appendix the general simulation settings used for the Urban Weather Generator (UWG) simulations included in **Paper 2** are fully detailed in Table [A.1](#).

Table A.1 Meteorological and site parameters

Parameter	Dimension	Value
Location	[-]	Geneva (Switzerland)
Latitude	[°]	46.20
Longitude	[°]	6.14
Daytime boundary layer height ¹	[m]	1000
Nighttime boundary layer height ¹	[m]	50
Inversion height ¹	[m]	150
Temperature measurement at reference site ¹	[m]	2
Air velocity measurements height ¹	[m]	10
Circulation velocity coefficient ¹	[-]	1.2
Exchange velocity coefficient ¹	[-]	1.0
Heat flux threshold for daytime conditions ²	[W/m ²]	150
Heat flux threshold for nighttime conditions ²	[W/m ²]	20
Latent fraction of trees ²	[-]	0.6
Latent fraction of grass ²	[-]	0.4
Albedo of vegetation	[-]	0.25
Begin month for vegetation participation	[-]	April
End month for vegetation participation	[-]	October
Urban parameters		
City diameter ³	[m]	7500
Fraction of HVAC waste heat released to urban canyon	[-]	1
Road pavement conductivity	[W/mK]	0.75
Road pavement volumetric heat capacity	[J/m ³ K]	1600000
Road pavement albedo	[-]	0.05
Roof albedo	[-]	0.2
Wall albedo	[-]	0.2
Glazing ratio of buildings	[-]	0.25
Solar Heat Gain Coefficient from windows	[-]	0.5
Building HVAC system and internal loads		
Occupancy ⁴	[m ² /pers]	30
Sensible heat per occupant ^{1,2}	[W]	100
Latent heat fraction from occupant ^{1,2}	[-]	0.3
Radiant heat fraction from occupant ^{1,2}	[-]	0.2
Lighting intensity ⁴	[W/m ²]	3.5
Radiant heat fraction from light ^{1,2}	[-]	0.7
Electric equipment intensity ⁴	[W/m ²]	15
Radiant heat fraction from equipment ^{1,2}	[-]	0.5
Heating set point ⁴	[°C]	20

¹ (Bueno et al., 2012)² (Bueno et al., 2014)³ Measured with GIS tools⁴ (Tardioli et al., 2020)

Appendix B

This Appendix includes the complete list as well as the description and the equations of the morphological parameters used for the study reported in **Paper 4**.

Table B.1 Building Parameters and Descriptions

Name	Description	Symbol	Equation	Unit
Building height	Building height	H	-	[m]
Building area	Building footprint area	A	-	[m ²]
Building floor area	Total floor area of the building	fA	$fA = A \cdot n_{\text{floors}}$	[m ²]
Building volume	Building volume	V	$V = A \cdot H$	[m ³]
Building perimeter	Sum of lengths of the building exterior walls	P	-	[m]
Building longest axis length	Diameter of the minimal circumscribed circle	LaL	-	[m]
Building volume to façade ratio	Ratio between building volume and total area of façades	VFR	$VFR = \frac{V}{P \cdot H}$	$\left[\frac{m^3}{m^2}\right]$
Building fractal dimension	Statistical index of the complexity of a geometry	FrD	$FrD = \frac{2 \log(P/2)}{\log(A)}$	-

Table B.1 Building Parameters and Descriptions (continued)

Name	Description	Symbol	Equation	Unit
Building form factor	Quantity representing the 3D shape characteristics	FoF	$FoF = \frac{A}{(V)^{2/3}}$	-
Tessellation area	Area of the tessellation cell	A_{tess}	-	$[m^2]$
Tessellation longest axis length	Diameter of the minimal circumscribed circle	LaL_{tess}	-	$[m]$
Building circular compactness	Index of the similarity of a shape with a circle	Cco	$Cco = \frac{A}{A_c}$	-
Building square compactness	Measure of the compactness of the building footprint	Sqco	$Sqco = \left(\frac{4\sqrt{A}}{P}\right)^2$	-
Building squareness	Mean deviation μ of each corner from 90 degrees	Squ	$Squ = \frac{1}{N_{cor}} \sum_{i=1}^{N_{cor}} \mu_i$	-
Building Rectangularity	Index of the similarity of a shape with a rectangle	Rec	$Rec = \frac{A}{A_{MBR}}$	-
Building shape index	Shape index of the building footprint	ShIdx	$ShIdx = \frac{\sqrt{\frac{A}{\pi}}}{0.5 \cdot LaL}$	-
Building equivalent rectangular index	Measure of shape complexity based on the area	ERI	$ERI = \sqrt{\frac{A}{A_{MBR}}} \cdot \frac{P_{MBR}}{P}$	-
Building elongation	Measure of the deviation of the building shape from a square	Elo	$Elo = \frac{L_{MBR}}{l_{MBR}}$	-

Table B.1 Building Parameters and Descriptions (continued)

Name	Description	Symbol	Equation	Unit
Coverage area ratio	Ratio between the building footprint area and tessellation cell area	CAR	$CAR = \frac{A}{A_{\text{tess}}}$	-
Floor area ratio	Ratio between building total floor area and tessellation cell area	FAR	$FAR = \frac{fA}{A_{\text{tess}}}$	-
Rugosity	Ratio between building volume and tessellation cell area	Rug	$Rug = \frac{V}{A_{\text{tess}}}$	$\left[\frac{m^3}{m^2}\right]$
Shared walls ratio of adjacent buildings	Ratio between the length of shared perimeter and building perimeter	SWR	$SWR = \frac{P_{\text{shared}}}{P}$	-
Number of neighbors	Number of neighboring buildings	N_{neigh}	-	-
Alignment	Mean deviation of solar orientation of neighboring buildings	Ali	$Ali = \frac{1}{N_{\text{neigh}}} \sum_{j \in \text{neigh}} \text{dev}_{\text{sol}}(j)$	-
Building adjacency	Ratio between joined adjacent structures and neighboring buildings	Adj	$Adj = \frac{N_{\text{neigh,join}}}{N_{\text{neigh}}}$	-
Mean inter-building distance	Mean distance between the building and adjacent buildings	\bar{d}	$\bar{d} = \frac{1}{N_{\text{neigh}}} \sum_{j \in \text{neigh}} d(j)$	$[m]$
Mean coverage area ratio	Mean coverage area ratio of neighboring tessellation cells	\overline{CAR}	$\overline{CAR} = \frac{1}{N_{\text{neigh}}} \sum_{j \in \text{neigh}} CAR(j)$	-
Mean floor area ratio	Mean floor area ratio of neighboring tessellation cells	\overline{FAR}	$\overline{FAR} = \frac{1}{N_{\text{neigh}}} \sum_{j \in \text{neigh}} FAR(j)$	-

Table B.1 Building Parameters and Descriptions (continued)

Name	Description	Symbol	Equation	Unit
Covered area	Total area covered by the building and its neighbors	CovA	$CovA = A + \sum_{j \in \text{neigh}} A(j)$	$[m^2]$
Average building area	Mean footprint area of neighboring constructions	\bar{A}	$\bar{A} = \frac{1}{N_{\text{neigh}}} \sum_{j \in \text{neigh}} A(j)$	$[m^2]$
Average building height	Mean height of neighboring constructions	\bar{H}	$\bar{H} = \frac{1}{N_{\text{neigh}}} \sum_{j \in \text{neigh}} H(j)$	$[m]$
Average building volume	Mean volume of neighboring constructions	\bar{V}	$\bar{V} = \frac{1}{N_{\text{neigh}}} \sum_{j \in \text{neigh}} V(j)$	$[m^3]$
Average building total floor area	Mean total floor area of neighboring constructions	\overline{fA}	$\overline{fA} = \frac{1}{N_{\text{neigh}}} \sum_{j \in \text{neigh}} fA(j)$	$[m^2]$
Average tessellation area	Mean tessellation area of neighboring cells	$\overline{A_{\text{tess}}}$	$\overline{A_{\text{tess}}} = \frac{1}{N_{\text{neigh}}} \sum_{j \in \text{neigh}} A_{\text{tess}}(j)$	$[m^2]$

